

University of Nottingham
UK | CHINA | MALAYSIA

Advanced X-ray Photoelectron Spectroscopy of N-based Ionic Liquids

Ana R. Santos, MEng (Hons)

Thesis submitted to the University of Nottingham for the degree of Doctor of Philosophy

August 2017

Declaration

This work has not previously been accepted in substance for any degree and is not being concurrently submitted in candidature for any degree.

Signed _____
(Candidate)

Date _____

Statement 1

This Thesis is the result of my own investigations, except where otherwise stated. Other sources are acknowledged by footnotes giving explicit references. Bibliographies are appended.

Signed _____
(Candidate)

Date _____

Signed _____
(Supervisor)

Date _____

Statement 2

I hereby give consent for my Thesis, if accepted, to be available for photocopying and for inter-library loan, and for the title and summary to be made available to outside organisations.

Signed _____
(Candidate)

Date _____

Acknowledgements

I would like to thank my supervisor, Prof. Peter Licence for his excellent guidance and support throughout this Ph.D. project. His constant enthusiasm and encouragement has been invaluable, and I can honestly say it has been great fun being a part of the Licence group for the past 4 years! We moved to the new GSK Carbon Neutral Laboratories in my final year of studies, and I had the enormous pleasure to follow Pete in this huge endeavour of which I am immensely proud of!

I would also like to thank Dr. Emily Smith for XPS training and continuous patience throughout my time in Nottingham. I extend my gratitude to Clive Dixon and Martin Dellar; the Nottingham Nanoscale and Microscale Research Centre (NMRC); and the University of Nottingham for funding.

I would like to thank the recent members of the Licence group for providing a great work environment, always being a source of knowledge and support: Coby, Dan, Zoë, Ejike, Ste, Mags, Astrid, Calum, Laís and Patrick. I would also like to extend my thanks to Sheridan, John, and Ryan for being great Masters students and specially Ryan for his contribution to this work. A special thank you goes to Luiz, for the all the precious thought-provoking discussions and travel expeditions we shared during his time in Nottingham. Finally, Becca, this work would have been impossible to achieve alone – I thank you the most for continuous support, ideas, critical advice, and constructive criticism of any drafts I have sent you! You never gave up on me, thank you so much!

Lastly, I extend my gratitude to my better half Frankie, for putting up with me and being by my side through my best and my worst; my best friend Kiki who I missed terribly – you are my soulmate always and forever; and my family, in particular my parents, Cristina and João, for their continuous love and support despite the distance, *saudade* and all the important moments I have missed. You have always been and always will be in my heart - I will always be grateful to you.

Abstract

X-ray photoelectron spectroscopy (XPS) has been used to probe the influence of cation structure on fundamental interactions within Ionic Liquid (IL) systems. A series of guanidinium-based ILs have been investigated and cation-anion interactions have been studied to determine the effect of a highly charge delocalised cationic core on the electronic environment of the anion. These and sulfur-based cations were developed, and ^{13}C-NMR comparisons addressed, along with the influence of sulfur functionalisation upon the electronic environments of the cationic component. These materials were then used to probe the composition and structural orientation of ions of the IL surface with resource to angle-resolved XPS (ARXPS) and particularly, energy-resolved XPS (ERXPS). Appropriate methodologies for both techniques were developed and fully verified, and the position of the anion ($[NTf_2]^-$) relative to cation (imidazolium, guanidinium and thioimidazolium) was found to support previous findings in the literature using other spectroscopic techniques. Additionally, ERXPS allowed for relative depth profiles not only of the anionic component, but also of the sulfur in the cationic component for the thioimidazolium bis(trifluoromethanesulfonyl)imide IL series.

Abbreviations & Acronyms

$[X]^-$	Anion
ARXPS	Angle-resolved X-ray photoelectron spectroscopy
a.u.	Arbitrary units
BE	Binding energy
BNC	Bayonet Neill-Concelman
Br^-	Bromide anion
$C_{aliphatic}$	Aliphatic carbon component
C_{core}	Core carbon component
$CDCl_3$	Deuterated chloroform
CHA	Concentric hemispheric analyser
$C_{hetero\ (methyl/S)}$	Heteroatom carbon component
C_{inter}	Intermediate carbon component
Cl^-	Chloride anion
CF_3	Trifluoromethane group
C_n	Carbon component(s) of n
$[C_1ImC_pSC_m]^+$	1-Alkyl-3-(2-alkyllthio)methylimidazolium cation
$[C_n(C_1Im)_2]^{2+}$	1,n-Bis(3-methylimidazolium-1-yl)alkane dication
$[(C_1Im)C_nPyr]^{2+}$	1,n-(3-Methylimidazolium-1-yl)(pyridinium-N-yl)alkane dication
CPS	Counts per second
DASSA	Dual analyser system for surface analysis
DLD	Delay line detector
DMSO-d_6	Deuterated dimethyl sulfoxide
ESCA	Electron spectroscopy for chemical analysis
ESI-MS	Electrospray ionisation mass spectrometry
e_A^-	Auger electron
e_p^-	Photoelectron
EDG	Electron donating group
ERXPS	Energy-resolved X-ray photoelectron spectroscopy

eV	Electron volts
EWG	Electron withdrawing group
FAT	Fixed analyser transmission
$[FSI]^-$	Bis(fluorosulfonyl)imide anion
FWHM	Full width at half maximum
h	Planck's constant (6.626×10^{-34} $m^2 \cdot kg \cdot s^{-1}$)
$[HSO_4]^-$	Hydrogen sulfate anion
HREELS	High-resolution electron energy loss spectroscopy
HOMO	Highest occupied molecular orbital
I^-	Iodide anion
IC	Ion chromatography
ID	Information depth
IL	Ionic liquid
IR	Infrared spectroscopy
J	Coupling constant
KE	Kinetic energy
LEIS	Low-energy ion scattering
LUMO	Lowest unoccupied molecular orbital
MD	Molecular dynamics
MIES	Metastable impact electron spectroscopy
mA	Milliampere
mbar	Millibar
$[MeSO_4]^-$	Methyl sulfate anion
n	Number of carbon atoms in an aliphatic chain
N_{anion}	Anionic nitrogen component
N_{cation}	Cationic nitrogen component
NBO	Natural bond order
NICISS	Neutral impact collision ion scattering spectroscopy
NPA	Natural population analysis
nm	Nanometer
NMR	Nuclear magnetic resonance

ppm	Parts per million
RBS	Rutherford backscattering
RSF	Relative sensitivity factor
S_{anion}	Anionic sulfur component
S_{cation}	Cationic sulfur component
SFG	Sum-frequency generation
$[SCN]^-$	Thiocyanate anion
SILP	Supported ionic liquid phase
UHV	Ultra-high vacuum ($\leq 1 \times 10^{-8}$ mbar)
UPS	Ultraviolet photoelectron spectroscopy
V	Volts
VOC	Volatile organic compound
XAS	X-ray absorption spectroscopy
XPS	X-ray photoelectron spectroscopy
δ	Chemical shift
ε_0	Vacuum permittivity
θ	Emission angle
λ_{AL}	Attenuation length
λ_{IMFP}	Inelastic mean free path
µm	Micrometre
ν	Frequency
Φ	Work function

Table of Structural Abbreviations

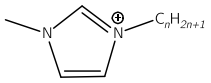
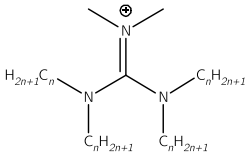
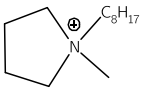
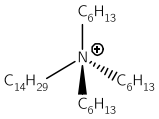
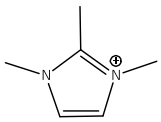
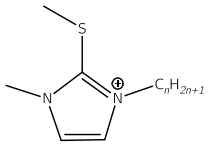
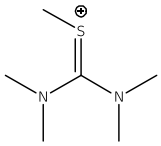
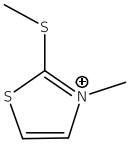
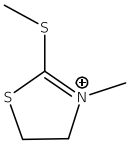
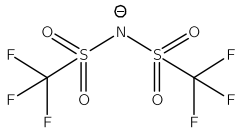
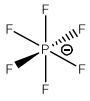
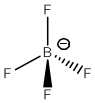
Structure	Name	Abbreviation
	1-Alkyl-3-methylimidazolium	$[C_nC_1Im]^+$
	Tetra-alkyl-dimethylguanidinium	$[(C_nC_m)_2dmg]^+$
	1-Octyl-1-methylpyrrolidinium	$[C_8C_1Pyrr]^+$
	Trihexyl(tetradecyl)ammonium	$[N_{6,6,6,14}]^+$
	1,2,3-Trimethylimidazolium	$[C_1C_1C_1Im]^+$
	1-Methyl-3-alkyl-2-methylthioimidazolium	$[C_n(C_1)_2ThioIm]^+$
	Pentamethylthiuronium	$[(C_1)_5TU]^+$
	3-Methyl-2-(methylthio)thiazolium	$[(C_1)_2Thio]^+$
	3-Methyl-2-methylsulfanyl-4,5-dihydro-1,3-thiazolium	$[(C_1)_2Thiz]^+$
	Bis(trifluoromethanesulfonyl)imide	$[NTf_2]^-$
	Hexafluorophosphate	$[PF_6]^-$
	Tetrafluoroborate	$[BF_4]^-$

Table of Contents

ACKNOWLEDGEMENTS ..... **II**

ABSTRACT ..... **III**

ABBREVIATIONS & ACRONYMS ..... **IV**

TABLE OF CONTENTS ..... **VIII**

1. INTRODUCTION **1**

1.1. Overview 1

1.1.1. Background 2

1.2. Ionic Liquid Properties 3

1.3. Functional Ionic Liquids 5

1.4. Probing Surface Interface using UHV Techniques 7

1.4.1. Impurity Detection 8

1.4.2. Composition 9

1.4.2.1. ARXPS 9

1.4.2.2. ERXPS 10

1.5. Aims and Objectives 11

2. X-RAY PHOTOELECTRON SPECTROSCOPY (XPS) **13**

2.1. X-ray Photoelectron Spectroscopy of Ionic Liquids 13

2.1.1. Principles of XPS 14

2.1.2. XPS Experiment 15

2.1.3. XP Spectra 17

2.1.3.1. Survey Scan 17

2.1.3.2. High-Resolution Scan 19

2.1.4. Information from XP Spectra 20

2.1.4.1. Semi-Quantitative Analysis 20

2.1.4.2. Chemical State Analysis 20

2.1.5. Charge Neutralisation and Charge Correction 21

2.1.6. Surface Cleaning with Argon Sputtering 23

2.2. XPS Instrumentation 24

2.3. Sample Preparation 25

2.4. XPS Analysis 26

2.5. Information Depth for ARXPS and ERXPS 27

3. FIRST XPS OF GUANIDINIUM IONIC LIQUIDS 29
3.1. Introduction 29
3.2. XPS of Guanidinium Ionic Liquids 31
3.2.1. Purity and Quantification 31
3.2.2. Development of C 1s Fitting Model 38
3.2.3. Effect of Alkyl Chain Length on Cationic Core 40
3.2.4. Effect of the Anion 43
3.3. Comparison of Guanidinium and Other Nitrogenous Ionic Liquids 43
3.4. Ionic Liquid Mixtures 46
3.4.1. Effect of the Anion 47
3.4.2. Effect of the Cation 53
3.5. Conclusions 57

4. PROBING THE STRUCTURE OF GUANIDINIUM IONIC LIQUIDS – THE USE OF SULFUR-BASED ANALOGUES 59
4.1. Introduction 59
4.2. XPS of Guanidinium and Sulfur-based Ionic Liquids 60
4.2.1. Purity and Quantification 60
4.2.2. Development of C 1s Fitting Models 61
4.2.3. Effect of Sulfur Functionalisation 66
4.3. Comparisons to ^{13}C-NMR 73
4.4. Conclusions 76

5. DEPTH PROFILING OF IONIC LIQUIDS – AN ARXPS AND ERXPS STUDY 79
5.1. Introduction 79
5.2. Surface Sensitivity and Information Depth 83
5.3. Angle-Resolved XPS 84
5.3.1. Principles 84
5.3.2. Sample Preparation 85
5.3.3. Data Analysis and Processing 88
5.4. ARXPS Analysis of Ionic Liquids 91
5.4.1. Experimental Methodology 91
5.4.2. ARXPS of Imidazolium Ionic Liquids 93
5.4.3. Comparison with Other Nitrogenous Cation Families 100
5.5. High-Energy XPS 103
5.5.1. Ag L_α' X-ray Source 103
5.5.2. Energy Range 104
5.5.3. Intensity and Broadening of Photoelectron Peaks 106
5.5.4. Binding Energy Analysis 111
5.6. Energy-Resolved XPS 115
5.6.1. Principles 115

5.6.2. Data Analysis and Processing 117
5.7. ERXPS Analysis of Ionic Liquids 120
5.7.1. Experimental Methodology 120
5.7.2. ERXPS of Imidazolium Ionic Liquids 133
5.8. Conclusions 137

6. CONCLUSIONS AND FUTURE WORK 139
6.1. Summary 139
6.2. Outlook and Future Work 140

7. SYNTHESIS OF IONIC LIQUIDS 147
7.1. Materials 147
7.2. Instrumentation 147
7.3. Guanidinium-based Ionic Liquids 153
7.4. Pyrrolidinium-based Ionic Liquids 169
7.5. Imidazolium- and Sulfur-based Ionic Liquids 173
7.6. Dicationic-based Ionic Liquids 217

REFERENCES 241

APPENDICES 255
Appendix A: XP Spectra for Chapter 3 255
Appendix B: XP Spectra for Chapter 4 281
Appendix C: XP Spectra for Chapter 5 295

1. Introduction

1.1. Overview

The Ionic Liquid (IL) literature has grown at an extraordinary rate since the late 1990's. This alone does not indicate in which direction the field is moving, or indeed, whether ionic liquids are fulfilling their potential as "designer solvents". This effect is making it increasingly difficult to assess the important research underlying and fundamental understanding of ionic liquids.[1]

Understanding how ionic liquids interact with materials at a molecular level is of particular importance. Progress is hampered by a lack of fundamental knowledge of the physical chemistry at the intermolecular interface. Empirical choice of liquid media for processes and devices – through trial and error – faces difficulties because of the huge variety of molecular and ionic solvents available. The selection and design of the best solvents and electrolytes would be far more efficient if structure/property correlations guided it.[2] The appropriate choice of resources, ionic liquids, molecular simulations, and experimental physical chemistry has the potential to help answer vital questions towards the optimisation of current and novel applications.

Studies on ionic interactions drive the development of many demanding applications in biology, chemistry, and material science. Complex ionic systems are challenging for structural and mechanistic studies in solution, and none of the currently available analytic methods can offer a complete characterisation. The dynamic behaviour and flexible nature of ion-solvent assemblies induce another dimension of structural variation. Thus, comprehensive data analysis is imperative, along with a stronger link with other experimental and theoretical fields, to fully overcome the almost seemingly arbitrary choice upon liquid media for a given purpose.

1.1.1. Background

One of the most important components of "chemistry" is the study of materials and reactions in solution.[3, 4] Generally, a solvent is needed to form a homogeneous solution in which solutes are dissolved. However, several drawbacks are associated with the use of solvents, namely environmental, health, or safety issues, which are currently subject to strict regulation.[5] It is simply not viable to replace all solvents in a short period of time with one, more environmentally benign, alternative. Consequently, most processes will still need to be conducted in either traditional or novel solvents. The current question chemists ask themselves is not if a solvent is needed, but rather what solvent is right for a specific reaction.[5] The introduction of cleaner technologies towards a sustainable future, has become a major concern throughout academia, industry, and now governments - recognised by the 2016 United Nations Convention on Climate Change – better known as the Paris Agreement. Thus, the search for alternatives to the most harmful solvents has become not only a priority, but a necessity.

Advances in theoretical, computational, and experimental techniques have provided unprecedented information upon the physical structure of liquids,[6-10] suggesting that liquids possess reasonably well-defined structure in the bulk phase and at interfaces, and that this structure underpins solvent behaviour.[5] Ionic liquids (ILs) are solvents that can participate in a variety of attractive interactions ranging from the weak, nonspecific, and isotropic forces (*e.g.*, van der Waals,[11] solvophobic,[12] dispersion[13] forces) to strong (Coulombic), specific, and anisotropic forces (*e.g.*, hydrogen bonding,[14] halogen bonding,[15] dipole–dipole, magnetic dipole, electron pair donor/acceptor interactions). The diversity and strength of intermolecular forces in ILs fine-tune local arrangements in the bulk and near interfaces.[5]

The sheer breadth of cations and anions available to make ionic liquids means that there is a true possibility to design ionic liquids to be environmentally benign and high-performance solvents/catalysts in their respective applications.

Although ILs were initially labelled as "green solvents" due to their negligible vapour pressures, recent toxicology,[16] biodegradability[17] and life cycle analysis[18] has shown that these might have even greater environmental impact than conventional volatile organic compounds (VOCs). Consequently, an ionic liquid needs to be reused many times to suppress the impact of its synthesis. Examples of the application of ILs in industry have been extensive reviewed, notable specific examples where intermolecular interactions and knowledge of them can impact upon productivity/performance: 1) BASIL™ (biphasic acid scavenging utilising ionic liquids developed by BASF) process[19] – control of phase boundary is key; 2) Alkylation cleaner - Chevron[20, 21] will be changing from hydrofluoric acid to an ionic liquid system as Lewis acid catalyst; 3) Lunar Mirror[22] – formation of eutectics to supress melting points while keeping low volatility. But mostly, ILs are still currently limited to small-scale applications.[5, 23] This can be attributed, in part, to the lack of understanding on how structural changes to an IL can influence its physicochemical properties and hence function.[5] As such, it has become increasingly important to understand ILs at a molecular level through fundamental investigations into their physicochemical and structural properties,[5, 24, 25] and with this knowledge it is certain that the utilisation of ILs and novel solvents in new and existing commercial applications will continue to increase.

1.2. Ionic Liquid Properties

The combined properties of low volatility, tunability and outstanding solvation ability define ILs as attractive alternatives to typical solvents and they have found use in many applications.[26, 27] However, the use of ILs often results in reduced efficiencies or deviations from expected behaviour. It is simply not realistic to change from a conventional solvent to an IL and expect an improved

outcome.[5] These results are usually attributed to high viscosity (mass transport effects) or the presence of contaminants[28] (*e.g.*, water, halide salts, organics). However, in most cases, the physical arrangement of ions in the bulk or at interfaces plays a key role in determining process efficiency. The general lack of understanding of IL structure and how it differs from traditional molecular solvents is the main challenge - ILs are not simply another class of solvents.[5] It has been found that even structurally similar ILs can dramatically change reaction outcomes.[29]

It is the IL chemical structure that allows for these materials to be liquids even at room temperatures (T_m < 25 °C). The anion and cation are chosen to destabilise the solid-phase crystal. Thus, while there are no set rules to making an IL, in general this can be achieved within a relatively large window of ion structures by balancing ion–ion interactions and symmetry as shown in Figure 1.1.[5]

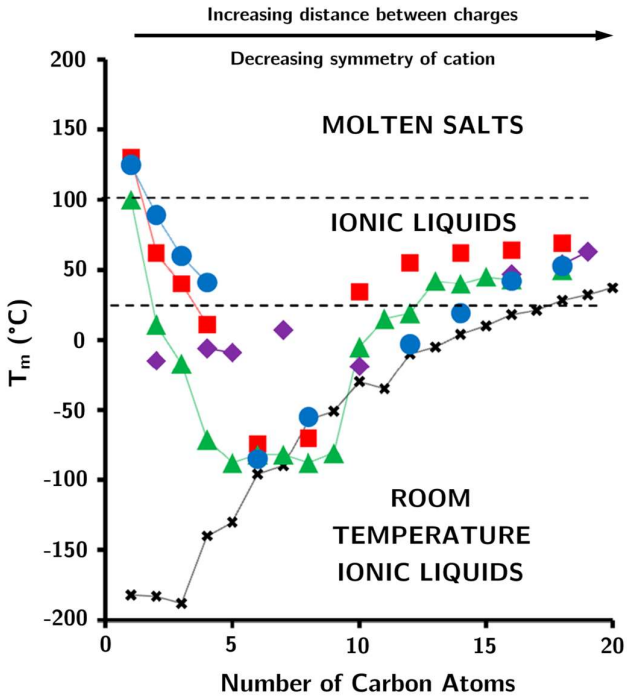


Figure 1.1. Melting point (T_m) as a function of cation alkyl chain length (*n*) for salts systems with 1-*n*-alkyl-3-methylimidazolium cations. *n*-Alkane data (n = 1– 20, ✖) are also shown for comparison. The trend in T_m is consistent across all salts: low *n* values T_m > 100 °C; intermediate *n* values 50 °C < T_m < 100 °C then T_m < 25 °C; and large *n* values 50 °C < T_m < 100 °C. Dashed lines indicate the boundaries between molten salts (T_m > 100 °C) ILs (T_m ≤ 100 °C) and RTILs (T_m ≤ 25 °C). Hexafluorophosphate ($[PF_6]^-$, red ■), tetrafluoroborate ($[BF_4]^-$, green▲), bis(trifluoromethanesulfonyl)imide ($[NTf_2]^-$, purple ◆), and chloride (Cl^-, blue ●); data sourced from references 30-33. Figure adapted from reference 5.

For instance, the cation alkyl chain must be long enough to reduce Coulombic forces and disrupt lattice packing, but not be too long ($\approx n < 12$) as this will increase the melting point despite the enhanced asymmetry; cohesive interactions increase with length of nonpolar groups as per linear alkanes.[5] However, Davis *et al.* recently showed a way around this and developed low melting salts from very long chain ($n > 16$) cations by introducing a *cis* double bond "kink" on the alkyl group.[34] This is similar to homeoviscous adaptation in cell membranes[35, 36] and highlights the complex array of packing and chemical factors that controls IL melting points.

Changing physicochemical properties, such as density, melting point, viscosity, conductivity or surface tension in ILs can be achieved with minimal structure variation and/or functionalisation. Thus, a study of the relationship between structure and physicochemical properties could enable designing ILs with tailored capabilities. These IL features will be discussed further in the following *Section 1.3*.

1.3. Functional Ionic Liquids

Structure–activity relationships,[37] and pursuing the functionalisation of ions, have been suggested as approaches to consider in order to finally create sustainable ionic liquids. Bio-based ionic liquids might be a step in the right direction. As such, chiral and amino acid-based ILs have been synthesised in the past, and their possible applications studied.[38, 39] Remarkably, the first naturally occurring IL has recently been discovered, thus highlighting the possibility that ILs may exist in nature to play specific biological roles.[40]

So far, functionalised ILs are generally recognised as ILs with functional groups in the cation. However, these ILs usually have higher melting points and viscosities compared to conventional ionic liquids with the same anions. Viscosity is an extremely important feature of ILs, especially in industrial and electrochemical device applications. To overcome this problem, functionalised anions have been probed and shown to lower the IL viscosity. Asymmetrical

anions with higher content of fluorine atoms has been shown to also reduce significantly the viscosity and increase hydrophobicity of the resulting ionic liquid. Synthesis of ionic liquids that incorporate more hydrophobic structural elements, while keeping their melting points below room temperature and low viscosities, continues to be a challenge.

Hydrophobicity can also be achieved by increasing the alkyl chain length of the cation. Although it is well known that ether functionalised ILs have lower melting points and viscosities when compared to their alkyl counterparts,[41] the synthesis of long ether functionalised side chains for imidazolium salts from parent molecules is problematic. Braun *et al.*[42] and O'Brien *et al.*[43] have recently developed a series of novel bio-inspired lipidic long chain ionic liquids containing phosphonyl and thioalkyl functional groups accomplished through "click" chemistry. Interestingly, long chain phosphonyl ILs were found to have lower melting points than their alkyl counterpart. Additionally, the same trends in melting point depression were observed for the thioethers as they were for the ethers. Incorporating sulfur as a heteroatom in the main chain also shown that melting point reduction is achieved without an accompanying vulnerability to sidechain scission – observed in unsaturated alkyl chains - making these ILs attractive candidates for investigation in a variety of practical applications.[43]

Tuning surface properties such as surface tension and wettability has important implications in both fundamental and technological advances; the anion effect offered by functionalised ILs on surface wettability is of practical significance to the adsorption on molecular surfaces and can be used for design of micro fluidics and micro devices used in anion sensing and in biomedical areas.[44] Hydrophilicity has a major impact upon the wettability of polar surfaces as pointed out by Cláudio *et al.*,[45] the higher the anion hydrogen-bond basicity, *i.e.*, the ability of the IL anion to accept protons, the easier it is for the IL to wet a polar surface (lower contact angles) while the opposite trend is observed on non-polar surfaces. The cation nature and alkyl side chain lengths have however a smaller impact on the wetting ability of ILs. Furthermore, for ILs with the same anion

and longer alkyl side chains, the contact angle values become increasingly more similar amongst the several surfaces since the hydrogen-bonding interactions become less significant.[46]

A detailed understanding of IL surfaces and interfaces and related processes at the molecular level is indispensable for predicting macroscopic surface and interface properties.[47-49] Surface termination, orientation of the outermost species (or end groups of larger anions or cations), segregation effects, surface contaminations, etc. are only some of the most important scientific challenges to be addressed.

1.4. Probing Surface Interface using UHV Techniques

To date, almost every known physical chemistry technique has been used to investigate structure in ILs. IL surface properties have been examined by a number of (non-vacuum related) surface sensitive techniques such as sum-frequency generation (SFG),[47, 50-58] X-ray reflectivity and neutron reflectometry,[58-60] surface tension measurements,[55, 61, 62] and molecular dynamic (MD) simulations have also been conducted.[63-69] Due to the high vapour pressure of typical liquids and their subsequent rate of evaporation, surface sensitive ultra-high vacuum (UHV) based techniques were limited to the analysis of compounds in the solid state. However, from 2005 it was realised that, due to their low vapor pressures, the bulk and surface properties of ILs can also be probed under UHV conditions. Since then, many surface science techniques have successfully contributed to an increasingly detailed understanding not only of the IL/vacuum interface, but also of IL bulk properties.[70] These techniques include X-ray photoelectron spectroscopy (XPS),[71-91] X-ray absorption spectroscopy (XAS),[92] low energy ion scattering (LEIS),[76] metastable ion spectroscopy (MIES),[71-73] Rutherford backscattering (RBS),[93] high-resolution electron energy loss spectroscopy (HREELS),[72] to name only a few. A particularly useful surface science method is XPS, also referred as electron spectroscopy for chemical analysis (ESCA), which allows for the determination

of the chemical composition of the surface and the surface-near bulk and oxidation state of the analysed atoms. Additionally, as core level binding energies are sensitive to small changes in electronic environment, much like the chemical shift in nuclear magnetic resonance (NMR) spectroscopy, the chemical state of atoms can be probed. The timescale of the XPS experiment renders it ideal to monitor processes and reactions, however data collection times must be considered. Examples of the use of XPS include the study of reactions in ILs or at IL–substrate or IL–electrode interfaces *in situ*, as a function of time or temperature.[74, 85, 94-98]. Many significant contributions have been provided by XPS in the field of IL surface characterisation, with emphasis on impurity detection and surface composition of ILs.[99] This will be further discussed in the following *Sections 1.4.1, and 1.4.2.*

1.4.1. Impurity Detection

Ultrapure ILs with nominal impurity levels are paramount for the determination of IL properties and structure. As mentioned in *Section 1.2,* IL impurities are mostly water, halides, and organics (which may be chromophoric) - carried over from synthesis including silicone grease.[100] ILs are generally air- and water-stable, however, all ILs are hygroscopic to some extent.[101] Water is generally removed by heating under vacuum conditions ($\approx 10^{-2}$ mbar).[100, 102] However, in order to remove the majority of water present in ILs (down to ≤ 10 ppm), higher vacuum ($\approx 10^{-5}$ mbar) has found to be necessary.[102, 103] The salt metathesis route has become the standard synthetic method for ILs, that gives the IL and a water-soluble halide salt.[86] Complete removal of the halide salt is difficult and commonly requires multiple washes with water; this generally involves loss of IL, adds water that subsequently has to be removed, and is not always successful.[100]

The XPS allows not only to check that the expected elements are present but also to check for impurities and dissolved species. Halide detection is possible even for relatively low concentrations, which is dependent on the sensitivity of the instrument.[80] Chromophores are more difficult to detect, mainly due to their

very low concentration, but also because they are generally composed of carbon, hydrogen, nitrogen, and oxygen atoms, which are present in most ILs.[49]

One of the most common problems associated with XPS is the observation of hydrocarbon-based impurities on the sample surface. In the case of IL-based measurements, this is most likely due to surface contamination as a result of silicone[74, 77, 82, 83, 95, 104] and organics,[74, 83, 105, 106] which can be attributed to either synthetic or handling procedures. The data published thus far suggests that the silicone is preferentially segregated towards the surface of the sample. Although surface segregated contaminants have not shown a direct effect upon the chemical environment of ILs by XPS,[74, 77, 107, 108] these can significantly impact upon the surface ion distribution and function of an IL especially at the IL/vacuum interface. It should be noted that many of the other surface sensitive techniques applied to the study of ILs are not as element specific as XPS and are consequently not capable of identifying impurities such as silicone.[49] Therefore, XPS provides high confidence levels in sample integrity and physical properties which helps characterise surface chemistry, orientation and possible contaminations.

1.4.2. Composition

1.4.2.1. ARXPS

XPS and in particular angle-resolved XPS (ARXPS) studies upon neat, functionalised, mixtures and IL solutions under different experimental conditions have been demonstrated to be very powerful probes of the IL surfaces.[49, 74-76, 78, 109, 110]

The information depth (ID) of standard XP experiments at 0° is between 7 – 9 nm, which is not particularly surface sensitive. However, by increasing the angle, the surface sensitivity is greatly increased; at 80°, the ID is 1 – 1.5 nm. Maier and co-workers studied a wide range of different IL systems using ARXPS.[82, 83, 86, 104] In the particular case of the 1-alkyl-3-methylimidazolium ILs, it was shown

that for $[C_nC_1Im][NTf_2]$, where n = 2 - 16, there is more alkyl chain present in the near-surface region than expected by stoichiometry, agreeing with previous conclusions of Lockett *et al.*[81, 104] Whether the alkyl chain is located on the cation or the anion, results for sum-frequency generation (SFG),[55, 58, 104] X-ray reflectivity,[58] metastable ion spectroscopy (MIES),[111] and simulations[63] agree with these findings. By varying the anion, $[C_8C_1Im][X]$,[82] it was shown that more alkyl chain is present in the near-surface region for those ILs containing smaller anions such as halides and $[BF_4]^-$.

ARXPS has been demonstrated to be a powerful technique to characterise and quantify the IL composition in the near-surface region with high accuracy, and that information on molecular orientation, surface contaminants, enrichment effects and chemical state of the IL or dissolved metal complexes can be determined.[48, 49, 77-79, 81, 90, 104, 112]

1.4.2.2. ERXPS

The chemical composition and the molecular arrangement at the near-surface region can be different to that in the bulk due to unbalanced forces which are present as result of the anisotropic environment. To explain macroscopic surface and bulk properties such as surface tension and solubility, a molecular perspective of the surface and the bulk is vital. Applications of ILs which involve reactions at interfaces, such as gas-separation processes as well as applications which involve processes in the bulk, *i.e.* solvation of metal catalysts, have increased greatly in recent years.[26, 47, 70] Hence, there is an increasing interest in obtaining depth profiles of ILs.[113, 114]

The ID for energy-resolved XPS (ERXPS) experiments is solely a function of attenuation length and hence kinetic energy of the escaping photoelectron. Therefore, this information depth is dependent upon the core orbital from which it originated. Blundell *et al.* demonstrated the use of a Ag L_α' X-ray source to investigate depth profiling of ILs containing the $[NTf_2]^-$ anion. Using sulfur as a probe of depth, the required photoelectron emissions were obtained using

calculated attenuation lengths values where it was found that the S 2p signal gives a "bulk sensitive" representation of the sulfur concentration in the sample, in contrast to the S 1s signal which gives a "surface sensitive" representation.

The surface ordering of the cation was found to be heavily dependent upon surface orientation of the anion, with similar trends observed as to those obtained through ARXPS. ERXPS can therefore be used to complement information given by ARXPS as both depth profiling techniques were supportive to each other, and provide further evidence of surface preferential orientation.[114]

Surface termination and positioning of the outermost species (or end groups of larger anions or cations), segregation effects, surface contaminations, etc. are only some of the most important scientific challenges to be addressed.[99]

1.5. Aims and Objectives

To fully understand the structure-property relationships of ionic liquids it is necessary to characterise neat ILs at a molecular level. Binding energies obtained from XPS have provided extensive information on the effect of structural changes to local electronic environment and also cation-anion interactions. Additionally, the surface sensitive nature of XPS enables depth-profiling experiments to determine the nature of the IL/vacuum interface. However, the majority of these studies have been focused on nonfunctionalised, heterocyclic cations with particular emphasis on the imidazolium-based systems. The work in this *Thesis* addresses this gap in knowledge through XPS investigations into guanidinium and sulfur containing cations, and the influence of cation functionalisation. A summary of the principles of XPS are described in *Chapter 2*.

In *Chapter 3* XPS is used to gather the first binding energy data for guanidinium-based ILs; the influence of cation structure on cation-anion interactions is the emphasis of this *Chapter*, with three main questions: (i) How does the charge delocalisation of the cation core influence cation-anion interactions? (ii) Are the

trends in anionic influence exhibited in other ILs families also applicable to this class of IL? (iii) How do cation mixtures impact upon the anionic component?

Chapter 4 describes the use of XPS binding energies information for cyclic and acyclic sulfur-based ILs along with appropriate comparisons to ^{13}C-NMR. The effect of sulfur functionalisation in both cyclic and exocyclic cation structure is also addressed.

Chapter 5 describes the use of XPS to characterise the surface structure for a range of imidazolium, guanidinium and sulfur-based ILs. The primary focus is to determine if the ionic components exhibit different surface preferences and investigate these effects upon a range of ILs families. To investigate this, two depth profiling techniques are used: angle-resolved XPS (ARXPS) and energy-resolved XPS (ERXPS) by means of the commercially available Al K_α' for the first, and Ag L_α' X-ray source for the latter.

2. X-ray Photoelectron Spectroscopy (XPS)

2.1. X-ray Photoelectron Spectroscopy of Ionic Liquids

X-ray photoelectron spectroscopy (XPS) is a surface sensitive analytical technique and is perhaps the most common and prominent ultra-high vacuum (UHV) based electron spectroscopy method.[115] This technique is valued for its capacity to provide unique information on chemical composition, chemical state identification and even composition depth profiles of the near-surface region ($\leq$ 10 nm) enabled by the measurement of binding energies of core level electrons ejected from a sample *via* X-ray irradiation UHV conditions.[116]

ILs may be introduced into UHV chambers without incurring significant evaporation.[48, 74, 112, 117-120] This lack of volatility has allowed XPS to become a prominent analytical method for the investigation of the physiochemical properties of IL samples.[82, 88, 94, 121, 122]

These materials were found to be resistant to X-ray beam damage and provided a strong photoelectron flux, resulting in short collection times and excellent XPS data. Subsequent investigations using other imidazolium ILs provided an updated fitting model that was shown to effectively fit the profiles of multiple IL C 1s spectra.[74]

XPS of ILs has rapidly expanded to include the monitoring of *in situ* organic reactivity using ILs as solvents,[85, 123] the speciation of organometallics in ILs,[107, 124] the investigations of cation-anion interactions[88, 108, 125] and the XPS analysis of a wide range of unique IL systems,[122, 126-129] to name a few.

2.1.1. Principles of XPS

XPS is based upon the basic principle of the photoelectric effect. In a standard XPS experiment, a sample is irradiated with X-ray photons, which can penetrate many micrometres into the bulk material. On collision with an electron the incident photon is annihilated with complete energy transfer to the electron. If the energy transferred is sufficient the electron will be ejected from the atom as a photoelectron, as illustrated by Figure 2.1.

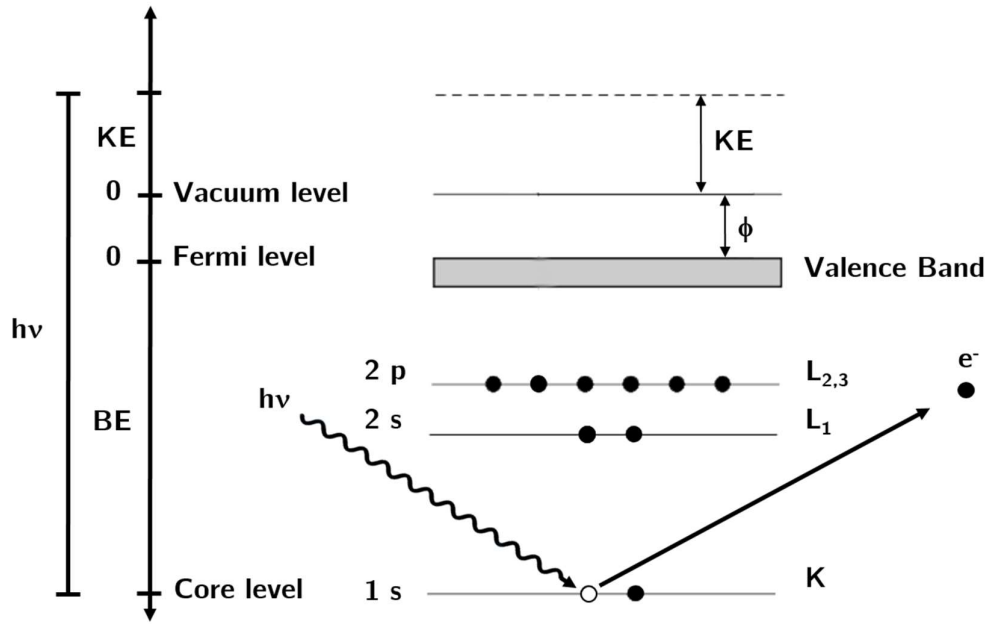


Figure 2.1. Schematic describing the Photoelectric Effect. An X-ray photon of energy ($h\nu$) collides with a core level electron in the initial state, thus ejecting it from the atom. This results in a final state with a core hole. The KE of the emitted photoelectron, e^-, is related to $h\nu$, BE and Φ_S as described in Equation 2.1.

The attenuation length (average distance travelled between two inelastic events without elastic events) of an emitted photoelectron is dependent on the X-ray energy. For the typical Al K_α X-ray source ($h\nu$ = 1486.6 eV) the subsequent information depth (ID) is approximately 10 nm, depending of the nature of the medium.[130] Consequently, only photoelectrons emitted in the near-surface region can escape and will be detected, thus defining the surface sensitive nature of XPS.

The kinetic energy (KE) of an emitted photoelectron (which has not suffered energy losses due to inelastic collisions) can be measured. This value is discrete in nature and is dependent upon the energy of the incident X-ray photon ($h\nu$), the binding energy (BE), and the work function of the spectrometer (Φ_s), as shown by Equation 2.1:

$$KE = h\nu - BE - \Phi_s \qquad \textbf{2.1.}$$

The binding energy is measured relative to the Fermi level (highest occupied quantum level) of the sample, and is regarded as the energy gap between the initial and final states of the photoelectron process; its value is both element and orbital specific. The spectrometer work function Φ_s, describes the energy required to remove an electron from the Fermi level to the vacuum level, the spectrometer automatically corrects for this value during analysis (typically $\approx$ 4.5 eV).[130] Consequently, as KE, $h\nu$ and Φ_s are either known or can be measured, the binding energy can be derived using Equation 2.1.

XPS experiments are generally performed under UHV conditions. This is to minimise gas phase collisions of emitted photoelectrons, which would otherwise result in significant scattering and hence low detection. Additionally, at UHV the impingement rate of gas molecules with the surface is very low, thus promoting a clean surface for analysis. Volatile contaminants, and dissolved gases, present in the sample will also be removed under UHV conditions, thus improving surface purity.[49]

2.1.2. XPS Experiment

A simplified schematic of a typical XP spectrometer is shown in Figure 2.2. X-rays are produced by bombarding a metal anode with high energy electrons. In this work both aluminium and silver anodes are utilised. Subsequently, the electron bombardment results in the emission of X-rays of energy characteristic to the source, *e.g.* Al K_α = 1486.6 eV or Ag L_α' = 2984.3 eV. Additional radiation including X-ray satellites, Bremsstrahlung radiation and Auger emissions are also produced to a lesser intensity.[115]

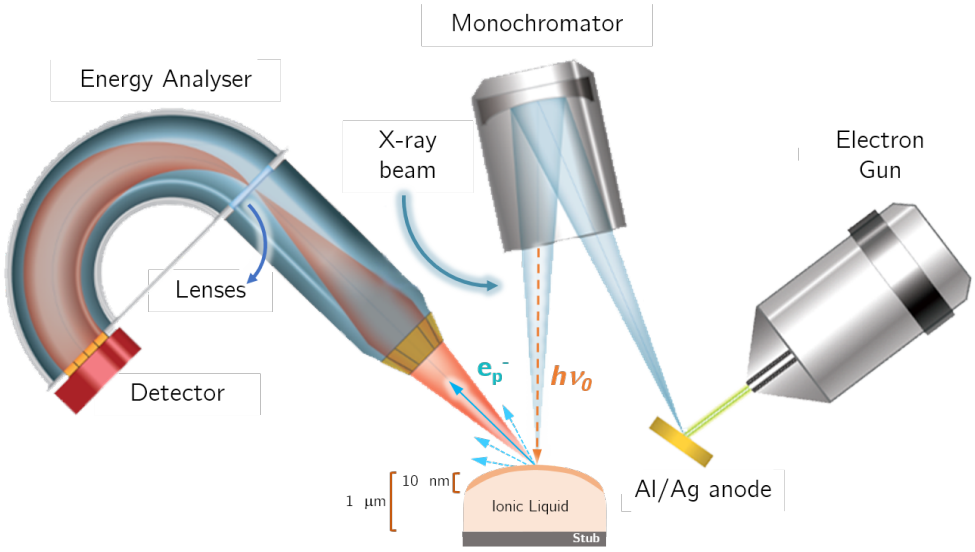


Figure 2.2. Schematic of XP spectrometer set-up. Figure adapted from reference 131.

The line width of the generated X-rays is reduced by diffraction against a quartz crystal monochromator; with reductions from 0.9 eV to approximately 0.25 eV for Al K_α, and from 2.6 to 1.2 eV for Ag L_α'.[116] In addition, the monochromator removes any additional spectral lines, and focuses the X-rays onto a small spot (down to 10 µm) on the sample surface.[130] The monochromator also provides a greater degree of separation between the sample and source, thus minimising sample damage from exposure to heat and back-scattered electrons.

Photoelectrons emitted from the sample pass through transfer lenses to the analyser. The most commonly employed analyser is the concentric hemispherical analyser (CHA), in which emitted photoelectrons pass between two concentric plates set at different voltages. Typically, the CHA works in combination with transfer lenses in fixed analyser transmission (FAT) mode.

In this mode, the voltage of the concentric plates is fixed for a given photoelectron kinetic energy – known as the pass energy. Before reaching the analyser, the photoelectrons must first pass through a series of electrostatic transfer lenses which slow down the photoelectrons to the required pass energy and focus them towards the analyser. Therefore, in order to obtain a photoelectron spectrum, the lens voltages are scanned to focus, sequentially, photoelectrons of varying kinetic energies to the required pass energy. As the

pass energy remains constant throughout the energy range, the resolution (in eV) is constant across the entire width of the spectrum.[116]

A typical detector consists of an electron multiplier, to count individual electrons arriving at the detector, and a delay line detector (DLD). The two most common multipliers used are channel electron multipliers and channel plates.

2.1.3. XP Spectra

XPS can provide two types of spectra for data analysis: survey (or wide) scans and high-resolution scans. For a survey scan, photoelectrons emitted from the entire energy range of the spectrometer are recorded, this is typically used to determine sample purity and elemental composition. High-resolution scans focus upon a specific energy region and are used to determine binding energies with higher accuracy. Hydrogen and helium are undetectable by XPS due their low photoionisation cross-section.[132]

2.1.3.1. Survey Scan

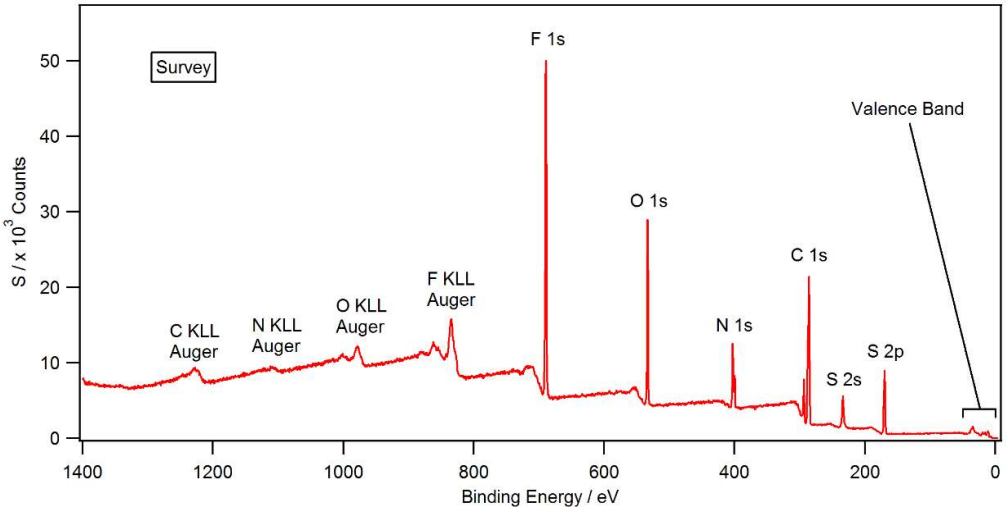


Figure 2.3. Survey (wide) XP spectra of $[C_8C_1Im][NTf_2]$ acquired with Al K_α X-rays. Charge corrected by referencing the $C_{aliphatic}$ 1s photoelectron emission peak to 285.0 eV.

An example survey scan for the ionic liquid $[C_8C_1Im][NTf_2]$ is presented in Figure 2.3. In this case, the spectrum was acquired with the Al K_α X-ray source and the energy range subsequently covers 0 – 1400 eV. Survey scans are often recorded with a step size of 0.5 eV and a pass energy of 80 eV, allowing for

greater signal intensity but at the cost of spectral resolution. The spectrum consists of a series of peaks situated on a background that decreases in a step like manner after each spectral feature, from high to low binding energy. The steps often appear due to emitted photoelectrons which experience energy losses *via* inelastic scattering before escaping the surface and consequently, contribute to the background signal. The main photoelectron lines occur in the energy range 35 – 800 eV and are distinct sharp peaks. Photoelectron binding energies are both element and orbital specific, thus each element has a characteristic set of spectral lines, which can be used for element identification.

In addition to core photoemissions, survey scans contain Auger peaks at higher BEs (800 - 1400 eV) and valence band signals at lower BEs (0 - 35 eV), in the case of the Al K_α X-ray source. Auger peaks can arise from internal atom de-excitation of the core holes produced by photoemission, as illustrated by Figure 2.4. In this example, a K level core hole is "filled" by an L_1 level electron, energy equal to the difference in binding energy of the K and L_1 levels is released and is sufficient to eject an electron from the $L_{2,3}$ level. This is known as a $KL_1L_{2,3}$ transition; however, it should be noted that other combinations exist.

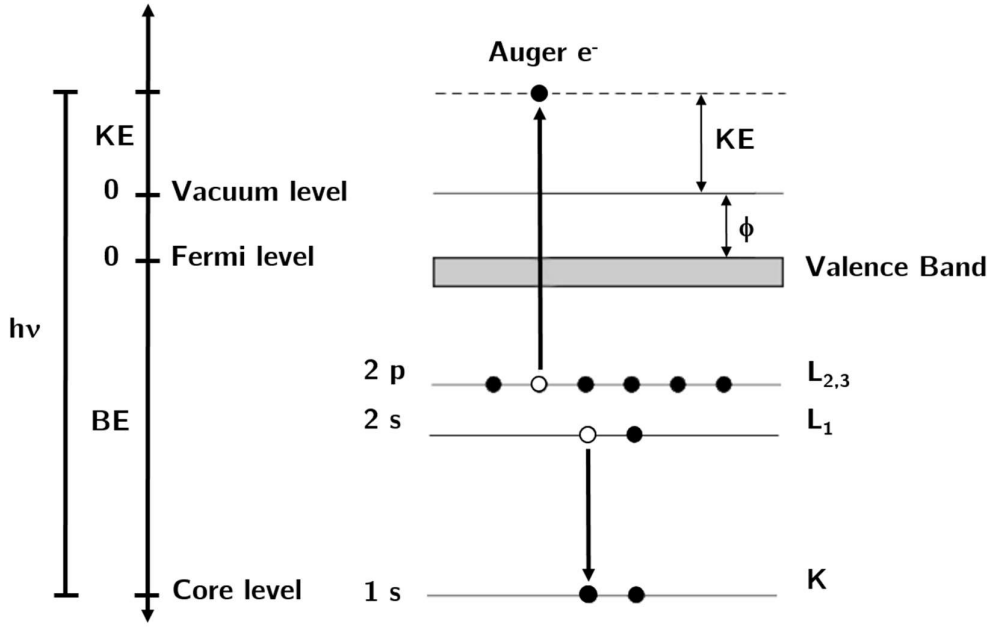


Figure 2.4. Schematic illustrating Auger electron emission after initial photoionisation. This example illustrates a $KL_1L_{2,3}$ Auger transition. An electron fills the core hole "falling" from the L_1 level to K level. Energy liberated is transferred to an electron in the $L_{2,3}$ level, which is ejected from the atom.

The kinetic energy of the emitted Auger electron is only dependent on the energy levels of the element. Subsequently, Auger kinetic energies are characteristic of the emitting atom, and can be used for element identification using the kinetic energy scale.

2.1.3.2. High-Resolution Scan

High-resolution scans focus on a narrow energy range (typically between 10 – 50 eV) which usually contain a core photoelectron line, as exemplified by the C 1s high-resolution scan for $[C_8C_1Im][NTf_2]$, Figure 2.5. In contrast to survey scans, these are measured with a smaller energy step size (0.1 eV) and lower pass energy (20 eV), in combination with longer acquisition times, which significantly improves spectra resolution - albeit at a cost to the signal-to-noise ratio. Consequently, high-resolution spectrum enables a greater degree of accuracy in binding energy analysis, which provides crucial information on element/component electronic environments.

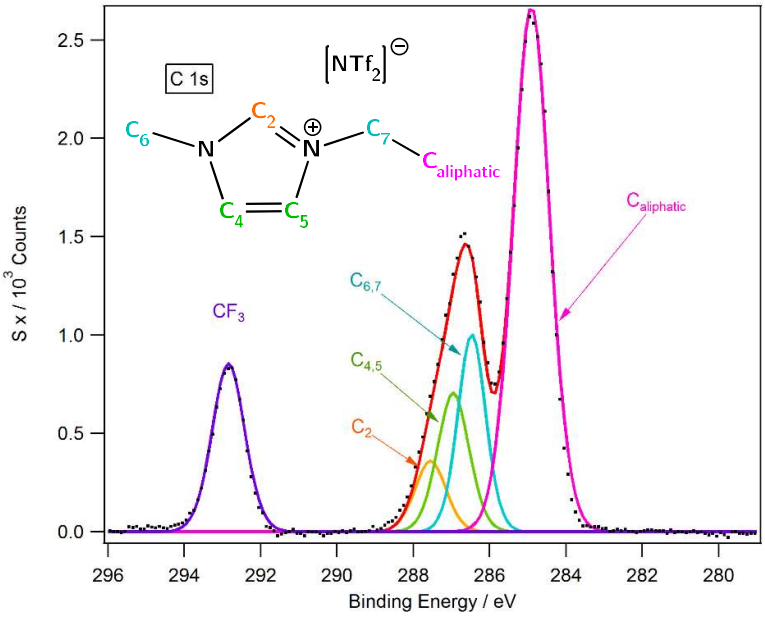


Figure 2.5. C 1s high-resolution spectrum including component fittings for $[C_8C_1Im][NTf_2]$. Charge corrected by referencing the $C_{aliphatic}$ 1s photoelectron emission peak to 285.0 eV. The resulting sum of components, envelope (red) is partially omitted to show the CF_3 and aliphatic components.

As shown in Figure 2.5, there is more than one C 1s environment in $[C_8C_1Im][NTf_2]$, and if these are particularly close in energy, it is not always

possible to resolve different contributions to the photoelectron emission spectra. It is, therefore, important to develop fitting models that accurately describe the different chemical environments of an element in order to determine their binding energies. C 1s fitting models have previously been described by the Licence group for imidazolium,[108] pyrrolidinium,[125] pyridinium,[129] ammonium and phosphonium ILs.[127] In this *Thesis* C 1s fitting models for guanidinium and sulfur-functionalised ILs have been developed and described (see *Chapter 3, Section 3.2.2.* and *Chapter 4, Section 4.2.2.*).

2.1.4. Information from XP Spectra

2.1.4.1. Semi-Quantitative Analysis

As mentioned previously in *Section 2.1.3*, each element (excluding hydrogen and helium) exhibit at least one core level line in the photoelectron spectrum. From these photoemission lines, peak positions - when measured on a binding energy scale - are sufficiently unique to allow elemental identification. Therefore, a single survey scan can provide complete elemental analysis.[130] Typical survey scan detection limits are 0.1 atomic% for elements with low photoelectron cross-section core levels. Therefore, any element present in lower concentrations will go undetected by XPS.[133]

The intensity of a specific photoelectron peak is dependent on its photoelectron cross-section - which is element and orbital specific – consequently, a direct comparison of peak areas does not provide useful information on relative atomic concentrations. Therefore, scaling of each photoelectron peak with the empirically derived relative sensitivity factor (RSF) is required. In this work, RSFs were obtained from the Kratos library for the semi-quantitatively determination of relative atomic concentrations (accuracy 10 – 20%).[134]

2.1.4.2. Chemical State Analysis

XPS is capable of quantifying and identifying the various chemical states of elements in a particular sample. The measured binding energy of a photoelectron

line is a function of the local chemical environment of the atom it originated from. Therefore, factors such as type of bonding, oxidation state and intra or inter-molecular interactions can influence the electron density of an atom, and hence cause a measurable shift in binding energy.[135]

For larger electron densities, the electrostatic shielding from the nuclear charge is greater and hence the core level electron experiences a lower effective electrostatic interaction to the nucleus. This will give rise to lower BEs signals. Analogously, a decrease in electron density of an atom, which may be caused by an increase in oxidation state or neighbouring electron withdrawing atoms/groups, generally results in an increase in binding energy.

Photoelectron lines corresponding to different chemical environments of the same element can therefore be distinguished from each other as seen from the C 1s region in Figure 2.5. Curve deconstruction may be required, as mentioned in *Section 2.1.3.2* to resolve the different components in order to accurately measure their binding energies. The associated experimental error with binding energy measurements is set by the manufacturer and stated as ± 0.1 eV.

2.1.5. Charge Neutralisation and Charge Correction

Binding energies from XPS are measured relative to the energy of the Fermi level, as stated in *Section 2.1.1*. When photoelectrons are emitted from a sample surface, positive holes are left behind. In the case of conducting samples in electrical contact with the spectrometer, the Fermi levels of the sample and spectrometer align. Consequently, the positive holes are quickly dissipated by the flow of electrons from spectrometer to sample.

However, for insulating compounds, no such equilibrating mechanism exists *i.e.* the Fermi levels of the sample and spectrometer are not aligned. As such, during photoelectron emission, a build-up of positive charge accumulates at the sample surface, thus its potential with respect to the spectrometer changes with time and it is no longer correctly compensated for. This substantial, positive potential

differential results in the entire XP spectrum to shift towards lower kinetic energies - higher apparent binding energies - which will also lead to line broadening and diminished spectral resolution.[108] In these cases, charge control methods need to be applied to compensate for surface charging.

The most utilised charge control approach is charge neutralisation. This method involves flooding the surface with low energy electrons to neutralise the positive charge. Generally, charge neutralisation results in overcompensation and the surface will become to some extent negatively charged, causing the observed BEs to subtly shift to lower energies.

In order to produce reliable and obtain accurate BEs, that may be used to compare signals across multiple data sets, it is necessary to use charge correction methods (even after charge neutralisation). Usually, charge correction involves calibrating the spectrum by referencing to a photoelectron peak of known binding energy. There are several approaches for charge correction, however referencing to an internal standard is the most commonly applied. The reason for this is that surface charging effects will be experienced equally by the reference and the sample.

Ionic liquids are conducting when in the liquid state; hence, charge control methods (*i.e.* charge neutralisation) are not usually required for liquid ILs. However, as ILs are ionic conductors, rather than electron conductors, they act as insulators when in the solid state.[108] Highly viscous materials, such as surfactant or wax-like ILs, may act as insulators as well. Therefore, charge neutralisation must be applied in the case of these samples to prevent surface charging.[72, 74, 95]

In order to measure true binding energy values for ILs, the application of charge correction methods is standard for all types of ionic liquid. It has become common practice to charge correct BEs by referencing the spectra to the signal corresponding to the aliphatic carbon atoms ($C_{aliphatic}$ 1s = 285.0 eV) present in most ILs.[72, 81, 88, 108, 136, 137] Spectra that are referenced this way appear to

provide consistent BEs of fluorine environments, for different anions. Hence, charge correction to the F 1s signal of $[NTf_2]^-$ anion is also a viable method of spectral calibration used in this work.

2.1.6. Surface Cleaning with Argon Sputtering

XPS is highly surface sensitive and even small levels of contaminants can have a profound effect on the measured spectra. An undesired feature associated with contaminants is unexpected photoelectron lines which can be excessively intense and/or overlap with photoelectron lines of the sampled material. This can prevent accurate determination of elemental composition and chemical state analysis of the sample. If the contamination is surface segregated, argon ion sputtering can be used to etch the surface and remove the contaminant, with typical sputter energies in the range of 0.5 – 10 keV. This process involves bombarding the surface with a beam of energetic argon ions, which removes the top few layers of atoms, thus exposing a clean surface that is free of contaminant below. In this *Thesis*, all materials that showed additional photoelectron lines were etched using the argon gas cluster ion source in order to minimise surface damage relative to sputtering with monoatomic Ar^+ ions (5 keV). The cluster sizes used can be differed from Ar_{500}^+ to Ar_{1000}^+ so that the partition energy can be varied from 0.5 eV (*e.g.* 0.5 keV/1000 cluster) to 20 eV per Ar atom. The schematic diagram in Figure 2.6 shows the interaction of a gas cluster with an ideal surface where the damage induced by the impact is localised at the surface, and comparison to a monoatomic ion beam.

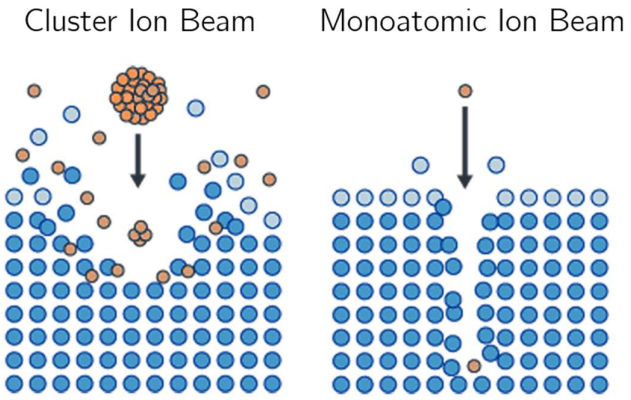


Figure 2.6. When using an ion cluster source, the energy per element is small, diminishing damage at the vicinity of the surface (left). Ions penetrate deep into the substrate causing extensive sample damage when using a monoatomic ion beam (right). Figure adapted from reference 138.

2.2. XPS Instrumentation

***Aluminium Source Experiments*:** XP spectra were recorded using a Kratos Axis Ultra spectrometer employing a focused, monochromated Al K_α source ($h\nu$ = 1486.6 eV), hybrid (magnetic/electrostatic) optics, concentric hemispherical analyser (CHA), a multi-channel plate and delay line detector (DLD) with an X-ray incident angle of 30° (relative to the surface normal). X-ray gun power was set to 120 W (10 mA, 12 kV). Spectra were recorded using an entrance aperture 300 µm × 700 µm with a pass energy of 80 eV and step size 0.5 eV for survey spectra, and pass energy 20 eV and step size 0.1 eV for high-resolution spectra. Acquisition times for survey scans and high-resolution scans were 1200 s and 600 s respectively.

***Silver Source Experiments*:** XP spectra were recorded using a Kratos Axis Ultra Spectrometer in which the Al K_α source was substituted with a monochromated Ag L_α' source ($h\nu$ = 2984.3 eV) operated at the same X-ray gun power (120 W) with minor adjustments to the gun position and monochromating crystals. All spectra were recorded with an entrance aperture of 300 µm × 700 µm with pass energy of 160 eV and step size 1.0 eV for survey spectra, and pass energy of 40 eV and step size 0.2 eV for high-resolution spectra. Acquisition times for surveys scans and high-resolution scans were 2400 s and 1200 s respectively.

For both sources binding energy calibration was made using Au $4f_{7/2}$ (83.96 eV), Ag $3d_{5/2}$ (368.21 eV) and Cu $2p_{3/2}$ (932.62 eV). The resolution of the photoelectron detector was based on the Ag $3d_{5/2}$ peak full width half maximum (FWHM), with the values obtained for each source as follows: Al K_α (Ag $3d_{5/2}$ FWHM = 0.55 eV); Ag L_α' (Ag $3d_{5/2}$ FWHM = 0.90 eV).

Charge neutralisation (used for solid samples only) was applied using a standard Kratos charge neutraliser consisting of a filament, coaxial with the electrostatic and magnetic transfer lenses, and a balance plate which creates a potential between the neutraliser and sample. Charge neutralisation was applied at 1.9 A filament current and 3.3 V balance plate voltage. Sample stubs were earthed *via* the instrument stage using a standard Bayonet Neill-Concelman (BNC) connector.

2.3. Sample Preparation

The preparation method for each sample is dependent on the nature of the material to be analysed, and the type of experiment.

***For standard XP experiments*:** liquid samples were prepared by placing a small drop (≈ 10 mg) of ionic liquid onto a stainless steel multi-sample bar; solid samples were fixed to the bar using double-sided adhesive tape or placed in a stainless-steel powder stub.

***For ARXPS and ERXPS experiments*:** Previous procedure involved placing a small drop (≈ 10 mg) of a liquid sample on a stainless-steel sample bar and cast into a thin film (approx. thickness 0.1 – 0.5 mm). After performing several measurements on the same sample with this methodology, the results were not reproducible. A full description of these results and changes to this technique is provided in *Chapter 5, Section 5.3.2.*

Samples were then pre-pumped in a preparative chamber to pressures lower than 1×10^{-6} mbar before transfer to the main analytical chamber. Pressure in the main chamber consistently remained $\leq 1 \times 10^{-8}$ mbar during XPS measurements.

2.4. XPS Analysis

Data was analysed using the CASAXPS (Version 2.3.17 dev 6.6) software. The Al K_α source was used to determine elemental composition using relative sensitivity factors (RSFs) taken from the Kratos library (RSF F 1s = 1) and used to determine relative atomic percentages from high-resolution scans of the most intense photoelectron peak for each element. Depending on background shape a two-point linear, shirley or spline linear background subtraction was performed to measure peak areas. Peaks were fitted using GL (30) lineshapes (70% Gaussian, 30% Lorentzian).

For ILs with a long alkyl chain ($n \geq 8$) charge referencing was achieved by setting the experimentally determined binding energy of the aliphatic component ($C_{aliphatic}$) equal to 285.0 eV. For compounds with a short alkyl chain ($n < 8$) charge referencing was achieved by setting the measured binding energy of the cationic heteroatom photoelectron emission peak equal to that for its long chain analogue, *i.e.* N_{cation} 1s for $[(C_4C_1)_2dmg][NTf_2]$ was set equal to 400.7 eV (where 400.7 eV is the measured binding energy of N_{cation} 1s for $[(C_8C_1)_2dmg][NTf_2]$). If neither charge referencing method is applicable to the IL investigated, it is stated otherwise within the text with an alternative provided.

ARXPS experiments at grazing emission angle ($\theta \geq 70°$) give significantly lower signal intensity than experiments at normal emission angle ($\theta = 0°$). Therefore, to aid visual interpretation of the ARXPS spectra presented, each spectrum recorded $\theta = 80°$ is normalised to the intensity of the C_{CF_3} 1s photoelectron emission peak recorded for the respective ionic liquid at $\theta = 0°$. This peak was selected for normalisation as the C_{CF_3} 1s moiety is present in all ILs in the same stoichiometry, and the C_{CF_3} 1s peak is easily identifiable with a binding energy well separated from any other photoelectron emission signals. This technique does not affect the relative ratios of different elements within the IL, thus provides a visual comparison of the same region for an IL on changes to emission

angle. Therefore, any changes in intensity of an element with emission angle can be observed.

2.5. Information Depth for ARXPS and ERXPS

The information depth (ID) can be defined as the depth, within the sample, from which 95.7% of the measured signal will originate and can be expressed by Equation 2.2.:

$$ID = 3\lambda_{AL}\cos\theta \qquad \textbf{2.2.}$$

For the lower energy, Al K_α X-ray source, ID varies mainly with $\cos\theta$, where θ is the electron emission angle relative to the surface normal. At the kinetic energies measured here ($\approx$ 800 – 1400 eV) the attenuation length (λ_{AL}) of photoelectrons in organic compounds is of the order of $\approx$ 3 nm.[139] From this, the ID in each of angle-resolved geometries employed in the ARXPS experiments can be estimated. Therefore, when $\theta = 0°$, ID = 7 – 9 nm (*N.B.* this value is also dependent on the kinetic energy of the escaping photoelectron, and therefore the identity of the element probed) and for $\theta = 80°$, ID = 1 – 1.5 nm. It should be noted that at 80°, 65% of the signal intensity arises from the uppermost 0.3 – 0.5 nm; this is less than the width of a single molecule for most ILs. An increase in element/component intensity with increasing θ, and thus with increasing surface sensitivity, indicates a higher concentration of this element in the top most layers.

When using the higher energy Ag L_α' X-ray source for ERXPS studies, a fixed normal emission angle of $\theta = 0°$ is used. Consequently, ID can be simplified to $ID = 3\lambda_{AL}$, thus ID is solely a function of attenuation length and hence kinetic energy. As a larger kinetic range is investigated $\approx$ 100 – 2800 eV, ID will be very dependent on the kinetic energy of an escaping photoelectron, and hence the core orbital from which it originated. A full description of this technique is provided in *Chapter 5, Section 5.2*

3. First XPS of Guanidinium Ionic Liquids

3.1. Introduction

The high nitrogen content of guanidinium cations leads to high energy density yet remarkable thermal and chemical stability providing interest as potential high-energy materials.[140-142] Moreover, the high degree of delocalisation of the cationic centre, the tuneability of the alkyl functionality of the nitrogen atoms, and other characteristic properties are making the synthesis and the application of guanidinium salts increasingly popular. [142-151] It has been proposed that guanidinium ILs are more environmental friendly solvents which have good designability, and more potential than traditional imidazolium ILs.[152]

Remarkably, guanidinium-based ILs have been showing clear signs of stabilisation[153] and disruption of peptides and proteins,[154-157] as well dissolution of biomolecules of interest such as cellulose.[158] This shows the incredible potential of these molecules to be designed as task-specific solvents, which increases the need to recognise the main interactions between solute and the IL solvent system, but also how these ILs interact on a molecular level, hence the effect upon inter-ion interactions must be explored.

Binding energies obtained from X-ray photoelectron spectroscopy (XPS) from ionic liquid solutions can help to characterise the main interactions occurring between the ionic liquid solvent and the solute and can be used to investigate the nature of the intermolecular interactions within ions, providing both elemental and chemical information.

XPS has been a valuable technique in a wide range of different fields, providing vital information in areas such as bulk and surface composition of ILs systems,[78, 104] *in situ* reaction monitoring,[123] and cation–anion interactions.[127] Not surprisingly, imidazolium and pyrrolidinium cation–anion interactions have been the emphasis of research, where the focus of interest has been on the effect of the anion upon the electronic environment of the cation, but interestingly there

are fewer studies into the nature of the cation and its influence.[88, 125, 127] These results can be correlated to NMR spectroscopy,[124] theoretical calculations[159] and Kamlet–Taft parameters[160] aiming for a better understanding of ionic liquid properties.[88]

XPS studies upon the cation–anion interactions can also help raise some light regarding interaction between the ion pair and solute molecules. Depending on the cation structure, the cation-anion interaction could be significantly weaker, which could be an explanation for the ability of the anion to be more readily available to interact with solute molecules. The high degree of charge delocalisation of the cationic core may be used as an indicator of cation–anion interaction. For instance, the charge on pyrrolidinium ILs is localised on the single nitrogen atom, whereas in the imidazolium ILs is distributed across the two nitrogen atoms. This results in a higher measured N 1s binding energy on the pyrrolidinium cation (when the anion is the same), evidencing a stronger interaction with the anion.[125] These results could be indispensable for the development of appropriate force fields for molecular simulations of guanidinium ionic liquids, which are crucial for molecular understanding of ILs properties and interactions with other molecules.[161-164] One recent theory paper even predicted the distilability of some guanidinium carboxylates using a combination of molecular dynamics and *ab initio* approaches.[165] Furthermore, XPS has also been used to monitor the electronic environment of the constituent atoms for a binary IL mixture by varying the composition of the anionic components, highlighting how IL mixtures can be used to tune the electronic environment of their cation–anion system.[110]

Research into ILs based on the guanidinium cation may be of particular importance, as they can offer interesting physicochemical properties, in comparison to other nitrogen based relatives, given by the high degree of delocalisation of the cationic core. Additionally, it has been reported that cyclic guanidinium cations are similar, in terms of their performance and robustness,

to more traditional families of ionic liquids when exposed to energetic radiolytic sources.[150]

The work herein utilises XPS to probe cation–anion interactions for guanidinium-based ILs and how the cationic structure influences cationic N 1s binding energies. Additionally, development of an appropriate fitting model for unresolved C 1s photoemission spectra is also presented. Moreover, stability to prolonged exposure to X-ray irradiation and/or argon etching is further investigated in *Section 3.2.1*. Finally, comparisons to other nitrogen-based ionic liquids, as a new potential system for binary IL mixtures will be discussed.

3.2. XPS of Guanidinium Ionic Liquids

3.2.1. Purity and Quantification

XP survey and high-resolution scans were used to establish elemental composition and purity for each ionic liquid presented in this study. Attaining high purity of ionic liquids is essential for the reliable characterisation of their physical and chemical properties. Figure 3.1. shows the survey scan for the solid $[(C_8C_1)_2dmg][BF_4]$ which exhibits all the expected photoelectron and Auger lines.

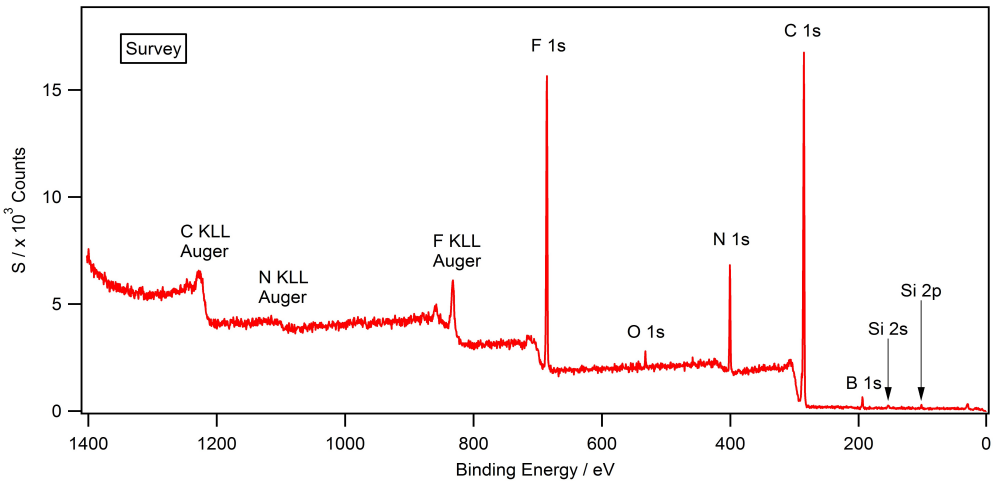


Figure 3.1. Survey XP spectrum for $[(C_8C_1)_2dmg][BF_4]$. O 1s and Si 2s/2p photoelectron lines are clearly visible indicating surface contamination.

Earlier XPS studies, in the field of ionic liquids, have shown the presence of hydrocarbon and silicon-based impurities in the near-surface region, which cannot be detected by NMR or other bulk sensitive techniques.[74, 75, 95] Some of the samples investigated in this work exhibited additional O 1s and Si 2s/Si 2p signals (see *Appendix A*). This does not appear to be systematic or linked with any component in either the sample or indeed the synthetic route to the material. In fact, CHN microanalysis found in *Chapter 7, Section 7.3* supports the high purity of this ionic liquid series. Furthermore, there are no photoelectron signals for metal-based cations or halide anions that may be carried over from earlier synthetic steps and anion metathesis chemistry involved in the preparation of these materials. These extra photoemission lines are likely to originate from laboratory high-vacuum silicon grease and/or glassware, which is used during synthesis and instrumentation handling. Several publications in the literature support that additional silicon peaks from these sources have no apparent effect on the recorded binding energies.[74, 77, 107, 108] Silicon grease, and other surface contaminants, can be removed by argon bombardment, a description of this procedure is provided in *Chapter 2, Section 2.1.6*. The experimental stoichiometries, which have been calculated from signal areas of high-resolution spectra, are presented in Table 3.1.

Table 3.1. Measured experimental and nominal (in brackets) stoichiometries for the guanidinium-based ionic liquids studied in this work. Highlighted stoichiometries that fall outside the experimental error of ± 20%.

		Composition[a] (%)													
Compound		C 1s		N 1s		F 1s		O 1s		S 2p		P 2p		B 1s		Cl 2p	
RSF[74,134]		0.278		0.477		1.000		0.780		0.668		0.486		0.159		0.891	
$[(C_8C_1)_2dmg]^+$	Cl^-	85.7	(84.0)	10.8	(12.0)	-		-		-		-		-		3.5	(4.0)
$[(C_4C_1)_2dmg]^+$	Cl^-	78.6	(76.5)	16.4	(17.6)	-		-		-		-		-		5.1	(5.9)
$[(C_4C_4)_2dmg]^+$	Cl^-	83.9	(82.6)	12.4	(13.0)	-		-		-		-		-		3.7	(4.3)
$[(C_8C_1)_2dmg]^+$	$[BF_4]^-$	74.5	(72.4)	9.3	(10.3)	12.0	(13.8)	-		-		-		4.3	(3.4)	-	
[b]$[(C_8C_1)_2dmg]^+$	$[BF_4]^-$	73.0[b]	(72.4)	9.2[b]	(10.3)	14.0[b]	(13.8)	-		-		-		3.9[b]	(3.4)	-	
$[(C_4C_1)_2dmg]^+$	$[BF_4]^-$	68.8	(61.9)	11.2	(14.3)	14.3	(19.0)	-		-		-		5.6	(4.8)	-	
$[(C_4C_4)_2dmg]^+$	$[BF_4]^-$	72.4	(70.4)	10.3	(11.1)	13.5	(14.8)	-		-		-		3.8	(3.7)	-	
$[(C_8C_1)_2dmg]^+$	$[PF_6]^-$	68.9	(67.7)	8.6	(9.7)	19.4	(19.4)	-		-		3.1	(3.2)	-		-	
$[(C_4C_1)_2dmg]^+$	$[PF_6]^-$	62.1	(56.5)	12.6	(13.0)	22.2	(26.1)	-		-		3.1	(4.3)	-		-	
$[(C_4C_4)_2dmg]^+$	$[PF_6]^-$	69.1	(65.5)	9.1	(10.3)	18.6	(20.7)	-		-		3.2	(3.4)	-		-	
$[(C_8C_1)_2dmg]^+$	$[NTf_2]^-$	61.4	(59.0)	10.0	(10.3)	14.9	(15.4)	9.0	(10.3)	4.7	(5.1)	-		-		-	
$[(C_4C_1)_2dmg]^+$	$[NTf_2]^-$	53.7	(48.4)	12.3	(12.9)	16.9	(19.4)	11.6	(12.9)	5.5	(6.5)	-		-		-	
$[(C_4C_4)_2dmg]^+$	$[NTf_2]^-$	59.8	(56.8)	10.6	(10.8)	14.8	(16.2)	10.2	(10.8)	4.5	(5.4)	-		-		-	

[a] Relative sensitivity factors (RSF) taken from the Kratos Library. *N.B.* Hydrogen is undetectable by XPS due its low photoionisation cross-section; consequently, reported stoichiometries are determined without consideration of hydrogen content.

[b] Measured experimental and nominal (in brackets) stoichiometries for $[(C_8C_1)_2dmg][BF_4]$ after argon-etching studies.

It should be noted here that some isolated photoemission lines, of elements that constitute the IL, exhibit errors that are slightly larger than anticipated (and do not lie within the acceptable ± 20%), which again does not seem to be systematic. This higher/lower composition of a given element, could be explained by preferential orientation, anion segregation and bulk or surface impurities within a sample. Further investigations into surface composition and the nature of contaminants, *i.e.* bulk or surface impurities, are described below.

In the particular case of $[(C_4C_1)_2dmg][BF_4]$, where the experimentally determined stoichiometries for nitrogen and fluorine exceed the error, and O 1s and Si 2s/Si 2p signals are present, elemental microanalysis was used to determine the C, H and N content. The CHN microanalysis for $[(C_4C_1)_2dmg][BF_4]$ demonstrates the high purity for this compound where C 49.66 (49.54), H 9.49 (9.59), N 13.12 (13.33) theoretical values are shown in brackets.

Also, for $[(C_8C_1)_2dmg][BF_4]$, C 59.10 (59.01), H 10.91 (10.85), N 9.81 (9.83) was determined. Hence, the results of CHN microanalysis are within the error for this experimental technique (± 0.4%) which strongly suggests that the error observed in percentage quantification by XPS is a result of surface segregation or related phenomenon, which could be very small in terms of mol fraction.

It has been previously shown that surface contaminants such as oxygen and silicon can be removed *via* successive cycles of argon ion bombardment.[74] A significant challenge in etching samples which are granular solids is the disturbance and dispersal of solid particles within the chamber by electrostatic effects. Solid samples that required argon bombardment were initially prepared by placing a small amount of solid in a stainless-steel stub, heating the sample until melted (≈ 40 - 60°C, 1 x 10^{-9} mbar), followed by argon bombardment (Ar_{500}^+ accelerated to 5 keV). Figure 3.2 (red) shows the XPS spectrum of $[(C_8C_1)_2dmg][BF_4]$ after this experiment.

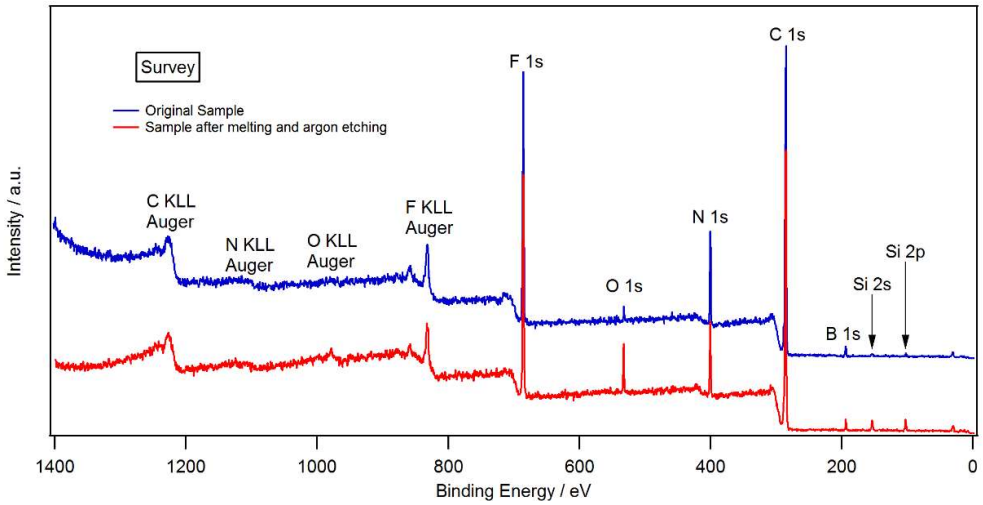


Figure 3.2. Survey XP spectrum for $[(C_8C_1)_2dmg][BF_4]$. O 1s and Si 2s/2p photoelectron lines are clearly visible indicating surface contamination (blue). Survey XP spectrum for $[(C_8C_1)_2dmg][BF_4]$ after melting, followed by argon bombardment (red). XP spectra offset vertically for clarity.

It is clear to see that the O 1s and Si 2s/2p photoelectron lines are still visible, which demonstrates that argon bombardment did not remove the contaminant. This result can be explained by the nature of the sample and the experiment; by heating the sample to the melt and maintaining this temperature, the mobility of the ions and contaminants is increased, consequently the rate of surface segregation of impurities also increase. Therefore, the removal of a surface segregated layer of impurities by argon bombardment is successful but is quickly replaced by a new layer of segregated contaminant. To examine this possibility, the sample was prepared by placing a small amount of solid in a stainless-steel powder stub, heating the sample until melted, then allowing it to cool and form a glass, followed by argon bombardment. Forming a glass instead of a granular solid allows argon etching of the surface without any disturbance of solid particles and reduces the mobility of ions and contaminants, thus reducing surface segregation between scans. If silicon and oxygen were still present, this would suggest that the impurities were part of the bulk, however if they were removed, it would prove that these were surface contaminants and therefore not representative of the bulk. Figure 3.3 (red) shows the XPS spectrum of $[(C_8C_1)_2dmg][BF_4]$ after this experiment and Table 3.1 shows experimental stoichiometries now within the experimental error.

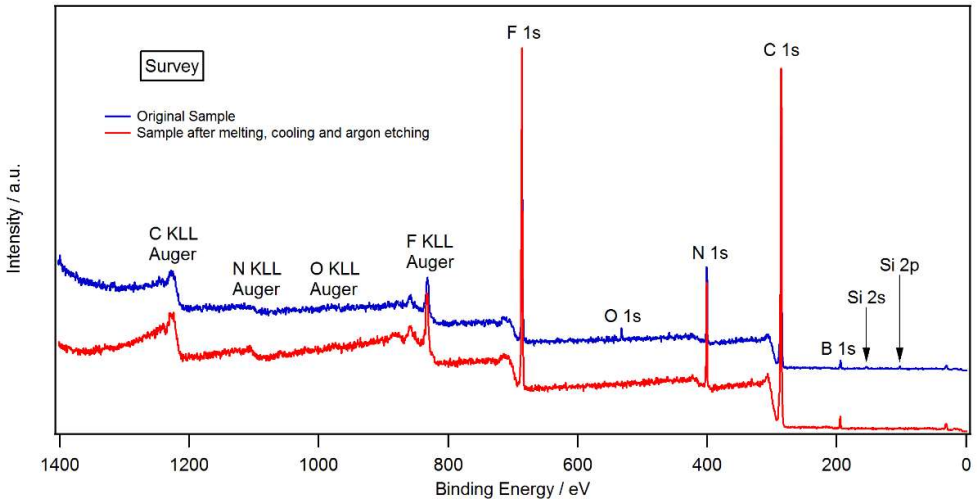


Figure 3.3. Survey XP spectrum for $[(C_8C_1)_2dmg][BF_4]$. O 1s and Si 2s/2p photoelectron lines are clearly visible indicating surface contamination (blue). Survey XP spectrum for $[(C_8C_1)_2dmg][BF_4]$ after melting, then cooling, followed by argon bombardment (red). XP spectra offset vertically for clarity.

Although surface etching displayed that oxygen and silicon can be removed for the compounds with a long alkyl chain ($n \geq 8$), irreversible changes to the sample occurred for compounds with a short alkyl chain ($n < 8$). Figure 3.4 illustrates a comparison of N 1s and C 1s high-resolution scans for $[(C_4C_1)_2dmg][BF_4]$ before and after argon bombardment. The full width at half maximum (FWHM) of the N 1s peak for the $[(C_4C_1)_2dmg]$ series is consistently equal to 1.1 eV when analysed without etching (see *Appendix A,* for all FWHM on the guanidinium ILs family); however, after argon bombardment, a broadening effect is clear to see on the N 1s region, as the Gaussian–Lorentzian shape is visibly lost with an associated increase of the FWHM. The same behaviour can also be seen in the C 1s region. This effect to the sample prevents the deconstruction of the different carbon environments, which is required to charge reference the $C_{aliphatic}$ to 285.0 eV. In summary, ILs with short alkyl chain ($n < 8$) seem to be unstable under argon bombardment, which is consistent with previous results.[126]

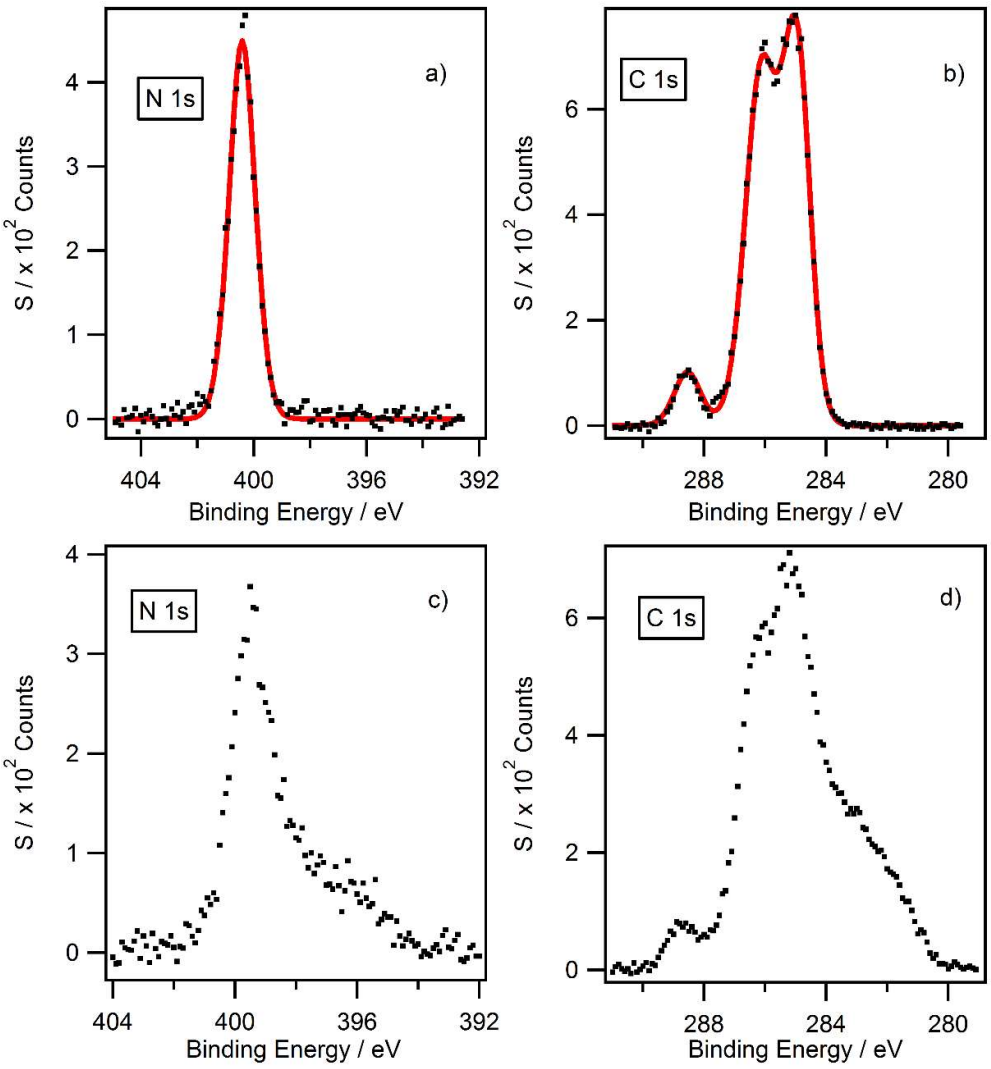


Figure 3.4. XPS high-resolution Spectra for the N 1s a) and c) and C 1s b) and d) of $[(C_4C_1)_2dmg][BF_4]$ before (top) and after (bottom) argon bombardment. N 1s spectra are truncated to 404-392 eV and C 1s to 279-290 eV to highlight changes to the lineshape. Spectra showing the full region are shown in *Appendix A*.

Subsequently, we have shown that heating the sample to the melt, then allowing it to cool prior to argon bombardment, does indeed remove the surface contaminants for compounds with long alkyl chain ($n \geq 8$). Thus, experimental values determined by XPS are now within the error of the nominal stoichiometry of ± 20%, and the majority are well within ± 10%, for compounds with long alkyl chain ($n \geq 8$). For shorter alkyl chain ($n < 8$) compounds, the surface contaminants could not be removed by argon bombardment alone, nevertheless quantification obtained by CHN microanalysis indicates the silicon and oxygen impurities observed by XPS originate through surface-segregation rather than

bulk contamination. This is further reinforced by the argon-etching studies upon the longer-chain analogues.

3.2.2. Development of C 1s Fitting Model

Diversity in the electronic environments of carbon often leads to unresolved peaks in the C 1s high-resolution XP spectrum. Therefore, it is essential that an appropriate fitting model is developed to describe these environments.

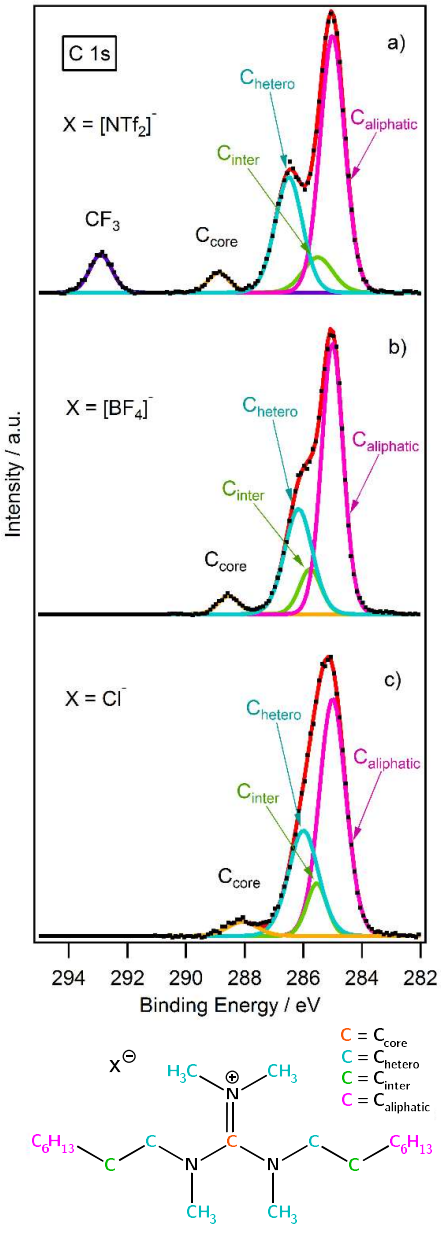


Figure 3.5. High-resolution XP spectra of the C 1s region with component fittings for a) $[(C_8C_1)_2dmg][NTf_2]$, b) $[(C_8C_1)_2dmg][BF_4]$ and c) $[(C_8C_1)_2dmg]Cl$. Intensities are normalised to the N_{cation} 1s photoemission peak for $[(C_8C_1)_2dmg][BF_4]$. All XP spectra charge corrected to $C_{aliphatic}$ = 285.0 eV.

Figure 3.5 shows some examples of the C 1s region for $[(C_8C_1)_2dmg]X$ (X = Cl^-, $[BF_4]^-$, $[NTf_2]^-$). In the case of $[(C_8C_1)_2dmg][NTf_2]$, there are four clear peaks, two of which are unresolved. The peak at ≈ 293 eV is assigned to the CF_3 group of the $[NTf_2]^-$ anion as seen previously for other $[NTf_2]^-$ based ionic liquids.[88, 108, 125, 127] For all the ILs investigated a small, well-defined peak is also observed, at a lower binding energy of 288–290 eV, alongside two unresolved peaks between 283–288 eV. Consequently, a suitable multicomponent model must be developed and applied in the deconstruction of the measured photoemission envelopes. Therefore, a series of multicomponent models have been developed to deconvolute these C 1s regions. Other robust C 1s models have been developed for a range of ionic liquid families, including: dialkyl-imidazolium, alkyl-pyridinium, pyrrolidinium, quaternary ammonium and phosphonium based ILs.[108, 125, 127] Herein we present first XPS data and appropriate fitting models for a range of guanidinium based cations.

A four-component model was applied to describe the guanidinium cation. The carbon structure of $[(C_8C_1)_2dmg]^+$ (Figure 3.5) can be grouped into four different chemical environments. The carbon bound exclusively to nitrogen (C_{core}) is expected to have the highest binding energy as it is directly bound to three electron-withdrawing nitrogen atoms. The label C_{hetero} is given to the first carbon of the alkyl-chain which is bound to a single nitrogen atom, and is expected to be at lower binding energy to C_{core}. This is followed by (C_{inter}), designated as an ''intermediate'' carbon environment, where the electron withdrawing impact of the nitrogen centre is less noticeable, resulting in an even lower binding energy. The remaining carbons are outside of the reach of the inductive effect of the cationic core and form the aliphatic component ($C_{aliphatic}$).

It is important that parameter constraints are utilised to ensure that the calculated model accurately describes the chemical environments of the compound. Component areas are constrained to their nominal stoichiometries, for example $C_{aliphatic}$: C_{hetero} : C_{inter} : C_{core} for $[(C_8C_1)_2dmg][BF_4]$ equates to 12 : 6 : 2 : 1. However, approximately 20% of all photoelectrons originating

from carbon atoms involved in unsaturated bonding will be affected by shake up/off phenomena and the corresponding C 1s peaks should be fitted to account for this, *i.e.* by reducing the total component area for C_{core} by 20%.[74] As the peak areas for the signals characteristic of aliphatic carbons are not affected by shake up/off phenomenon, the relative peak area ratios for the four cationic components can now be set to 12 : 6 : 2 : 0.8, correspondingly. Additionally, the FWHM for each component was constrained to be between 0.8 and 1.3 eV. Binding energy constraints were not applied as the binding energy shift between C_{hetero}, C_{inter} and C_{core} is expected to be dependent upon the nature of the anion.[88, 125] The fitting envelopes (red curve), shown in Figure 3.5a–c, correspond well to the experimental spectra (black dots). C 1s fittings for $[(C_8C_1)_2dmg][PF_6]$ and $[(C_4C_1)_2dmg][X]$ (X = Cl^-, $[BF_4]^-$, $[PF_6]^-$, $[NTf_2]^-$) are included in *Appendix A* and are also in agreement with the experimental spectra.

3.2.3. Effect of Alkyl Chain Length on Cationic Core

The binding energies measured for all compounds investigated in this study are displayed in Table 3.2. To extract reliable binding energies, a suitable charge-referencing method must be applied. In the case of ionic liquids with a long alkyl chain ($n \geq 8$), charge-referencing can be accomplished by setting the binding energy of the aliphatic carbon component ($C_{aliphatic}$) equal to an internal reference value, which is 285.0 eV.[88, 108, 125]

However, for ionic liquids with shorter alkyl chains, indirect charge referencing is achieved by setting the measured binding energy of N_{cation} 1s equal to that of their long-chain equivalent.[88]

To determine that this charge referencing technique is viable, a series of short alkyl chain analogues were evaluated.

The cation size has been reduced to $[(C_4C_1)_2dmg]^+$ and $[(C_4C_4)_2dmg]^+$ to evaluate whether the length of the alkyl chain impacts on cation–anion interactions. A comparison between the binding energies in Table 3.2 for the

same anion, show that a decrease in alkyl chain length has negligible impact upon the electronic environment of the anion. For example, N_{cation} 1s for $[(C_4C_1)_2dmg][BF_4]$ is set to 400.4 eV (where 400.4 eV is the measured binding energy of N_{cation} 1s for $[(C_8C_1)_2dmg][BF_4]$), which has been charge referenced by setting $C_{aliphatic}$ to 285.0 eV.

It must be stressed, however, that this procedure is only valid for a series of ionic liquids containing structurally similar cations and identical anions as it has been shown that the nature of the anion does affect the binding energy of N_{cation} 1s.[88, 108, 125, 127, 129] The influence of the anion on cation photoemissions will be discussed further in *Section 3.2.3*.

Table 3.2. Experimental binding energies in eV for the ionic liquids studied in this work. The associated experimental error is 0.1 eV. $[(C_8C_1)_2dmg]^+$ compounds charge corrected by setting $C_{aliphatic}$ 1s to 285.0 eV. The corrected N_{cation} 1s values were then used to charge reference the smaller chain analogues where the anion is kept the same.

		Binding Energy / eV											
Compound		Cation					Anion						
Cation	Anion	$C_{aliphatic}$ 1s	C_{inter} 1s	C_{hetero} 1s	C_{core} 1s	N_{cation} 1s	C_{CF3} 1s	N_{anion} 1s	O 1s	F 1s	S $2p_{3/2}$	P $2p_{3/2}$	B 1s	Cl $2p_{3/2}$
$[(C_8C_1)_2dmg]^+$	Cl^-	285.0	285.5	286.0	288.1	400.1	-	-	-	-	-	-	-	196.4
$[(C_4C_1)_2dmg]^+$	Cl^-	284.7	285.3	285.8	288.2	400.1	-	-	-	-	-	-	-	196.4
$[(C_4C_4)_2dmg]^+$	Cl^-	284.9	285.4	286.0	288.2	400.1	-	-	-	-	-	-	-	196.4
$[(C_8C_1)_2dmg]^+$	$[BF_4]^-$	285.0	285.8	286.2	288.5	400.4	-	-	-	685.7	-	-	194.0	-
$[(C_4C_1)_2dmg]^+$	$[BF_4]^-$	284.9	285.3	286.2	288.5	400.4	-	-	-	685.6	-	-	193.8	-
$[(C_4C_4)_2dmg]^+$	$[BF_4]^-$	284.9	285.4	286.2	288.6	400.4	-	-	-	685.5	-	-	193.8	-
$[(C_8C_1)_2dmg]^+$	$[PF_6]^-$	285.0	285.6	286.4	288.8	400.7	-	-	-	686.5	-	136.3	-	-
$[(C_4C_1)_2dmg]^+$	$[PF_6]^-$	285.1	285.5	286.4	288.8	400.7	-	-	-	686.5	-	136.5	-	-
$[(C_4C_4)_2dmg]^+$	$[PF_6]^-$	285.2	285.8	286.5	288.8	400.7	-	-	-	686.5	-	136.4	-	-
$[(C_8C_1)_2dmg]^+$	$[NTf_2]^-$	285.0	285.5	286.5	288.9	400.7	292.9	399.3	532.6	688.8	168.9	-	-	-
$[(C_4C_1)_2dmg]^+$	$[NTf_2]^-$	285.1	285.5	286.5	288.9	400.7	293.0	399.5	532.7	688.9	169.0	-	-	-
$[(C_4C_4)_2dmg]^+$	$[NTf_2]^-$	285.2	285.5	286.5	288.8	400.7	293.0	399.4	532.6	688.9	168.9	-	-	-

3.2.4. Effect of the Anion

XPS has been successfully used to probe cation–anion interactions in ionic liquids.[88, 122, 125, 127] It has been previously acknowledged that anion basicity influences the electronic environment of the cation, and is thought to occur through a transfer of charge from anion to cation. This is reflected in the binding energy of the N_{cation} 1s, C_{core} 1s and C_{hetero} 1s where the binding energies follows the trend $[NTf_2]^-$ > $[BF_4]^-$ > Cl^-.[88, 108, 127] Unsurprisingly, the same trend is also observed for guanidinium-based ionic liquids which can be seen in Figure 3.6.

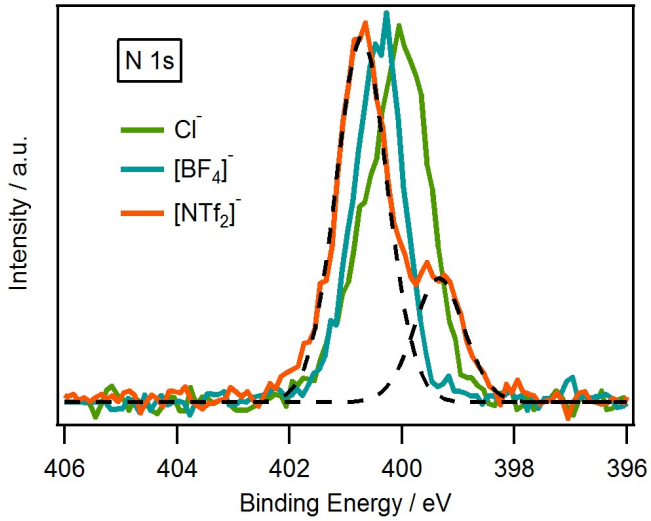


Figure 3.6. N 1s XP spectra of $[(C_8C_1)_2dmg][NTf_2]$, $[(C_8C_1)_2dmg][BF_4]$ and $[(C_8C_1)_2dmg][Cl]$. Intensities are normalised to the N_{cation} 1s peak for $[(C_8C_1)_2dmg][BF_4]$. XP spectra were charge corrected by referencing the aliphatic C 1s photoemission peak to 285.0 eV. Deconstruction of the N 1s XP photoemission peaks (dashed line) for the $[(C_8C_1)_2dmg][NTf_2]$ highlighting the two nitrogen electronic environments, N_{cation} at higher binding energy and N_{anion} at lower binding energy.

3.3. Comparison of Guanidinium and Other Nitrogenous Ionic Liquids

Having obtained reliable and reproducible binding energies, comparisons can be made between N 1s binding energies of $[NTf_2]^-$ guanidinium-based ILs with other nitrogen-based cations such as pyrrolidinium,[125] imidazolium[88] and ammonium.[127] Normalisation was accomplished using the F 1s photoelectron peak for the $[NTf_2]^-$ anion for $[C_8C_1Pyrr][NTf_2]$.

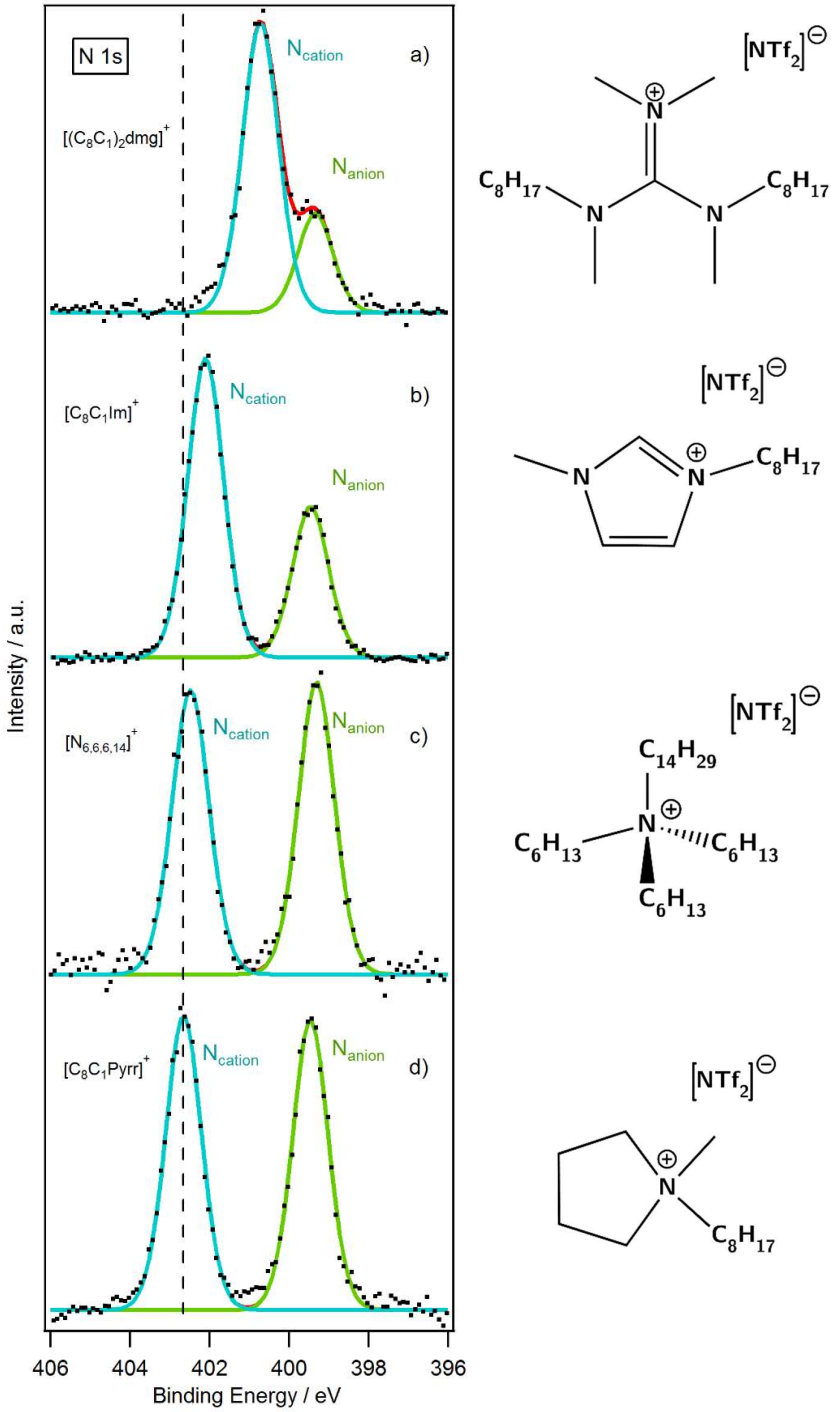


Figure 3.7. N 1s XP spectra of a) $[(C_8C_1)_2dmg][NTf_2]$, b) $[C_8C_1Im][NTf_2]$, c) $[N_{6,6,6,14}][NTf_2]$ and d) $[C_8C_1Pyrr][NTf_2]$. Intensities are normalised to the F 1s peak for $[C_8C_1Pyrr][NTf_2]$. XP spectra were charge corrected by referencing the aliphatic C 1s photoemission peak to 285 eV. Dashed line to guide the reader's eye only.

As shown in Figure 3.7a, there are two nitrogen peaks which correspond to two nitrogen electronic environments, *i.e.* the three nitrogen atoms of the cation

and the single nitrogen atom of the $[NTf_2]^-$ anion. Considering the stoichiometry of the molecule the ratio of N_{cation} : N_{anion} is expected to be 3 : 1. The N 1s high-resolution scan shows that these results are in good agreement with the expected ratio. Figure 3.7b, illustrates two nitrogen peaks which correspond to two nitrogen electronic environments in the imidazolium ionic liquid. However, the ratio of N_{cation} to N_{anion} was expected to be 2 : 1 from the stoichiometry of the molecule, and the N 1s high-resolution scan was in good agreement with this. Similarly, this is also true for the pyrrolidinium and ammonium ionic liquid, Figure 3.7c–d, where the ratio of N_{cation} to N_{anion} was expected to be 1 : 1 and these results were also in good agreement with the expected ratio.

Table 3.3. N_{cation} 1s Binding Energies for various nitrogen-based cations with long alkyl chain (n ≥ 8).

	$[(C_8C_1)_2dmg][NTf_2]$	$[C_8C_1Im][NTf_2]$	$[N_{6,6,6,14}][NTf_2]$	$[C_8C_1Pyrr][NTf_2]$
N_{cation} 1s BE (eV)	400.7	402.1	402.5	402.7

Interestingly, there is a notable difference between the binding energies of the N_{cation} 1s peak for the four ionic liquids families, Table 3.3. Looking firstly at the pyrrolidinium cation, it noticeably possesses the highest binding energy for the N_{cation} 1s peak. The reason for this may be explained by the charge being localised entirely on the single nitrogen atom of the pyrrolidinium ring. The ammonium cation shows a binding energy very similar to the pyrrolidinium, due to the charge being localised on a single nitrogen atom. For the imidazolium, however, the positive charge is distributed across the π-ring system resulting in a slightly lower binding energy by 0.6 eV. The N_{cation} 1s peak for the guanidinium cation occurs at an even lower binding energy with a striking difference of 2.0 eV from that of the pyrrolidinium cation. This can be explained by considering that the positive charge of the guanidinium cation is distributed across three nitrogen atoms as opposed to just one in the pyrrolidinium cation. This is further reinforced by the FWHM of the N_{cation} 1s where for $[C_8C_1Im][NTf_2]$, $[N_{6,6,6,14}][NTf_2]$ and $[C_8C_1Pyrr][NTf_2]$ are equal to 1.0 eV, and to 1.1 eV for $[(C_8C_1)_2dmg][NTf_2]$ representing a single nitrogen electronic environment.

3.4. Ionic Liquid Mixtures

Present activity surrounding the applications of ionic liquids has focused on their use as solvents for chemicals synthesis.[26, 27, 166-169]

The ability to design ionic liquids by selection of cations and anions is extensive and recent attempts have been made to take this idea further by using mixtures of ionic liquids. The use and study of ionic liquid mixtures are still in their early stages. This could be due to the even larger number of ionic combinations, not to mention that ionic liquid mixtures can be prepared by mixing not only ILs, but also for example, an IL with higher melting salts.

It is well documented that some ionic liquids, notably $[C_4C_1Im]Cl$, can dissolve cellulose. Though, to use cellulose as a feedstock for industrially more valuable chemicals, further processing is necessary, usually in the form of a second independent reaction step. By using mixtures of $[C_4C_1Im][HSO_4]$ (3.5 mmol) in $[C_4C_1Im]Cl$ (20 g) it was possible to achieve this process in a one-pot reaction, where the cellulose is dissolved by the chloride while the acidic ionic liquid is used for the catalytic conversion of the dissolved cellulose to low-molecular weight products.[170]

Another suggested use of mixtures of ionic liquids is for ruthenium catalysed hydroformylation reactions in mixtures of $[C_4C_1Im][NTf_2]$ with $[C_4C_1Im]Cl$, which showed increasing conversion rates with decreasing chloride concentrations indicating higher reactivity due to better solubility of the reactants.[171]

$[C_1C_4Pyrr][NTf_2]$ and $[C_1C_3Pyrr][FSI]$, and their binary mixtures were investigated to better understand their behaviour as electrolyte components in supercapacitor and lithium battery systems. The IL mixtures showed excellent low temperature properties far exceeding those of the pure IL materials. For example, at −40 °C the conductivity of binary mixtures was found to be up to four orders of magnitude higher than that of the pure ILs.[172]

Based on the numerous unforeseen physicochemical properties reported in the literature, it is suggested that mixtures of ILs should not be compared to mixtures of organic solvents. The individual ions which comprise each IL can interact independently with the other ions, and thus can lead to new and unexpected properties. These mixtures can show unique melting points and glass transition temperatures, often forming eutectic regions, disruptions in glass transitions, or even acting as a single set of ions.[173, 174] For example, the equimolar mixing of $[C_3C_1Pyrr][NTf_2]$ and $[C_4C_1Pyrr][NTf_2]$ exhibited only a single melting transition (T_m = −25 °C) as was also found for the two IL parents albeit at higher temperatures (10 °C for $[C_3C_1Pyrr][NTf_2]$ and −7 °C for $[C_4C_1Pyrr][NTf_2]$).[174] Other papers have reported unique ionic interactions occurring in mixtures of ionic liquids with ions, solutes, or solvents.[175-177]

The use of more systematic spectroscopic analysis methods is strongly recommended to support future studies of ionic liquid mixtures, to better understand the complex interactions between the various ions; with particular emphasis on the study of ionic combinations of ions with wildly different properties, sizes, *etc*. Some examples of potential design of melting point or phase transition behaviour have been published, however, the most promising properties of ionic liquid mixtures could be chemical, and it should be possible to design and modify ionic liquid mixtures toward specific ends. For instance, ionic liquid mixtures often exhibit improved solvent properties not readily apparent from those of the two-ion IL parents.

3.4.1. Effect of the Anion

The electronic environment within ionic liquids is one of the dominating factors governing the properties exhibited by ionic liquids and the interactions of their constituting ions with solutes. The ability to fine tune the electronic environment of ions within ionic liquid systems signifies a step forward towards the development of a material with a very specific series of physical and chemical properties to match a given application.

In 2014 Villar-Garcia *et al.* showed that changes in the composition of ionic liquid mixtures can be used to tune the electronic environment (*i.e.* the distribution of electron density) of their ions, both anions and cations.

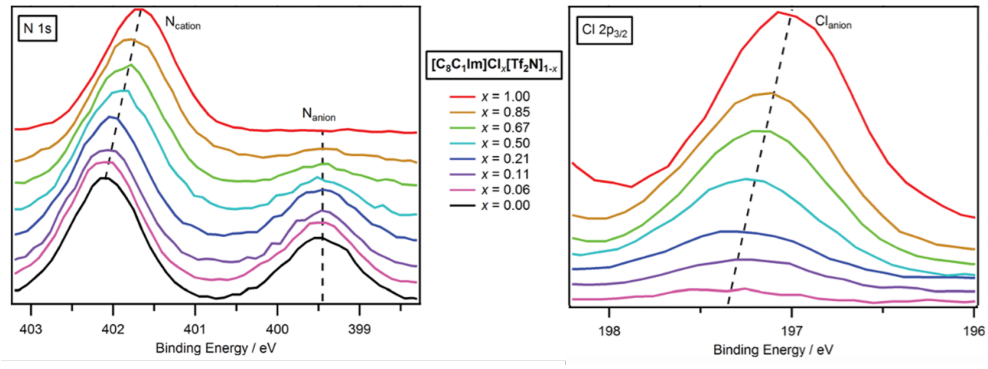


Figure 3.8. High-resolution XP spectra of the different mixture systems: N 1s and Cl $2p_{3/2}$ for $[C_8C_1Im]Cl_x[NTf_2]_{1-x}$. Data recorded for the neat ionic liquids is also included for comparison. In this case the intensity of the photoemission peaks have been normalised to the intensity of the N_{cation} 1s peak, so the natural change in peak areas with composition can be also visualised. All XP spectra are charge corrected by setting the aliphatic carbon signal, $C_{aliphatic}$ 1s, to 285.0 eV and offset vertically for clarity. Dashed lines to guide the reader's eye only.[110]

Figure 3.8 illustrates how the electronic environment of both anions and cations within ionic liquids can be tuned using mixtures, showing the N 1s and Cl $2p_{3/2}$ high-resolution XP spectra of the different $[C_8C_1Im]Cl_x[NTf_2]_{1-x}$ mixtures and respective neat ionic liquids. It can be clearly seen that for this mixture of anions of different basicity, the binding energy of the N_{cation} 1s peak changes in a quasi-linear behaviour from the characteristic energy of one of the neat ionic liquids to the other. This data agrees with the well reported structure of ionic liquid mixtures consisting of a randomly distributed mixture of all component ions.[178-180] Consequently, the cations in the ionic liquid mixture are all interacting with a statistically similar environment which is composed of an average number of both anions at the same time.[181] As a result of this mixed interaction, the net amount of charge transferred to each cation in the mixture is identical, *i.e.* the electronic environment of the cation is now distinct to that of the two neat ionic liquids.

In this study, the presence of poorly coordinating $[NTf_2]^-$ will lead to a reduction in the number of basic anions in the coordination sphere of the cation. As $[NTf_2]^-$ anions transfer less electronic charge to the cation than Cl^- anions, the cations

within the mixture will have more capacity to accept electron density from Cl^- anions. Consequently, the Cl^- anions will be able to transfer more electronic charge to these cations. This larger donation of charge will leave the Cl^- anion with less electron density and therefore, their electrons will exhibit higher binding energies than the Cl^- anion electrons in neat $[C_8C_1Im]Cl$. This shows that the final electronic environment of the cation depends upon the nature and relative percentages of the anions present in the mixture. Moreover, the presence of other anions also affects the electronic environment of the anion.

In *Section 3.3* a notable difference of 2.0 eV in the N_{cation} 1s between the guanidinium and the pyrrolidinium cations provide an opportunity to explore mixtures of these two cations and assess the effect of the cation upon the anion electronic environment. Furthermore, correlating with Villar-Garcia's results, in a mixture of two different cations with the same anion, charge transfer and anion–cation interactions, could mean that the anion will be interacting with both types of cations at the same time. Hence an impact on the electronic environment could potentially be expected upon both anion and cation.

To explore this assumption, ionic liquid mixtures of $[(C_8C_1)_2dmg]^+$ and $[C_8C_1Pyrr]^+$, coupled with three different anions were investigated. The choice of aliphatic component ($n \geq 8$), was intended to ease charge-referencing by setting the binding energy of the aliphatic carbon component ($C_{aliphatic}$) equal to the internal reference value, which is 285.0 eV. The anions were chosen accordingly with anion basicity as this influences the electronic environment of the cation where binding energies follow the trend $[NTf_2]^- > [BF_4]^- > Cl^-$, as seen previously in this *Section 3.2.4*.

Figure 3.9a shows the N 1s region of cation mixtures when paired with $[NTf_2]^-$ anion. The anion does not seem to have any impact upon the N_{cation} electronic environment as the elemental binding energy of the cations in the mixture remained unchanged when compared with the neat ionic liquids that constitute it, Table 3.4.

In regards to the $[BF_4]^-$ anion, which is more coordinating than the $[NTf_2]^-$ anion, some impact is expected upon the cations electronic environment. Though, there is no significant shift for the N_{cation} on both cations, Figure 3.9b.

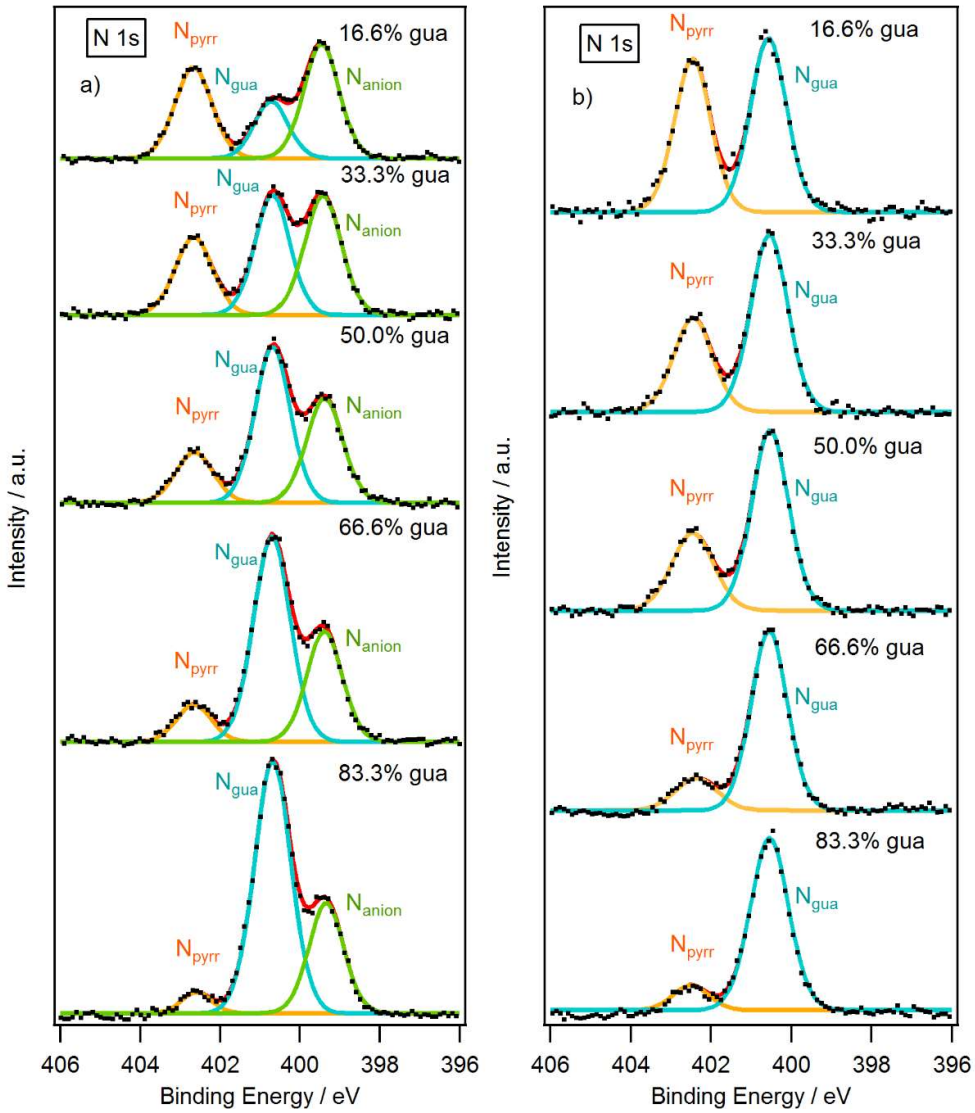


Figure 3.9. N 1s region for the mixtures of $[(C_8C_1)_2dmg]^+$ and $[C_8C_1Pyrr]^+$ when paired with a) $[NTf_2]^-$ and b) $[BF_4]^-$ anions. $[NTf_2]^-$ mixtures normalised to the N_{anion} 1s and $[BF_4]^-$ mixtures normalised to $[(C_8C_1)_2dmg]^+$ N_{cation} 1s, spectra offset vertically for clarity.

When paired with a more coordinating and more basic Cl^- anion, the single ILs show a window of 2.0 eV on the N 1s region, Table 3.4. On a mixture of these two cations, the anion could potentially have a significant impact on the N_{cation} 1s environment. The anion, while interacting with both types of cations at the same time, can on average influence a shift on each individual N_{cation} 1s

environment towards the neat ILs, while depending on the mixture ratio. The mixture shows two cation environments, though a slight shift from the neat ILs can be observed, Figure 3.10. The binding energy N_{cation} 1s for the neat $[(C_8C_1)_2dmg]Cl$ is 400.1 eV, while the N_{cation} 1s for $[C_8C_1Pyrr]Cl$ is 402.1 eV and although the mixtures varied from 402.2 to 401.9 eV, the difference is only slightly outside the experimental error. The mixture nevertheless seems to shift consistently with the mixture composition towards the neat ILs.

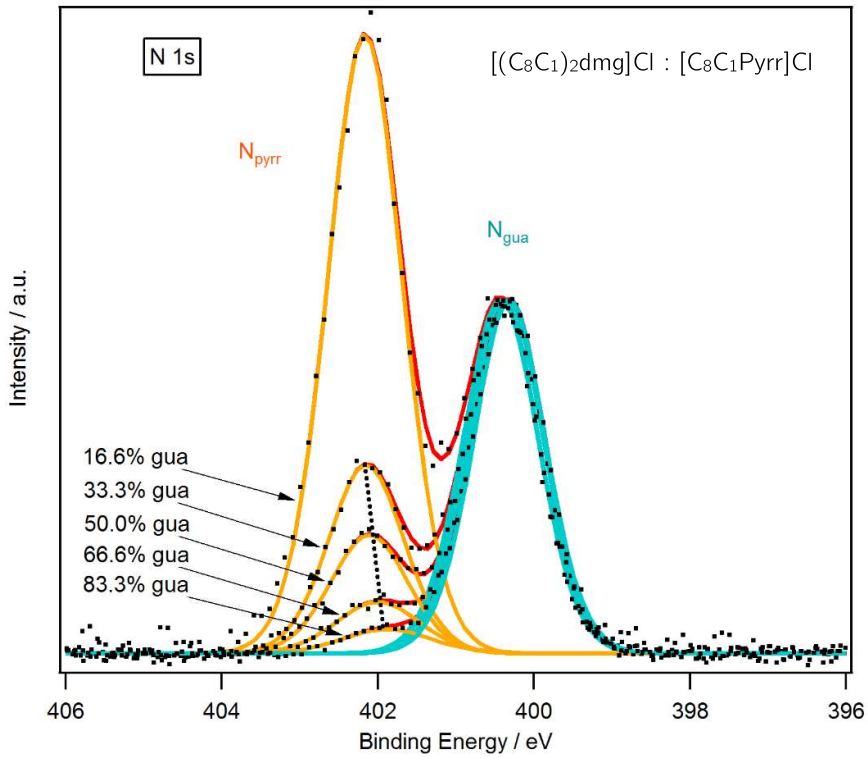


Figure 3.10. N 1s region for the mixture of ionic liquids with two different cations when paired with Cl^- anion. Mixture normalised to the $[(C_8C_1)_2dmg]^+$ N_{cation} 1s. Noteceable shift can be acknowledge on the N_{cation} 1s of the $[C_8C_1Pyrr]^+$ cation. Dotted line to guide the reader's eye only.

Table 3.4. Experimental binding energies in eV for $[(C_8C_1)_2dmg]^+$ and $[C_8C_1Pyrr]^+$ with Cl^-, $[BF_4]^-$ and $[NTf_2]^-$ anions and respective mixtures. The associated experimental error is 0.1 eV (*binding energies with 2 decimal points to show trend only). All compounds charge corrected by setting $C_{aliphatic}$ 1s to 285.0 eV. Neat ILs highlighted to aid comparison.

		Binding Energy / eV												
Compound		Cation						Anion						
Cation	Anion	$C_{aliphatic}$ 1s	C_{inter} 1s	C_{hetero} 1s	C_{core} 1s	N_{gua} 1s	N_{pyrr} 1s	C_{CF3} 1s	N_{anion} 1s	O 1s	F 1s	S $2p_{3/2}$	*B 1s	*Cl $2p_{3/2}$
$[C_8C_1Pyrr]^+$	Cl^-	285.0	285.5	286.1	-	-	402.1	-	-	-	-	-	-	196.88
16.6% $[(C_8C_1)_2dmg]^+$	Cl^-	285.0	285.5	286.2	288.4	400.4	402.2	-	-	-	-	-	-	196.71
33.3% $[(C_8C_1)_2dmg]^+$	Cl^-	285.0	285.5	286.2	288.5	400.4	402.1	-	-	-	-	-	-	196.62
50.0% $[(C_8C_1)_2dmg]^+$	Cl^-	285.0	285.6	286.1	288.5	400.4	402.1	-	-	-	-	-	-	196.59
66.6% $[(C_8C_1)_2dmg]^+$	Cl^-	285.0	285.6	286.1	288.4	400.3	402.0	-	-	-	-	-	-	196.51
83.3% $[(C_8C_1)_2dmg]^+$	Cl^-	285.0	285.6	286.0	288.4	400.3	401.9	-	-	-	-	-	-	196.48
$[(C_8C_1)_2dmg]^+$	Cl^-	285.0	285.5	286.0	288.1	400.1	-	-	-	-	-	-	-	196.42
$[C_8C_1Pyrr]^+$	$[BF_4]^-$	285.0	285.5	286.5	-	-	402.4	-	-	-	685.9	-	194.14	-
16.6% $[(C_8C_1)_2dmg]^+$	$[BF_4]^-$	285.0	285.5	286.5	288.7	400.6	402.5	-	-	-	685.8	-	194.16	-
33.3% $[(C_8C_1)_2dmg]^+$	$[BF_4]^-$	285.0	285.6	286.5	288.7	400.6	402.4	-	-	-	685.8	-	194.08	-
50.0% $[(C_8C_1)_2dmg]^+$	$[BF_4]^-$	285.0	285.7	286.4	288.6	400.5	402.4	-	-	-	685.7	-	194.05	-
66.6% $[(C_8C_1)_2dmg]^+$	$[BF_4]^-$	285.0	285.8	286.4	288.6	400.5	402.4	-	-	-	685.7	-	194.02	-
83.3% $[(C_8C_1)_2dmg]^+$	$[BF_4]^-$	285.0	285.7	286.4	288.6	400.5	402.5	-	-	-	685.7	-	193.99	-
$[(C_8C_1)_2dmg]^+$	$[BF_4]^-$	285.0	285.8	286.2	288.5	400.4	-	-	-	-	685.7	-	193.98	-
$[C_8C_1Pyrr]^+$	$[NTf_2]^-$	285.0	285.7	286.8	-	-	402.7	293.0	399.5	532.7	688.8	169.0	-	-
16.6% $[(C_8C_1)_2dmg]^+$	$[NTf_2]^-$	285.0	285.7	286.7	288.9	400.7	402.7	293.0	399.5	532.7	688.8	169.0	-	-
33.3% $[(C_8C_1)_2dmg]^+$	$[NTf_2]^-$	285.0	285.7	286.7	288.9	400.7	402.7	292.9	399.4	532.6	688.8	169.0	-	-
50.0% $[(C_8C_1)_2dmg]^+$	$[NTf_2]^-$	285.0	285.7	286.6	288.9	400.7	402.7	292.9	399.4	532.6	688.8	169.0	-	-
66.6% $[(C_8C_1)_2dmg]^+$	$[NTf_2]^-$	285.0	285.7	286.6	288.9	400.7	402.7	292.9	399.4	532.6	688.8	168.9	-	-
83.3% $[(C_8C_1)_2dmg]^+$	$[NTf_2]^-$	285.0	285.7	286.5	288.9	400.7	402.6	292.9	399.3	532.6	688.8	168.9	-	-
$[(C_8C_1)_2dmg]^+$	$[NTf_2]^-$	285.0	285.5	286.5	288.9	400.7	-	292.9	399.3	532.6	688.8	168.9	-	-

3.4.2. Effect of the Cation

As mentioned previously, the remarkable difference of 2.0 eV in the N_{cation} between the guanidinium and the pyrrolidinium cations provides an opportunity to explore mixtures of these two cations and assess the effect of the cation upon the anion electronic environment. Although no significant impact upon the cation mixture by the anion can be found, the cation mixture could still have an impact upon the electronic environment of the anion. Particularly when coupled with the Cl^- anion, the individual anion binding energies differ quite considerably from the pyrrolidinium to the guanidinium cation.

The poorly coordinating $[NTf_2]^-$ has shown that its electronic environment remains unaffected regardless of the cation to which it is paired to, for all the cation families studied so far, including the ones in this *thesis*.[88, 125, 127, 129] Consequently, when paired with the $[NTf_2]^-$ anion, the cation mixture does not seem to have any impact upon the anion electronic environment. This can be seen for the N_{anion} 1s, Figure 3.9a and for the F 1s region, Figure 3.11a. These findings validate Villar-Garcia's results as seen for the N_{anion} in Figure 3.8.

Looking at the $[BF_4]^-$ anion, some impact is expected upon its electronic environment. The shift for the F 1s however is within the experimental error and therefore cannot be acknowledged, Figure 3.11b while the B 1s peak is only slightly outside the experimental error, Figure 3.12 and Table 3.4.

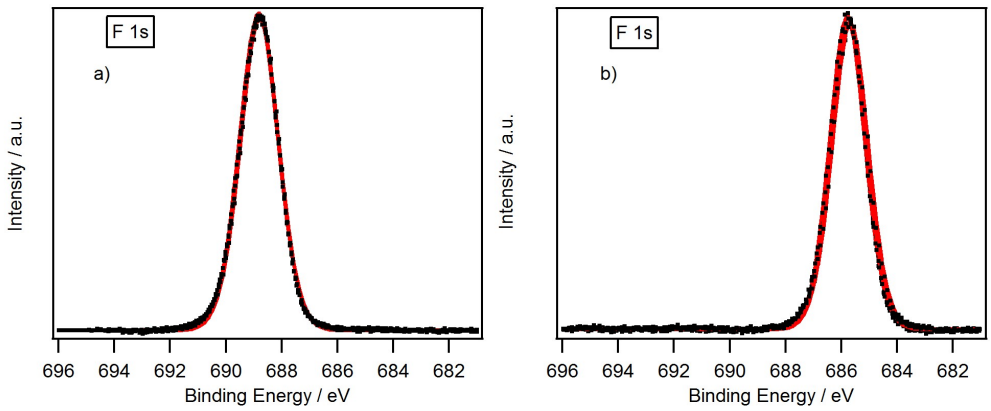


Figure 3.11. F 1s region for the mixtures of ionic liquids with two different cations when paired with a) $[NTf_2]^-$ and b) $[BF_4]^-$ anions. $[NTf_2]^-$ mixtures normalised to the N_{anion} 1s and $[BF_4]^-$ mixtures normalised to $[(C_8C_1)_2dmg]^+$ N_{cation} 1s.

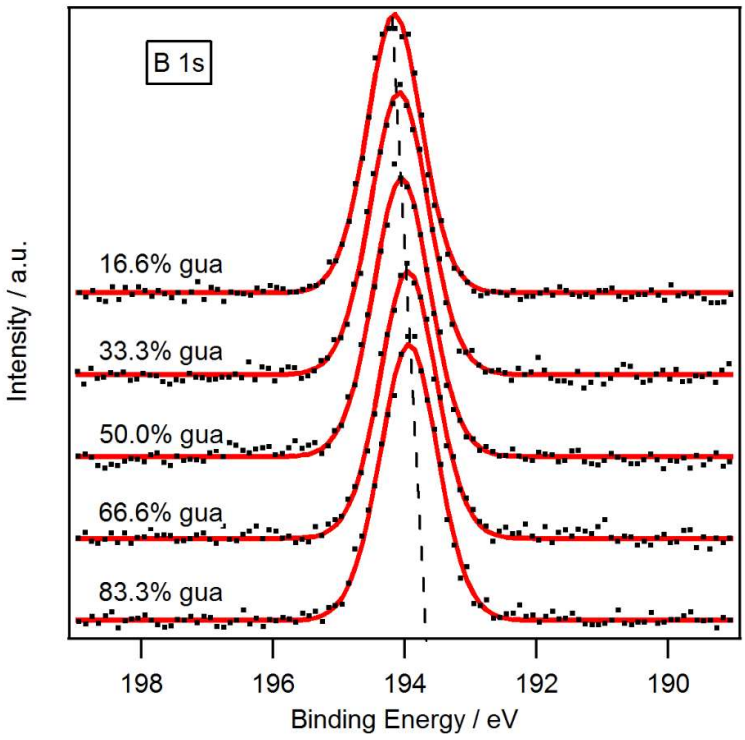


Figure 3.12. B 1s region for the mixture of ionic liquids with two different cations when paired with the $[BF_4]^-$ anion. $[BF_4]^-$ mixtures normalised to $[(C_8C_1)_2dmg]^+$ N_{cation} 1s, spectra offset vertically for clarity. Dashed line to guide the reader's eye only.

On the other hand, for mixtures with the Cl^- anion, more impact is expected from the mixture of the two cations. The neat ILs shows a difference of 0.5 eV on the Cl $2p_{3/2}$ region (196.9 eV $[C_8C_1Pyrr]^+$ to 196.4 eV $[(C_8C_1)_2dmg]^+$), validating this assumption. However, for these mixtures the obtained binding energies always lie within the experimental error (varying from 196.7 eV to 196.5 eV) although a shift towards the neat IL when varying the mixture composition can be acknowledged, Figure 3.13 and Table 3.4. Consequently, there is an impact on the anion electronic environment caused by the mixture of ILs, when compared to the neat ILs.

The difference in binding energy between the neat ILs and resulting mixture might not be as wide-ranging as expected but a series of entirely new electronic environments was developed. A change in the physicochemical properties of the resulting mixtures might however, justify using these mixtures instead of the neat ILs for a given application.

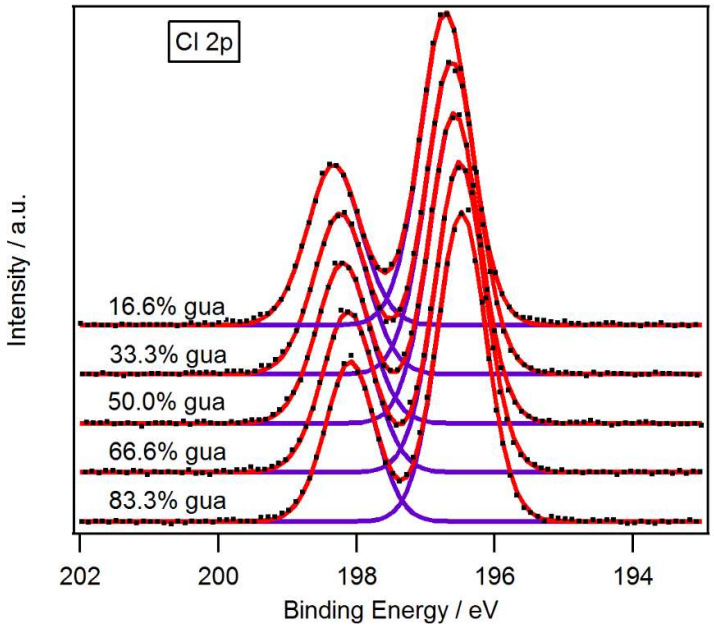


Figure 3.13. Cl 2p region for the mixture of ionic liquids with two different cations when paired with the Cl^- anion. Cl^- mixtures normalised to $[(C_8C_1)_2dmg]^+$ N_{cation} 1s, spectra offset vertically for clarity.

It should be noted that the full width at half maximum (FWHM) of the photoemission envelopes in the mixture spectra were comparable to those exhibited by the neat ionic liquid spectra, Table 3.5. This observation clearly illustrates that the XP spectra of the mixtures are not composed of a superposition of the XP spectra of each neat ionic liquid, but a new signal corresponding to a series of entirely new electronic environments.

Table 3.5. Measured experimental full width at half maximum in eV for $[(C_8C_1)_2dmg]^+$ and $[C_8C_1Pyrr]^+$ with Cl^-, $[BF_4]^-$ and $[NTf_2]^-$ anions and respective mixtures. Neat ILs highlighted to aid comparison.

Compound		FWHM / eV												
		Cation						Anion						
Cation	Anion	$C_{aliphatic}$ 1s	C_{inter} 1s	C_{hetero} 1s	C_{core} 1s	N_{gua} 1s	N_{pyrr} 1s	C_{CF3} 1s	N_{anion} 1s	O 1s	F 1s	S $2p_{3/2}$	B 1s	Cl $2p_{3/2}$
$[C_8C_1Pyrr]^+$	Cl^-	0.9	1.1	1.1	-	-	1.0	-	-	-	-	-	-	0.9
16.6% $[(C_8C_1)_2dmg]^+$	Cl^-	1.0	1.1	1.1	1.0	1.1	1.1	-	-	-	-	-	-	0.9
33.3% $[(C_8C_1)_2dmg]^+$	Cl^-	1.0	1.1	1.1	0.9	1.1	1.1	-	-	-	-	-	-	0.9
50.0% $[(C_8C_1)_2dmg]^+$	Cl^-	1.0	1.0	1.1	0.9	1.1	1.1	-	-	-	-	-	-	0.9
66.6% $[(C_8C_1)_2dmg]^+$	Cl^-	1.0	1.0	1.1	0.9	1.0	1.2	-	-	-	-	-	-	0.9
83.3% $[(C_8C_1)_2dmg]^+$	Cl^-	1.0	0.9	1.1	0.9	1.0	1.2	-	-	-	-	-	-	0.9
$[(C_8C_1)_2dmg]^+$	Cl^-	1.0	0.9	1.1	1.0	1.1	-	-	-	-	-	-	-	1.0
$[C_8C_1Pyrr]^+$	$[BF_4]^-$	1.0	1.0	1.1	-	-	1.1	-	-	-	1.5	-	1.0	-
16.6% $[(C_8C_1)_2dmg]^+$	$[BF_4]^-$	1.0	1.0	1.1	0.8	1.1	1.1	-	-	-	1.5	-	1.0	-
33.3% $[(C_8C_1)_2dmg]^+$	$[BF_4]^-$	1.0	1.1	1.1	0.8	1.1	1.1	-	-	-	1.5	-	1.0	-
50.0% $[(C_8C_1)_2dmg]^+$	$[BF_4]^-$	1.0	1.1	1.1	0.9	1.1	1.1	-	-	-	1.5	-	1.0	-
66.6% $[(C_8C_1)_2dmg]^+$	$[BF_4]^-$	1.0	1.1	1.1	0.8	1.1	1.1	-	-	-	1.5	-	1.0	-
83.3% $[(C_8C_1)_2dmg]^+$	$[BF_4]^-$	1.0	1.1	1.1	0.9	1.1	1.1	-	-	-	1.5	-	1.0	-
$[(C_8C_1)_2dmg]^+$	$[BF_4]^-$	1.0	1.1	1.1	0.9	1.1	-	-	-	-	1.4	-	0.9	-
$[C_8C_1Pyrr]^+$	$[NTf_2]^-$	1.0	1.0	1.1	-	-	1.0	1.0	1.1	1.2	1.6	1.0	-	-
16.6% $[(C_8C_1)_2dmg]^+$	$[NTf_2]^-$	1.0	1.0	1.1	0.9	1.0	1.1	1.0	1.0	1.2	1.6	0.9	-	-
33.3% $[(C_8C_1)_2dmg]^+$	$[NTf_2]^-$	1.0	1.0	1.1	0.8	1.1	1.1	1.0	1.0	1.2	1.6	0.9	-	-
50.0% $[(C_8C_1)_2dmg]^+$	$[NTf_2]^-$	1.0	1.1	1.1	0.8	1.1	1.1	1.0	1.0	1.2	1.6	1.0	-	-
66.6% $[(C_8C_1)_2dmg]^+$	$[NTf_2]^-$	1.0	1.1	1.1	0.8	1.0	1.0	1.0	1.1	1.2	1.6	0.9	-	-
83.3% $[(C_8C_1)_2dmg]^+$	$[NTf_2]^-$	1.0	1.1	1.1	0.8	1.0	1.0	1.0	1.1	1.2	1.6	0.9	-	-
$[(C_8C_1)_2dmg]^+$	$[NTf_2]^-$	1.0	1.1	1.1	0.9	1.1	-	1.0	1.0	1.2	1.6	0.9	-	-

3.5. Conclusions

The successful measurement of XP spectra for a range of guanidinium-based ionic liquids, varying both cation aliphatic chain length, *n*, and the anion, demonstrates that this class of ILs are stable to measure under X-ray irradiation. Experimentally, an effective method of etching solid samples by heating to the melt, followed by cooling to form a glassy state solid, was applied to avoid the scattering of powder during argon bombardment. Surface contaminants were thus successfully removed *via* this method. However, ILs with shorter alkyl chains ($n < 8$) were observed to be less stable and have been shown to decompose under argon bombardment.[126, 182]

The electronic environments of all elements were identified and an appropriate fitting model for the C 1s region was developed. The binding energy of the aliphatic carbon ($C_{aliphatic}$ 1s) was shown to be reliable and robust as an internal charge reference. Variation of the cation bound alkyl chain length, with a common anion, was shown to have minimal impact on the electronic environment of the anion.

Comparison of binding energies for different nitrogen-based cationic structures revealed significant differences. This could be explained by considering that the positive charge of the guanidinium cation is well distributed across three nitrogen atoms, as opposed to just one in the pyrrolidinium cation, reflecting the weak bond between the guanidinium cation and the anion through the delocalisation of the positive charge around the three-nitrogen centre.

The observed electronic environments in the mixtures are the sum of long range anion–cation interactions and charge transfer events and are consequently, distinct and unique for every mixture. As mentioned previously in *Section 3.4*, the most promising properties of ionic liquid mixtures could be chemical, and although the difference in binding energy between the neat ILs and resulting mixture was somewhat lower than expected, a series of entirely new electronic environments could be acknowledged.

This research not only furthers our understanding of inter-ion interactions of ILs, but also provides a step towards being able to predict how changing the different components of an ionic liquid will impact upon their respective electronic environments, a step that is key to developing the ability to tune an ionic liquid system to meet a given purpose.

4. Probing the Structure of Guanidinium Ionic Liquids – The Use of Sulfur-based Analogues

4.1. Introduction

The chemistry of bio-based ligands, derived from the chiral pool, usually mimics natural systems. In the case of natural receptors, the archetypal example of a binding host is the guanidinium ion, which naturally occurs as a part of arginine residues.[183] Amino acid-based ILs have been synthesised in the past, and their possible applications on the dissolution of biomolecules studied.[38, 39] They are ideal candidates for chiral systems as the chiral cations/anions starting materials are renewable naturally occurring compounds and typically non-toxic.[184]

Similarly, thiouronium salts have an important role as reaction intermediates in the synthesis of thiols[185] and guanidinium salts,[186] and they are also used as peptide coupling agents.[187] The guanidine moiety has shown a remarkable difference in its chemical environment when compared to other nitrogen-based cations. The measured binding energies for the N_{cation} 1s component for the guanidinium ILs showed a large shift to lower binding energies when compared to other families of ionic liquids. These results suggest a weaker anion/cation interaction thus the anion should be more able to interact with a solid matrix and become more active in dissolution.

Remarkably, the C_{core} 1s for the guanidinium ILs also presents an interesting route of research. Cremer *et al.* acknowledged a significant shift in the ^{13}C-NMR for the C_2 position on imidazolium ILs when compared to its methylated version. However, no noticeable difference in the C_{hetero} electronic environment by XPS could be seen. On the other hand, this disruption on the ability to form hydrogen bonding with the anion *via* the C_2 position, showed an impact on the binding energy of the N_{cation} to lower binding energies.[88] This, combined with the results

from *Chapter 3* may allow us to design an ionic liquid with higher solvation ability by decreasing even further the anion/cation interactions through functionalisation of the cation especially when choosing weakly coordinating anions.

Replacement of one nitrogen atoms in the guanidinium moiety by another element, sulfur, aims to explore this assumption. The resulting thiourea moiety is abundant in nature, biodegradable and used widely in organocatalysis.[188-190] Sulfur is a bigger atom than nitrogen and the larger orbital sizes will have an influence on resonance structure which in theory should be seen as a shift in binding energy by XPS.

XPS and NMR were explored further to provide a better understanding on the specific interactions within ionic liquids, where the effect on changing a heteroatom is compared *i.e.* replacing a nitrogen from the guanidinium moiety. This was also carried out for cyclic counterparts *i.e.* replacing the methyl group on the C_2 position from the imidazolium moiety. Ionic liquids incorporating these and other structural changes were synthesised to allow analysis of the core carbon environment and will be discussed further in *Section 4.2.3 and Section 4.3*.

4.2. XPS of Guanidinium and Sulfur-based Ionic Liquids

4.2.1. Purity and Quantification

XP survey and high-resolution scans were used to establish elemental composition and purity for each ionic liquid. Spectra showing all regions are shown in *Appendix B* for all ionic liquids investigated in this *Chapter*. The experimental stoichiometries, which have been calculated from signal areas of high-resolution spectra, are presented in Table 4.1 and are all within experimental error.

Table 4.1. Measured experimental and nominal (in brackets) stoichiometries for guanidinium, sulfur and imidazolium based ionic liquids studied in this work. Associated experimental error is ± 10 - 20%.

	Composition (%)				
Compound	C 1s	N 1s	O 1s	F 1s	S 2p
[a]RSF[74,134]	0.278	0.477	0.780	1.000	0.668
$[(C_1C_1)_2dmg][NTf_2]$	39.9 (36.0)	16.7 (16.0)	14.4 (16.0)	22.6 (24.0)	6.4 (8.0)
$[(C_1)_5TU][NTf_2]$	37.8 (33.3)	11.5 (12.5)	14.2 (16.7)	23.3 (25.0)	13.3 (12.5)
$[C_1(C_1)_2ThioIm][NTf_2]$	36.6 (33.3)	11.7 (12.5)	14.2 (16.7)	24.4 (25.0)	13.1 (12.5)
$[(C_1)_2Thio][NTf_2]$	32.3 (30.4)	9.1 (8.7)	16.4 (17.4)	27.2 (26.1)	15.0 (17.4)
$[(C_1)_2Thiz][NTf_2]$	33.8 (30.4)	9.1 (8.7)	16.2 (17.4)	25.0 (26.1)	15.8 (17.4)
$[C_1C_1Im][NTf_2]$	35.3 (31.8)	14.3 (13.6)	16.0 (18.2)	25.9 (27.3)	8.5 (9.1)
$[C_1C_1C_1Im][NTf_2]$	38.2 (34.8)	14.6 (13.0)	15.8 (17.4)	23.4 (26.1)	8.1 (8.7)

[a] Relative sensitivity factors (RSF) taken from the Kratos Library. *N.B.* Hydrogen is undetectable by XPS due its low photoionisation cross-section; consequently, reported stoichiometries are determined without consideration of hydrogen content.[132]

As the cations investigated do not contain an alkyl chain with a length of eight carbons or more, charge referencing could not be accomplished by setting the $C_{aliphatic}$ 1s to 285.0 eV. Instead, the anion was kept the same, the weakly coordinating $[NTf_2]^-$ anion, which allowed us to charge reference to the F 1s photoemission peak to 688.8 eV, hence comparisons between different cations can be made.

4.2.2. Development of C 1s Fitting Models

As seen in the guanidinium series, different electronic environments of carbon often lead to unresolved peaks. For the imidazolium family, a model has been previously reported in the literature, Figure 4.1.[74, 75] Each component is colour coded to the attached structure, C_2 (orange), $C_{4,5}$, (green), $C_{6,7}$ (blue), $C_{aliphatic}$ (pink) and the CF_3 (purple).* In this model, the $C_{4,5}$ component appears at a higher BE than the $C_{6,7}$ component, this assignment has been made through chemical intuition.

* Note that C_2, $C_{4,5}$, $C_{6,7}$ are used to describe imidazolium/cyclic-based systems and C_{core}, C_{inter}, C_{hetero}, respectively, to acyclic-based systems (given the short aliphatic length of acyclic compounds in this *Chapter* there is no C_{inter} component). In addition, $S_{cation\ exocyclic}$ denotes the sulfur bound to the C_2/C_{core} position and $S_{cation\ cyclic}$ the sulfur located in the ring. $C_{S/MethylC_2}$ refers to a methyl group substituted either in the exocyclic sulfur or on the C_2/C_{core} position, respectively.

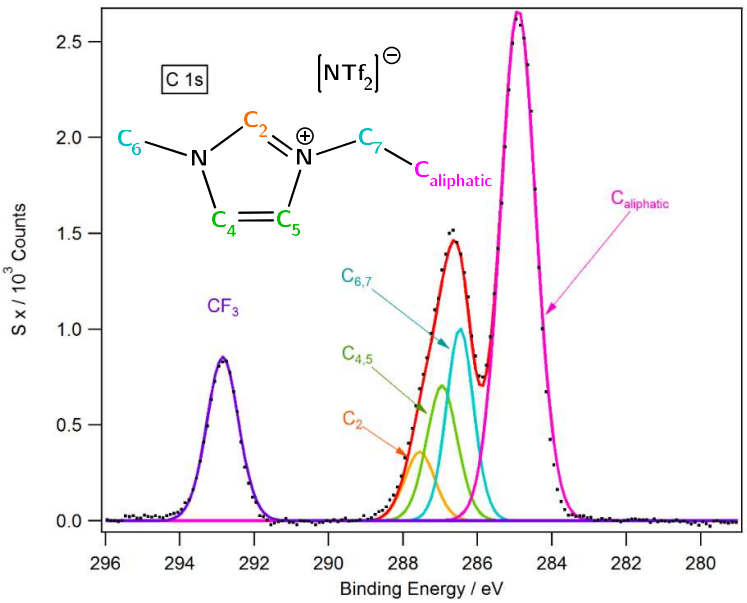


Figure 4.1. Current fitting model for the $[C_8C_1Im][NTf_2]$ C 1s region, showing the $C_{6,7}$ (blue) component at a lower BE than the $C_{4,5}$ (green) component. The resulting sum of components, envelope (red) is partially omitted to show the CF_3 and aliphatic components.

However, to fully verify the validity of this model, functionalisation of the C_4 position of the imidazolium ring was performed in order to accurately determine peak positions, as described by Coby Clarke.[191]

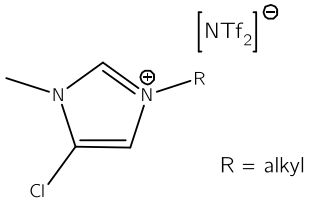


Figure 4.2. Structure of the $[C_1C_n\text{-4-ClIm}][NTf_2]$ ILs used to investigate peak fitting of the C 1s electronic environments. These imidazolium salts are abbreviated in order to denote that the chlorine is bound to the C_4 carbon. Full XP spectra of $[C_1C_8\text{-4-ClIm}][NTf_2]$ in *Appendix B*.

The comparison of chlorinated imidazolium salts, Figure 4.2, relative to non-chlorinated analogues has provided an alternative imidazolium C 1s fitting model to the previously model developed initially by the Licence group. Through the shifting of electron density, chlorination of the C_4 carbon of the imidazolium ring allowed the exact location of the $C_{4,5}$ component to be identified. It was concluded that the C_5 photoemission is most likely coincident with the C_4 signal due to similarity of local environment and these were found to be assigned to the $C_{6,7}$ component previous location. The updated peak fitting of $[C_8C_1Im][NTf_2]$ C 1s region is displayed in Figure 4.3.[191]

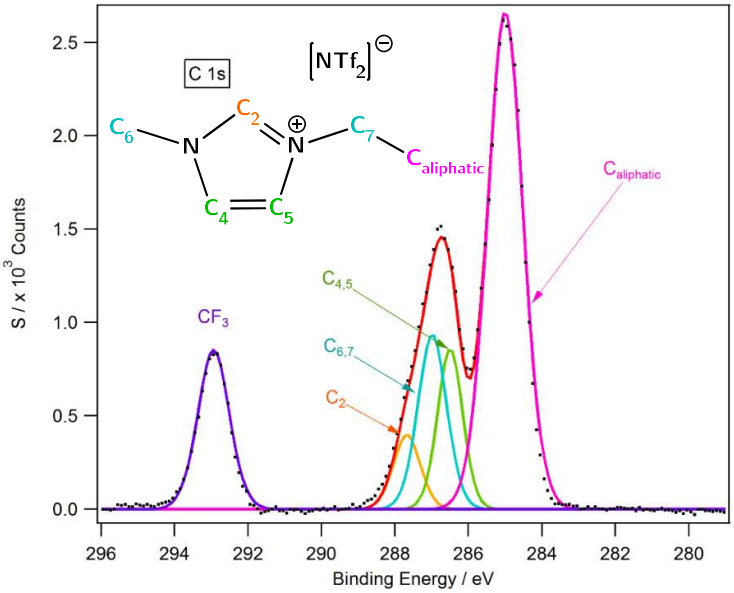


Figure 4.3. The updated fitting model for the $[C_8C_1Im][NTf_2]$ C 1s region, showing the $C_{6,7}$ component at a higher BE than the $C_{4,5}$ component. The resulting sum of components, envelope (red) is partially omitted to show the CF_3 and aliphatic component colours.

Functionalisation of the C_4 component with an electron withdrawing group (EWG) will directly affect the ring electronic environments, thus shifting $C_{4,5}$ towards higher BEs. To fully verify this fitting model, further investigation upon these systems is necessary through a series of functionalised compounds in different positions of the ring (*e.g.* C_6 position), with substituents that will allow evaluation of both electron donating (EDG) and withdrawing groups and comparisons to HOMO/LUMO calculations. This *Chapter* presents a range of ILs that have been functionalised with sulfur, Figure 4.4. These materials were design to have similarities with the guanidinium and imidazolium structures. Consequently, the C 1s fitting model for the thiouronium IL was adapted from the model developed in *Chapter 3* for the guanidinium ILs. All other cyclic sulfur containing ILs C 1s fitting models were adapted from the current imidazolium model described above, and appropriate fitting has been established for these functionalised systems.

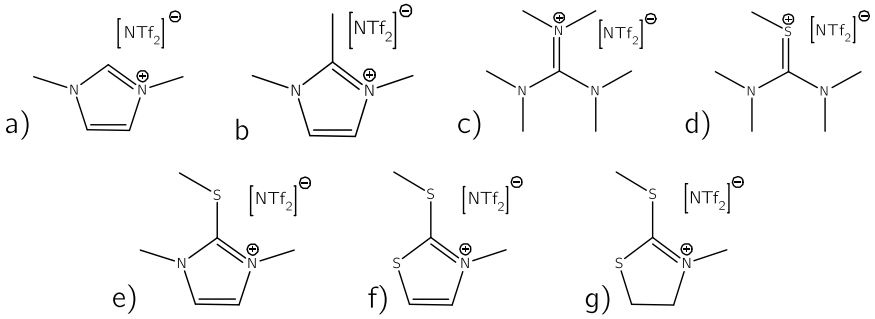


Figure 4.4. Structures and abbreviations of the ILs probed in this *Chapter*. Top, left to right: a) $[C_1C_1Im][NTf_2]$, b) $[C_1C_1C_1Im][NTf_2]$, c) $[(C_1C_1)_2dmg][NTf_2]$ and d) $[(C_1)_5TU][NTf_2]$. Bottom, left to right: e) $[C_1(C_1)_2ThioIm][NTf_2]$, f) $[(C_1)_2Thio][NTf_2]$ and g) $[(C_1)_2Thiz][NTf_2]$.

Table 4.2. Experimental binding energies in eV for guanidinium, sulfur-based and imidazolium ionic liquids studied in this work. The associated experimental error is 0.1 eV. All compounds charge corrected by setting F 1s to 688.8 eV of the corresponding $[NTf_2]^-$ anion.

Compound		Binding Energy / eV												
		Cation							Anion					
Cation	Anion	$C_{2/core}$ 1s	$C_{6,7/hetero}$ 1s	$C_{4,5/inter}$ 1s	$C_{S/MethylC_2}$ 1s	N_{cation} 1s	$S_{cation\ exocyclic}$ $2p_{3/2}$	$S_{cation\ cyclic}$ $2p_{3/2}$	C_{CF3} 1s	N_{anion} 1s	O 1s	F 1s	S_{anion} $2p_{3/2}$
$[(C_1C_1)_2dmg]^+$	$[NTf_2]^-$	288.9	286.5	-	-	400.8	-	-	292.9	399.4	532.6	688.8	169.0
$[(C_1)_5TU]^+$	$[NTf_2]^-$	288.6	286.6	-	286.2	401.1	164.7	-	292.9	399.4	532.6	688.8	169.0
$[C_1(C_1)_2ThioIm\ ]^+$	$[NTf_2]^-$	288.0	286.9	286.6	285.8	402.0	164.8	-	292.9	399.4	532.6	688.8	168.9
$[(C_1)_2Thio]^+$	$[NTf_2]^-$	288.1	286.9	286.6	285.9	402.2	164.9	165.9	292.9	399.4	532.6	688.8	168.9
$[(C_1)_2Thiz]^+$	$[NTf_2]^-$	288.4	286.9	286.7	286.1	401.5	165.1	-	292.9	399.4	532.6	688.8	169.0
$[(C_1C_1)Im]^+$	$[NTf_2]^-$	287.6	286.9	286.5	-	402.1	-	-	292.9	399.4	532.6	688.8	168.9
$[(C_1C_1C_1)Im]^+$	$[NTf_2]^-$	287.9	286.9	286.4	286.1	401.8	-	-	292.9	399.4	532.6	688.8	168.9

Table 4.3. FWHM in eV for guanidinium, sulfur-based and imidazolium ionic liquids studied in this work.

Compound		FWHM / eV											
		Cation							Anion				
Cation	Anion	$C_{2/core}$ 1s	$C_{6,7/hetero}$ 1s	$C_{4,5/inter}$ 1s	$C_{S/MethylC_2}$ 1s	N_{cation} 1s	$S_{cation\ exocyclic}$ $2p_{3/2}$	$S_{cation\ cyclic}$ $2p_{3/2}$	C_{CF3} 1s	N_{anion} 1s	O 1s	F 1s	S_{anion} $2p_{3/2}$
$[(C_1C_1)_2dmg]^+$	$[NTf_2]^-$	1.0	1.1	-	-	1.1	-	-	1.1	1.2	1.2	1.7	1.0
$[(C_1)_5TU]^+$	$[NTf_2]^-$	0.8	1.2	-	1.2	1.1	1.0	-	1.0	1.0	1.2	1.6	1.0
$[C_1(C_1)_2ThioIm]^+$	$[NTf_2]^-$	0.9	1.2	0.9	1.0	1.0	0.9	-	1.0	1.0	1.2	1.6	0.9
$[(C_1)_2Thio]^+$	$[NTf_2]^-$	0.8	1.2	0.9	0.9	1.0	1.1	1.0	0.9	1.0	1.1	1.6	0.9
$[(C_1)_2Thiz]^+$	$[NTf_2]^-$	0.8	1.1	1.1	1.0	1.1	0.9	-	1.0	1.0	1.1	1.6	0.9
$[(C_1C_1)Im]^+$	$[NTf_2]^-$	1.0	1.1	0.9	-	1.0	-	-	1.0	1.0	1.2	1.6	0.9
$[(C_1C_1C_1Im]^+$	$[NTf_2]^-$	1.0	1.2	1.0	1.2	1.1	-	-	1.1	1.2	1.2	1.7	1.0

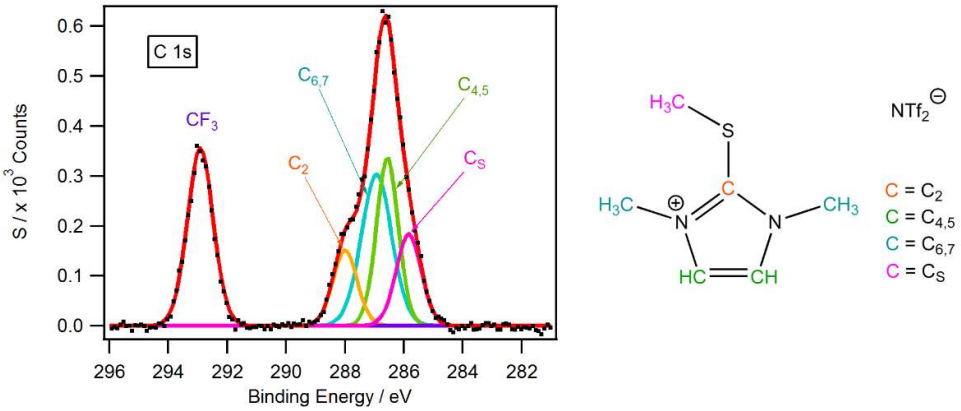


Figure 4.5. Fitting model for the C 1s region of cyclic thioimidazoliums adapted from the imidazolium model as described in this *Section*.

The C 1s fitting model for $[C_1(C_1)_2ThioIm][NTf_2]$ applying the model described is shown in Figure 4.5 and good agreement with the experimental data can be acknowledged. The measured BEs and FWHMs for all compounds investigated in this *Chapter* are presented in Table 4.2 and Table 4.3, respectively. Charge referencing to the F 1s region provides good agreement between samples and comparisons can be made. Although the C 1s fitting model used has not been fully verified for $[(C_1)_5TU][NTf_2]$, $[C_1(C_1)_2ThioIm][NTf_2]$, $[(C_1)_2Thio][NTf_2]$ and $[(C_1)_2Thiz][NTf_2]$ ionic liquids, the aim of this *Chapter* is to compare the C_2/C_{core} 1s peak and correlate it with ^{13}C-NMR. Consequently, the full comprehensive accuracy of the model should not have a relevant impact upon this study.

4.2.3. Effect of Sulfur Functionalisation

The remarkably high S 2p BE for the $[C_1(C_1)_2ThioIm]^+$ cation indicates a charge transfer between the imidazolium ring and the thio-methyl group in 2-position, leading to a significantly reduced electron density at the sulfur, Figure 4.6.

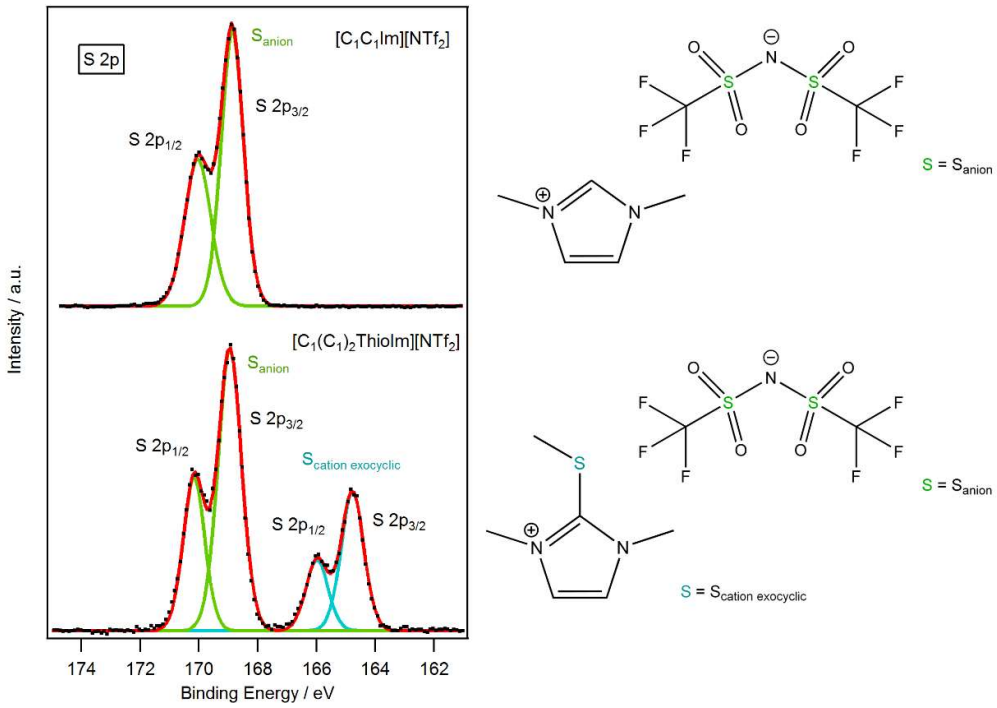


Figure 4.6. High-resolution XP spectra of the S 2p region for (top) $[C_1C_1Im][NTf_2]$ and (bottom) $[C_1(C_1)_2ThioIm][NTf_2]$, showing the lower BE of the $S_{cation\ exocyclic}$ 2p.

As a result of this effect, an enhanced electron density within the imidazolium ring is expected and a shift towards lower BEs of the C 1s components should be seen. However, the XP spectra of $[C_1(C_1)_2ThioIm][NTf_2]$ and $[C_1C_1Im][NTf_2]$, in Figure 4.7 reveal no significant shift towards lower BEs of the C 1 s signals of the imidazolium ring in $[C_1(C_1)_2ThioIm][NTf_2]$ compared to $[C_1C_1Im][NTf_2]$. Therefore, the assumed increase in electron density in the imidazolium ring of $[C_1(C_1)_2ThioIm][NTf_2]$ cannot be acknowledged. In fact, the C_2 carbon atom of $[C_1(C_1)_2ThioIm][NTf_2]$ exhibits a shift of 0.4 eV towards higher BE, which is likely due to the fact that the neighbouring S is more electronegative than hydrogen in $[C_1C_1Im][NTf_2]$.

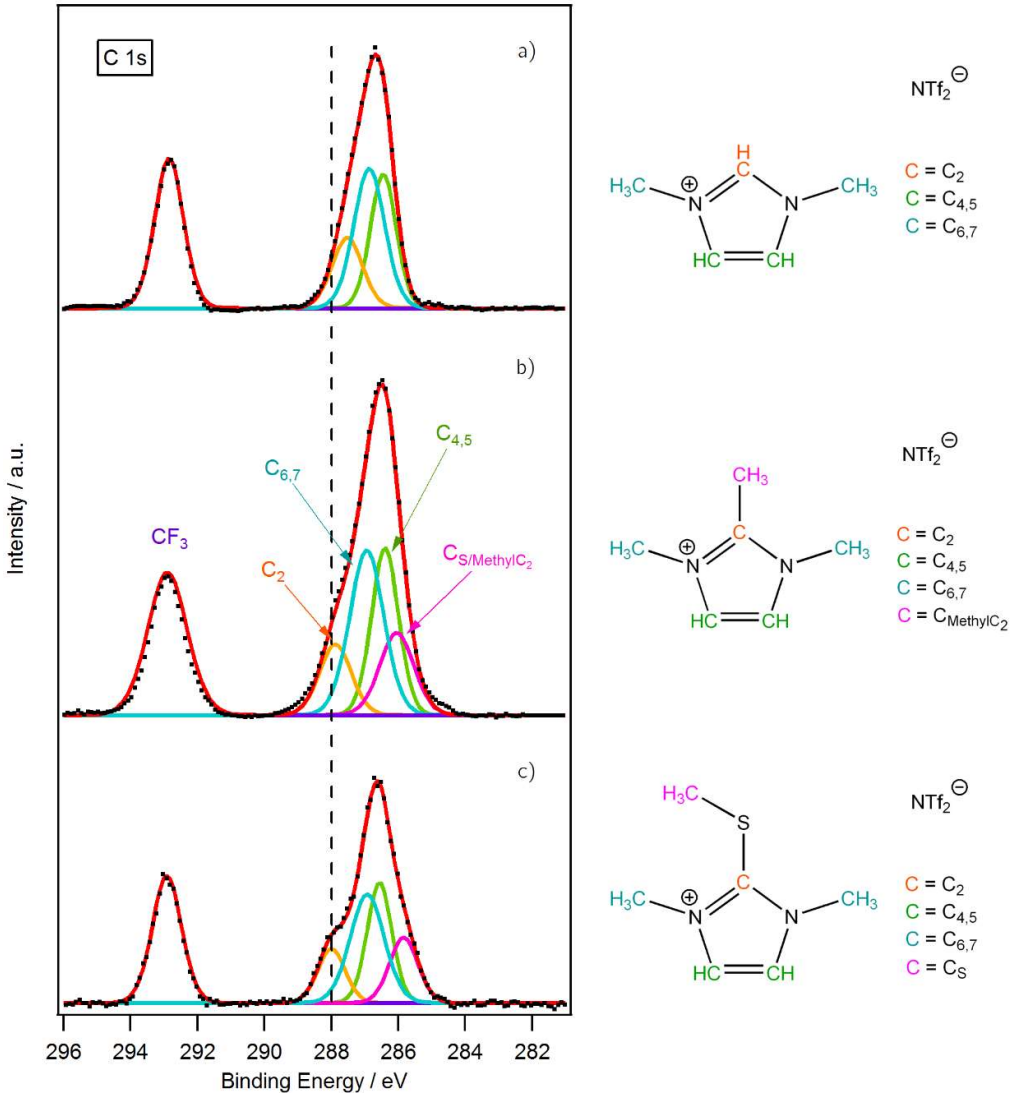


Figure 4.7. High-resolution XP spectra of the C 1s region with component fittings for a) $[C_1C_1Im][NTf_2]$, b) $[C_1C_1C_1Im][NTf_2]$, and c) $[C_1(C_1)_2ThioIm][NTf_2]$. All XP spectra charge corrected to F 1s = 688.8 eV. Intensities are normalised to the C_{CF_3} 1s photoemission peak for $[C_1C_1Im][NTf_2]$.

Cremer *et al.*,[88] followed by Taccardi *et al.*,[192] reported that $[C_1C_1C_1Im][NTf_2]$ does not exhibit a similar high BE shift when compared to $[C_1C_1Im][NTf_2]$. This is a good example where a monochromated source can provide additional information and perhaps result in incorrect assumptions. In fact, Cremer *et al.*, totals all carbon contributions of the imidazolium head group into C_{hetero} (*i.e.*, C_2, $C_{4,5}$ and $C_{6,7}$). Consequently, the overall contributions when compared to other ILs might be well within the experimental error and therefore, lead to the conclusion that the methylated version of the imidazolium cation has little

effect in the hydrogen bonding strength between anion and cation.[88] However, as a result of the monochromated source, the BEs presented in this work provide further evidence that the C_2 methylated imidazolium cation ($[C_1C_1C_1Im]^+$), has the same effect on the imidazolium ring as the sulfur in $[C_1(C_1)_2ThioIm]^+$ cation. Indeed the $C_{4,5}$ 1s and $C_{6,7}$ 1s components of $[C_1C_1Im][NTf_2]$ and $[C_1C_1C_1Im][NTf_2]$ are within the experimental error, however, there is a shift towards higher BEs, of the C_2 1s in the methylated IL, comparable with the shift of the C_2 1s of the thio-methylated version.

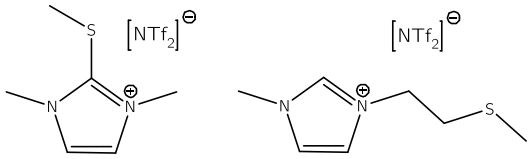


Figure 4.8. Structures and abbreviations of the ILs investigated by Taccardi *et al.*[192] Left, $[C_1(C_1)_2ThioIm][NTf_2]$ and right, $[C_1C_1ThioC_2Im][NTf_2]$.

Taccardi *et al.*,[192] also compared a structural isomer of the $[C_1(C_1)_2ThioIm]^+$ cation, containing the sulfur atom as part of a thioether group within the alkyl side chain, $[C_1C_1ThioC_2Im]^+$, Figure 4.8. Remarkably, the BE of exocyclic sulfur attached in 2-position of $[C_1(C_1)_2ThioIm][NTf_2]$ is shifted by 1.0 eV towards higher BE in comparison to the thioether S 2p signal of the $[C_1C_1ThioC_2Im]^+$ cation, Figure 4.9.

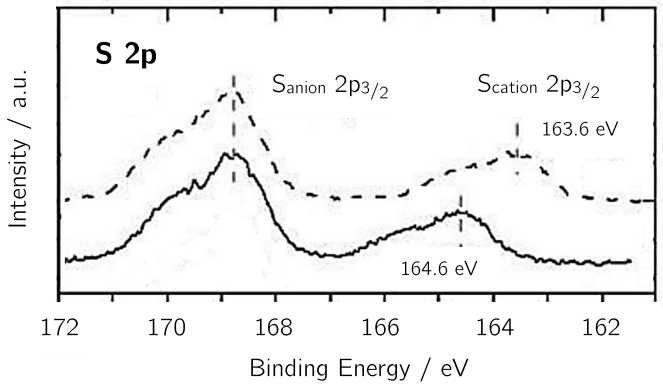


Figure 4.9. S 2p XP spectra of $[C_1C_1ThioC_2Im][NTf_2]$ (dashed), and $[C_1(C_1)_2ThioIm][NTf_2]$ (solid); spectra are offset for clarity. Figure obtained from Taccardi *et al.*[192] (modified to contain only these two ILs).

This difference is very large for an environment of neighbours with identical electronegativity. These results suggest that the positive charge of the

$[C_1(C_1)_2ThioIm]^+$ cation extends to a considerable amount over the thio-group. This consequently clarifies why the electronic environment of the C_2 methylated version of the imidazolium is very similar to the thio-methylated counterpart.

In the case of $[(C_1)_2Thio][NTf_2]$ and $[(C_1)_2Thiz][NTf_2]$, where one nitrogen has been substituted by another atom of sulfur, notable differences can be acknowledged. In fact, although the C_2 1s in $[(C_1)_2Thio][NTf_2]$ is incredibly similar to $[C_1(C_1)_2ThioIm][NTf_2]$, when removing a double bond in the imidazolium ring, $[(C_1)_2Thiz][NTf_2]$, a considerable shift towards higher BEs can be seen, Table 4.2. This shows that the positive charge is now localised between the S-C_2-N bonds, not being shared by the entire ring structure. This results in a more electron deficient C_2 1s environment. Another interesting find is the S 2p region for these ILs, Figure 4.10. Although the S 2p from the cyclic sulfur has roughly the same electronic environment than the exocyclic sulfur for $[(C_1)_2Thiz][NTf_2]$ ionic liquid (Figure 4.10c), it displays a new, higher BE peak in the $[(C_1)_2Thio][NTf_2]$ counterpart (Figure 4.10b). The cyclic sulfur seems to be more electron poor than the exocyclic sulfur, which suggests that the delocalisation of the positive charge is now shared, resulting in a lower BE in the C_2 1s of $[(C_1)_2Thio][NTf_2]$ and therefore a higher BE in $[(C_1)_2Thiz][NTf_2]$.

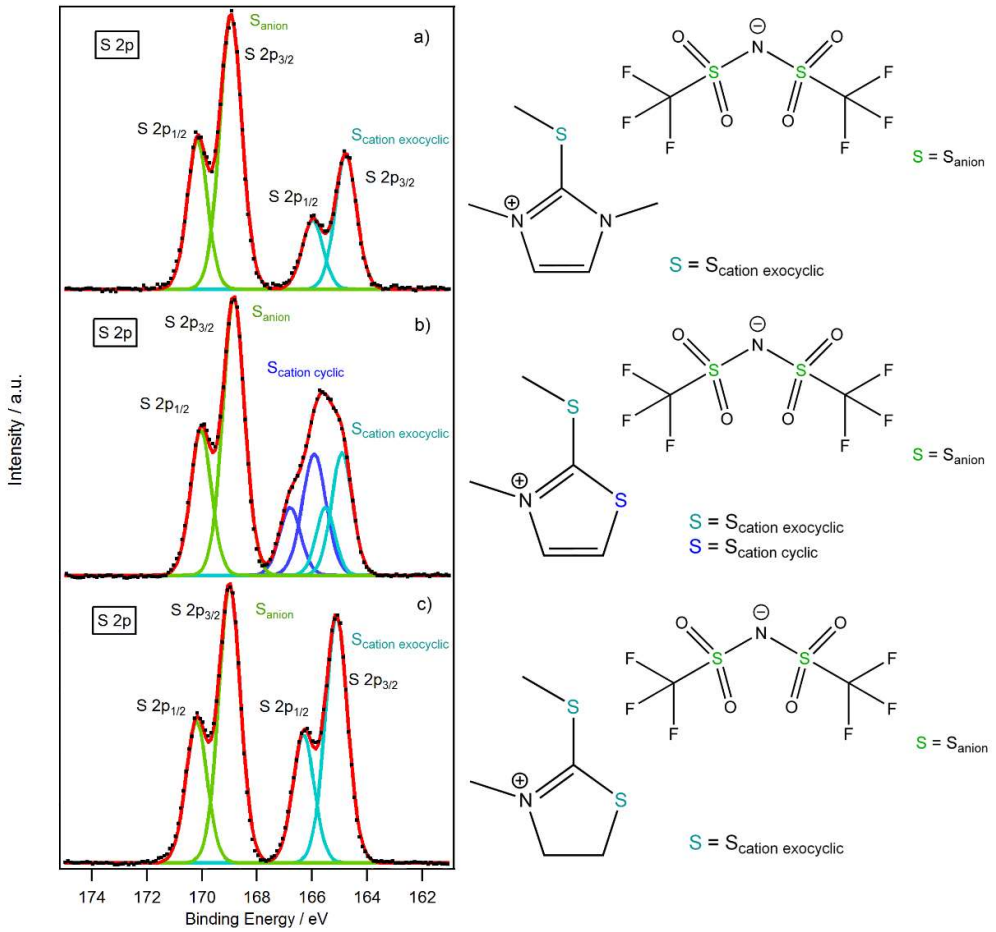


Figure 4.10. High-resolution XP spectra of the S 2p region with component fittings for a) $[C_1(C_1)_2ThioIm][NTf_2]$, b) $[(C_1)_2Thio][NTf_2]$, and c) $[(C_1)_2Thiz][NTf_2]$. All XP spectra charge corrected to F 1s = 688.8 eV. Intensities are normalised to the S_{anion} 2p photoemission peak for $[C_1(C_1)_2ThioIm][NTf_2]$.

In the particular case of the acyclic ILs described in this work, the substitution of one of the nitrogen atoms upon the guanidinium moiety shows the opposite trend regarding the C_{core} 1s BE shift. The guanidinium cation core, as seen in *Chapter 3*, has a remarkable resonance structure which surrounds the carbon at the centre, resulting in a more electron poor environment. Herein, the addition of sulfur disrupts this resonance structure, providing a more localised charge between the N-C_{core}-N and/or S-C_{core}-N bond. The C_{core} in the case of the acyclic thiouronium cation is however more electron deficient than the C_2 in the $[C_1(C_1)_2ThioIm][NTf_2]$ IL, only comparable with the $[(C_1)_2Thiz][NTf_2]$, Figure 4.11. These results suggest that the positive charge is clearly more

localised in these cases when compared with the resonance structure of the ring or the guanidinium moeity.

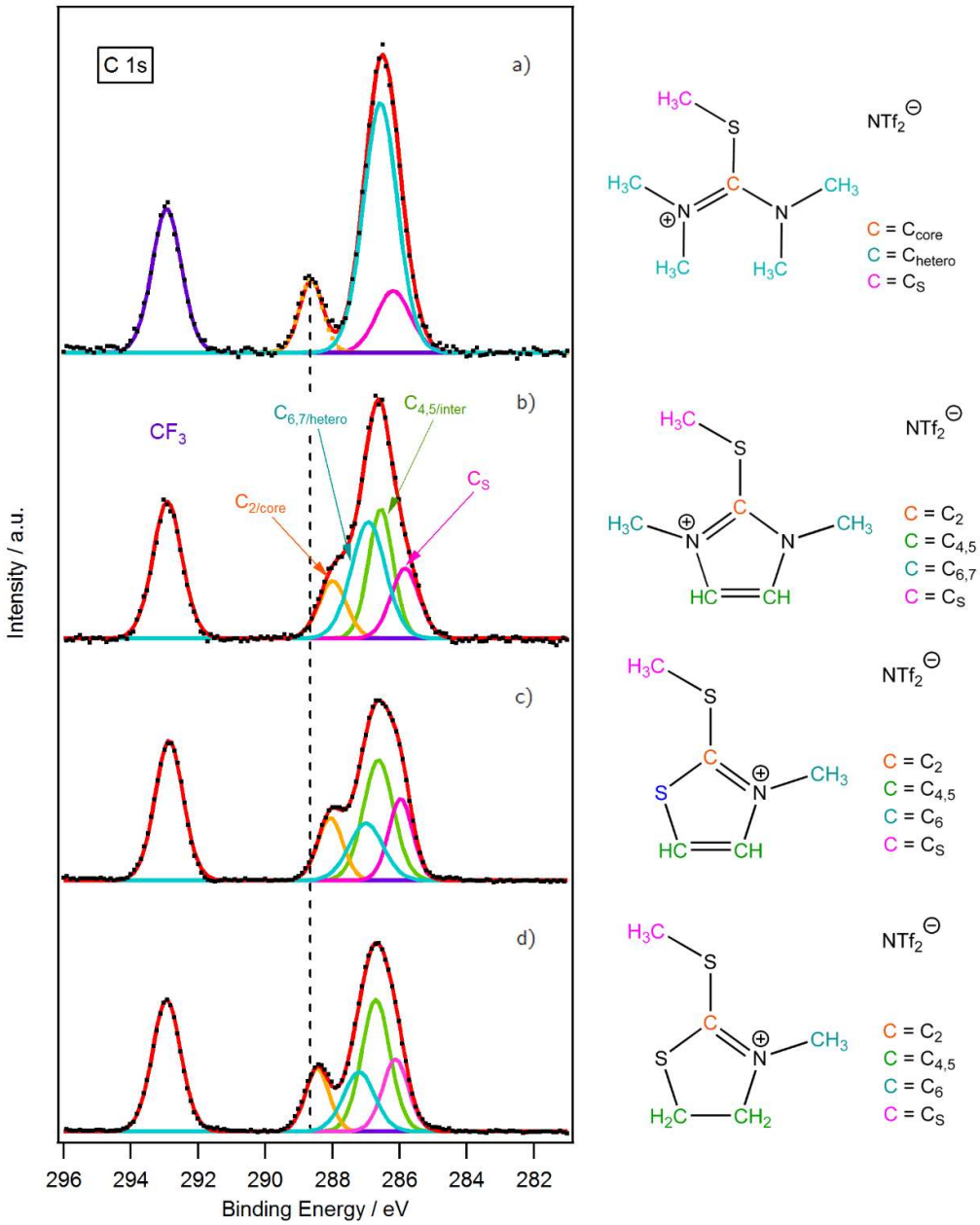


Figure 4.11. High-resolution XP spectra of the C 1s region with component fittings for a) $[(C_1)_5TU][NTf_2]$, b) $[C_1(C_1)_2ThioIm][NTf_2]$, c) $[(C_1)_2Thio][NTf_2]$ and d) $[(C_1)_2Thiz][NTf_2]$. All XP spectra charge corrected to F 1s = 688.8 eV. Intensities are normalised to the C_{CF_3} 1s photoemission peak for $[(C_1)_5TU][NTf_2]$.

The opposite trend of $C_{2/core}$ 1s could be seen upon the N_{cation} 1s BEs of all ILs investigated, Table 4.2. This suggests that the charge transfer between cation

and anion is weakened, especially in the guanidinium core, as result of its higher degree of charge delocalisation.

4.3. Comparisons to ^{13}C-NMR

It is well known that solvents can have significant impact upon electronic interactions between cation and anion. As such, to eliminate potential solvent/solute interactions, NMR measurements should be done on the neat IL (with solvent in an insert). As all ILs studied herein were solids (with the exception of $[(C_1)_2Im][NTf_2]$), ^{13}C-NMRs were performed in DMSO-d_6. Nevertheless, although this solvent effect can occur, a reliable standard is provided by the CF_3 of the $[NTf_2]^-$ anion.

Cremer *et al.*[88] reported a systematic XPS, NMR and theoretical study upon $[C_8C_1Im]X$ and $[C_8C_1C_1Im]X$ for Br^- and $[NTf_2]^-$. Natural bond order (NBO) calculations shown that for less basic and less strongly coordinating anions, the on-top configuration is energetically favoured; this also holds true for $[C_8C_1C_1Im]X$ ILs, where the most acidic proton in 2-position is substituted by a neutral methyl group. It was concluded that despite the considerably lower contribution of hydrogen bond type interactions in the methylated $[C_8C_1C_1Im]X$ ILs (deduced from NBO analysis and ^{1}H-NMR), the anion-dependent charge transfer is nearly identical to that for the non-methylated homologue ILs (deduced by natural population analysis of atomic charges (NPA) and XPS). However, as seen in *Section 4.2.3*, XPS shows a shift towards higher BEs, of the C_2 1s on the methylated IL which was missed previously in this publication.

From the ^{13}C-NMR measurements, Figure 4.12, it can be seen that the peak assigned to C_2 undergoes a clear downfield shift of about 8 ppm towards higher values upon methylation, which is a general feature in aromatic systems, when a proton is substituted with a methyl group.[193]

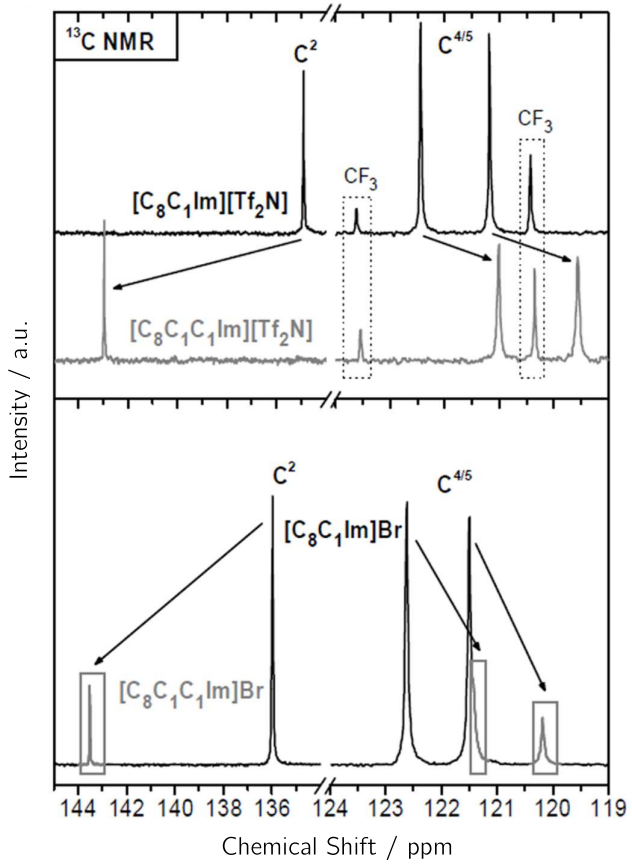


Figure 4.12. Imidazolium ring signals in ^{13}C-NMR of [C_8C_1Im][NTf_2] (black curves) and [$C_8C_1C_1$Im][NTf_2] (grey curves) (top) and of the 5:1 mixture of [C_8C_1Im]Br:[$C_8C_1C_1$Im]Br (bottom black curve, with [$C_8C_1C_1$Im]Br contributions in grey) are compared (signals originating from the [NTf_2]$^-$ anion in this region are indicated by dotted boxes). [$C_8C_1C_1$Im]Br is solid at room temperature, and therefore could not be measured in pure form. The differential ppm shifts due to methylation at C_2 are marked by arrows. Figure obtained from Cremer *et al.*[88]

This shift is commonly assigned to a change in electron current at the ^{13}C nucleus resulting from the different bonding environment (exchange of s-type(H) with sp^3-type(C) orbital).[193] In contrast, the $C_{4,5}$ signals undergo a highfield shift of ≈ 1.5 ppm, which can be assigned to the molecular changes due to methylation. This shift upon the C_2 is very similar in the case of [$C_1(C_1)_2$ThioIm][NTf_2] which correlates with XPS findings in *Section 4.2.3*. A shift downfield is also seen in [$(C_1)_2$Thio][NTf_2] and [$(C_1)_2$Thiz][NTf_2], and although this shift follows the same trend in XPS (towards higher BEs), the shift in the ^{13}C-NMR is more pronounced, showing that this effect cannot be solely explained by aromaticity effects, Figure 4.13.

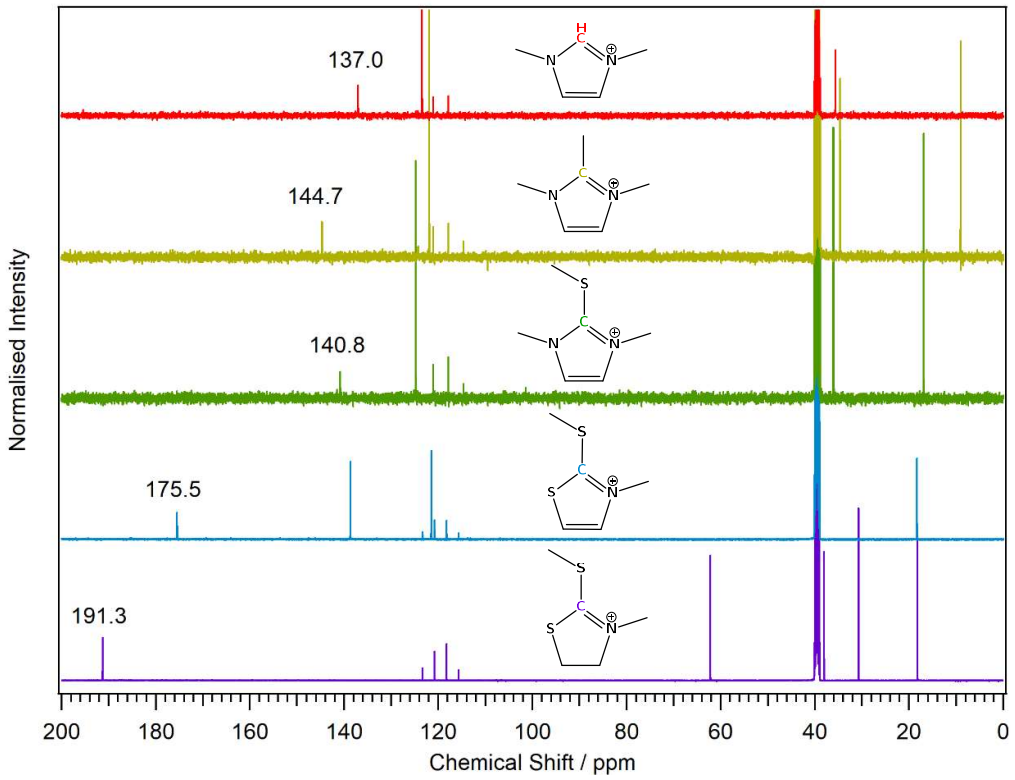


Figure 4.13. ^{13}C-NMR of $[C_1C_1Im][NTf_2]$ (red), $[C_1C_1C_1Im][NTf_2]$ (yellow), $[C_1(C_1)_2ThioIm][NTf_2]$ (green), $[(C_1)_2Thio][NTf_2]$ (blue) and $[(C_1)_2Thiz][NTf_2]$ (purple). The ppm values at C_2 are marked. Data offset vertically for clarity.

Not surprisingly, the guanidinium moiety also presents a downfield shift in ^{13}C-NMR upon the C_{core} when compared to the C_2 imidazolium cation which correlates with its higher BE found by XPS, Figure 4.13. Upon sulfur substitution of one of the nitrogen atoms, XPS showed a shift towards lower BEs, showing that the charge delocalisation is more effective on the guanidinium cation, which should be reflected in ^{13}C-NMR as a higher shift downfield. However, not only the thiouronium displays a higher shift downfield, Figure 4.14, this difference is larger than 10 ppm. Notably, the acyclic $[(C_1)_5TU][NTf_2]$ has a C_{core} BE similar to the C_2 of $[(C_1)_2Thiz][NTf_2]$, but its ^{13}C-NMR shift is comparable with $[(C_1)_2Thio][NTf_2]$ instead, Figure 4.13.

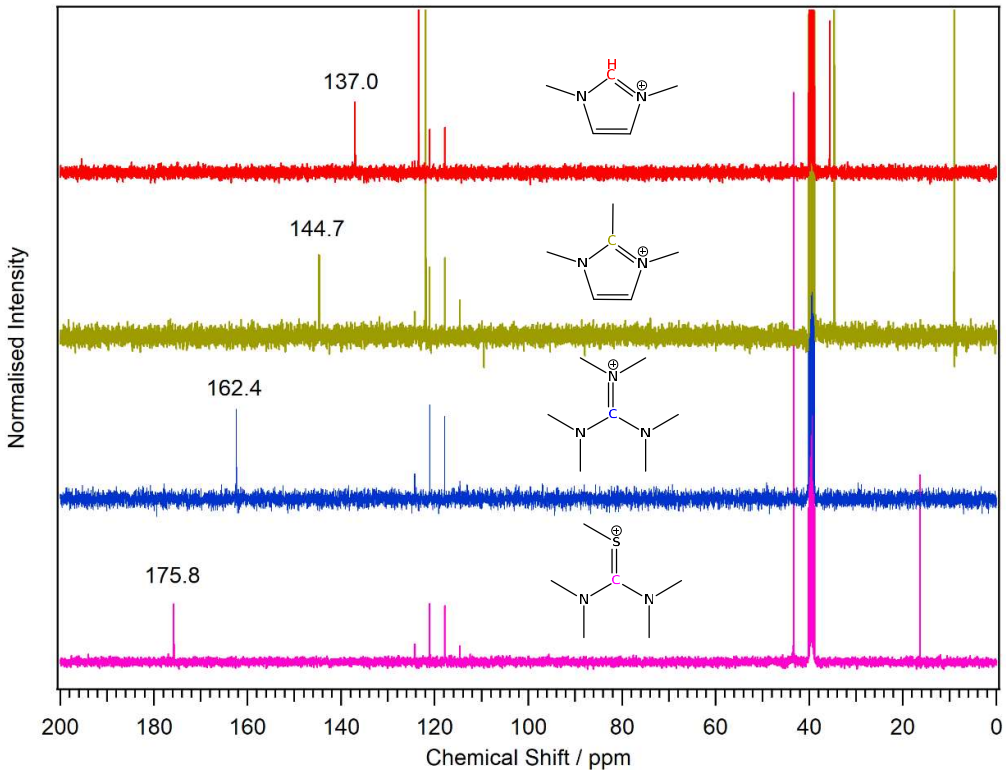


Figure 4.14. ^{13}C-NMR of $[C_1C_1Im][NTf_2]$ (red), $[C_1C_1C_1Im][NTf_2]$ (yellow), $[(C_1C_1)_2dmg][NTf_2]$ (dark blue) and $[(C_1)_5TU][NTf_2]$ (pink). The ppm values at $C_{2/core}$ are marked. Data offset vertically for clarity.

It seems that some compensating effects are present, such as changes in the ring current, hybridisation re-arrangements accompanied by anisotropy changes, different degree of orbital mixing, *etc.*, which are known to have an impact on local shielding constants in ^{13}C-NMR. Clearly, although ^{13}C-NMR correlates to some extend with XPS, with the exception of $[(C_1)_5TU][NTf_2]$, the variation between shifts is incredibly more pronounced in ^{13}C-NMR.

4.4. Conclusions

Sulfur functionalisation of cyclic and acyclic ILs has shown notable impact upon the chemical environment of surrounding atoms. Regardless of presence or absence of aromaticity, functionalisation tends to disrupt the charge delocalisation upon the cation core. This can be seen in methylated and thio-methylated counterparts, resulting in a higher BE when compared to the non-methylated version. This effect is also present in ^{13}C-NMR, seen as a shift downfield. This suggests that $C_{2/core}$ is more deshielded, due to removal of

electron density, or other effects. Additionally, the anion was kept the same for all ILs, as the $[NTf_2]^-$ anion transfers less charge to the cation core, providing a better comparison between different cation families. ^{13}C-NMR seems to be more sensitive than XPS regarding functionalisation at the cation core. Structural changes seem to have a clear effect upon the $C_{2/core}$ chemical shift, whereas by XPS this effect is less apparent, in some cases within the experimental error. Although there seems to be an apparent correlation between the $C_{2/core}$ 1s BE and ^{13}C-NMR $C_{2/core}$ shifts for most ILs studied in this work, this effect is more pronounced in ^{13}C-NMR, and for the acyclic ILs this relationship cannot be acknowledged. In fact, the guanidinium IL shows the higher C_{core} 1s BE of all ILs, followed by the thiouronium, however, the thiouronium displays a higher downfield chemical shift in ^{13}C-NMR for the C_{core}.

Computational methods can provide further information in order to fully understand changes how changes in the cation structure impacts upon its chemical environment, ring current effects, re-arrangements, degree of orbital mixing, *etc.* which could explain the higher impact upon ^{13}C-NMR *versus* XPS. This study would also provide a better understanding and interpretation of force field parameters (*e.g.*, effective charges) used in molecular dynamics simulations.

Consequently, there seems to be a strong effect upon ^{13}C-NMR on $C_{2/core}$ chemical shift upon functionalisation, which could help identify specific interactions within ionic liquids, therefore aiding upon a choice of IL for a specific application. However, this effect does not fully correlate with XPS findings. This suggests that other interactions have an influence in the recorded data, for example, the use of solvents in the NMR technique which could also add other solvent interactions, complicated shielding effects, *etc.* and therefore showing an impact on the chemical shifts. Additionally, it has been reported that this effect is a consequence of carbon shifts being strongly affected by additive contributions of substituents in α, β, γ and δ positions.[194, 195] As such, ^{13}C-NMR does not seem to always provide a reliable indicator of the chemistry

of the compound; proton NMR, however, is much less influenced by these effects and provides a better description of the chemical environment (which in the case of the compounds studied in this work cannot be investigated). Furthermore, NMR is undeniably a bulk sensitive analytical tool whereas XPS is regarded a surface sensitive technique. It is important to therefore, not make conventions between different cations, based in one technique alone, as more evidence upon cation-anion interactions, orbital mixing, *etc.* is necessary to fully understand how these can interact with solute molecules.

5. Depth Profiling of Ionic Liquids – An ARXPS and ERXPS study

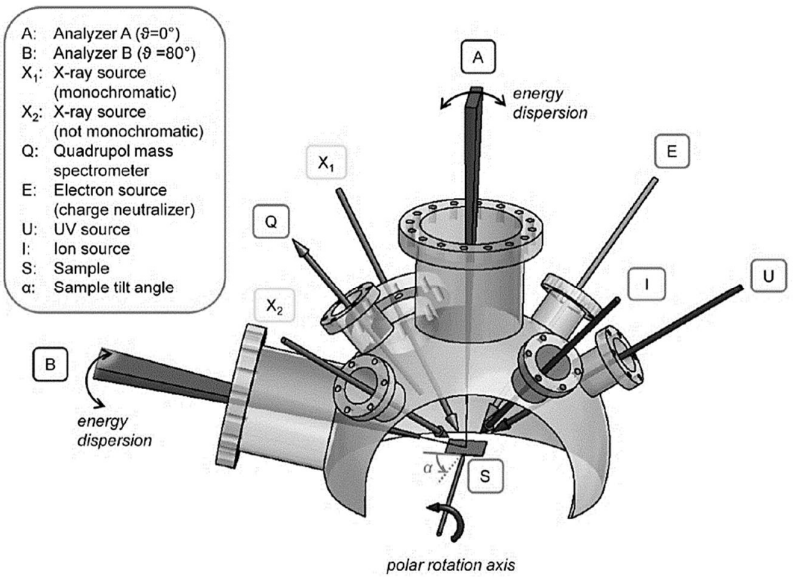
5.1. Introduction

Advances within the field of ionic liquid-based technologies require a broad understanding of their surface properties, as an extensive range of chemical reactions take place mostly at interface discontinuities. Understanding the ionic liquid–gas interface[47, 70] is crucial for a wide range of applications such as gas capture/storage/separation,[196-201] nanoparticle and thin film preparation,[202-206] and supported ionic liquid phase (SILP) catalysis,[207, 208] to name a few.

The ionic liquid–vacuum surface has been studied mostly in four different areas: spectroscopy,[50, 58, 60, 71-73, 78, 81, 82, 90, 104, 111, 209-214] scattering,[76, 215-227] sticking probability/temperature programmed desorption,[95, 117, 228] and molecular dynamics (MD) simulations.[63, 65, 214, 229-241] Ultra-high vacuum techniques (UHV) have been used to probe the IL-vacuum interface, including laboratory and synchrotron based X-ray photoelectron spectroscopy (XPS),[78, 82, 83, 104, 209, 242, 243] ultraviolet photoelectron spectroscopy (UPS),[71, 92, 111, 211, 244] metastable impact electron spectroscopy (MIES),[71, 72, 111] low energy ion scattering (LEIS),[76, 245-247] Rutherford backscattering (RBS),[93, 221, 248, 249] and neutral impact collision ion scattering spectroscopy (NICISS).[113, 222, 224] These methods probe different depths, for instance, while the information depth for Al source XPS is about 7 – 9 nm, for angle-resolved X-ray photoelectron spectroscopy (ARXPS) is about 1 – 1.5 nm [78, 81, 82, 90, 104, 209] However, MIES[71-73, 111, 211] and atom/molecule scattering,[215-220] owing to the reactivity/size of the probe, are considerably more surface sensitive than ARXPS,[78, 81, 82, 90, 104, 209] as these techniques probe primarily the molecular layer of an ionic liquid which is in contact with the vacuum.[246] Different surface sensitive techniques also provide different information, consequently an array of techniques are needed to fully understand the ionic liquid–vacuum surface.

ARXPS has recurrently been used for depth profiling studies onto ionic liquid systems. All ARXPS studies on ILs reported so far involved sample rotation with respect to a fixed electron analyser in order to change the electron emission angle. This rotation is done by mounting the sample on a rotatable manipulator. In liquid samples, there is the intrinsic problem that the liquid film might simply drip off the support. Rotation is only possible for very thin liquid layers of up to 0.5 mm thickness, as long as sufficiently viscous ILs are used. Such layers can be prepared by manually spreading a drop of liquid onto a flat solid support. In these cases, one must ensure that the analyser only detects electrons from the sample centre, in order to have a well-defined emission angle. Due to gravity, the liquid film at the bottom part of tilted samples is thicker than at the centre or upper parts, producing a curved surface layer. Additionally, the sample might also form a sessile shape influenced by the solid support, surface composition and sample purity. Surface tension, interfacial tension and wettability of ionic liquids have a crucial impact upon their shape, especially when dealing with relatively large surface areas and/or curved interfaces, therefore, capillary pressure must be taken into account.

Niedermaier *et al.* have recently developed a dual analyser system for surface analysis (DASSA), dedicated to ARXPS of liquid surfaces and interfaces.[250] DASSA not only enables fast ARXPS, but allows UV photoelectron spectroscopy, imaging XPS, and low-energy ion scattering (LEIS) at the horizontal surface plane of macroscopically thick non-volatile liquid samples. It comprises a UHV chamber equipped with two electron analysers mounted for simultaneous measurements in 0° and 80° emission relative to the surface normal. A scheme of this apparatus is described in Figure 5.1.



Angle definition	Angle value
ASB	80°
X_1SA	54.7°
X_1SB	54.7°
X_2SA	54.7°
X_2SB	54.7°
USA	55°
USB	135°
ISA	45°
QSA	40°
QSB	40°

Figure 5.1. Scheme of the DASSA analysis chamber with its multiple excitation sources and the two analysers. The table on the right gives critical angles between components. The angles' center point is always the sample center (S).[250]

The incidence angle is therefore constant, ruling out the risk of temporal sample changes between consecutive measurements in standard ARXPS that occurs upon sample rotation. Additionally, IL films of different thickness even for liquid samples can be probed since these are horizontally mounted samples. This is of particular importance as comparison of different layer thicknesses can shed light on to what extent processes such as ion charge transport play a role on how charge compensation takes place in ILs.[250]

However, this new concept also poses some drawbacks. Not only this setup had to be modified to particular specifications, the transmission function, relative sensitivity factors (RSFs) and geometric corrections had to be acquired and optimised. Reference measurements confirmed the identical performance of both analysers and RSFs for numerous elements have been determined for the new instrument using clean ionic liquids, but further investigation is required in this field. Additionally, DASSA comprises a monochromated Al K_α radiation ($h\nu$ = 1486.6 eV) X-ray source and a non-monochromated X-ray source that can emit either Al K_α or Mg K_α radiation ($h\nu$ = 1253.6 eV). In the particular case of the Licence group instrument, although only one analyser is present, an additional monochromated high-energy Ag L_α' ($h\nu$ = 2984.3 eV) X-ray source

is available. This means that i) higher energy radiation is sufficient to eject core level electrons (which otherwise would not be ejected with a lower energy source) - Therefore, binding energies for deeper core levels provided; ii) Higher energy radiation emits electrons with higher kinetic energies – Therefore, information depth increases.

As for DASSA, the high-energy XPS (also termed energy-resolved XPS, ERXPS) no geometry change to the sample is required, thus enabling repeated analysis of a consistently level surface thereby minimising error caused by physical shifting of the sample. Additionally, depth profiling data can be obtained from a single experiment as opposed to repeated experiments in which the emission angle is altered (ARXPS) or photon-energy varied (synchrotron-based ERXPS) thus minimising X-ray exposure and hence sample damage. Furthermore, higher energy core orbitals can be probed, elucidating further information concerning ionic liquid electronic environments, which is imperative to understanding ionic liquids at a molecular level.

Recently, Blundell *et al.* demonstrated the use of the Ag L_{α}' X-ray source to investigate depth profiling of the sulfur atom of the $[NTf_2]^-$ anion. A cationic dependence upon surface ordering of the anion was demonstrated, with similar trends observed as to those obtained through ARXPS. It was found that both depth profiling techniques were supportive and additive to each other.[114] ERXPS can then be used to complement information given by ARXPS. Due to a lack of a dual analyser for ARXPS experiments, the sample holder had to be tilted in order to change the detection angle of emitted photoelectrons. This, as mentioned by Niedermaier *et al.* restricts the liquid systems studied to very thin viscous IL films coating a flat solid support (multistage stainless-steel bar). To overcome this problem, in this work a full description and development of an add-on bar to the multistage bar is investigated and appropriate comparisons to the previous methodology acknowledged.

Subsequently, this work aims to combine ARXPS and ERXPS, using the $[NTf_2]^-$ anion as a probe of sulfur enrichment on the surface interface, for a range of IL families. This study will include the frequently studied imidazolium cation, with different aliphatic chain lengths towards a better understanding of the arrangement of the ILs components at the IL/vacuum interface.

5.2. Surface Sensitivity and Information Depth

As described in *Chapter 2, Section 2.5.*, the surface sensitivity of XPS experiments is influenced by two main factors: i) electron emission angle, θ and ii) the attenuation length, λ_{AL}, of the emitted photoelectrons (*N.B.* this value is also dependent upon the photoelectron kinetic energy). A measure of surface sensitivity is provided by the information depth (ID) which is defined as the depth at which 95.7% of the signal originates; the dependence of ID upon θ and λ_{AL} is shown by Equation 2.2 ($ID = 3\lambda_{AL}\cos\theta$).

It should be noted that definitions for inelastic mean free path (λ_{IMFP}) and attenuation length (λ_{AL}) are often used interchangeably in the literature. Herein, λ_{IMFP} is defined as the average distance travelled by an electron of a specific energy between two inelastic events, with elastic scattering included. Whereas, λ_{AL} is defined as the average distance travelled by an electron of a specific energy between two inelastic events without elastic scattering. Consequently, λ_{AL} is used to describe depth, rather than λ_{IMFP}, as it does not include elastic scattering events which can cause an overestimated depth, and is typically 20% smaller than λ_{IMFP}.[116, 130]

Subsequently, two techniques which tune surface sensitivity of an XPS experiment will be studied: (1) angle-resolved XPS (ARXPS), based on varying the detection angle (θ) of the emitted photoelectrons and (2) energy-resolved XPS (ERXPS), utilising the dependence of λ_{AL} on the kinetic energy of the emitted photoelectron.

5.3. Angle-Resolved XPS

5.3.1. Principles

Of the two methods ARXPS is the most commonly employed to obtain a depth profile for ionic liquid systems. Typically, the lower energy Al K_α X-ray source is used due to its higher signal intensity, and ID varies chiefly with θ. The emission angle, θ, can be varied with respect to the surface normal by rotation of the sample stage with respect to the concentric hemispherical analyser (CHA), as illustrated by the schematic in Figure 5.2.

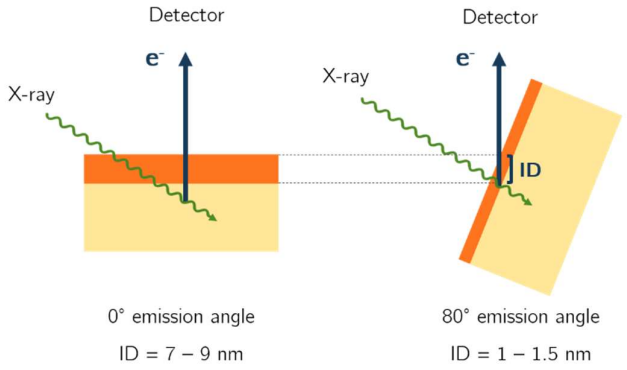


Figure 5.2. Schematic detailing the influence of sample geometry on information depth when recording XP spectra at normal emission angle, θ = 0° (left); and at grazing emission angle, θ = 80° (right).

By increasing the emission angle, the distance that an emitted photoelectron must travel through the sample is increased, thus only photoelectrons that have escaped from a shallower depth are detected. At the kinetic energies measured here using the Al K_α source (≈ 800 – 1400 eV) the attenuation length of photoelectrons in organic compounds is of the order ≈ 3 nm.[139] From this, the ID for each of the angle-resolved geometries employed in the ARXPS experiments can be estimated. Subsequently, at a normal emission angle (θ = 0°) ID is between 7 – 9 nm, and on increasing emission angle to 70° then 80° the measured ID changes to 2 – 3 nm and 1 – 1.5 nm respectively.[49] At θ = 80°, approximately 65% of the measured signal arises from the topmost 0.3 – 0.5 nm of the sample; this is smaller than the size of most IL ions, highlighting the high degree of surface sensitivity this technique provides.

In a typical ARXPS experiment a series of spectra are recorded in the "bulk sensitive" geometry, where θ = 0°, and with increasing emission angle to more "surface sensitive" geometries *i.e.* 70° ≤ θ ≤ 85°. For a homogeneous and isotropic arrangement of ions in an ionic liquid, identical core photoelectron intensities would be observed for all emission angles. However, a preferential increase in a core photoelectron emission intensity with increasing θ, and thus increasing surface sensitivity, indicates a higher surface concentration for the respective element/component in comparison to the bulk.

5.3.2. Sample Preparation

As stated in *Chapter 2, Section 2.2.*, the experimental geometric change in the case of ARXPS, brings additional measuring uncertainty relative to the sample shape. As result, for some samples, after taking the XP spectra on three different positions, the obtained data did not exhibited reproducibility. This could be seen in the case where samples showed an inability to form a thin flat film, and rather a droplet shape.

Liquids can interact with two main types of solid surfaces. Usually, solid surfaces have been divided into high-energy and low-energy types. Solids such as metals, glasses, and ceramics are known as "high-energy" because it takes a large input of energy to break the chemical bonds that hold them together (*e.g.*, covalent, ionic, or metallic). Most molecular liquids achieve complete wetting with high-energy surfaces, Figure 5.3.

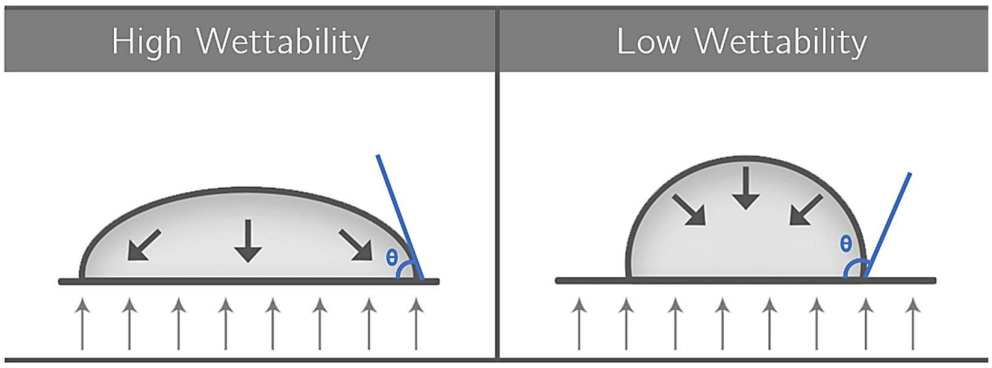


Figure 5.3. Wettability of fluids onto a solid surface; 0 < θ < 90° High degree of wettability, small contact angle; 90° < θ < 180° Low degree of wettability, large contact angle.

In traditional XPS experiments a stainless steel multi-sample bar is used, to increase the wettability of fluids on the solid surface. However, not all metal supports provide a high degree of wettability. In fact, it has been found that for a range of ILs in gold on mica substrate these have formed droplets or islands rather than thin films.[251] In the case of materials such as ionic liquids, the resulting low wettability on the surface and small contact angle can be explained by the presence of surface contaminants, high degree of hydrophobicity, and surface tension. According to Santos and Baldelli,[55] shorter alkyl chains, whether attached to the cation or the anion, lead to higher surface tension. Consequently, the increase in the internal contact angle of the sample results in a larger than expected information depth. This is of particularly importance for ARXPS experiments, as this effect can have an enormous impact on the recorded data, Figure 5.4.

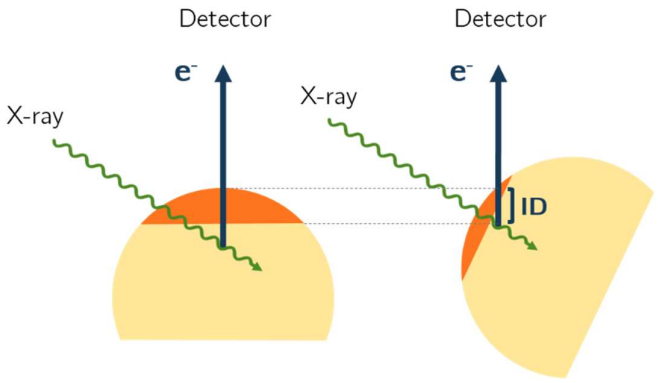


Figure 5.4. ARXPS on a sample with increased internal contact angle

To minimise this effect, found especially in materials with surface impurities (see *Chapter 2, Section 2.1.6.* on how to remove silicon and other surface impurities), a new methodology was developed which involved designing an add-on bar to the stainless steel multi-sample bar already used, Figure 5.5.



Figure 5.5. New add-on stainless steel bar for ARXPS experiments, placed on top of the stainless steel multi-sample bar already used for XPS experiments.

This new bar has been cut to have wells (4 x 4 mm) with approximate depth of 20 μm with an internal circular design that should minimise the contact angle formed by the sample droplet. Each well should therefore have a minimal amount of sample necessary for a flat surface, Figure 5.6 and Figure 5.7, since any excess material can be scrapped off.

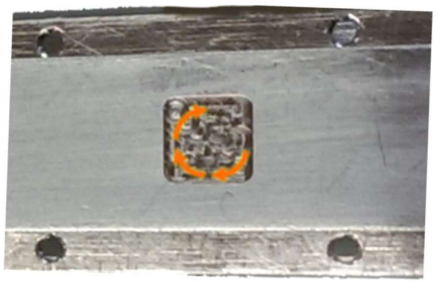


Figure 5.6. Detail of add-on stainless steel bar for ARXPS experiments, showing internal circular design minimising the droplet shape of samples during the angular experiment.

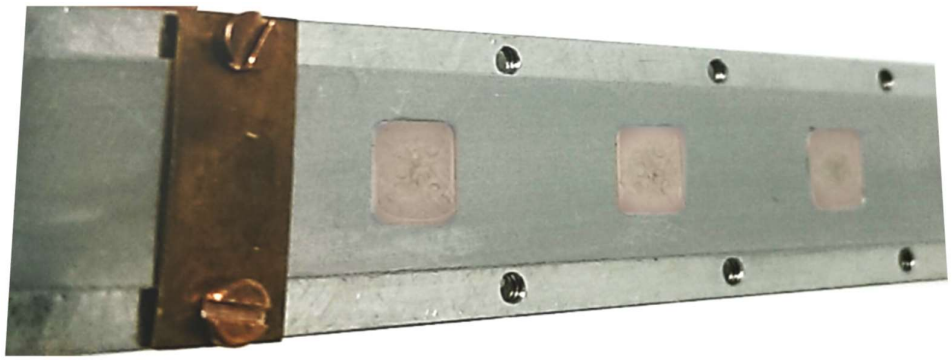


Figure 5.7. Upright sideways detail of add-on stainless steel bar for ARXPS experiments, showing liquid samples with no droplet effect, providing a completely flat surface during the angular experiment.

It is important to note that enough material must be used in order to allow adhesion of the fluid to the walls of the wells, which will cause an upward force

on the liquid at the edges while the surface tension holds the surface flat. An illustration of this phenomenon can be seen in Figure 5.8.



Figure 5.8. Effect of adhesive forces and surface tension applied to fluids on the walls of the wells when enough material is used to cover the well.

Inversely, if the amount of sample is not enough, the cohesive forces within the sample will result in the increase of contact angle and low wettability onto the surface, Figure 5.9. Consequently, this results in an increase of information depth in ARXPS studies.

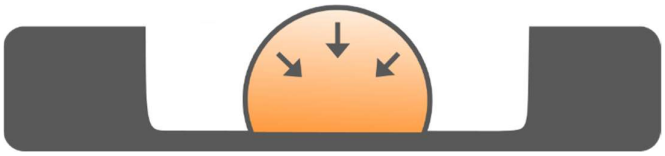


Figure 5.9. Effect of cohesive forces and surface tension applied to fluids when not using enough material to cover the well.

Experiments with and without this add-on bar have been performed and discussed further in *Section 5.4.1.*

5.3.3. Data Analysis and Processing

XP spectra have been obtained at two emission angles, 0° and 80°, with respect to the surface normal for imidazolium bis(trifluoromethanesulfonyl)imide-based ionic liquids, using the Al K_α X-ray source. Experimental stoichiometries were determined from the high-resolution scans for each element and are presented in Table 5.1.

Stoichiometries determined at the electron emission angle θ = 0° (ID = 7 – 9 nm) agree very well to the nominal stoichiometry and are within the experimental error for all ionic liquids studied and are well within ± 10% for the majority. Shake up/off phenomena has been taken into account when calculating atomic percentages for the elements involved in double bonding (see

Appendix C). Nonetheless, experimental O 1s stoichiometry is systematically lower than the nominal value. This suggests that the RSF, taken from the Kratos Library, for this element is not ideally suited for the compounds under investigation. Similar deviations in stoichiometry have been reported elsewhere.[83, 90, 209] Small deviations in RSF values have minimal impact on the conclusions made as this study is focused on changes in stoichiometric ratio with respect to emission angle.

Table 5.1. Measured experimental and nominal stoichiometries (in number of atoms) for the imidazolium-based ionic liquids studied with ARXPS in this work. The experimental values are obtained from XP spectra at θ = 0° and 80°. Associated experimental error is ± 10 - 20%.

		Composition (number of atoms)									
		Cation				Anion					
Coumpound		$C_{aliphatic}$ 1s	$C_{4,5}$ 1s	$C_{6,7}$ 1s	C_2 1s	N_{cation} 1s	C_{CF3} 1s	N_{anion} 1s	O 1s	F 1s	S 2p
	[a]RSF[74,134]	0.278	0.278	0.278	0.278	0.477	0.278	0.477	0.780	1.000	0.668
$[C_2C_1Im][NTf_2]$	**Nominal**	**1**	**2**	**2**	**1**	**2**	**2**	**1**	**4**	**6**	**2**
	0°	1.2	1.9	2.3	0.9	2.0	2.3	1.0	3.5	6.0	1.8
	80°	1.2	1.8	2.2	0.9	1.8	2.2	1.0	3.5	6.5	1.8
$[C_3C_1Im][NTf_2]$	**Nominal**	**2**	**2**	**2**	**1**	**2**	**2**	**1**	**4**	**6**	**2**
	0°	2.3	1.9	2.3	0.9	2.0	2.3	1.0	3.5	6.0	1.8
	80°	2.3	1.8	2.1	0.9	1.8	2.2	0.9	3.5	6.7	1.7
$[C_4C_1Im][NTf_2]$	**Nominal**	**4**	**2**	**2**	**1**	**2**	**2**	**1**	**4**	**6**	**2**
	0°	3.5	1.9	2.3	0.9	2.0	2.3	1.0	3.5	5.9	1.8
	80°	3.8	1.9	2.3	0.9	1.9	2.3	1.0	3.3	5.7	1.9
$[C_6C_1Im][NTf_2]$	**Nominal**	**6**	**2**	**2**	**1**	**2**	**2**	**1**	**4**	**6**	**2**
	0°	5.7	1.8	2.3	0.9	1.9	2.3	1.0	3.4	5.7	1.9
	80°	5.8	1.9	2.3	1.1	1.9	2.2	1.0	3.3	5.8	1.8
$[C_8C_1Im][NTf_2]$	**Nominal**	**8**	**2**	**2**	**1**	**2**	**2**	**1**	**4**	**6**	**2**
	0°	7.9	1.8	2.3	0.9	1.9	2.3	1.0	3.4	5.7	1.8
	80°	8.4	1.8	2.3	0.9	1.7	2.3	0.9	3.2	5.8	1.7
$[C_{10}C_1Im][NTf_2]$	**Nominal**	**10**	**2**	**2**	**1**	**2**	**2**	**1**	**4**	**6**	**2**
	0°	10.0	1.8	2.2	0.9	1.9	2.2	1.0	3.5	5.8	1.8
	80°	10.7	1.8	2.2	0.9	1.6	2.2	0.9	3.2	5.9	1.6
$[C_{12}C_1Im][NTf_2]$	**Nominal**	**12**	**2**	**2**	**1**	**2**	**2**	**1**	**4**	**6**	**2**
	0°	12.2	1.8	2.2	0.9	1.9	2.2	1.0	3.4	5.6	1.8
	80°	13.7	1.7	2.1	0.9	1.6	2.2	0.9	3.0	5.5	1.6

[a] Relative sensitivity factors (RSF) taken from the Kratos Library. Stoichiometries determined without consideration of H content.

5.4. ARXPS Analysis of Ionic Liquids

5.4.1. Experimental Methodology

Earlier attempts at recording Angle-Resolved experiments of ionic liquids were carried out by placing a small drop (≈ 10 mg) of a liquid sample on a stainless-steel sample bar and cast into a thin film (approximate thickness 0.1 – 0.5 mm), see *Chapter 2, Section 2.2*. However, if one considers a sequential series of data sets, in some cases significant change can be noted. Figure 5.10 shows the XP spectra of the F 1s and C 1s region for $[C_8C_1Im][NTf_2]$.

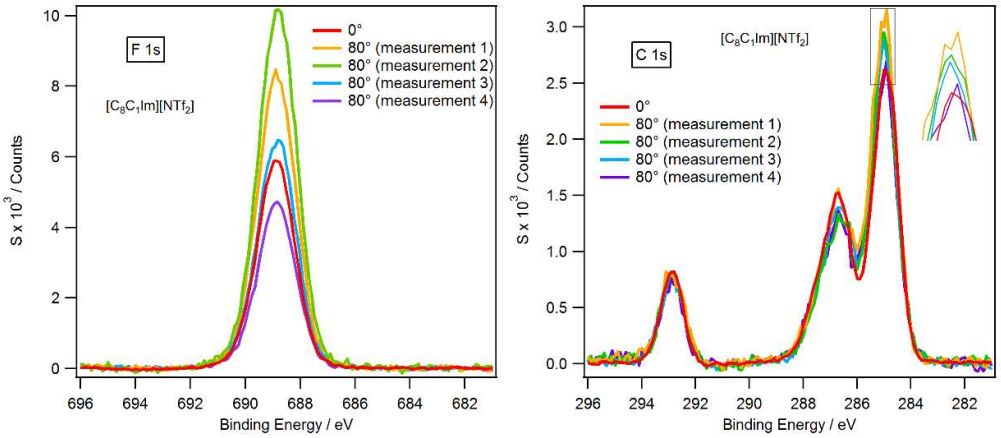


Figure 5.10. High-resolution XP spectra of the F 1s and C 1s region for $[C_8C_1Im][NTf_2]$, recorded at 0° (red) and 80° (orange, green, blue and purple) electron emission angle, θ, with respect to the surface normal. ARXPS measurements achieved by placing a small drop on a stainless-steel sample bar as a thin film. $[C_8C_1Im][NTf_2]$ charge corrected by referencing $C_{aliphatic}$ 1s to 285.0 eV. Spectra recorded at θ = 80° normalised to the intensity of the C_{CF3} 1s photoelectron emission peak recorded at θ = 0°.

The lack of reproducibility of the current method is noteworthy, especially for the F 1s region. Each measurement (average of three different positions) arises from a fresh sample drop of ionic liquid, from the same ionic liquid batch, thus any deviations within measurements are not caused by different origins of the sample. Additionally, all the imidazolium ionic liquids explored within this *Chapter* were free of any surface contaminants, hence discarding the impact of this variable on the recorded spectra. Although the imidazolium series were able to form a thin flat film, for the ionic liquids that exhibited surface contaminants, such as the $[C_n(C_1)_2ThioIm][NTf_2]$ series, a droplet shape was visually observed even at 0°. Rotation of the sample around an axis will clearly introduce errors

such as sample height and the geometry of the surface as the angle vary from 0° to 80°. To overcome this issue, a new methodology involving a new add-on bar, was developed as described previously in *Section 5.3.2*. It is important to verify the reliability of both methods, as such, imidazolium based ionic liquids were chosen as this specific family of ILs has been extensively investigated. From Figure 5.11, the consistency between measurements can easily be acknowledged. These measurements were performed exactly at the same conditions as described above to eliminate further error deviations.

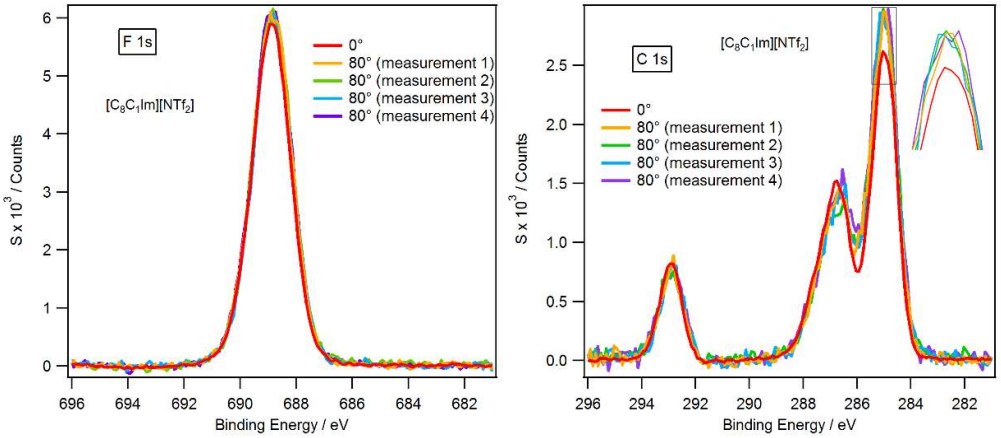


Figure 5.11. High-resolution XP spectra of the F 1s and C 1s region for $[C_8C_1Im][NTf_2]$, recorded at 0° (red) and 80° (orange, green, blue and purple) electron emission angle, θ, with respect to the surface normal. ARXPS measurements achieved by using the new add-on bar. $[C_8C_1Im][NTf_2]$ charge corrected by referencing $C_{aliphatic}$ 1s to 285.0 eV. Spectra recorded at θ = 80° normalised to the intensity of the C_{CF3} 1s photoelectron emission peak recorded at θ = 0°.

Additionally, both measurements 4 (purple) were recorded after 24 hours of the sample being at 80° emission angle. From Figure 5.10, inconsistency between measurements can be observed for the F 1s photoemission peak, suggesting rather a concave shape, possibly caused by excessive amount and/or viscosity of the sample. It is important to stress that although no visual droplet shape could be acknowledged for the imidazolium series, the recorded data as seen in Figure 5.10 provides evidence of different information depths within measurements. The validity of the new methodology is further reinforced as for measurement 4, negligible deviation can be observed, Figure 5.11, demonstrating little variation on the sample shape and consequently reliable reproducibility of the recorded data.

Additional studies on the imidazolium series using this new approach are discussed further in *Section 5.4.2*. Furthermore, for consistency, this methodology is employed for angle-resolved studies on all ionic liquids investigated in this *Thesis*.

5.4.2. ARXPS of Imidazolium Ionic Liquids

ARXPS has been used for depth profiling studies onto ionic liquid systems. These investigations predominantly focus on the heavily studied 1-alkyl-3-methylimidazolium cation,[78, 81, 82, 90, 104] with only a few of ARXPS studies addressing the structurally distinct pyrrolidinium cation,[90, 209] and more recently, quaternary ammonium and phosphonium cations.[114] An interesting trend for the IL/vacuum interface in 1-alkyl-3-methylimidazolium-based ILs arising from these investigations suggest that for sufficient chain length ($n \geq 4$) (seen as a significant increase in intensity of the $C_{aliphatic}$ 1s component with increasing emission angle), the alkyl chains are projected towards the vacuum forming an aliphatic overlayer, with a polar sublayer of positively and negatively charged head groups residing underneath, as illustrated in Figure 5.12.[78, 81, 82, 90, 104, 242, 243] A systematic investigation into this effect as a function of alkyl chain length has also shown that the degree of surface enrichment increases with the length of the alkyl chain.[78, 104, 99]

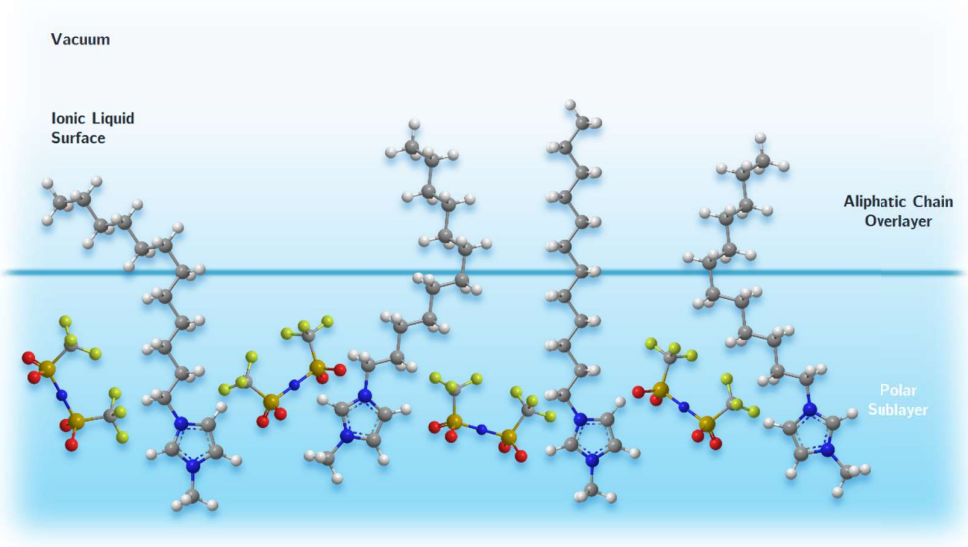


Figure 5.12. Schematic illustrating the surface structure for $[C_{12}C_1Im][NTf_2]$ as described in the literature.

This observation appears to hold true for the 1-alkyl-1-methylpyrrolidinium analogues,[90, 209] thus an increase on the data collection upon structurally diverse cations is imperative to shed some light into this phenomenon.

Moreover, ARXPS is instructive for determining depth distribution of certain elements, *i.e.* the surface composition but is not sensitive enough to detailed geometry effects such as molecular orientation.[104] ARXPS probes the top 1 – 1.5 nm of the IL surface interface and although some assumptions can be drawn in respects to the topmost surface composition, little can be acknowledged in regards to the arrangement/conformation of the ionic liquid constituents.

To investigate the surface composition and arrangement of the IL components at the IL/vacuum interface, a series of $[C_nC_1Im][NTf_2]$ ILs, with n = 2 to 12 were studied. As described in *Section 5.1*, the 1-alkyl-3-methylimidazolium ILs have been studied extensively within the literature, however, in this work ARXPS measurements were necessary to enable direct comparisons to highlight subtle changes within ARXPS and ERXPS data.

To aid visual interpretation of the ARXPS spectra presented, each spectrum recorded θ = 80° is normalised to the area of the C_{CF_3} 1s photoelectron emission peak recorded for the respective ionic liquid at θ = 0°. This peak was selected for normalisation as the C_{CF_3} 1s moiety is present in all ILs in the same stoichiometry, the C_{CF_3} 1s peak is easily identifiable with a binding energy well separated from any other photoelectron emission signals and as shown in Table 5.1, the composition of the C_{CF_3} 1s seems barely unaffected by the change in geometry. It should be stressed that due to the liquid state of the samples, a fluid and dynamic nature exists as a result of molecular tumbling, thus the data obtained represents an average of the true situation at any time.

For this family of ILs, an enrichment of the alkyl chains at the outer surface was found at the expense of the imidazolium head groups and the anions, with increasing chain length. In addition, both anions and cationic head groups are

located approximately at the same distance from the outer surface, with the anion slightly above the imidazolium ring.[78]

Visual comparison of the C 1s photoelectron emission at 0° and 80° for each ionic liquid studied is presented in Figure 5.13, highlighting the differences in surface enrichment for each cation.

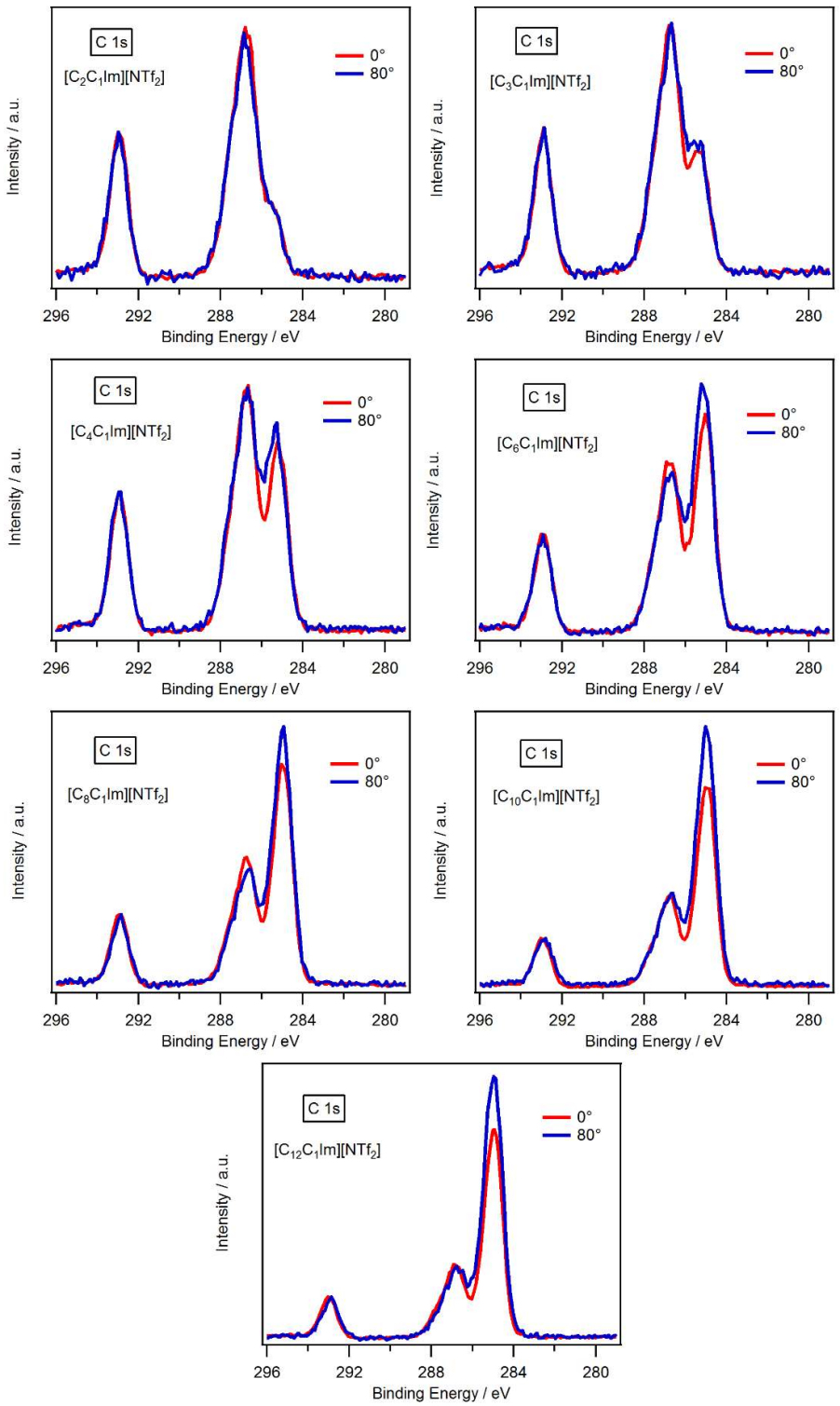


Figure 5.13. High-resolution XP spectra of the C 1s region for the imidazolium bis(trifluoromethanesulfonyl)imide-based ionic liquids studied in this *Chapter*, recorded at 0° (red) and 80° (blue) electron emission angle, θ, with respect to the surface normal. $[C_nC_1Im][NTf_2]$ with $n \geq 8$, charge corrected by referencing $C_{aliphatic}$ 1s to 285.0 eV. $[C_nC_1Im][NTf_2]$ with $n < 8$ were charge corrected by referencing N_{cation} 1s to the value obtained for $[C_8C_1Im][NTf_2]$. Spectra recorded at θ = 80° normalised to the intensity of the C_{CF_3} 1s photoelectron emission peak recorded for the respective ionic liquid at θ = 0°.

These results are in good agreement with the literature, showing an enrichment of the aliphatic component as the chain length increases.[78] Moreover, for $[C_nC_1Im][NTf_2]$ when n = 2, 3, small changes are observed with change in the emission angle, indicating a homogenous distribution and orientation of the ions at the surface. Simultaneously, from Table 5.1, the intensities of the C_{inter} 1s and N_{cation} 1s decrease (this effect is slightly less prominent in the C_{hetero} 1s and N_{anion} 1s). This behaviour indicates that the alkyl chains are enriched in the near-surface region and carbon atoms from the ring as well as the nitrogen atoms are depleted. Information on the relative position of the imidazolium ring of the cation and the anion can be taken from the comparison between N_{cation} 1s and N_{anion} 1s, which shows a tendency of the anion nitrogen to be located slightly above the imidazolium ring.

There is agreement between several experiments[76, 90, 111, 215-217, 221] and MD simulations[217, 230, 235, 240] that for $[C_nC_1Im][NTf_2]$ the $[NTf_2]^-$ anion is at the ionic liquid–vacuum outer atomic surface, even when n = 10 and 12. The anion orientation reported for $[NTf_2]^-$ suggests that the CF_3 groups are near the vacuum and the $[(SO_2)_2N]$ groups are towards the bulk, Figure 5.14.[90, 221, 230, 233, 235, 238, 240]

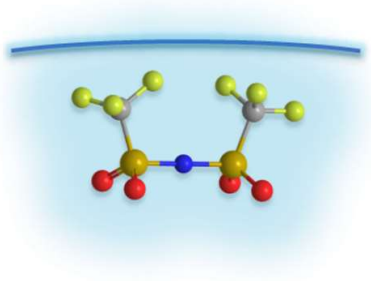


Figure 5.14. Suggested orientation of the $[NTf_2]^-$ anion at the ionic liquid-vacuum outer surface.[90, 221, 230, 233, 235, 238, 240]

The F 1s photoelectron emission at 0° and 80° for each ionic liquid studied is presented in Figure 5.15. Interestingly, the surface enrichment is more evident for $[C_nC_1Im][NTf_2]$ when n = 2, 3 and 10, 12. These results suggest that the position of the anion changes as the aliphatic component increases.

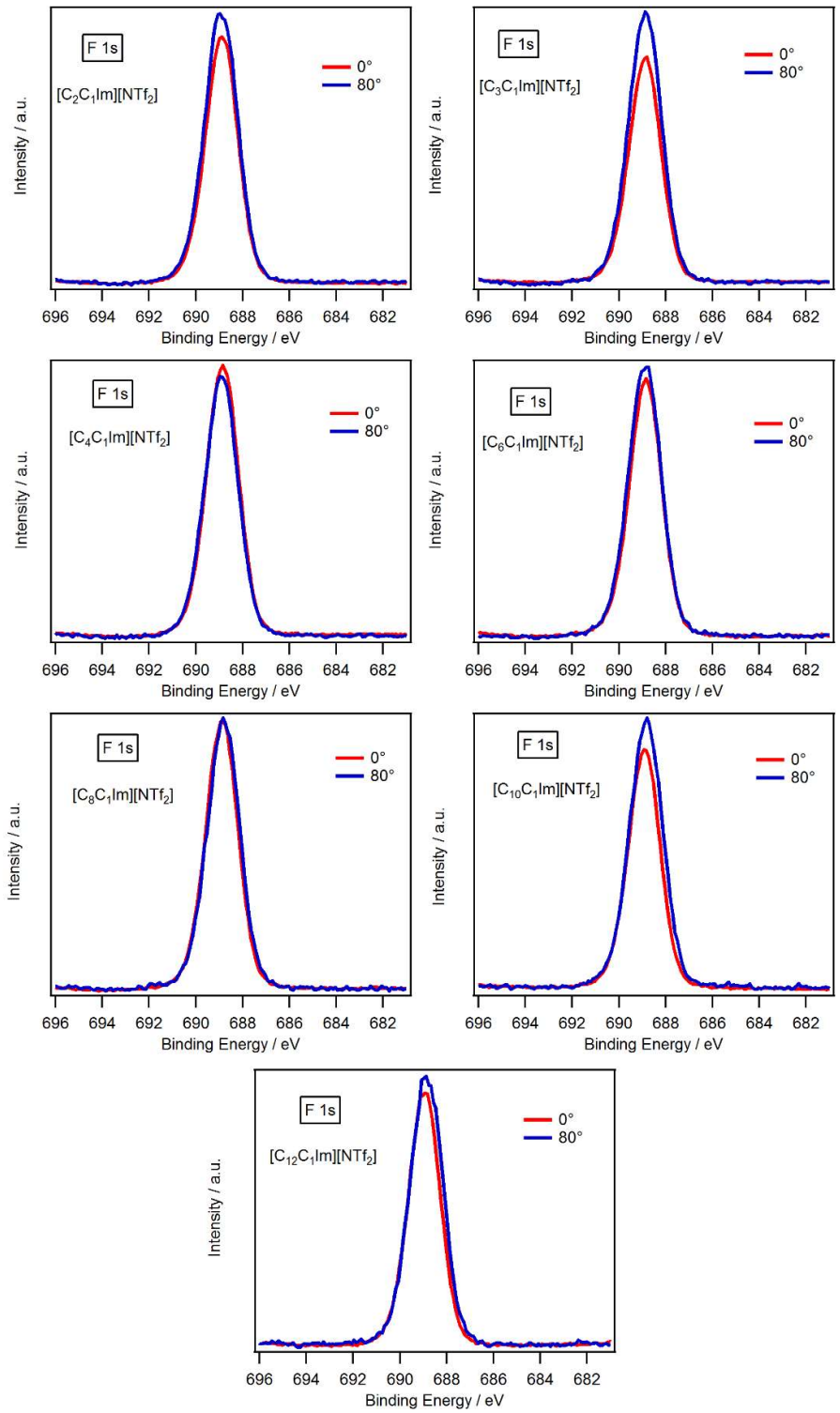


Figure 5.15. High-resolution XP spectra of the F 1s region for the imidazolium bis(trifluoromethanesulfonyl)imide-based ionic liquids studied in this *Chapter*, recorded at 0° (red) and 80° (blue) electron emission angle, θ, with respect to the surface normal. $[C_nC_1Im][NTf_2]$ with $n < 8$ were charge corrected by referencing N_{cation} 1s to the value obtained for $[C_8C_1Im][NTf_2]$. Spectra recorded at θ = 80° normalised to the intensity of the C_{CF_3} 1s photoelectron emission peak recorded for the respective ionic liquid at θ = 0°.

One explanation for these results, could mean approximately perpendicular orientation of the chains to the surface in short chain length cations, and an arrangement approximately parallel to the surface in long chain length cations. An illustration can be seen in Figure 5.16.

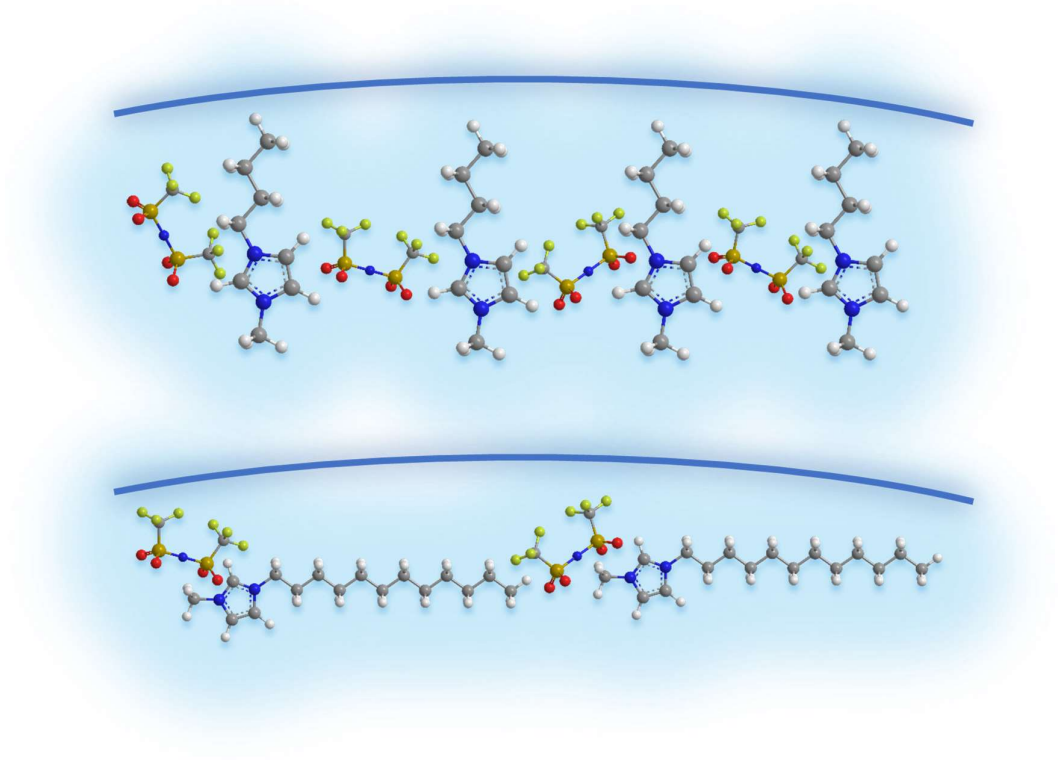


Figure 5.16. Schematic illustrating the possible surface structure for short chain length ILs with perpendicular orientation (top) and long chain length ILs with parallel orientation (bottom). Anion represented always above the cationic head group in accordance with the interpretation of the results discussed in this *Section and in Section 5.7.2*.

Maier *et al.* suggested that in the case of perpendicular orientation of the chains to the surface, this would result in an alkyl overlayer of larger thickness but diluted alkyl chains which seems to be unfavourable due to reduction in attractive van-der-Waals interactions between neighbouring alkyl chains. In contrast, for parallel orientation of the chains to the surface, the first molecular layer would be characterised by a very dense alkyl overlayer of narrow vertical width above the polar headgroups which is unlikely due to steric repulsive interactions.[78] More likely is an intermediate tilt angle for the mean alkyl chain orientation in a similar manner as it is known for long-chain self-assembled monolayers, as represented in Figure 5.17.[252]

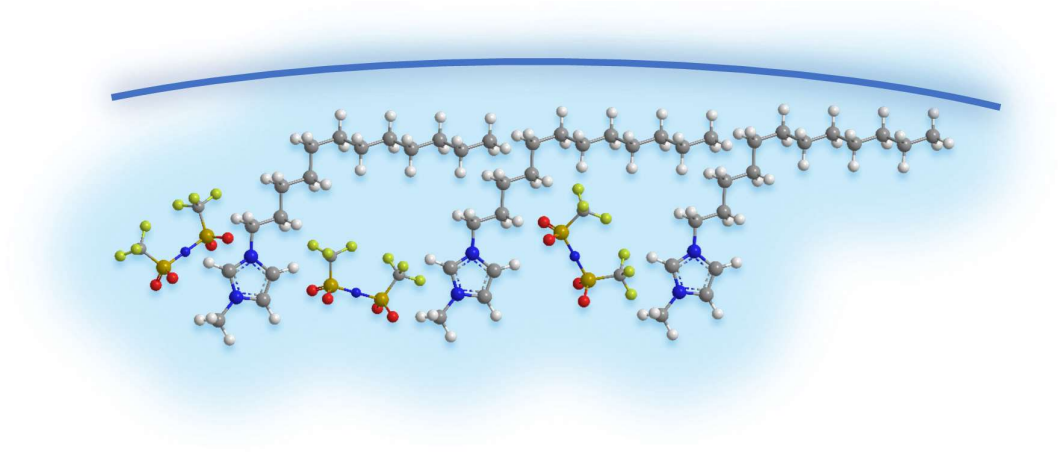


Figure 5.17. Schematic illustrating the surface structure with a chain tilt orientation for long chain length ILs.

This data suggests that for short chains, there is a perpendicular orientation, with the anion above the cation. A less prominent enrichment of the $C_{aliphatic}$ 1s and F 1s components for n = 4, 6, 8 suggest that the cation and anion are sinking towards the bulk, with the alkyl chain pointing towards the vacuum layer. However, there is a n for which an increase of the $C_{aliphatic}$ 1s component can be seen, along with an increase of the F 1s component. This observation suggests that an alkyl chain tilt, as described in Figure 5.17, is the more likely conformation at the near surface region. The F 1s component increase for n = 10, 12 also suggest that the anion is more at the surface for longer alkyl chains.

Nevertheless, the exact orientation of the ILs components cannot be determined directly using ARXPS without additional assumptions concerning ion distribution. In *Section 5.7.2.* ERXPS investigations on the 1-alkyl-3-methylimidazolium family are shown and appropriate discussions addressed to aid understanding on ion orientation/arrangement.

5.4.3. Comparison with Other Nitrogenous Cation Families

Of all bis(trifluoromethanesulfonyl)imide-based ionic liquids studied in *Chapter 3*, only $[(C_8C_1)_2dmg][NTf_2]$ was liquid at room temperature. Visual comparison of the F 1s and C 1s photoelectron emission at 0° and 80° is presented in Figure 5.18, highlighting the differences in surface enrichment.

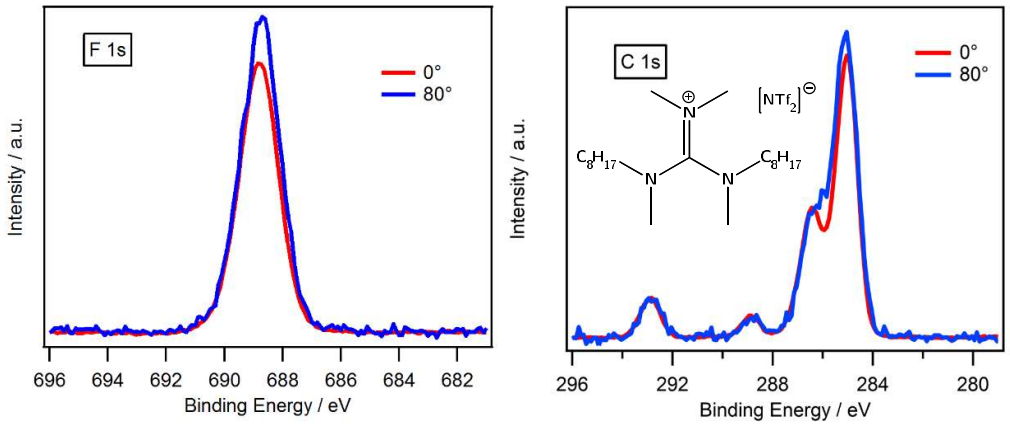


Figure 5.18. High-resolution XP spectra of the F 1s and C 1s region for $[(C_8C_1)_2dmg][NTf_2]$, recorded at 0° (red) and 80° (blue) electron emission angle, θ, with respect to the surface normal. Spectra charge corrected by referencing $C_{aliphatic}$ 1s to 285.0 eV. Spectra recorded at θ = 80° normalised to the intensity of the C_{CF_3} 1s photoelectron emission peak recorded for the respective ionic liquid at θ = 0°.

As expected, the guanidinium cation has an increase on the $C_{aliphatic}$ 1s, suggesting an enrichment of the aliphatic chain at the surface. Surprisingly, this effect on the aliphatic component is comparable to the $[C_8C_1Im][NTf_2]$ counterpart, even though the guanidinium studied here has two octyl chains, when compared to one octyl chain in the imidazolium cation.

Interestingly, the surface enrichment of the F 1s component is slightly more evident in the case of $[(C_8C_1)_2dmg][NTf_2]$ than for $[C_8C_1Im][NTf_2]$. This indicates that the anion sits at the surface also for the guanidinium cation, as seen in the imidazolium series, and seems to be more at surface when compared to its the imidazolium counterpart.

In the case of the thioimidazolium series, $[C_n(C_1)_2ThioIm]$ with n = 1, 4, 8, developed to aim further comparison with ERXPS in *Section 5.7*, the F 1s and C 1s photoelectron emission at 0° and 80° can be seen in Figure 5.19.

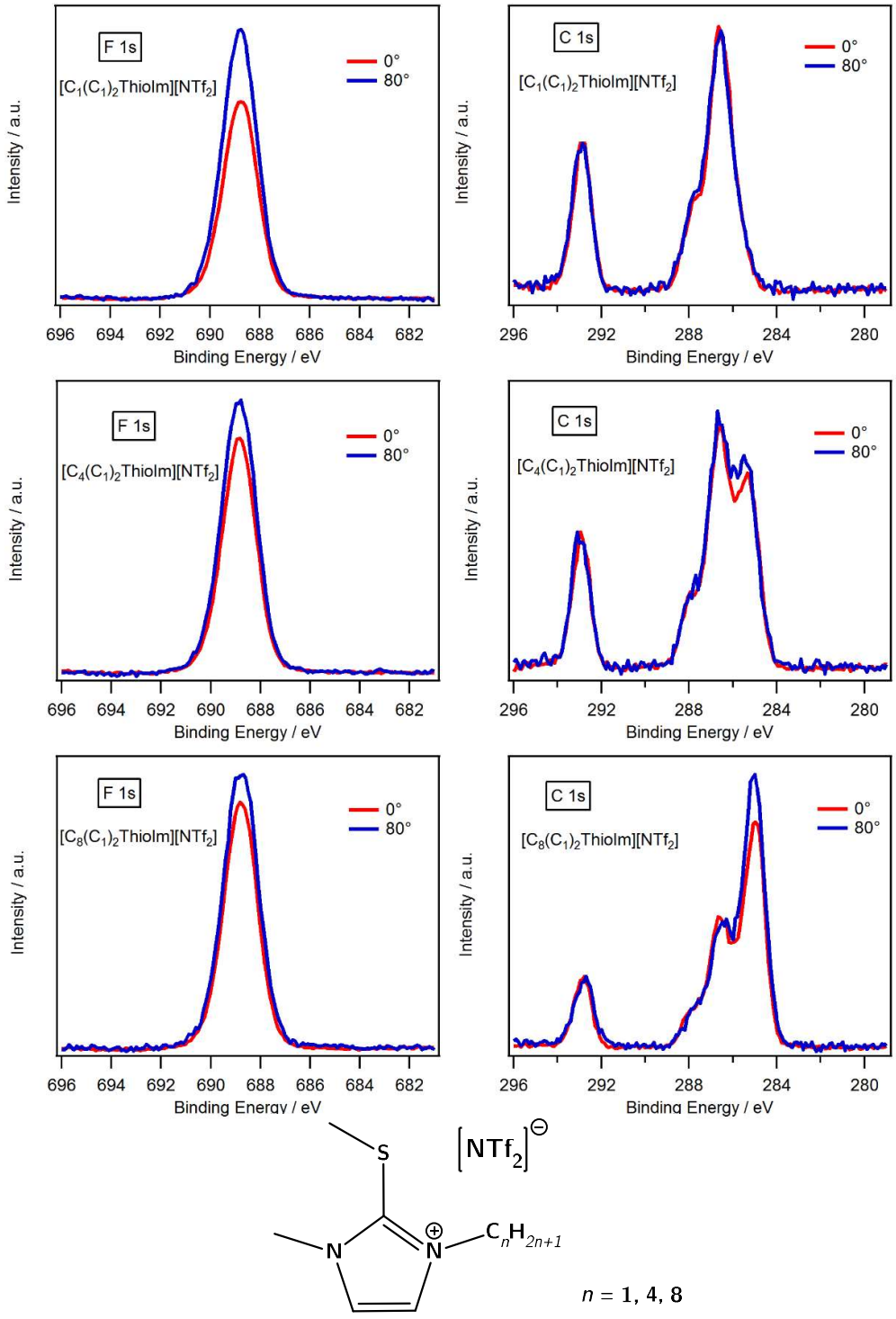


Figure 5.19. High-resolution XP spectra of the F 1s and C 1s region for the thioimidazolium bis(trifluoromethanesulfonyl)imide-based ionic liquids studied in this *Chapter*, recorded at 0° (red) and 80° (blue) electron emission angle, θ, with respect to the surface normal. $[C_n(C_1)_2\text{ThioIm}][NTf_2]$ with $n < 8$ were charge corrected by referencing N_{cation} 1s to the equivalent value obtained for $[C_8(C_1)_2\text{ThioIm}][NTf_2]$. Spectra recorded at θ = 80° normalised to the intensity of the C_{CF_3} 1s photoelectron emission peak recorded for the respective ionic liquid at θ = 0°.

As acknowledged for the imidazolium series, the thioimidazolium series also display an increase in the aliphatic component at 80°, as the alkyl chain is increased. As expected, this impact is more evident for $[C_8(C_1)_2ThioIm][NTf_2]$, showing comparable increase to the aliphatic component as for the $[C_8C_1Im][NTf_2]$ ionic liquid.

An increase of the F 1s component was also expected, especially for short chain ionic liquids. Interestingly, the $[C_1(C_1)_2ThioIm][NTf_2]$ displays a higher content of F 1s component when compared to short chain imidazoliums. Additionally, the same can be seen for the $[C_4(C_1)_2ThioIm][NTf_2]$. Whereas for $[C_4C_1Im][NTf_2]$ no enrichment can be acknowledged, the thioimidazolium shows F 1s enrichment at the surface.

These results suggest that the anion not only sits on the top of the cation, similarly as for the imidazolium series, but also can be found more at the surface when compared to a similar chain imidazolium.

5.5. High-Energy XPS

5.5.1. Ag L_α' X-ray Source

One of the most important characteristics of XPS using conventional sources such as Al K_α ($h\nu$ = 1486.6 eV) or Mg K_α ($h\nu$ = 1253.6 eV) is the surface sensitivity of the technique. Using a source with higher photon energy will increase the kinetic energy level of the conventional peaks but will also introduce new lines, which may have low kinetic energy levels. In the evolving years of XPS the choice of a suitable photon source for higher energy XPS was a matter of some compromise. This is because as the energy was increased to increase the analysis depth, the natural line width and therefore also the chemical resolution was degraded. In spite of this, much useful work was done by several workers who moved to higher energy sources such as Si K_α ($h\nu$ = 1739.4 eV),[253] Zr L_α' ($h\nu$ = 2042.4 eV),[254] Ag L_α' ($h\nu$ = 2984.3 eV),[255] and Ti K_α ($h\nu$ = 4510.9 eV)[256, 257]. The Ti and Zr induced spectra highlighted an additional

problem with higher energy photon sources, that of spectral features resulting from X-ray satellites and the presence of an intense Bremsstrahlung component. As a solution to this, the use of a standard monochromator geometry was proposed, which would take second order reflections from a Ag L_{α}' source.[255, 258] The use of the monochromated source dramatically improved the quality of the spectra.[259] These high-energy sources raise the depth limit for collection of chemically specific data to the order of 25 nm. Monochromatisation of the X-rays is therefore essential to eliminate unwanted X-ray lines, Bremstrahlung radiation and X-ray satellites. This is crucial to improve resolution and avoid complications resulting from the overlap of peaks due to different X-ray lines. Monochromatisation reduces the spectral background by removal of the Bremstrahlung component, improves the signal-to-noise ratio of Auger peaks, and makes it possible to see weak Auger signals. The ability to focus the X-ray beam onto the correct position on the sample is another benefit of monochromatisation.

5.5.2. Energy Range

The kinetic energy of an emitted photoelectron is dependent on the energy of the incident radiation. Consequently, on consideration of the Einstein equation ($KE = h\nu - BE - \Phi_S$, Equation 2.1.), where KE = kinetic energy, $h\nu$ = energy of incident radiation, BE = binding energy, and Φ_S = spectrometer work function – the binding energy of a photoelectron peak should not change between X-ray sources.

This is clearly seen by a comparison of survey spectra for $[(C_8C_1)_2dmg][NTf_2]$ obtained with the Al K_{α} and Ag L_{α}' sources between the energy range 0 –1400 eV, Figure 5.20. Additionally, due to the higher energy of the Ag L_{α}' X-rays, which is approximately twice that of Al K_{α} radiation, a broader energy range of photoelectron emissions can be observed, thus core orbitals of higher binding energy can be detected *i.e.* the S 1s photoelectron emission at ≈ 2500 eV.

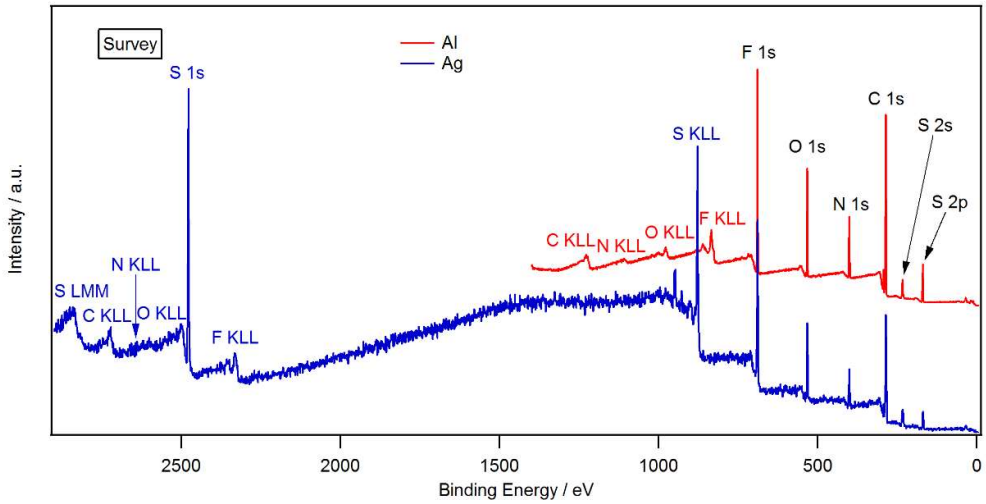


Figure 5.20. Survey XP spectra for $[(C_8C_1)_2dmg][NTf_2]$ using Al K_α and Ag L_α' X-ray sources; showing photoelectron emissions detected by both sources (black labels); Auger emissions for Al source (red labels); Auger and photoelectron emissions for Ag source (blue labels). Spectra normalised to intensity of the F 1s photoelectron emission peak obtained using the Al K_α source and offset vertically for clarity.

In contrast, Auger electron emissions have a kinetic energy that is independent to the energy of the incident radiation as they arise from internal atom deexcitation. As a binding energy scale is used in an XP spectrum for the analysis of photoelectron emissions, the apparent "binding energy" of the Auger emissions will vary as the energy of the X-ray source is changed. This is clearly exhibited by Figure 5.20 where the Auger emissions using the Al K_α source occur between 800 – 1400 eV, whereas the same Auger emissions occur at 2300 – 2800 eV using the Ag L_α' source. As only photoelectron emissions are analysed in this study the binding energy scale is used throughout.

The dependency of the kinetic energy for any given photoelectron emission on the energy of the incident radiation also has implications on the depth of the sample probed. For example, radiation of higher energy will result in a higher kinetic energy of the emitted photoelectron. In turn, this results in a longer attenuation length, and hence a greater probability of it escaping from deeper within the sample. As such the Ag L_α' source can probe deeper within a sample, in comparison to Al K_α radiation, thereby elucidating further information on the bulk structure of ionic liquids.

It should be noted that in order to calculate XPS sensitivity factors for a particular analyser, it is necessary to determine its efficiency for focusing and discriminating electrons as a function of their energy, also known as the transmission function.[260] Relative sensitivity factors (RSFs) for the softer Al K_α source, *i.e.* for photoelectron kinetic energies in the range 0 – 1500 eV, are well-defined in the literature enabling elemental quantification.[74, 134] In contrast, for the harder Ag L_α' source no sensitivity factors or transmission function protocol currently exists for photoelectron kinetic energies in the range 1500 – 2900 eV. Consequently, for depth profiling experiments using the Ag L_α' X-ray source a qualitative approach is utilised and is discussed further in *Section 5.6*.

5.5.3. Intensity and Broadening of Photoelectron Peaks

The energy of the Ag L_α' X-rays ($h\nu$ = 2984.3 eV) are approximately twice that of the Al K_α source ($h\nu$ = 1486.6 eV). For each source, the same spectrometer set-up is used with only minor adjustments to the X-ray gun position and the quartz crystal monochromator.

The same quartz crystal monochromator is allowed for use with each source as an integer number of Al K_α and Ag L_α' X-ray wavelengths (0.834 nm and 0.415 nm respectively) equate to the spacing between the quartz (1010) planes (0.425 nm) at an angle close to 78.5°.[115] The Bragg diffraction principle stipulates that for constructive interference of reflected photons to occur they must satisfy the conditions outlined in Equation 5.1:

$$n\lambda = 2d\sin\theta \qquad \textbf{5.1}$$

where n = order of diffraction, λ = wavelength, d = crystal spacing, and θ = angle of diffraction.

Consequently, as the wavelength for Ag L_α' is half that of Al K_α, the Bragg diffraction criteria is satisfied to first order for Al K_α and second order for Ag L_α'. The combination of Bragg diffraction and a slight concavity of the

quartz crystal results in a focused X-ray beam at the sample surface, see Figure 5.21.

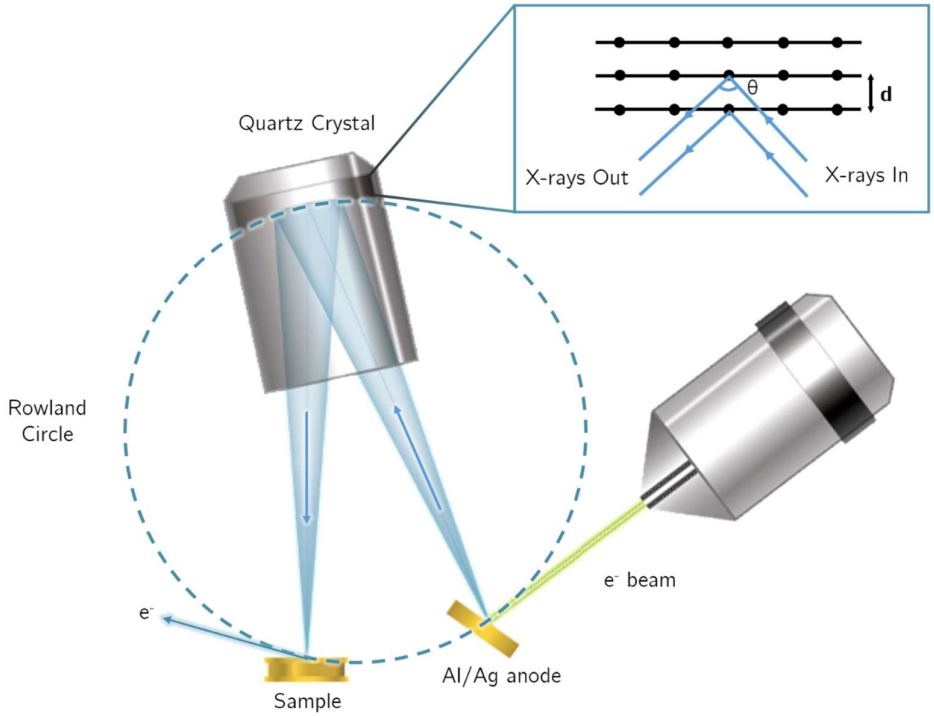


Figure 5.21. Schematic illustrating the XPS monochromator geometry in which X-rays generated at the anode are reflected off quartz crystal and focused at the sample. The inset describes the Bragg diffraction criterion for constructive interference of the scattered X-rays. (Adapted from reference 131)

An increase in order of diffraction is accompanied by a significant decrease in X-ray beam intensity. Consequently, the signal intensity when using the Ag L_{α}' source is considerably reduced in comparison to the Al K_{α} source, as demonstrated by the unnormalised survey spectra Figure 5.22 and C 1s spectra for $[(C_8C_1)_2dmg][NTf_2]$ obtained from each source in Figure 5.23.

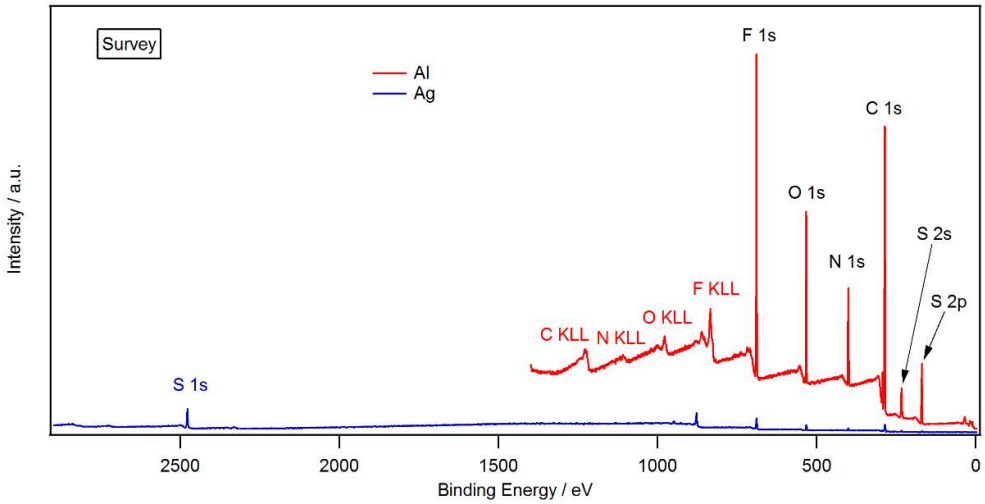


Figure 5.22. Comparison of survey XP spectra for $[(C_8C_1)_2dmg][NTf_2]$ using Al K_α and Ag L_α' X-ray sources; showing photoelectron emissions detected by both sources (black labels); Auger emissions for Al source (red labels); S 1s photoelectron emission for Ag source (blue label). Spectra offset vertically for clarity.

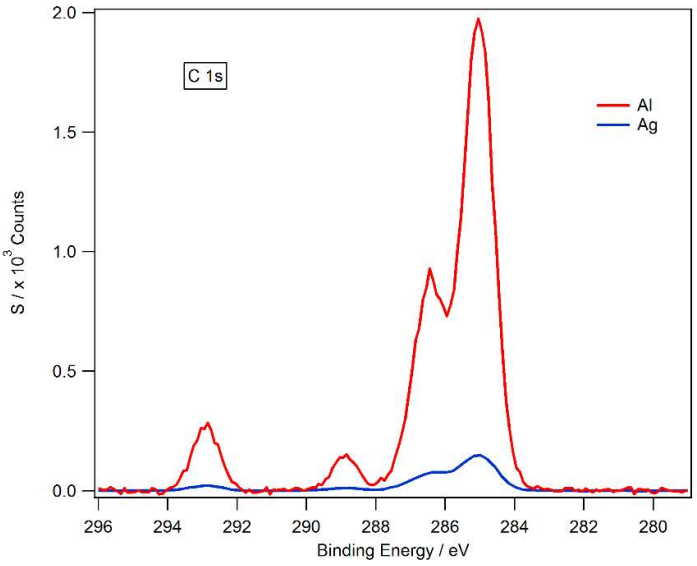


Figure 5.23. Comparison of C 1s high-resolution spectra intensity for $[(C_8C_1)_2dmg][NTf_2]$ obtained with Ag L_α' source (blue) and Al K_α (red). Spectra charge corrected by referencing $C_{aliphatic}$ 1s = 285.0 eV

As a result, longer acquisition times must be employed when using the Ag L_α' X-ray source to obtain spectra comparable in quality to the Al K_α source, see *Chapter 2 Section 2.2.* for details. Furthermore, in order to obtain a visual comparison of spectra obtained from the two different sources an appropriate normalisation procedure must be applied.

With increasing order of diffraction, a wider energy distribution of the respective X-ray beam will result *i.e.* X-ray linewidth will increase with diffraction order. Consequently, as Ag L_α' X-rays satisfy second order diffraction conditions a larger linewidth of ≈ 1.2 eV occurs in comparison to $\approx 0.2 - 0.3$ eV for Al K_α.[115] As such, the photoelectron peaks obtained using the Ag L_α' X-ray source are typically broader than when obtained using the Al K_α source. For example, when using the Ag $3d_{5/2}$ peak to determine energy resolution, a full width half maximum (FWHM) of < 0.55 eV is obtained using the Al K_α source in comparison to 0.9 eV for Ag L_α'. This is also exemplified in Figure 5.24, which shows a visual comparison of the high-resolution spectra obtained with each X-ray source for all regions for $[(C_8C_1)_2dmg][NTf_2]$. It can be seen that the FWHM for the photoelectron peaks detected with the Ag L_α' source are typically ≈ 0.1 eV larger than those obtained with the Al K_α source.

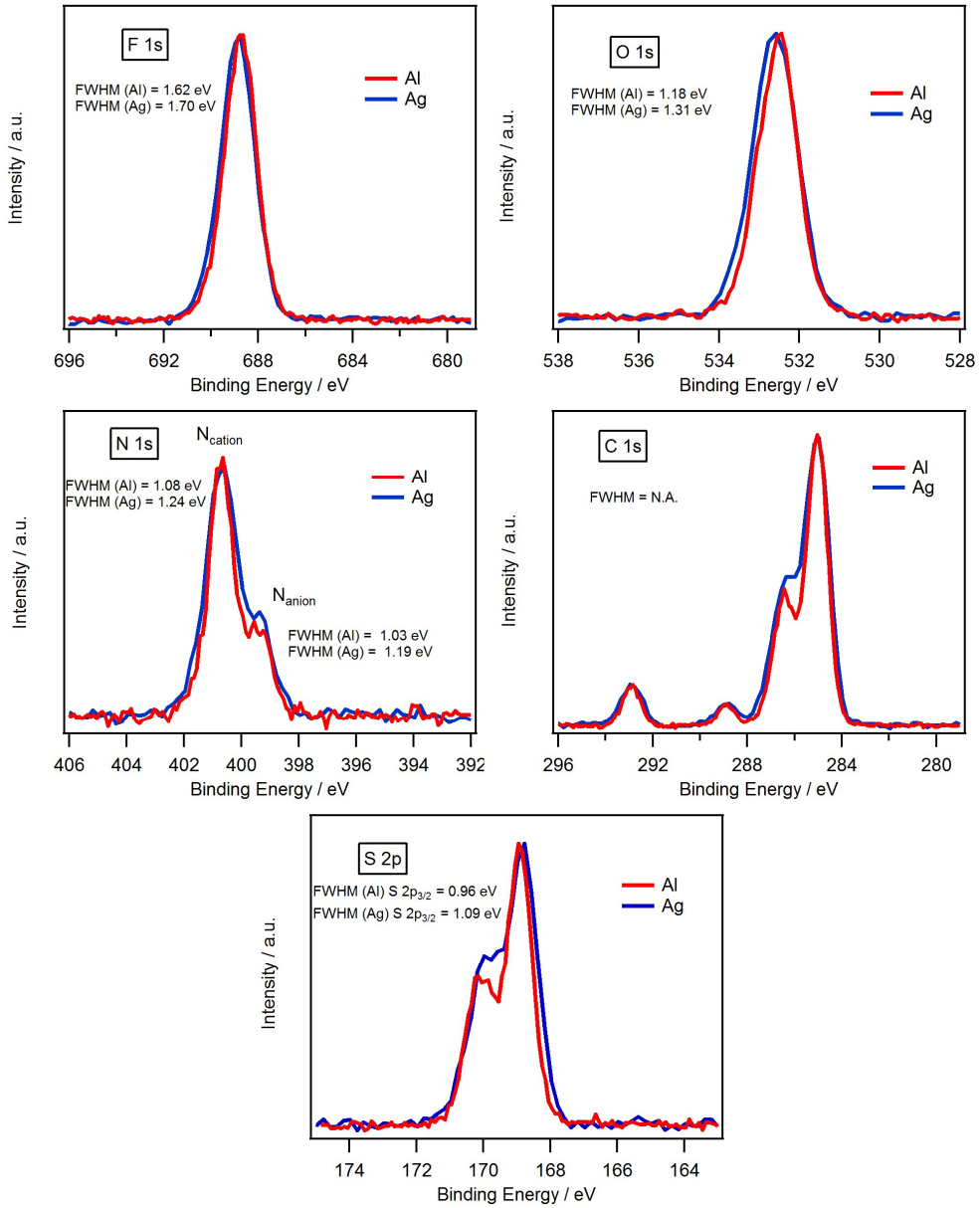


Figure 5.24. Comparison of XP spectra obtained with Ag L_{α}' source (blue) and Al K_{α} source (red) for all regions for $[(C_8C_1)_2dmg][NTf_2]$. Spectra charge corrected by referencing $C_{aliphatic}$ 1s = 285.0 eV and normalised to the intensity of the respective photoelectron peak obtained using the Al K_{α} X-ray source (N_{cation} 1s, CF_3 1s and S $2p_{3/2}$ in the case of N 1s, C 1s and S 2p respectively). The associated experimental error is ± 0.1 eV (FWHM of the respective regions with 2 decimal points to show trend only).

The FWHM for the C 1s regions are not stated as the C 1s spectra consists of several components, consequently the FWHM of the respective components are dependent on the constraints used in the fitting model. However, a slight broadening in line shape can be observed for the Ag L_{α}' C 1s region in Figure 5.24.

Due to the broader line shape of photoelectron emissions resulting from the Ag L_α' source the FWHM constraints for the C 1s fitting model have to be slightly modified. The fitting model is followed exactly as previously described for the Al K_α source, see *Chapter 3, Sections 3.2.3*, however the FWHM is constrained to be between 0.8 – 1.5 eV instead of 0.8 – 1.3 eV.

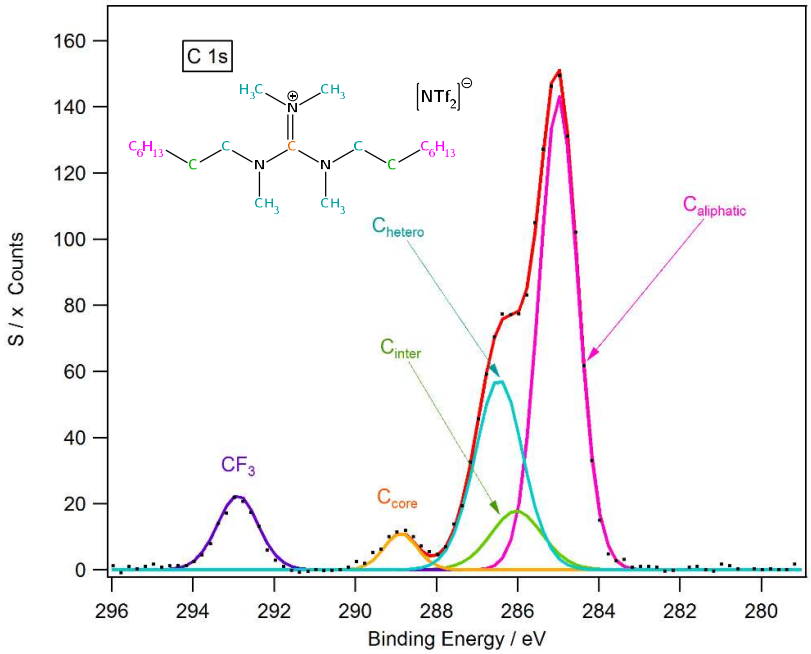


Figure 5.25. High-resolution C 1s spectra obtained with the Ag L_α' source for $[(C_8C_1)_2dmg][NTf_2]$ including colour coded component fittings for $C_{aliphatic}$ (pink), C_{hetero} (blue), C_{inter} (green), C_{core} (orange) and C_{CF_3} (purple); fitting envelope (red); counts (black dots). Spectra charge corrected by referencing $C_{aliphatic}$ 1s to 285.0 eV**.** The resulting sum of components, envelope (red) is partially omitted to show the CF_3, C_{core} and aliphatic components.

A representative example of the C 1s fitting model for $[(C_8C_1)_2dmg][NTf_2]$ is provided in Figure 5.25. The fitting envelope (red trace) demonstrates excellent agreement to the experimental spectra (black dots) highlighting the validity of the fitting model. C 1s component fittings for all ionic liquids investigated with the Ag L_α' X-ray source are included in *Appendix C*, and are also in good agreement with the experimental spectra.

5.5.4. Binding Energy Analysis

A comparison of binding energies obtained with the Ag L_α' and Al K_α source has been made upon a series of structurally diverse ionic liquids comprising the

$[NTf_2]^-$ anion for consistency. A range of monocations were selected: $[C_nC_1Im]^+$, $[C_n(C_1)_2ThioIm]^+$ and $[(C_8C_1)_2dmg]^+$. The anion was chosen such that all ILs include an element that has higher energy core orbitals which can only be detected with the higher energy Ag L_α' source *i.e.* S 1s photoelectron emissions. The $[C_n(C_1)_2ThioIm]^+$ series was chosen as both anion and cation include sulfur, providing more information upon the anion/cation relative position.

Ionic liquids containing the $[NTf_2]^-$ anion did not show any indication of beam damage. In addition, there was no evidence of contaminants in the majority of ILs studied, especially in the imidazolium series, such as laboratory grease. Moreover, all peaks in the survey spectra could be assigned to elements within the respective ionic liquids, highlighting the high purity for this particular series of ionic liquids, see *Appendix C*. Furthermore, these compounds were in liquid state at room temperature, therefore they emitted superior photoelectron flux in comparison to solid samples. This enabled the measurement of high quality spectra with excellent resolution.

The measured binding energies for both sources display excellent agreement with values within the experimental error (± 0.1 eV), see Table 5.2, Table 5.3, *etc*. Accordingly, the Ag L_α' X-ray source provides robust chemical state analysis for a variety of ionic liquids, as well as the characterisation of previously inaccessible higher energy core orbitals such as Si 1s and S 1s.

The added value of the high-energy Ag L_α' X-ray source, however, is its ability to provide another approach to depth profiling based on detecting two different core photoelectron emissions (which have a large difference in binding energy) from the same element.

Bis(trifluoromethanesulfonyl)imide-based ionic liquids were investigated further in a depth profiling study to determine the influence of the cation on the ionic liquid/vacuum interface, this is discussed in detail in the following sections.

Table 5.2. Experimental binding energies in eV for the imidazolium bis(trifluoromethanesulfonyl)imide-based ionic liquids studied. The associated experimental error is ± 0.1 eV. $[C_nC_1Im][NTf_2]$ with $n \geq 8$ charge corrected by referencing $C_{aliphatic}$ 1s to 285.0 eV. $[C_nC_1Im][NTf_2]$ with $n < 8$ charge corrected by referencing N_{cation} 1s to the value obtained for $[C_8C_1Im][NTf_2]$ using the same X-ray source.

		Binding Energy / eV										
		Cation					Anion					
Ionic Liquid		$C_{aliphatic}$ 1s	$C_{4,5}$ 1s	$C_{6,7}$ 1s	C_2 1s	N_{cation} 1s	C_{CF_3} 1s	N_{anion} 1s	O 1s	F 1s	S_{anion} $2p_{3/2}$	S_{anion} 1s
Al K_α Source												
$[C_2C_1Im]$	$[NTf_2]$	285.5	286.6	287.0	287.7	402.1	293.0	399.5	532.7	688.9	169.0	-
$[C_3C_1Im]$	$[NTf_2]$	285.4	286.5	287.0	287.7	402.1	292.9	399.5	532.7	688.9	168.9	-
$[C_4C_1Im]$	$[NTf_2]$	285.2	286.6	287.0	287.7	402.1	292.9	399.5	532.7	688.9	169.0	-
$[C_6C_1Im]$	$[NTf_2]$	285.1	286.5	287.0	287.7	402.1	292.9	399.5	532.7	688.9	169.0	-
$[C_8C_1Im]$	$[NTf_2]$	285.0	286.5	287.0	287.7	402.1	292.9	399.5	532.7	688.9	169.0	-
$[C_{10}C_1Im]$	$[NTf_2]$	285.0	286.6	287.0	287.7	402.1	293.0	399.5	532.7	688.9	169.0	-
$[C_{12}C_1Im]$	$[NTf_2]$	285.0	286.6	287.0	287.7	402.1	293.0	399.5	532.7	688.9	169.0	-
Ag L_α' Source												
$[C_2C_1Im]$	$[NTf_2]$	285.5	286.6	287.2	287.7	402.1	293.0	399.5	532.7	689.0	168.9	2478.2
$[C_3C_1Im]$	$[NTf_2]$	285.4	286.5	287.0	287.8	402.1	293.0	399.5	532.7	689.0	168.9	2478.2
$[C_4C_1Im]$	$[NTf_2]$	285.2	286.5	287.1	287.7	402.1	293.0	399.5	532.7	689.0	168.9	2478.2
$[C_6C_1Im]$	$[NTf_2]$	285.1	286.5	287.0	287.8	402.1	293.0	399.5	532.7	689.0	168.9	2478.2
$[C_8C_1Im]$	$[NTf_2]$	285.0	286.5	287.0	287.8	402.1	293.0	399.5	532.7	688.9	168.9	2478.2
$[C_{10}C_1Im]$	$[NTf_2]$	285.0	286.5	287.1	287.7	402.1	293.0	399.5	532.7	689.0	169.0	2478.2
$[C_{12}C_1Im]$	$[NTf_2]$	285.0	286.5	287.1	287.8	402.1	293.0	399.5	532.7	689.0	169.0	2478.2

Table 5.3. Experimental binding energies in eV for the Thioimidazolium bis(trifluoromethanesulfonyl)imide-based ionic liquids studied. The associated experimental error is ± 0.1 eV. $[C_8(C_1)_2ThioIm][NTf_2]$ charge corrected by referencing $C_{aliphatic}$ 1s to 285.0 eV. $[C_1(C_1)_2ThioIm][NTf_2]$ and $[C_4(C_1)_2ThioIm][NTf_2]$ charge corrected by referencing N_{cation} 1s to the value obtained for $[C_8(C_1)_2ThioIm][NTf_2]$ using the same X-ray source.

Compound		Binding Energy / eV													
		Cation								Anion					
Cation	Anion	C_2 1s	$C_{6,7}$ 1s	$C_{4,5}$ 1s	C_S 1s	$C_{aliphatic}$ 1s	N_{cation} 1s	$S_{exocyclic}$ $2p_{3/2}$	$S_{exocyclic}$ 1s	C_{CF_3} 1s	N_{anion} 1s	O 1s	F 1s	S_{anion} $2p_{3/2}$	S_{anion} 1s
Al K_α Source															
$[C_1(C_1)_2ThioIm]$	$[NTf_2]$	288.0	286.9	286.6	285.8	-	402.0	164.8	-	292.9	399.4	532.6	688.8	168.9	-
$[C_4(C_1)_2ThioIm]$	$[NTf_2]$	288.0	286.9	286.5	285.9	285.2	402.0	164.8	-	292.9	399.4	532.6	688.8	168.9	-
$[C_8(C_1)_2ThioIm]$	$[NTf_2]$	287.9	286.9	286.5	285.9	285.0	402.0	164.8	-	292.9	399.4	532.6	688.9	168.9	-
Ag L_α' Source															
$[C_1(C_1)_2ThioIm]$	$[NTf_2]$	287.9	286.9	286.5	285.8	-	402.0	164.7	2473.0	292.9	399.4	532.7	688.9	168.8	2478.2
$[C_4(C_1)_2ThioIm]$	$[NTf_2]$	288.0	286.8	286.6	286.0	285.2	402.0	164.7	2473.0	292.9	399.4	532.7	688.9	168.8	2478.2
$[C_8(C_1)_2ThioIm]$	$[NTf_2]$	288.0	286.9	286.6	286.0	285.0	402.0	164.7	2473.0	292.9	399.4	532.7	689.0	168.8	2478.2

5.6. Energy-Resolved XPS

5.6.1. Principles

In the case of ERXPS the dependence of λ_{AL} on the kinetic energy of the emitted photoelectron is exploited in order to depth profile a sample. Unlike ARXPS, a fixed geometry is employed with a normal emission angle of $\theta = 0°$. Consequently, ID can be simplified to $ID = 3\lambda_{AL}$, thus ID is solely a function of attenuation length and hence kinetic energy. This can be achieved in two ways. Firstly, by looking at spectra of the same core photoelectron emission but changing the energy of the incident radiation, thereby varying photoelectron kinetic energy, and hence the depth which is probed. Typically, this procedure requires the use of synchrotron radiation sources as they can provide high intensity X-ray photons that can be tuned across a broad range of energies. The most surface sensitive mode for synchrotron depth profiling experiments are at a photon energy about 50 eV higher than the binding energy of the core level photoelectron emission examined, in which the surface layer probed is around several atoms thick.[90]

The second ERXPS approach can be accomplished by looking at two different core photoelectron emissions from the same element using the same X-ray source. Importantly, the binding energy difference – and consequently, the kinetic energy difference – between the two photoelectron emissions must be sufficiently large, therefore high energy X-ray sources such as Ag L_α' are required to detect core levels of higher energy.

In contrast to ARXPS there are only few reported examples of using ERXPS to probe the IL/vacuum interface, and these have been limited to variable-photon energy experiments which require a synchrotron source.[81, 90] Although many synchrotron facilities exist, obtaining time on them can be difficult and also expensive. Recently in the Licence group, ERXPS studies onto quaternary ammonium and phosphonium cations were compared to ARXPS utilising this approach with similar trends observed.[114] Herein, this approach of utilising a

high-energy laboratory Ag L_{α}' X-ray source for the depth profiling of a series of bis(trifluoromethanesulfonyl)imide-based ionic liquids is described.

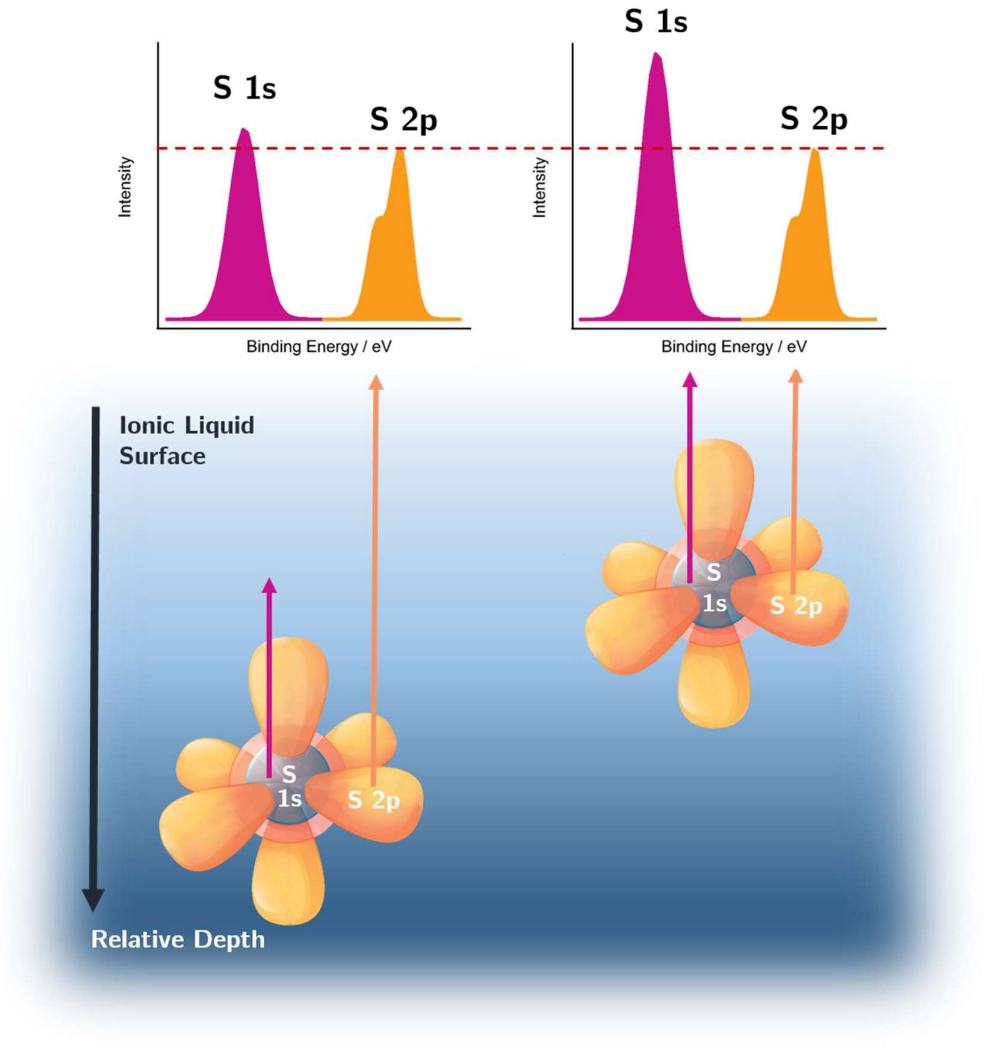


Figure 5.26. Schematic representation illustrating the influence of depth of the sulfur atom from the $[NTf_2]^-$ anion on the corresponding S 1s and S 2p photoelectron emission intensities. The higher kinetic energy of an emitted S 2p photoelectron results in a higher probability of its escape from within the bulk (ID = 15.9 nm), thus the intensity the S 2p photoelectron emission signal remains constant regardless of the depth of the emitting sulfur atom. In contrast, the lower kinetic energy of an emitted S 1s photoelectron reduces its probability of escape from within the bulk (ID = 4.2 nm). Consequently, the change in intensity of the S 1s photoelectron emission peak provides information on the surface concentration of sulfur, *i.e.* high sulfur surface concentration increases the S 1s signal, whereas low sulfur surface concentration decreases the S 1s signal (relative to S 2p).

A qualitative approach is used to determine differences in sulfur surface enrichment between samples. By comparison of the peak area ratio of S 1s : S 2p between different samples a relative depth profile can be obtained, whereby the area for S 2p is effectively constant (as it is representative of the bulk) and the area for S 1s will vary with surface enrichment of sulfur, thus

affecting the ratio of S 1s : S 2p accordingly for each sample. Therefore, a comparison of this ratio between different samples will show any differences with respect to sulfur surface enrichment relative to each other; this method is illustrated by the schematic presented in Figure 5.26 and explained further in *Section 5.7*.

5.6.2. Data Analysis and Processing

Depth profile of an element within an ionic liquid can be obtained if two core photoelectron emissions from that element can be detected, most importantly they must also have a wide separation in energy. By using the higher energy Ag L_{α}' X-ray source photoelectron emissions at higher binding energy can be detected, as shown in Figure 5.20. ERXPS, was therefore used to obtain a depth profile for the sulfur atom of the $[NTf_2]^-$ anion through comparison of the S 1s and S 2p photoelectron peaks for the ionic liquids. It is important to note that no geometry change to the sample is required, *i.e.* all spectra are recorded at fixed emission angle $\theta = 0°$, consequently any error introduced by a change in geometry is removed.

This approach is based on the fact that the depth from which a photoelectron is able to escape is dependent on the kinetic energy of the photoelectron. A higher kinetic energy will allow the photoelectron to travel for a longer distance in the sample without experiencing energy loss through collisions *i.e.* it has a longer attenuation length, λ_{AL}.

The binding energies for S 2p and S 1s core orbitals for all ionic liquids studied are respectively ≈ 169 eV and 2478 eV, as discussed further (Table 5.2, Table 5.3, *etc.*). This corresponds to kinetic energies of S 2p ≈ 2816 eV and S 1s ≈ 507 eV. Consequently, a photoelectron emitted from the S 2p orbital has a greater probability of escaping from deeper in the sample than an S 1s photoelectron. The NIST Electron Inelastic-Mean-Free-Path Database was used to estimate λ_{AL} for S 2p and S 1s photoelectrons for each ionic liquid to give approximate values of 5.3 nm and 1.4 nm respectively.[261] This was achieved by

using the database to first calculate the inelastic mean free path (λ_{IMFP}) for each ionic liquid using the TPP-2M method.[262] This calculation can only be carried out up to a kinetic energy of 2000 eV.[†] Consequently, extrapolation of the obtained data set up to 3000 eV is required to obtain an estimate λ_{IMFP} in the energy range 2000 – 3000 eV. The resultant plots of λ_{IMFP} *versus* kinetic energy for each ionic liquid are presented in Figure 5.27.

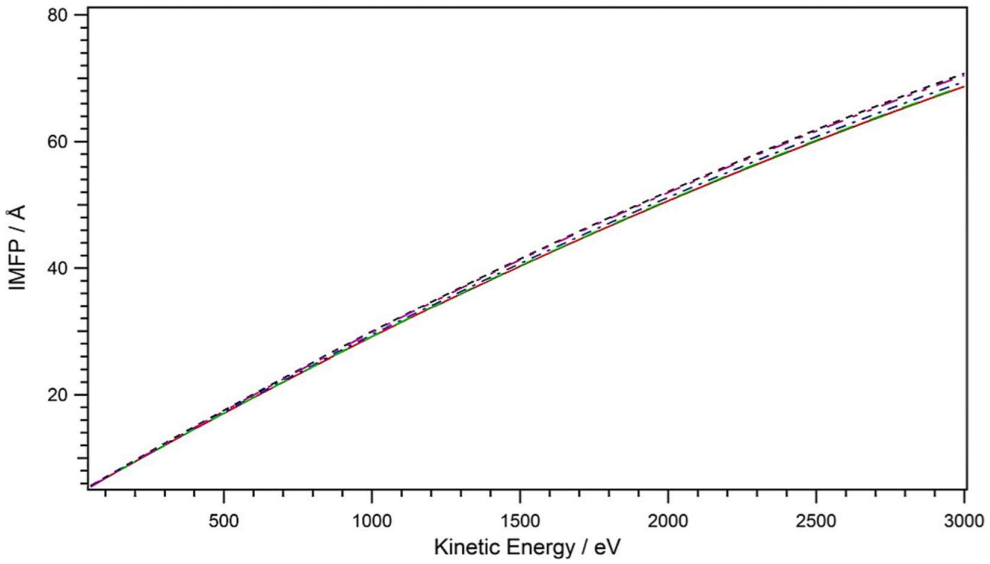


Figure 5.27. Calculated λ_{IMFP} values for the kinetic energy range 0 – 3000 eV for an array of ionic liquids studied.

The attenuation length is typically 20% smaller than the calculated inelastic mean free path as it does not include elastic scattering events;[116, 130] subsequently, this is accounted for in the estimation of λ_{AL} in this work. Figure 5.28 provides a representative example of this procedure for $[C_8C_1Im][NTf_2]$. This shows a plot of the calculated λ_{IMFP} for the energy range 50 – 3000 eV (solid line), and the estimated λ_{AL} (dashed line) – which is 80% of λ_{IMFP}.

[†] The TPP-2M method depends on the molecular weight, density, and number of valence electrons of the compounds analysed. Recently this methodology has been verified for XPS experiments and consistency between experimental methods and computed IMFPs has been found.[263] However, uncertainty of data is about ± 10% as this method assumes homogeneous depth composition of the sample.

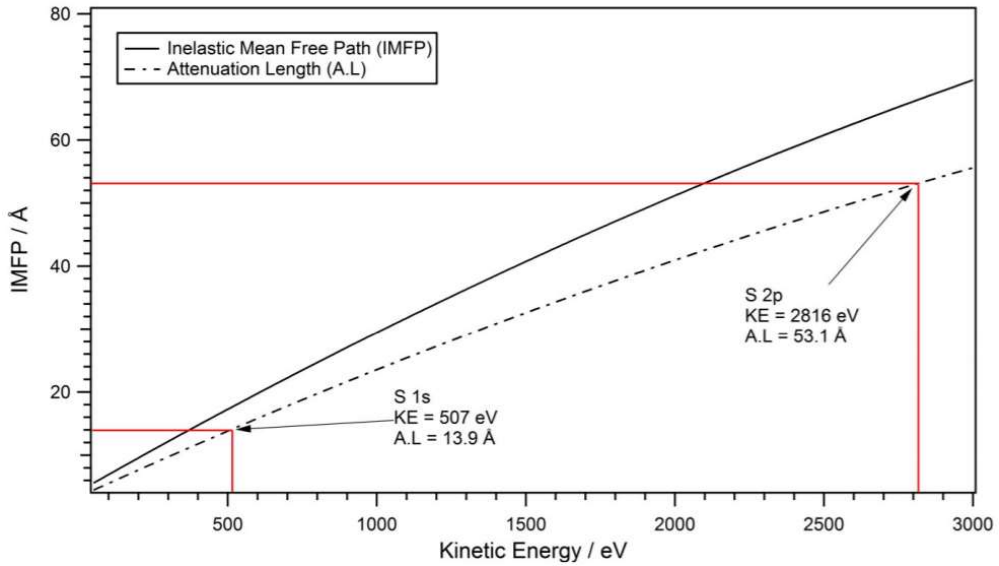


Figure 5.28. Plot describing the calculated λ_{IMFP} (solid black line) and estimated λ_{AL} (dashed line) for $[C_8C_1Im][NTf_2]$. Highlighting the λ_{AL} values obtained for S 1s and S 2p photoelectrons.

The corresponding λ_{AL} values can then be determined for the required kinetic energies. The λ_{IMFP} and λ_{AL} values obtained for each ionic liquid are presented in Table 5.4. The values are consistent between compounds and are therefore not sensitive to the ionic liquid.

Table 5.4. λ_{IMFP} and λ_{AL} values for the S 2p and S 1s photoelectrons for a range of $[NTf_2]^-$ ionic liquids studied in this work.

	S 2p		S 1s	
	λ_{IMFP} (nm)	λ_{AL} (nm)	λ_{IMFP} (nm)	λ_{AL} (nm)
$[C_8C_1Im][NTf_2]$	6.7	5.3	1.7	1.4
$[(C_8C_1)_2dmg][NTf_2]$	6.8	5.4	1.8	1.4
$[C_8(C_1)_2ThioIm][NTf_2]$	6.6	5.3	1.7	1.4

As this technique uses a fixed geometry of the sample *i.e.* an emission angle where $\theta = 0°$, ID can be expressed as $ID = 3\lambda_{AL}$. The information depths for the required photoelectron emissions were obtained using the calculated λ_{AL} values to give an S 1s ID = 4.2 nm and S 2p ID = 15.9 nm. Consequently, the S 2p signal gives a "bulk sensitive" representation of the sulfur concentration in the sample, in contrast to the S 1s signal which gives a "surface sensitive" representation.

Due to the different cross-sections of the two sulfur orbitals (S 2p and S 1s), and hence different RSF values, a direct comparison of peak areas does not

provide quantitative information on sulfur surface enrichment within a sample. To achieve this, the area ratio of S 1s : S 2p must first be determined for a homogeneously disordered ionic liquid sample, this can then be used to construct the currently unknown RSF for the S 1s peak by multiplication of the known S 2p RSF by the appropriate factor (obtained from the area ratio of S 1s : S 2p). Once attained the S 1s and S 2p signals can be quantified and directly compared for any sample, thus providing a measure of sulfur surface enrichment. However, as previously discussed many ionic liquids show significant surface ordering and therefore do not contain a homogeneous distribution of ions, thus if quantitative conclusions are to be drawn from data produced by such high-energy sources, it is essential to directly determine the electron attenuation length over the full kinetic energy range as well as RSF of a wide range of elements.

5.7. ERXPS Analysis of Ionic Liquids

5.7.1. Experimental Methodology

For ARXPS experiments, the 1-alkyl-3-methylimidazolium series was chosen to investigate the validity of our new methodology. This seems appropriate, as previously ARXPS studies onto this ILs moiety has been shown in the literature and comparisons can be made. However, for ERXPS experiments, the thioimidazolium series seemed a more appropriate set of ILs, probing not only the sulfur containing anion, but also the sulfur containing cation. Figure 5.29 illustrates general S 1s and S 2p regions, exemplified here for the $[C_1(C_1)_2ThioIm][NTf_2]$ ionic liquid.

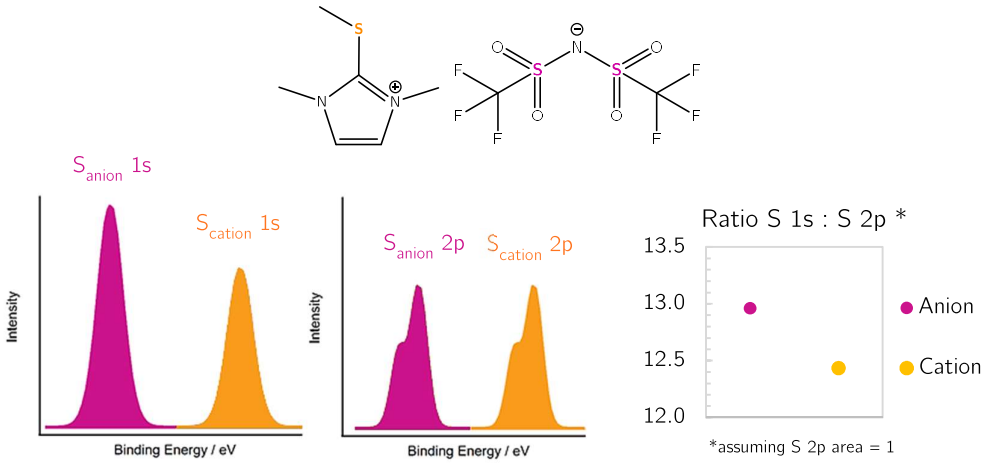


Figure 5.29. Illustration of S 1s and S 2p photoelectron emission intensities exemplified for the $[C_1(C_1)_2ThioIm][NTf_2]$ ionic liquid and visual representation of the area ratio between S 1s and S 2p for the respective anion and cation.

As mentioned in *Section 5.6.1*, the area for S 2p is effectively constant (as it is representative of the bulk) but the area for S 1s will vary with surface enrichment of sulfur, thus affecting the ratio of S 1s : S 2p accordingly for each sample. Therefore, for this particular family of ILs, a comparison of this area ratio between S_{anion} 1s : S_{anion} 2p and S_{cation} 1s : S_{cation} 2p will show any differences with respect to sulfur surface enrichment relative to each other. For visual comparison, all experimental points reflect the ratio of S 1s : S 2p when S 2p equals to 1 (for instance, 13 : 1 ratio, is represented as the *y* axis equal to 13, the *x* axis serves only to distinguish between anion and cation). Furthermore, the S_{anion} 1s : S_{cation} 1s could also be probed, providing additional information on surface enrichment of sulfur. Suitable comparisons between imidazolium and other cation families are discussed further in *Section 5.7.2*.

Upon measuring the Ag source XP spectra for the $[C_n(C_1)_2ThioIm][NTf_2]$ ionic liquid series, the $[C_1(C_1)_2ThioIm][NTf_2]$ shown a surface silicon impurity through the Si 1s peak at ≈ 1900 eV (and respective Si KLL ≈ 1400 eV) as seen in Figure 5.30.

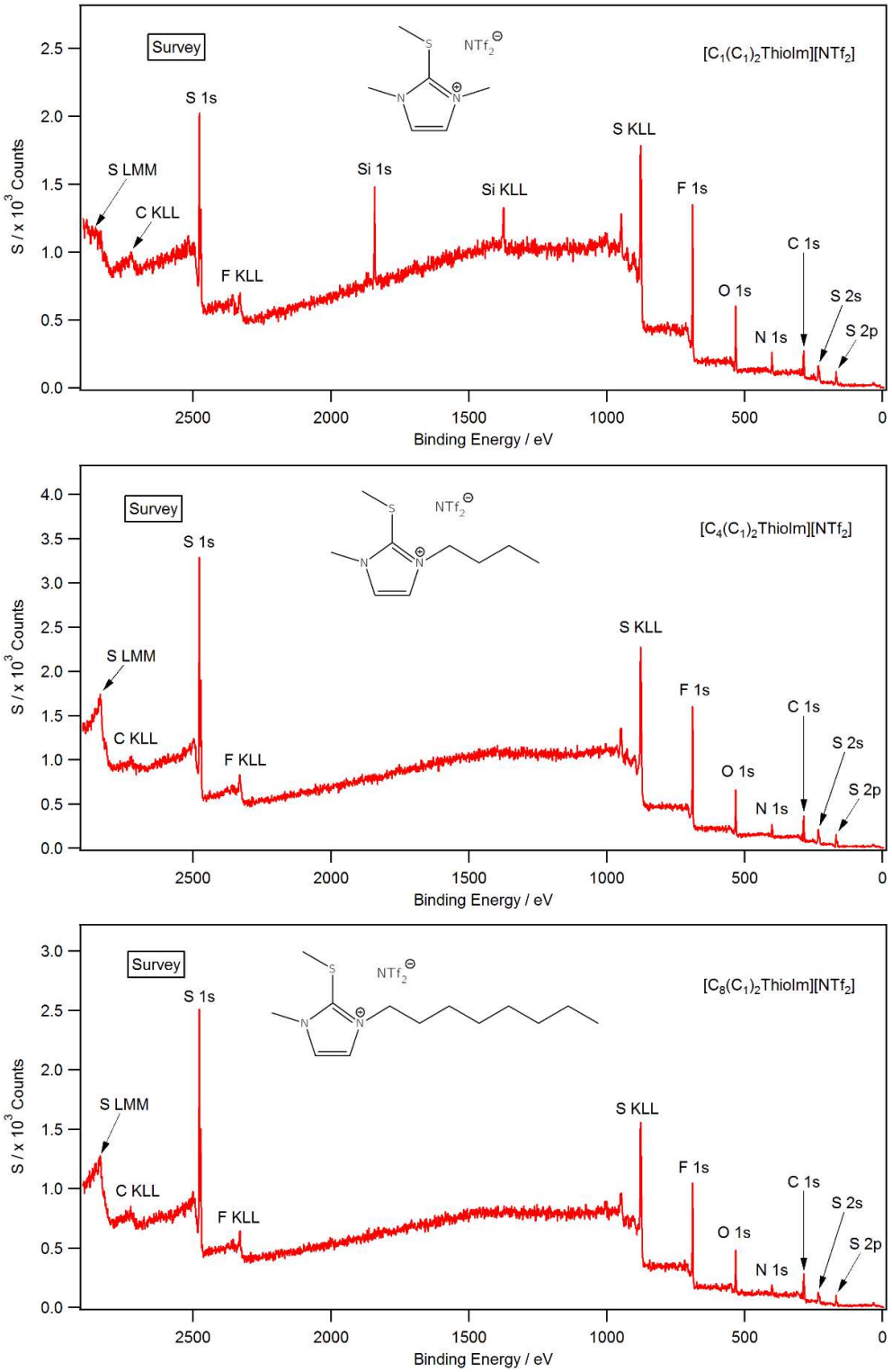


Figure 5.30. Survey scans for the $[C_n(C_1)_2\text{ThioIm}][NTf_2]$ series before any argon bombardment/heating experiments.

The noticeable silicon segregation in one of the ILs probed poses a challenge. Although surface contaminants can be removed by argon bombardment (proving they are not representative of the bulk as shown previously in *Chapter 3, Section 3.2.1*), for depth profiling studies this surface contamination may alter the arrangement and composition at the surface, which could result in inaccurate representation of the IL orientation in the IL/vacuum layer.

In order to investigate the effect of surface contamination upon depth profiles of this family of ILs, the design of experiments is a crucial step. As such, the XP Spectra measurements of these ILs were performed to the samples in steps:

- Firstly, analysis of the ILs XP spectra as shown in Figure 5.30 will allow a comparison before and after any treatment, showing the initial preferential surface rearrangement.
- Secondly, sputtering and heating experiments were performed. Sputtering was done first, for 5 minutes, in order to remove any surface contaminants. All three ionic liquids were liquids at the conditions of the experiments, thus it would be expected to the surface to rearrange itself to its preferential conformation. Nevertheless, it has been found that $[NTf_2]^-$ ionic liquids viscosities tend to increase with increase of alkyl chain length,[264] which might slow down this process.
- In the case of this rearrangement being slower in one IL when compared to others, heating for 30 minutes at 150 °C (no decomposition was observed for this IL family) was achieved in order to decrease viscosity, allowing free movement of ions. Before taking a spectrum, the surface was allowed to cool down overnight. This let the ILs to rearrange gradually and reduce the ions movement at the surface.
- If any surface contaminants segregated back to the surface (caused by the drive of ions upon heating) etching would be applied once again. This would allow additional comparison with the previous etching done before heating.

On Figure 5.31 there is a representative trend of the ratio between S 1s : S 2p areas for the first set of XP spectra for this family of ILs. The first anion/cation pair represents $[C_1(C_1)_2ThioIm][NTf_2]$, the second $[C_4(C_1)_2ThioIm][NTf_2]$ and the third $[C_8(C_1)_2ThioIm][NTf_2]$.

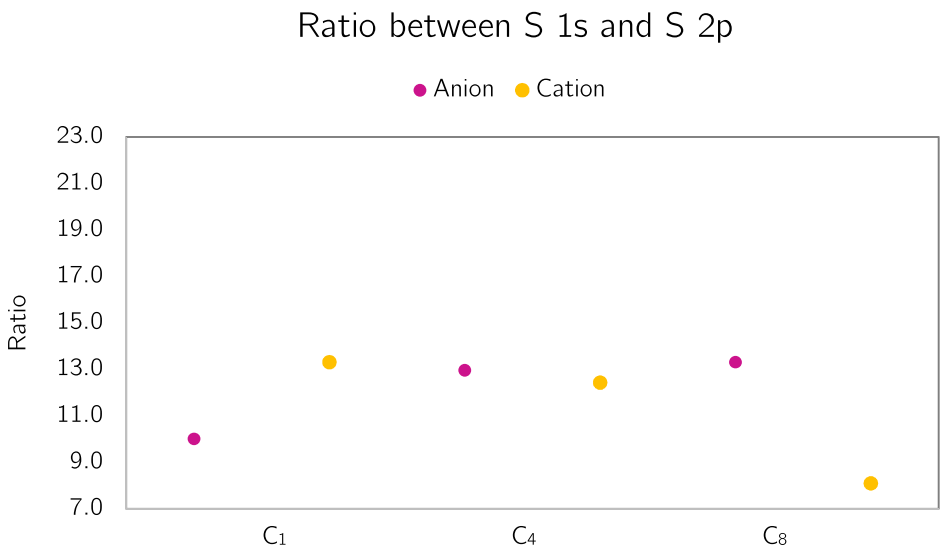


Figure 5.31. Ratio between S 1s and S 2p - Before any argon etching or heating experiments

This data highlights that there is a large level of ambiguity between samples; there seems to be no apparent correlation between the distance of the anion towards the cation and its relative position, neither a correlation between the cation depth relative to the alkyl chain length. Although the S 1s and S 2p ratio does not immediately shows a link between the position of the anion towards the cation, for the $[C_1(C_1)_2ThioIm][NTf_2]$ the trend is the opposite than for the $[C_8(C_1)_2ThioIm][NTf_2]$. Should the position of the cation stay unaltered regardless of the alkyl chain length? Or is this apparently arbitrary? Should the distance between anion and cation remain constant regardless the alkyl chain length? The variation between the ratio of the S 1s of the anion and the S 1s of the cation also emphasises a lack of correlation, as this ratio should validate the distance between the anion and the cation and the standard deviation is about 90% between measurements, Figure 5.32.

The presence of silicon within at least one of the samples might be the reason for this apparent randomness of position/distance as discussed above.

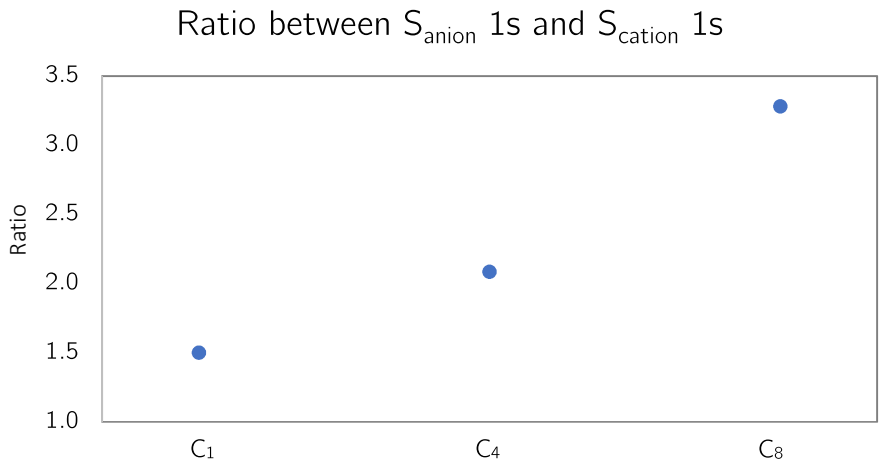


Figure 5.32. Ratio between S_{anion} 1s and S_{cation} 1s - Before any argon etching or heating experiments

After etching (5 min each)

In order to remove the surface contamination, argon bombardment was performed for 5 min in each sample. Although only one of the samples showed contamination, etching was done in all three sample for consistency. In addition, it has been reported that on the surface discontinuity, ILs tend to orientate and pair on a specific manner which them becomes slightly more arbitrary and free from orientation constrains, deeper within the sample.[70] Etching will then expose the first layers of the IL that are more random and less constrained. This noticeably creates another question upon the depth profile studies. By etching a sample are we manipulating the surface composition to a specific orientation/position? Or are the surface contaminants constraining the ability of the surface chemistry of ILs for specific applications? All three XP spectra are now clean from impurities and the survey spectrum for $[C_1(C_1)_2ThioIm][NTf_2]$ can be seen below, Figure 5.33.

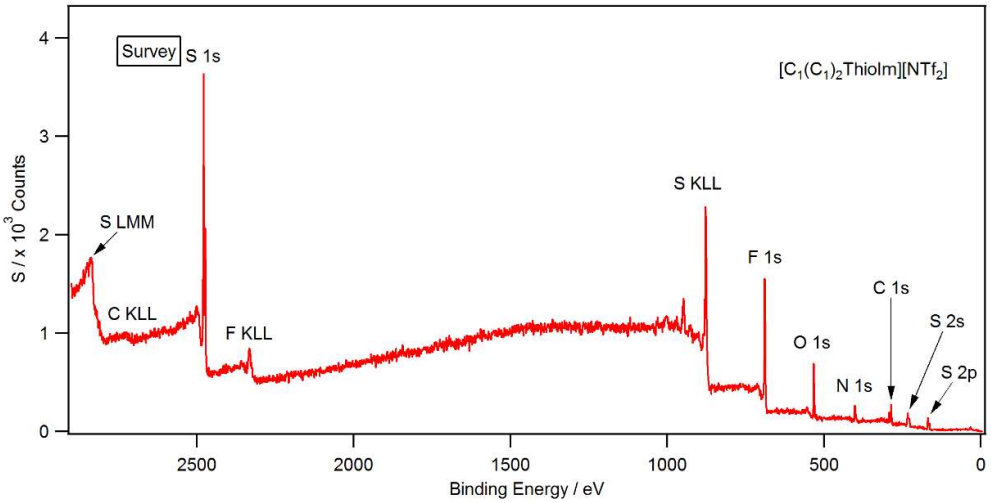


Figure 5.33. Survey scan for the $[C_1(C_1)_2Thiolm][NTf_2]$ IL after argon bombardment for 5 min.

By taking look at Figure 5.34, a clearer and define trend can easily be acknowledged. There is a preferential position of the anion to be at the surface when compared to the cation in all three ILs studied. Moreover, there seems to be a consistency within the distance between the anion and the cation as well, with a standard deviation of 14%. There seems however, to be a very similar depth for this set of ILs regardless of the alkyl chain length. This observation is somewhat surprising, as one would expect smaller cations to be more at the surface when compared to longer alkyl chain length counterparts.

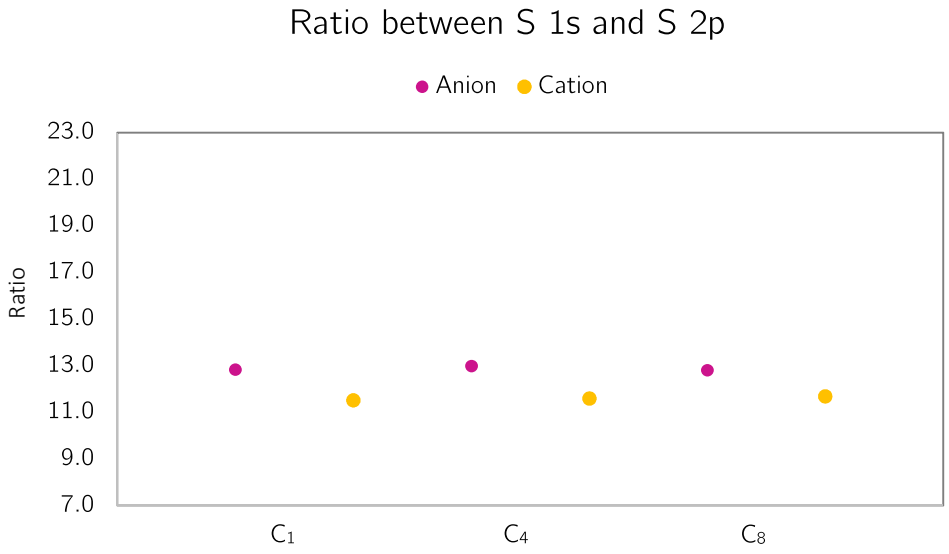


Figure 5.34. Ratio between S 1s and S 2p - After etching.

Furthermore, the ratio between S_{anion} 1s and S_{cation} 1s also falls into the assumption that some validation should be seen between the distance of anion and cation, now with a standard deviation of 3%, Figure 5.35.

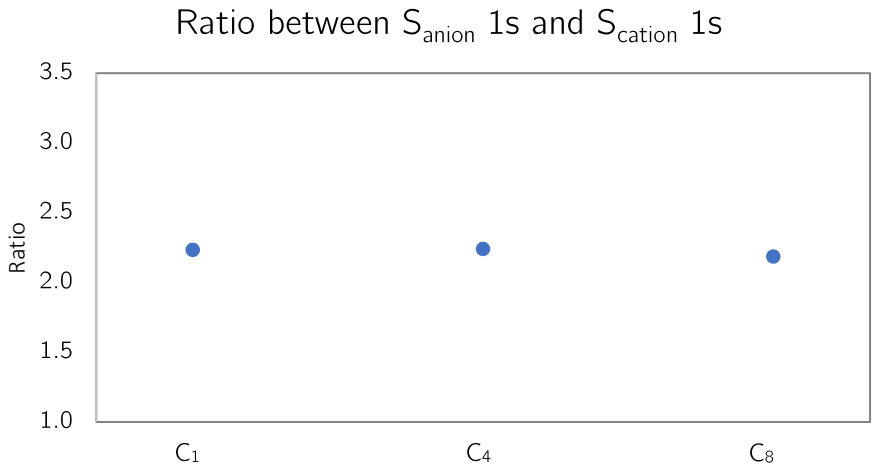


Figure 5.35. Ratio between S_{anion} 1s and S_{cation} 1s - After etching for 5 min.

After heating (30 min at 150 °C, then let cool)– no etching

Heating at approximately 150 °C for 30 min followed by allowing the surface to naturally cool down to 25 °C, was performed to allow the IL surface to move itself onto its preferential conformation after being etch. Ideally this would not segregate any surface contaminants present still within the sample and would answer the questions on the manipulation of the surface composition to a specific orientation/position from etching studies and the effect of surface contaminants on the surface chemistry of ILs. The silicon impurity present on the $[C_1(C_1)_2ThioIm][NTf_2]$ segregated to the surface and is still present, Figure 5.36. This correlates with the findings on *Chapter 3, Section 3.2.1*, for the guanidinium series.

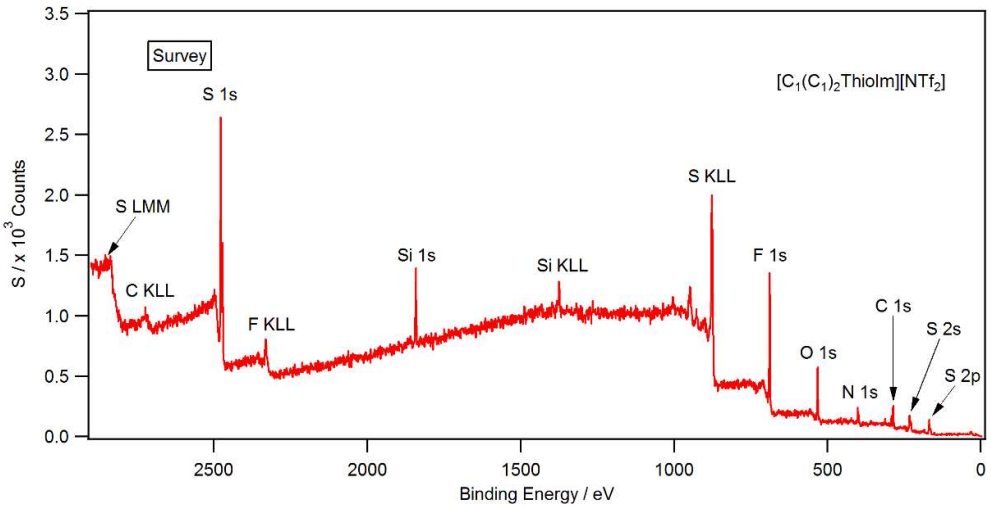


Figure 5.36. Survey scan for the $[C_1(C_1)_2ThioIm][NTf_2]$ IL after argon bombardment for 5 min, followed by heating and let it cool.

However, with reference to Figure 5.37, although the relative position of anions and cations have changed for the three ILs, the general position of anion *vs* cation within the same IL, have not. The anion remains above the cation for all three ILs, however, there is no longer a noticeable correlation. Unlike previously after etching, there seems to be a completely different depth for these three ILs. The $[C_8(C_1)_2ThioIm][NTf_2]$ seems to be relatively more at the surface when compared to the small $[C_1(C_1)_2ThioIm][NTf_2]$, which was not expected. This result leads to the hypothesis that the surface contaminants do affect the relative depth of the components of the ILs and therefore have a clear impact on the relative surface composition and geometry.

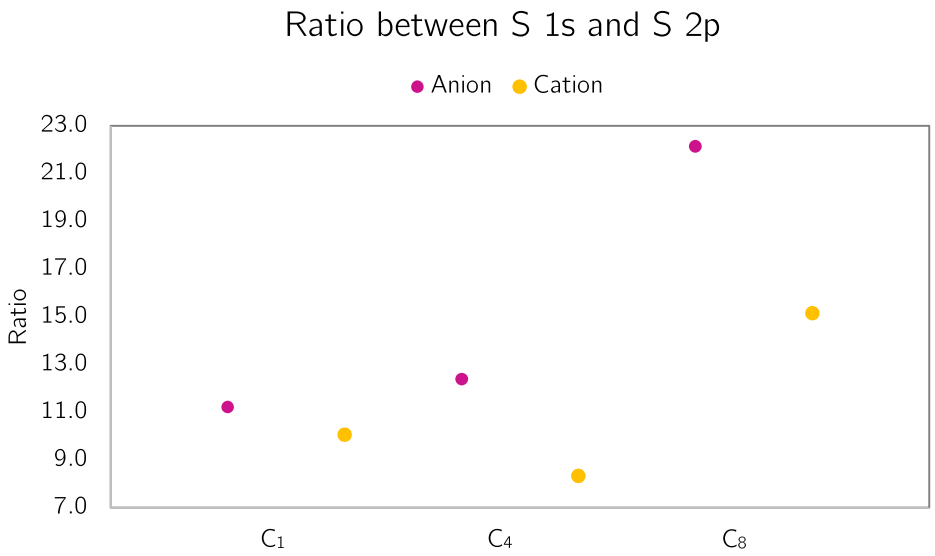


Figure 5.37. Ratio between S 1s and S 2p - After heating and let it cool

Furthermore, the anion/cation distance correlation is again affected by surface segregation as the standard deviation for the ratio between the S 1s of the anion and the S 1s of the cation is now 42%, Figure 5.38.

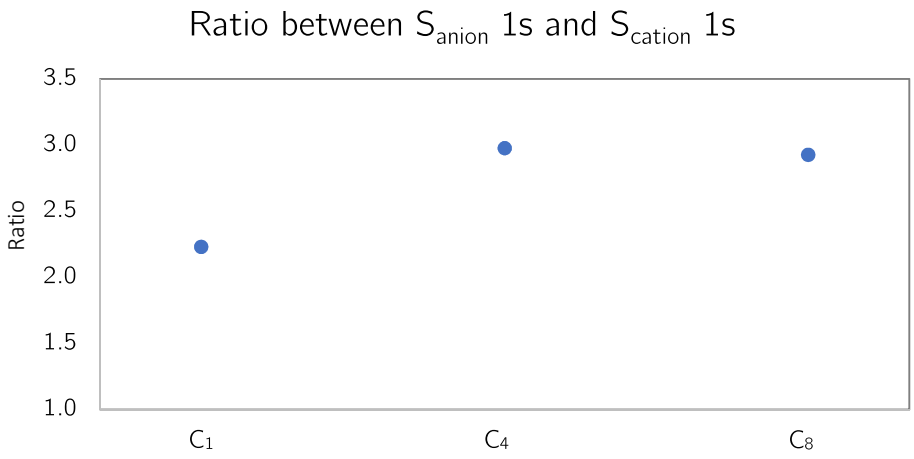


Figure 5.38. Ratio between S_{anion} 1s and S_{cation} 1s - After heating and let it cool

After heating, let cool and etching (5 min each)

The three samples were etched again for another 5 min and a strong correlation between anion/cation distance and position can be seen once more, Figure 5.39. Although the depth between cations with different alkyl chain lengths does not seem to be consistent, there is a clear trend forming within the three

ILs – towards a deeper cation when increasing the alkyl chain length and consequently a deeper anion pair.

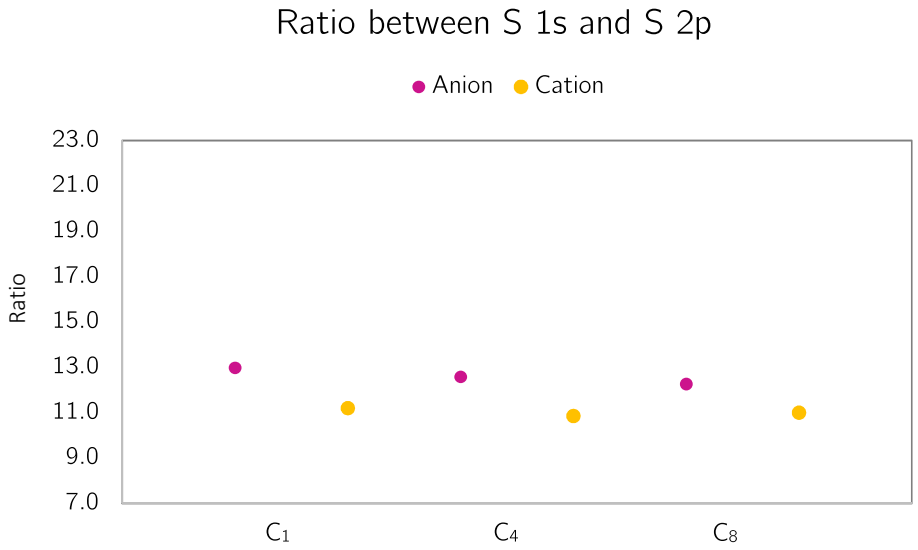


Figure 5.39. Ratio between S 1s and S 2p - After etching, heating, let it cool and etched again

The ratio between S 1s of the anion and the S 1s of the cation falls again into the assumption that some validation can be seen between the distance of anion and cation, now with a standard deviation of 5%, Figure 5.40.

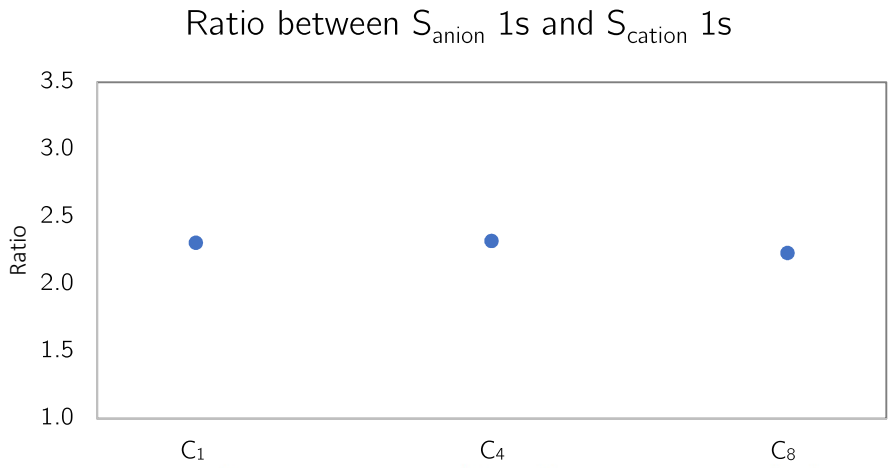


Figure 5.40. Ratio between S_{anion} 1s and S_{cation} 1s - After etching, heating, let it cool and etched again

Further etching (10 min each)

Additional studies onto etching times could potentially decrease the standard deviation of these measurements and should in principle give appropriate information relative to surface position/orientation. An additional exposure to argon bombardment for further 10 min does indeed refer to a decrease up to

4% of standard deviation, Figure 5.41. The anion seems to be consistently on the top and at relative same distance towards the cation, regardless of the alkyl chain length.

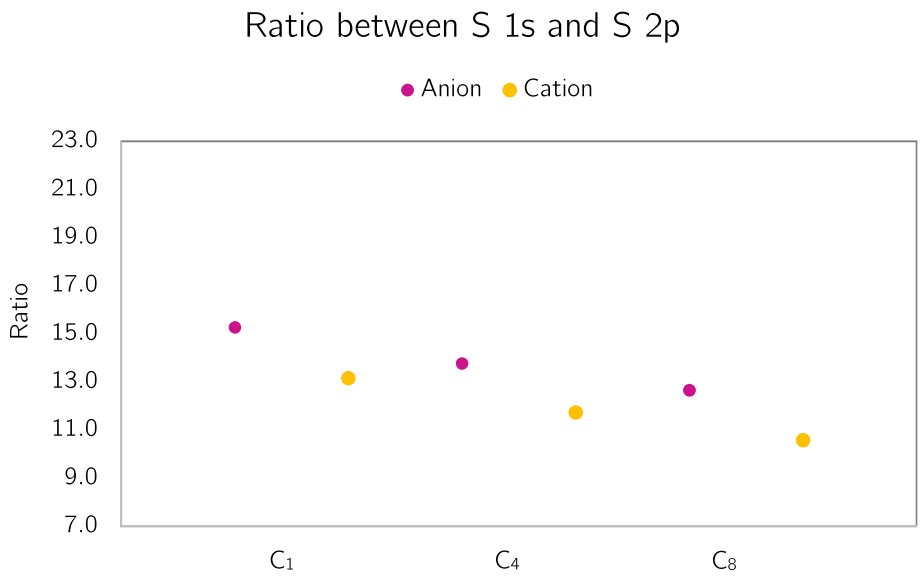


Figure 5.41. Ratio between S 1s and S 2p – After further etching

These results support the previous hypothesis - towards a deeper cation when increasing the alkyl chain length and consequently a deeper anion pair. Furthermore, the correlation on the distance between cation and anion is again reinforced by this study, Figure 5.42.

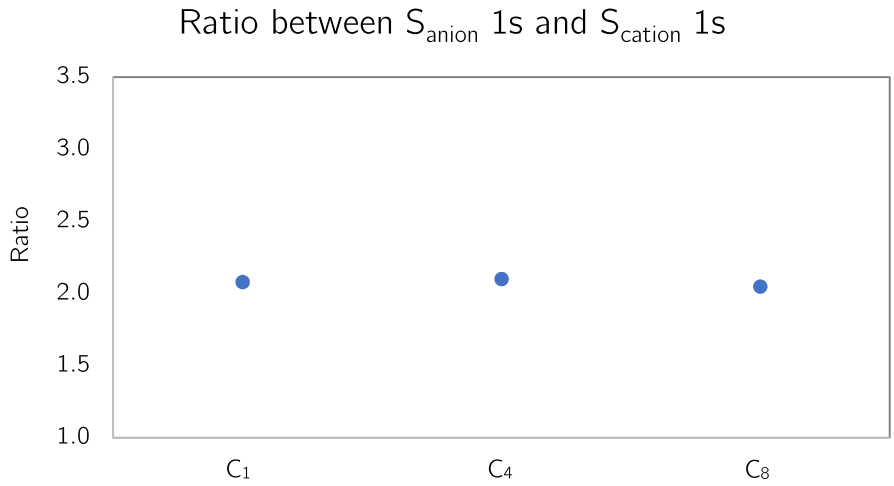


Figure 5.42. Ratio between S_{anion} 1s and S_{cation} 1s - After further etching

The position between the anion and the cation does not seem to be arbitrary. The anion seems to have a preferential 'on top' position relative to the cation that is paired with, Table 5.5.

Table 5.5. Ratio of S 1s to S 2p photoelectron emission peak area for the $[C_n(C_1)_2ThioIm][NTf_2]$ ionic liquid series after heating/etching studies. Area measured from high-resolution spectra with an associated error of ± 5%.

Ionic Liquid	Photoelectron emission peak area S_{anion} 1s : S_{anion} 2p	Photoelectron emission peak area S_{cation} 1s : S_{cation} 2p
$[C_1(C_1)_2ThioIm][NTf_2]$	15.3 : 1	13.2 : 1
$[C_4(C_1)_2ThioIm][NTf_2]$	13.8 : 1	11.7 : 1
$[C_8(C_1)_2ThioIm][NTf_2]$	12.7 : 1	10.6 : 1

Additionally, there seems to be a correlation of the distance between the anion and the cation. Surprisingly, the anion appears to consistently sit at relatively the same distance of the cation regardless of the alkyl chain length, for this specific family of ILs. Furthermore, the alkyl chain length seems to influence the relative position of the cation showing a promising hypothesis towards a 'sinking' of longer cations *versus* small cations. As observed in ARXPS studies in *Section 5.4*, there seems to be an alkyl chain length to which a parallel conformation is preferred at the surface, for the 1-alkyl-3-methylimidazolium IL family. This observation may vary depending on the degree of functionality in the alkyl chain, cation/anion interaction, and structural constrains.

The presence of surface contaminants has shown an effect on the measured depth of the ions that constitute the ionic liquid. This effect is not uniform throughout, having a different impact on anion/cation which can be seen from the discrepancy between measurements. Etching studies has shown that by removing the surface contaminants the deeper layers of IL are being exposed, which seem to show an apparent consistency of ion pairing. As mentioned before, specific orientation of ILs are reported on the surface, which then becomes more arbitrary and free from orientation constrains, deeper within the bulk. This could mean that by removing the first few layers of the sample, we are no longer probing the considered surface area, and probing deeper within the bulk of the sample. However, our etching studies reveal some structure and orientation within the cation/anion pair, which suggests some layering effects

that have been linked to the near surface region. Furthermore, as the IL samples studied in this work were liquids, these materials can easily segregate and reorganise at the surface, which is a challenge to very viscous/solid samples. These findings underpin the necessity to produce ultrapure materials to fully understand and characterise their surface chemistry and consequently develop informed materials for a specific application.

5.7.2. ERXPS of Imidazolium Ionic Liquids

The S 1s and S 2p peak areas for each of the 1-alkyl-3-methylimidazolium ionic liquids studied were measured from the respective high-resolution spectra with an average taken for three different positions on the sample to obtain the peak area ratio as presented in Table 5.6.

Table 5.6. Ratio of S 1s to S 2p photoelectron emission peak area for the imidazolium ionic liquids studied in this work. Areas measured from high-resolution spectra with an associated error of ± 5%.

Ionic Liquid	Photoelectron emission peak area S 1s : S 2p
$[C_2C_1Im][NTf_2]$	19.0 : 1
$[C_3C_1Im][NTf_2]$	17.6 : 1
$[C_4C_1Im][NTf_2]$	17.1 : 1
$[C_6C_1Im][NTf_2]$	19.0 : 1
$[C_8C_1Im][NTf_2]$	19.0 : 1
$[C_{10}C_1Im][NTf_2]$	17.0 : 1
$[C_{12}C_1Im][NTf_2]$	17.4 : 1

It is apparent that the concentration of the $[NTf_2]^-$ anion in the near-surface region appears highly dependent on the alkyl chain length. For $[C_nC_1Im][NTf_2]$ when the alkyl chain is short, *i.e.* $n = 2$, 3, and 4 it seems that there is a decrease in surface concentration of the sulfur atom of the $[NTf_2]^-$ anion. This leads to the assumption that the surface is constructed of an alkyl chain overlayer, with a sublayer of charge-bearing head groups residing underneath. A greater surface presence of sulfur is observed for $[C_nC_1Im][NTf_2]$ when increasing the alkyl chain length, and for $n = 6$, and 8 it seems apparent that the anion is at about the same distance related to the surface as it is for a very short alkyl chain ($n = 2$). In comparison to the ARXPS findings in *Section 5.4.2*, where an enrichment of the F 1s component can be barely be acknowledged for $n = 6$, and 8, these

results seem contradictory. However, the merge of the observed data provided by these two techniques supports the assumption that for a given alkyl chain length, the aliphatic component becomes parallel to the surface. In ARXPS there is a clear increase of the aliphatic component for n = 6 and 8, showing that at the topmost surface, the surface is constituted mainly by the alkyl chain. However, ERXPS suggests that the sulfur present in the anion is closer to the surface than it is for shorter alkyl chains *i.e.* n = 3, and 4. It is important to have into account that for Al source ARXPS experiments, the information depth is about 1.5 nm and that for the S 1s in Ag source ERXPS experiments the information depth is about 4.2 nm. Combining these results, and considering the depth range of both techniques, this suggests that for $n > 4$ (the exact size to which this phenomenon can be seen has not been studied in this work, other techniques have been reported elsewhere[70]), the alkyl chain length starts to tilt towards a parallel conformation at the surface, dragging the cation headgroup and the anion towards the surface. For longer alkyl chains, a reduction in surface concentration of sulfur also supports the assumption of parallel orientation of the chains to the surface, in addition to the $C_{aliphatic}$ 1s enrichment in ARXPS studies. However, stacking of very long alkyl chains may limit the amount of anion at the surface, pushing it towards the bulk, resulting in a decrease of sulfur composition. This also seems to hold true for $[(C_8C_1)_2dmg][NTf_2]$, as ERXPS suggests that the sulfur present in the anion is closer to the surface for $[C_8C_1Im][NTf_2]$ than it is for the $[(C_8C_1)_2dmg][NTf_2]$, compare Table 5.6 with Table 5.7, contrary to ARXPS results where higher F 1s enrichment can be seen for the guanidinium cation when compared to its imidazolium counterpart.

Table 5.7. Ratio of S 1s to S 2p photoelectron emission peak area for $[(C_8C_1)_2dmg][NTf_2]$. Area measured from high-resolution spectra with an associated error of ± 5%.

Ionic Liquid	Photoelectron emission peak area S 1s : S 2p
$[(C_8C_1)_2dmg][NTf_2]$	14.7 : 1

Additionally, in the particular case of $[C_4C_1Im][NTf_2]$, ARXPS indicated that no such ordering occurs at the IL/vacuum interface and a homogeneous distribution of ions exists. This is supported by a reduction of the S 1s : S 2p ratio, which

indicates a reduction in surface concentration of sulfur, and hence a greater proportion of the sulfur signal arises from the bulk. As both ARXPS and ERXPS studies on $[C_4C_1Im][NTf_2]$ provide evidence for a homogeneous distribution of ions, this IL could be used in future studies as an appropriate reference sample to estimate the currently unknown S 1s RSF. This would enable quantitative data on sulfur surface enrichment to be obtained through future ERXPS investigations. RSFs were not extracted for the ionic liquids in this study as the current dataset is limited to ILs of the $[NTf_2]^-$ variety, thus the resultant RSFs may not be applicable to other cations and anions. Therefore, it is important for robust testing against a variety of ionic liquids, alongside using other techniques to confirm the homogeneous nature of the ILs discussed above, before extracting and reporting RSF values.

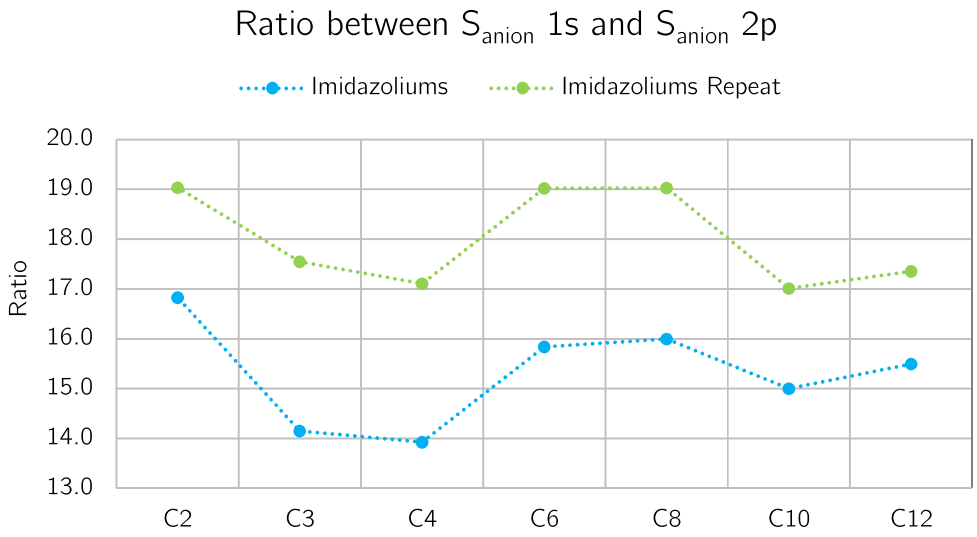


Figure 5.43. Ratio between S_{anion} 1s and S_{anion} 2p for the imidazolium series with the $[NTf_2]^-$ anion, before any treatment (blue), and after etching/heating studies (green).

A visual representation of the imidazolium series measured on a first instance and after etching/heating studies, Table 5.6 (as described in *Section 5.7.1*) is represented in Figure 5.43. This series was free of surface contaminants and the same depth profiles were obtained after these studies. These results show the same trend between measurements, however a difference in the absolute value of depth can be acknowledged. At the point of the research this variation cannot be fully explained, although some loss of intensity - caused by the wear of the

anode - was observed between measurements. Figure 5.44 shows the S 1s and S 2p Ag L_{α}' source XP spectra of $[C_2C_1Im][NTf_2]$ recorded one year apart.

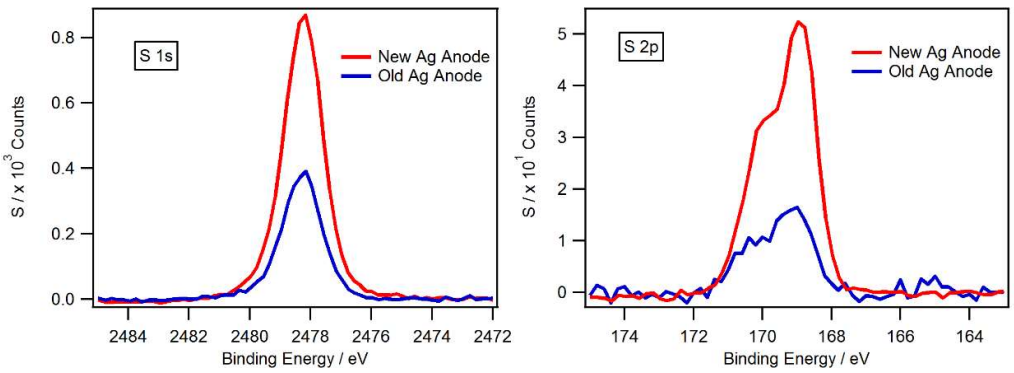


Figure 5.44. Significant decrease of XP spectra resolution of $[C_2C_1Im][NTf_2]$ recorded when the Ag anode was new (red) and after one year of use (blue).

Not only a reduction of intensity could be seen for the S 1s region, the magnitude of this effect is by far superior in the case of the S 2p region. The lack of definition of this region greatly impacts the fitting of components on the recorded data. Consequently, the ratios obtained will have a higher associated error.

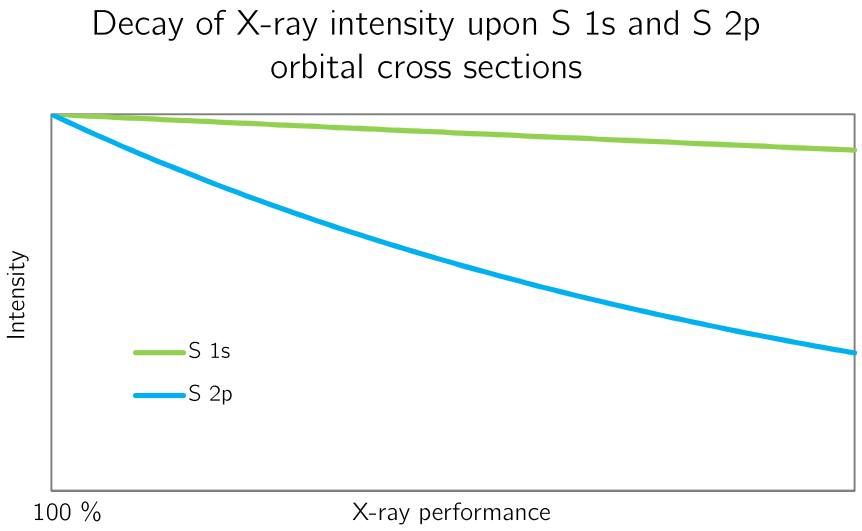
Nevertheless, some experiments could be designed to probe the full accuracy of these measurements and instrument calibration, as suggested in *Section 5.8*.

5.8. Conclusions

ARXPS and ERXPS have been used to probe sulfur enrichment on the surface interface, for a range of IL families. Although tilting of the sample was necessary for ARXPS studies, the design, manufacture, and application of a new add-on bar was accomplished, and its reliability verified. Additionally, for samples which present surface contaminants, a full methodology was developed. This is of particular importance for ERXPS investigations, as surface segregation of impurities show a tremendous impact on the recorded information. Moreover, the robustness of the fitting model for the C 1s region of the guanidinium series developed in *Chapter 3,* and thioimidazolium series in *Chapter 4*, was further reinforced by Ag source data. The information collected from ERXPS shows a high degree of confidence capable of providing depth profiles within a series of imidazolium ionic liquids, and provisional comparable data between this series and other nitrogenous cations counterparts. ERXPS investigations upon a series of ILs shows that the $[NTf_2]^-$ anion sits consistently above the cation. This observation has been reported in the literature by other spectroscopic techniques and theoretical calculations and the data presented in this *Thesis* provides further evidence that ERXPS is a powerful and extremely useful tool for depth profile studies.

Further investigation upon absolute values of depth is necessary along with appropriate design of experiments towards the diagnostic of source lifespan. For any X-ray source, the aluminium/silver coating on the anode will wear with use, affecting the intensity of the X-rays and the instrument's sensitivity. For Ag source experiments, where the intensity - and therefore the area measured - has a huge impact in the resulting ratio, this could mean significantly misinterpretation of the depth probed. This will affect orbital cross sections differently, S 1s and S 2p, in the case of this work, where the loss of intensity will greatly affect the S 2p area at a higher rate than the S 1s area. A theoretical interpretation of this is represented, Graphic 5.1.

Graphic 5.1. Proposed depreciation of X-ray performance caused by anode wear.



A potential diagnosis for good data versus bad data could mean the development of a solid-state standard, possibly a thin coated stub with known layers of specific sulfur containing materials, Figure 5.45. This would allow the depth profile of a known material, and consequently measure the associated error of each experiment prior to analysis.

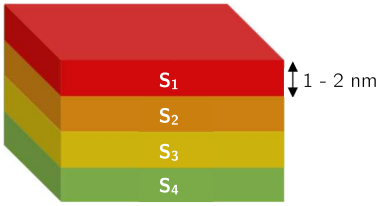


Figure 5.45. Design of a thin film with coated layers of sulfur containing compounds.

6. Conclusions and Future Work

6.1. Summary

The anion ability to interact with solute molecules seems to be heavily depend on the cation structure and consequently, cation-anion interactions. XPS studies upon this phenomenon can develop further understanding on the fundamental interactions between ion pair and solute molecules. This work described the successful measurement of XP spectra and development of appropriate fitting model for the C 1s region for a range of guanidinium-based ionic liquids which exhibit high degree of delocalisation of the cationic centre. Varying both cation aliphatic chain length, n, and the anion, demonstrates that this class of ILs are stable to measure under X-ray irradiation. Surface contaminants were successfully removed however, ILs with shorter alkyl chains ($n < 8$) were observed to be more prone to damage and less stable under argon bombardment, when utilising a Ar_{500}^{+} cluster ion beam accelerated to 5 keV. Comparison of binding energies for different nitrogen-based cationic structures revealed that the positive charge of the guanidinium cation is well distributed across three nitrogen atoms, as opposed to just one in the pyrrolidinium cation, reflecting the weak bond between the guanidinium cation and the anion through the delocalisation of the positive charge around the three-nitrogen centre. Mixtures of these two distinct cations were investigated and although the difference in binding energy between the neat ILs and resulting mixture was lower than expected, a series of entirely new electronic environments could be acknowledged and physicochemical properties relevant towards specific applications.

In order to further investigate the effect of charge delocalisation upon the cation core, sulfur functionalisation of cyclic and acyclic ILs was attained and XP data recorded. Functionalisation shows notable impact upon the chemical environment of surrounding atoms, as it tends to disrupt the charge

delocalisation upon the cation core. Comparison to ^{13}C-NMR was accomplished and found to be more sensitive than XPS regarding functionalisation at the cation core, however ^{13}C-NMR does not seem to always provide a reliable indicator of the chemistry of the compound. Structural changes seem to have a clear effect upon the $C_{2/core}$ chemical shift, whereas by XPS this effect is less apparent. This effect does not fully correlate with XPS findings which suggests that other interactions have an influence in the recorded data.

In order to understand surface-based applications of ILs it is crucial to first understand their surface assembly, with the ultimate goal of developing design rules such that the structure for any given IL can be predicted. Herein, ARXPS and ERXPS have been used to probe sulfur enrichment on the surface interface, for a range of IL families. A relevant impact on the recorded information was found on samples which present surface contaminants. Furthermore, the lifetime of the anode has been found to have an enormous effect upon the recorded data for depth profile accuracy and appropriate experiments/solutions have been suggested. In spite of this, information collected from ERXPS shows a high degree of confidence capable of providing trend depth profiles within a series of imidazolium ionic liquids. Remarkably, ERXPS investigations upon a series of ILs shows that the $[NTf_2]^-$ anion sits consistently above the cation. This observation has been reported in the literature by other spectroscopic techniques and theoretical calculations and the data presented in this *Thesis* provides further evidence that ERXPS is a powerful and extremely useful tool for depth profile studies.

6.2. Outlook and Future Work

Decomposition of ionic liquids with argon sputtering has been previously reported in the literature. Taylor and Licence acknowledged decomposition using a 4 keV monoatomic ion beam upon Ferrocenyl and Ferrocenium-based ILs. Further studies showed decomposition even with lower accelerations of 0.5 keV.[126] The use of a monoatomic ion beam increases the damage at the

surface, as shown in *Section 2.1.6*, Figure 2.6. In the case of guanidinium ILs where signs of degradation was recorded ($n < 8$) using a Ar_{500}^+ with 5 keV, increasing the cluster size to Ar_{1000}^+ and decreasing acceleration to 0.5 keV could potentially decrease surface damage. Experiments varying both cluster size and energy applied can provide relevant information upon stability of this IL family.

Additional theoretical and computational studies upon different cation structures would provide further information on how these changes impact upon chemical environment, ring current effects, re-arrangements, degree of orbital mixing, *etc*. A better understanding and interpretation of force field parameters used in molecular dynamics simulations can also be investigated.

Depth profiles studies are of particular importance as the constituents of the liquid-vacuum interface are crucial for specific applications, such as catalysis, gas capture/storage/separation and SILP chemistries. Herein, depth profiles of a range of ILs was achieved, with emphasis upon thioimidazolium ILs paired with the $[NTf_2]^-$ anion. This family of materials permitted probing of sulfur enrichment at the surface not only by ARXPS but also by ERXPS. The Ag L_α' source XPS use for depth profiles is restricted to compounds containing elements with higher energy orbitals, *e.g.* sulfur, phosphorous and chlorine, allowing for photoemission lines S 1s, P 1s and Cl 1s respectively, to be recorded. Moreover, the reduced intensity of the Ag L_α' line, compared to Al K_α, requires longer acquisition times promoting an increased risk of sample damage. It has been proposed that there is a specific alkyl chain length for which the aliphatic component becomes parallel to the surface. This could be acknowledged for the imidazolium series and seems to be strongly depend upon the cationic structure. Further studies upon these materials is expected to provide further evidence of surface rearrangement. Mitchell[265] proposed (although building these assumptions solely upon standard XPS studies) that for asymmetric dication ILs with short chain linkers, these can experience a smaller degree of bending because of repulsions caused by the positive charge carriers. As the chain length

is increased, there is a greater ability for bending of the alkyl chain before issues of repulsion apply. The longer the alkyl chain, the more bending can occur. A schematic of this arrangement is presented in Figure 6.1.

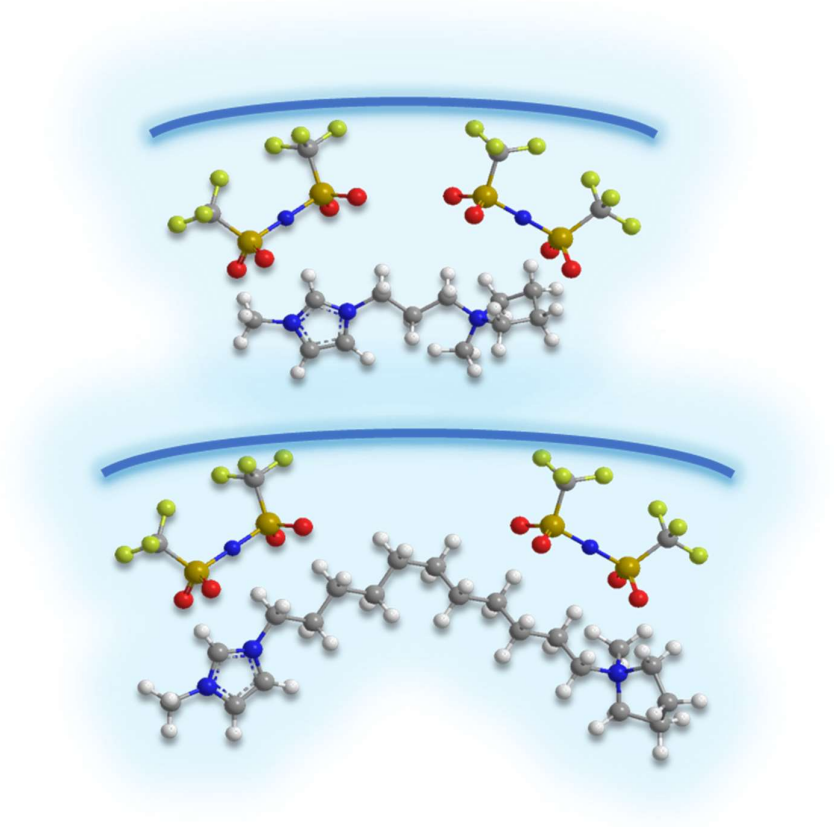


Figure 6.1. Predicted bending of asymmetric ionic liquids *e.g.* $[(C_1Im)C_n(C_1Pyrr)]2[NTf_2]$, as alkyl chain linker length is increased.

Based on this assumption and considering the limitations of using the Ag L_α' source for depth profiling, the system in Figure 6.2 is proposed.

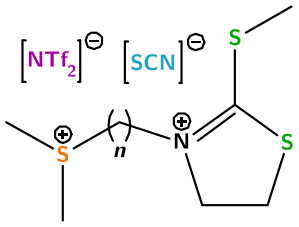


Figure 6.2. Asymmetric dication ionic liquid family proposed for depth profile studies.

This system allows for S 1s and S 2p photoelectron emissions to be recorded from four different chemical environments as illustrated in Figure 6.3.

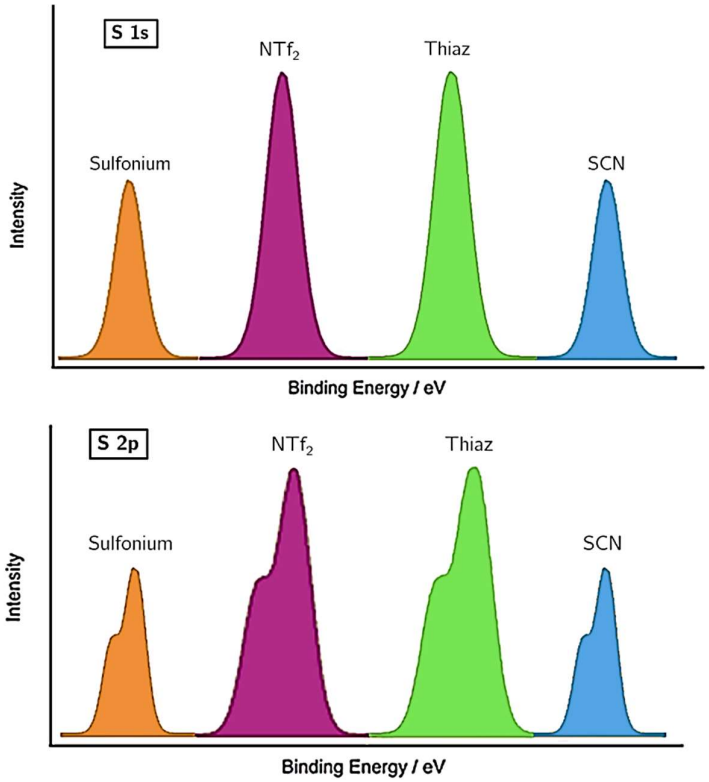


Figure 6.3. Representation of (top) S 1s and (bottom) S 2p for the different chemical environments on the proposed asymmetric dication (the intensity is represented to match the number of sulfur elements present in each component – the relative true intensity will depend on its respective depth).

A proposed synthesis for this IL family can be seen below in Figure 6.4:

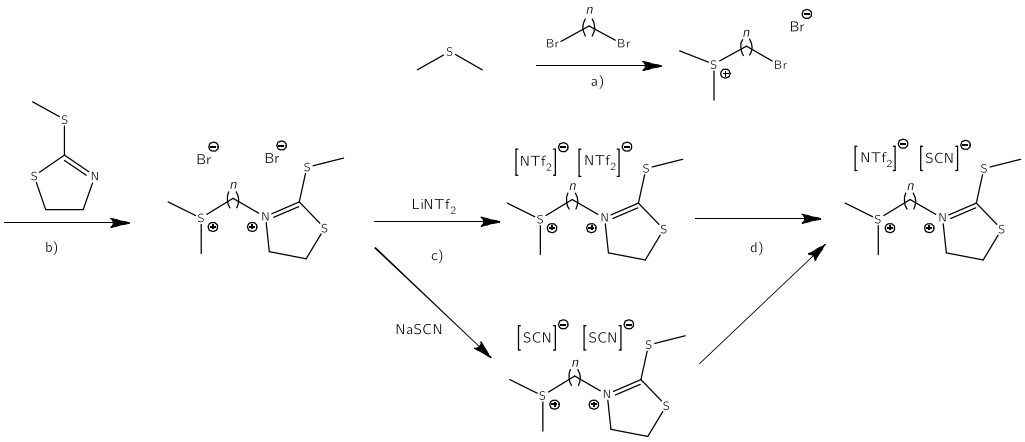


Figure 6.4. Proposed synthetic route for asymmetric dication with four different sulfur chemical environments towards accurate depth profiling.

The final step d) involves a 1 : 1 mixture of both asymmetric dications ($[NTf_2]^-$ and $[SCN]^-$). Anion metathesis prior to step b) has been attempted previously in the Licence group, however it has been found that carrying out with alkylation after metathesis will result in partially loss of the anion previously exchanged.[266]

Depth profiles of dications pose a challenge. In the case of $[(C_1Im)C_n(C_1Pyrr)]2[NTf_2]$, Figure 6.1, where the cation does not have a sulfur element to be probed, both anions would have the same sulfur chemical environment. Thus, if one anion is at a different depth compared to the other, the S 1s area would be an average of both anion sulfur contributions. Nevertheless, as symmetric dication imidazoliums, $[C_n(C_1Im)_2]2[NTf_2]$, and asymmetric imidazolium-pyridiniums, $[(C_1Im)C_nPyr]2[NTf_2]$, (where n = 6, 8, 10, 12) sets of ILs have been synthesised previously in the Licence group, Ag L_α' source measurements were performed. Remarkably, the same depth profile trend for the $[NTf_2]^-$ anions was seen for the two counterparts, Figure 6.5. The actual surface position of these materials cannot be confirmed for the reason explained above, however, it is interesting that both dications, regardless of symmetry, show the same average of depth. This suggests that these might have the same rearrangement at the surface, regardless of the cation structure. This also suggests that the alkyl chain length has strong effect upon the surface structure and positioning of ionic liquids.

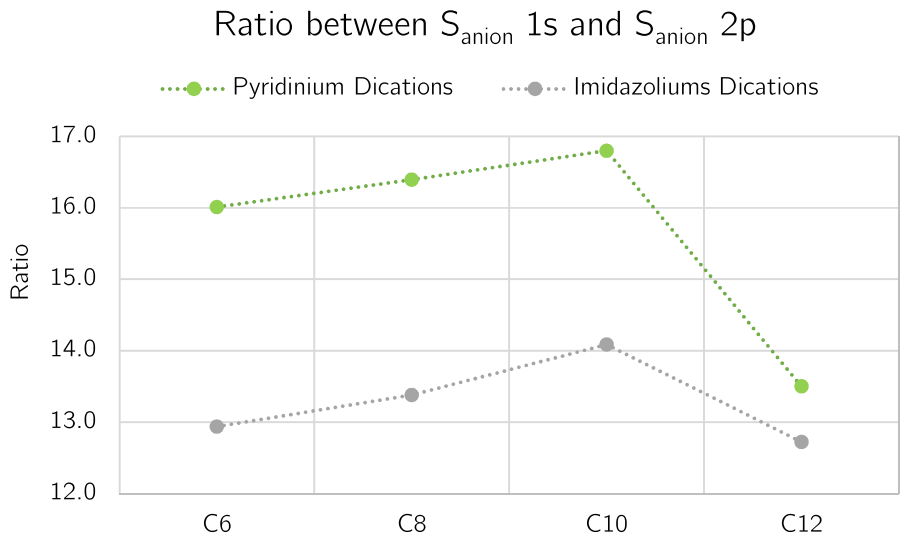


Figure 6.5. Ratio between S_{anion} 1s and S_{anion} 2p for symmetric imidazolium (grey) and asymmetric imidazolium-pyridinium (green) bis(trifluoromethanesulfonyl)imide-based dication ILs - After etching, heating, let it cool and etched again.

In addition, a series of alkyl chain sulfur functionalised imidazolium ILs have been synthesised as described in Figure 6.6.

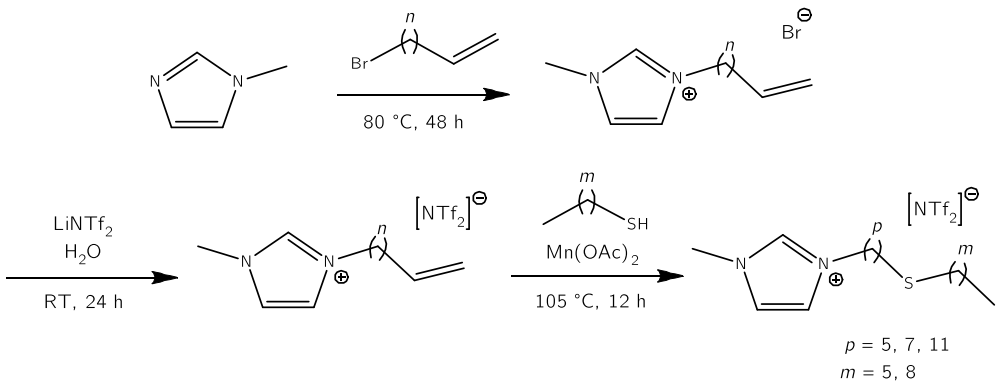


Figure 6.6. Synthetic route for alkyl chain sulfur functionalised imidazolium bis(trifluoromethanesulfonyl)imide-based ILs, $[C_1ImC_pSC_m][NTf_2]$.

These were designed with the aim of correlate these materials with the imidazolium series investigated in *Chapter 5, Section 5.7.2*. Preliminary depth profiles of these materials can be seen in Figure 6.7.

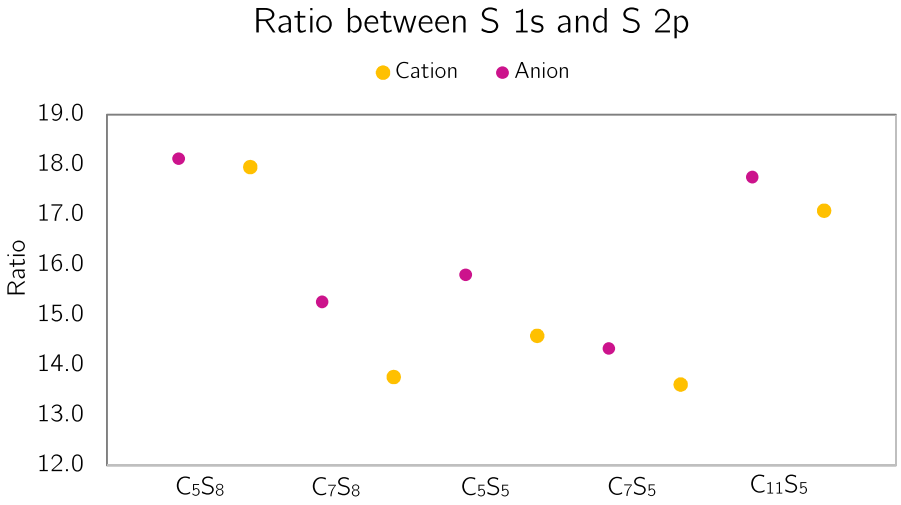


Figure 6.7. Ratio between S 1s and S 2p for alkyl chain sulfur functionalisation imidazolium ILs - After etching, heating, let it cool and etched again.

However, as the sulfur position within the alkyl chain and the alkyl chain length varies, the relative position to the anion seems to change. This could be a result of a tilt in the chain upon functionalisation. To fully understand the relative position of both sulfur elements, additional chain lengths should be synthesised and studied. Furthermore, changing to a cation that has sulfur within its structure would help identify the position of all constituents, cation, anion and alkyl chain.

7. Synthesis of Ionic Liquids

7.1. Materials

Compounds investigated herein were prepared in our laboratory using modified literature procedures. Chemical precursors were obtained from commercial suppliers and used without further purification unless otherwise stated. Lithium bis(trifluoromethanesulfonyl)imide was obtained from 3M. All water used in this work was Millipore Milli-Q 18 MΩ ultrapure and deionised. All solvents were analytical reagent grade with exception to anhydrous solvents (≥ 99.7%).

7.2. Instrumentation

All compounds were dried *in vacuo* ($p \leq 10^{-3}$ mbar) at 50 °C and stored under argon before being characterised by ^{1}H, ^{13}C, and ^{19}F-{^{1}H} and ^{31}P-{^{1}H} NMR when appropriate (recorded at room temperature on a Bruker AV3400HD or Bruker DPX300 spectrometer); Chemical shifts (δ) are reported in parts per million (ppm) with reference to residual traces of protonated solvents in commercial NMR solvents: protonated chloroform (δ_H 7.27) and $CDCl_3$ (δ_C 77.0), and protonated dimethyl sulfoxide (δ_H 2.50) and DMSO-*d*$_6$ (δ_C 39.5); Coupling constants (*J*) are given in Hz and multiplicities were labelled singlet (s), doublet (d), triplet (t), quartet (q), quintet (quin), sextet (sxt), septet (spt), double doublet (dd), triple triplet (tt) and multiplet (m).

Note: ^{1}H-NMR and ^{19}F-NMR chemical shifts are represented together in the compound structure when applicable. ^{13}C-NMR chemical shifts are represented separately paired with ^{31}P-NMR when appropriate.

Further characterisation methods also included IR (Perkin Elmer 1600 FT spectrometer); ESI-MS (Brücker MicroTOF 62 spectrometer); DSC (TA-Q2000) and XPS (Kratos Axis Ultra Spectrometer). For synthesis which involved anion exchange chemistries, Ion Chromatography (Dionex ICS-3000

machine fitted with AS20 analytical column and AG20 guard column) showed that residual halide was below the detection limits of the instrument (≈ 10 ppm).

Differential Scanning Calorimetry (DSC)

Approximately 3 mg of the sample of interest was loaded into a T_{zero} (for solid samples) or hermetic (viscous liquids) DSC pan and sealed.

The sample sequence was as follows:

1° Cycle

Ramp at 10 °C·min^{-1} from 25 °C to -90 °C

Isothermal for 5 min

Ramp at 10 °C·min^{-1} from -90 °C to 200 °C

Isothermal for 5 min

Ramp at 10 °C·min^{-1} from 200 °C to -90 °C

Isothermal for 5 min

2° Cycle

Ramp at 10 °C·min^{-1} from -90 °C to 200 °C

Isothermal for 5 min

Ramp at 10 °C·min^{-1} from 200 °C to -90 °C

Table 7.1. Phase transitions for all guanidinium ILs studied in *Chapter 3*.

Ionic Liquid	T_c/T_g (°C)	T_m (°C)
$[(C_4C_4)_2dmg][Cl]$	-55.3	82.0
$[(C_4C_4)_2dmg][BF_4]$	-57.7	74.5
$[(C_4C_4)_2dmg][PF_6]$	-	58.7
$[(C_4C_4)_2dmg][NTf_2]$	7.7	59.9
$[(C_4C_1)_2dmg][Cl]$	-	-
$[(C_4C_1)_2dmg][BF_4]$	17.6	67.6
$[(C_4C_1)_2dmg][PF_6]$	-10.5	62.8
$[(C_4C_1)_2dmg][NTf_2]$	-	62.1
$[(C_8C_1)_2dmg][Cl]$	23.0	45.8
$[(C_8C_1)_2dmg][BF_4]$	33.2	61.2
$[(C_8C_1)_2dmg][PF_6]$	-31.6	21.0
$[(C_8C_1)_2dmg][NTf_2]$	-	-

List of Experiments

7.3.1. Hexamethylguanidinium bis(trifluoromethanesulfonyl)imide, $[(C_1C_1)_2dmg][NTf_2]$ 153
7.3.2. Tetrabutyldimethylguanidinium chloride, $[(C_4C_4)_2dmg][Cl]$..... 154
7.3.3. Tetrabutyldimethylguanidinium hexafluorophosphate, $[(C_4C_4)_2dmg][PF_6]$ 155
7.3.4. Tetrabutyldimethylguanidinium tetrafluoroborate, $[(C_4C_4)_2dmg][BF_4]$ 156
7.3.5. Tetrabutyldimethylguanidinium bis(trifluoromethylsulfonyl)imide, $[(C_4C_4)_2dmg][NTf_2]$ 157
7.3.6. Butylmethyldimethylguanidinium chloride, $[(C_4C_1)_2dmg][Cl]$..... 158
7.3.7. Butylmethyldimethylguanidinium hexafluorophosphate, $[(C_4C_1)_2dmg][PF_6]$ 159
7.3.8. Butylmethyldimethylguanidinium tetrafluoroborate, $[(C_4C_1)_2dmg][BF_4]$..... 160
7.3.9. Butylmethyldimethylguanidinium bis(trifluoromethylsulfonyl)imide, $[(C_4C_1)_2dmg][NTf_2]$ 161
7.3.10. Methyloctyldimethylguanidinium chloride, $[(C_8C_1)_2dmg][Cl]$ 163
7.3.11. Methyloctyldimethylguanidinium hexafluorophosphate, $[(C_8C_1)_2dmg][PF_6]$ 164
7.3.12. Methyloctyldimethylguanidinium tetrafluoroborate, $[(C_8C_1)_2dmg][BF_4]$..... 165
7.3.13. Methyloctyldimethylguanidinium bis(trifluoromethylsulfonyl)imide, $[(C_8C_1)_2dmg][NTf_2]$ 167
7.4.1. 1-Octyl-1-methylpyrrolidinium bromide, $[C_8C_1Pyrr]Br$..... 169
7.4.2. 1-Octyl-1-methylpyrrolidinium chloride, $[C_8C_1Pyrr]Cl$ 169
7.4.3. 1-Octyl-1-methylpyrrolidinium tetrafluoroborate, $[C_8C_1Pyrr][BF_4]$ 170
7.4.4. 1-Octyl-1-methylpyrrolidinium bis(trifluoromethanesulfonyl)imide, $[C_8C_1Pyrr][NTf_2]$..... 171
7.5.1. 1,2,3-Trimethylimidazolium iodide, $[C_1C_1C_1Im][I]$..... 173
7.5.2. 1,2,3-Trimethylimidazolium bis(trifluoromethylsulfonyl)imide, $[(C_1)_3Im][NTf_2]$..... 173
7.5.3. 1,3-Dimethylimidazolium methyl sulfate, $[C_1C_1C_1Im][MeSO_4]$ 174
7.5.4. 1,3-Dimethylimidazolium bis(trifluoromethylsulfonyl)imide, $[C_1C_1Im][NTf_2]$ 175
7.5.5. 1-Ethyl-3-methylimidazolium bis(trifluoromethanesulfonyl)imide, $[C_2C_1Im][NTf_2]$ 176
7.5.6. 1-Propyl-3-methylimidazolium chloride, $[C_3C_1Im]Cl$..... 177

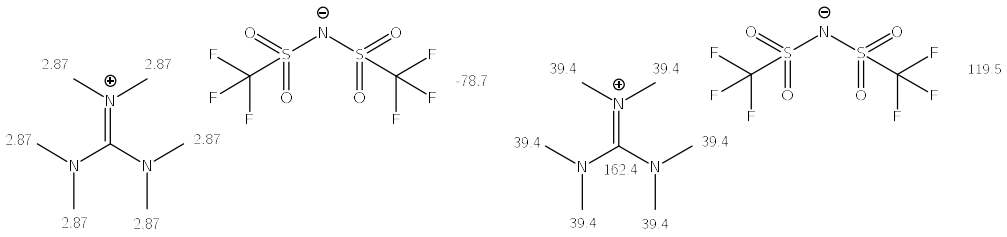
7.5.7. 1-Propyl-3-methylimidazolium bis(trifluoromethanesulfonyl)imide, [C_3C_1Im][NTf_2]..... 177
7.5.8. 1-Butyl-3-methylimidazolium chloride, [C_4C_1Im]Cl..... 178
7.5.9. 1-Butyl-3-methylimidazolium bis(trifluoromethanesulfonyl)imide, [C_4C_1Im][NTf_2]..... 179
7.5.10. 1-Hexyl-3-methylimidazolium chloride, [C_6C_1Im]Cl..... 180
7.5.11. 1-Hexyl-3-methylimidazolium bis(trifluoromethanesulfonyl)imide, [C_6C_1Im][NTf_2]..... 181
7.5.12. 1-Octyl-3-methylimidazolium chloride, [C_8C_1Im]Cl..... 182
7.5.13. 1-Octyl-3-methylimidazolium bis(trifluoromethanesulfonyl)imide, [C_8C_1Im][NTf_2]..... 182
7.5.14. 1-Decyl-3-methylimidazolium chloride, [$C_{10}C_1$Im]Cl..... 183
7.5.15. 1-Decyl-3-methylimidazolium bis(trifluoromethanesulfonyl)imide, [$C_{10}C_1$Im][NTf_2] 184
7.5.16. 1-Dodecyl-3-methylimidazolium chloride, [$C_{12}C_1$Im]Cl..... 185
7.5.17. 1-Dodecyl-3-methylimidazolium bis(trifluoromethanesulfonyl)imide, [$C_{12}C_1$Im][NTf_2] 186
7.5.18. Pentamethylthiouronium iodide, [$(C_1)_5$TU][I]..... 187
7.5.19. Pentamethylthiouronium bis(trifluoromethanesulfonyl)imide, [$(C_1)_5$TU][NTf_2] 187
7.5.20. 1,3-Dimethylimidazoline-2-thione..... 189
7.5.21. 1,3-Dimethyl-2-methylthioimidazolium iodide, [$C_1(C_1)_2$ThioIm][I] ... 190
7.5.22. 1,3-Dimethyl-2-methylthioimidazolium bis(trifluoromethanesulfonyl)imide, [$C_1(C_1)_2$ThioIm][NTf_2]..... 190
7.5.23. Butylimidazole..... 191
7.5.24. 1-Butyl-3-methylimidazolium methyl sulfate, [C_4C_1Im][$MeSO_4$] 192
7.5.25. 1-Butyl-3-methylimidazoline-2-thione..... 193
7.5.26. 1-Butyl-2,3-dimethylthioimidazolium iodide, [$C_4(C_1)_2$ThioIm][I] 194
7.5.27. 1-Butyl-2,3-dimethylthioimidazolium hexafluorophosphate, [$C_4(C_1)_2$ThioIm][PF_6] 194
7.5.28. 1-Butyl-2,3-dimethylthioimidazolium bis(trifluoromethylsulfonyl)imide, [$C_4(C_1)_2$ThioIm] [NTf_2] 195
7.5.29. Octylimidazole 196
7.5.30. 1-Octyl-3-methylimidazolium methyl sulfate, [C_8C_1Im][$MeSO_4$] 197
7.5.31. 1-Octyl-3-methylimidazoline-2-thione..... 198
7.5.32. 1-Octyl-2,3-dimethylthioimidazolium iodide, [$C_8(C_1)_2$ThioIm][I] 199
7.5.33. 1-Octyl-2,3-dimethylthioimidazolium hexafluorophosphate, [$C_8(C_1)_2$ThioIm][PF_6] 200
7.5.34. 1-Octyl-2,3-dimethylthioimidazolium bis(trifluoromethylsulfonyl)imide, [$C_8(C_1)_2$ThioIm][NTf_2]..... 201

7.5.35. 3-Methyl-2-(methylthio)thiazolium iodide, $[(C_1)_2Thio]I$ 202
7.5.36. 3-Methyl-2-(methylthio)thiazolium bis(trifluoromethylsulfonyl)imide, $[(C_1)_2Thio][NTf_2]$ 202
7.5.37. 3-Methyl-2-methylsulfanyl-4,5-dihydro-1,3-thiazolium iodide, $[(C_1)_2Thiz]I$ 203
7.5.38. 3-Methyl-2-methylsulfanyl-4,5-dihydro-1,3-thiazolium bis(trifluoromethylsulfonyl)imide, $[(C_1)_2Thiz][NTf_2]$ 204
7.5.39. 1-Methyl-3-undecenylimidazolium bromide, $[C_1ImC_{11}ene]Br$ 205
7.5.40. 1-Methyl-3-undecenylimidazolium bis(trifluoromethylsulfonyl)imide, $[C_1ImC_{11}ene][NTf_2]$ 206
7.5.41. 1-Methyl-3-undecyl-thia-pentylimidazolium bis(trifluoromethylsulfonyl)imide, $[C_1ImC_{11}SC_5][NTf_2]$ 207
7.5.42. 1-Methyl-3-heptenylimidazolium bromide, $[C_1ImC_7ene]Br$ 208
7.5.43. 1-Methyl-3-heptenylimidazolium bis(trifluoromethylsulfonyl)imide, $[C_1ImC_7ene][NTf_2]$ 209
7.5.44. 1-Methyl-3-heptylthiaoctylimidazolium bis(trifluoromethylsulfonyl)imide, $[C_1ImC_7SC_8][NTf_2]$ 210
7.5.45. 1-Methyl-3-heptylthiapentylimidazolium bis(trifluoromethylsulfonyl)imide, $[C_1ImC_7SC_5][NTf_2]$ 211
7.5.46. 1-Methyl-3-pentenylimidazolium bromide, $[C_1ImC_5ene]Br$ 212
7.5.47. 1-Methyl-3-pentenylimidazolium bis(trifluoromethylsulfonyl)imide, $[C_1ImC_5ene][NTf_2]$ 213
7.5.48. 1-Methyl-3-pentylthiaoctylimidazolium bis(trifluoromethylsulfonyl)imide, $[C_1ImC_5SC_8][NTf_2]$ 214
7.5.49. 1-Methyl-3-pentylthiapentylimidazolium bis(trifluoromethylsulfonyl)imide, $[C_1ImC_5SC_5][NTf_2]$ 215
7.6.1. 1,6-Bis(3-methylimidazolium-1-yl)hexane dibromide, $[C_6(C_1Im)_2]2Br$ 217
7.6.2. 1,6-Bis(3-methylimidazolium-1-yl)hexane di[bis(trifluoromethanesulfonyl)imide], $[C_6(C_1Im)_2]2[NTf_2]$ 218
7.6.3. 1,8-Bis(3-methylimidazolium-1-yl)octane dibromide, $[C_8(C_1Im)_2]2Br$ 219
7.6.4. 1,8-Bis(3-methylimidazolium-1-yl)octane di[bis(trifluoromethanesulfonyl)imide], $[C_8(C_1Im)_2]2[NTf_2]$ 220
7.6.5. 1,10-Bis(3-methylimidazolium-1-yl)decane dibromide, $[C_{10}(C_1Im)_2]2Br$ 221
7.6.6. 1,10-Bis(3-methylimidazolium-1-yl)decane di[bis(trifluoromethanesulfonyl)imide], $[C_{10}(C_1Im)_2]2[NTf_2]$ 222
7.6.7. 1,12-Bis(3-methylimidazolium-1-yl)dodecane dibromide, $[C_{12}(C_1Im)_2]2Br$ 223

7.6.8. 1,12-Bis(3-methylimidazolium-1-yl)dodecane di[bis(trifluoromethanesulfonyl)imide], $[C_{12}(C_1Im)_2]2[NTf_2]$ 224
7.6.9. 6-Bromohexylpyridinium bromide, $[Pyr(C_6)Br]Br$ 225
7.6.10. 1,6-(3-Methylimidazolium-1-yl)(pyridinium-N-yl)hexane dibromide, $[Pyr(C_6)Im]2Br$ 226
7.6.11. 1,6-(3-Methylimidazolium-1-yl)(pyridinium-N-yl)hexane di[bis(trifluoromethanesulfonyl)imide], $Pyr(C_6)Im]2[NTf_2]$ 227
7.6.12. 8-Bromooctylpyridinium bromide, $[Pyr(C_8)Br]Br$ 228
7.6.13. 1,8-(3-Methylimidazolium-1-yl)(pyridinium-N-yl)octane dibromide, $[Pyr(C_8)Im]2Br$ 229
7.6.14. 1,8-(3-Methylimidazolium-1-yl)(pyridinium-N-yl)octane di[bis(trifluoromethanesulfonyl)imide], $[Pyr(C_8)Im]2[NTf_2]$ 231
7.6.15. 10-Bromodecylpyridinium bromide, $[Pyr(C_{10})Br]Br$ 232
7.6.16. 1,10-(3-Methylimidazolium-1-yl)(pyridinium-N-yl)decane dibromide, $[Pyr(C_{10})Im]2Br$ 233
7.6.17. 1,10-(3-Methylimidazolium-1-yl)(pyridinium-N-yl)decane di[bis(trifluoromethanesulfonyl)imide], $[Pyr(C_{10})Im]2[NTf_2]$ 234
7.6.18. 12-Bromododecylpyridinium bromide, $[Pyr(C_{12})Br]Br$ 235
7.6.19. 1,12-(3-Methylimidazolium-1-yl)(pyridinium-N-yl)dodecane dibromide, $[Pyr(C_{12})Im]2Br$ 237
7.6.20. 1,12-(3-Methylimidazolium-1-yl)(pyridinium-N-yl)dodecane di[bis(trifluoromethanesulfonyl)imide], $[Pyr(C_{12})Im]2[NTf_2]$ 238

7.3. Guanidinium-based Ionic Liquids

7.3.1. Hexamethylguanidinium bis(trifluoromethanesulfonyl)imide, $[(C_1C_1)_2dmg][NTf_2]$



Hexa-methyl-guanidinium chloride (0.50 g, 2.78 mmol) was transferred to a round bottom flask followed by the addition of water (5 mL). Lithium bis(trifluoromethanesulfonyl)imide (0.960 g, 3.34 mmol) in water (5 mL) was added and the mixture stirred at 0 °C and gradually allowed to warm up to room temperature for 24 h. Dichloromethane (10 mL) was added to extract the ionic liquid and washed with cold water (5 x 5 mL). The organic layer was collected, the solvent removed and stirred *in vacuo* overnight at 50 °C. The salt $[(C_1C_1)_2dmg][NTf_2]$ (1.11 g, 94.0%) was obtained as a white solid powder.

^{1}H NMR (400 MHz, DMSO-d_6): δ 2.87 (s, 18 H);

^{13}C NMR (100 MHz, DMSO-d_6): δ 162.4, 119.9 (q, $^{1}J_{C\text{-}F}$ = 322 Hz, 1 C), 39.4;

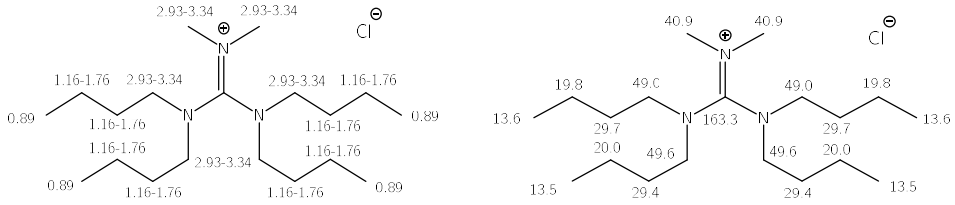
^{19}F NMR (376 MHz, DMSO-d_6): δ -78.7 (s, 6 F).

ESI-MS (+ve) $[C_7H_{18}N_3]^+$: calcd 144.1495, found 144.1484.

ESI-MS (-ve) $[C_2F_6NO_4S_2]^-$: calcd 279.9178, found 279.9175.

CHN Analysis: Calc. for $[(C_1C_1)_2dmg][NTf_2]$, ($C_9H_{18}F_6N_4O_4S_2$): N 13.20, C 25.47, H 4.28. Found: N 13.00, C 25.51, H 4.07.

7.3.2. Tetrabutyldimethylguanidinium chloride, $[(C_4C_4)_2dmg][Cl]$[142]



To a suspension of phosgene iminium chloride (2.10 g, 13.0 mmol) in anhydrous dichloromethane (20 mL) at 0 °C (ice bath) was added dropwise a mixture of dibutylamine (4.60 mL, 27.3 mmol) and triethylamine (3.99 mL, 28.6 mmol) in dichloromethane (30 mL). After 30 min at 0 °C (complete solubilisation of the phosgene iminium salt), the reaction was stirred at room temperature for 4 h. The solvent was removed *in vacuo* and an aqueous solution of NaOH (2 M, 20 mL) was added. The mixture was washed with diethyl ether (2 x 25 mL) and the pH adjusted to 7 by dropwise addition of hydrochloric acid (37%). The water was removed *in vacuo*, the residue extracted with dichloromethane (50 mL), the solvent evaporated and the residue left *in vacuo* overnight at 50 °C. The salt $[(C_4C_4)_2dmg][Cl]$ (3.73 g, 82.1%) was obtained as a light yellow hygroscopic solid wax.

^{1}H NMR (400 MHz, $CDCl_3$): δ 2.93 - 3.34 (m, 14 H), 1.16 - 1.76 (m, 16 H), 0.89 (t, J = 7.2 Hz, 12 H);

^{13}C NMR (100 MHz, $CDCl_3$): δ 163.3, 49.6 and 49.0 (rotamers), 40.9, 29.7 and 29.4 (rotamers), 20.0 and 19.8 (rotamers), 13.6 and 13.5 (rotamers).

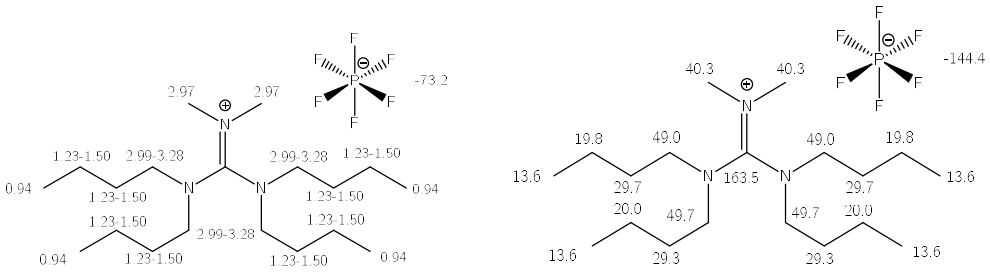
ESI-MS (+ve) $[C_{19}H_{42}N_3]^+$: calcd 312.3373, found 312.3371.

CHN Analysis: Calc. for $[(C_4C_4)_2dmg]Cl$, ($C_{19}H_{42}ClN_3$): N 12.07, C 65.57, H 12.16. Found: N 12.45, C 65.98, H 11.83.

DSC: A glass transition was observed at -55.3 °C and a melting transition was observed at 82.0 °C.

Data in agreement with literature values.[142]

7.3.3. Tetrabutyldimethylguanidinium hexafluorophosphate, $[(C_4C_4)_2dmg][PF_6]$[142]



[**CAUTION**! Release of HF from HPF_6 occurs upon contact with water. Thick protective gloves should always be worn]

Compound **7.3.2.** (3.50 g, 10.1 mmol) was transferred to a round bottom flask followed by the addition of water (20 mL). HPF_6 (1.67 mL, 12.1 mmol) 60% w/w solution (10 mL) was added and the mixture stirred at 0 °C and gradually allowed to warm up to room temperature for 24 h. Dichloromethane (20 mL) was added to recover the ionic liquid and washed with cold water (5 x 5 mL). The organic layer was collected, the solvent removed and stirred *in vacuo* overnight at 50 °C. The salt $[(C_4C_4)_2dmg][PF_6]$ (4.51 g, 98.3%) was obtained as a light yellow solid powder.

^{1}H NMR (400 MHz, $CDCl_3$): δ 3.28 - 2.99 (m, 8 H), 2.97 (s, 6 H), 1.50 - 1.23 (m, 16 H), 0.94 (t, J = 7.2 Hz, 12 H);

^{13}C NMR (100 MHz, $CDCl_3$): δ 163.5, 49.7 and 49.0 (rotamers), 40.3, 29.7 and29.3 (rotamers), 20.0 and19.8 (rotamers), 13.6;

^{19}F NMR (376 MHz, $CDCl_3$): δ -73.2 (d, $^{1}J_{F\text{-}P}$ = 712 Hz, 6 F);

^{31}P NMR (160 MHz, $CDCl_3$): δ -144.4 (spt, $^{1}J_{P\text{-}F}$ = 712 Hz, 1 P).

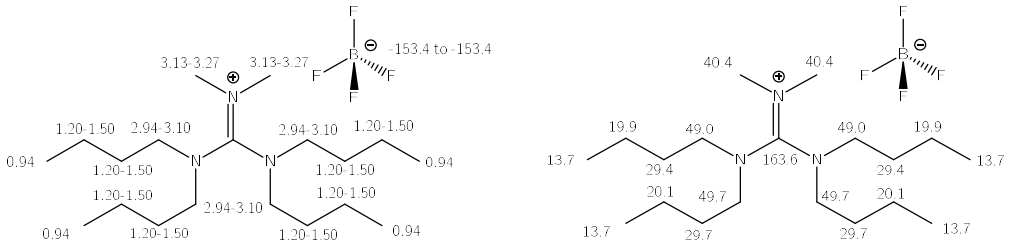
ESI-MS (+ve) $[C_{19}H_{42}N_3]^+$: calcd 312.3373, found 312.3365.

CHN Analysis: Calc. for $[(C_4C_4)_2dmg][PF_6]$, ($C_{19}H_{42}F_6N_3P$): N 9.18, C 49.88, H 9.25. Found: N 9.27, C 49.53, H 9.40.

DSC: A melting transition was observed at 58.7 °C.

Data in agreement with literature values.[142]

7.3.4. Tetrabutyldimethylguanidinium tetrafluoroborate, $[(C_4C_4)_2dmg][BF_4]$[142]



Compound **7.3.2.** (2.00 g, 5.75 mmol) was transferred to a round bottom flask followed by the addition of water (20 mL). $NaBF_4$ (0.76 g, 6.89 mmol) in water (10 mL) was added and the mixture stirred at 0 °C and gradually allowed to warm up to room temperature for 24 h. Dichloromethane (20 mL) was added to recover the ionic liquid and washed with cold water (5 x 5 mL). The organic layer was collected, the solvent removed and stirred *in vacuo* overnight at 50 °C. The salt $[(C_4C_4)_2dmg][BF_4]$ (2.20 g, 96.2%) was obtained as a white solid powder.

^{1}H NMR (400 MHz, $CDCl_3$): δ 3.27 - 3.13 (m, 6 H), 3.10 - 2.94 (m, 8 H), 1.50 - 1.20 (m, 16 H), 0.94 (t, J = 7.2 Hz, 12 H);

^{13}C NMR (100 MHz, $CDCl_3$): δ 163.6, 49.7 and 49.0 (rotamers), 40.4, 29.7 and 29.4 (rotamers), 20.1 and19.9 (rotamers), 13.7;

^{19}F NMR (376 MHz, $CDCl_3$): δ -153.4 to -153.4 (m), -153.4 (br. s);

ESI-MS (+ve) $[C_{19}H_{42}N_3]^+$: calcd 312.3373, found 312.3366.

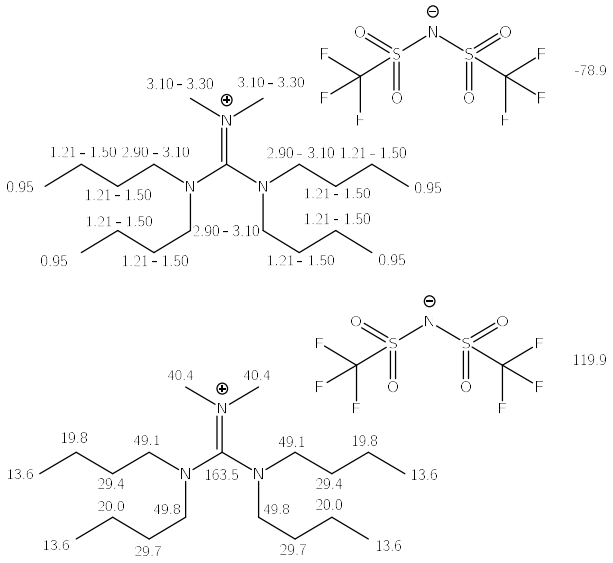
CHN Analysis: Calc. for $[(C_4C_4)_2dmg][BF_4]$, ($C_{19}H_{42}F_4N_3B$): N 10.52, C 57.14, H 10.60. Found: N 10.67, C 57.35, H 10.31.

DSC: A glass transition was observed at -57.7 °C and a melting transition was observed at 74.5 °C.

Data in agreement with literature values.[142]

Note: In the ^{19}F NMR, two equidistant signals were observed: a broad singlet for coupling between ^{10}B-F and a quartet (recorded most of the times as a multiplet) for coupling between ^{11}B-F).

7.3.5. Tetrabutyldimethylguanidinium bis(trifluoromethylsulfonyl)imide, $[(C_4C_4)_2dmg][NTf_2]$



Compound **7.3.2.** (1.50 g, 4.31 mmol) was transferred to a round bottom flask followed by the addition of water (15 mL). $LiNTf_2$ (1.48 g, 5.17 mmol) in water (10 mL) was added and the mixture stirred at 0 °C and gradually allowed to warm up to room temperature for 24 h. Dichloromethane (15 mL) was added to recover the ionic liquid and washed with cold water (5 x 5 mL). The organic layer was collected, the solvent removed and stirred *in vacuo* overnight at 50 °C. The salt $[(C_4C_4)_2dmg][NTf_2]$ (2.53 g, 99.1%) was obtained as a white solid powder.

^{1}H NMR (400 MHz, $CDCl_3$): δ 3.30 - 3.13 (m, 6 H), 3.10 - 2.90 (m, 8 H), 1.50 - 1.21 (m, 16 H), 0.95 (t, J = 7.2 Hz, 12 H);

^{13}C NMR (100 MHz, $CDCl_3$): δ 163.5, 119.9 (q, $^1J_{C\text{-}F}$ = 322 Hz, 1 C), 49.8 and 49.1 (rotamers), 40.4, 29.7 and 29.4 (rotamers), 20.0 and 19.8 (rotamers), 13.6;

^{19}F NMR (376 MHz, $CDCl_3$): δ -78.9 (s, 6 F).

IR $\nu_{max}(CHCl_3)\cdot cm^{-1}$ 3045, 2965, 2936, 2877, 1578, 1539, 1460, 1421, 1351, 1192, 1136, 1060, 890.

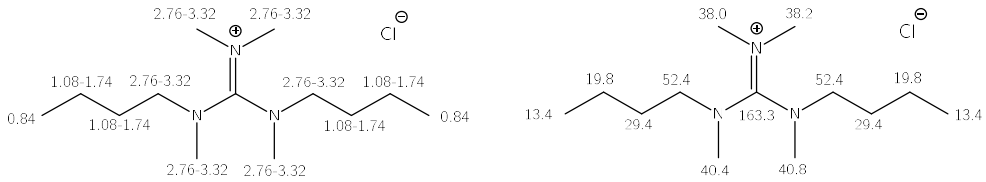
ESI-MS (+ve) $[C_{19}H_{42}N_3]^+$: calcd 312.3373, found 312.3369.

ESI-MS (-ve) $[C_2F_6NO_4S_2]^-$: calcd 279.9178, found 279.9177.

CHN Analysis: Calc. for $[(C_4C_4)_2dmg][NTf_2]$, ($C_{21}H_{42}F_6N_4O_4S_2$): N 9.45, C 42.55, H 7.14. Found: N 9.22, C 42.57, H 7.02.

DSC: A glass transition was observed at 7.7 °C and a melting transition was observed at 59.9 °C.

7.3.6. Butylmethyldimethylguanidinium chloride, $[(C_4C_1)_2dmg][Cl]$[142]



To a suspension of phosgene iminium chloride (5.00 g, 30.8 mmol) in anhydrous dichloromethane (40 mL) at 0 °C (ice bath) was added dropwise a mixture of methylbutylamine (7.66 mL; 64.7 mmol) and triethylamine (9.44 mL; 67.8 mmol) in dichloromethane (50 mL). After 30 min at 0 °C (complete solubilisation of the phosgene iminium salt), the reaction was stirred at room temperature for 4 h. The solvent was removed *in vacuo* and an aqueous solution of NaOH (2 M, 30 mL) was added. The mixture was washed with diethyl ether (2 x 50 mL) and the pH adjusted to 7 by dropwise addition of hydrochloric acid (37%). The water was removed *in vacuo*, the residue extracted with dichloromethane (100 mL), the solvent evaporated and the residue left *in vacuo* overnight. The salt $[(C_4C_1)_2dmg][Cl]$ (6.91 g, 85.6%) was obtained as a yellow viscous liquid.

^{1}H NMR (400 MHz, $CDCl_3$): δ 3.32 - 2.76 (m, 16 H), 1.74 - 1.08 (m, 8 H), 0.84 (t, J = 7.2 Hz, 6 H);

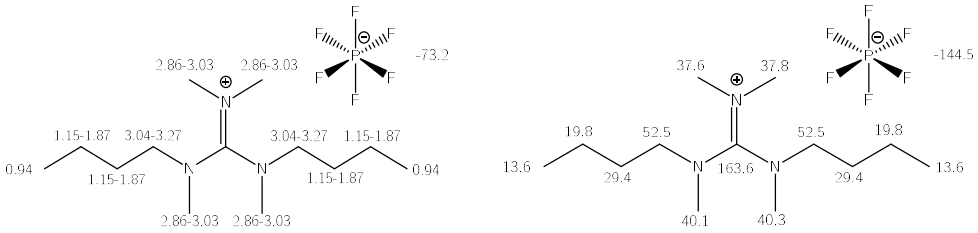
^{13}C NMR (100 MHz, $CDCl_3$): δ 163.3, 52.4, 40.8 and 40.4 (rotamers), 38.2 and 38.0 (rotamers), 29.4, 19.8, 13.4.

ESI-MS (+ve) $[C_{13}H_{30}N_3]^+$: calcd 228.2434, found 228.2433.

CHN Analysis: Calc. for $[(C_4C_1)_2dmg]Cl$, ($C_{21}H_{42}ClN_3$): N 15.93, C 59.18, H 11.46. Found: N 15.68, C 59.23, H 11.79.

Data in agreement with literature values.[142]

7.3.7. Butylmethyldimethylguanidinium hexafluorophosphate, $[(C_4C_1)_2dmg][PF_6]$[142]



[**CAUTION!** Release of HF from HPF_6 occurs upon contact with water. Thick protective gloves should always be worn]

Compound **7.3.6**. (0.660 g, 2.50 mmol) was transferred to a round bottom flask followed by the addition of water (5 mL). HPF_6 (0.420 mL, 3.00 mmol) 60% w/w solution in water (5 mL) was added and the mixture stirred at 0 °C and gradually allowed to warm up to room temperature for 24 h. Dichloromethane (10 mL) was added to recover the ionic liquid and washed with cold water (5 x 5 mL). The organic layer was collected, the solvent removed and stirred *in vacuo* overnight at 50 °C. The salt $[(C_4C_1)_2dmg][PF_6]$ (0.850 g, 91.4%) was obtained as a light yellow solid powder.

^{1}H NMR (400 MHz, $CDCl_3$): δ 3.27 - 3.04 (m, 4 H), 3.03 - 2.86 (m, 12 H), 1.87 - 1.15 (m, 8 H), 0.94 (t, J = 7.2 Hz, 6 H);

^{13}C NMR (100 MHz, $CDCl_3$): δ 163.6, 52.5, 40.3 and 40.1 (rotamers), 37.8 and 37.6 (rotamers), 29.4, 19.8, 13.6;

^{19}F NMR (376 MHz, $CDCl_3$): δ -73.2 (d, $^1J_{F\text{-}P}$ = 712 Hz, 6 F);

^{31}P NMR (160 MHz, $CDCl_3$): δ -144.5 (spt, $^1J_{P\text{-}F}$ = 712 Hz, 1 P).

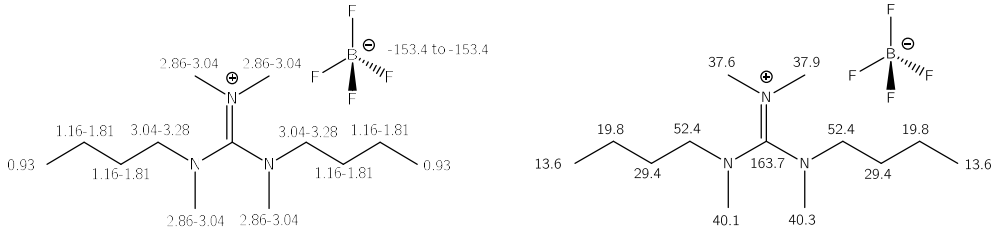
ESI-MS (+ve) $[C_{13}H_{30}N_3]^+$: calcd 228.2434, found 228.2429.

CHN Analysis: Calc. for $[(C_4C_1)_2dmg][PF_6]$, ($C_{21}H_{42}F_6N_3P$): N 11.25, C 41.82, H 8.10. Found: N 11.01, C 41.99, H 8.33.

DSC: A glass transition was observed at -10.5 °C and a melting transition was observed at 62.8 °C.

Data in agreement with literature values.[142]

7.3.8. Butylmethyldimethylguanidinium tetrafluoroborate, $[(C_4C_1)_2dmg][BF_4]$[142]



Compound **7.3.6**. (0.830 g, 3.14 mmol) was transferred to a round bottom flask followed by the addition of water (5 mL). $NaBF_4$ (0.410 g, 3.78 mmol) in water (5 mL) was added and the mixture stirred at 0 °C and gradually allowed to warm up to room temperature for 24 h. Dichloromethane (10 mL) was added to recover the ionic liquid and washed with cold water (5 x 5 mL). The organic layer was collected, the solvent removed and stirred *in vacuo* overnight at 50 °C. The salt $[(C_4C_1)_2dmg][BF_4]$ (0.880 g, 88.0%) was obtained as a light yellow solid powder.

^{1}H NMR (400 MHz, $CDCl_3$): δ 3.28 - 3.04 (m, 4 H); 3.04 - 2.86 (m, 12 H), 1.81 - 1.16 (m, 8 H), 0.93 (t, J = 7.2 Hz, 6H);

^{13}C NMR (100 MHz, $CDCl_3$): δ 163.7, 52.4, 40.3 and 40.1 (rotamers), 37.9 and 37.6 (rotamers), 29.4, 19.8, 13.6;

^{19}F NMR (376 MHz, $CDCl_3$): δ -153.4 (q, J = 1.1 Hz), -153.3 (br. s);

ESI-MS (+ve) $[C_{13}H_{30}N_3]^+$: calcd 228.2434, found 228.2438.

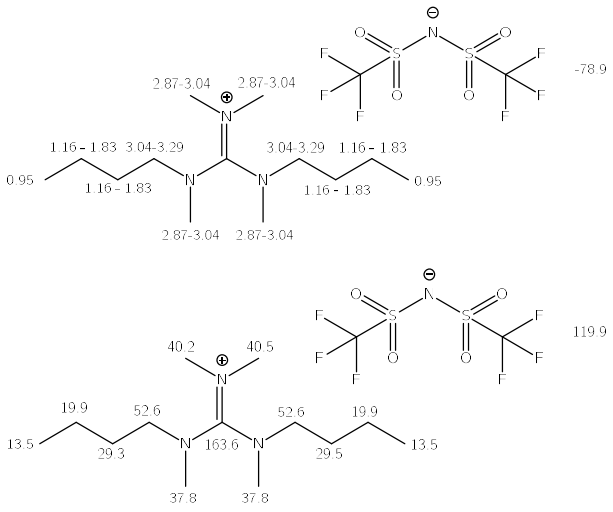
CHN Analysis: Calc. for $[(C_4C_1)_2dmg][BF_4]$, ($C_{21}H_{42}F_4N_3B$): N 13.33, C 49.54, H 9.59. Found: N 13.61, C 49.43, H 9.32.

DSC: A glass transition was observed at 17.6 °C and a melting transition was observed at 67.6 °C.

Data in agreement with literature values.[142]

Note: In the ^{19}F NMR, two equidistant signals were observed: a broad singlet for coupling between ^{10}B-F and a quartet (recorded most of the times as a multiplet) for coupling between ^{11}B-F).

7.3.9. Butylmethyldimethylguanidinium bis(trifluoromethylsulfonyl)imide, $[(C_4C_1)_2dmg][NTf_2]$



Compound **7.3.6**. (0.440 g, 1.67 mmol) was transferred to a round bottom flask followed by the addition of water (5 mL). $LiNTf_2$ (0.570 g, 2.00 mmol) in water (5 mL) was added and the mixture stirred at 0 °C and gradually allowed to

warm up to room temperature for 24 h. Dichloromethane (10 mL) was added to recover the ionic liquid and washed with cold water (5 x 5 mL). The organic layer was collected, the solvent removed and stirred *in vacuo* overnight at 50 °C. The salt $[(C_4C_1)_2dmg][NTf_2]$ (0.81 g, 96.6%) was obtained as a light yellow powder.

^{1}H NMR (400 MHz, $CDCl_3$): δ 3.29 - 3.04 (m, 4 H), 3.04 - 2.87 (m, 12 H), 1.83 - 1.16 (m, 8 H), 0.95 (t, J = 7.2 Hz, 6 H);

^{13}C NMR (100 MHz, $CDCl_3$): δ 163.6, 119.9 (q, $^1J_{C\text{-}F}$ = 322 Hz, 1 C), 52.6, 40.5 and 40.2 (rotamers), 37.8, 29.5 and 29.3 (rotamers), 19.9, 13.5;

^{19}F NMR (376 MHz, $CDCl_3$): δ -78.9 (s, 6 F).

IR $\nu_{max}(CHCl_3)\cdot cm^{-1}$ 3045, 2965, 2936, 2877, 1569, 1468, 1408, 1350, 1192, 1136, 1060, 893.

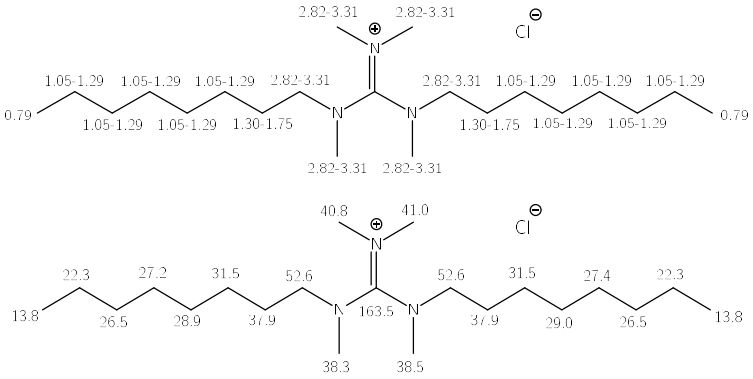
ESI-MS (+ve) $[C_{13}H_{30}N_3]^+$: calcd 228.2434, found 228.2436.

ESI-MS (-ve) $[C_2F_6NO_4S_2]^-$: calcd 279.9178, found 279.9174.

CHN Analysis: Calc. for $[(C_4C_1)_2dmg][NTf_2]$, ($C_{15}H_{30}F_6N_4O_4S_2$): N 11.02, C 35.43, H 5.95. Found: N 10.79, C 35.47, H 5.84.

DSC: A melting transition was observed at 62.1 °C.

7.3.10. Methyloctyldimethylguanidinium chloride, $[(C_8C_1)_2dmg][Cl]$



To a suspension of phosgene iminium chloride (4.06 g, 25.0 mmol) in anhydrous dichloromethane (40 mL) at 0 °C (ice bath) was added dropwise a mixture of methyloctylamine (9.52 mL, 52.5 mmol) and triethylamine (7.67 mL, 55.0 mmol) in dichloromethane (50 mL). After 30 min at 0 °C (complete solubilisation of the phosgene iminium salt), the reaction was stirred at room temperature for 4 h. The solvent was removed *in vacuo* and an aqueous solution of NaOH (2 M, 30 mL) was added. The mixture was washed with diethyl ether (2 x 50 mL) and the pH adjusted to 7 by dropwise addition of hydrochloric acid (37%). The water was removed *in vacuo*, the residue extracted with dichloromethane (100 mL), the solvent evaporated and the residue left *in vacuo* overnight. The salt $[(C_8C_1)_2dmg][Cl]$ (7.62 g, 81.7%) was obtained as a light yellow wax.

^{1}H NMR (400 MHz, $CDCl_3$): δ 3.31 - 2.82 (m, 16 H), 1.75 - 1.30 (m, 4 H), 1.29 - 1.05 (m, 20 H), 0.79 (t, J = 6.8 Hz, 6 H);

^{13}C NMR (100 MHz, $CDCl_3$): δ 163.5, 52.6, 41.0 and 40.8 (rotamers), 38.5 and 38.3 (rotamers), 37.9, 31.5, 29.0 and 28.9 (rotamers), 27.4 and 27.2 (rotamers), 26.5, 22.3, 13.8.

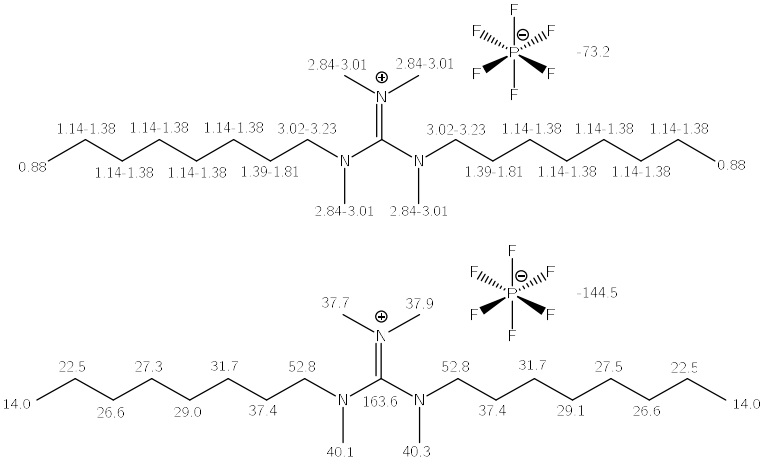
IR $\nu_{max}(CHCl_3)\cdot cm^{-1}$ 2930, 2858, 2463, 1566, 1467, 1408, 1378, 1247, 1063, 898.

ESI-MS (+ve) $[C_{21}H_{46}N_3]^+$: calcd 340.3686, found 340.3677.

CHN Analysis: Calc. for $[(C_8C_1)_2dmg]Cl{\cdot}3H_2O$, ($C_{21}H_{52}ClN_3O_3$): N 9.77, C 58.64, H 12.19. Found: N 9.81, C 58.51, H 11.91.

DSC: A glass transition was observed at 23.0 °C and a melting transition was observed at 45.8 °C.

7.3.11. Methyloctyldimethylguanidinium hexafluorophosphate, $[(C_8C_1)_2dmg][PF_6]$



[**CAUTION!** Release of HF from HPF_6 occurs upon contact with water. Thick protective gloves should always be worn]

Compound **7.3.10**. (1.09 g, 2.90 mmol) was transferred to a round bottom flask followed by the addition of water (10 mL). HPF_6 (0.480 mL, 3.50 mmol) 60% w/w in water (10 mL) was added and the mixture stirred at 0 °C and gradually allowed to warm up to room temperature for 24 h. Dichloromethane (10 mL) was added to recover the ionic liquid and washed with cold water (5 x 5 mL). The organic layer was collected, the solvent removed and stirred *in vacuo* overnight at 50 °C. The salt $[(C_8C_1)_2dmg][PF_6]$ (1.38 g, 98.0%) was obtained as a light yellow liquid.

^{1}H NMR (400 MHz, $CDCl_3$): δ 3.23 - 3.02 (m, 4 H), 3.01 - 2.84 (m, 12 H), 1.81 - 1.39 (m, 4 H), 1.38 - 1.14 (m, 20 H), 0.88 (t, J = 6.8 Hz, 6 H);

^{13}C NMR (100 MHz, $CDCl_3$): δ 163.6, 52.8, 40.3 and 40.1 (rotamers), 37.9 and 37.7 (rotamers), 37.4, 31.7, 29.1 and 29.0 (rotamers), 27.5 and 27.3 (rotamers), 26.6, 22.5, 14.0;

^{19}F NMR (376 MHz, $CDCl_3$): δ -73.2 (d, $^1J_{F\text{-}P}$ = 712 Hz, 6 F);

^{31}P NMR (160 MHz, $CDCl_3$): δ -144.5 (spt, $^1J_{P\text{-}F}$ = 712 Hz, 1 P).

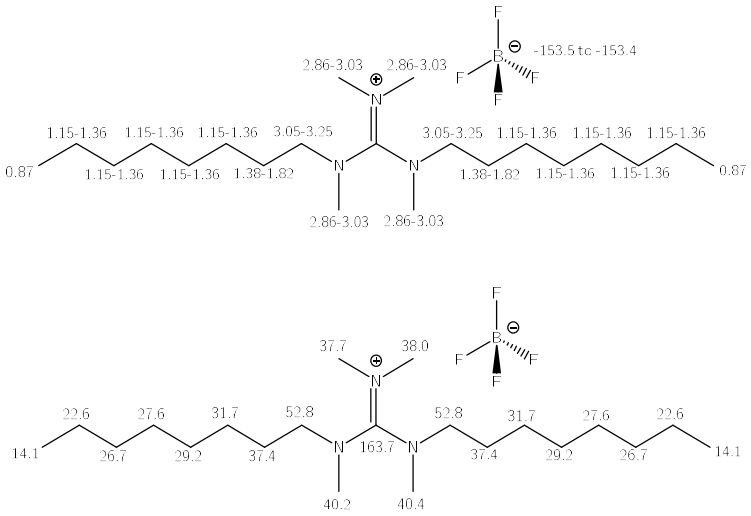
IR $\nu_{max}(CHCl_3)\cdot cm^{-1}$ 3046, 2930, 2858, 1570, 1467, 1409, 1250, 849.

ESI-MS (+ve) $[C_{21}H_{46}N_3]^+$: calcd 340.3686, found 340.3678.

CHN Analysis: Calc. For $[(C_8C_1)_2dmg][PF_6]$, ($C_{21}H_{46}F_6N_3P$): N 8.65, C 51.94, H 9.55. Found: N 8.73, C 51.91, H 9.36.

DSC: A glass transition was observed at -31.6 °C and a melting transition was observed at 21.0 °C.

7.3.12. Methyloctyldimethylguanidinium tetrafluoroborate, $[(C_8C_1)_2dmg][BF_4]$



Compound **7.3.10**. (1.09 g, 2.90 mmol) was transferred to a round bottom flask followed by the addition of water (10 mL). $NaBF_4$ (0.380 g, 3.49 mmol) in water (10 mL) was added and the mixture stirred at 0 °C and gradually allowed to warm up to room temperature for 24 h. Dichloromethane (10 mL) was added

to recover the ionic liquid and washed with cold water (5 x 5 mL). The organic layer was collected, the solvent removed and stirred *in vacuo* overnight at 50 °C. The salt $[(C_8C_1)_2dmg][BF_4]$ (1.14 g, 92%) was obtained as a light yellow powder.

^{1}H NMR (400 MHz, $CDCl_3$): δ 3.25 - 3.05 (m, 4 H), 3.03 - 2.86 (m, 12 H), 1.82 - 1.38 (m, 4 H), 1.36 - 1.15 (m, 20 H), 0.87 (t, J = 6.8 Hz, 6 H);

^{13}C NMR (100 MHz, $CDCl_3$): δ 163.7, 52.8, 40.4 and 40.2 (rotamers), 38.0 and 37.7 (rotamers), 37.4, 31.7, 29.2, 27.6, 26.7, 22.6, 14.1;

^{19}F NMR (376 MHz, $CDCl_3$): δ -153.5 to -153.4 (m), -153.4 (br. s).

IR $\nu_{max}(CHCl_3)\cdot cm^{-1}$ 3045, 2930, 2858, 1570, 1467, 1409, 1378, 1286, 1242, 1060, 899.

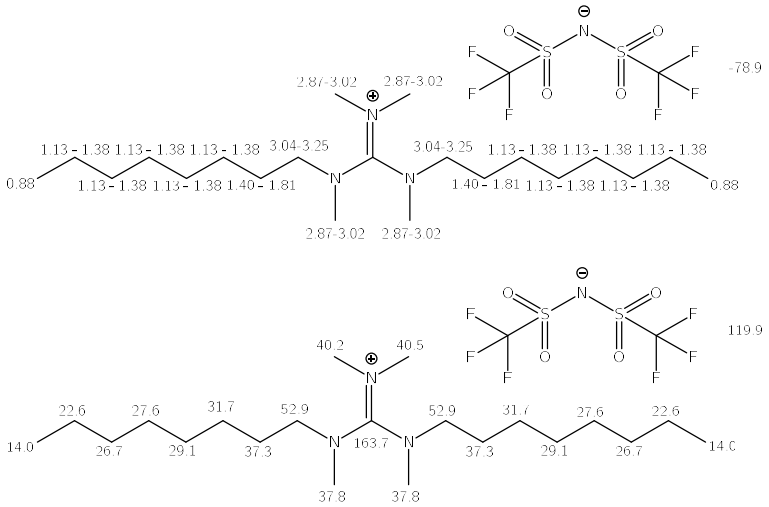
ESI-MS (+ve) $[C_{21}H_{46}N_3]^+$: calcd 340.3686, found 340.3681.

CHN Analysis: Calc. for $[(C_8C_1)_2dmg][BF_4]$, ($C_{21}H_{46}F_4N_3B$): N 9.83, C 59.01, H 10.85. Found: N 9.81, C 59.10, H 10.91.

DSC: A glass transition was observed at 33.2 °C and a melting transition was observed at 61.2 °C.

Note: In the ^{19}F NMR, two equidistant signals were observed: a broad singlet for coupling between ^{10}B-F and a quartet (recorded most of the times as a multiplet) for coupling between ^{11}B-F).

7.3.13. Methyloctyldimethylguanidinium bis(trifluoromethylsulfonyl)imide, $[(C_8C_1)_2dmg][NTf_2]$



Compound **7.3.10.** (0.510 g, 1.36 mmol) was transferred to a round bottom flask followed by the addition of water (5 mL). $LiNTf_2$ (0.470 g, 1.63 mmol) in water (5 mL) was added and the mixture stirred at 0 °C and gradually allowed to warm up to room temperature for 24 h. Dichloromethane (10 mL) was added to recover the ionic liquid and washed with cold water (5 x 5 mL). The organic layer was collected, the solvent removed and stirred *in vacuo* overnight at 50 °C. The salt $[(C_8C_1)_2dmg][NTf_2]$ (0.830 g, 98.1%) was obtained as a light yellow liquid.

^{1}H NMR (400 MHz, $CDCl_3$): δ 3.25 - 3.04 (m, 4 H), 3.02 - 2.87 (m, 12 H), 1.81 - 1.40 (m, 4 H), 1.38 - 1.13 (m, 20 H), 0.88 (t, J = 6.8 Hz, 6 H);

^{13}C NMR (100 MHz, $CDCl_3$): δ 163.7, 119.9 (q, $^1J_{C\text{-}F}$ = 322 Hz, 1 C), 52.9, 40.5 and 40.2 (rotamers), 37.8, 37.3, 31.7, 29.1, 27.6, 26.7, 22.6, 14.0;

^{19}F NMR (376 MHz, $CDCl_3$): δ -78.9 (s, 6 F).

IR $\nu_{max}(CHCl_3)\cdot cm^{-1}$ 3045, 2931, 2858, 1569, 1467, 1408, 1350, 1192, 1135, 1060, 898.

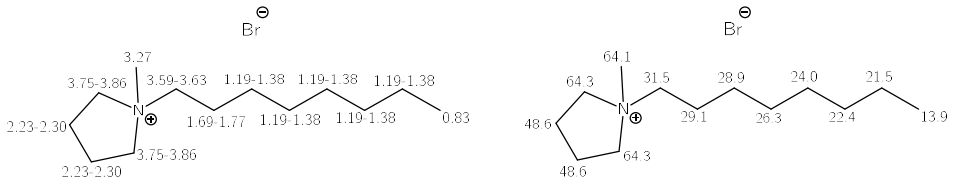
ESI-MS (+ve) $[C_{21}H_{46}N_3]^+$: calcd 340.3686, found 340.3677.

ESI-MS (-ve) $[C_2F_6NO_4S_2]^-$: calcd 279.9178, found 279.9175.

CHN Analysis: Calc. for $[(C_8C_1)_2dmg][NTf_2]$, ($C_{23}H_{46}F_6N_4O_4S_2$): N 9.03, C 44.50, H 7.47. Found: N 9.11, C 44.62, H 7.33.

7.4. Pyrrolidinium-based Ionic Liquids

7.4.1. 1-Octyl-1-methylpyrrolidinium bromide, $[C_8C_1Pyrr]Br$[267]



To a stirring solution of 1-methylpyrrolidine (20.0 mL, 188 mmol) in ethyl acetate (15 mL), 1-bromooctane (40 mL, 232.0 mmol) was added dropwise at room temperature. The reaction mixture was heated to 40 °C and stirred for 48 h. The solvent was removed and the crude solid recrystallized from acetonitrile/ethyl acetate and dried *in vacuo* at 50 °C to yield a off-white solid (33.0 g, 63.9%).

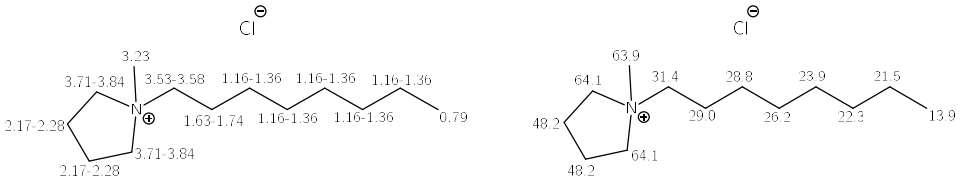
^{1}H NMR (400 MHz, $CDCl_3$): δ 3.86 - 3.75 (m, 4 H), 3.63 - 3.59 (m, 2 H), 3.27 (s, 3 H), 2.30 - 2.23 (m, 4 H), 1.77 - 1.69 (m, 2 H), 1.38 - 1.19 (m, 10 H), 0.83 (t, J = 7.0 Hz, 3 H);

^{13}C NMR (100 MHz, $CDCl_3$): δ 64.3, 64.1, 48.6, 31.5, 29.1, 28.9, 26.3, 24.0, 22.4, 21.5, 13.9.

ESI-MS (+ve) $[C_{13}H_{28}N]^+$: calcd 198.2216, found 198.2210.

Data in agreement with literature values.[267]

7.4.2. 1-Octyl-1-methylpyrrolidinium chloride, $[C_8C_1Pyrr]Cl$[268]



Compound **7.4.1.** (7.20 g, 25.9 mmol) was dissolved in methanol (100 mL) and eluted through a column containing Amberlite-IRA400 (Cl) ion-exchange resin

(80.0 g) at a drop rate of 1 mL·min^{-1}. The solvent was removed and the product was dried *in vacuo* at 50 °C to yield an off-white solid (5.68 g, 93%).

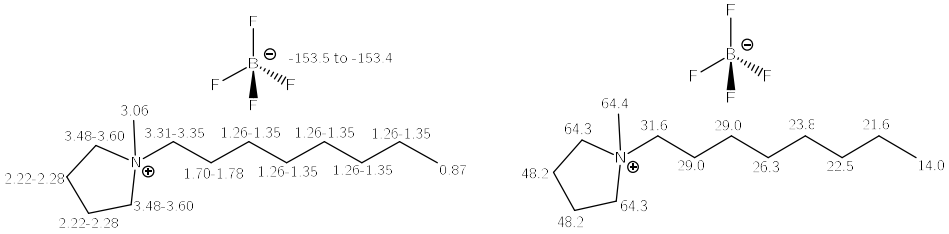
^{1}H NMR (300 MHz, $CDCl_3$): δ 3.84 - 3.71 (m, 4 H), 3.58 - 3.53 (m, 2 H), 3.23 (s, 3 H), 2.28 - 2.17 (m, 4 H), 1.74 - 1.63 (m, 2 H), 1.36 - 1.16 (m, 10 H), 0.79 (t, *J* = 7.0 Hz, 3 H);

^{13}C NMR (75 MHz, $CDCl_3$): δ 64.1, 63.9, 48.2, 31.4, 29.0, 28.8, 26.2, 23.9, 22.3, 21.5, 13.9.

ESI-MS (+ve) $[C_{13}H_{28}N]^+$: calcd 198.2216, found 198.2222.

Data in agreement with literature values.[269]

7.4.3. 1-Octyl-1-methylpyrrolidinium tetrafluoroborate, $[C_8C_1Pyrr][BF_4]$[267]



To a solution of compound **7.4.1** (6.82 g, 24.5 mmol) in water (25 mL), a solution of sodium tetrafluoroborate (3.24 g, 29.5 mmol) in water (25 mL) was added dropwise. The reaction mixture was stirred overnight at room temperature. Dichloromethane (75 mL) was added and the organic layer separated and washed with water (5 x 30 mL). The solvent was removed and the product was dried *in vacuo* at 50 °C to yield a white solid (6.37 g, 91.5%).

^{1}H NMR (400 MHz, $CDCl_3$): δ 3.60 - 3.48 (m, 4 H), 3.35 - 3.31 (m, 2 H), 3.06 (s, 3 H), 2.28 - 2.22 (m, 4 H), 1.78 - 1.70 (m, 2 H), 1.35 - 1.26 (m, 10 H), 0.87 (t, *J* = 7.0 Hz, 3 H);

^{13}C NMR (100 MHz, $CDCl_3$): δ 64.4, 64.3, 48.2, 31.6, 29.0, 29.0, 26.3, 23.8, 22.5, 21.6, 14.0;

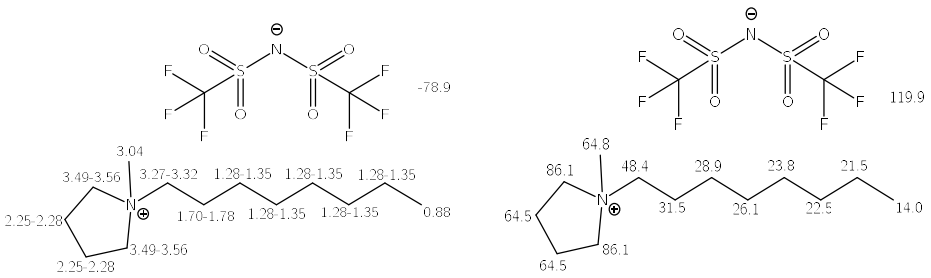
^{19}F NMR (376 MHz, $CDCl_3$): δ -151.5 (q, J = 1.1 Hz), -151.4 (br. s);

ESI-MS (+ve) $[C_{13}H_{28}N]^+$: calcd 198.2216, found 198.2220.

Data in agreement with literature values.[267]

Note: In the ^{19}F NMR, two equidistant signals were observed: a broad singlet for coupling between ^{10}B-F and a quartet (recorded most of the times as a multiplet) for coupling between ^{11}B-F).

7.4.4. 1-Octyl-1-methylpyrrolidinium bis(trifluoromethanesulfonyl)imide, $[C_8C_1Pyrr][NTf_2]$[267]



To a solution of compound **7.4.1.** (5.82 g, 20.9 mmol) in water (25 mL), a solution of lithium bis(trifluoromethane)sulfonimide (7.21 g, 25.1 mmol) in water (25 mL) was added dropwise. The reaction mixture was stirred overnight at room temperature. Dichloromethane (75 mL) was added and the organic layer separated and washed with water (5 x 30 mL). The solvent was removed and the product was dried *in vacuo* at 50 °C to yield a white solid (9.40 g, 94.3%).

^{1}H NMR (400 MHz, $CDCl_3$): δ 3.56 - 3.49 (m, 4 H), 3.32 - 3.27 (m, 2 H), 3.04 (s, 3 H), 2.28 - 2.25 (m, 4 H), 1.78 – 1.70 (m, 2 H), 1.35 – 1.28 (m, 10 H), 0.88 (t, J = 7.0 Hz, 3 H);

^{13}C NMR (100 MHz, $CDCl_3$): δ 119.9 (q, $^1J_{C\text{-}F}$ = 322 Hz, 1 C), 86.1, 64.8, 64.5, 48.4, 31.5, 28.9, 26.1, 23.8, 22.5, 21.5, 14.0;

^{19}F NMR (376 MHz, $CDCl_3$): δ -78.9 (s, 6 F).

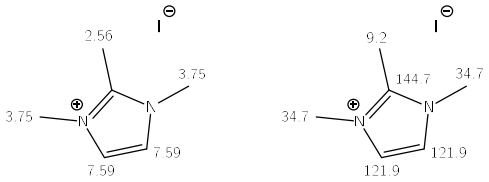
ESI-MS (+ve) $[C_{13}H_{28}N]^+$: calcd 198.2216, found 198.2222.

ESI-MS (-ve) $[C_2F_6NO_4S_2]^-$: calcd 279.9178, found 279.9177.

Data in agreement with literature values.[267]

7.5. Imidazolium- and Sulfur-based Ionic Liquids

7.5.1. 1,2,3-Trimethylimidazolium iodide, $[C_1C_1C_1Im][I]$



[**CAUTION!** Iodomethane is a strong alkylating agent. Thick protective gloves should be worn at all times]

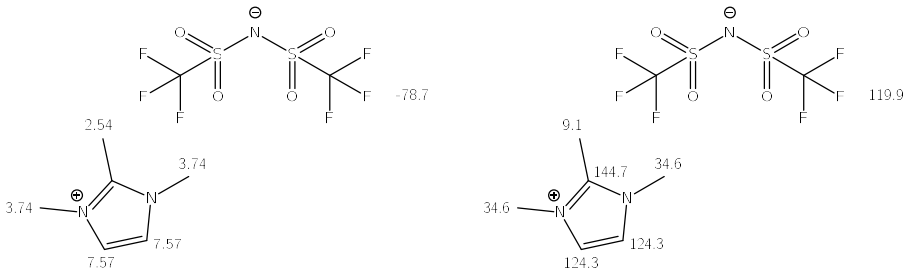
DimethylImidazole (2.02 g, 21.0 mmol) was dissolved in dry diethyl ether (20 mL). Iodomethane (3.92 mL, 63.0 mmol) was added to the solution in one portion. The mixture was refluxed 24 h, then cooled and recrystallised from acetonitrile/ethyl acetate. The product was filtered and dried *in vacuo* overnight at 50 °C. The salt (4.65 g, 92.9%) was obtained as a white powder.

^{1}H NMR (400 MHz, DMSO-d_6): δ 7.59 (s, 2 H), 3.75 (s, 6 H), 2.56 (s, 3 H);

^{13}C NMR (100 MHz, DMSO-d_6): δ 144.7, 121.9, 34.7, 9.2.

ESI-MS (+ve) $[C_6H_{11}N_2]^+$: calcd 111.0917, found 111.0925.

7.5.2. 1,2,3-Trimethylimidazolium bis(trifluoromethylsulfonyl)imide, $[C_1C_1C_1Im][NTf_2]$



Compound **7.5.1.** (0.610 g, 2.56 mmol) was transferred to a round bottom flask followed by the addition of water (5 mL). $LiNTf_2$ (0.880 g, 3.07 mmol) in water (5 mL) was added and the mixture stirred at 0 °C and gradually allowed to warm up to room temperature for 24 h. Dichloromethane (10 mL) was added

to recover the ionic liquid and washed with cold water (5 x 5 mL). The organic layer was collected, the solvent removed and dried *in vacuo* overnight at 50 °C. The salt (0.990 g, 98.7%) was obtained as white powder.

^{1}H NMR (400 MHz, DMSO-d_6): δ 7.57 (s, 2 H), 3.74 (s, 6 H), 2.54 (s, 3 H);

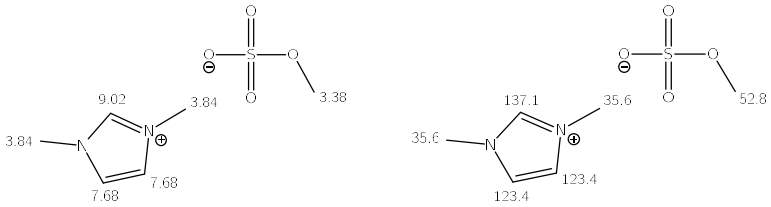
^{13}C NMR (100 MHz, DMSO-d_6): δ 144.7, 121.9, 119.9 (q, $^{1}J_{C\text{-}F}$ = 322 Hz, 1 C), 34.6, 9.1;

^{19}F NMR (376 MHz, DMSO-d_6): δ -78.7 (s, 6 F).

ESI-MS (+ve) $[C_6H_{11}N_2]^+$: calcd 111.0917, found 111.0929.

ESI-MS (-ve) $[C_2F_6NO_4S_2]^-$: calcd 279.9173, found 279.9181.

7.5.3. 1,3-Dimethylimidazolium methyl sulfate, $[C_1C_1Im][MeSO_4]$[268]



[**CAUTION!** Dimethyl sulfate is a strong alkylating agent. Thick protective gloves should be worn at all times]

Dimethyl sulfate (47.8 mL, 0.504 mol) was added dropwise to a solution of 1-methylimidazole (39.4 g, 0.480 mol) in toluene under argon (150 mL) cooled in an ice-bath at a rate to maintain the reaction temperature below 40 °C (the reaction is highly exothermic). Formation of the IL product was immediate and caused the initially clear solution to become opaque, followed by byphasic separation of the toluene solution and the formation of a denser IL phase. After addition of the dimethyl sulfate, the reaction mixture was stirred at room temperature for 24 h. The upper, organic phase was decanted and the lower, IL phase was washed with toluene (5 x 50 mL), the residual organic solvents were

removed and the product stirred *in vacuo* overnight at 50 °C. The salt (98.3 g, 98.3%) was obtained as a colourless liquid.

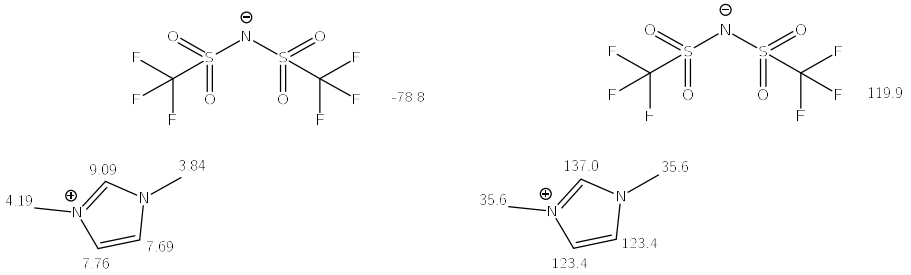
^{1}H NMR (400 MHz, DMSO-d_6): δ 9.02 (s, 1 H), 7.68 (d, J = 1.6 Hz, 2 H), 3.84 (s, 6 H), 3.38 (s, 3 H);

^{13}C NMR (100 MHz, DMSO-d_6): δ 137.1, 123.4, 52.8, 35.6.

ESI-MS (+ve) $[C_5H_9N_2]^+$: calcd 97.0760, found 97.0776.

Data in agreement with literature values.[268]

7.5.4. 1,3-Dimethylimidazolium bis(trifluoromethylsulfonyl)imide, $[C_1C_1Im][NTf_2]$[270]



Compound **7.5.3**. (1.10 g, 5.30 mmol) was transferred to a round bottom flask followed by the addition of water (10 mL). $LiNTf_2$ (1.83 g, 6.36 mmol) in water (10 mL) was added and the mixture stirred at 0 °C and gradually allowed to warm up to room temperature for 24 h. Dichloromethane (20 mL) was added to recover the ionic liquid and washed with cold water (5 x 5 mL). The organic layer was collected, the solvent removed and dried *in vacuo* overnight at 50 °C. The salt (1.98 g, 99.1%) was obtained as colourless liquid.

^{1}H NMR (400 MHz, DMSO-d_6): δ 9.09 (br. s, 1 H), 7.76 (t, J = 1.8 Hz, 1 H), 7.69 (t, J = 1.8 Hz, 1 H), 4.19 (s, 3 H), 3.84 (s, 3 H);

^{13}C NMR (100 MHz, DMSO-d_6): δ 137.0, 123.4, 119.9 (q, $^{1}J_{C\text{-}F}$ = 322 Hz, 1 C), 35.6;

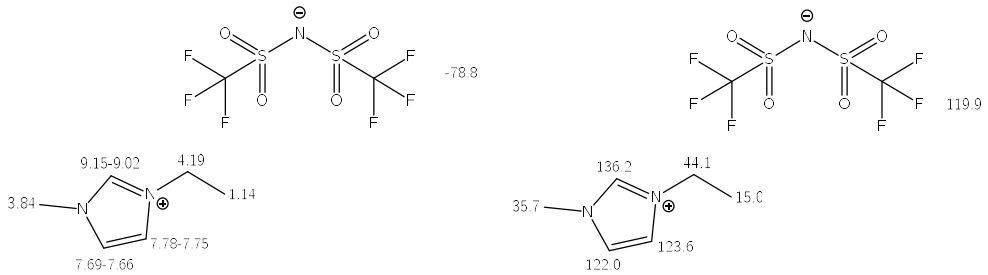
^{19}F NMR (376 MHz, DMSO-d_6): δ -78.8 (s, 6 F).

ESI-MS (+ve) $[C_5H_9N_2]^+$: calcd 97.0760, found 97.0777.

ESI-MS (-ve) $[C_2F_6NO_4S_2]^-$: calcd 279.9173, found 279.9185.

Data in agreement with literature values.[270]

7.5.5. 1-Ethyl-3-methylimidazolium bis(trifluoromethanesulfonyl)imide, $[C_2C_1Im][NTf_2]$[270]



To a solution of 1-ethyl-1-methylimidazolium chloride (1.87 g, 12.8 mmol) in water (10 mL), a solution of lithium bis(trifluoromethane)sulfonimide (4.40 g, 15.3 mmol) in water (10 mL) was added dropwise. The reaction mixture was stirred overnight at room temperature. Dichloromethane (50 mL) was added and the organic layer separated and washed with water (5 x 15 mL). The solvent was removed and the product was dried *in vacuo* at 50 °C to yield a colourless liquid (4.70 g, 94.3%).

^{1}H NMR (400 MHz, DMSO-d_6): δ 9.09 (br. s, 1 H), 7.76 (t, J = 1.8 Hz, 1 H), 7.67 (t, J = 1.8 Hz, 1 H), 4.19 (q, J = 7.4 Hz, 2 H), 3.84 (s, 3 H), 1.41 (t, J = 7.4 Hz, 3 H);

^{13}C NMR (100 MHz, DMSO-d_6): δ 136.2, 123.6, 122.0, 119.9 (q, $^1J_{C\text{-}F}$ = 322 Hz, 1 C), 44.1, 35.7, 15.0;

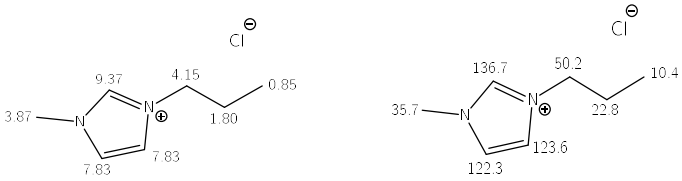
^{19}F NMR (376 MHz, DMSO-d_6): δ -78.8 (s, 6 F).

ESI-MS (+ve) $[C_6H_{11}N_2]^+$: calcd 111.0917 found 111.0931.

ESI-MS (-ve) $[C_2F_6NO_4S_2]^-$: calcd 279.9173, found 279.9187.

Data in agreement with literature values.[270]

7.5.6. 1-Propyl-3-methylimidazolium chloride, $[C_3C_1Im]Cl$



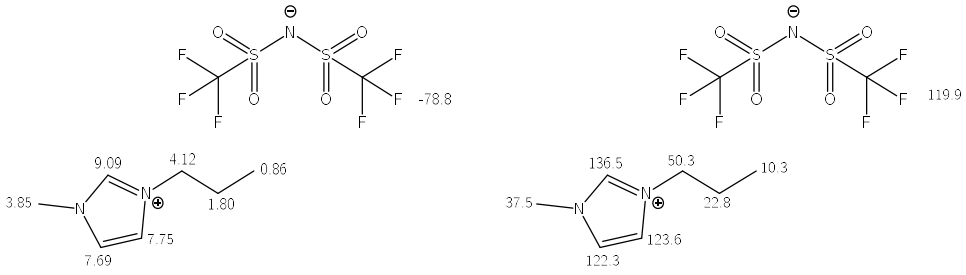
To a stirring solution of 1-methylimidazole (4.96 mL, 62.2 mmol) in acetonitrile (10 mL), 1-chloropropane (6.59 mL, 74.7 mmol) was added dropwise at room temperature. The reaction mixture was heated to 40 °C and stirred for 48 h. The solvent was removed and the crude solid recrystallized from acetonitrile/ethyl acetate and dried *in vacuo* at 50 °C to yield a light yellow hygroscopic solid (7.32 g, 73.2%).

^{1}H NMR (400 MHz, DMSO-d_6): δ 9.37 (br. s, 1 H), 7.83 (t, J = 1.8 Hz, 1 H), 7.76 (t, J = 1.8 Hz, 1 H), 4.15 (t, J = 7.4 Hz, 2 H), 3.87 (s, 3 H), 1.80 (sxt, J = 7.4 Hz, 2 H), 0.85 (t, J = 7.4 Hz, 3 H);

^{13}C NMR (100 MHz, DMSO-d_6): δ 136.7, 123.6, 122.3, 50.2, 35.7, 22.8, 10.4.

ESI-MS (+ve) $[C_7H_{13}N_2]^+$: calcd 125.1073 found 125.1061.

7.5.7. 1-Propyl-3-methylimidazolium bis(trifluoromethanesulfonyl)imide, $[C_3C_1Im][NTf_2]$



To a solution of compound **7.5.6** (1.98 g, 12.3 mmol) in water (10 mL), a solution of lithium bis(trifluoromethane)sulfonimide (4.25 g, 14.8 mmol) in water (10 mL) was added dropwise. The reaction mixture was stirred overnight at room temperature. Dichloromethane (50 mL) was added and the organic

layer separated and washed with water (5 x 15 mL). The solvent was removed and the product was dried *in vacuo* at 50 °C to yield a colourless liquid (4.75 g, 95.1%).

^{1}H NMR (400 MHz, DMSO-d_6): δ 9.09 (br. s, 1 H), 7.75 (t, J = 1.8 Hz, 1 H), 7.69 (t, J = 1.8 Hz, 1 H), 4.12 (t, J = 7.4 Hz, 2 H), 3.85 (s, 3 H), 1.80 (sxt, J = 7.4 Hz, 2 H), 0.86 (t, J = 7.4 Hz, 3 H);

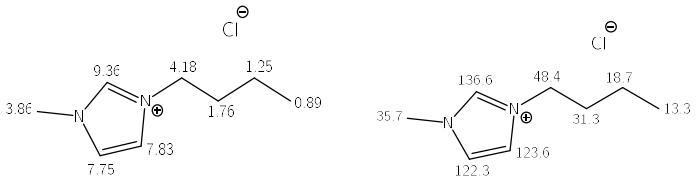
^{13}C NMR (100 MHz, DMSO-d_6): δ 136.5, 123.6, 122.3, 119.9 (q, $^{1}J_{C\text{-}F}$ = 322 Hz, 1 C), 50.3, 35.7, 22.8, 10.3;

^{19}F NMR (376 MHz, DMSO-d_6): δ -78.8 (s, 6 F).

ESI-MS (+ve) $[C_7H_{13}N_2]^+$: calcd 125.1073 found 125.1070.

ESI-MS (-ve) $[C_2F_6NO_4S_2]^-$: calcd 279.9173, found 279.9171.

7.5.8. 1-Butyl-3-methylimidazolium chloride, $[C_4C_1Im]Cl$[271]



To a stirring solution of 1-methylimidazole (4.56 mL, 57.3 mmol) in acetonitrile (10 mL), 1-chlorobutane (7.15 mL, 68.7 mmol) was added dropwise at room temperature. The reaction mixture was heated to 40 °C and stirred for 48 h. The solvent was removed and the crude solid recrystallized from acetonitrile/ethyl acetate and dried *in vacuo* at 50 °C to yield a white hygroscopic solid (6.73 g, 67.3%).

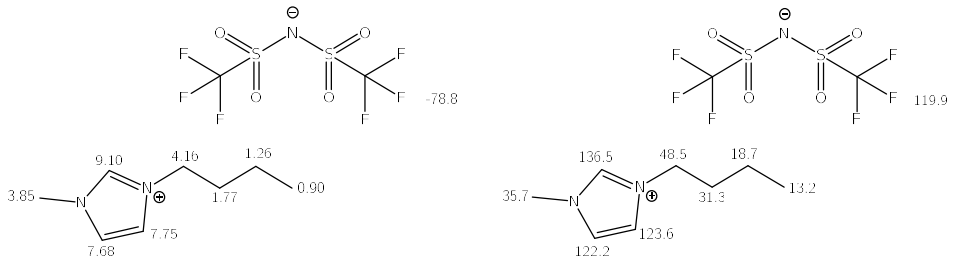
^{1}H NMR (400 MHz, DMSO-d_6) δ 9.36 (br. s, 1 H), 7.83 (t, J = 1.8 Hz, 1 H), 7.75 (t, J = 1.8 Hz, 1 H), 4.18 (t, J = 7.4 Hz, 2 H), 3.86 (s, 3 H), 1.76 (quin, J = 7.4 Hz, 2 H), 1.25 (sxt, J = 7.4 Hz, 2 H), 0.89 (t, J = 7.4 Hz, 3 H);

^{13}C NMR (100 MHz, DMSO-d_6): δ 136.6, 123.6, 122.3, 48.4, 35.7, 31.3, 18.7, 13.3.

ESI-MS (+ve) $[C_8H_{15}N_2]^+$: calcd 139.1230 found 139.1247.

Data in agreement with literature values.[271]

7.5.9. 1-Butyl-3-methylimidazolium bis(trifluoromethanesulfonyl)imide, $[C_4C_1Im][NTf_2]$[270]



To a solution of coumpound **7.5.8.** (2.08 g, 11.9 mmol) in water (10 mL), a solution of lithium bis(trifluoromethane)sulfonimide (4.11 g, 14.3 mmol) in water (10 mL) was added dropwise. The reaction mixture was stirred overnight at room temperature. Dichloromethane (50 mL) was added and the organic layer separated and washed with water (5 x 15 mL). The solvent was removed and the product was dried *in vacuo* at 50 °C to yield a colourless liquid (9.82 g, 98.2%).

^{1}H NMR (400 MHz, DMSO-d_6): δ 9.10 (br. s, 1 H), 7.75 (t, J = 1.8 Hz, 1 H), 7.68 (t, J = 1.8 Hz, 1 H), 4.16 (t, J = 7.4 Hz, 2 H), 3.85 (s, 3 H), 1.77 (quin, J = 7.4 Hz, 2 H), 1.26 (sxt, J = 7.4 Hz, 2 H), 0.90 (t, J = 7.4 Hz, 3 H);

^{13}C NMR (100 MHz, DMSO-d_6): δ 136.5, 123.6, 122.2, 119.9 (q, $^1J_{C\text{-}F}$ = 322 Hz, 1 C), 48.5, 35.7, 31.3, 18.7, 13.2;

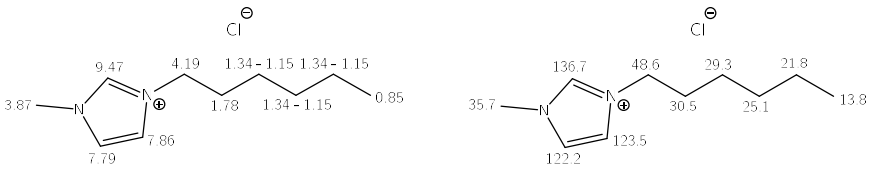
^{19}F NMR (376 MHz, DMSO-d_6): δ -78.8 (s, 6 F).

ESI-MS (+ve) $[C_8H_{15}N_2]^+$: calcd 139.1230 found 139.1243.

ESI-MS (-ve) $[C_2F_6NO_4S_2]^-$: calcd 279.9173, found 279.9190.

Data in agreement with literature values.[270]

7.5.10. 1-Hexyl-3-methylimidazolium chloride, $[C_6C_1Im]Cl$[271]



To a stirring solution of 1-methylimidazole (3.93 mL, 4.93 mmol) in acetonitrile (10 mL), 1-chlorohexane (8.12 mL, 5.92 mmol) was added dropwise at room temperature. The reaction mixture was heated to 40 °C and stirred for 48 h. The solvent was removed, the crude was re-dissolved in a minimal amount of acetonitrile, then washed with ethyl acetate and dried *in vacuo* at 50 °C to yield a yellow hygroscopic liquid (6.18 g, 61.8%).

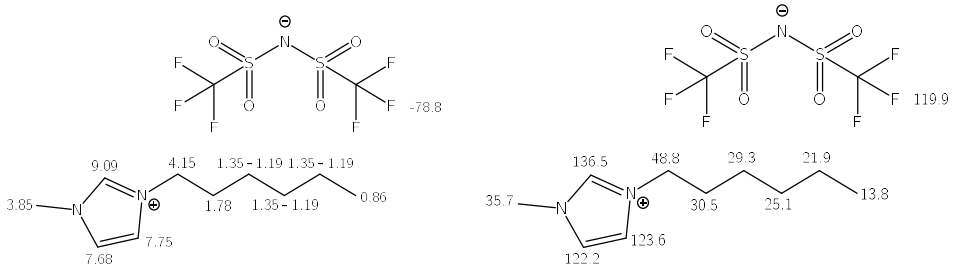
^{1}H NMR (400 MHz, DMSO-d_6) δ 9.47 (br. s, 1 H), 7.86 (t, J = 1.8 Hz, 1 H), 7.79 (t, J = 1.8 Hz, 1 H), 4.19 (t, J = 7.4 Hz, 2 H), 3.87 (s, 3 H), 1.78 (quin, J = 7.4 Hz, 2 H), 1.34 - 1.15 (m, 6 H), 0.85 (t, J = 7.4 Hz, 3 H);

^{13}C NMR (100 MHz, DMSO-d_6): δ 136.7, 123.5, 122.2, 48.6, 35.7, 30.5, 29.3, 25.1, 21.8, 13.8.

ESI-MS (+ve) $[C_{10}H_{19}N_2]^+$: calcd 167.1543 found 167.1550.

Data in agreement with literature values.[271]

7.5.11. 1-Hexyl-3-methylimidazolium bis(trifluoromethanesulfonyl)imide, $[C_6C_1Im][NTf_2]$[270]



To a solution of compound **7.5.10.** (2.27 g, 11.2 mmol) in water (10 mL), a solution of lithium bis(trifluoromethane)sulfonimide (3.85 g, 13.4 mmol) in water (10 mL) was added dropwise. The reaction mixture was stirred overnight at room temperature. Dichloromethane (50 mL) was added and the organic layer separated and washed with water (5 x 15 mL). The solvent was removed and the product was dried *in vacuo* at 50 °C to yield a light yellow liquid (4.87 g, 97.3%).

^{1}H NMR (400 MHz, DMSO-d_6): δ 9.09 (br. s, 1 H), 7.75 (t, J = 1.8 Hz, 1 H), 7.68 (t, J = 1.8 Hz, 1 H), 4.15 (t, J = 7.4 Hz, 2 H), 3.85 (s, 3 H), 1.78 (quin, J = 7.4 Hz, 2 H), 1.35 - 1.19 (m, 6 H), 0.86 (t, J = 7.4 Hz, 3 H);

^{13}C NMR (100 MHz, DMSO-d_6): δ 136.5, 123.6, 122.2, 119.9 (q, $^{1}J_{C\text{-}F}$ = 322 Hz, 1 C), 48.8, 35.7, 30.5, 29.3, 25.1, 21.9, 13.8;

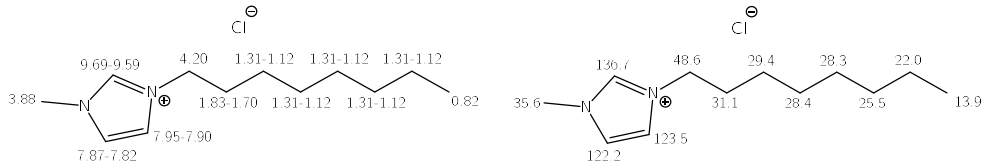
^{19}F NMR (376 MHz, DMSO-d_6): δ -78.8 (s, 6 F).

ESI-MS (+ve) $[C_{10}H_{19}N_2]^+$: calcd 167.1543 found 167.1551.

ESI-MS (-ve) $[C_2F_6NO_4S_2]^-$: calcd 279.9173, found 279.9198.

Data in agreement with literature values.[270]

7.5.12. 1-Octyl-3-methylimidazolium chloride, $[C_8C_1Im]Cl$[271]



To a stirring solution of 1-methylimidazole (3.45 mL, 43.3 mmol) in acetonitrile (10 mL), 1-chlorooctane (8.83 mL, 52.0 mmol) was added dropwise at room temperature. The reaction mixture was heated to 40 °C and stirred for 48 h. The solvent was removed, the crude was re-dissolved in a minimal amount of acetonitrile, then washed with ethyl acetate and dried *in vacuo* at 50 °C to yield a light yellow hygroscopic liquid (6.74 g, 67.4%).

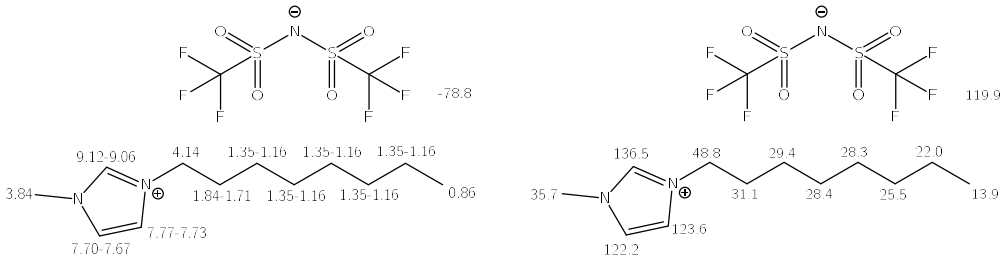
^{1}H NMR (400 MHz, DMSO-d_6) δ 9.65 (br.s, 1 H), 7.92 (t, J = 1.8 Hz, 1 H), 7.85 (t, J = 1.8 Hz, 1 H), 4.20 (t, J = 7.4 Hz, 2 H), 3.88 (s, 3 H), 1.78 (quin, J = 7.4 Hz, 2 H), 1.31 - 1.12 (m, 10 H), 0.82 (t, J = 7.4 Hz, 3 H);

^{13}C NMR (100 MHz, DMSO-d_6) δ 136.7, 123.5, 122.2, 48.6, 35.6, 31.1, 29.4, 28.4, 28.3, 25.5, 22.0, 13.9.

ESI-MS (+ve) $[C_{12}H_{23}N_2]^+$: calcd 195.1856, found 195.1859.

Data in agreement with literature values.[271]

7.5.13. 1-Octyl-3-methylimidazolium bis(trifluoromethanesulfonyl)imide, $[C_8C_1Im][NTf_2]$[270]



To a solution of compound **7.5.12.** (2.89 g, 10.5 mmol) in water (10 mL), a solution of lithium bis(trifluoromethane)sulfonimide (3.62 g, 12.6 mmol) in water (10 mL) was added dropwise. The reaction mixture was stirred overnight

at room temperature. Dichloromethane (50 mL) was added and the organic layer separated and washed with water (5 x 15 mL). The solvent was removed, and the product was dried *in vacuo* at 50 °C to yield a colourless liquid (4.79 g, 95.8%).

^{1}H NMR (400 MHz, DMSO-d_6) δ 9.10 (br. s, 1 H), 7.75 (t, J = 1.8 Hz, 1 H), 7.68 (t, J = 1.8 Hz, 1 H), 4.14 (t, J = 7.4 Hz, 2 H), 3.84 (s, 3 H), 1.78 (quin, J = 7.4 Hz, 2 H), 1.35 - 1.16 (m, 10 H), 0.86 (t, J = 7.4 Hz, 3 H);

^{13}C NMR (100 MHz, DMSO-d_6) δ 136.5, 123.6, 122.2, 119.9 (q, $^{1}J_{C\text{-}F}$ = 322 Hz, 1 C), 48.8, 35.7, 31.1, 29.4, 28.4, 28.3, 25.5, 22.0, 13.9;

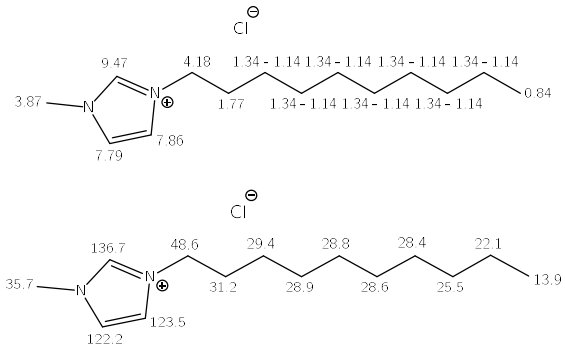
^{19}F NMR (376 MHz, DMSO-d_6) δ -78.8 (s, 6 F)

ESI-MS (+ve) $[C_{12}H_{23}N_2]^+$: calcd 195. 1856, found 195.1863.

ESI-MS (-ve) $[C_2F_6NO_4S_2]^-$: calcd 279.9173, found 279.9180.

Data in agreement with literature values.[270]

7.5.14. 1-Decyl-3-methylimidazolium chloride, $[C_{10}C_1Im]Cl$



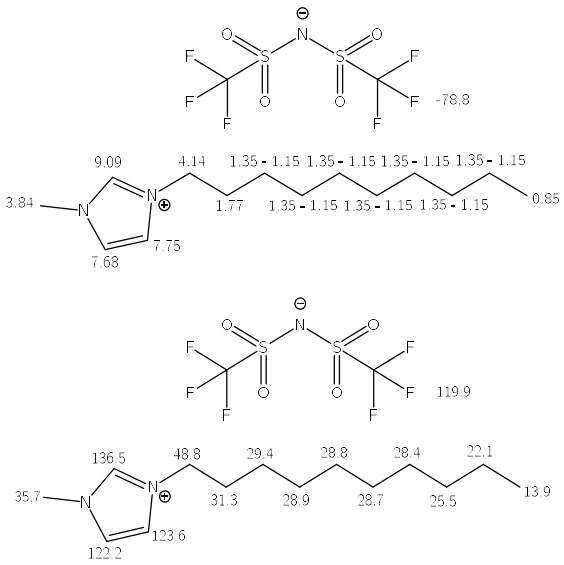
To a stirring solution of 1-methylimidazole (3.08 mL, 38.6 mmol) in acetonitrile (10 mL), 1-chlorodecane (9.44 mL, 46.4 mmol) was added dropwise at room temperature. The reaction mixture was heated to 40 °C and stirred for 48 h. The solvent was removed and the crude solid recrystallized from acetonitrile/ethyl acetate and dried *in vacuo* at 50 °C to yield a white hygroscopic solid (7.21 g, 72.1%).

^{1}H NMR (400 MHz, DMSO-d_6) δ 9.47 (br. s, 1 H), 7.86 (t, J = 1.8 Hz, 1 H), 7.79 (t, J = 1.8 Hz, 1 H), 4.18 (t, J = 7.4 Hz, 2 H), 3.87 (s, 3 H), 1.77 (quin, J = 7.4 Hz, 2 H), 1.34 - 1.14 (m, 14 H), 0.84 (t, J = 7.4 Hz, 3 H);

^{13}C NMR (100 MHz, DMSO-d_6) δ 136.7, 123.5, 122.2, 48.6, 35.7, 31.2, 29.4, 28.9, 28.8, 28.6, 28.4, 25.5, 22.1, 13.9.

ESI-MS (+ve) $[C_{14}H_{27}N_2]^+$: calcd 223.2169, found 223.2188.

7.5.15. 1-Decyl-3-methylimidazolium bis(trifluoromethanesulfonyl)imide, $[C_{10}C_1Im][NTf_2]$



To a solution of compound **7.5.14.** (2.57 g, 9.93 mmol) in water (10 mL), a solution of lithium bis(trifluoromethane)sulfonimide (3.42 g, 11.9 mmol) in water (10 mL) was added dropwise. The reaction mixture was stirred overnight at room temperature. Dichloromethane (50 mL) was added and the organic layer separated and washed with water (5 x 15 mL). The solvent was removed, and the product was dried *in vacuo* at 50 °C to yield a colourless liquid (4.72 g, 94.3%).

^{1}H NMR (400 MHz, DMSO-d_6) δ 9.09 (br. s, 1 H), 7.75 (t, J = 1.8 Hz, 1 H), 7.68 (t, J = 1.8 Hz, 1 H), 4.14 (t, J = 7.4 Hz, 2 H), 3.84 (s, 3 H), 1.77 (quin, J = 7.4 Hz, 2 H), 1.35 - 1.15 (m, 14 H), 0.85 (t, J = 7.4 Hz, 3 H);

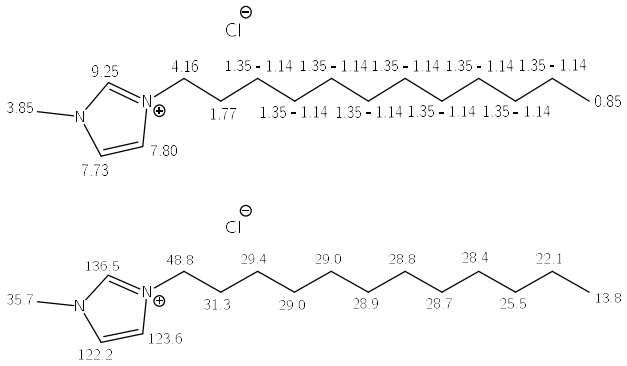
^{13}C NMR (100 MHz, DMSO-d_6) δ 136.5, 123.6, 122.2, 119.9 (q, $^{1}J_{C\text{-}F}$ = 322 Hz, 1 C), 48.8, 35.7, 31.3, 29.4, 28.9, 28.8, 28.7, 28.4, 25.5, 22.1, 13.9;

^{19}F NMR (376 MHz, DMSO-d_6) δ -78.8 (s, 6 F).

ESI-MS (+ve) $[C_{14}H_{27}N_2]^+$: calcd 223.2169, found 223.2188.

ESI-MS (-ve) $[C_2F_6NO_4S_2]^-$: calcd 279.9173, found 279.9171.

7.5.16. 1-Dodecyl-3-methylimidazolium chloride, $[C_{12}C_1Im]Cl$[271]



To a stirring solution of 1-methylimidazole (2.78 mL, 34.9 mmol) in acetonitrile (10 mL), 1-chlorododecane (9.88 mL, 41.8 mmol) was added dropwise at room temperature. The reaction mixture was heated to 40 °C and stirred for 48 h. The solvent was removed and the crude solid recrystallised from acetonitrile/ethyl acetate and dried *in vacuo* at 50 °C to yield a white hygroscopic solid (9.22 g, 92.2%).

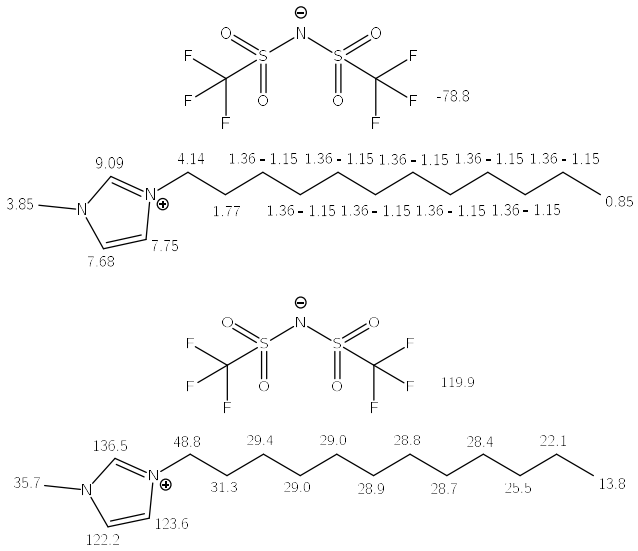
^{1}H NMR (400 MHz, DMSO-d_6) δ 9.25 (br. s, 1 H); 7.80 (t, J = 1.8 Hz, 1 H), 7.73 (t, J = 1.8 Hz, 1 H), 4.16 (t, J = 7.4 Hz, 2 H), 3.85 (s, 3 H), 1.77 (quin, J = 7.4 Hz, 2 H), 1.35 - 1.14 (m, 18 H), 0.85 (t, J = 7.4 Hz, 3 H);

^{13}C NMR (100 MHz, DMSO-d_6) δ 136.5, 123.6, 122.2, 48.8, 35.7, 31.3, 29.4, 29.0, 29.0, 28.9, 28.8, 28.7, 28.4, 25.5, 22.1, 13.8.

ESI-MS (+ve) $[C_{16}H_{31}N_2]^+$: calcd 251.2482, found 251.2499.

Data in agreement with literature values.[271]

7.5.17. 1-Dodecyl-3-methylimidazolium bis(trifluoromethanesulfonyl)imide, $[C_{12}C_1Im][NTf_2]$[270]



To a solution of compound **7.5.16.** (2.70 g, 9.41 mmol) in water (10 mL), a solution of lithium bis(trifluoromethane)sulfonimide (3.24 g, 11.3 mmol) in water (10 mL) was added dropwise. The reaction mixture was stirred overnight at room temperature. Dichloromethane (50 mL) was added and the organic layer separated and washed with water (5 x 15 mL). The solvent was removed and the product was dried *in vacuo* at 50 °C to yield a colourless liquid (4.58 g, 91.5%).

^{1}H NMR (400 MHz, DMSO-d_6) δ 9.09 (br. s, 1 H), 7.75 (t, J = 1.8 Hz, 1 H), 7.68 (t, J = 1.8 Hz, 1 H), 4.14 (t, J = 7.4 Hz, 2 H), 3.85 (s, 3 H), 1.77 (quin, J = 7.4 Hz, 2 H), 1.36 - 1.15 (m, 18 H), 0.85 (t, J = 7.4 Hz, 3 H);

^{13}C NMR (100 MHz, DMSO-d_6) δ 136.5, 123.6, 122.2, 119.9 (q, $^1J_{C\text{-}F}$ = 322 Hz, 2 C), 48.8, 35.7, 31.3, 29.4, 29.0, 29.0, 28.9, 28.8, 28.7, 28.4, 25.5, 22.1, 13.8;

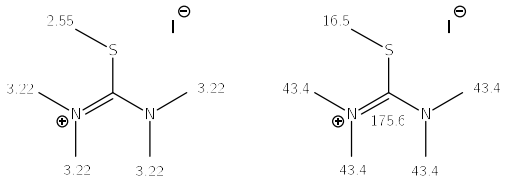
^{19}F NMR (376 MHz, DMSO-*d6*) δ -78.8 (s, 6 F).

ESI-MS (+ve) $[C_{16}H_{31}N_2]^+$: calcd 251.2482, found 251.2499.

ESI-MS (-ve) $[C_2F_6NO_4S_2]^-$: calcd 279.9173, found 279.9176.

Data in agreement with literature values.[270]

7.5.18. Pentamethylthiouronium iodide, $[(C_1)_5TU][I]$



[**CAUTION!** Iodomethane is a strong alkylating agent. Thick protective gloves should be worn at all times]

To a solution of tetramethylthiourea (1.00 g, 7.57 mmol) in 8 mL of dried methanol at 0 °C under argon, was added iodomethane (870 µL, 14.1 mmol) dropwise. After 16 h stirring at room temperature, the solvent was removed *in vacuo*. The product was stirred *in vacuo* overnight at 50 °C. The salt (2.07 g, 99.0%) was obtained as a light yellow hygroscopic powder.

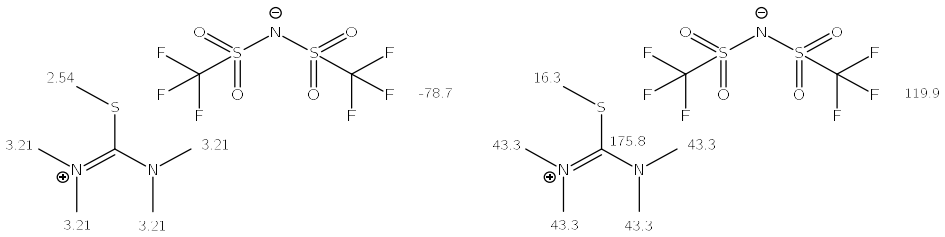
^{1}H NMR (400 MHz, DMSO-d_6): δ 3.22 (s, 12 H), 2.55 (s, 3 H);

^{13}C NMR (100 MHz, DMSO-d_6): δ 175.6, 43.4, 16.5.

ESI-MS (+ve) $[C_6H_{15}N_2S]^+$: calcd 147.0950, found 147.0872.

Data in agreement with literature values.[272]

7.5.19. Pentamethylthiouronium bis(trifluoromethanesulfonyl)imide, $[(C_1)_5TU][NTf_2]$



Compound **7.5.18.** (1.92 g, 7.02 mmol) was transferred to a round bottom flask followed by the addition of water (15 mL). Lithium bis(trifluoromethanesulfonyl)imide (2.42 g, 8.42 mmol) in water (15 mL) was added and the mixture stirred at 0 °C and gradually allowed to warm up to room

temperature for 24 h. Dichloromethane (20 mL) was added to recover the ionic liquid and washed with cold water (5 x 5 mL). The organic layer was collected, the solvent removed and stirred *in vacuo* overnight at 50 °C. The salt (2.81 g, 93.6%) was obtained as a white powder.

^{1}H NMR (400 MHz, DMSO-d_6): δ 3.21 (s, 12 H), 2.54 (s, 3 H);

^{13}C NMR (100 MHz, DMSO-d_6): δ 175.8, 119.9 (q, $^{1}J_{C\text{-}F}$ = 322 Hz, 1 C), 43.3, 16.3;

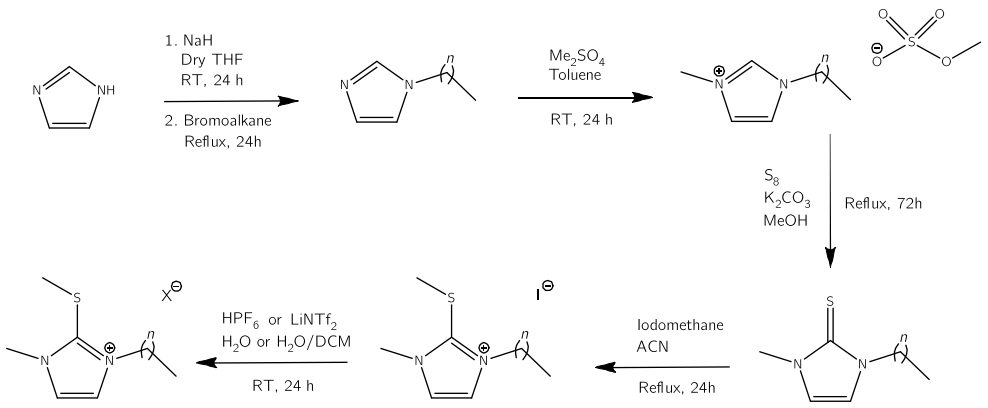
^{19}F NMR (376 MHz, DMSO-d_6): δ -78.7 (s, 6 F).

ESI-MS (+ve) $[C_6H_{15}N_2S]^+$: calcd 147.0950, found 147.0941.

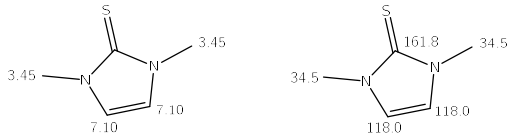
ESI-MS (-ve) $[C_2F_6NO_4S_2]^-$: calcd 279.9173, found 279.9193.

CHN Analysis: Calc. for $[(C_1)_5TU][NTf_2]$, ($C_8H_{15}F_6N_3O_4S_3$): N 9.83, C 22.48, H 3.54. Found: N 9.43, C 22.43, H 3.25.

Multi-Step Synthesis of ThioImidazoliums:



7.5.20. 1,3-Dimethylimidazoline-2-thione[273]



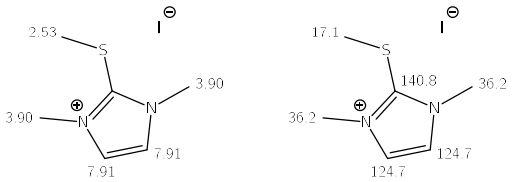
A mixture of compound **7.5.3.** (8.12 g, 39.0 mmol), sulphur (1.30 g, 40.5 mmol), and potassium carbonate (6.73 g, 48.7 mmol) in methanol (50 mL) was refluxed for 72 h. After removal of the solvent, the residue was recrystallised from boiling water (the amount necessary to obtain a clear solution). The colourless product was filtrated, washed with water (5 x 10 mL) and dried *in vacuo*. The product (3.62 g, 72.4%) was obtained as a white powder.

^{1}H NMR (400 MHz, DMSO-d_6): δ 7.10 (s, 2 H), 3.45 (s, 6 H);

^{13}C NMR (100 MHz, DMSO-d_6): δ 161.8, 118.0, 34.5.

Data in agreement with literature values.[273]

7.5.21. 1,3-Dimethyl-2-methylthioimidazolium iodide, $[C_1(C_1)_2ThioIm][I]$[274]



[**CAUTION!** Iodomethane is a strong alkylating agent. Thick protective gloves should be worn at all times]

Compound **7.5.20.** (1.04 g, 8.14 mmol) was dissolved in acetonitrile (50 mL) and iodomethane (1.52 mL, 0.02 mol) was added to the solution in one portion. The mixture was refluxed for 24 h, then cooled and recrystallised from ethyl acetate. The product was filtered and dried *in vacuo* overnight at 50 °C. The salt (1.98 g, 90.7%) was obtained as a white powder.

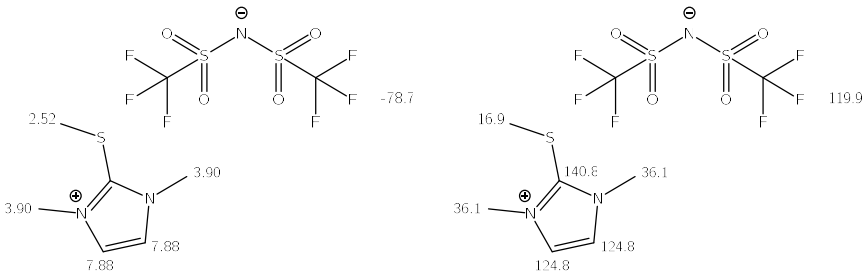
^{1}H NMR (400 MHz, DMSO-d_6): δ 7.91 (s, 2 H), 3.90 (s, 6 H), 2.53 (s, 3 H);

^{13}C NMR (100 MHz, DMSO-d_6): δ 140.8, 124.7, 36.2, 17.1.

ESI-MS (+ve) $[C_6H_{11}N_2S]^+$: calcd 143.0637, found 143.0593.

Data in agreement with literature values.[274]

7.5.22. 1,3-Dimethyl-2-methylthioimidazolium bis(trifluoromethanesulfonyl)imide, $[C_1(C_1)_2ThioIm][NTf_2]$



Compound **7.5.21.** (0.770 g, 2.83 mmol) was transferred to a round bottom flask followed by the addition of water (5 mL). Lithium bis(trifluoromethanesulfonyl)imide (0.980 g, 3.40 mmol) in water (5 mL) was added and the mixture stirred at 0 °C and gradually allowed to warm up to room

temperature for 24 h. Dichloromethane (10 mL) was added to recover the ionic liquid and washed with cold water (5 x 5 mL). The organic layer was collected, the solvent removed and stirred *in vacuo* overnight at 50 °C. The salt (1.19 g, 99.6%) was obtained as a colourless viscous liquid.

^{1}H NMR (400 MHz, DMSO-d_6): δ 7.88 (br.s, 2 H), 3.90 (s, 6 H), 2.52 (s, 3 H);

^{13}C NMR (100 MHz, DMSO-d_6): δ 140.8, 124.8, 119.9 (q, $^{1}J_{C\text{-}F}$ = 322 Hz, 1 C), 36.1, 16.9;

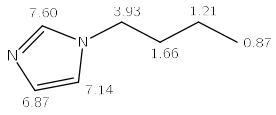
^{19}F NMR (376 MHz, DMSO-d_6): δ -78.7 (s, 6 F).

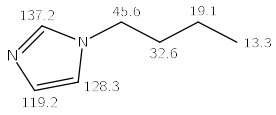
ESI-MS (+ve) $[C_6H_{11}N_2S]^+$: calcd 143.0637, found 143.0890.

ESI-MS (-ve) $[C_2F_6NO_4S_2]^-$: calcd 279.9173, found 279.9171.

CHN Analysis: Calc. for $[C_1(C_1)_2\text{ThioIm}][NTf_2]$, ($C_8H_{11}F_6N_3O_4S_3$): N 9.93, C 22.70, H 2.62. Found: N 9.84, C 22.72, H 2.34.

7.5.23. Butylimidazole





[**CAUTION:** In contact with water sodium hydride liberates extremely flammable hydrogen gas]

Imidazole (21.9 g, 322 mmol) was dissolved in dry THF (200 mL) under an inert atmosphere and sodium hydride (60% in mineral oil, 12.9 g, 322 mmol, 1.0 eq.) was slowly added, ensuring that the temperature remained cool (**CAUTION:** flammable hydrogen gas is liberated). After the sodium hydride had reacted and the evolution of gas had ceased, the mixture was stirred for further 24 h at room temperature. Bromobutane (44.1 g, 322 mmol, 1.0 eq.) was dissolved in dry THF (≈ 1:1 v/v) and the solution was added dropwise to the sodium imidazolate. After further 2 h the mixture was heated to reflux and

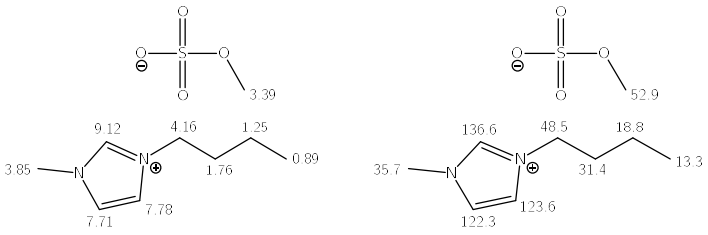
left for 24 h. The mixture was cooled and filtered to remove the insoluble salt, evaporation of the solvent yielded a pale-yellow oil that was purified by reduced pressure distillation (70-72 °C, 9 x 10^{-2} mbar) to yield a colourless oil (33.0 g, 82.4%).

^{1}H NMR (400 MHz, DMSO-d_6): δ 7.60 (s, 1 H), 7.14 (t, J = 1.1 Hz, 1 H), 6.87 (t, J = 1.1 Hz, 1 H), 3.93 (t, J = 7.4 Hz, 2 H), 1.66 (quin, J = 7.4 Hz, 2 H), 1.21 (sxt, J = 7.4 Hz, 2 H), 0.87 (t, J = 7.4 Hz, 3 H);

^{13}C NMR (100 MHz, DMSO-d_6): δ 137.2, 128.3, 119.2, 45.6, 32.6, 19.1, 13.3.

ESI-MS (+ve) [$C_7H_{12}N_2$]: calcd 124.1000, found 124.1086.

7.5.24. 1-Butyl-3-methylimidazolium methyl sulfate, [C_4C_1Im][MeSO$_4$]



[**CAUTION!** Dimethyl sulfate is a strong alkylating agent. Thick protective gloves should be worn at all times]

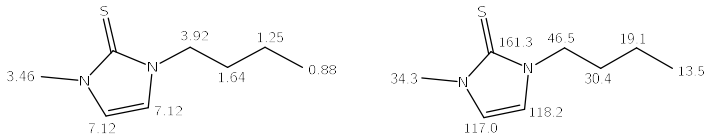
Dimethyl sulfate (25.2 mL, 0.266 mol) was added dropwise to a solution of compound **7.5.23** (26.3 mL, 0.200 mol) in toluene under argon (150 mL) cooled in an ice-bath at a rate to maintain the reaction temperature below 40 °C (the reaction is highly exothermic). Formation of the IL product was immediate and caused the initially clear solution to become opaque, followed by byphasic separation of the toluene solution and the formation of a denser IL phase. After addition of the dimethyl sulfate, the reaction mixture was stirred at room temperature for 24 h. The upper, organic phase was decanted and the lower, IL phase was washed with toluene (3 x 50 mL), the residual organic solvents were removed, and the product stirred *in vacuo* overnight at 50 °C. The salt (44.5 g, 88.9%) was obtained as a colourless liquid.

^{1}H NMR (400 MHz, DMSO-d_6): δ 9.12 (s, 1 H), 7.78 (t, J = 1.8 Hz, 1 H), 7.71 (t, J = 1.8 Hz, 1 H), 4.16 (t, J = 7.4 Hz, 2 H), 3.85 (s, 3 H), 3.39 (s, 3 H), 1.76 (quin, J = 7.4 Hz, 2 H), 1.25 (sxt, J = 7.4 Hz, 2 H), 0.89 (t, J = 7.4 Hz, 3 H);

^{13}C NMR (100 MHz, DMSO-d_6): δ 136.6, 123.6, 122.3, 52.9, 48.5, 35.7, 31.4, 18.8, 13.3.

ESI-MS (+ve) $[C_8H_{15}N_2]^+$: calcd 139.1230, found 139.1234.

7.5.25. 1-Butyl-3-methylimidazoline-2-thione



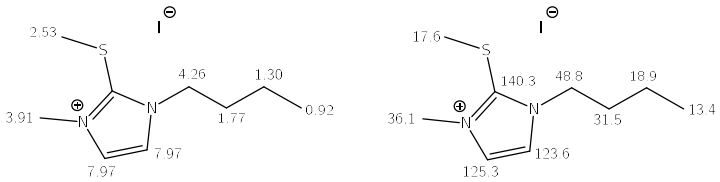
A mixture of compound **7.5.24.** (22.1 g, 88.0 mmol), sulphur (2.94 g, 92 mmol), and potassium carbonate (15.2 g, 110 mmol) in methanol (150 mL) was refluxed for 72 h. After removal of the solvent, the residue was dissolved in ethyl acetate and washed with water (5 x 20 mL). The product (8.24 g, 54.9%) was dried *in vacuo* at 50°C and was obtained as an orange viscous liquid.

^{1}H NMR (400 MHz, DMSO-d_6): δ 7.12 (dd, J = 6.2, 2.4 Hz, 2 H), 3.92 (t, J = 7.4 Hz, 2 H), 3.46 (s, 3 H), 1.64 (quin, J = 7.4 Hz, 2 H), 1.25 (sxt, J = 7.4 Hz, 2 H), 0.88 (t, J = 7.4 Hz, 3 H);

^{13}C NMR (100 MHz, DMSO-d_6): δ 161.3, 118.2, 117.0, 46.5, 34.3, 30.4, 19.1, 13.5.

ESI-MS (+ve) $[C_8H_{14}N_2S]$: calcd 170.0878, found 170.0955.

7.5.26. 1-Butyl-2,3-dimethylthioimidazolium iodide, $[C_4(C_1)_2ThioIm][I]$



[**CAUTION!** Iodomethane is a strong alkylating agent. Thick protective gloves should be worn at all times]

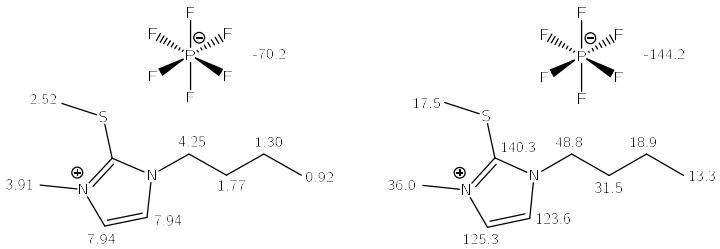
Compound **7.5.25.** (7.09 g, 42.0 mmol) was dissolved in acetonitrile (50 mL) and iodomethane (17.7 mL, 125 mol) was added to the solution in one portion. The mixture was refluxed 24 h, then cooled and recrystallised from ethyl acetate. The product was filtered and dried *in vacuo* overnight at 50 °C. The salt (12.3 g, 94.6%) was obtained as a white powder.

^{1}H NMR (400 MHz, DMSO-d_6): δ 7.97 (dd, J = 10.5, 2.0 Hz, 2 H), 4.26 (t, J = 7.4 Hz, 2 H), 3.91 (s, 3 H), 2.53 (s, 3 H), 1.77 (quin, J = 7.4 Hz, 2 H), 1.30 (sxt, J = 7.4 Hz, 2 H), 0.92 (t, J = 7.4 Hz, 3 H);

^{13}C NMR (100 MHz, DMSO-d_6): δ 140.3, 125.3, 123.6, 48.8, 36.1, 31.5, 18.9, 17.6, 13.4.

ESI-MS (+ve) $[C_9H_{17}N_2S]^+$: calcd 185.1107, found 185.1111.

7.5.27. 1-Butyl-2,3-dimethylthioimidazolium hexafluorophosphate, $[C_4(C_1)_2ThioIm][PF_6]$



[**CAUTION!** Release of HF from HPF_6 occurs upon contact with water. Thick protective gloves should always be worn]

Compound **7.5.26.** (0.950 g, 3.03 mmol) was transferred to a round bottom flask followed by the addition of water (10 mL). HPF_6 (0.510 mL, 3.63 mmol) 60% w/w in water (10 mL) was added and the mixture stirred at 0 °C and gradually allowed to warm up to room temperature for 24 h. Dichloromethane (20 mL) was added to recover the ionic liquid and washed with cold water (5 x 10 mL). The organic layer was collected, the solvent removed and stirred dried *in vacuo* overnight at 50 °C. The salt (0.950 g, 95.0%) was obtained as a white powder.

^{1}H NMR (400 MHz, DMSO-d_6): δ 7.94 (dd, J = 9.8, 2.0 Hz, 2 H), 4.25 (t, J = 7.4 Hz, 2 H), 3.91 (s, 3 H), 2.52 (s, 3 H), 1.77 (quin, J = 7.4 Hz, 2 H), 1.30 (sxt, J = 7.4 Hz, 2 H), 0.92 (t, J = 7.4 Hz, 3 H);

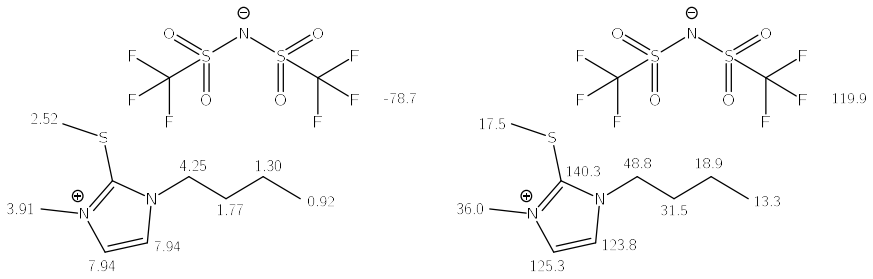
^{13}C NMR (100 MHz, DMSO-d_6): δ 140.3, 125.3, 123.6, 48.8, 36.0, 31.5, 18.9, 17.5, 13.3;

^{19}F NMR (376 MHz, DMSO-d_6): δ -70.2 (d, $^{1}J_{F\text{-}P}$ = 710 Hz, 6 F);

^{31}P NMR (160 MHz, DMSO-d_6): δ -144.2 (spt, $^{1}J_{P\text{-}F}$ = 710 Hz, 1 P).

ESI-MS (+ve) $[C_9H_{17}N_2S]^+$: calcd 185.1107, found 185.1137.

7.5.28. 1-Butyl-2,3-dimethylthioimidazolium bis(trifluoromethylsulfonyl)imide, $[C_4(C_1)_2ThioIm][NTf_2]$



Compound **7.5.26.** (0.810 g, 2.58 mmol) was transferred to a round bottom flask followed by the addition of water (10 mL). $LiNTf_2$ (0.890 g, 3.10 mmol) in water (10 mL) was added and the mixture stirred at 0 °C and gradually allowed to warm up to room temperature for 24 h. Dichloromethane (20 mL)

was added to recover the ionic liquid and washed with cold water (5 x 10 mL). The organic layer was collected, the solvent removed and stirred *in vacuo* overnight at 50 °C. The salt (1.16 g, 97.4%) was obtained as a colourless liquid.

^{1}H NMR (500 MHz, DMSO-d_6): δ 7.94 (dd, J = 12.0, 2.2 Hz, 2 H), 4.25 (t, J = 7.4 Hz, 2 H), 3.91 (s, 3 H), 2.52 (s, 3 H), 1.77 (quin, J = 7.4 Hz, 2 H), 1.30 (sxt, J = 7.4 Hz, 2 H), 0.92 (t, J = 7.4 Hz, 16 H);

^{13}C NMR (125 MHz, DMSO-d_6): δ 140.3, 125.3, 123.6, 119.9 (q, $^{1}J_{C\text{-}F}$ = 322 Hz, 1 C), 48.8, 36.0, 31.5, 18.9, 17.5, 13.3;

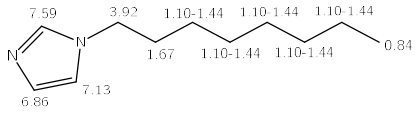
^{19}F NMR (376 MHz, DMSO-d_6): δ -78.7 (s, 6 F).

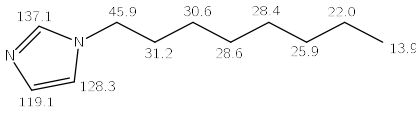
ESI-MS (+ve) $[C_9H_{17}N_2S]^+$: calcd 185.1107, found 185.1114.

ESI-MS (-ve) $[C_2F_6NO_4S_2]^-$: calcd 279.9173, found 279.9176.

CHN Analysis: Calc. for $[C_4(C_1)_2\text{ThioIm}][NTf_2]$, ($C_{11}H_{17}F_6N_3O_4S_3$): N 9.03, C 28.39, H 3.68. Found: N 9.26, C 28.43, H 3.71.

7.5.29. Octylimidazole





[**CAUTION:** In contact with water sodium hydride liberates extremely flammable hydrogen gas]

Imidazole (15.1 g, 222 mmol) was dissolved in dry THF (200 mL) under an inert atmosphere and sodium hydride (60% in mineral oil, 8.87 g, 222 mmol, 1.0 eq.) was slowly added, ensuring that the temperature remained cool (**CAUTION:** flammable hydrogen gas is liberated). After the sodium hydride had reacted and the evolution of gas had ceased, the mixture was stirred for further 24 h at room temperature. Bromooctane (42.9 g, 222 mmol, 1.0 eq.) was dissolved in dry THF (≈ 1:1 v/v) and the solution was added dropwise to the sodium imidazolate. After further 2 h the mixture was heated to reflux and

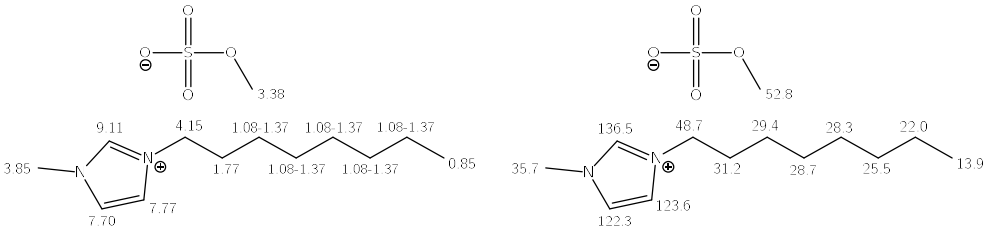
left for 24 h. The mixture was cooled and filtered to remove the insoluble salt, evaporation of the solvent yielded a pale-yellow oil that was purified by reduced pressure distillation (70-72 °C, 9 x 10^{-2} mbar) to yield a colourless oil (29.9 g, 74.8%).

^{1}H NMR (400 MHz, DMSO-d_6): δ 7.59 (s, 1 H), 7.13 (br. s, 1 H), 6.86 (br. s, 1 H), 3.92 (t, J = 7.2 Hz, 2 H), 1.67 (quin, J = 7.2 Hz, 2 H), 1.44 - 1.10 (m, 10 H), 0.84 (t, J = 7.2 Hz, 3 H);

^{13}C NMR (100 MHz, DMSO-d_6): δ 137.1, 128.3, 119.1, 45.9, 31.2, 30.6, 28.6, 28.4, 25.9, 22.0, 13.9.

ESI-MS (+ve) [$C_{11}H_{20}N_2$]: calcd 180.1626, found 180.1703.

7.5.30. 1-Octyl-3-methylimidazolium methyl sulfate, [C_8C_1Im][$MeSO_4$]



[**CAUTION!** Dimethyl sulfate is a strong alkylating agent. Thick protective gloves should be worn at all times]

Dimethyl sulfate (3.25 mL, 34.3 mmol) was added dropwise to a solution of compound **7.5.29.** (5.88 g, 32.6 mmol) in toluene under argon (50 mL) cooled in an ice-bath at a rate to maintain the reaction temperature below 40 °C (the reaction is highly exothermic). Formation of the IL product was immediate and caused the initially clear solution to become opaque, followed by byphasic separation of the toluene solution and the formation of a denser IL phase. After addition of the dimethyl sulfate, the reaction mixture was stirred at room temperature for 24 h. The upper, organic phase was decanted and the lower, IL phase was washed with toluene (5 x 50 mL), the residual organic solvents were

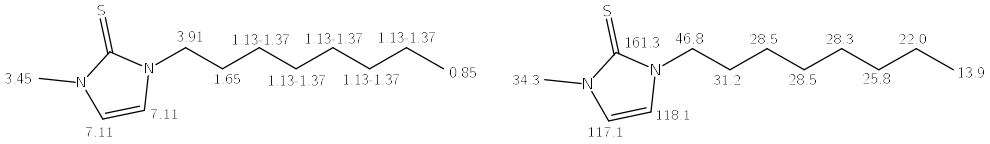
removed and the product stirred under *vacuo* overnight at 50 °C. The salt (8.43 g, 84.3%) was obtained as a colourless liquid.

^{1}H NMR (400 MHz, DMSO-d_6): δ 9.11 (s, 1 H), 7.77 (s, 1 H), 7.70 (s, 1 H), 4.15 (t, J = 7.2 Hz, 2 H), 3.85 (s, 3 H), 3.38 (s, 3 H), 1.77 (quin, J = 6.7 Hz, 2 H), 1.37 - 1.08 (m, 10 H), 0.85 (t, J = 6.7 Hz, 3 H);

^{13}C NMR (100 MHz, DMSO-d_6): δ 136.5, 123.6, 122.3, 52.8, 48.8, 35.7, 31.2, 29.4, 28.7, 28.3, 25.5, 22.0, 13.9,

ESI-MS (+ve) $[C_{12}H_{23}N_2]^+$: calcd 195.1861, found 195.1862.

7.5.31. 1-Octyl-3-methylimidazoline-2-thione



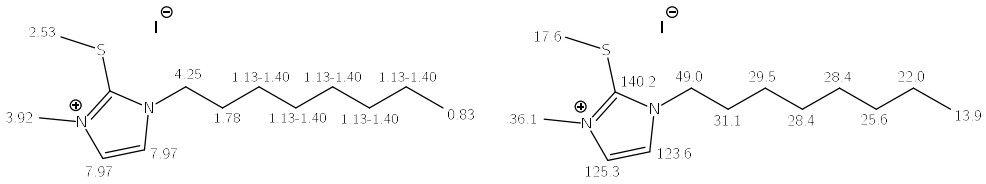
A mixture of compound **7.5.30.** (4.74 g, 15.5 mmol), sulphur (1.98 g, 61.8 mmol), and potassium carbonate (10.3 g, 74.2 mmol) in methanol (100 mL) was refluxed for 72 h. After removal of the solvent, the residue was dissolved in ethyl acetate and washed with water (5 x 20 mL). The product (2.92 g, 83.4%) was dried *in vacuo* at 50°C and was obtained as an orange viscous liquid.

^{1}H NMR (400 MHz, DMSO-d_6): δ 7.11 (dd, J = 7.2, 2.40 Hz, 2 H), 3.91 (t, J = 7.2 Hz, 2 H), 3.45 (s, 3 H), 1.65 (quin, J = 7.2 Hz, 2 H), 1.37 - 1.13 (m, 10 H), 0.85 (t, J = 7.2 Hz, 3 H);

^{13}C NMR (100 MHz, DMSO-d_6): δ 161.3, 118.1, 117.1, 46.8, 34.3, 31.2, 28.5, 28.5, 28.3, 25.8, 22.0, 13.9.

ESI-MS (+ve) $[C_{12}H_{22}N_2S]$: calcd 226.1504, found 226.1578.

7.5.32. 1-Octyl-2,3-dimethylthioimidazolium iodide, [$C_8(C_1)_2$ThioIm][I]



[**CAUTION!** Iodomethane is a strong alkylating agent. Thick protective gloves should be worn at all times]

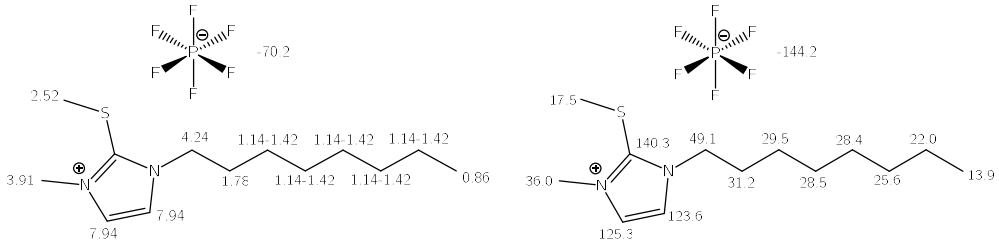
Compound **7.5.31.** (2.37 g, 10.5 mmol) was dissolved in acetonitrile (20 mL) and iodomethane (1.95 mL, 31.4 mmol) was added to the solution in one portion. The mixture was refluxed 24 h, then cooled and recrystallised from ethyl acetate. The product was filtered and dried *in vacuo* overnight at 50 °C. The salt (2.84 g, 71.1%) was obtained as a light yellow liquid.

^{1}H NMR (400 MHz, DMSO-d_6): δ 7.97 (dd, J = 11.7, 2.1 Hz, 2 H), 4.25 (t, J = 7.2 Hz, 2 H), 3.92 (s, 3 H), 2.53 (s, 3 H), 1.78 (quin, J = 7.2 Hz, 2 H), 1.40 - 1.13 (m, 10 H), 0.83 (t, J = 7.2 Hz, 1 H);

^{13}C NMR (100 MHz, DMSO-d_6): δ 140.2, 125.3, 123.6, 49.0, 36.1, 31.1, 29.5, 28.4, 28.4, 25.6, 22.0, 17.6, 13.9;

ESI-MS (+ve) $[C_{13}H_{25}N_2S]^+$: calcd 241.1733, found 241.1739.

7.5.33. 1-Octyl-2,3-dimethylthioimidazolium hexafluorophosphate, $[C_8(C_1)_2ThioIm][PF_6]$



[**CAUTION!** Liberation of HF from HPF_6 occurs upon contact with water. Thick protective gloves should always be worn]

Compound **7.5.32.** (0.480 g, 1.29 mmol) was transferred to a round bottom flask followed by the addition of water (5 mL). HPF_6 (0.220 mL, 1.15 mmol) 60% w/w in water (5 mL) was added and the mixture stirred at 0 °C and gradually allowed to warm up to room temperature for 24 h. Dichloromethane (10 mL) was added to recover the ionic liquid and washed with cold water (5 x 5 mL). The organic layer was collected, the solvent removed and stirred dried *in vacuo* overnight at 50 °C. The salt (0.470 g, 93.6%) was obtained as a colourless viscous liquid.

^{1}H NMR (400 MHz, DMSO-d_6): δ 7.94 (dd, J = 11.0, 2.0 Hz, 2 H), 4.24 (t, J = 7.2 Hz, 2 H), 3.91 (s, 3 H), 2.52 (s, 3 H), 1.78 (quin, J = 7.2 Hz, 2 H), 1.42 -1.14 (m, 10 H), 0.86 (t, J = 7.2 Hz, 3 H);

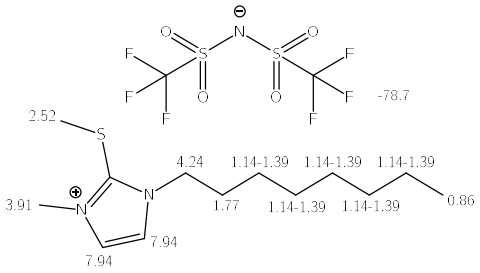
^{13}C NMR (100 MHz, DMSO-d_6): δ 140.3, 125.3, 123.6, 49.1, 36.0, 31.2, 29.5, 28.5, 28.4, 25.6, 22.0, 17.5, 13.9;

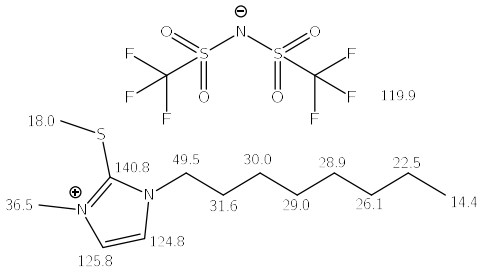
^{19}F NMR (376 MHz, DMSO-d_6): δ -70.2 (d, $^1J_{F\text{-}P}$ = 712 Hz, 6 F);

^{31}P NMR (160 MHz, DMSO-d_6): δ -144.2 (spt, $^1J_{P\text{-}F}$ = 712 Hz, 1 P).

ESI-MS (+ve) $[C_{13}H_{25}N_2S]^+$: calcd 241.1733, found 241.1737.

7.5.34. 1-Octyl-2,3-dimethylthioimidazolium bis(trifluoromethylsulfonyl)imide, $[C_8(C_1)_2ThioIm][NTf_2]$





Compound **7.5.32.** (0.530 g, 1.44 mmol) was transferred to a round bottom flask followed by the addition of water (5 mL). $LiNTf_2$ (0.500 g, 1.73 mmol) in water (5 mL) was added and the mixture stirred at 0 °C and gradually allowed to warm up to room temperature for 24 h. Dichloromethane (10 mL) was added to recover the ionic liquid and washed with cold water (5 x 5 mL). The organic layer was collected, the solvent removed and dried *in vacuo* overnight at 50 °C. The salt (0.710 g, 95.2%) was obtained as a colourless liquid.

^{1}H NMR (400 MHz, DMSO-d_6): δ 7.94 (m, 2 H), 4.24 (t, J = 7.5 Hz, 2 H), 3.91 (s, 3 H), 2.52 (s, 3 H), 1.78 (quin, J = 7.5 Hz, 2 H), 1.39 - 1.14 (m, 10 H), 0.86 (t, J = 7.5 Hz, 3 H);

^{13}C NMR (100 MHz, DMSO-d_6): δ 140.8, 125.8, 124.8, 119.9 (q, $^{1}J_{C\text{-}F}$ = 322 Hz, 1 C), 49.5, 36.5, 31.6, 30.0, 29.0, 28.9, 26.1, 22.5, 18.0, 14.4;

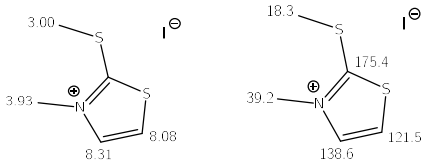
^{19}F NMR (376 MHz, DMSO-d_6): δ -78.7 (s, 6 F).

ESI-MS (+ve) $[C_{13}H_{25}N_2S]^+$: calcd 241.1733, found 241.1758.

ESI-MS (-ve) $[C_2F_6NO_4S_2]^-$: calcd 279.9173, found 279.9191.

CHN Analysis: Calc. for $[C_8(C_1)_2ThioIm][NTf_2]$, ($C_{15}H_{25}F_6N_3O_4S_3$): N 8.06, C 34.54, H 4.83. Found: N 8.33, C 34.86, H 4.45.

7.5.35. 3-Methyl-2-(methylthio)thiazolium iodide, $[(C_1)_2Thio]I$



[**CAUTION!** Iodomethane is a strong alkylating agent. Thick protective gloves should be worn at all times]

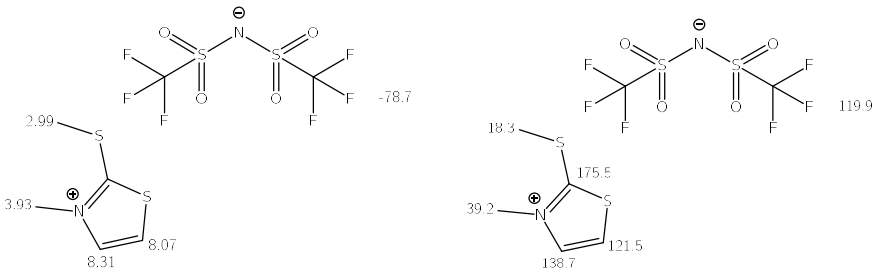
2-(methylthio)thiazole (3.78 mL, 36.6 mmol) was dissolved in acetonitrile (10 mL) and iodomethane (6.84 mL, 110 mmol) was added to the solution in one portion. The mixture was refluxed 24 h, then cooled and recrystallised from ethyl acetate. The product was filtered and dried *in vacuo* overnight at 50 °C. The salt (7.81 g, 71.8%) was obtained as a white powder.

^{1}H NMR (400 MHz, DMSO-d_6): δ 8.31 (d, J = 4.1 Hz, 1 H), 8.08 (d, J = 4.1 Hz, 1 H), 3.93 (s, 3 H), 3.00 (s, 3 H);

^{13}C NMR (100 MHz, DMSO-d_6): δ 175.4, 138.6, 121.5, 39.2, 18.3.

ESI-MS (+ve) $[C_5H_8NS_2]^+$: calcd 146.0093, found 146.0090.

7.5.36. 3-Methyl-2-(methylthio)thiazolium bis(trifluoromethylsulfonyl)imide, $[(C_1)_2Thio][NTf_2]$



Compound **7.5.35.** (1.28 g, 4.69 mmol) was transferred to a round bottom flask followed by the addition of water (10 mL). $LiNTf_2$ (1.62 g, 5.63 mmol) in water (10 mL) was added and the mixture stirred at 0 °C and gradually allowed to warm up to room temperature for 24 h. Dichloromethane (20 mL) was added to recover the ionic liquid and washed with cold water (5 x 5 mL). The organic

layer was collected, the solvent removed and dried *in vacuo* overnight at 50 °C. The salt (1.90 g, 95.2%) was obtained as a white powder.

^{1}H NMR (400 MHz, DMSO-d_6): δ 8.31 (d, J = 4.1 Hz, 1 H), 8.07 (d, J = 4.1 Hz, 1 H), 3.93 (s, 3 H), 2.99 (s, 3 H);

^{13}C NMR (100 MHz, DMSO-d_6): δ 175.5, 138.7, 121.5, 119.9 (q, $^{1}J_{C\text{-}F}$ = 322 Hz, 1 C), 39.2, 18.3;

^{19}F NMR (376 MHz, DMSO-d_6): δ -78.7 (s, 6 F).

ESI-MS (+ve) $[C_5H_8NS_2]^+$: calcd 146.0093, found 146.0090.

ESI-MS (-ve) $[C_2F_6NO_4S_2]^-$: calcd 279.9173, found 279.9196.

CHN Analysis: Calc. for $[(C_1)_2\text{Thio}][NTf_2]$, ($C_7H_8F_6N_2O_4S_3$): N 6.57, C 19.72, H 1.89. Found: N 6.77, C 19.83, H 1.90.

7.5.37. 3-Methyl-2-methylsulfanyl-4,5-dihydro-1,3-thiazolium iodide, $[(C_1)_2\text{Thiz}]I$



[**CAUTION!** Iodomethane is a strong alkylating agent. Thick protective gloves should be worn at all times]

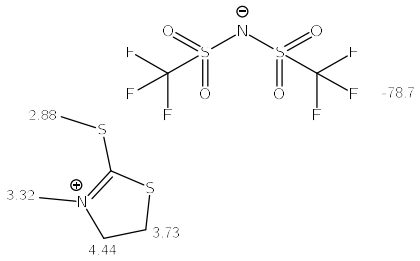
2-(methylthio)-4,5-dihydrothiazole (3.95 mL, 36.3 mmol) was dissolved in acetonitrile (10 mL) and iodomethane (6.95 mL, 110 mmol) was added to the solution in one portion. The mixture was refluxed 24 h, then cooled and recrystallised from ethyl acetate. The product was filtered and dried *in vacuo* overnight at 50 °C. The salt (0.748 g, 74.8%) was obtained as a white powder.

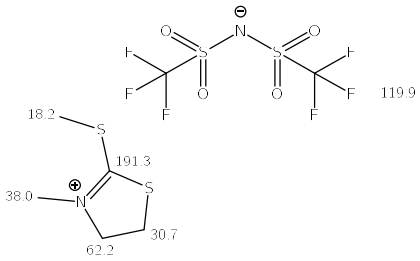
^{1}H NMR (400 MHz, DMSO-d_6): δ 4.45 (t, J = 8.8 Hz, 2 H), 3.74 (t, J = 8.8 Hz, 2 H), 3.31 (s, 3 H), 2.88 (s, 3 H);

^{13}C NMR (100 MHz, DMSO-d_6): δ 191.3, 62.2, 38.1, 30.8, 18.3.

ESI-MS (+ve) $[C_5H_{10}NS_2]^+$: calcd 148.0249, found 148.0251.

7.5.38. 3-Methyl-2-methylsulfanyl-4,5-dihydro-1,3-thiazolium bis(trifluoromethylsulfonyl)imide, $[(C_1)_2Thiz][NTf_2]$





Compound **7.5.37.** (1.28 g, 4.67 mmol) was transferred to a round bottom flask followed by the addition of water (10 mL). $LiNTf_2$ (1.61 g, 5.60 mmol) in water (10 mL) was added and the mixture stirred at 0 °C and gradually allowed to warm up to room temperature for 24 h. Dichloromethane (20 mL) was added to recover the ionic liquid and washed with cold water (5 x 10 mL). The organic layer was collected, the solvent removed and dried *in vacuo* overnight at 50 °C. The salt (1.86 g, 93.1%) was obtained as a white powder.

^{1}H NMR (400 MHz, DMSO-d_6): δ 4.44 (t, J = 8.8 Hz, 2 H), 3.73 (t, J = 8.8 Hz, 2 H), 3.32 (s, 3 H), 2.88 (s, 3 H);

^{13}C NMR (100 MHz, DMSO-d_6): δ 191.3, 119.9 (q, $^1J_{C\text{-}F}$ = 322 Hz, 1 C), 62.2, 38.0, 30.7, 18.2;

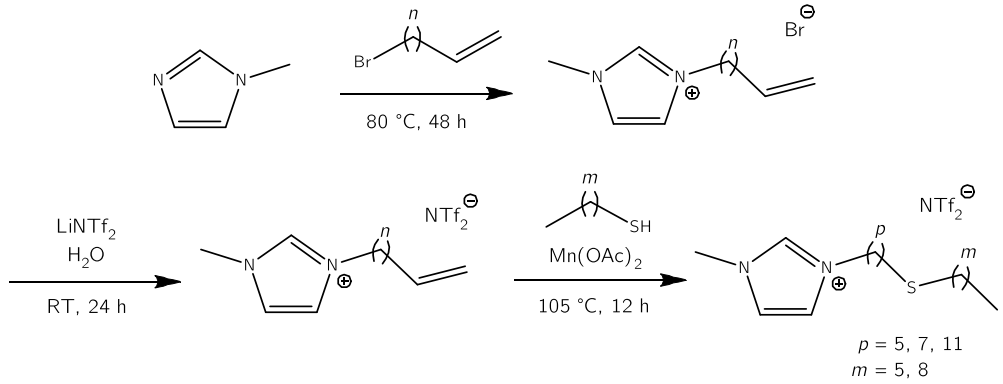
^{19}F NMR (376 MHz, DMSO-d_6): δ -78.7 (s, 6 F).

ESI-MS (+ve) $[C_5H_{10}NS_2]^+$: calcd 148.0249, found 148.0247.

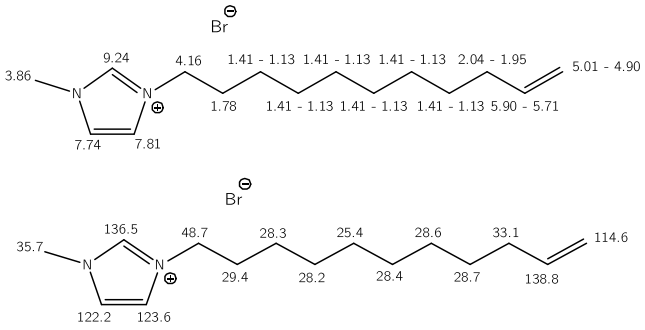
ESI-MS (-ve) $[C_2F_6NO_4S_2]^-$: calcd 279.9173, found 279.9175.

CHN Analysis: Calc. for $[(C_1)_2Thiz][NTf_2]$, ($C_7H_{10}F_6N_2O_4S_3$): N 6.54, C 19.63, H 2.35. Found: N 6.62, C 19.78, H 2.52.

Multi-Step Synthesis of Sulfur-Chain Imidazoliums:[42, 275]



7.5.39. 1-Methyl-3-undecenylimidazolium bromide, [C_1ImC_{11}ene]Br[275]



To a stirring solution of 1-methylimidazole (1.39 mL, 15.9 mmol) in acetonitrile (10 mL), 11-bromo-1-undecene (3.48 mL, 17.4 mmol) was added dropwise at room temperature. The reaction mixture was heated to 80 °C and stirred for 48 h. The solvent was removed and the crude recrystallised from acetonitrile/ethyl acetate and dried *in vacuo* overnight at 50 °C to yield a yellow viscous liquid (3.78 g, 76.2%).

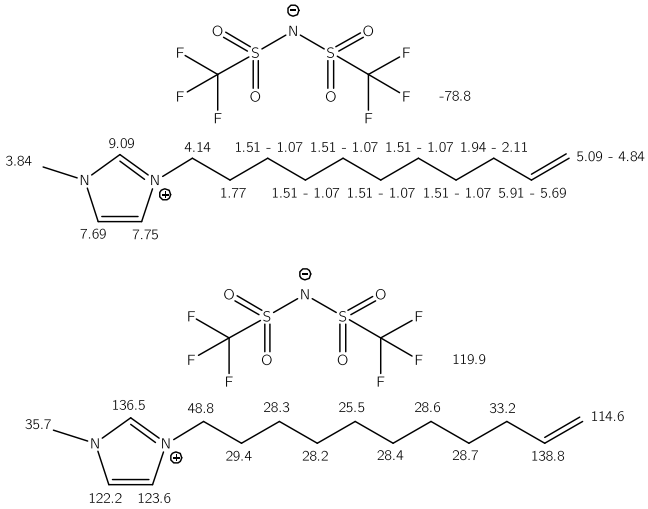
^{1}H NMR (400 MHz, DMSO-d_6): δ 9.24 (br. s, 1 H), 7.81 (t, J = 1.8 Hz, 1 H), 7.74 (t, J = 1.8 Hz, 1 H), 5.90 – 5.71 (m, 1 H), 5.01 - 4.90 (m, 2H), 4.16 (t, J = 7.2 Hz, 2 H), 3.86 (s, 3 H), 2.04 - 1.95 (m, 2 H), 1.78 (quint, J = 7.2 Hz, 2 H) 1.41- 1.13 (m, 12 H);

^{13}C NMR (100 MHz, DMSO-d_6): δ 138.8, 136.5, 123.6, 122.2, 114.6, 48.7, 35.7, 33.1, 29.4, 28.7, 28.6, 28.4, 28.3, 28.2, 25.4.

ESI-MS (+ve) $[C_{15}H_{27}N_2]^+$: calcd 235.2169, found 235.2190.

Data in agreement with literature values.[275]

7.5.40. 1-Methyl-3-undecenylimidazolium bis(trifluoromethylsulfonyl)imide, $[C_1ImC_{11}ene][NTf_2]$[275]



To a solution of compound **7.5.39** (6.12 g, 19.4 mmol) in water (15 mL), a solution of lithium bis(trifluoromethane)sulfonimide (6.68 g, 23.3 mmol) in water (15 mL) was added dropwise. The reaction mixture was stirred overnight at room temperature. Dichloromethane (50 mL) was added and the organic layer separated and washed with water (5 x 15 mL). The solvent was removed, and the product was dried *in vacuo* at 50 °C to yield a yellow viscous liquid (9.73 g, 97.3%).

^{1}H NMR (400 MHz, DMSO-d_6): δ 9.09 (br. s, 1 H), 7.75 (t, J = 1.8 Hz, 1 H), 7.69 (t, J =1.8 Hz, 1 H), 5.91 - 5.69 (m, 1 H), 5.09 - 4.84 (m, 2 H), 4.14 (t, J = 7.2 Hz, 2 H), 3.84 (s, 3 H), 1.94 - 2.11 (m, 2 H), 1.77 (quin, J = 7.2 Hz, 2 H), 1.51 - 1.07 (m, 12 H);

^{13}C NMR (100 MHz, DMSO-d_6): δ 138.8, 136.5, 123.6, 122.2, 119.9 (q, $^1J_{C\text{-}F}$ = 322 Hz, 1 C), 114.6, 48.8, 35.7, 33.2, 29.4, 28.7, 28.4, 28.3, 28.2, 25.5;

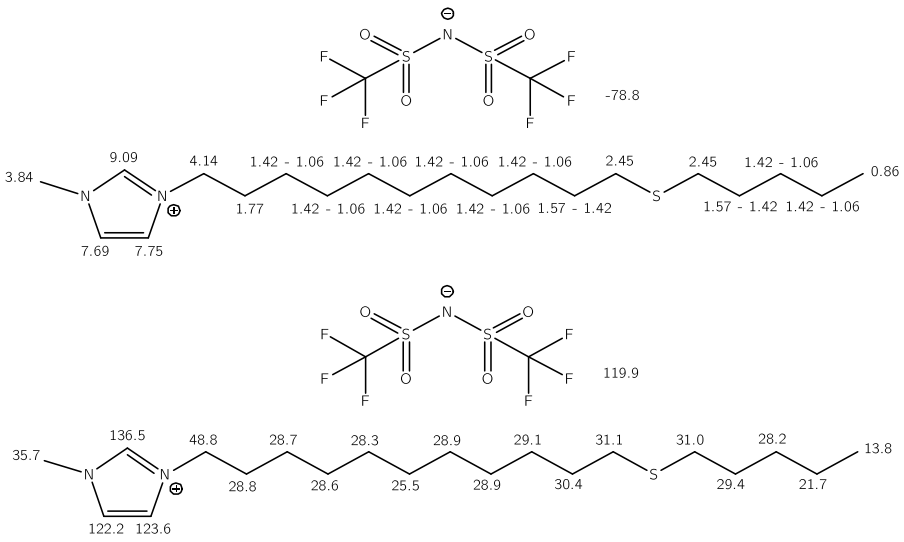
^{19}F NMR (376 MHz, DMSO-d_6) δ -78.8 (s, 6 F).

ESI-MS (+ve) $[C_{15}H_{27}N_2]^+$: calcd 235.2169, found 235.2191.

ESI-MS (-ve) $[C_2F_6NO_4S_2]^-$: calcd 279.9173, found 279.9187.

Data in agreement with literature values.[275]

7.5.41. 1-Methyl-3-undecyl-thia-pentylimidazolium bis(trifluoromethylsulfonyl)imide, $[C_1ImC_{11}SC_5][NTf_2]$[43]



[**CAUTION!** Thiols have strong odours similar to natural gas. Oxidation is most easily accomplished using a bleach solution]

A mixture of 1-pentanethiol (3.60 mL, 29.0 mmol), $Mn(OAc)_2$ (0.56 g, 3.20 mmol) was stirred at room temperature until a homogenous mixture was observed. Then compound **7.5.40** (1.66 g, 3.20 mmol) was added to the mixture and was stirred at 105 °C for 12 h. The residue was then washed with hexane (5 × 10 mL) and cold water (5 × 5 mL), followed by removal of residual solvents *in vacuo* overnight at 50 °C. The salt (1.38 g, 68.8%) was obtained as yellow viscous liquid.

^{1}H NMR (400 MHz, DMSO-d_6): δ 9.09 (br. s, 1 H), 7.75 (br. s, 1 H), 7.69 (br. s, 1 H), 4.14 (t, J = 7.2 Hz, 2 H), 3.84 (s, 3 H), 2.45 (t, J = 7.2 Hz, 4 H), 1.77 (quin, J = 7.2 Hz, 2 H), 1.57 - 1.42 (m, 4 H), 1.42 - 1.06 (m, 18 H), 0.86 (t, J = 7.2 Hz, 3 H);

^{13}C NMR (100 MHz, DMSO-d_6): δ 136.5, 123.6, 122.2, 119.9 (q, $^{1}J_{C\text{-}F}$ = 322 Hz, 1 C), 48.8, 35.7, 31.1, 31.0, 30.4, 29.4, 29.1, 28.9, 28.9, 28.8, 28.7, 28.6, 28.3, 28.2, 25.5, 21.7, 13.8;

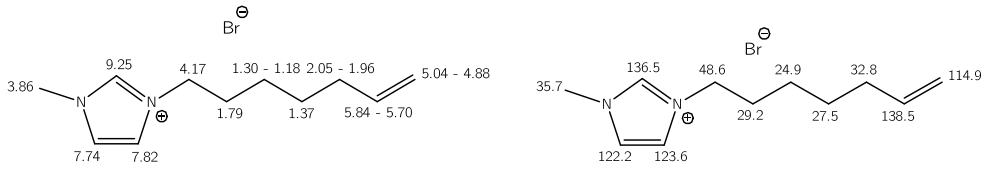
^{19}F NMR (376 MHz, DMSO-d_6) δ -78.8 (s, 6 F).

ESI-MS (+ve) $[C_{20}H_{39}N_2S]^+$: calcd 339.2828, found 339.2826.

ESI-MS (-ve) $[C_2F_6NO_4S_2]^-$: calcd 279.9173, found 279.9170.

Data in agreement with literature values.[43]

7.5.42. 1-Methyl-3-heptenylimidazolium bromide, [C_1ImC_7ene]Br[275]



To a stirring solution of 1-methylimidazole (2.47 mL, 28.2 mmol) in acetonitrile (15 mL), 7-bromo-1-heptene (4.29 mL, 31.0 mmol) was added dropwise at room temperature. The reaction mixture was heated to 80 °C and stirred for 48 h. The solvent was removed and the crude recrystallized from acetonitrile/ethyl acetate and dried *in vacuo* overnight at 50 °C to yield a yellow viscous liquid (5.93 g, 81.3%).

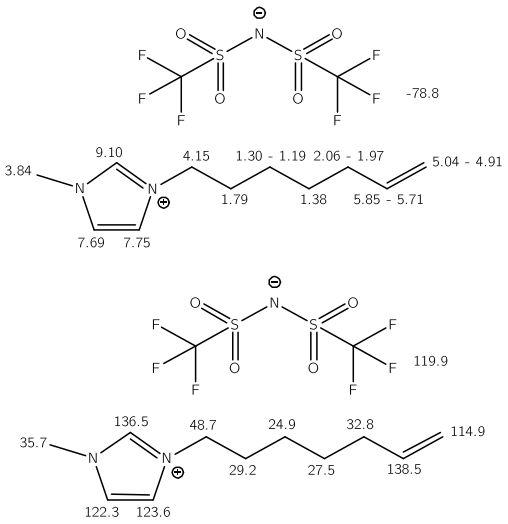
^{1}H NMR (400 MHz, DMSO-d_6): δ 9.25 (br. s, 1 H), 7.82 (t, J = 1.8 Hz, 1 H), 7.74 (t, J = 1.8 Hz, 1 H), 5.84 - 5.70 (m, 1 H), 5.04 - 4.88 (m, 2 H), 4.17 (t, J = 7.2 Hz, 2 H), 3.86 (s, 3 H), 2.05 - 1.96 (m, 2 H), 1.79 (quin, J = 7.2 Hz, 2 H), 1.37 (quin, J = 7.2 Hz, 2 H), 1.30 - 1.18 (m, 2 H);

^{13}C NMR (100 MHz, DMSO-d_6): δ 138.5, 136.5, 123.6, 122.2, 114.9, 48.6, 35.7, 32.8, 29.2, 27.5, 24.9.

ESI-MS (+ve) $[C_{11}H_{19}N_2]^+$: calcd 179.1543, found 179.1552.

Data in agreement with literature values.[275]

7.5.43. 1-Methyl-3-heptenylimidazolium bis(trifluoromethylsulfonyl)imide, $[C_1ImC_7ene][NTf_2]$[275]



Coumpound **7.5.42** (3.39 g, 13.1 mmol) was transferred to a round bottom flask followed by the addition of water (15 mL). $LiNTf_2$ (4.50 g, 15.7 mmol) in water (10 mL) was added and the mixture stirred at 0 °C and gradually allowed to warm up to room temperature for 24 h. Dichloromethane (15 mL) was added to recover the ionic liquid and washed with cold water (5 x 10 mL). The organic layer was collected, the solvent removed and dried *in vacuo* overnight at 50 °C. The salt (5.74 g, 95.6%) was obtained as yellow viscous liquid.

^{1}H NMR (400 MHz, DMSO-d_6): δ 9.10 (br. s, 1 H), 7.75 (t, J = 1.8 Hz, 1 H), 7.69 (t, J = 1.8 Hz, 1 H), 5.85 - 5.71 (m, 1 H), 5.04 - 4.91 (m, 2 H), 4.15 (t, J = 7.2 Hz, 2 H), 3.84 (s, 3 H), 2.06 - 1.97 (m, 2 H), 1.79 (quin, J = 7.2 Hz, 2 H), 1.38 (quin, J = 7.2 Hz, 2 H), 1.30 - 1.19 (m, 2 H);

^{13}C NMR (100 MHz, DMSO-d_6): δ 138.5, 136.5, 123.6, 122.3, 119.9 (q, $^1J_{C\text{-}F}$ = 322 Hz, 1 C), 114.9, 48.7, 35.7, 32.8, 29.2, 27.5, 24.9;

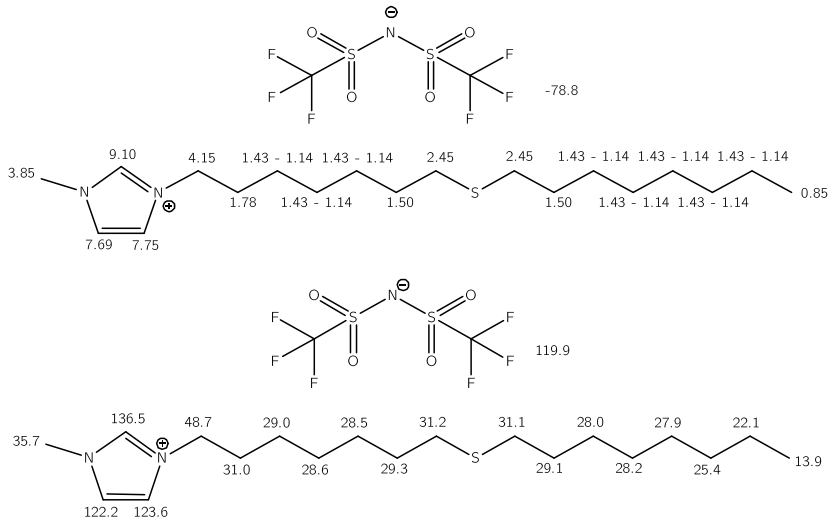
^{19}F NMR (376 MHz, DMSO-d_6) δ -78.8 (s, 6 F).

ESI-MS (+ve) $[C_{11}H_{19}N_2]^+$: calcd 179.1543, found 179.1549.

ESI-MS (-ve) $[C_2F_6NO_4S_2]^-$: calcd 279.9173, found 279.9177.

Data in agreement with literature values.[275]

7.5.44. 1-Methyl-3-heptylthiaoctylimidazolium bis(trifluoromethylsulfonyl)imide, $[C_1ImC_7SC_8][NTf_2]$[43]



[**CAUTION!** Thiols have strong odours similar to natural gas. Oxidation is most easily accomplished using a bleach solution]

A mixture of 1-octanethiol (7.74 mL, 446 mmol), $Mn(OAc)_2$ (0.857 g, 49.5 mmol) was stirred at room temperature until a homogenous mixture was observed. Then coumpound **7.5.43** (2.28 g, 49.5 mmol) was added to the mixture and was stirred at 105 °C for 12 h. The residue was then washed with hexanes (5 × 10 mL) and cold water (5 × 5 mL), followed by removal of residual solvents *in vacuo* overnight at 50 °C. The salt (2.11 g, 70.4%) was obtained as viscous yellow liquid.

^{1}H NMR (400 MHz, DMSO-d_6): δ 9.10 (br. s, 1 H), 7.75 (t, J = 1.8 Hz, 1 H), 7.69 (t, J = 1.8 Hz, 1 H), 4.15 (t, J = 7.2 Hz, 2 H), 3.85 (s, 3 H), 2.45 (t, J = 7.2 Hz, 4 H), 1.78 (quin, J = 7.2 Hz, 2 H), 1.50 (quin, J = 7.2 Hz, 4 H) 1.43 - 1.14 (m, 16 H), 0.85 (t, J = 7.2 Hz, 3 H);

^{13}C NMR (100 MHz, DMSO-d_6): δ 136.5, 123.6, 122.2, 119.9 (q, $^1J_{C\text{-}F}$ = 322 Hz, 1 C), 48.7, 35.7, 31.2, 31.1, 31.0, 29.3, 29.1, 29.0, 28.6, 28.5, 28.2, 28.0, 27.9, 25.4, 22.1, 13.9;

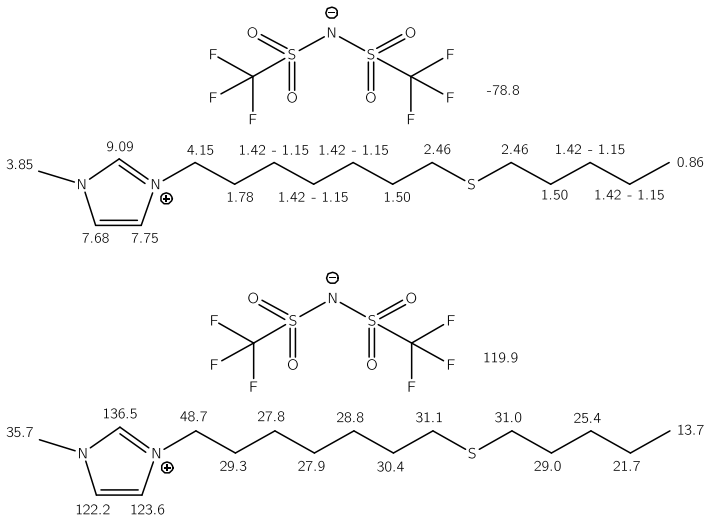
^{19}F NMR (376 MHz, DMSO-d_6) δ -78.8 (s, 6 F).

ESI-MS (+ve) $[C_{19}H_{37}N_2S]^+$: calcd 325.2672, found 325.2673.

ESI-MS (-ve) $[C_2F_6NO_4S_2]^-$: calcd 279.9173, found 279.9169.

Data in agreement with literature values.[43]

7.5.45. 1-Methyl-3-heptylthiapentylimidazolium bis(trifluoromethylsulfonyl)imide, $[C_1ImC_7SC_5][NTf_2]$[43]



[**CAUTION!** Thiols have strong odours similar to natural gas. Oxidation is most easily accomplished using a bleach solution]

A mixture of 1-pentanethiol (5.92 mL, 47.9 mmol), $Mn(OAc)_2$ (0.921 g, 5.32 mmol) was stirred at room temperature until a homogenous mixture was observed. Then compound **7.5.45** (2.45 g, 5.32 mmol) was added to the mixture and was stirred at 105 °C for 12 h. The residue was then washed with hexanes (5 × 10 mL) and cold water (5 × 5 mL), followed by removal of residual solvents *in vacuo* overnight at 50 °C. The salt (2.05 g, 68.3%) was obtained as viscous yellow liquid.

^{1}H NMR (400 MHz, DMSO-d_6): δ 9.09 (br. s, 1 H), 7.75 (t, J = 1.8 Hz, 1 H), 7.68 (t, J = 1.8 Hz, 1 H), 4.15 (t, J = 7.2 Hz, 2 H), 3.85 (s, 3 H), 2.46 (t, J = 7.2 Hz, 4 H), 1.78 (quin, J = 7.2 Hz, 2 H), 1.50 (quin, J = 7.2 Hz, 4 H), 1.42 - 1.15 (m, 10 H), 0.86 (t, J= 7.2 Hz, 3 H);

^{13}C NMR (100 MHz, DMSO-d_6): δ 136.5, 123.6, 122.2, 119.9 (q, $^{1}J_{C\text{-}F}$ = 322 Hz, 1 C), 48.7, 35.7, 31.1, 31.0, 30.4, 29.3, 29.0, 28.8, 27.9, 27.8, 25.4, 21.7, 13.7;

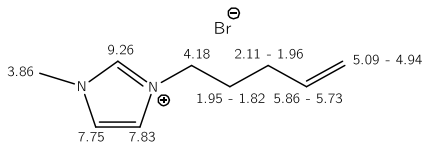
^{19}F NMR (376 MHz, DMSO-d_6) δ -78.8 (s, 6 F).

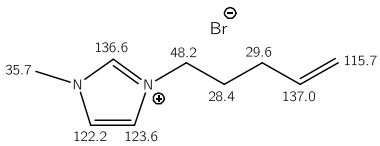
ESI-MS (+ve) $[C_{16}H_{31}N_2S]^+$: calcd 283.2208, found 283.2214.

ESI-MS (-ve) $[C_2F_6NO_4S_2]^-$: calcd 279.9173, found 279.9173.

Data in agreement with literature values.[43]

7.5.46. 1-Methyl-3-pentenylimidazolium bromide, [C_1ImC_5ene]Br[275]





To a stirring solution of 1-methylimidazole (3.79 mL, 47.6 mmol) in acetonitrile (20 mL), 5-bromo-1-pentene (5.13 mL, 43.3 mmol) was added dropwise at room temperature. The reaction mixture was heated to 80 °C and stirred for 48 h. The solvent was removed and the crude recrystallized from acetonitrile/ethyl acetate and dried *in vacuo* overnight at 50 °C to yield a yellow viscous liquid (8.37 g, 83.7%).

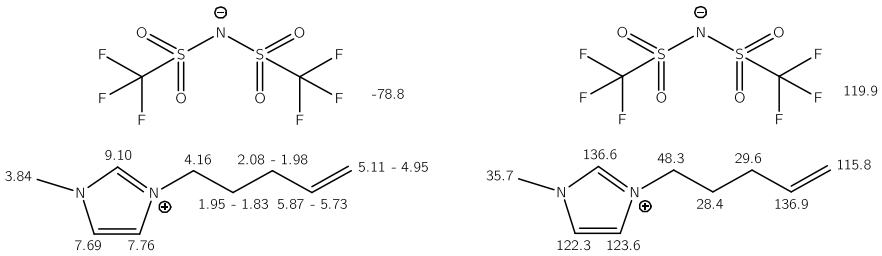
^{1}H NMR (400 MHz, DMSO-d_6): δ 9.26 (br. s, 1 H), 7.83 (t, J = 1.8 Hz, 1 H), 7.75 (t, J = 1.8 Hz, 1 H), 5.86 - 5.73 (m, 1H), 5.09 - 4.94 (m, 2 H), 4.18 (t, J = 7.2 Hz, 2 H), 3.86 (s, 3 H), 2.11 - 1.96 (m, 2 H), 1.95 - 1.82 (m, 2 H);

^{13}C NMR (100 MHz, DMSO-d_6): δ 137.0, 136.6, 123.6, 122.2, 115.7, 48.2, 35.7, 29.6, 28.4.

ESI-MS (+ve) $[C_9H_{15}N_2]^+$: calcd 151.1235, found 151.1240.

Data in agreement with literature values.[275]

7.5.47. 1-Methyl-3-pentenylimidazolium bis(trifluoromethylsulfonyl)imide, $[C_1ImC_5ene][NTf_2]$[275]



Coumpound **7.5.46** (5.36 g, 23.2 mmol) was transferred to a round bottom flask followed by the addition of water (15 mL). $LiNTf_2$ (7.99 g, 27.8 mmol) in water (20 mL) was added and the mixture stirred at 0 °C and gradually allowed to warm up to room temperature for 24 h. Dichloromethane (30 mL) was added to recover the ionic liquid and washed with cold water (5 x 15 mL). The organic layer was collected, the solvent removed and dried *in vacuo* overnight at 50 °C. The salt (9.88 g, 98.8%) was obtained as yellow viscous liquid.

^{1}H NMR (400 MHz, DMSO-d_6): δ 9.10 (br. s, 1 H), 7.76 (t, J = 1.8 Hz, 1 H), 7.69 (t, J = 1.8 Hz, 1 H), 5.87 - 5.73 (m, 1H), 5.11 - 4.95 (m, 2 H), 4.16 (t, J = 7.2 Hz, 2 H), 3.84 (s, 3 H), 2.08 - 1.98 (m, 2 H), 1.95 - 1.83 (m, 2 H);

^{13}C NMR (100 MHz, DMSO-d_6): δ 136.9, 136.6, 123.6, 122.3, 119.9 (q, $^1J_{C\text{-}F}$ = 322 Hz, 1 C), 115.8, 48.3, 35.7, 29.6, 28.4;

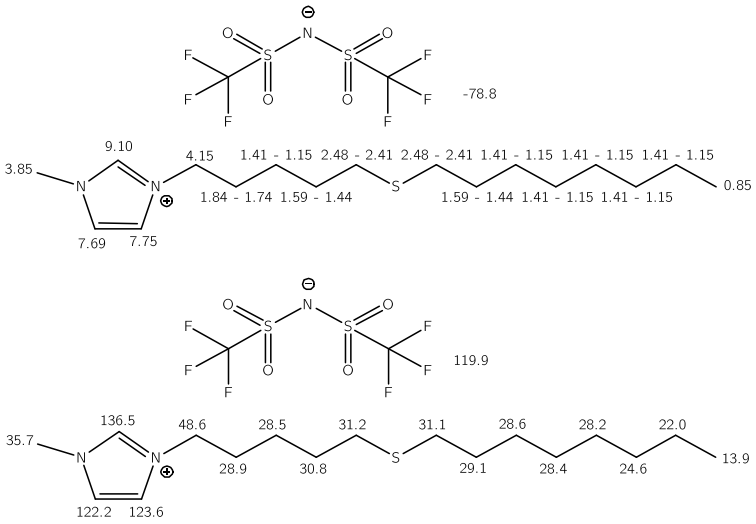
^{19}F NMR (376 MHz, DMSO-d_6) δ -78.8 (s, 6 F).

ESI-MS (+ve) $[C_9H_{15}N_2]^+$: calcd 151.1235, found 151.1229.

ESI-MS (-ve) $[C_2F_6NO_4S_2]^-$: calcd 279.9173, found 279.9181.

Data in agreement with literature values.[275]

7.5.48. 1-Methyl-3-pentylthiaoctylimidazolium bis(trifluoromethylsulfonyl)imide, $[C_1ImC_5SC_8][NTf_2]$[43]



[**CAUTION!** Thiols have strong odours similar to natural gas. Oxidation is most easily accomplished using a bleach solution]

A mixture of 1-octanethiol (8.11 mL, 46.7 mmol), $Mn(OAc)_2$ (0.899 g, 5.19 mmol) was stirred at room temperature until a homogenous mixture was observed. Then compound **7.5.47** (2.24 g, 5.19 mmol) was added to the mixture and was stirred at 105 °C for 12 h. The residue was then washed with hexanes (5 × 10 mL) and cold water (5 × 5 mL), followed by removal of residual solvents *in vacuo* overnight at 50 °C. The salt (2.48 g, 82.7%) was obtained as viscous yellow liquid.

^{1}H NMR (400 MHz, DMSO-d_6): δ 9.10 (br. s, 1 H), 7.75 (t, J = 1.8 Hz, 1 H), 7.69 (t, J = 1.8 Hz, 1 H), 4.15 (t, J = 7.2 Hz, 2 H), 3.85 (s, 3H), 2.48 - 2.41 (m, 4 H), 1.84 - 1.74 (m, 2 H), 1.59 - 1.44 (m, 4 H), 1.41 - 1.15 (m, 12 H), 0.85 (t, J = 7.2 Hz, 3 H);

^{13}C NMR (100 MHz, DMSO-d_6): δ 136.5, 123.6, 122.2, 119.9 (q, $^1J_{C\text{-}F}$ = 322 Hz, 1 C), 48.6, 35.7, 31.2, 31.1, 30.8, 29.1, 28.9, 28.6, 28.5, 28.4, 28.2, 24.6, 22.0, 13.9;

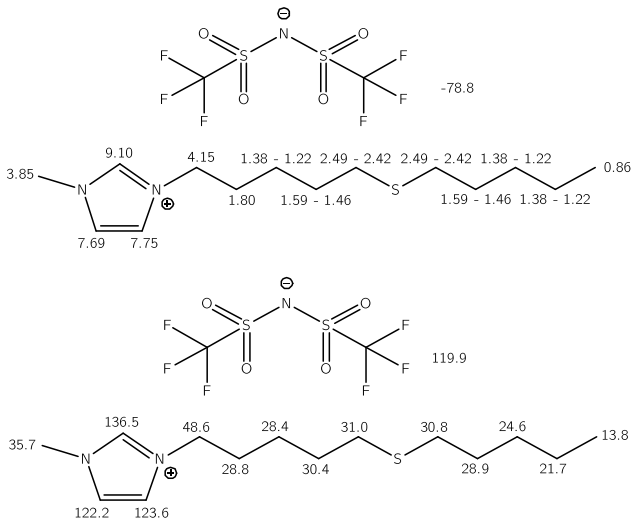
^{19}F NMR (376 MHz, DMSO-d_6) δ -78.8 (s, 6 F).

ESI-MS (+ve) $[C_{17}H_{33}N_2S]^+$: calcd 297.2364, found 297.2359.

ESI-MS (-ve) $[C_2F_6NO_4S_2]^-$: calcd 279.9173, found 279.9179.

Data in agreement with literature values.[43]

7.5.49. 1-Methyl-3-pentylthiapentylimidazolium bis(trifluoromethylsulfonyl)imide, $[C_1ImC_5SC_5][NTf_2]$[43]



[**CAUTION!** Thiols have strong odours similar to natural gas. Oxidation is most easily accomplished using a bleach solution]

A mixture of 1-pentanethiol (6.23 mL, 50.4 mmol), $Mn(OAc)_2$ (0.969 g, 5.60 mmol) was stirred at room temperature until a homogenous mixture was observed. Then compound **7.5.47** (2.42 g, 5.60 mmol) was added to the mixture and was stirred at 105 °C for 12 h. The residue was then washed with hexanes (5 × 10 mL) and cold water (5 × 5 mL), followed by removal of residual solvents *in vacuo* overnight at 50 °C. The salt (2.10 g, 69.9%) was obtained as viscous yellow liquid.

^{1}H NMR (400 MHz, DMSO-d_6): δ 9.10 (br. s, 1 H), 7.75 (t, J = 1.8 Hz, 1 H), 7.69 (t, J = 1.8 Hz, 1 H), 4.15 (t, J = 7.2 Hz, 2 H), 3.85 (s, 3 H), 2.49 - 2.42 (m, 4 H), 1.80 (quin, J = 7.2 Hz, 2 H), 1.59 - 1.46 (m, 4 H), 1.38 - 1.22 (m, 6 H), 0.86 (t, J = 7.2 Hz, 3 H);

^{13}C NMR (100 MHz, DMSO-d_6): δ 136.5, 123.6, 122.2, 119.9 (q, $^{1}J_{C\text{-}F}$ = 322 Hz, 1 C),48.6, 35.7, 31.0, 30.8, 30.4, 28.9, 28.8, 28.4, 24.6, 21.7, 13.8;

^{19}F NMR (376 MHz, DMSO-d_6) δ -78.8 (s, 6 F).

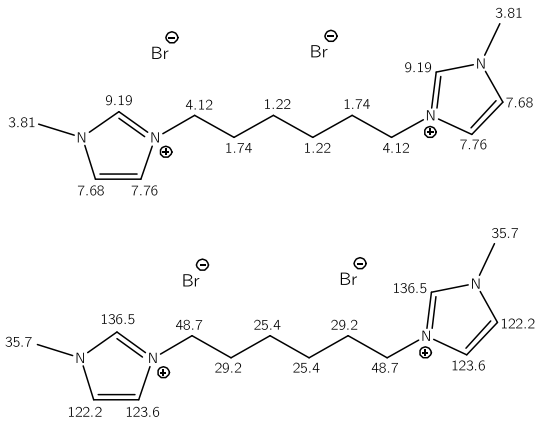
ESI-MS (+ve) $[C_{14}H_{27}N_2S]^+$: calcd 255.1895, found 255.1899.

ESI-MS (-ve) $[C_2F_6NO_4S_2]^-$: calcd 279.9173, found 279.9182.

Data in agreement with literature values.[43]

7.6. Dicationic-based Ionic Liquids

7.6.1. 1,6-Bis(3-methylimidazolium-1-yl)hexane dibromide, $[C_6(C_1Im)_2]2Br$[276]



To a stirring solution of 1-methylimidazole (4.30 mL, 53.9 mmol) in acetonitrile (15 mL), 1,6-dibromohexane (3.77 mL, 24.5 mmol) was added dropwise at room temperature. The reaction mixture was heated to 40 °C and stirred for 48 h. The solvent was removed and the crude recrystallized from acetonitrile/ethyl acetate and dried *in vacuo* at 50 °C to yield a white powder (8.17 g, 81.7%).

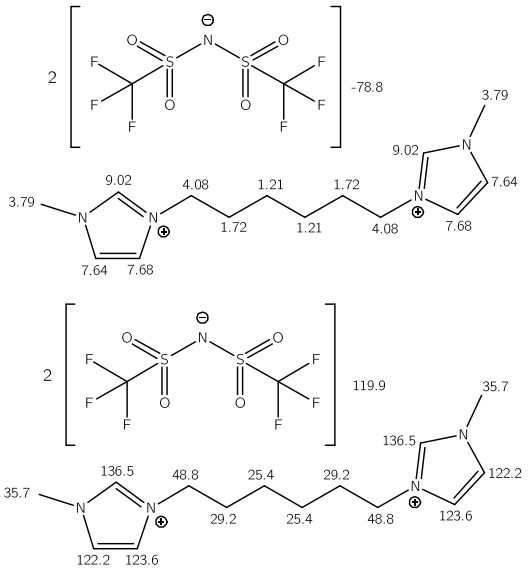
^{1}H NMR (400 MHz, DMSO-d_6): δ 9.19 (s, 2 H), 7.76 (t, J = 1.8 Hz, 2 H), 7.68 (t, J = 1.8 Hz, 2 H), 4.12 (t, J = 7.2 Hz, 4 H), 3.81 (s, 6 H), 1.74 (quin, J = 7.4 Hz, 4 H), 1.22 (m, 4 H);

^{13}C NMR (100 MHz, DMSO-d_6): δ 136.5, 123.6, 122.2, 48.7, 35.7, 29.2, 25.4.

ESI-MS (+ve) $[C_{14}H_{24}N_4]^{2+}$: calcd 124.0995, found 124.0989.

Data in agreement with literature values.[276]

7.6.2. 1,6-Bis(3-methylimidazolium-1-yl)hexane di[bis(trifluoromethanesulfonyl)imide], $[C_6(C_1Im)_2]2[NTf_2]$[276]



Compound **7.6.1** (2.52 g, 6.18 mmol) was transferred to a round bottom flask followed by the addition of water (5 mL). $LiNTf_2$ (4.26 g, 14.4 mmol) in water (5 mL) was added and the mixture stirred at 0 °C and gradually allowed to warm up to room temperature for 24 h. Dichloromethane (10 mL) was added to recover the ionic liquid and washed with cold water (5 x 5 mL). The organic layer was collected, the solvent removed and dried *in vacuo* overnight at 50 °C. The salt (4.72 g, 94.4%) was obtained as slightly yellow liquid.

^{1}H NMR (400 MHz, DMSO-d_6): δ 9.02 (s, 2 H), 7.68 (t, J = 1.8 Hz, 2 H), 7.64 (t, J = 1.8 Hz, 2 H), 4.08 (t, J = 7.2 Hz, 4 H), 3.79 (s, 6 H), 1.72 (quin, J = 7.4 Hz, 4 H), 1.21 (m, 4 H);

^{13}C NMR (100 MHz, DMSO-d_6): δ 136.5, 123.6, 122.2, 119.9 (q, $^1J_{C\text{-}F}$ = 322 Hz, 1 C),48.8, 35.7, 29.2, 25.4.

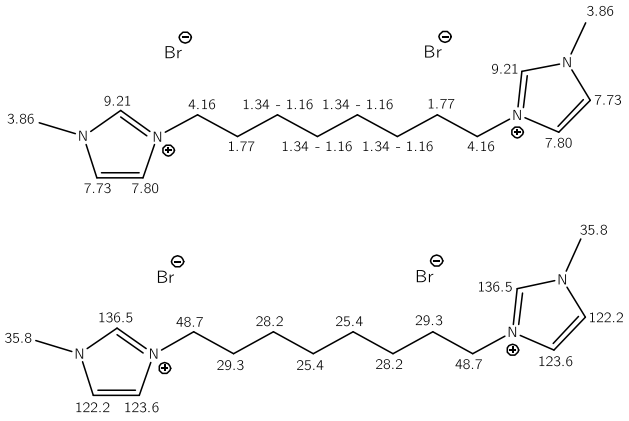
^{19}F NMR (376 MHz, DMSO-d_6) δ -78.8 (s, 6 F).

ESI-MS (+ve) $[C_{14}H_{24}N_4]^{2+}$: calcd 124.0995, found 124.0990.

ESI-MS (-ve) $[C_2F_6NO_4S_2]^-$: calcd 279.9173, found 279.9173.

Data in agreement with literature values.[276]

7.6.3. 1,8-Bis(3-methylimidazolium-1-yl)octane dibromide, $[C_8(C_1Im)_2]2Br$[276]



To a stirring solution of 1-methylimidazole (4.02 mL, 50.4 mmol) in acetonitrile (15 mL), 1,8-dibromooctane (4.22 mL, 22.9 mmol) was added dropwise at room temperature. The reaction mixture was heated to 40 °C and stirred for 48 h. The solvent was removed and the crude recrystallized from acetonitrile/ethyl acetate and dried *in vacuo* at 50 °C to yield a white powder (8.88 g, 88.8%).

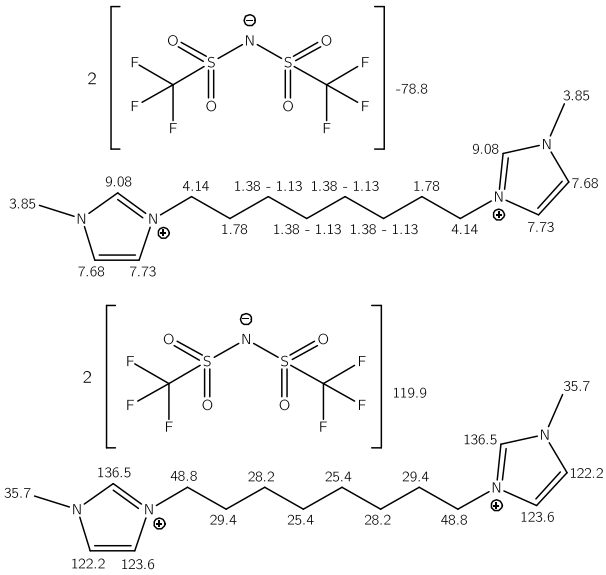
^{1}H NMR (400 MHz, DMSO-d_6): δ 9.21 (s, 2 H), 7.80 (t, J = 1.8 Hz, 2 H), 7.73 (t, J = 1.8 Hz, 2 H), 4.16 (t, J = 7.2 Hz, 4 H), 3.86 (s, 6 H), 1.77 (quin, J = 7.4 Hz, 4 H), 1.34 – 1.16 (m, 8 H);

^{13}C NMR (100 MHz, DMSO-d_6): δ 136.5, 123.6, 122.2, 48.7, 35.8, 29.3, 28.2, 25.4.

ESI-MS (+ve) $[C_{16}H_{28}N_4]^{2+}$: calcd 138.1151, found 138.1162.

Data in agreement with literature values.[276]

7.6.4. 1,8-Bis(3-methylimidazolium-1-yl)octane di[bis(trifluoromethanesulfonyl)imide], $[C_8(C_1Im)_2]2[NTf_2]$[276]



Compound **7.6.3** (2.61 g, 5.98 mmol) was transferred to a round bottom flask followed by the addition of water (5 mL). $LiNTf_2$ (4.12 g, 14.3 mmol) in water (5 mL) was added and the mixture stirred at 0 °C and gradually allowed to warm up to room temperature for 24 h. Dichloromethane (10 mL) was added to recover the ionic liquid and washed with cold water (5 x 5 mL). The organic layer was collected, the solvent removed and dried *in vacuo* overnight at 50 °C. The salt (4.94 g, 98.7%) was obtained as yellow liquid.

^{1}H NMR (400 MHz, DMSO-d_6): δ 9.08 (s, 2 H), 7.73 (t, J = 1.8 Hz, 2 H), 7.68 (t, J = 1.8 Hz, 2 H), 4.14 (t, J = 7.4 Hz, 4 H), 3.85 (s, 6 H), 1.78 (quin, J = 7.2 Hz, 4 H), 1.38 – 1.13 (m, 8 H);

^{13}C NMR (100 MHz, DMSO-d_6): δ 136.5, 123.6, 122.2, 119.9 (q, $^1J_{C\text{-}F}$ = 322 Hz, 1 C), 48.8, 35.7, 29.4, 28.2, 25.4;

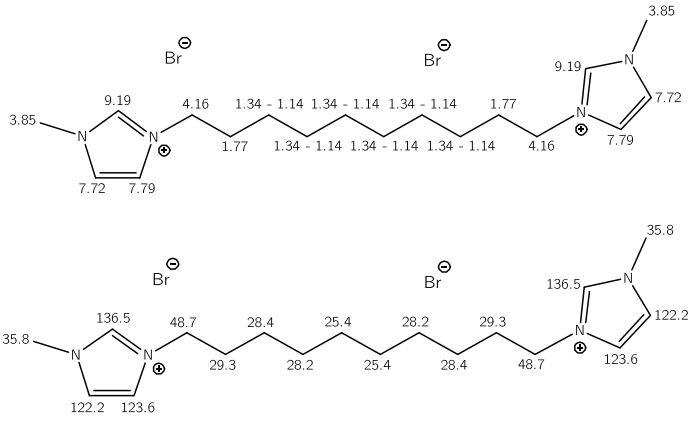
^{19}F NMR (376 MHz, DMSO-d_6) δ -78.8 (s, 6 F).

ESI-MS (+ve) $[C_{16}H_{28}N_4]^{2+}$: calcd 138.1151, found 138.1149.

ESI-MS (-ve) $[C_2F_6NO_4S_2]^-$: calcd 279.9173, found 279.9180.

Data in agreement with literature values.[276]

7.6.5. 1,10-Bis(3-methylimidazolium-1-yl)decane dibromide, $[C_{10}(C_1Im)_2]2Br$[276]



To a stirring solution of 1-methylimidazole (3.78 mL, 47.4 mmol) in acetonitrile (15 mL), 1,10-dibromodecane (4.84 mL, 21.5 mmol) was added dropwise at room temperature. The reaction mixture was heated to 40 °C and stirred for 48 h. The solvent was removed and the crude recrystallized from acetonitrile/ethyl acetate and dried *in vacuo* at 50 °C to yield a white powder (8.64 g, 86.4%).

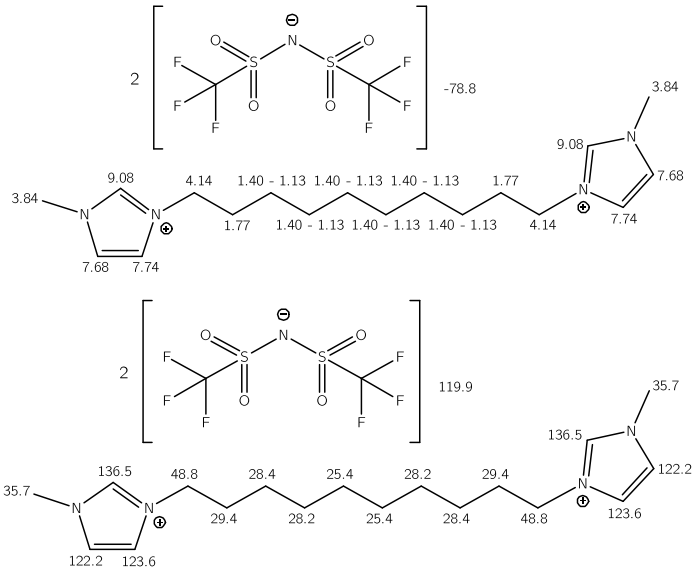
^{1}H NMR (400 MHz, DMSO-d_6): δ 9.19 (s, 2 H), 7.79 (t, J = 1.8 Hz, 2 H), 7.72 (t, J = 1.8 Hz, 2 H), 4.16 (t, J = 7.2 Hz, 4 H), 3.85 (s, 6 H), 1.77 (quin, J = 7.4 Hz, 4 H), 1.34 – 1.14 (m, 12 H);

^{13}C NMR (100 MHz, DMSO-d_6): δ 136.5, 123.6, 122.2, 48.7, 35.8, 29.3, 28.4, 28.2, 25.4.

ESI-MS (+ve) $[C_{18}H_{32}N_4]^{2+}$: calcd 152.1308, found 152.1303.

Data in agreement with literature values.[276]

7.6.6. 1,10-Bis(3-methylimidazolium-1-yl)decane di[bis(trifluoromethanesulfonyl)imide], $[C_{10}(C_1Im)_2]2[NTf_2]$[276]



Compound **7.6.5** (2.68 g, 5.78 mmol) was transferred to a round bottom flask followed by the addition of water (5 mL). $LiNTf_2$ (3.98 g, 13.9 mmol) in water (5 mL) was added and the mixture stirred at 0 °C and gradually allowed to warm up to room temperature for 24 h. Dichloromethane (10 mL) was added to recover the ionic liquid and washed with cold water (5 x 5 mL). The organic layer was collected, the solvent removed and dried *in vacuo* overnight at 50 °C. The salt (4.83 g, 96.6%) was obtained as colourless liquid.

^{1}H NMR (400 MHz, DMSO-d_6): δ 9.08 (s, 2 H), 7.74 (t, J = 1.8 Hz, 2 H), 7.68 (t, J = 1.8 Hz, 2 H), 4.14 (t, J = 7.2 Hz, 4 H), 3.84 (s, 6 H), 1.77 (quin, J = 7.2 Hz, 4 H), 1.40 – 1.13 (m, 12 H);

^{13}C NMR (100 MHz, DMSO-d_6): δ 136.5, 123.6, 122.2, 119.9 (q, $^1J_{C\text{-}F}$ = 322 Hz, 1 C), 48.8, 35.7, 29.4, 28.4, 28.2, 25.4;

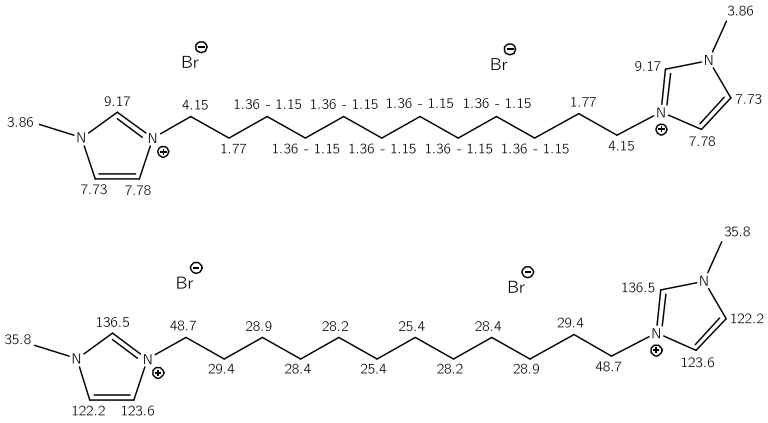
^{19}F NMR (376 MHz, DMSO-d_6) δ -78.8 (s, 6 F).

ESI-MS (+ve) $[C_{18}H_{32}N_4]^{2+}$: calcd 152.1308, found 152.1310.

ESI-MS (-ve) $[C_2F_6NO_4S_2]^-$: calcd 279.9173, found 279.9170.

Data in agreement with literature values.[276]

7.6.7. 1,12-Bis(3-methylimidazolium-1-yl)dodecane dibromide, $[C_{12}(C_1Im)_2]2Br$[276]



To a stirring solution of 1-methylimidazole (3.56 mL, 44.7 mmol) in acetonitrile (15 mL), 1,12-dibromododecane (6.66 g, 20.3 mmol) was added dropwise at room temperature. The reaction mixture was heated to 40 °C and stirred for 48 h. The solvent was removed and the crude recrystallized from acetonitrile/ethyl acetate and dried *in vacuo* at 50 °C to yield a colourless liquid (8.27 g, 82.7%).

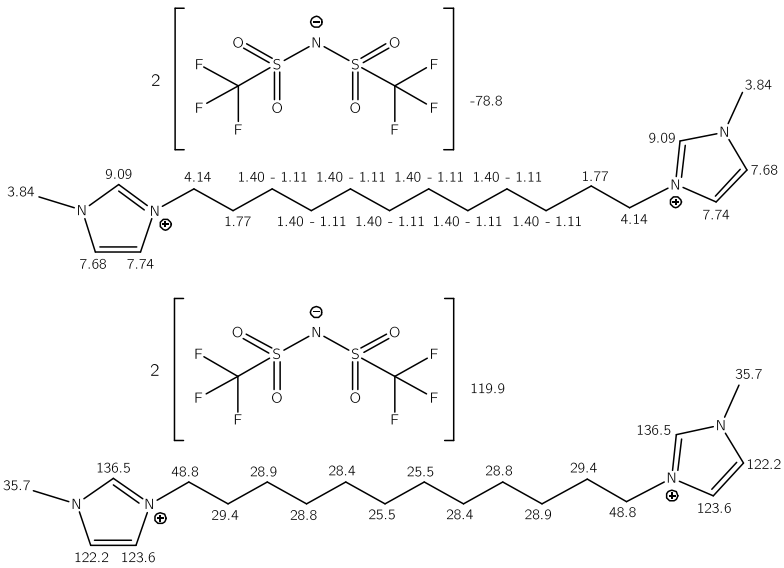
^{1}H NMR (400 MHz, DMSO-d_6): δ 9.17 (s, 2 H), 7.78 (t, J = 1.8 Hz, 2 H), 7.73 (t, J = 1.8 Hz, 2 H), 4.15 (t, J = 7.2 Hz, 4 H), 3.86 (s, 6 H), 1.77 (quin, J = 7.4 Hz, 4 H), 1.36 – 1.15 (m, 16 H);

^{13}C NMR (100 MHz, DMSO-d_6): δ 136.5, 123.6, 122.2, 48.7, 35.8, 29.4, 28.9, 28.4, 28.2, 25.4.

ESI-MS (+ve) $[C_{20}H_{36}N_4]^{2+}$: calcd 166.1465, found 166.1462.

Data in agreement with literature values.[276]

7.6.8. 1,12-Bis(3-methylimidazolium-1-yl)dodecane di[bis(trifluoromethanesulfonyl)imide], $[C_{12}(C_1Im)_2]2[NTf_2]$[276]



Compound **7.6.7** (2.76 g, 5.60 mmol) was transferred to a round bottom flask followed by the addition of water (5 mL). $LiNTf_2$ (3.86 g, 13.4 mmol) in water (5 mL) was added and the mixture stirred at 0 °C and gradually allowed to warm up to room temperature for 24 h. Dichloromethane (10 mL) was added to recover the ionic liquid and washed with cold water (5 x 5 mL). The organic layer was collected, the solvent removed and dried *in vacuo* overnight at 50 °C. The salt (4.58 g, 91.6%) was obtained as colourless liquid.

^{1}H NMR (400 MHz, DMSO-d_6): δ 9.09 (s, 2 H), 7.74 (t, J = 1.8 Hz, 2 H), 7.68 (t, J = 1.8 Hz, 2 H), 4.14 (t, J = 7.2 Hz, 4 H), 3.84 (s, 6 H), 1.77 (quin, J = 7.2 Hz, 4 H), 1.40 – 1.11 (m, 16 H);

^{13}C NMR (100 MHz, DMSO-d_6): δ 136.5, 123.6, 122.2, 119.9 (q, $^1J_{C\text{-}F}$ = 322 Hz, 1 C), 48.8, 35.7, 29.4, 28.9, 28.8, 28.4, 25.5;

^{19}F NMR (376 MHz, DMSO-d_6) δ -78.8 (s, 6 F).

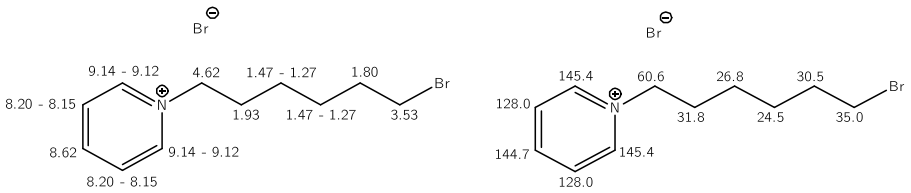
ESI-MS (+ve) $[C_{20}H_{36}N_4]^{2+}$: calcd 166.1465, found 166.1460.

ESI-MS (-ve) $[C_2F_6NO_4S_2]^-$: calcd 279.9173, found 279.9181.

Data in agreement with literature values.[276]

7.6.9. 6-Bromohexylpyridinium bromide, [Pyr(C_6)Br]Br

(Synthesised by Steven Maxwell-Hogg, as described by Zoë Disley)[277]



A three-neck round bottom flask, fitted with a reflux condenser and a pressure-equalised addition funnel, was charged with dibromohexane (48.3 g, 0.198 mol). A solution of pyridine (4.90 g, 61.9 mmol) in dichloromethane (75 mL) was added dropwise at room temperature whilst stirring. The resulting mixture was refluxed and stirred at 50-60 °C for 10 h. The solvents were removed under pressure leaving a pale yellow waxy solid. The solid was dissolved in methanol (50 mL) and the unreacted dibromohexane was washed out thoroughly with hexane (5 x 30 mL). The resulting mixture was purified by silica column chromatography (DCM/MeOH = 7/1) to give a yellow viscous liquid which was dried *in vacuo* (9.34 g, 46.7%).

^{1}H NMR (300 MHz, DMSO-d_6): δ 9.14 – 9.12 (m, 2 H), 8.62 (tt, J = 7.8 Hz, 1.3 Hz, 1 H), 8.20 – 8.15 (m, 2 H), 4.62 (t, J = 7.4 Hz, 2 H), 3.53 (t, J = 7.2 Hz, 2 H), 1.93 (quin, J = 7.4 Hz, 2 H), 1.80 (quin, J = 7.2 Hz, 2 H), 1.47 - 1.27 (m, 4 H);

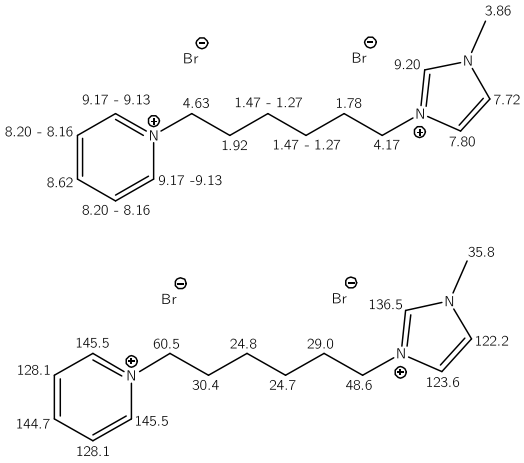
^{13}C NMR (75 MHz, DMSO-d_6): δ 145.4, 144.7, 128.0, 60.6, 35.0, 31.8, 30.5, 26.8, 24.5.

IR $\nu_{max}(CHCl_3)\cdot cm^{-1}$ 3024, 2924, 2855, 1632, 1498, 1488, 1477, 1253.

ESI-MS (+ve) $[C_{11}H_{17}BrN]^+$: calcd 242.0539, found 242.0544.

CHN Analysis Calc. for [Pyr(C_6)Br]Br, ($C_{11}H_{17}Br_2N$): C, 40.90; H, 5.30; N, 4.34. Found C 40.73, H 5.32, N 4.38.

7.6.10. 1,6-(3-Methylimidazolium-1-yl)(pyridinium-N-yl)hexane dibromide, [Pyr(C_6)Im]2Br (Synthesised by Ryan Clark)[266]



To a solution of compound **7.6.9** (7.18 g, 22.2 mmol) in methanol (20 mL), 1-methylimidazole (3.54 mL, 44.4 mmol) was added dropwise with stirring, turning the yellow solution clear, and the reaction mixture was left stirring at room temperature for 96 h, affording a clear, yellow solution. The crude was precipitated using ethyl acetate, then dissolved in the minimal amount of methanol and precipitated using ethyl acetate again. The solution was left in the freezer overnight to afford a white flaky solid, which was filtered and dried *in vacuo* at 50 °C overnight to give a white powder (8.75 g, 97.2%).

^{1}H NMR (300 MHz, DMSO-d_6): δ 9.20 (br. s, 1 H), 9.17 - 9.13 (m, 2 H), 8.62 (tt, J = 7.8 Hz, 1.3 Hz, 1 H), 8.20 – 8.16 (m, 2 H), 7.80 (t, J = 1.8 Hz, 1 H), 7.72 (t, J = 1.8 Hz, 1 H), 4.63 (t, J = 7.4 Hz, 2 H), 4.17 (t, J = 7.2 Hz, 2 H), 3.86 (s, 3 H), 1.92 (quin, J = 7.4 Hz, 2 H), 1.78 (quin, J = 7.2 Hz, 2 H), 1.47 - 1.27 (m, 4 H);

^{13}C NMR (75 MHz, DMSO-d_6): δ 145.5, 144.7, 136.5, 128.1, 123.6, 122.2, 60.5, 48.6, 35.8, 30.4, 29.0, 24.8, 24.7.

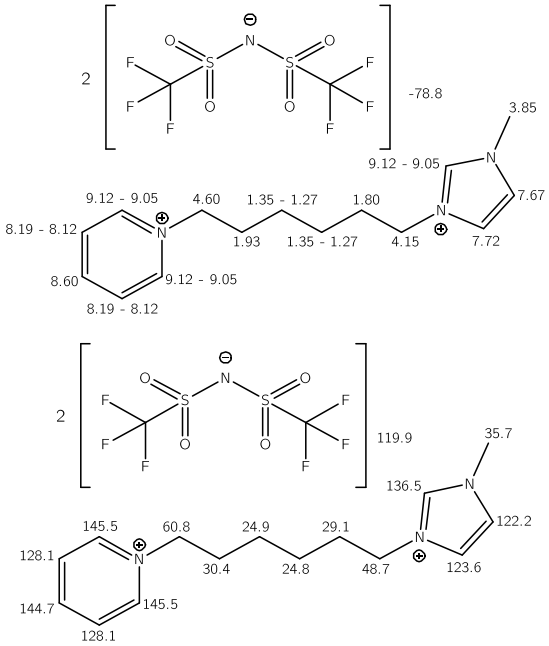
IR $\nu_{max}(CHCl_3)\cdot cm^{-1}$ 3049, 2931, 2855, 1634, 1569, 1498, 1486, 1482.

ESI-MS (+ve) $[C_{15}H_{23}N_3]^{2+}$: calcd 122.5941, found 122.5939.

CHN Analysis Calc. for [Pyr(C_6)Im]2Br·H_2O, ($C_{15}H_{26}N_3Br_2O$): C 42.57, H 5.95, N 9.93. Found C 42.23, H 5.91, N 9.81.

7.6.11. 1,6-(3-Methylimidazolium-1-yl)(pyridinium-N-yl)hexane di[bis(trifluoromethanesulfonyl)imide], Pyr(C_6)Im]2[NTf_2]

(Synthesised by Ryan Clark)[266]



Compound **7.6.10** (2.51 g, 6.21 mmol) was transferred to a round bottom flask followed by the addition of water (10 mL). $LiNTf_2$ (4.28 g, 14.9 mmol) in water (10 mL) was added and the mixture stirred at 0 °C and gradually allowed to warm up to room temperature for 24 h. Dichloromethane (20 mL) was added to recover the ionic liquid and washed with cold water (5 x 10 mL). The organic layer was collected, the solvent removed and dried *in vacuo* overnight at 50 °C. The salt (4.17 g, 83.4%) was obtained as colourless liquid.

^{1}H NMR (300 MHz, DMSO-d_6): δ 9.12 – 9.05 (m, 3 H), 8.60 (t, J = 7.8 Hz, 1 H), 8.19 – 8.12 (m, 2 H), 7.72 (t, J=1.8 Hz, 1 H), 7.67 (t, J = 1.8 Hz, 1 H), 4.60 (t, J = 7.4 Hz, 2 H), 4.15 (t, J = 7.2 Hz, 2 H), 3.85 (s, 3 H), 1.93 (quin, J = 7.4 Hz, 2 H), 1.80 (quin, J = 7.2 Hz, 2 H), 1.35 – 1.27 (m, 4 H);

^{13}C NMR (75 MHz, DMSO-d_6): δ 145.5, 144.7, 136.5, 128.1, 123.6, 122.2, 119.9 (q, $^1J_{C\text{-}F}$ = 322 Hz, 1 C), 60.8, 48.7, 35.7, 30.4, 29.1, 24.9, 24.8;

^{19}F NMR (282 MHz, DMSO-d_6) δ -78.8 (s, 6 F).

IR $\nu_{max}(CHCl_3)\cdot cm^{-1}$ 3098, 2924, 2855, 1637, 1573, 1498, 1489, 1482, 1347, 1173, 1131, 1050.

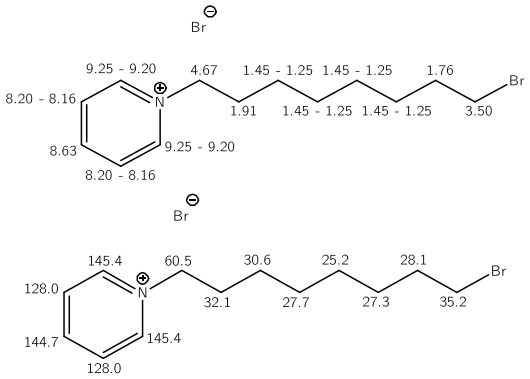
ESI-MS (+ve) $[C_{15}H_{23}N_3]^{2+}$: calcd 122.5941, found 122.5939.

ESI-MS (-ve) $[C_2F_6NO_4S_2]^-$: calcd 279.9173, found 279.9174.

CHN Analysis Calc. for [Pyr(C_6)Im]2[NTf_2], ($C_{19}H_{23}F_{12}N_5O_8S_4$): C 28.33, H 2.88, N 8.69. Found C 27.91, H 2.71, N 8.45.

7.6.12. 8-Bromooctylpyridinium bromide, [Pyr(C_8)Br]Br

(Synthesised by Ryan Clark)[266]



To pyridine (4.51 g, 57.0 mmol), a solution of 1,8-dibromooctane (49.6 g, 182 mmol) in dichloromethane (200 mL) was added dropwise with stirring. The reaction mixture was stirred at room temperature under argon for 96 h affording a cloudy layer and a viscous, milky white liquid layer. The dichloromethane was removed from the reaction mixture and the remaining mixture was dissolved in methanol, whereupon the two layers formed one homogenous, clear, colourless solution. This was then washed with hexane (10 × 50 mL) to remove unreacted 1,8-dibromooctane (Note: The methanol and hexane were miscible until a large amount of hexane was added). The excess methanol was removed in vacuo to give a viscous yellow solution and the product was dried *in vacuo* at 50 °C overnight to give a white paste that solidified into a waxy solid over 7 days (11.6 g, 57.9%).

^{1}H NMR (300 MHz, DMSO-d_6): δ 9.25 – 9.20 (m, 2 H), 8.63 (tt, J = 7.8 Hz, 1.3 Hz, 1 H), 8.20 – 8.16 (m, 2 H), 4.67 (t, J = 7.4 Hz, 2 H), 3.50 (t, J = 7.2 Hz, 2 H), 1.91 (quin, J = 7.4 Hz, 2 H), 1.76 (quin, J = 7.2 Hz, 2 H), 1.45 – 1.25 (m, 8 H);

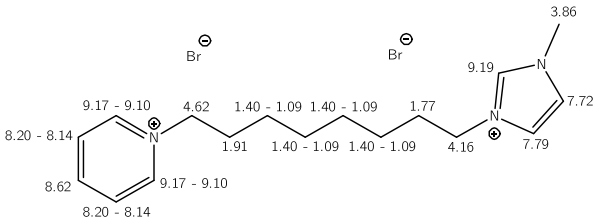
^{13}C NMR (75 MHz, DMSO-d_6): δ 145.4, 144.7, 128.0, 60.5, 35.2, 32.1, 30.6, 28.1, 27.7, 27.3, 25.2.

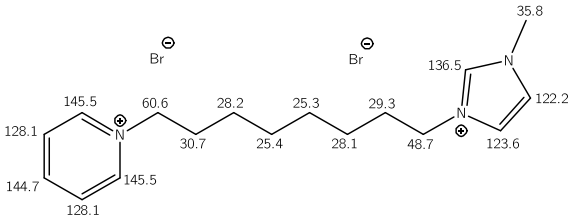
IR $\nu_{max}(CHCl_3)\cdot cm^{-1}$ 2992, 2925, 2855, 1630, 1504, 1485, 1470, 1243.

ESI-MS (+ve) $[C_{13}H_{21}BrN]^+$: calcd 270.0852, found 270.0849.

CHN Analysis Calc. for [Pyr(C_8)Br]Br, ($C_{13}H_{21}Br_2N$): C 44.47, H 6.03, N 3.99. Found C 44.40, H 6.35, N 3.86.

7.6.13. 1,8-(3-Methylimidazolium-1-yl)(pyridinium-N-yl)octane dibromide, [Pyr(C_8)Im]2Br (Synthesised by Ryan Clark)[266]





To a solution of compound **7.6.12** (8.10 g, 23.1 mmol) in methanol, 1-methylimidazole (3.68 mL, 46.2 mmol) was added dropwise with stirring. The reaction mixture was stirred for 96 h at room temperature under argon affording an orangey/yellow solution. The crude was precipitated using ethyl acetate collected by filtration, then purified by dissolving in methanol and precipitating with ethyl acetate, then leaving in the freezer overnight. The product was

collected by filtration and dried *in vacuo* at 50 °C overnight to afford a yellow powder (9.04 g, 90.4%).

^{1}H NMR (300 MHz, DMSO-d_6): δ 9.19 (s, 1 H), 9.17 – 9.10 (m, 2 H), 8.62 (tt, J = 7.8 Hz, 1.3 Hz, 1 H), 8.20 – 8.14 (m, 2 H), 7.79 (t, J = 1.8 Hz, 1 H), 7.72 (t, J = 1.8 Hz, 1 H), 4.62 (t, J = 7.4 Hz, 2 H), 4.16 (t, J = 7.2 Hz, 2 H), 3.86 (s, 3 H), 1.91 (quin, J = 7.4 Hz, 2 H), 1.77 (quin, J = 7.2 Hz, 2 H), 1.40 – 1.09 (m, 8 H);

^{13}C NMR (75 MHz, DMSO-d_6): δ 145.5, 144.7, 136.5, 128.1, 123.6, 122.2, 60.6, 48.7, 35.8, 30.7, 29.3, 28.2, 28.1, 25.4, 25.3.

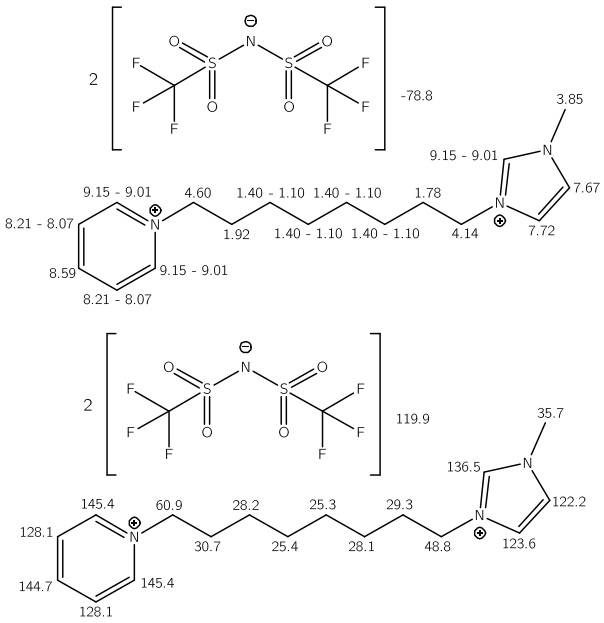
IR $\nu_{max}(CHCl_3)\cdot cm^{-1}$ 3025, 2924, 2852, 1631, 1562, 1503, 1483, 1469.

ESI-MS (+ve) $[C_{17}H_{27}N_3]^{2+}$: calcd 136.6097, found 136.6096.

CHN Analysis Calc. for [Pyr(C_6)Im]2Br, ($C_{17}H_{27}Br_2N_3$): C 47.13, H 6.28, N 9.70. Found C 46.84, H 6.58, N 9.56.

7.6.14. 1,8-(3-Methylimidazolium-1-yl)(pyridinium-N-yl)octane di[bis(trifluoromethanesulfonyl)imide], [Pyr(C_8)Im]2[NTf_2]

(Synthesised by Ryan Clark)[266]



Compound **7.6.13** (2.60 g, 6.00 mmol) was transferred to a round bottom flask followed by the addition of water (5 mL). $LiNTf_2$ (4.13 g, 14.4 mmol) in water (5 mL) was added and the mixture stirred at 0 °C and gradually allowed to warm up to room temperature for 24 h. Dichloromethane (10 mL) was added to recover the ionic liquid and washed with cold water (5 x 5 mL). The organic layer was collected, the solvent removed and dried *in vacuo* overnight at 50 °C. The salt (4.12 g, 82.3%) was obtained as white glass-like solid.

^{1}H NMR (300 MHz, DMSO-d_6): δ 9.15 - 9.01 (m, 3 H), 8.59 (tt, J = 7.8, 1.3 Hz, 1 H), 8.21 – 8.07 (m, 2 H), 7.72 (t, J = 1.8 Hz, 1 H), 7.67 (t, J = 1.8 Hz, 1 H), 4.60 (t, J = 7.4 Hz, 2 H), 4.14 (t, J = 7.2 Hz, 2 H), 3.85 (s, 3 H), 1.92 (quin, J = 7.4 Hz, 2 H), 1.78 (quin, J = 7.2 Hz, 2 H), 1.40 – 1.10 (m, 8 H);

^{13}C NMR (75 MHz, DMSO-d_6): δ 145.4, 144.7, 136.5, 128.1, 123.6, 122.2, 119.9 (q, $^1J_{C\text{-}F}$ = 322 Hz, 1 C), 60.9, 48.8, 35.7, 30.7, 29.3, 28.2, 28.1, 25.4, 25.3;

^{19}F NMR (282 MHz, DMSO-d_6) δ -78.8 (s, 6 F).

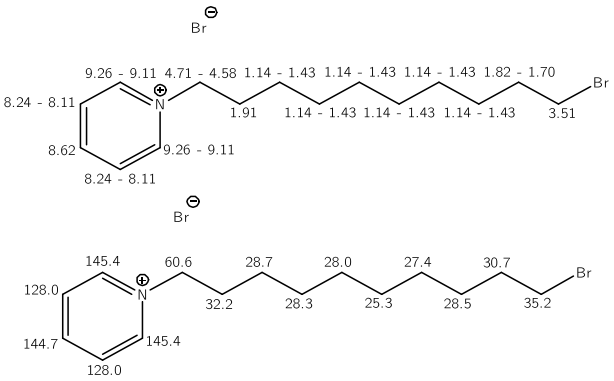
IR $\nu_{max}(CHCl_3)\cdot cm^{-1}$ 3094, 2938, 2855, 1636, 1570, 1503, 1492, 1470, 1326, 1172, 1133, 1051.

ESI-MS (+ve) $[C_{17}H_{27}N_3]^{2+}$: calcd 136.6097, found 136.6096.

ESI-MS (-ve) $[C_2F_6NO_4S_2]^-$: calcd 279.9173, found 279.9173.

CHN Analysis Calc. for [Pyr(C_8)Im]2[NTf_2], ($C_{21}H_{27}F_{12}N_5O_8S_4$): C 30.25, H 3.26, N 8.40. Found C 29.97, H 3.03, N 7.99.

7.6.15. 10-Bromodecylpyridinium bromide, [Pyr(C_{10})Br]Br



To pyridine (4.33 g, 54.8 mmol), a solution of 1,10-dibromodecane (82.2 g, 274 mmol) in dichloromethane (200 mL) was added dropwise with stirring. The reaction mixture was stirred at room temperature under argon for 96 h affording a cloudy layer and a viscous, milky white liquid layer. The dichloromethane was removed from the reaction mixture and the remaining mixture was dissolved in methanol, whereupon the two layers formed one homogenous, clear, colourless solution. This was then washed with hexane (10 × 50 mL) to remove unreacted 1,10-dibromodecane. The excess methanol was removed in vacuo to give a viscous yellow solution and the product was dried *in vacuo* at 50 °C overnight to give a white powder (12.5 g, 62.4%).

^{1}H NMR (300 MHz, DMSO-d_6): δ 9.26 – 9.11 (m, 2 H), 8.62 (tt, J = 7.8, 1.3 Hz, 1 H), 8.24 – 8.11 (m, 2 H), 4.71 - 4.58 (m, 2 H), 3.51 (t, J = 7.2 Hz, 2 H), 1.91 (quin, J = 7.4 Hz, 2 H), 1.82 – 1.70 (m, 2 H), 1.43 – 1.14 (m, 12 H);

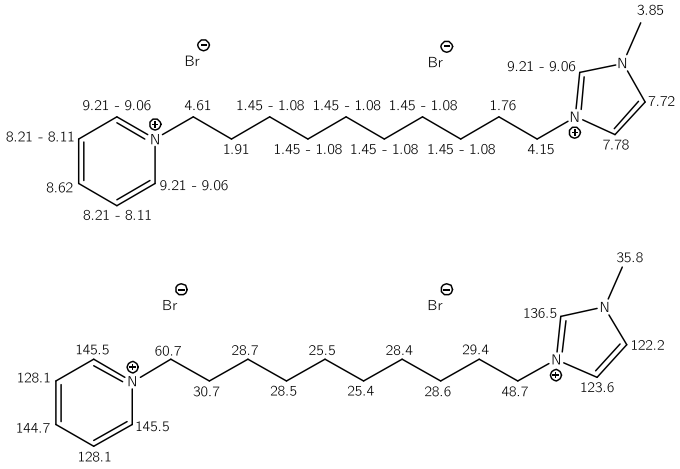
^{13}C NMR (75 MHz, DMSO-d_6): δ 145.4, 144.7, 128.0, 60.6, 35.2, 32.2, 30.7, 28.7, 28.6, 28.5, 28.3, 28.0, 27.4, 25.3.

IR $\nu_{max}(CHCl_3)\cdot cm^{-1}$ 2986, 2921, 2857, 1650, 1507, 1490, 1475, 1245.

ESI-MS (+ve) $[C_{15}H_{25}BrN]^+$: calcd 298.1165, found 298.1159.

CHN Analysis Calc. for [Pyr(C_{10})Br]Br, ($C_{15}H_{25}Br_2N$): C 47.51, H 6.65, N 3.69. Found C 47.73, H 6.45, N 3.82.

7.6.16. 1,10-(3-Methylimidazolium-1-yl)(pyridinium-N-yl)decane dibromide, [Pyr(C_{10})Im]2Br



To a solution of compound **7.6.15** (15.9 g, 43.6 mmol) in methanol, 1-methylimidazole (6.95 mL, 87.1 mmol) was added dropwise with stirring. The reaction mixture was stirred for 96 h at room temperature under argon affording an orangey/yellow solution. The crude was precipitated using ethyl acetate collected by filtration, then purified by dissolving in methanol and precipitating with ethyl acetate, then leaving in the freezer overnight. The product was collected by filtration and dried *in vacuo* at 50 °C overnight to afford a white powder (14.6 g, 73.0%).

^{1}H NMR (300 MHz, DMSO-d_6): δ 9.21 – 9.06 (m, 3 H), 8.62 (tt, J = 7.8, 1.3 Hz, 1 H), 8.21 – 8.11 (m, 2 H), 7.78 (t, J = 1.8 Hz, 1 H), 7.72 (t, J = 1.8 Hz,

1 H), 4.61 (t, J = 7.4 Hz, 2 H), 4.15 (t, J = 7.2 Hz, 2 H), 3.85 (s, 3 H), 1.91 (quin, J = 7.4 Hz, 2 H), 1.76 (quin, J = 7.2 Hz, 2 H), 1.45 – 1.08 (m, 12 H);

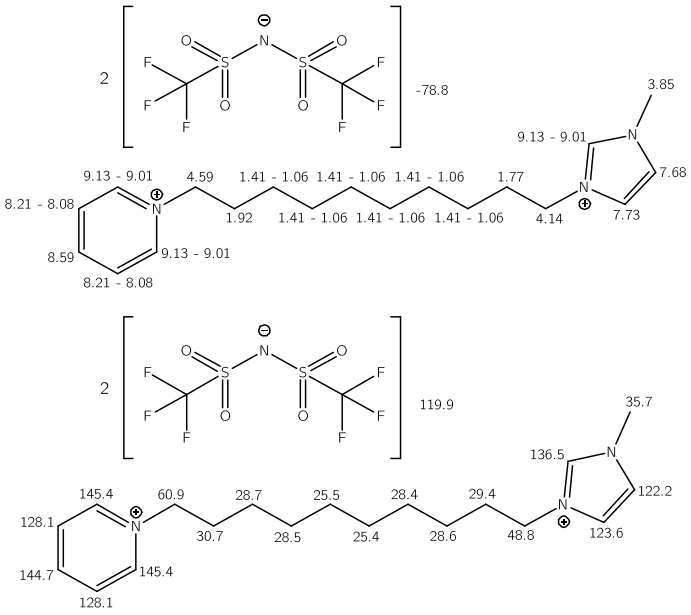
^{13}C NMR (75 MHz, DMSO-d_6): δ 145.5, 144.7, 136.5, 128.1, 123.6, 122.2, 60.7, 48.7, 35.8, 30.7, 29.4, 28.7, 28.4, 25.5, 25.4.

IR $\nu_{max}(CHCl_3)\cdot cm^{-1}$ 3027, 2921, 2848, 1638, 1561, 1509, 1487, 1462.

ESI-MS (+ve) $[C_{19}H_{31}N_3]^{2+}$: calcd 150.6254, found 150.6262.

CHN Analysis Calc. for [Pyr(C_{10})Im]2Br, ($C_{19}H_{31}Br_2N_3$): C 49.47, H 6.77, N 9.11. Found C 49.22, H 6.53, N 9.43.

7.6.17. 1,10-(3-Methylimidazolium-1-yl)(pyridinium-N-yl)decane di[bis(trifluoromethanesulfonyl)imide], [Pyr(C_{10})Im]2[NTf_2]



Compound **7.6.16** (2.67 g, 5.81 mmol) was transferred to a round bottom flask followed by the addition of water (5 mL). $LiNTf_2$ (4.00 g, 13.9 mmol) in water (5 mL) was added and the mixture stirred at 0 °C and gradually allowed to warm up to room temperature for 24 h. Dichloromethane (10 mL) was added to recover the ionic liquid and washed with cold water (5 x 5 mL). The organic

layer was collected, the solvent removed and dried *in vacuo* overnight at 50 °C. The salt (4.90 g, 97.9%) was obtained as colourless liquid.

^{1}H NMR (300 MHz, DMSO-d_6): δ 9.13 – 9.01 (m, 3 H), 8.59 (tt, J = 7.8, 1.3 Hz, 1 H), 8.21 – 8.08 (m, 2 H), 7.73 (t, J = 1.8 Hz, 1 H), 7.68 (t, J = 1.8 Hz, 1 H), 4.59 (t, J = 7.4 Hz, 2 H), 4.14 (t, J = 7.2 Hz, 2 H), 3.85 (s, 3 H), 1.92 (quin, J = 7.4 Hz, 2 H), 1.77 (quin, J = 7.2 Hz, 2 H), 1.41 – 1.06 (m, 12 H);

^{13}C NMR (75 MHz, DMSO-d_6): δ 145.4, 144.7, 136.5, 128.1, 123.6, 122.2, 119.9 (q, $^{1}J_{C\text{-}F}$ = 322 Hz, 1 C), 60.9, 48.8, 35.7, 30.7, 29.4, 28.7, 28.6, 28.5, 28.4, 25.5, 25.4;

^{19}F NMR (282 MHz, DMSO-d_6) δ -78.8 (s, 6 F).

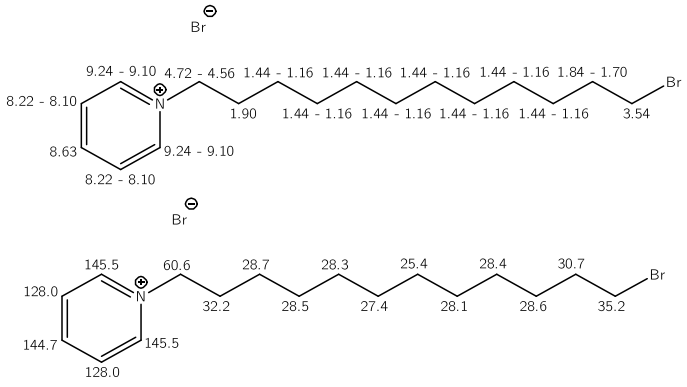
IR $\nu_{max}(CHCl_3)\cdot cm^{-1}$ 3090, 2934, 2857, 1630, 1574, 1507, 1499, 1473, 1321, 1170, 1135, 1055.

ESI-MS (+ve) $[C_{19}H_{31}N_3]^{2+}$: calcd 150.6254, found 150.6264.

ESI-MS (-ve) $[C_2F_6NO_4S_2]^-$: calcd 279.9173, found 279.9183.

CHN Analysis Calc. for [Pyr(C_{10})Im]2[NTf_2], ($C_{23}H_{31}F_{12}N_5O_8S_4$): C 32.06, H 3.63, N 8.13. Found C 31.87, H 3.51, N 7.97.

7.6.18. 12-Bromododecylpyridinium bromide, [Pyr(C_{12})Br]Br



To pyridine (3.88 g, 49.1 mmol), a solution of 1,12-dibromododecane (80.6 g, 246 mmol) in dichloromethane (200 mL) was added dropwise with stirring. The

reaction mixture was stirred at room temperature under argon for 96 h affording a cloudy layer and a viscous, milky white liquid layer. The dichloromethane was removed from the reaction mixture and the remaining mixture was dissolved in methanol, whereupon the two layers formed one homogenous, clear, colourless solution. This was then washed with hexane (10 × 50 mL) to remove unreacted 1,12-dibromododecane. The excess methanol was removed in vacuo to give a viscous yellow solution and the product was dried *in vacuo* at 50 °C overnight to give a white powder (12.6 g, 63.2%).

^{1}H NMR (300 MHz, DMSO-d_6): δ 9.24 – 9.10 (m, 2 H), 8.63 (tt, J = 7.8, 1.3 Hz, 1 H), 8.22 – 8.10 (m, 2 H), 4.72 - 4.56 (m, 2 H), 3.54 (t, J = 7.2 Hz, 2 H), 1.90 (quin, J = 7.4 Hz, 2 H), 1.84 – 1.70 (m, 2 H), 1.44 - 1.16 (m, 16 H);

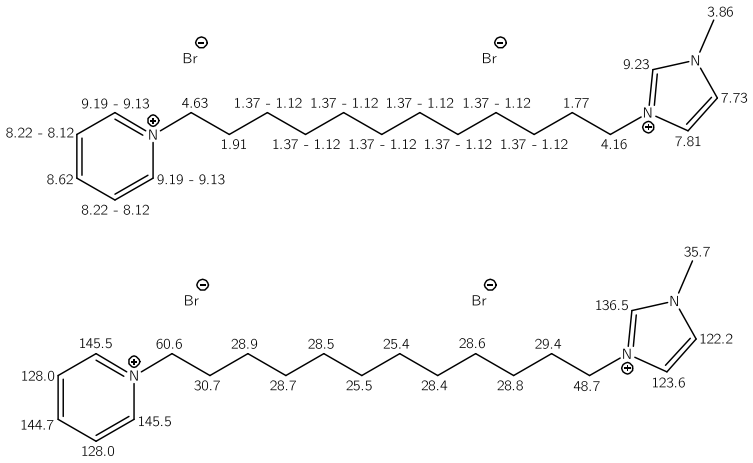
^{13}C NMR (75 MHz, DMSO-d_6): δ 145.5, 144.7, 128.0, 60.6, 35.2, 32.2, 30.7, 28.7, 28.6, 28.5, 28.4, 28.3, 28.1, 27.4, 25.4.

IR $\nu_{max}(CHCl_3)\cdot cm^{-1}$ 2983, 2920, 2855, 1654, 1509, 1492, 1477, 1243.

ESI-MS (+ve) $[C_{17}H_{29}BrN]^+$: calcd 326.1478, found 326.1488.

CHN Analysis Calc. for [Pyr(C_{12})Br]Br, ($C_{17}H_{29}Br_2N$): C 50.14, H 7.18, N 3.44. Found C 50.33, H 7.04, N 3.55.

7.6.19. 1,12-(3-Methylimidazolium-1-yl)(pyridinium-N-yl)dodecane dibromide, [Pyr(C_{12})Im]2Br



To a solution of compound **7.6.18** (16.6 g, 40.9 mmol) in methanol, 1-methylimidazole (6.71 g, 81.7 mmol) was added dropwise with stirring. The reaction mixture was stirred for 96 h at room temperature under argon affording an orangey/yellow solution. The crude was precipitated using ethyl acetate collected by filtration, then purified by dissolving in methanol and precipitating with ethyl acetate, then leaving in the freezer overnight. The product was collected by filtration and dried *in vacuo* at 50 °C overnight to afford a yellow/orange solid (14.4 g, 71.8%).

^{1}H NMR (300 MHz, DMSO-d_6): δ 9.23 (br. s, 1H), 9.19 – 9.13 (m, 2 H), 8.62 (tt, J = 7.8, 1.3 Hz, 1 H), 8.22 – 8.12 (m, 2 H), 7.81 (t, J = 1.8 Hz, 1 H), 7.73 (t, J = 1.8 Hz, 1 H), 4.63 (t, J = 7.4 Hz, 2 H), 4.16 (t, J = 7.2 Hz, 2 H), 3.86 (s, 3 H), 1.91 (quin, J = 7.4 Hz, 2 H), 1.77 (quin, J = 7.2 Hz, 2 H), 1.37 – 1.12 (m, 16 H);

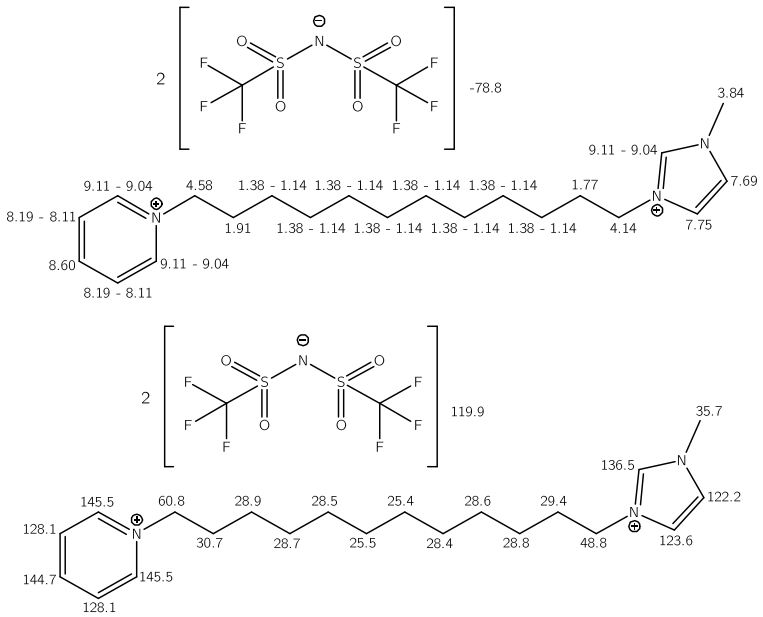
^{13}C NMR (75 MHz, DMSO-d_6): δ 145.5, 144.7, 136.5, 128.0, 123.6, 122.2, 60.6, 48.7, 35.7, 30.7, 29.4, 28.9, 28.8, 28.7, 28.6, 28.5, 28.4, 25.5, 25.4;

IR $\nu_{max}(CHCl_3)\cdot cm^{-1}$ 3023, 2927, 2842, 1639, 1564, 1503, 1480, 1466.

ESI-MS (+ve) $[C_{21}H_{35}N_3]^{2+}$: calcd 164.6410, found 164.6420.

CHN Analysis Calc. for [Pyr(C_{12})Im]2Br, ($C_{21}H_{35}Br_2N_3$): C 51.55, H 7.21, N 8.59. Found C 51.23, H 6.97, N 8.80.

7.6.20. 1,12-(3-Methylimidazolium-1-yl)(pyridinium-N-yl)dodecane di[bis(trifluoromethanesulfonyl)imide], [Pyr(C_{12})Im]2[NTf_2]



Compound **7.6.19** (2.65 g, 5.62 mmol) was transferred to a round bottom flask followed by the addition of water (5 mL). $LiNTf_2$ (3.87 g,13.5 mmol) in water (5 mL) was added and the mixture stirred at 0 °C and gradually allowed to warm up to room temperature for 24 h. Dichloromethane (10 mL) was added to recover the ionic liquid and washed with cold water (5 x 5 mL). The organic layer was collected, the solvent removed and dried *in vacuo* overnight at 50 °C. The salt (4.72 g, 94.3%) was obtained as colourless liquid.

^{1}H NMR (300 MHz, DMSO-d_6): δ 9.11 – 9.04 (m, 3 H), 8.60 (tt, J = 7.8, 1.3 Hz, 1 H), 8.19 – 8.11 (m, 2 H), 7.75 (t, J = 1.8 Hz, 1 H), 7.69 (t, J = 1.8 Hz, 1 H), 4.58 (t, J = 7.4 Hz, 2 H), 4.14 (t, J = 7.2 Hz, 2 H), 3.84 (s, 3 H), 1.91 (quin, J = 7.4 Hz, 2 H), 1.77 (quin, J = 7.2 Hz, 2 H), 1.38 – 1.14 (m, 16 H);

^{13}C NMR (75 MHz, DMSO-d_6): δ 145.5, 144.7, 136.5, 128.1, 123.6, 122.2, 119.9 (q, $^{1}J_{C\text{-}F}$ = 322 Hz, 1 C), 60.8, 48.8, 35.7, 30.7, 29.4, 28.9, 28.8, 28.7, 28.6, 28.5, 28.4, 25.5, 25.4;

^{19}F NMR (282 MHz, DMSO-d_6) δ -78.8 (s, 6 F).

IR $\nu_{max}(CHCl_3)\cdot cm^{-1}$ 3091, 2933, 2850, 1634, 1572, 1505, 1489, 1477, 1320, 1177, 1140, 1060.

ESI-MS (+ve) $[C_{21}H_{35}N_3]^{2+}$: calcd 164.6410, found 164.6413.

ESI-MS (-ve) $[C_2F_6NO_4S_2]^-$: calcd 279.9173, found 279.9180.

CHN Analysis Calc. for [Pyr(C_{12})Im]2[NTf_2], ($C_{25}H_{35}F_{12}N_5O_8S_4$): C 33.75, H 3.96, N 7.87. Found C 33.76, H 3.87, N 7.92.

References

1. M. Deetlefs, M. Fanselow and K. R. Seddon, *RSC Adv.*, 2016, **6**, 4280-4288.
2. A. Pádua, *Impact*, 2016, **Volume 2016**, 14-16.
3. R. Giernoth, *Solvents and Solvent Effects in Organic Chemistry*, Ed. by Reichardt, C. and Welton, T., Wiley-VCH, Weinheim, 4th edn., 2011.
4. G. Wypych, *Handbook of Solvents*, ChemTec Publishing, Ontario, Canada, 2001.
5. R. Hayes, G. G. Warr and R. Atkin, *Chem. Rev.*, 2015, **115**, 6357-6426.
6. T. Head-Gordon and G. Hura, *Chem. Rev.*, 2002, **102**, 2651-2669.
7. A. K. Soper, *Pure Appl. Chem.*, 2010, **82**, 1855-1867.
8. F. Paesani and G. A. Voth, *J. Phys. Chem. B*, 2009, **113**, 5702-5719.
9. T. F. Headen, C. A. Howard, N. T. Skipper, M. A. Wilkinson, D. T. Bowron and A. K. Soper, *J. Am. Chem. Soc.*, 2010, **132**, 5735-5742.
10. R. Böhmer, C. Gainaru and R. Richert, *Phys. Rep.*, 2014, **545**, 125-195.
11. V. A. Parsegian, *Van der Waals Forces: A Handbook for Biologists, Chemists, Engineers, and Physicists*, Cambridge University Press, New York, 2005.
12. A. Ray, *Nature*, 1971, **231**, 313-315.
13. J. Mahanty and B. W. Ninham, *Dispersion Forces*, Academic Press, London, 1976.
14. G. A. Jeffrey, *An Introduction to Hydrogen Bonding*, Oxford University Press, New York, 1997.
15. P. Metrangolo and G. Resnati, *Halogen Bonding: Fundamentals and Applications*, Springer, Berlin, 2008.
16. R. M. Cuéllar-Franca, P. García Gutiérrez, S. F. R. Taylor, C. Hardacre and A. Azapagic, *Faraday Discuss.*, 2016, **192**, 283-301.
17. M. C. Bubalo, K. Radošević, I. R. Redovniković, J. Halambek and V. G. Srček, *Ecotoxicol. Environ. Saf.*, 2014, **99**, 1-12.
18. Y. Zhang, B. R. Bakshi and E. S. Demessie, *Environ. Sci. Technol.*, 2008, **42**, 1724-1730.
19. M. Freemantle, *Chem. Eng. News*, 2003, **81**, 9.
20. CEN, Chevron embraces ionic liquids, [online], http://cen.acs.org/articles/94/i39/Chevron-embraces-ionic-liquids.html?type=paidArticleContent, (accessed 22 May 2017).
21. Honeywell, Introduces Ionic Liquids Alkylation Technology, [online], https://www.uop.com/?press_release=honeywell-uop-introduces-ionic-liquids, (accessed 22 May 2017).
22. NASA, Liquid Mirror Telescopes on the Moon, [online], https://science.nasa.gov/science-news/science-at-nasa/2008/09oct_liquidmirror, (accessed 9 January 2017).

23. L. Chen, M. Sharifzadeh, N. M. Dowell, T. Welton, N. Shah and J. P. Hallett, *Green Chem.*, 2014, **16**, 3098-3106.
24. H. Weingärtner, *Angew. Chem. Int. Ed.*, 2008, **47**, 654-670.
25. E. W. Castner, C. J. Margulis, M. Maroncelli and J. F. Wishart, *Annu. Rev. Phys. Chem.*, 2011, **62**, 85-105.
26. P. Wasserscheid and T. Welton, *Ionic Liquids in Synthesis*, Wiley-VCH, Weinheim, 2nd edn., 2008.
27. J. P. Hallett and T. Welton, *Chem. Rev.*, 2011, **111**, 3508-3576.
28. R. Sharma and R. K. Mahajan, *RSC Adv.*, 2014, **4**, 748-774.
29. M. J. Earle, S. P. Katdare and K. R. Seddon, *Org. Lett.*, 2004, **6**, 707-710.
30. I. López-Martin, E. Burello, P. N. Davey, K. R. Seddon and G. Rothenberg, *ChemPhysChem*, 2007, **8**, 690-695.
31. A. E. Bradley, C. Hardacre, J. D. Holbrey, S. Johnston, S. E. J. McMath and M. Nieuwenhuyzen, *Chem. Mater.*, 2002, **14**, 629-635.
32. S. V. Dzyuba and R. A. Bartsch, *ChemPhysChem*, 2002, **3**, 161-166.
33. C. M. Gordon, J. D. Holbrey, A. R. Kennedy and K. R. Seddon, *J. Mater. Chem.*, 1998, **8**, 2627-2636.
34. S. M. Murray, R. A. O'Brien, K. M. Mattson, C. Ceccarelli, R. E. Sykora, K. N. West and J. H. Davis, *Angew. Chem. Int. Ed.*, 2010, **49**, 2755-2758.
35. M. Sinensky, *Proc. Natl. Acad. Sci. USA*, 1974, **71**, 522-525.
36. R. Ernst, C. S. Ejsing and B. Antonny, *J. Mol. Biol.*, 2016, **428**, 4776-4791.
37. J. Ranke, S. Stolte, R. Störmann, J. Arning and B. Jastorff, *Chem. Rev.*, 2007, **107**, 2183-2206.
38. G. H. Tao, L. He, N. Sun and Y. Kou, *Chem. Commun.*, 2005, 3562-3564.
39. K. Fukumoto, M. Yoshizawa and H. Ohno, *J. Am. Chem. Soc.*, 2005, **127**, 2398-2399.
40. L. Chen, G. E. Mullen, M. Le Roch, C. G. Cassity, N. Gouault, H. Y. Fadamiro, R. E. Barletta, R. A. O'Brien, R. E. Sykora, A. C. Stenson, K. N. West, H. E. Horne, J. M. Hendrich, K. R. Xiang and J. H. Davis, *Angew. Chem. Int. Ed.*, 2014, **53**, 11762-11765.
41. Z. J. Chen, Y. N. Huo, J. Cao, L. Xu and S. G. Zhang, *Ind. Eng. Chem. Res.*, 2016, **55**, 11589-11596.
42. R. A. Braun, J. L. Bradfield, C. B. Henderson, N. Mobarrez, Y. H. Sheng, R. A. O'Brien, A. C. Stenson, J. H. Davis and A. Mirjafari, *Green Chem.*, 2015, **17**, 1259-1268.
43. R. A. O'Brien, A. Mirjafari, K. M. Mattson, S. M. Murray, N. Mobarrez, E. A. Salter, A. Wierzbicki, J. H. Davis and K. N. West, *J. Phys. Chem. B*, 2014, **118**, 10232-10239.
44. X. H. Li, D. B. Zhao, Z. F. Fei and L. F. Wang, *Sci. China Ser. B Chem.*, 2006, **49**, 385-401.

45. A. F. M. Cláudio, L. Swift, J. P. Hallett, T. Welton, J. A. P. Coutinho and M. G. Freire, *Phys. Chem. Chem. Phys.*, 2014, **16**, 6593-6601.
46. M. M. Pereira, K. A. Kurnia, F. L. Sousa, N. J. O. Silva, J. A. Lopes-da-Silva, J. A. P. Coutinho and M. G. Freire, *Phys. Chem. Chem. Phys.*, 2015, **17**, 31653-31661.
47. C. S. Santos and S. Baldelli, *Chem. Soc. Rev.*, 2010, **39**, 2136-2145.
48. H.-P. Steinrück, J. Libuda, P. Wasserscheid, T. Cremer, C. Kolbeck, M. Laurin, F. Maier, M. Sobota, P. S. Schulz and M. Stark, *Adv. Mater.*, 2011, **23**, 2571-2587.
49. K. R. J. Lovelock, I. J. Villar-Garcia, F. Maier, H.-P. Steinrück and P. Licence, *Chem. Rev.*, 2010, **110**, 5158-5190.
50. C. Aliaga, G. A. Baker and S. Baldelli, *J. Phys. Chem. B*, 2008, **112**, 1676-1684.
51. C. Aliaga and S. Baldelli, *J. Phys. Chem. B*, 2006, **110**, 18481-18491.
52. C. Aliaga, C. S. Santos and S. Baldelli, *Phys. Chem. Chem. Phys.*, 2007, **9**, 3683-3700.
53. S. Rivera-Rubero and S. Baldelli, *J. Phys. Chem. B*, 2006, **110**, 4756-4765.
54. C. S. Santos and S. Baldelli, *J. Phys. Chem. B*, 2007, **111**, 4715-4723.
55. C. S. Santos and S. Baldelli, *J. Phys. Chem. B*, 2009, **113**, 923-933.
56. C. S. Santos, S. Rivera-Rubero, S. Dibrov and S. Baldelli, *J. Phys. Chem. C*, 2007, **111**, 7682-7691.
57. T. Iimori, T. Iwahashi, K. Kanai, K. Seki, J. H. Sung, D. Kim, H. O. Hamaguchi and Y. Ouchi, *J. Phys. Chem. B*, 2007, **111**, 4860-4866.
58. Y. Jeon, J. Sung, W. Bu, D. Vaknin, Y. Ouchi and D. Kim, *J. Phys. Chem. C*, 2008, **112**, 19649-19654.
59. J. Bowers, M. C. Vergara-Gutierrez and J. R. P. Webster, *Langmuir*, 2004, **20**, 309-312.
60. E. Sloutskin, B. M. Ocko, L. Tamam, I. Kuzmenko, T. Gog and M. Deutsch, *J. Am. Chem. Soc.*, 2005, **127**, 7796-7804.
61. V. Halka, R. Tsekov and W. Freyland, *Phys. Chem. Chem. Phys.*, 2005, **7**, 2038-2043.
62. M. G. Freire, P. J. Carvalho, A. M. Fernandes, I. M. Marrucho, A. J. Queimada and J. A. P. Coutinho, *J. Colloid Interface Sci.*, 2007, **314**, 621-630.
63. W. Jiang, Y. T. Wang, T. Y. Yan and G. A. Voth, *J. Phys. Chem. C*, 2008, **112**, 1132-1139.
64. W. Jiang, T. Y. Yan, Y. T. Wang and G. A. Voth, *J. Phys. Chem. B*, 2008, **112**, 3121-3131.
65. R. M. Lynden-Bell and M. G. Del Pópolo, *Phys. Chem. Chem. Phys.*, 2006, **8**, 949-954.
66. R. M. Lynden-Bell, M. G. Del Pópolo , T. G. A. Youngs, J. Kohanoff, C. G. Hanke, J. B. Harper and C. C. Pinilla, *Acc. Chem. Res.*, 2007, **40**, 1138-1145.

67. N. Sieffert and G. Wipff, *J. Phys. Chem. C*, 2008, **112**, 6450-6461.
68. N. Sieffert and G. Wipff, *J. Phys. Chem. C*, 2008, **112**, 19590-19603.
69. T. M. Chang and L. X. Dang, *J. Phys. Chem. A*, 2009, **113**, 2127-2135.
70. K. R. J. Lovelock, *Phys. Chem. Chem. Phys.*, 2012, **14**, 5071-5089.
71. O. Höfft, S. Bahr, M. Himmerlich, S. Krischok, J. A. Schaefer and V. Kempter, *Langmuir*, 2006, **22**, 7120-7123.
72. S. Krischok, M. Eremtchenko, M. Himmerlich, P. Lorenz, J. Uhlig, A. Neumann, R. Öttking, W. J. D. Beenken, O. Höfft, S. Bahr, V. Kempter and J. A. Schaefer, *J. Phys. Chem. B*, 2007, **111**, 4801-4806.
73. S. Krischok, R. Öttking, W. J. D. Beenken, M. Himmerlich, P. Lorenz, O. Höfft, S. Bahr, V. Kempter and J. A. Schaefer, *Z. Phys. Chem.*, 2006, **220**, 1407-1416.
74. E. F. Smith, F. J. M. Rutten, I. J. Villar-Garcia, D. Briggs and P. Licence, *Langmuir*, 2006, **22**, 9386-9392.
75. E. F. Smith, I. J. Villar-Garcia, D. Briggs and P. Licence, *Chem. Commun.*, 2005, 5633-5635.
76. S. Caporali, U. Bardi and A. Lavacchi, *J. Electron Spectrosc. Relat. Phenom.*, 2006, **151**, 4-8.
77. J. M. Gottfried, F. Maier, J. Rossa, D. Gerhard, P. S. Schulz, P. Wasserscheid and H.-P. Steinrück, *Z. Phys. Chem.*, 2006, **220**, 1439-1453.
78. F. Maier, T. Cremer, C. Kolbeck, K. R. J. Lovelock, N. Paape, P. S. Schulz, P. Wasserscheid and H.-P. Steinrück, *Phys. Chem. Chem. Phys.*, 2010, **12**, 1905-1915.
79. F. Maier, J. M. Gottfried, J. Rossa, D. Gerhard, P. S. Schulz, W. Schwieger, P. Wasserscheid and H.-P. Steinrück, *Angew. Chem. Int. Ed.*, 2006, **45**, 7778-7780.
80. D. S. Silvester, T. L. Broder, L. Aldous, C. Hardacre, A. Crossley and R. G. Compton, *Analyst*, 2007, **132**, 196-198.
81. V. Lockett, R. Sedev, C. Bassell and J. Ralston, *Phys. Chem. Chem. Phys.*, 2008, **10**, 1330-1335.
82. C. Kolbeck, T. Cremer, K. R. J. Lovelock, N. Paape, P. S. Schulz, P. Wasserscheid, F. Maier and H.-P. Steinrück *J. Phys. Chem. B*, 2009, **113**, 8682-8688.
83. C. Kolbeck, M. Killian, F. Maier, N. Paape, P. Wasserscheid and H.-P. Steinrück, *Langmuir*, 2008, **24**, 9500-9507.
84. C. Kolbeck, J. Lehmann, K. R. J. Lovelock, T. Cremer, N. Paape, P. Wasserscheid, A. P. Fröba, F. Maier and H.-P. Steinrück, *J. Phys. Chem. B*, 2010, **114**, 17025-17036.
85. C. Kolbeck, I. Niedermaier, N. Taccardi, P. S. Schulz, F. Maier, P. Wasserscheid and H.-P. Steinrück, *Angew. Chem. Int. Ed.*, 2012, **51**, 2610-2613.
86. N. Paape, W. Wei, A. Bösmann, C. Kolbeck, F. Maier, H.-P. Steinrück, P. Wasserscheid and P. S. Schulz, *Chem. Comm.*, 2008, 3867-3869.

87. T. Cremer, M. Killian, J. M. Gottfried, N. Paape, P. Wasserscheid, F. Maier and H.-P. Steinrück, *ChemPhysChem*, 2008, **9**, 2185-2190.
88. T. Cremer, C. Kolbeck, K. R. J. Lovelock, N. Paape, R. Wölfel , P. S. Schulz, P. Wasserscheid, H. Weber, J. Thar, B. Kirchner, F. Maier and H.-P. Steinrück *Chem. - Eur. J.*, 2010, **16**, 9018-9033.
89. T. Cremer, M. Stark, A. Deyko, H.-P. Steinrück and F. Maier, *Langmuir*, 2011, **27**, 3662-3671.
90. V. Lockett, R. Sedev, S. Harmer, J. Ralston, M. Horne and T. Rodopoulos, *Phys. Chem. Chem. Phys.*, 2010, **12**, 13816-13827.
91. F. Maier, *Angew. Chem. Int. Ed.*, 2011, **50**, 10133-10134.
92. T. Nishi, T. Iwahashi, H. Yamane, Y. Ouchi, K. Kanai and K. Seki, *Chem. Phys. Lett.*, 2008, **455**, 213-217.
93. K. Nakajima, A. Ohno, M. Suzuki and K. Kimura, *Nucl. Instrum. Methods Phys. Res. Sect. B.*, 2009, **267**, 605-609.
94. A. W. Taylor, F. L. Qiu, I. J. Villar-Garcia and P. Licence, *Chem. Comm.*, 2009, 5817-5819.
95. K. R. J. Lovelock, E. F. Smith, A. Deyko, I. J. Villar-Garcia, P. Licence and R. G. Jones, *Chem. Commun.*, 2007, 4866-4868.
96. F. L. Qiu, A. W. Taylor, S. Men, I. J. Villar-Garcia and P. Licence, *Phys. Chem. Chem. Phys.*, 2010, **12**, 1982-1990.
97. R. Wibowo, L. Aldous, R. M. J. Jacobs, N. S. A. Manan and R. G. Compton, *Chem. Phys. Lett.*, 2011, **509**, 72-76.
98. D. Weingarth, A. Foelske-Schmitz, A. Wokaun and R. Kötz, *Electrochem. Commun.*, 2011, **13**, 619-622.
99. H.-P. Steinrück, *Phys. Chem. Chem. Phys.*, 2012, **14**, 5010-5029.
100. M. J. Earle, C. M. Gordon, N. V. Plechkova, K. R. Seddon and T. Welton, *Anal. Chem.*, 2007, **79**, 758-764.
101. K. R. Seddon, A. Stark and M. J. Torres, *Pure Appl. Chem.*, 2000, **72**, 2275-2287.
102. A. W. Taylor, K. R. J. Lovelock, A. Deyko, P. Licence and R. G. Jones, *Phys. Chem. Chem. Phys.*, 2010, **12**, 1772-1783.
103. K. R. J. Lovelock, Ph.D. Thesis, University of Nottingham, 2008.
104. K. R. J. Lovelock, C. Kolbeck, T. Cremer, N. Paape, P. S. Schulz, P. Wasserscheid, F. Maier and H.-P. Steinrück, *J. Phys. Chem. B*, 2009, **113**, 2854-2864.
105. Q. H. Zhang, S. M. Liu, Z. P. Li, J. Li, Z. J. Chen, R. F. Wang, L. J. Lu and Y. Q. Deng, *Chem. - Eur. J.*, 2009, **15**, 765-778.
106. H. Hashimoto, A. Ohno, K. Nakajima, M. Suzuki, H. Tsuji and K. Kimura, *Surf. Sci.*, 2010, **604**, 464-469.
107. A. W. Taylor, S. Men, C. J. Clarke and P. Licence, *RSC Adv.*, 2013, **3**, 9436-9445.
108. I. J. Villar-Garcia, E. F. Smith, A. W. Taylor, F. Qiu, K. R. J. Lovelock, R. G. Jones and P. Licence, *Phys. Chem. Chem. Phys.*, 2011, **13**, 2797-2808.

109. R. Fortunato, C. A. M. Afonso, J. Benavente, E. Rodriguez-Castellón and J. G. Crespo, *J. Membr. Sci.*, 2005, **256**, 216-223.
110. I. J. Villar-Garcia, K. R. J. Lovelock, S. Men and P. Licence, *Chem. Sci.*, 2014, **5**, 2573-2579.
111. T. Iwahashi, T. Nishi, H. Yamane, T. Miyamae, K. Kanai, K. Seki, D. Kim and Y. Ouchi, *J. Phys. Chem. C*, 2009, **113**, 19237-19243.
112. H.-P. Steinrück, *Surf. Sci.*, 2010, **604**, 481-484.
113. C. Ridings, G. G. Warr and G. G. Andersson, *Phys. Chem. Chem. Phys.*, 2012, **14**, 16088-16095.
114. R. K. Blundell, A. E. Delorme, E. F. Smith and P. Licence, *Phys. Chem. Chem. Phys.*, 2016, **18**, 6122-6131.
115. P. van der Heide, *X-ray Photoelectron Spectroscopy: An Introduction to Principles and Practices*, John Wiley & Sons, Inc., New Jersey, 2011.
116. J. F. Watts and J. Wolstenholme, *An Introduction to Surface Analysis by XPS and AES*, John Wiley & Sons, Inc., Great Britain, 2003.
117. A. Deyko and R. G. Jones, *Faraday Discuss.*, 2012, **154**, 265-288.
118. A. Deyko, K. R. J. Lovelock, J. A. Corfield, A. W. Taylor, P. N. Gooden, I. J. Villar-Garcia, P. Licence, R. G. Jones, V. G. Krasovskiy, E. A. Chernikova and L. M. Kustov, *Phys. Chem. Chem. Phys.*, 2009, **11**, 8544-8555.
119. J. P. Armstrong, C. Hurst, R. G. Jones, P. Licence, K. R. J. Lovelock, C. J. Satterley and I. J. Villar-Garcia, *Phys. Chem. Chem. Phys.*, 2007, **9**, 982-990.
120. K. R. J. Lovelock, A. Deyko, P. Licence and R. G. Jones, *Phys. Chem. Chem. Phys.*, 2010, **12**, 8893-8901.
121. P. Licence, *Angew. Chem. Int. Ed.*, 2012, **51**, 4789-4791.
122. B. B. Hurisso, K. R. J. Lovelock and P. Licence, *Phys. Chem. Chem. Phys.*, 2011, **13**, 17737-17748.
123. I. Niedermaier, C. Kolbeck, N. Taccardi, P. S. Schulz, J. Li, T. Drewello, P. Wasserscheid, H.-P. Steinrück and F. Maier, *ChemPhysChem*, 2012, **13**, 1725-1735.
124. M. Currie, J. Estager, P. Licence, S. Men, P. Nockemann, K. R. Seddon, M. Swadźba-Kwaśny and C. Terrade, *Inorg. Chem.*, 2013, **52**, 1710-1721.
125. S. Men, K. R. J. Lovelock and P. Licence, *Phys. Chem. Chem. Phys.*, 2011, **13**, 15244-15255.
126. A. W. Taylor and P. Licence, *ChemPhysChem*, 2012, **13**, 1917-1926.
127. R. K. Blundell and P. Licence, *Phys. Chem. Chem. Phys.*, 2014, **16**, 15278-15288.
128. A. R. Santos, R. K. Blundell and P. Licence, *Phy. Chem. Chem. Phys.*, 2015, **17**, 11839-11847.
129. S. Men, D. S. Mitchell, K. R. J. Lovelock and P. Licence, *ChemPhysChem*, 2015, **16**, 2211-2218.

130. D. Briggs and J. T. Grant, *Surface Analysis by Auger and X-ray Photoelectron Spectroscopy*, IM Publications LLP, Manchester, 2003.
131. ULVAC-PHI, XPS/ESCA, [online], https://www.phi.com/surface-analysis-techniques/xps-esca.html, (accessed 21 Jan 2017).
132. N. Stojilovic, *J. Chem. Educ.*, 2012, **89**, 1331-1332.
133. I. S. Tilinin, A. Jablonski and W. S. M. Werner, *Prog. Surf. Sci.*, 1996, **52**, 193-335.
134. C. D. Wagner, L. E. Davis, M. V. Zeller, J. A. Taylor, R. H. Raymond and L. H. Gale, *Surf. Interface Anal.*, 1981, **3**, 211-225.
135. A. D. Baker and D. Betteridge, *Photoelectron Spectroscopy: Chemical and Analytical Aspects*, Pergamon Press, 1972.
136. F. Bernardi, J. D. Scholten, G. H. Fecher, J. Dupont and J. Morais, *Chem. Phys. Lett.*, 2009, **479**, 113-116.
137. C. Paun, C. Stere, S. M. Coman, V. I. Parvulescu, P. Goodrich and C. Hardacre, *Catal. Today*, 2008, **131**, 98-103.
138. ULVAC-PHI, About Gas Cluster Ion Beams, [online], (accessed 17 May 2017).
139. R. F. Roberts, D. L. Allara, C. A. Pryde, D. N. E. Buchanan and N. D. Hobbins, *Surf. Interface Anal.*, 1980, **2**, 5-10.
140. J. Neutz, O. Grosshardt, S. Schäufele, H. Schuppler and W. Schweikert, *Propellants Explos. Pyrotech.*, 2003, **28**, 181-188.
141. H. Kunkel and G. Maas, *Eur. J. Org. Chem.*, 2007, 3746-3757.
142. N. M. M. Mateus, L. C. Branco, N. M. T. Lourenço and C. A. M. Afonso, *Green Chem.*, 2003, **5**, 347-352.
143. Y. Gao, S. W. Arritt, B. Twamley and J. M. Shreeve, *Inorg. Chem.*, 2005, **44**, 1704-1712.
144. H. Xie, S. Zhang and H. Duan, *Tetrahedron Lett.*, 2004, **45**, 2013-2015.
145. S. Li, Y. Lin, H. Xie, S. Zhang and J. Yu, *Org. Lett.*, 2006, **8**, 391-394.
146. S. Li, Y. Lin, J. Cao and S. Zhang, *J. Org. Chem.*, 2007, **72**, 4067-4072.
147. T. Jiang, H. Gao, B. Han, G. Zhao, Y. Chang, W. Wu, L. Gao and G. Yang, *Tetrahedron Lett.*, 2004, **45**, 2699-2701.
148. Y. Peng, G. Song and F. Huang, *Monatsh. Chem.*, 2005, **136**, 727-731.
149. P. Blondeau, M. Segura, R. Pérez-Fernández and J. de Mendoza, *Chem. Soc. Rev.*, 2007, **36**, 198-210.
150. I. A. Shkrob, T. W. Marin, J. R. Bell, H. Luo and S. Dai, *J. Phys. Chem. B*, 2013, **117**, 14400-14407.
151. K. A. Schug and W. Lindner, *Chem. Rev.*, 2005, **105**, 67-113.
152. R. F. M. Frade, A. A. Rosatella, C. S. Marques, L. C. Branco, P. S. Kulkarni, N. M. M. Mateus, C. A. M. Afonso and C. M. M. Duarte, *Green Chem.*, 2009, **11**, 1660-1665.
153. X. Q. Ding, Y. Z. Wang, Q. Zeng, J. Chen, Y. H. Huang and K. J. Xu, *Anal. Chim. Acta*, 2014, **815**, 22-32.
154. V. A. Sirotkin and R. Winter, *J. Phys. Chem. B*, 2010, **114**, 16881-16886.

155. R. D. Macdonald and M. Khajehpour, *Biophys. Chem.*, 2015, **196**, 25-32.
156. R. Singh, M. I. Hassan, A. Islam and F. Ahmad, *PLoS One*, 2015, **10**, 1-16.
157. J. N. Scott, N. V. Nucci and J. M. Vanderkooi, *J. Phys. Chem. A*, 2008, **112**, 10939-10948.
158. A. Brandt, J. Gräsvik, J. P. Hallett and T. Welton, *Green Chem.*, 2013, **15**, 550-583.
159. D. Weingarth, I. Czekaj, Z. F. Fei, A. Foelske-Schmitz, P. J. Dyson, A. Wokaun and R. Kötz, *J. Electrochem. Soc.*, 2012, **159**, H611-H615.
160. R. Lungwitz, M. Friedrich, W. Linert and S. Spange, *New J. Chem.*, 2008, **32**, 1493-1499.
161. X. M. Liu, S. J. Zhang, G. H. Zhou, G. W. Wu, X. L. Yuan and X. Q. Yao, *J. Phys. Chem. B*, 2006, **110**, 12062-12071.
162. X. Liu, G. Zhou, S. Zhang, G. Wu and G. Yu, *J. Phys. Chem. B*, 2007, **111**, 5658-5668.
163. X. Liu, G. Zhou and S. Zhang, *Fluid Phase Equilib.*, 2008, **272**, 1-7.
164. X. Liu, X. Zhang, G. Zhou, X. Yao and S. Zhang, *Sci. China Chem.*, 2012, **55**, 1573-1579.
165. G. Yu, X. Chen, C. Asumana, S. Zhang, X. Liu and G. Zhou, *AIChE J.*, 2011, **57**, 507-516.
166. F. Endres, D. MacFarlane and A. Abbott, *Electrodeposition from Ionic Liquids*, Wiley-VCH, Weinheim, 2008.
167. H. Ohno, *Electrochemical Aspects of Ionic Liquids*, John Wiley & Sons, Inc., New Jersey, 2005.
168. B. Kirchner, *''Ionic Liquids'' Topics in Current Chemistry*, Springer, Heidelberg, 2009.
169. N. V. Plechkova and K. R. Seddon, *Chem. Soc. Rev.*, 2008, **37**, 123-150.
170. J. X. Long, B. Guo, X. H. Li, Y. B. Jiang, F. R. Wang, S. C. Tsang, L. F. Wang and K. M. K. Yu, *Green Chem.*, 2011, **13**, 2334-2338.
171. K. Tominaga, *Catal. Today*, 2006, **115**, 70-72.
172. M. Kunze, S. Jeong, G. B. Appetecchi, M. Schönhoff, M. Winter and S. Passerini, *Electrochim. Acta*, 2012, **82**, 69-74.
173. G. Annat, M. Forsyth and D. R. MacFarlane, *J. Phys. Chem. B*, 2012, **116**, 8251-8258.
174. M. Kunze, S. Jeong, E. Paillard, M. Winter and S. Passerini, *J. Phys. Chem. C*, 2010, **114**, 12364-12369.
175. K. N. Marsh, J. A. Boxall and R. Lichtenthaler, *Fluid Phase Equilib.*, 2004, **219**, 93-98.
176. H. Niedermeyer, J. P. Hallett, I. J. Villar-Garcia, P. A. Hunt and T. Welton, *Chem. Soc. Rev.*, 2012, **41**, 7780-7802.
177. K. A. Fletcher, S. N. Baker, G. A. Baker and S. Pandey, *New J. Chem.*, 2003, **27**, 1706-1712.

178. M. Y. Lui, L. Crowhurst, J. P. Hallett, P. A. Hunt, H. Niedermeyer and T. Welton, *Chem. Sci.*, 2011, **2**, 1491-1496.
179. K. Shimizu, M. Tariq, L. P. N. Rebelo and J. N. Canongia Lopes, *J. Mol. Liq.*, 2010, **153**, 52-56.
180. J. M. Andanson, M. J. Beier and A. Baiker, *J. Phys. Chem. Lett.*, 2011, **2**, 2959-2964.
181. M. Brüssel, M. Brehm, T. Voigt and B. Kirchner, *Phys. Chem. Chem. Phys.*, 2011, **13**, 13617-13620.
182. K. R. J. Lovelock, J. P. Armstrong, P. Licence and R. G. Jones, *Phys. Chem. Chem. Phys.*, 2014, **16**, 1339-1353.
183. J. W. Steed, *Supramolecular Chemistry*, John Wiley & Sons, Ltd, Chichester, 2009.
184. H. Ohno and K. Fukumoto, *Acc. Chem. Res.*, 2007, **40**, 1122-1129.
185. F. A. Carey and R. J. Sundberg, *Advanced Organic Chemistry: Reactions and Synthesis*, Springer, New York, NY, 2007.
186. D. M. Kneeland, K. Ariga, V. M. Lynch, C. Y. Huang and E. V. Anslyn, *J. Am. Chem. Soc.*, 1993, **115**, 10042-10055.
187. F. Albericio, M. A. Bailén, R. Chinchilla, D. J. Dodsworth and C. Nájera, *Tetrahedron*, 2001, **57**, 9607-9613.
188. P. R. Schreiner, *Chem. Soc. Rev.*, 2003, **32**, 289-296.
189. P. K. Nanda, K. K. Rao, R. K. Kar and P. L. Nayak, *J. Therm. Anal. Calorim.*, 2007, **89**, 935-940.
190. C. Thomas and B. Bibal, *Green Chem.*, 2014, **16**, 1687-1699.
191. C. Clarke, Ph.D. Thesis, University of Nottingham, 2015.
192. N. Taccardi, I. Niedermaier, F. Maier, H.-P. Steinrück and P. Wasserscheid, *Chem. Eur. J.*, 2012, **18**, 8288-8291.
193. M. Hesse, H. Meier and B. Zeeh, *Spectroscopic Methods in Organic Chemistry*, Thieme, Stuttgart, New York, 2nd edn., 2007.
194. F. W. Wehrli, A. P. Marchand and S. Wehrli, *Interpretation of Carbon-13 NMR Spectra*, John Wiley & Sons, Chichester, 2nd edn., 1983.
195. J. Clayden, N. Greeves, S. Warren and P. Wothers, *Organic Chemistry*, Oxford University Press Inc., New York, United States, 2nd edn., 2001.
196. L. A. Blanchard, D. Hancu, E. J. Beckman and J. F. Brennecke, *Nature*, 1999, **399**, 28-29.
197. J. L. Anderson, J. K. Dixon and J. F. Brennecke, *Acc. Chem. Res.*, 2007, **40**, 1208-1216.
198. X. Han and D. W. Armstrong, *Acc. Chem. Res.*, 2007, **40**, 1079-1086.
199. C. F. Poole, *J. Chromatogr. A*, 2004, **1037**, 49-82.
200. C. F. Poole and S. K. Poole, *J. Sep. Sci.*, 2011, **34**, 888-900.
201. I. Niedermaier, M. Bahlmann, C. Papp, C. Kolbeck, W. Wei, S. K. Calderon, M. Grabau, P. S. Schulz, P. Wasserscheid, H.-P. Steinrück and F. Maier, *J. Am. Chem. Soc.*, 2014, **136**, 436-441.
202. J. Dupont and J. D. Scholten, *Chem. Soc. Rev.*, 2010, **39**, 1780-1804.

203. H. Wender, R. V. Gonçalves, A. F. Feil, P. Migowski, F. S. Poletto, A. R. Pohlmann, J. Dupont and S. R. Teixeira, *J. Phys. Chem. C*, 2011, **115**, 16362-16367.
204. T. Torimoto, T. Tsuda, K. Okazaki and S. Kuwabata, *Adv. Mater.*, 2010, **22**, 1196-1221.
205. S. Kuwabata, T. Tsuda and T. Torimoto, *J. Phys. Chem. Lett.*, 2010, **1**, 3177-3188.
206. E. F. Borra, O. Seddiki, R. Angel, D. Eisenstein, P. Hickson, K. R. Seddon and S. P. Worden, *Nature*, 2007, **447**, 979-981.
207. A. Riisager, R. Fehrmann, M. Haumann and P. Wasserscheid, *Top. Catal.*, 2006, **40**, 91-102.
208. A. Riisager, R. Fehrmann, M. Haumann and P. Wasserscheid, *Eur. J. Inorg. Chem.*, 2006, 695-706.
209. S. Men, B. B. Hurisso, K. R. J. Lovelock and P. Licence, *Phys. Chem. Chem. Phys.*, 2012, **14**, 5229-5238.
210. T. Iwahashi, T. Miyamae, K. Kanai, K. Seki, D. Kim and Y. Ouchi, *J. Phys. Chem. B*, 2008, **112**, 11936-11941.
211. A. Ulbrich, M. Reinmöller, W. J. D. Beenken and S. Krischok, *ChemPhysChem*, 2012, **13**, 1718-1724.
212. I. S. Martinez and S. Baldelli, *J. Phys. Chem. C*, 2010, **114**, 11564-11575.
213. I. S. Martinez, C. Santos and S. Baldelli, *ChemPhysChem*, 2012, **13**, 1818-1824.
214. E. Sloutskin, R. M. Lynden-Bell, S. Balasubramanian and M. Deutsch, *J. Chem. Phys.*, 2006, **125**, 1-7 (174715).
215. C. Waring, P. A. J. Bagot, J. M. Slattery, M. L. Costen and K. G. McKendrick, *J. Phys. Chem. A*, 2010, **114**, 4896-4904.
216. C. Waring, P. A. J. Bagot, J. M. Slattery, M. L. Costen and K. G. McKendrick, *J. Phys. Chem. Lett.*, 2010, **1**, 429-433.
217. B. H. Wu, J. M. Zhang, T. K. Minton, K. G. McKendrick, J. M. Slattery, S. Yockel and G. C. Schatz, *J. Phys. Chem. C*, 2010, **114**, 4015-4027.
218. J. R. Roscioli and D. J. Nesbitt, *J. Phys. Chem. Lett.*, 2010, **1**, 674-678.
219. J. R. Roscioli and D. J. Nesbitt, *J. Phys. Chem. A*, 2011, **115**, 9764-9773.
220. M. P. Ziemkiewich, A. Zutz and D. J. Nesbitt, *J. Phys. Chem. C*, 2012, **116**, 14284-14294.
221. K. Nakajima, A. Ohno, H. Hashimoto, M. Suzuki and K. Kimura, *J. Chem. Phys.*, 2010, **133**, 1 - 7 (044702).
222. T. Hammer, M. Reichelt and H. Morgner, *Phys. Chem. Chem. Phys.*, 2010, **12**, 11070-11080.
223. M. Reichelt, T. Hammer and H. Morgner, *Surf. Sci.*, 2011, **605**, 1402-1411.
224. C. Ridings, V. Lockett and G. Andersson, *Phys. Chem. Chem. Phys.*, 2011, **13**, 17177-17184.

225. C. Ridings, V. Lockett and G. Andersson, *Phys. Chem. Chem. Phys.*, 2011, **13**, 21301-21307.
226. C. Ridings, V. Lockett and G. Andersson, *Colloids Surf. A*, 2012, **413**, 149-153.
227. A. Ohno, H. Hashimoto, K. Nakajima, M. Suzuki and K. Kimura, *J. Chem. Phys.*, 2009, **130**, 1-5 (204705).
228. S. G. Hessey and R. G. Jones, *Chem. Sci.*, 2013, **4**, 2519-2529.
229. B. L. Bhargava and S. Balasubramanian, *J. Am. Chem. Soc.*, 2006, **128**, 10073-10078.
230. A. S. Pensado, P. Malfreyt and A. A. H. Pádua, *J. Phys. Chem. B*, 2009, **113**, 14708-14718.
231. A. S. Pensado, M. F. Costa Gomes, J. N. Canongia Lopes, P. Malfreyt and A. A. H. Pádua, *Phys. Chem. Chem. Phys.*, 2011, **13**, 13518-13526.
232. X. Paredes, J. Fernández, A. A. H. Pádua, P. Malfreyt, F. Malberg, B. Kirchner and A. S. Pensado, *J. Phys. Chem. B*, 2012, **116**, 14159-14170.
233. X. Paredes, J. Fernández, A. A. H. Pádua, P. Malfreyt, F. Malberg, B. Kirchner and A. S. Pensado, *J. Phys. Chem. B*, 2014, **118**, 731-742.
234. S. Yockel and G. C. Schatz, *J. Phys. Chem. B*, 2010, **114**, 14241-14248.
235. X. H. Li, G. C. Schatz and D. J. Nesbitt, *J. Phys. Chem. B*, 2012, **116**, 3587-3602.
236. G. Hantal, M. N. D. S. Cordeiro and M. Jorge, *Phys. Chem. Chem. Phys.*, 2011, **13**, 21230-21232.
237. G. Hantal, I. Voroshylova, M. N. D. S. Cordeiro and M. Jorge, *Phys. Chem. Chem. Phys.*, 2012, **14**, 5200-5213.
238. M. Lísal, Z. Posel and P. Izák, *Phys. Chem. Chem. Phys.*, 2012, **14**, 5164-5177.
239. M. Lísal and P. Izák *J. Chem. Phys.*, 2013, **139**, 1-15 (014704).
240. M. E. Perez-Blanco and E. J. Maginn, *J. Phys. Chem. B*, 2010, **114**, 11827-11837.
241. H. Xu, Z. Han, D. J. Zhang and J. H. Zhan, *ACS Appl. Mater. Interfaces*, 2012, **4**, 6646-6653.
242. C. Kolbeck, A. Deyko, T. Matsuda, F. T. U. Kohler, P. Wasserscheid, F. Maier and H.-P. Steinrück *ChemPhysChem*, 2013, **14**, 3726-3730.
243. C. Kolbeck, I. Niedermaier, A. Deyko, K. R. J. Lovelock, N. Taccardi, W. Wei, P. Wasserscheid, F. Maier and H.-P. Steinrück *Chem. Eur. J.*, 2014, **20**, 3954-3965.
244. D. Yoshimura, T. Yokoyama, T. Nishi, H. Ishii, R. Ozawa, H. Hamaguchi and K. Seki, *J. Electron Spectrosc. Relat. Phenom.*, 2005, **144**, 319-322.
245. A. Kauling, G. Ebeling, J. Morais, A. Pádua, T. Grehl, H. H. Brongersma and J. Dupont, *Langmuir*, 2013, **29**, 14301-14306.
246. I. J. Villar-Garcia, S. Fearn, G. F. De Gregorio, N. L. Ismail, F. J. V. Gschwend, A. J. S. McIntosh and K. R. J. Lovelock, *Chem. Sci.*, 2014, **5**, 4404-4418.

247. I. J. Villar-Garcia, S. Fearn, N. L. Ismail, A. J. S. McIntosh and K. R. J. Lovelock, *Chem. Comm.*, 2015, **51**, 5367-5370.
248. K. Nakajima, M. Miyashita, M. Suzuki and K. Kimura, *J. Chem. Phys.*, 2013, **139**, 1-8 (224701).
249. K. Nakajima, S. Nakanishi, Z. Chval, M. Lísal and K. Kimura, *J. Chem. Phys.*, 2016, **145**, 1-6 (184704).
250. I. Niedermaier, C. Kolbeck, H.-P. Steinrück and F. Maier, *Rev. Sci. Instrum.*, 2016, **87**, 1-14 (045105).
251. E. F. Smith, Ph.D. Thesis, University of Nottingham, 2015.
252. A. S. Duwez, *J. Electron Spectrosc. Relat. Phenom.*, 2004, **134**, 97-138.
253. J. E. Castle and R. H. West, *J. Electron Spectrosc. Relat. Phenom.*, 1980, **19**, 409-428.
254. R. H. West and J. E. Castle, *Surf. Interface Anal.*, 1982, **4**, 68-75.
255. M. J. Edgell, R. W. Paynter and J. E. Castle, *J. Electron Spectrosc. Relat. Phenom.*, 1985, **37**, 241-256.
256. D. T. Clark, M. M. Abushbak and W. J. Brennan, *J. Electron Spectrosc. Relat. Phenom.*, 1982, **28**, 11-21.
257. T. G. Vargo and J. A. Gardella, *J. Vac. Sci. Technol. A*, 1989, **7**, 1733-1741.
258. K. Yates and R. H. West, *Surf. Interface Anal.*, 1983, **5**, 133-138.
259. J. F. Watts, *J. Microsc.*, 1985, **140**, 243-260.
260. J. Carrazza and V. León, *Surf. Interface Anal.*, 1991, **17**, 225-229.
261. C. J. Powell and A. Jablonski, *NIST Electron Inelastic-Mean-Free-Path-Database - Version 1.2*, National Institute of Standards and Technology, Gaithersburg, MD, 2010.
262. S. Tanuma, C. J. Powell and D. R. Penn, *Surf. Interface Anal.*, 1994, **21**, 165-176.
263. C. J. Powell and A. Jablonski, *J. Electron Spectrosc. Relat. Phenom.*, 2017, **218**, 1-12.
264. S. J. Zhang, N. Sun, X. Z. He, X. M. Lu and X. P. Zhang, *J. Phys. Chem. Ref. Data*, 2006, **35**, 1475-1517.
265. D. S. Mitchell, Ph.D. Thesis, University of Nottingham, 2015.
266. R. Clark, M.Sci. Thesis, University of Nottingham, 2016.
267. M. Guncheva, M. Dimitrov, F. Napoly, M. Draye and B. Andrioletti, *J. Mol. Catal. B: Enzym.*, 2014, **102**, 72-80.
268. J. D. Holbrey, W. M. Reichert, R. P. Swatloski, G. A. Broker, W. R. Pitner, K. R. Seddon and R. D. Rogers, *Green Chem.*, 2002, **4**, 407-413.
269. G. Cravotto, E. C. Gaudino, L. Boffa, J. M. Lévêque, J. Estager and W. Bonrath, *Molecules*, 2008, **13**, 149-156.
270. P. Bonhôte, A. P. Dias, M. Armand, N. Papageorgiou, K. Kalyanasundaram and M. Grätzel, *Inorg. Chem.*, 1996, **35**, 1168-1178.
271. J. G. Huddleston, A. E. Visser, W. M. Reichert, H. D. Willauer, G. A. Broker and R. D. Rogers, *Green Chem.*, 2001, **3**, 156-164.

272. C. Sabot, K. A. Kumar, C. Antheaume and C. Mioskowski, *J. Org. Chem.*, 2007, **72**, 5001-5004.
273. G. Laus, V. Kahlenberg, K. Wurst, T. Müller, H. Kopacka and H. Schottenberger, *Z. Naturforsch B*, 2013, **68**, 1239-1252.
274. T. Yamada, Y. Kondo and S. Kusabayashi, *Bull. Chem. Soc. Jpn.*, 1982, **55**, 2911-2916.
275. M. S. Zayas, J. C. Gaitor, S. T. Nestor, S. Minkowicz, Y. H. Sheng and A. Mirjafari, *Green Chem.*, 2016, **18**, 2443-2452.
276. H. Shirota, T. Mandai, H. Fukazawa and T. Kato, *J. Chem. Eng. Data*, 2011, **56**, 2453-2459.
277. Z. B. C. Disley, M.Sci. Thesis, University of Nottingham, 2012.
278. R. K. Blundell, Ph.D. Thesis, University of Nottingham, 2016.

Appendices

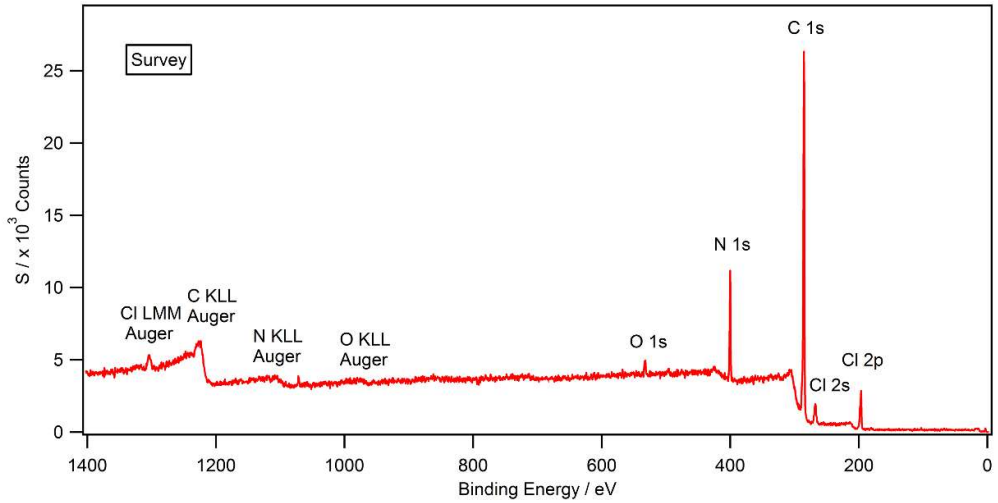
Appendix A: XP Spectra for Chapter 3

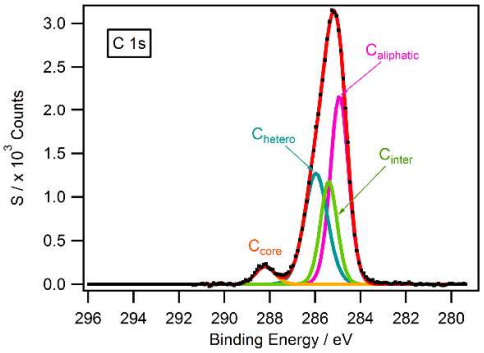
Spectra are charge corrected using an established internal reference method of setting the $C_{aliphatic}$ 1s component to 285.0 eV for ionic liquids with longer alkyl chains ($n \geq 8$). For ionic liquids with shorter alkyl chains ($n < 8$), indirect charge referencing is achieved by setting the measured binding energy of N_{cation} 1s equal to that of their long-chain equivalent A full description of this procedure is described within *Chapter 3, Section 3.2.3*.

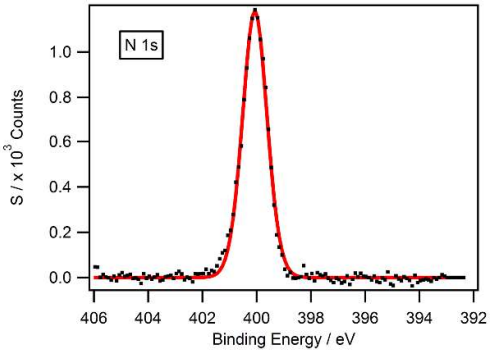
C 1s high-resolution spectra were fitted according to the models described in *Chapter 3, Section 3.2.2*. Cl 2p, S 2p and P 2p high-resolution spectra were fitted taking into account spin-orbit coupling, whereby the area ratio of $2p_{1/2}$: $2p_{3/2}$ components is set to 1 : 2. The O 1s and S 2p high-resolution spectra for ionic liquids containing the $[NTf_2]^-$ anion are affected by shake up/off phenomena and a 4% intensity loss (per oxygen/sulfur atom involved in double bonding) was taken into account when calculating atomic percentages for these elements. Likewise, the C_{core} 1s and N_{cation} 1s high-resolution spectra of all cations are affected by shake up/off phenomena and a 20% and 12%, respectively, intensity loss (per carbon/nitrogen atom involved in double bonding) was taken into account when calculating atomic percentages for these elements.[74]

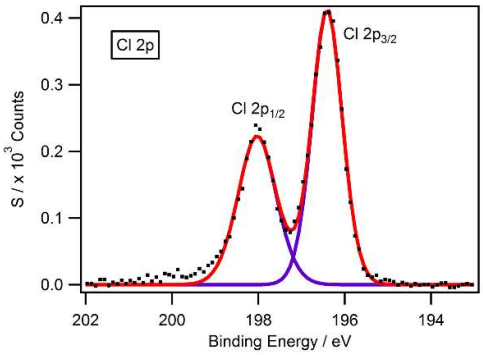
Binding energies, full width at half maximum and composition tables for all guanidinium ionic liquids investigated in *Chapter 3* can be found at the end of *Appendix A*.

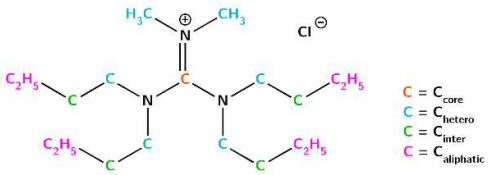
7.3.2. $[(C_4C_4)_2dmg][Cl]$ survey and high-resolution scans



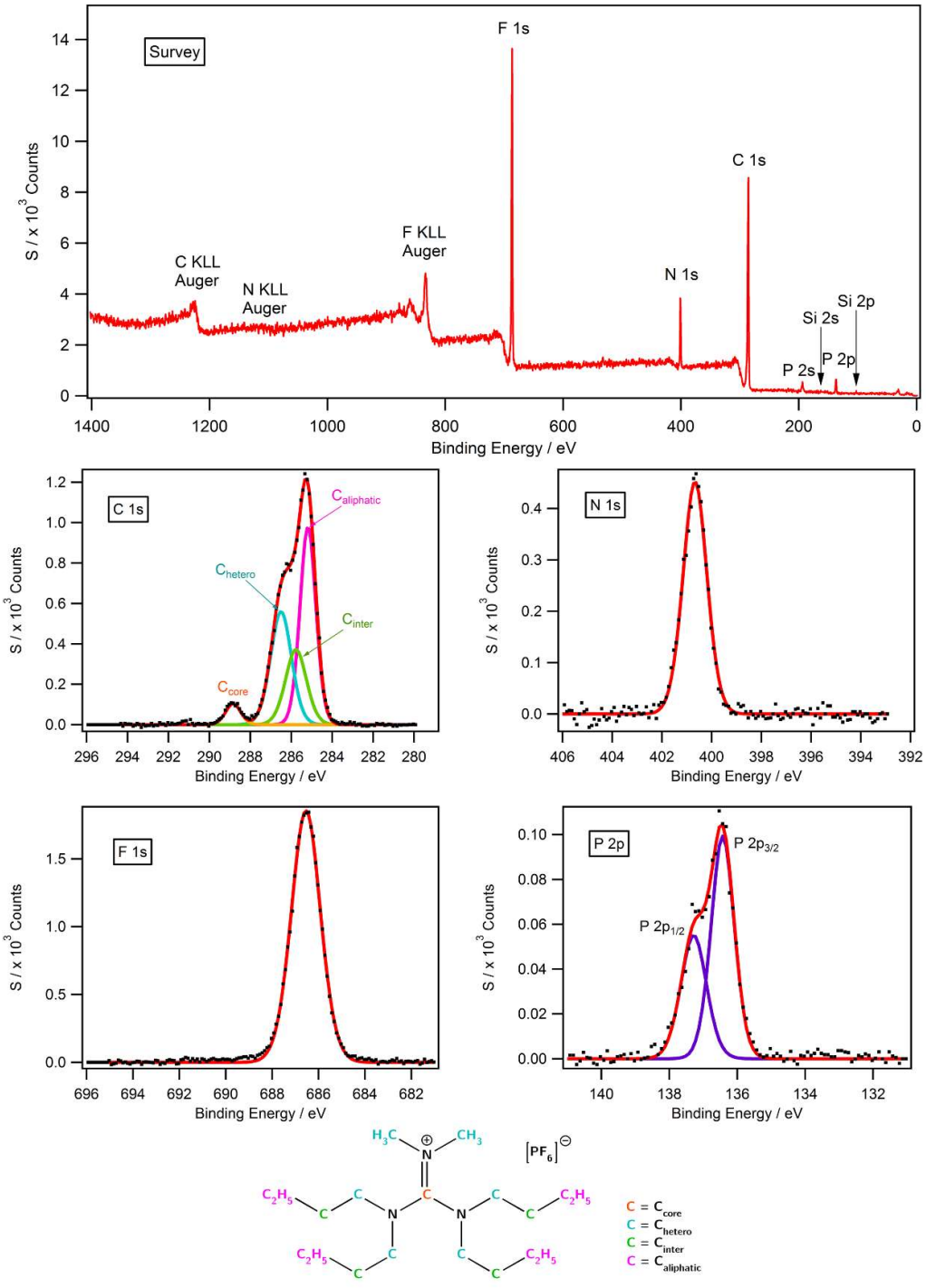




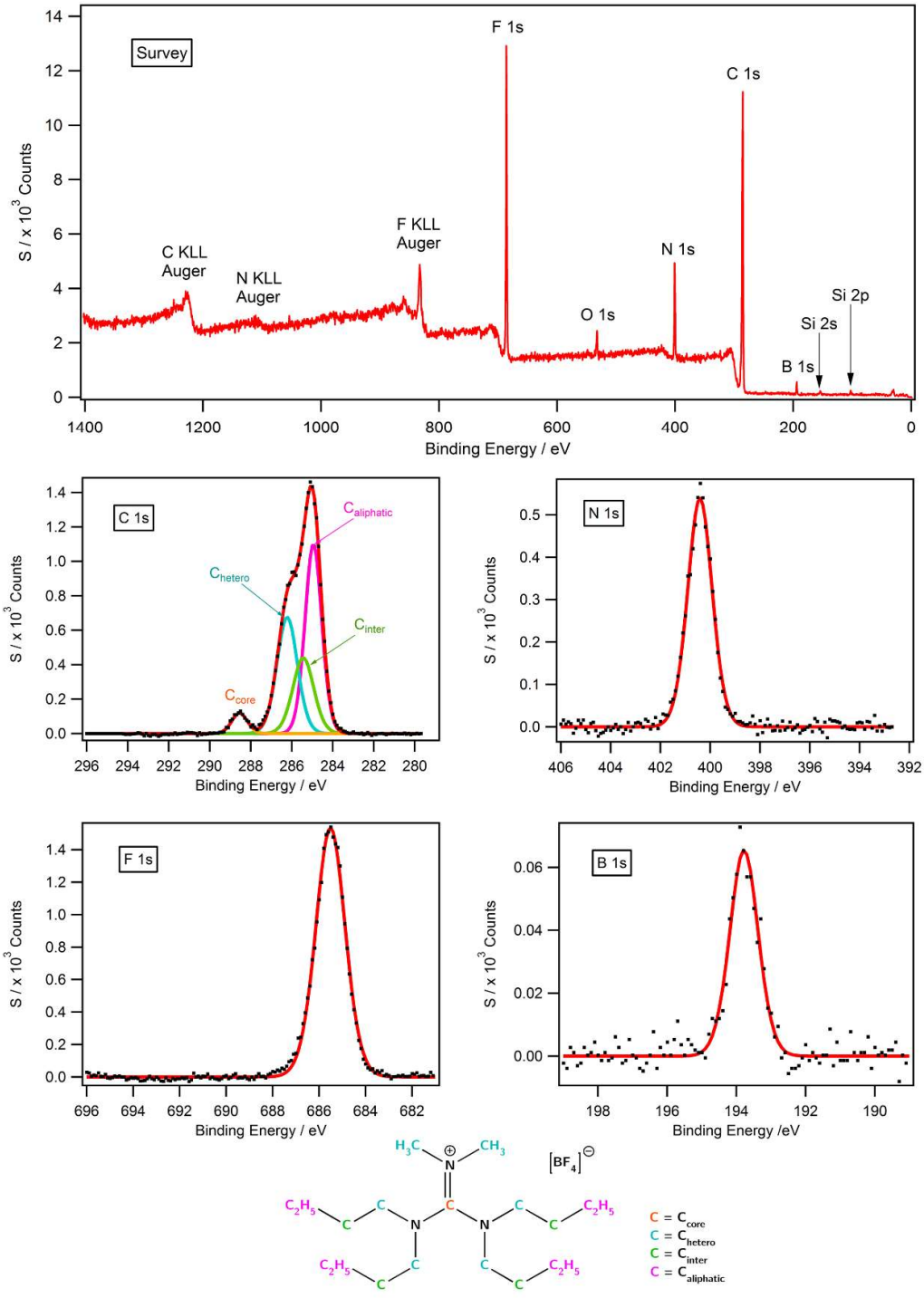




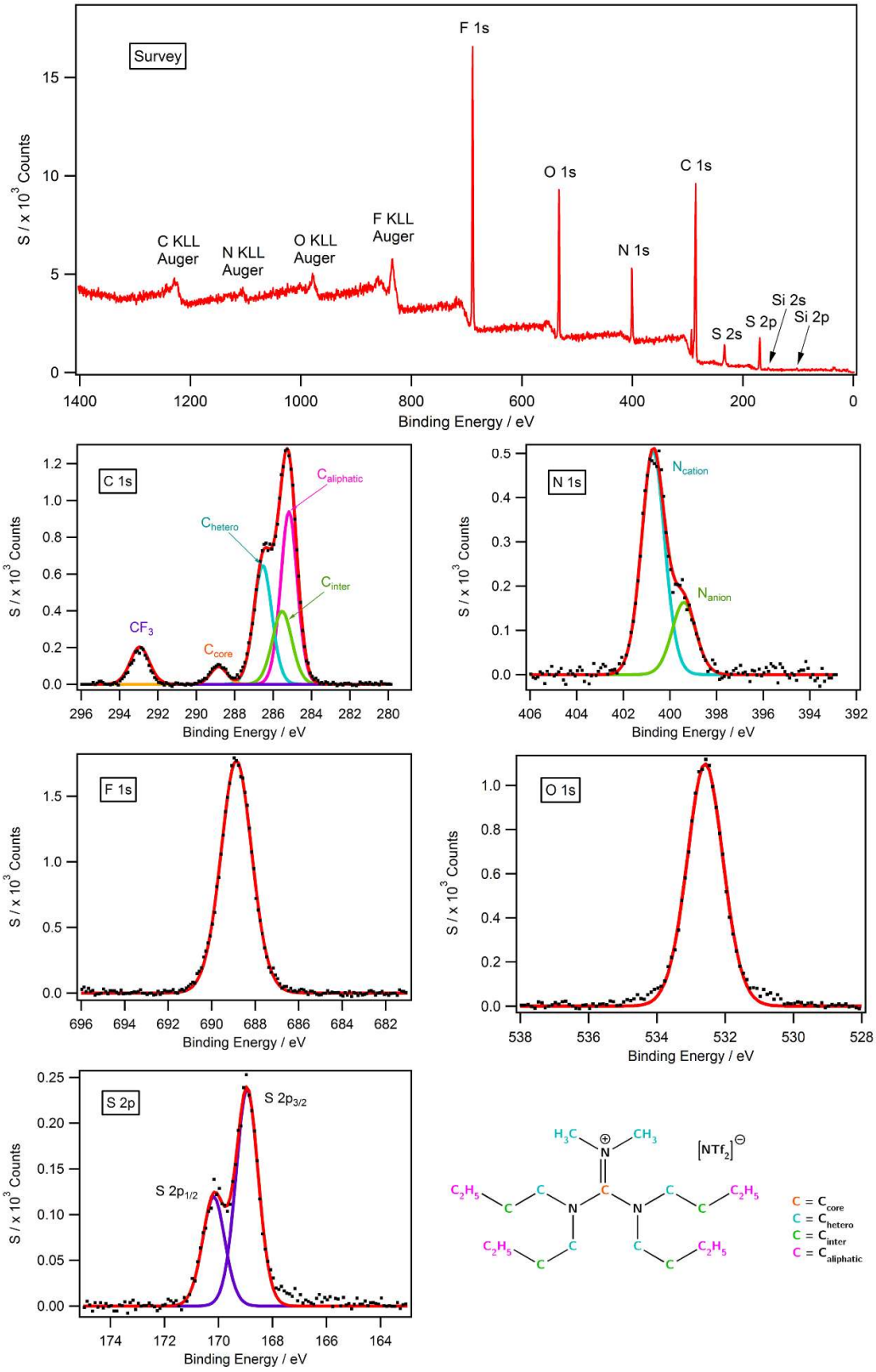
7.3.3. $[(C_4C_4)_2dmg][PF_6]$ survey and high-resolution scans



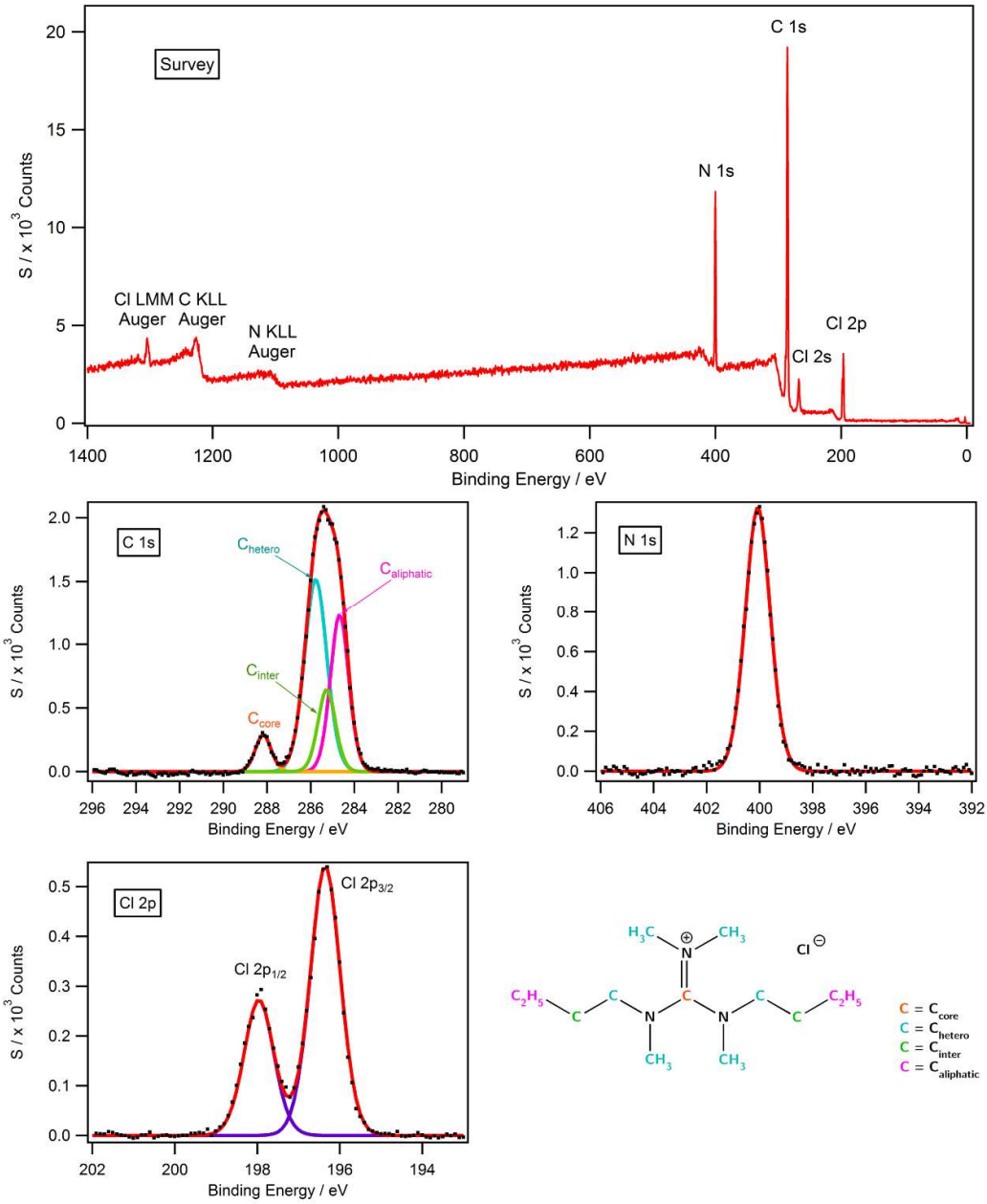
7.3.4. $[(C_4C_4)_2dmg][BF_4]$ survey and high-resolution scans



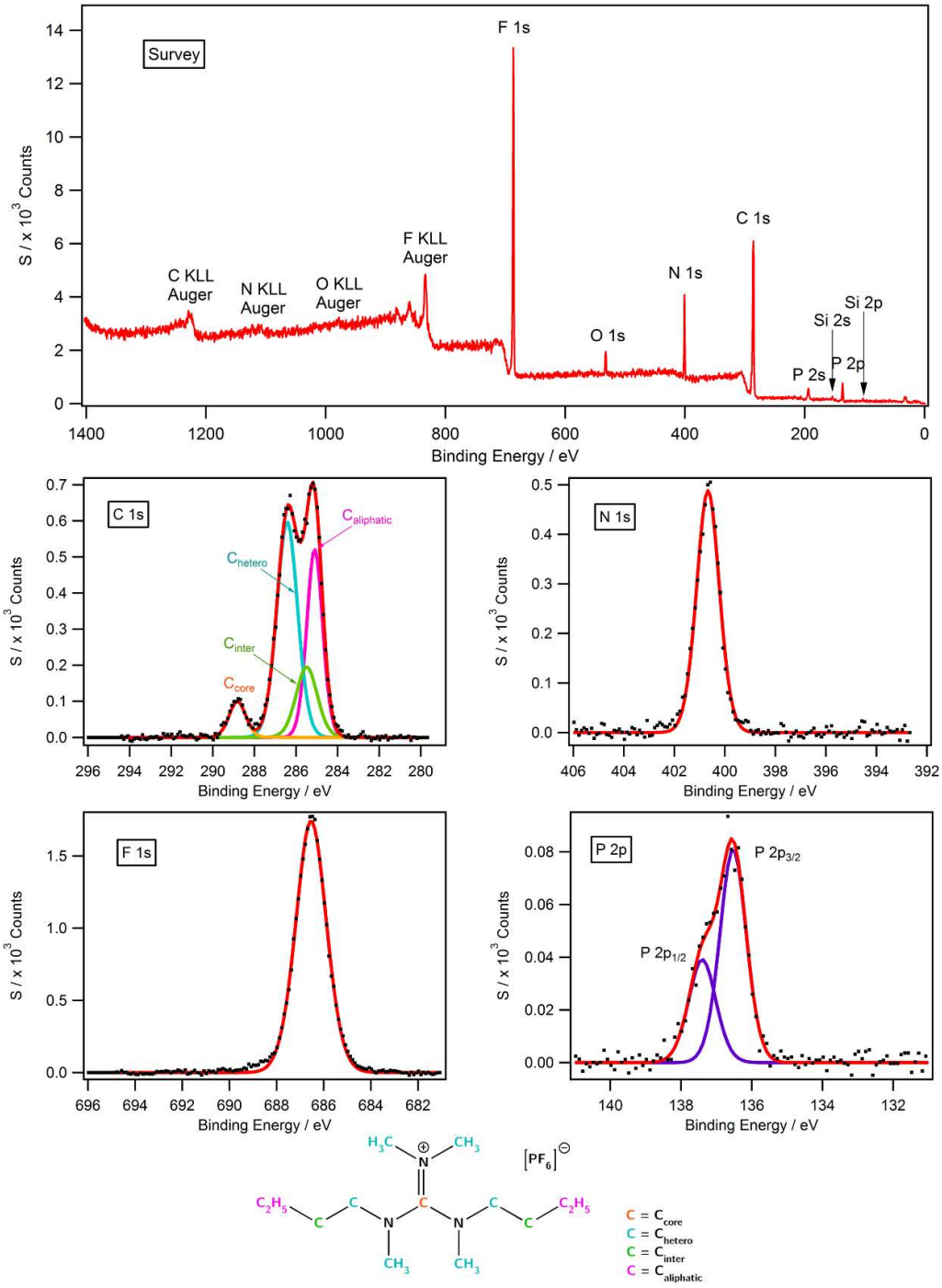
7.3.5. $[(C_4C_4)_2dmg][NTf_2]$ survey and high-resolution scans



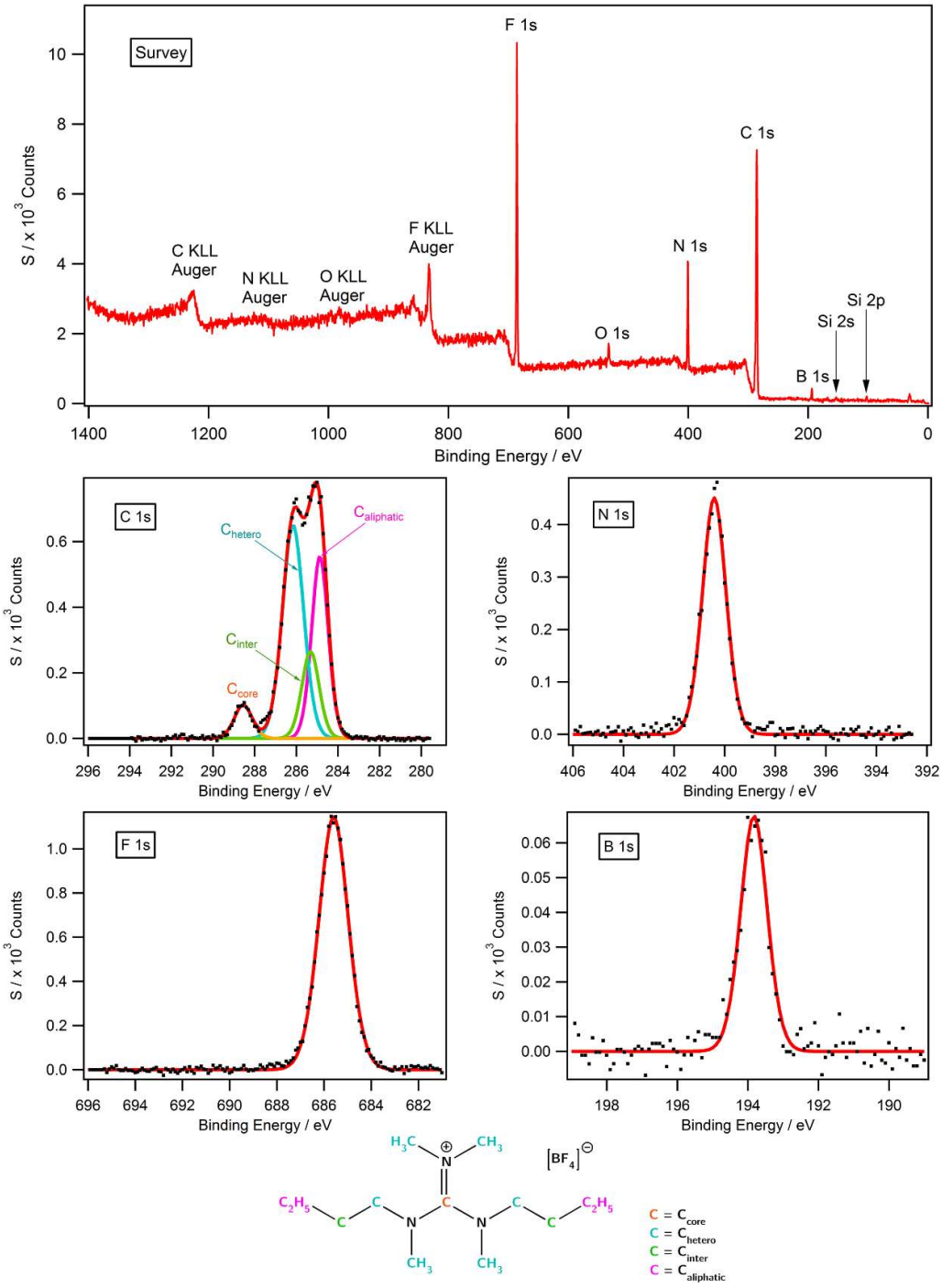
7.3.6. $[(C_4C_1)_2dmg][Cl]$ survey and high-resolution scans



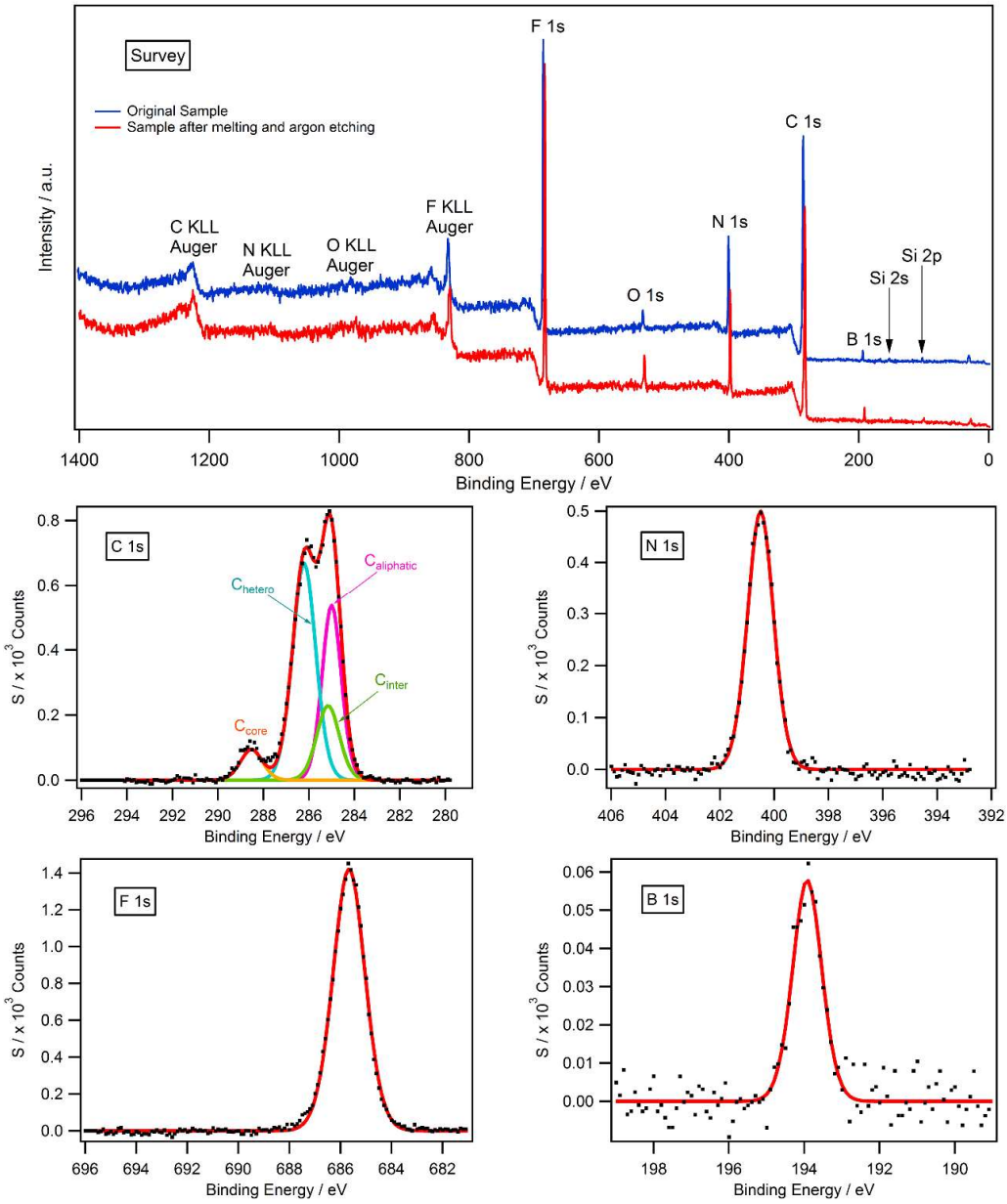
7.3.7. $[(C_4C_1)_2dmg][PF_6]$ survey and high-resolution scans



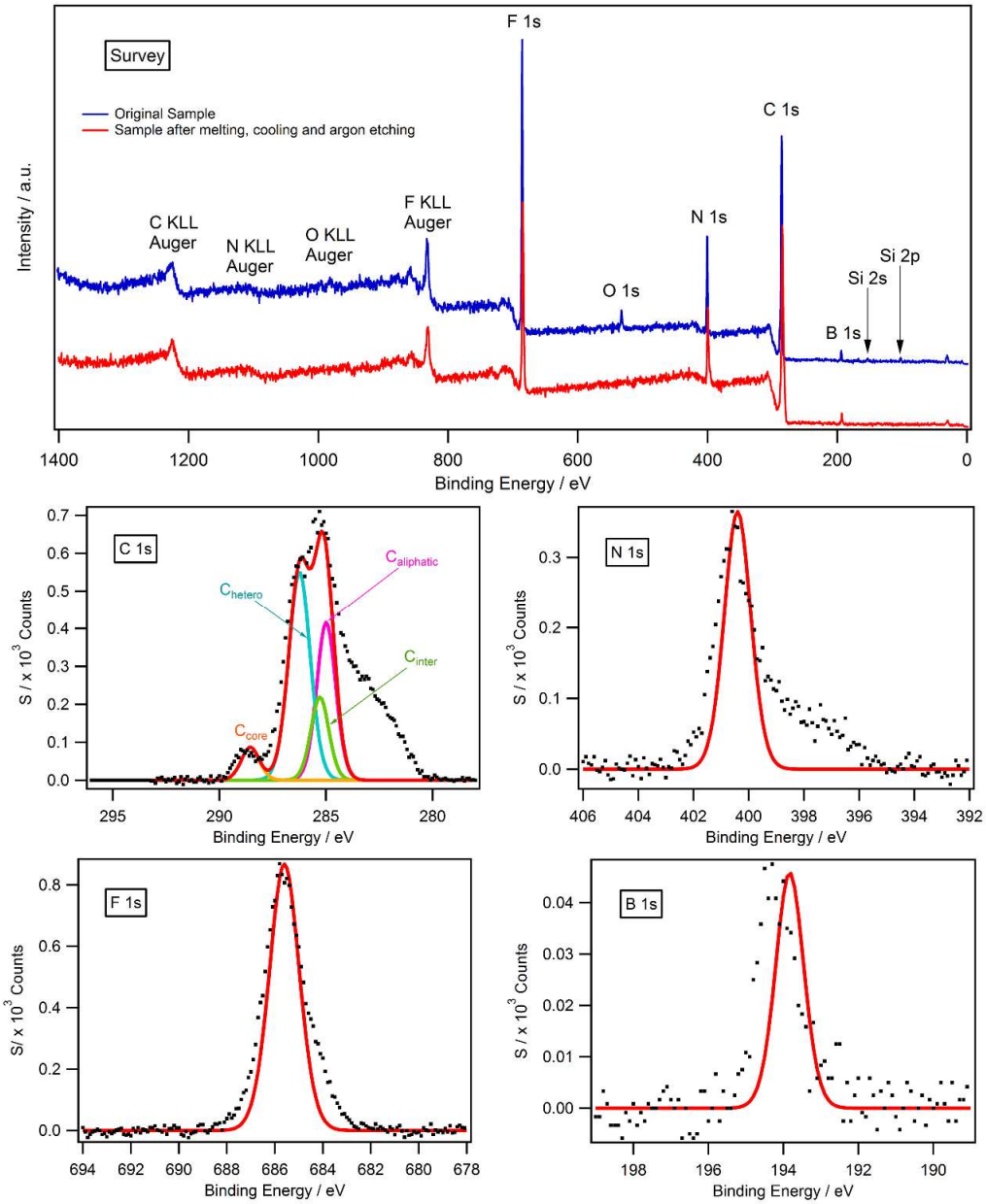
7.3.8. $[(C_4C_1)_2dmg][BF_4]$ survey and high-resolution scans



7.3.8. $[(C_4C_1)_2dmg][BF_4]$ survey and high-resolution scans – melting followed by argon etching

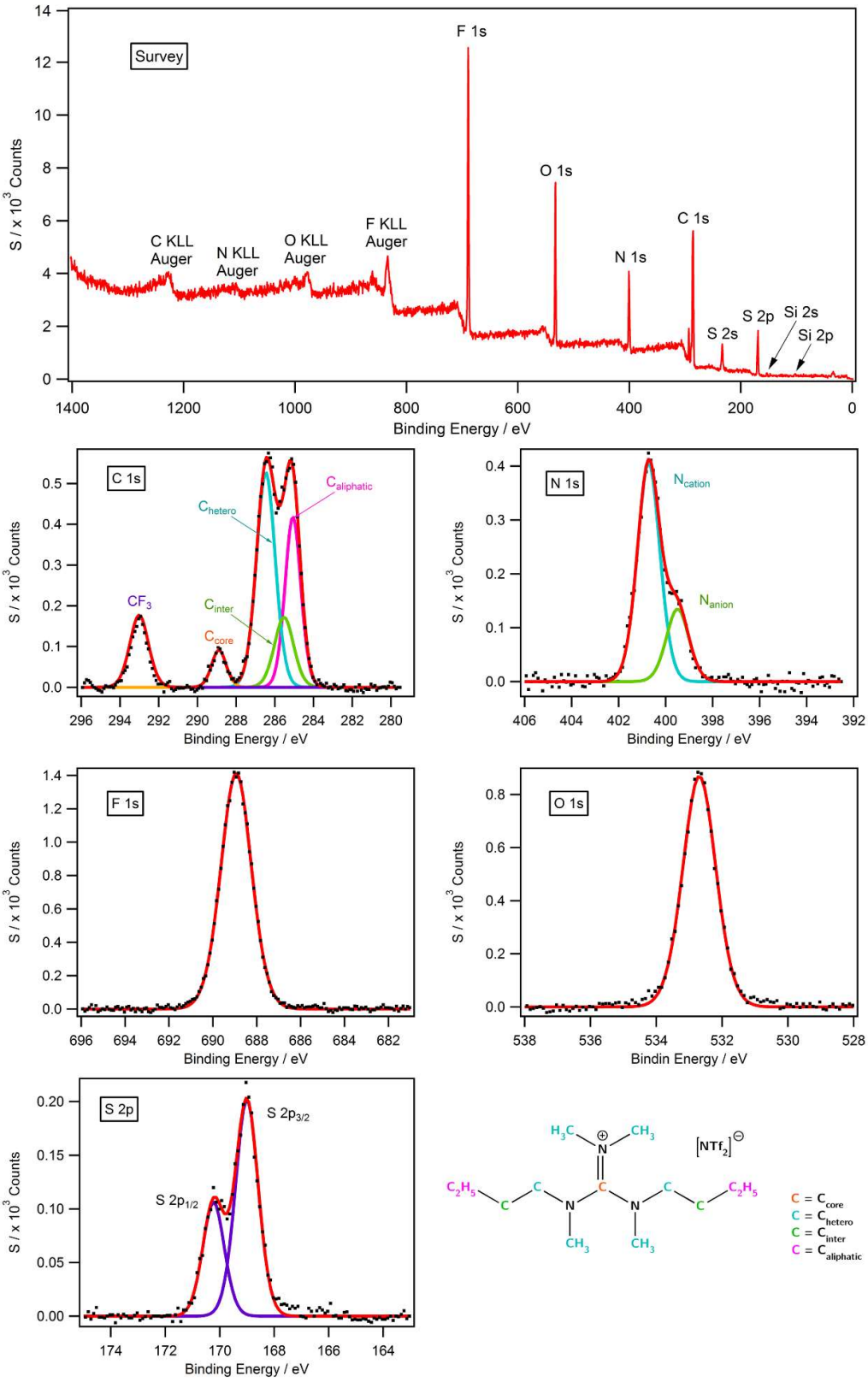


7.3.8. $[(C_4C_1)_2dmg][BF_4]$ survey and high-resolution scans – melting, followed by cooling to form a glassy state solid and finally argon etching‡

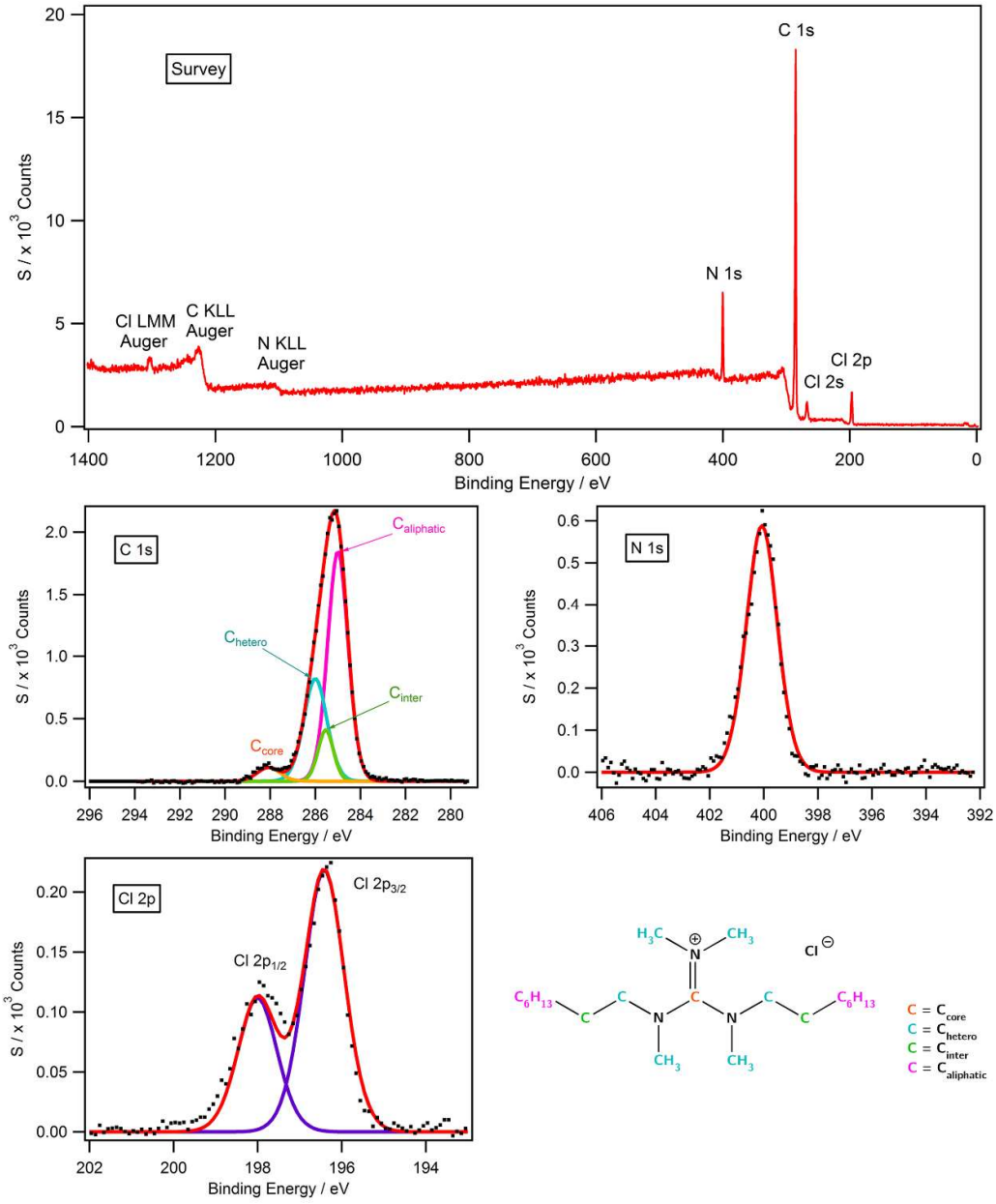


‡ XP spectra charge corrected to F 1s = 685.6 eV and model fitted to match original fitting for $[(C_4C_1)_2dmg][BF_4]$ to highlight extensive peak broadening as a result of the irreversible damage under the argon beam.

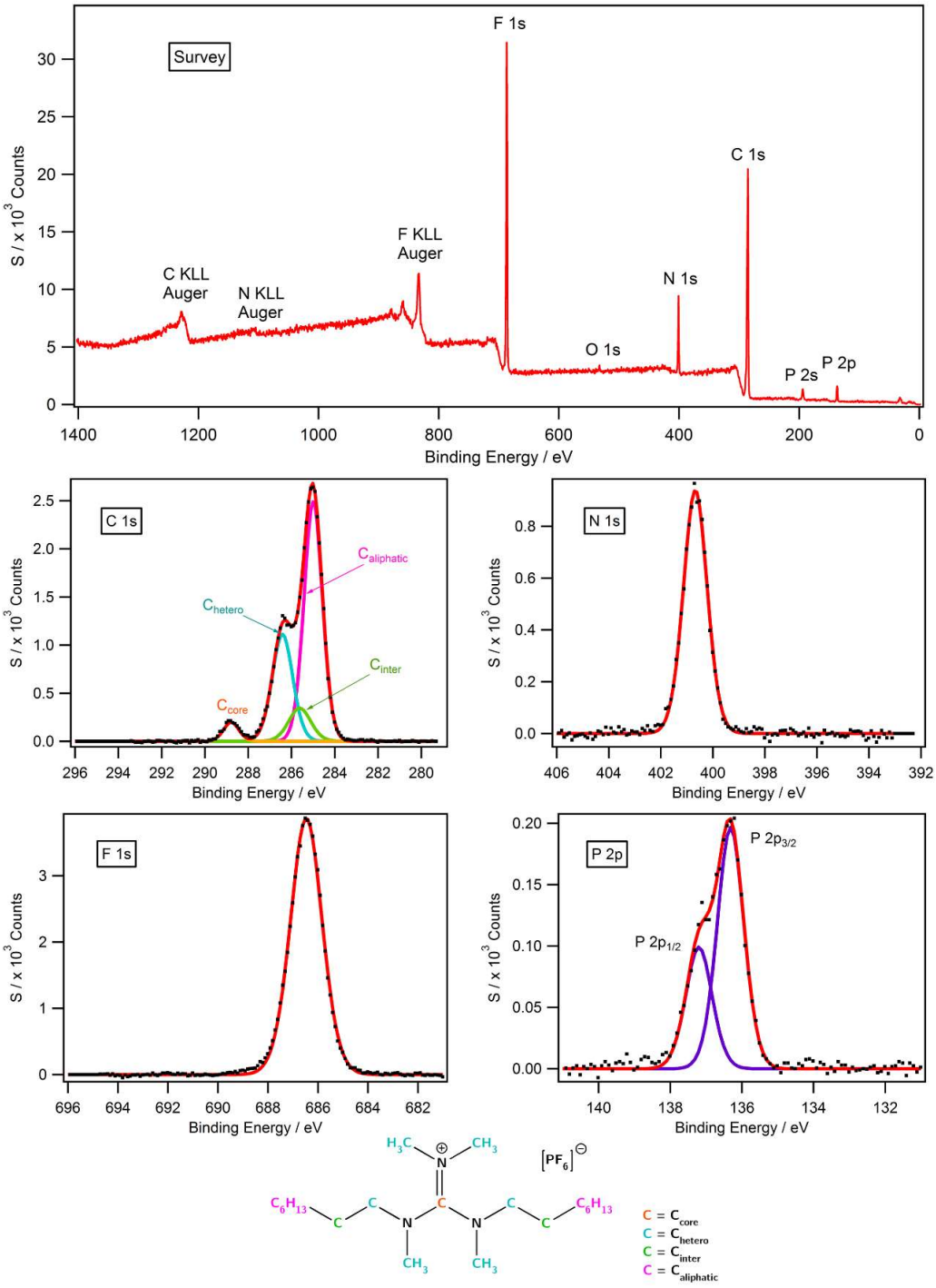
7.3.9. $[(C_4C_1)_2dmg][NTf_2]$ survey and high-resolution scans



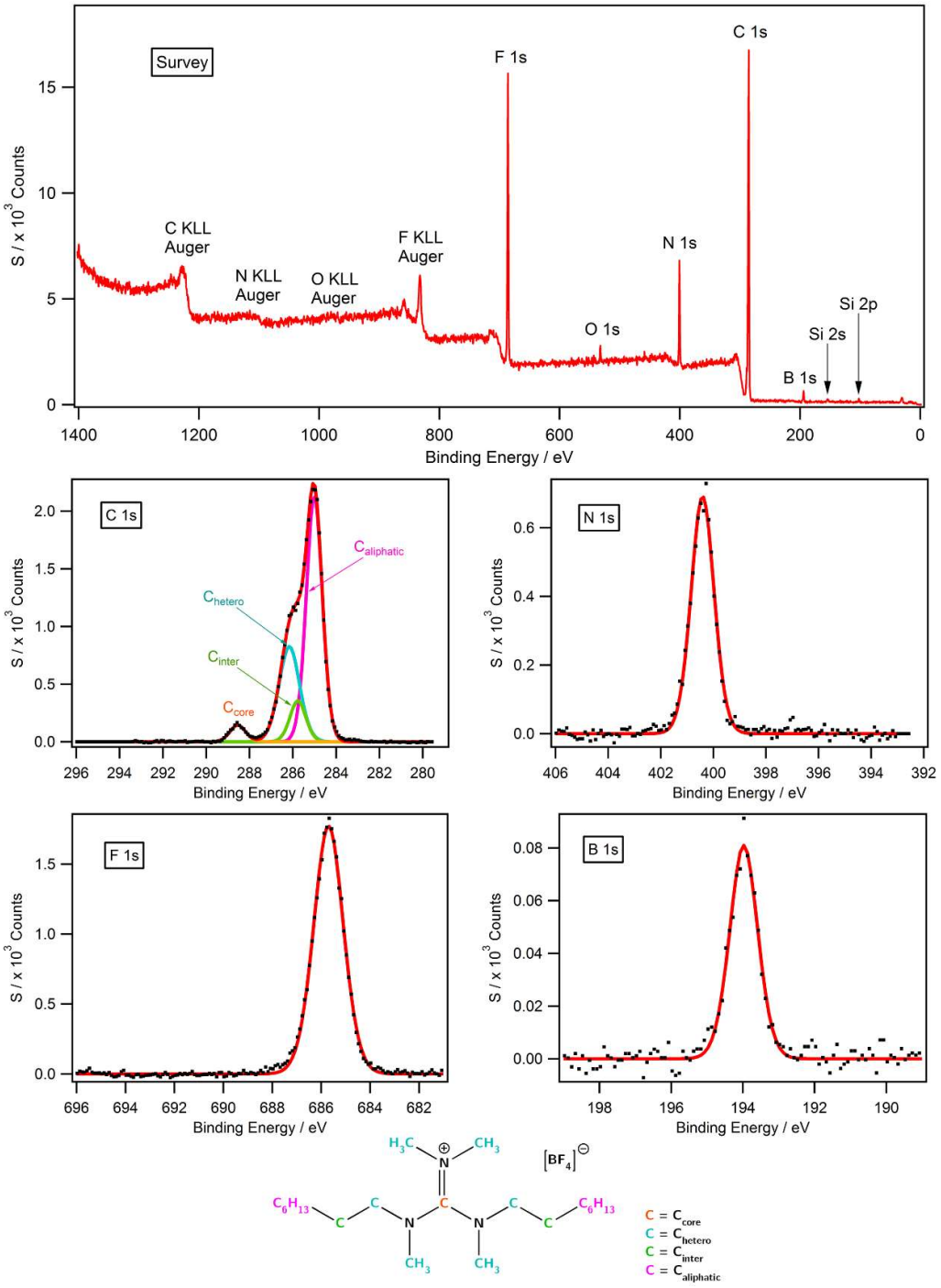
7.3.10. $[(C_8C_1)_2dmg][Cl]$ survey and high-resolution scans



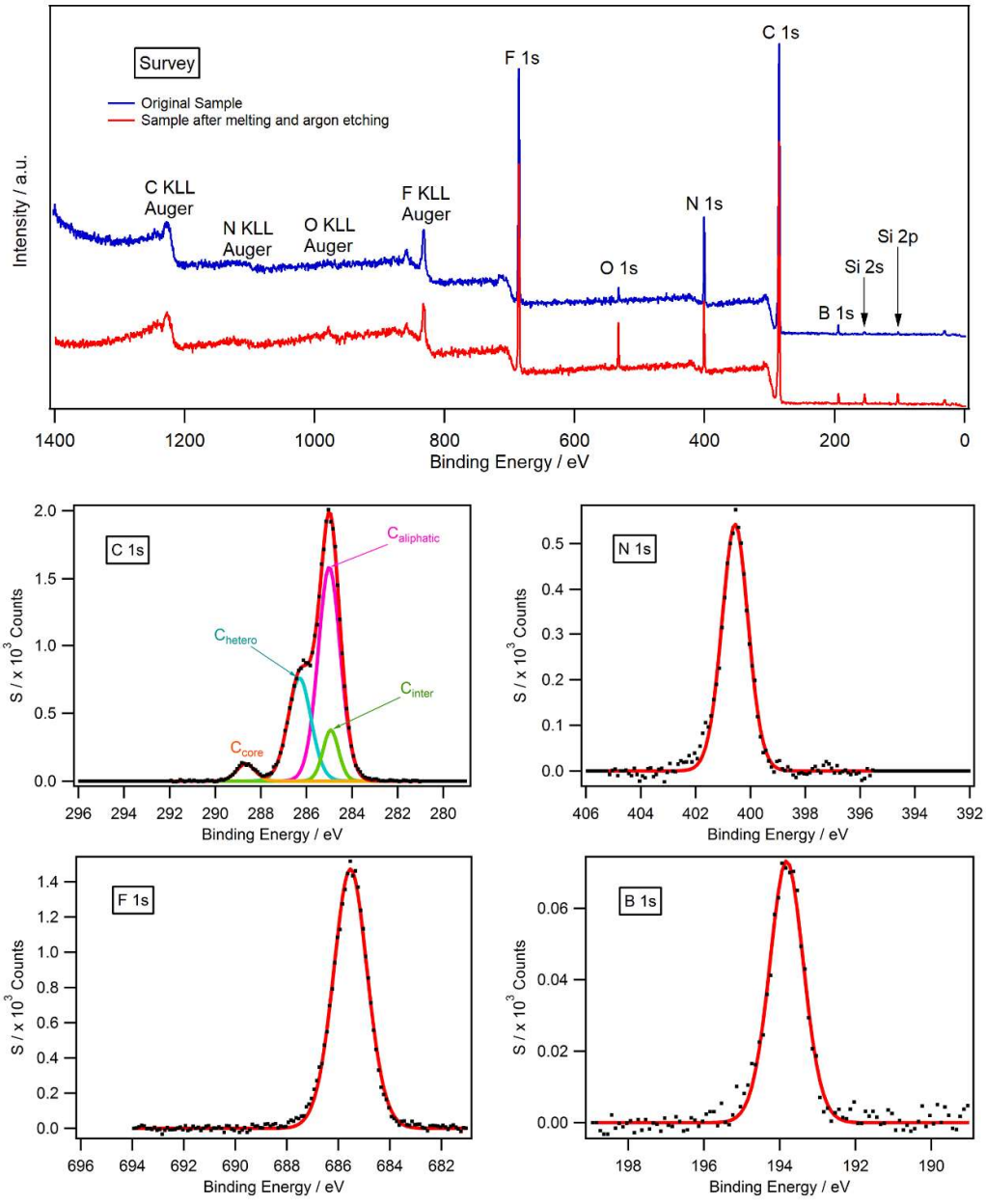
7.3.11. $[(C_8C_1)_2dmg][PF_6]$ survey and high-resolution scans



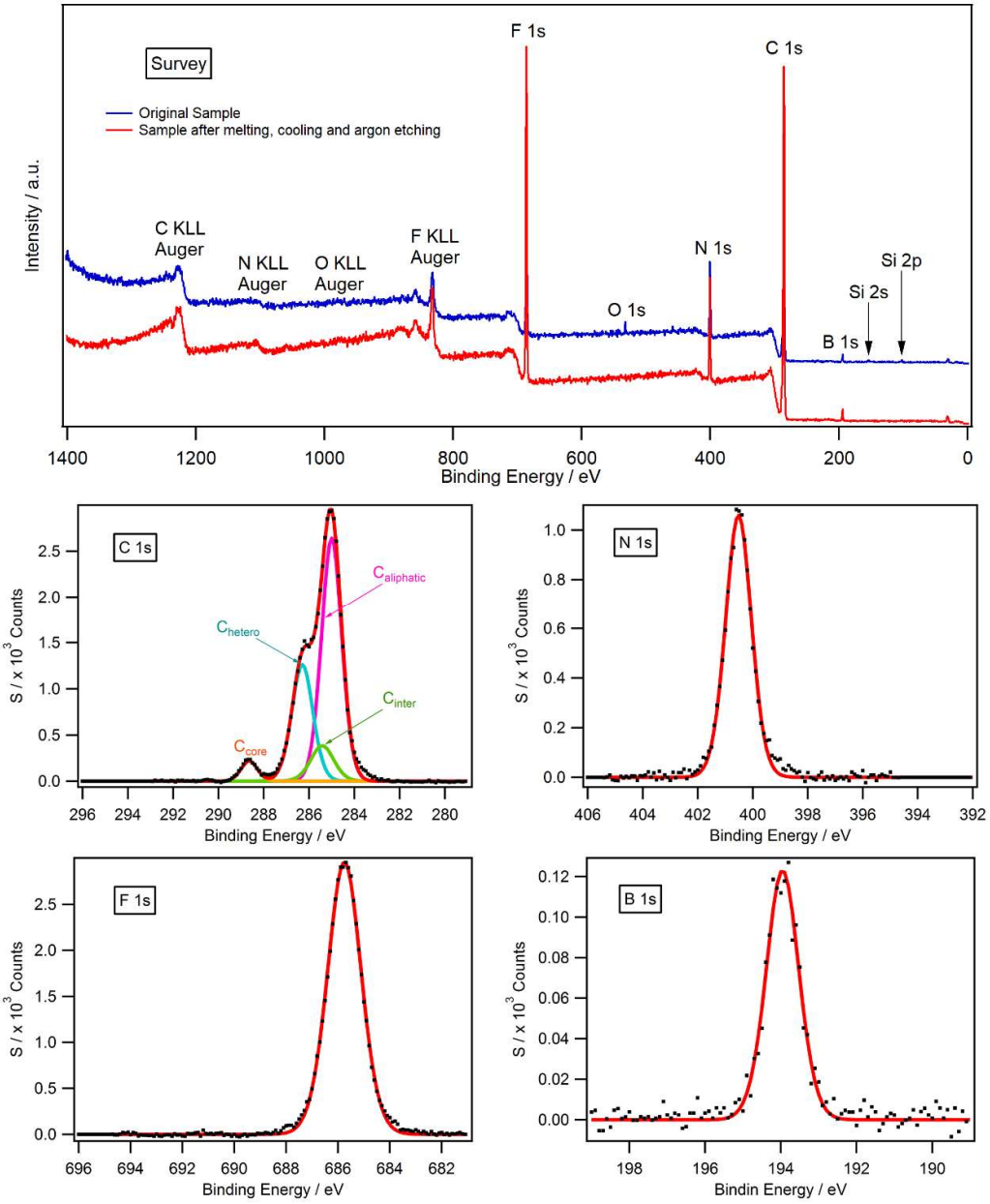
7.3.12. $[(C_8C_1)_2dmg][BF_4]$ survey and high-resolution scans



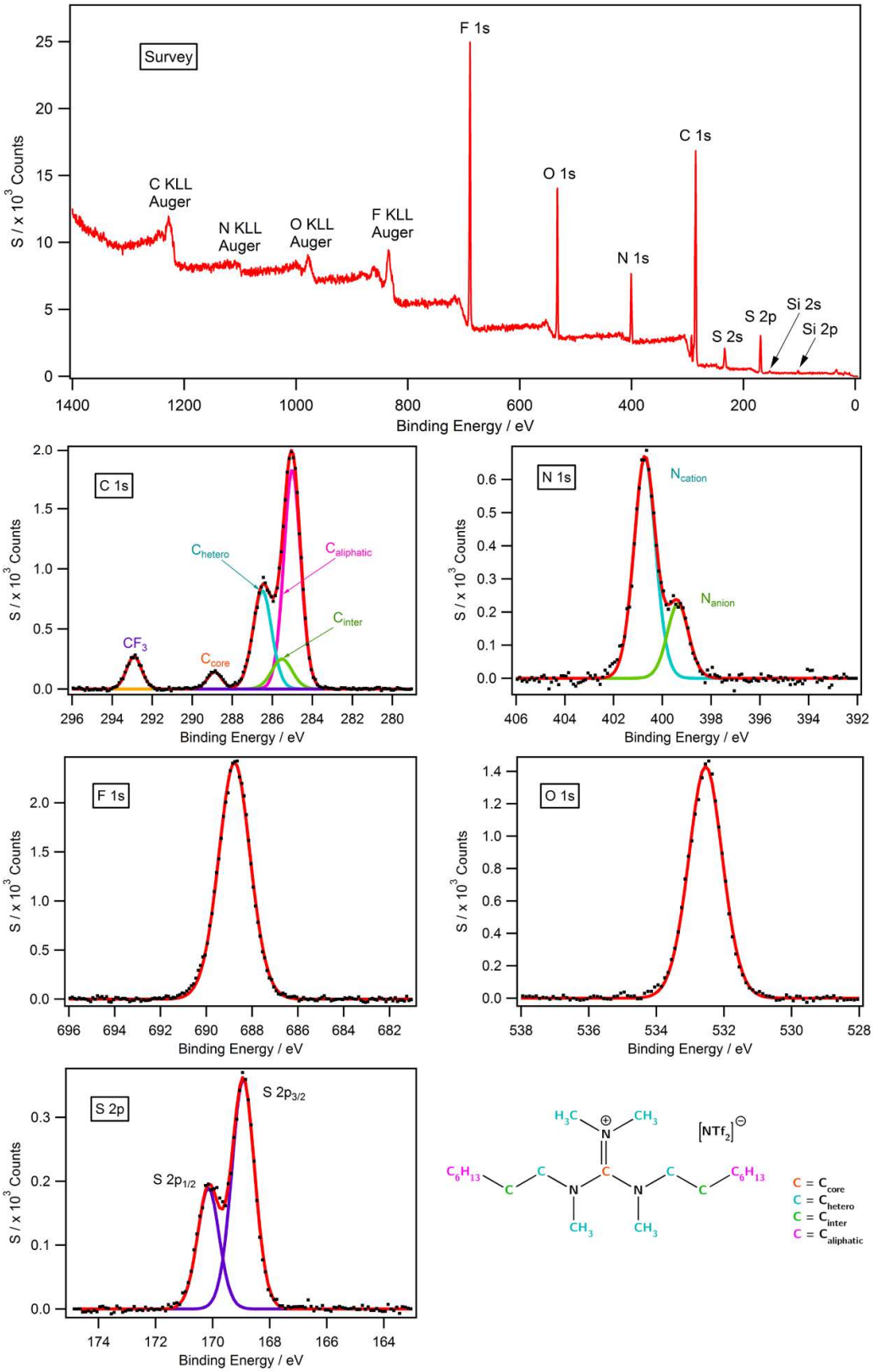
7.3.12. $[(C_8C_1)_2dmg][BF_4]$ survey and high-resolution scans – melting followed by argon etching



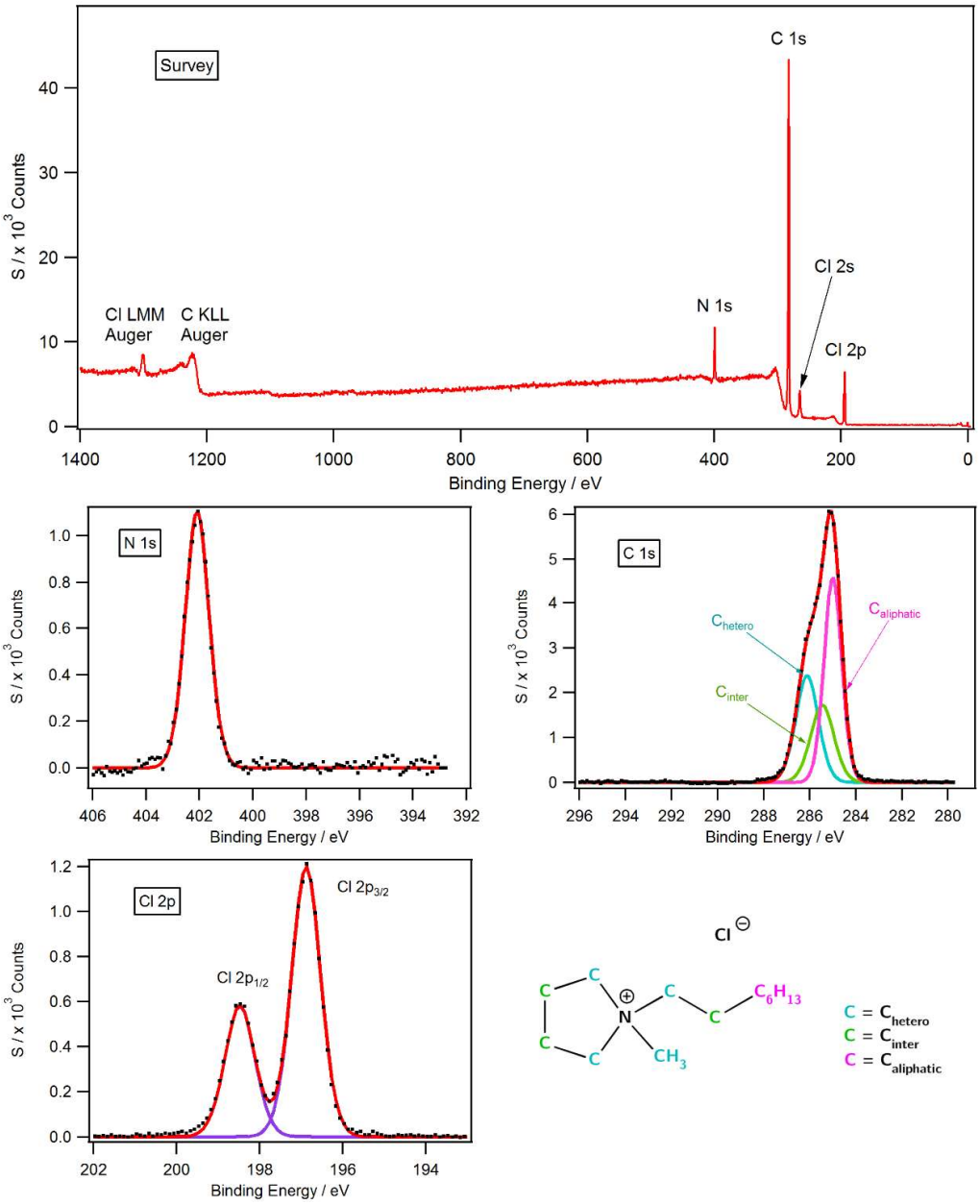
7.3.12. $[(C_8C_1)_2dmg][BF_4]$ survey and high-resolution scans – melting, followed by cooling to form a glassy state solid and finally argon etching



7.3.13. $[(C_8C_1)_2dmg][NTf_2]$ survey and high-resolution scans

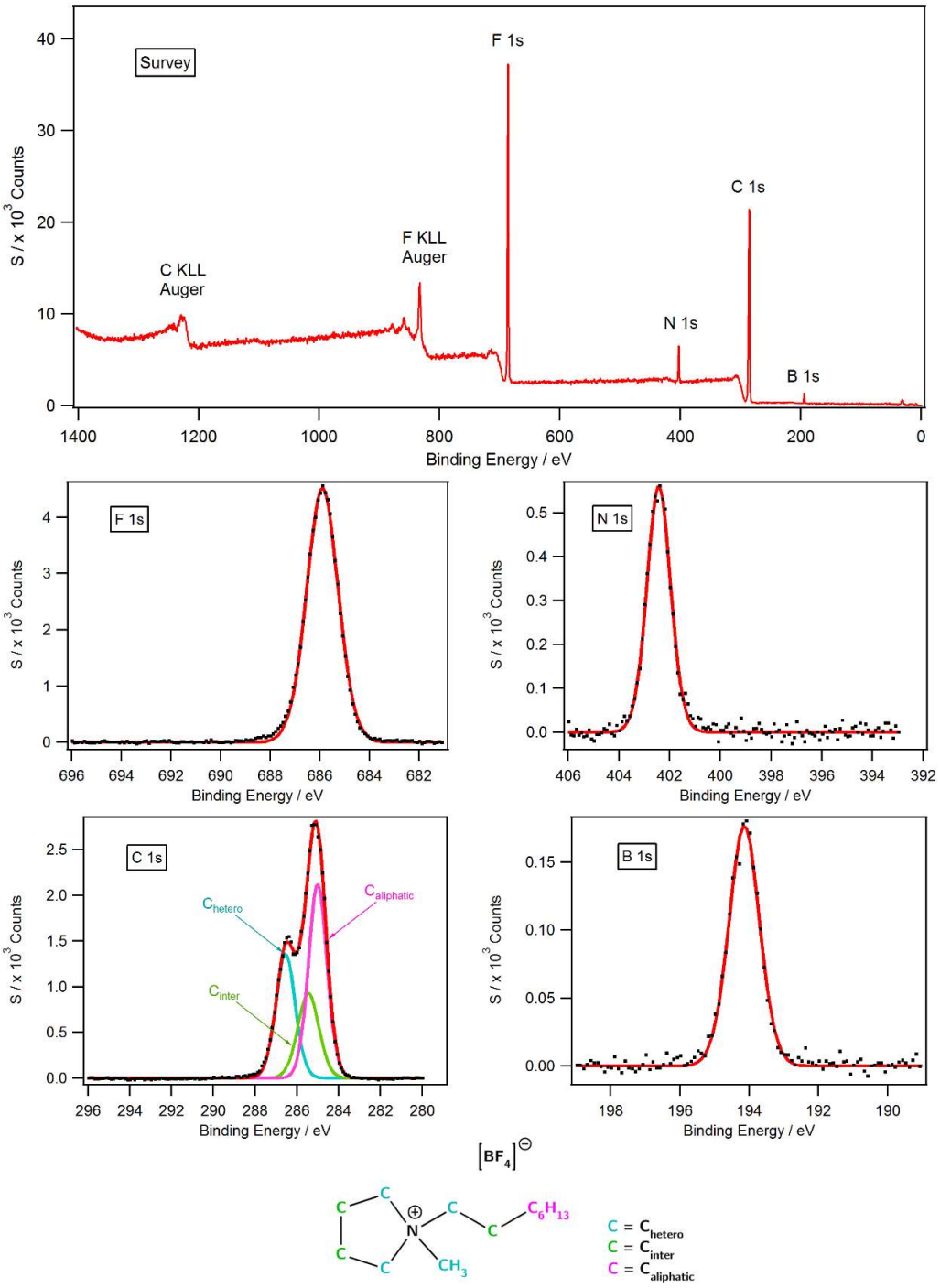


7.4.2. $[C_8C_1Pyrr]Cl$ survey and high-resolution scans§



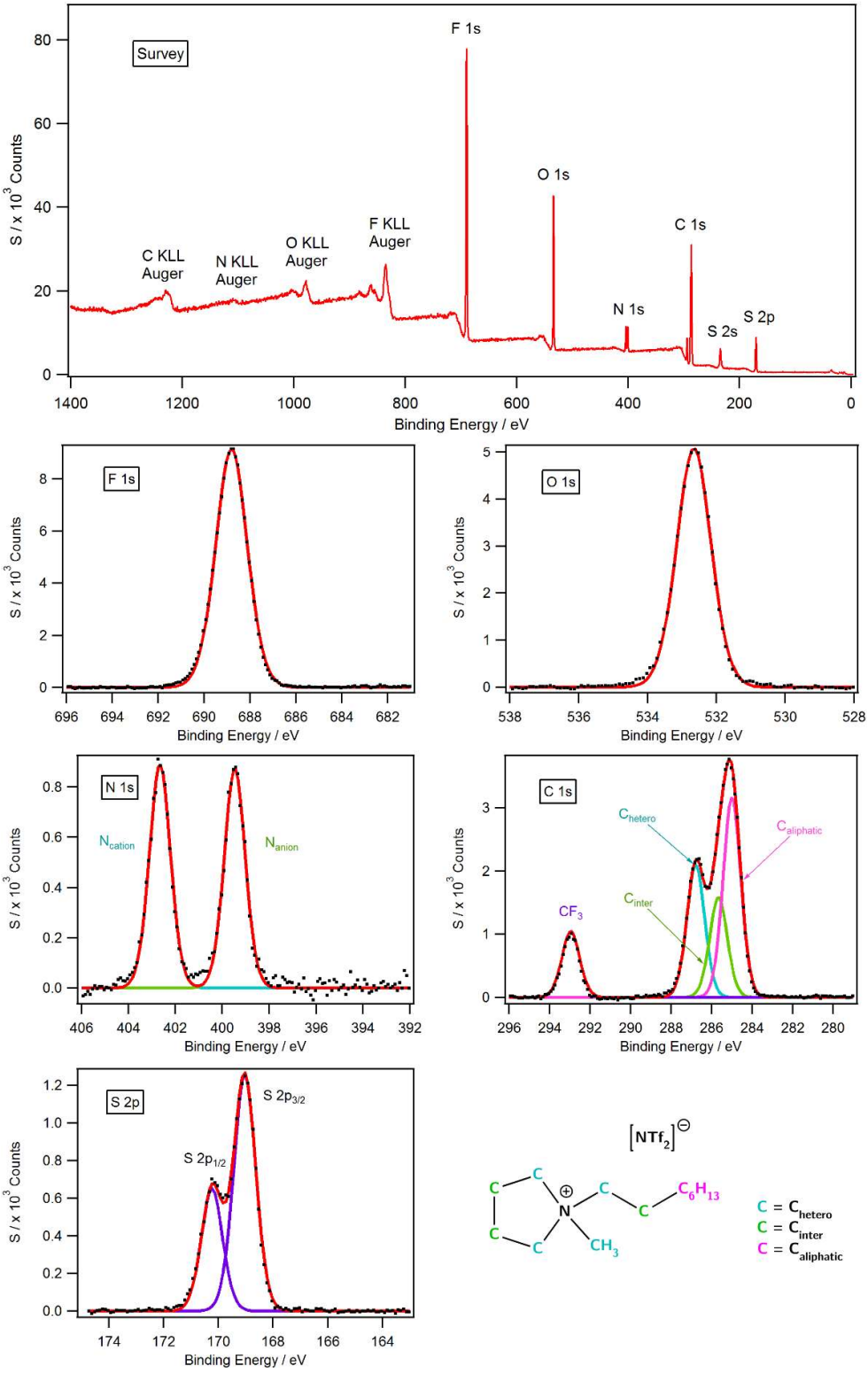
§ Experimental data in agreement with reference 278.

7.4.3. $[C_8C_1Pyrr][BF_4]$ survey and high-resolution scans**



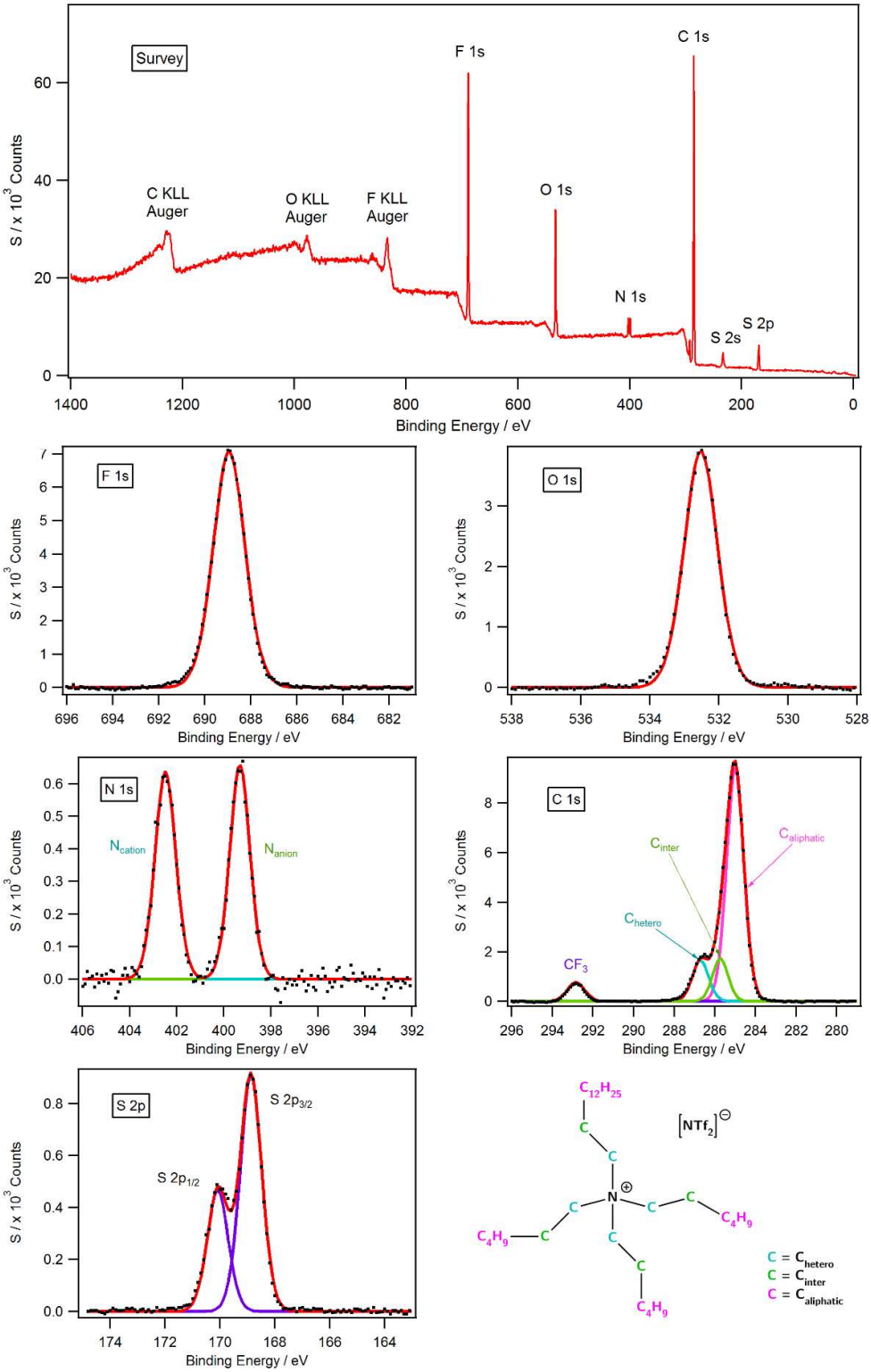
** Experimental data in agreement with reference 278.

7.4.4. $[C_8C_1Pyrr][NTf_2]$ survey and high-resolution scans[††]



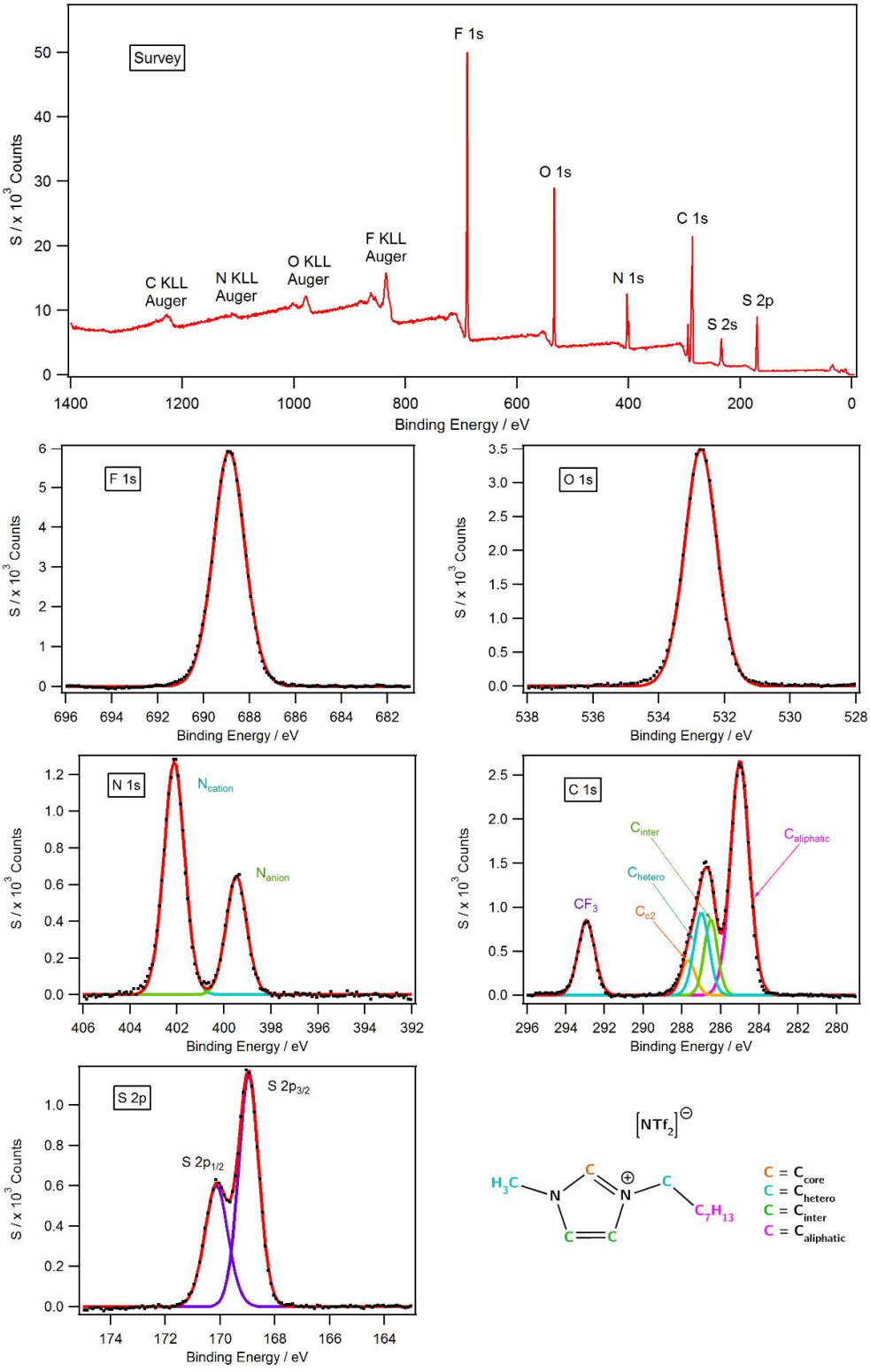
[††] Experimental data in agreement with reference 125.

$[N_{6,6,6,14}][NTf_2]$ survey and high-resolution scans[‡‡]



[‡‡] Experimental data obtained from reference 127.

7.5.13. $[C_8C_1Im][NTf_2]$ survey and high-resolution scans§§



§§ Experimental data in agreement with reference 108.

Table 3.1. Measured experimental and nominal (in brackets) stoichiometries for the guanidinium-based ionic liquids studied in this work. Highlighted stoichiometries that fall outside the experimental error of ± 20%.

		Composition[a] (%)													
Compound		C 1s		N 1s		F 1s		O 1s		S 2p		P 2p		B 1s		Cl 2p	
RSF[74,134]		0.278		0.477		1.000		0.780		0.668		0.486		0.159		0.891	
$[(C_8C_1)_2dmg]^+$	Cl^-	85.7	(84.0)	10.8	(12.0)	-		-		-		-		-		3.5	(4.0)
$[(C_4C_1)_2dmg]^+$	Cl^-	78.6	(76.5)	16.4	(17.6)	-		-		-		-		-		5.1	(5.9)
$[(C_4C_4)_2dmg]^+$	Cl^-	83.9	(82.6)	12.4	(13.0)	-		-		-		-		-		3.7	(4.3)
$[(C_8C_1)_2dmg]^+$	$[BF_4]^-$	74.5	(72.4)	9.3	(10.3)	12.0	(13.8)	-		-		-		4.3	(3.4)	-	
[b]$[(C_8C_1)_2dmg]^+$	$[BF_4]^-$	73.0[b]	(72.4)	9.2[b]	(10.3)	14.0[b]	(13.8)	-		-		-		3.9[b]	(3.4)	-	
$[(C_4C_1)_2dmg]^+$	$[BF_4]^-$	68.8	(61.9)	11.2	(14.3)	14.3	(19.0)	-		-		-		5.6	(4.8)	-	
$[(C_4C_4)_2dmg]^+$	$[BF_4]^-$	72.4	(70.4)	10.3	(11.1)	13.5	(14.8)	-		-		-		3.8	(3.7)	-	
$[(C_8C_1)_2dmg]^+$	$[PF_6]^-$	68.9	(67.7)	8.6	(9.7)	19.4	(19.4)	-		-		3.1	(3.2)	-		-	
$[(C_4C_1)_2dmg]^+$	$[PF_6]^-$	62.1	(56.5)	12.6	(13.0)	22.2	(26.1)	-		-		3.1	(4.3)	-		-	
$[(C_4C_4)_2dmg]^+$	$[PF_6]^-$	69.1	(65.5)	9.1	(10.3)	18.6	(20.7)	-		-		3.2	(3.4)	-		-	
$[(C_8C_1)_2dmg]^+$	$[NTf_2]^-$	61.4	(59.0)	10.0	(10.3)	14.9	(15.4)	9.0	(10.3)	4.7	(5.1)	-		-		-	
$[(C_4C_1)_2dmg]^+$	$[NTf_2]^-$	53.7	(48.4)	12.3	(12.9)	16.9	(19.4)	11.6	(12.9)	5.5	(6.5)	-		-		-	
$[(C_4C_4)_2dmg]^+$	$[NTf_2]^-$	59.8	(56.8)	10.6	(10.8)	14.8	(16.2)	10.2	(10.8)	4.5	(5.4)	-		-		-	

[a] Relative sensitivity factors (RSF) taken from the Kratos Library. *N.B.* Hydrogen is undetectable by XPS due its low photoionisation cross-section; consequently, reported stoichiometries are determined without consideration of hydrogen content.[132]

[b] Measured experimental and nominal (in brackets) stoichiometries for $[(C_8C_1)_2dmg][BF_4]$ after argon-etching studies.

Table 3.2. Experimental binding energies in eV for the ionic liquids studied in this work. The associated experimental error is 0.1 eV. $[(C_8C_1)_2dmg]^+$ compounds charge corrected by setting $C_{aliphatic}$ 1s to 285.0 eV. The corrected N_{cation} 1s values were then used to charge reference the smaller chain analogues where the anion is kept the same.

		Binding Energy / eV												
Compound		Cation					Anion							
Cation	Anion	$C_{aliphatic}$ 1s	C_{inter} 1s	C_{hetero} 1s	C_{core} 1s	N_{cation} 1s	C_{CF3} 1s	N_{anion} 1s	O 1s	F 1s	S $2p_{3/2}$	P $2p_{3/2}$	B 1s	Cl $2p_{3/2}$
$[(C_8C_1)_2dmg]^+$	Cl^-	285.0	285.5	286.0	288.1	400.1	-	-	-	-	-	-	-	196.4
$[(C_4C_1)_2dmg]^+$	Cl^-	284.7	285.3	285.8	288.2	400.1	-	-	-	-	-	-	-	196.4
$[(C_4C_4)_2dmg]^+$	Cl^-	284.9	285.4	286.0	288.2	400.1	-	-	-	-	-	-	-	196.4
$[(C_8C_1)_2dmg]^+$	$[BF_4]^-$	285.0	285.8	286.2	288.5	400.4	-	-	-	685.7	-	-	194.0	-
$[(C_4C_1)_2dmg]^+$	$[BF_4]^-$	284.9	285.3	286.2	288.5	400.4	-	-	-	685.6	-	-	193.8	-
$[(C_4C_4)_2dmg]^+$	$[BF_4]^-$	284.9	285.4	286.2	288.6	400.4	-	-	-	685.5	-	-	193.8	-
$[(C_8C_1)_2dmg]^+$	$[PF_6]^-$	285.0	285.6	286.4	288.8	400.7	-	-	-	686.5	-	136.3	-	-
$[(C_4C_1)_2dmg]^+$	$[PF_6]^-$	285.1	285.5	286.4	288.8	400.7	-	-	-	686.5	-	136.5	-	-
$[(C_4C_4)_2dmg]^+$	$[PF_6]^-$	285.2	285.8	286.5	288.8	400.7	-	-	-	686.5	-	136.4	-	-
$[(C_8C_1)_2dmg]^+$	$[NTf_2]^-$	285.0	285.5	286.5	288.9	400.7	292.9	399.3	532.5	688.8	168.9	-	-	-
$[(C_4C_1)_2dmg]^+$	$[NTf_2]^-$	285.1	285.5	286.5	288.9	400.7	293.0	399.5	532.7	688.9	169.0	-	-	-
$[(C_4C_4)_2dmg]^+$	$[NTf_2]^-$	285.2	285.5	286.5	288.8	400.7	293.0	399.4	532.6	688.9	168.9	-	-	-

Table 3.6. Measured experimental full width at half maximum for the guanidinium ionic liquids studied in this work.

Compound		FWHM / eV												
		Cation					Anion							
Cation	Anion	$C_{aliphatic}$ 1s	C_{inter} 1s	C_{hetero} 1s	C_{core} 1s	N_{cation} 1s	C_{CF_3} 1s	N_{anion} 1s	O 1s	F 1s	S $2p_{3/2}$	B 1s	P $2p_{3/2}$	Cl $2p_{3/2}$
$[(C_8C_1)_2dmg]^+$	Cl^-	1.0	0.9	1.1	1.0	1.1	-	-	-	-	-	-	-	1.0
$[(C_4C_1)_2dmg]^+$	Cl^-	1.0	0.9	1.2	0.8	1.1	-	-	-	-	-	-	-	0.9
$[(C_4C_4)_2dmg]^+$	Cl^-	0.9	0.9	1.2	1.0	1.0	-	-	-	-	-	-	-	0.9
$[(C_8C_1)_2dmg]^+$	$[BF_4]^-$	1.0	1.1	1.1	0.9	1.1	-	-	-	1.4	-	0.9	-	-
$[(C_4C_1)_2dmg]^+$	$[BF_4]^-$	0.9	1.1	1.2	1.0	1.1	-	-	-	1.5	-	0.9	-	-
$[(C_4C_4)_2dmg]^+$	$[BF_4]^-$	1.0	1.2	1.2	0.9	1.1	-	-	-	1.5	-	0.9	-	-
$[(C_8C_1)_2dmg]^+$	$[PF_6]^-$	1.0	1.2	1.1	0.8	1.0	-	-	-	1.5	-	-	0.9	-
$[(C_4C_1)_2dmg]^+$	$[PF_6]^-$	0.9	1.2	1.2	0.9	1.1	-	-	-	1.5	-	-	0.9	-
$[(C_4C_4)_2dmg]^+$	$[PF_6]^-$	0.9	1.2	1.2	0.9	1.1	-	-	-	1.5	-	-	0.9	-
$[(C_8C_1)_2dmg]^+$	$[NTf_2]^-$	1.0	1.1	1.1	0.9	1.1	1.0	1.0	1.2	1.6	0.9	-	-	-
$[(C_4C_1)_2dmg]^+$	$[NTf_2]^-$	1.0	1.2	1.1	0.9	1.1	1.1	1.1	1.2	1.6	1.0	-	-	-
$[(C_4C_4)_2dmg]^+$	$[NTf_2]^-$	1.0	1.2	1.1	1.0	1.1	1.1	1.2	1.2	1.6	1.0	-	-	-

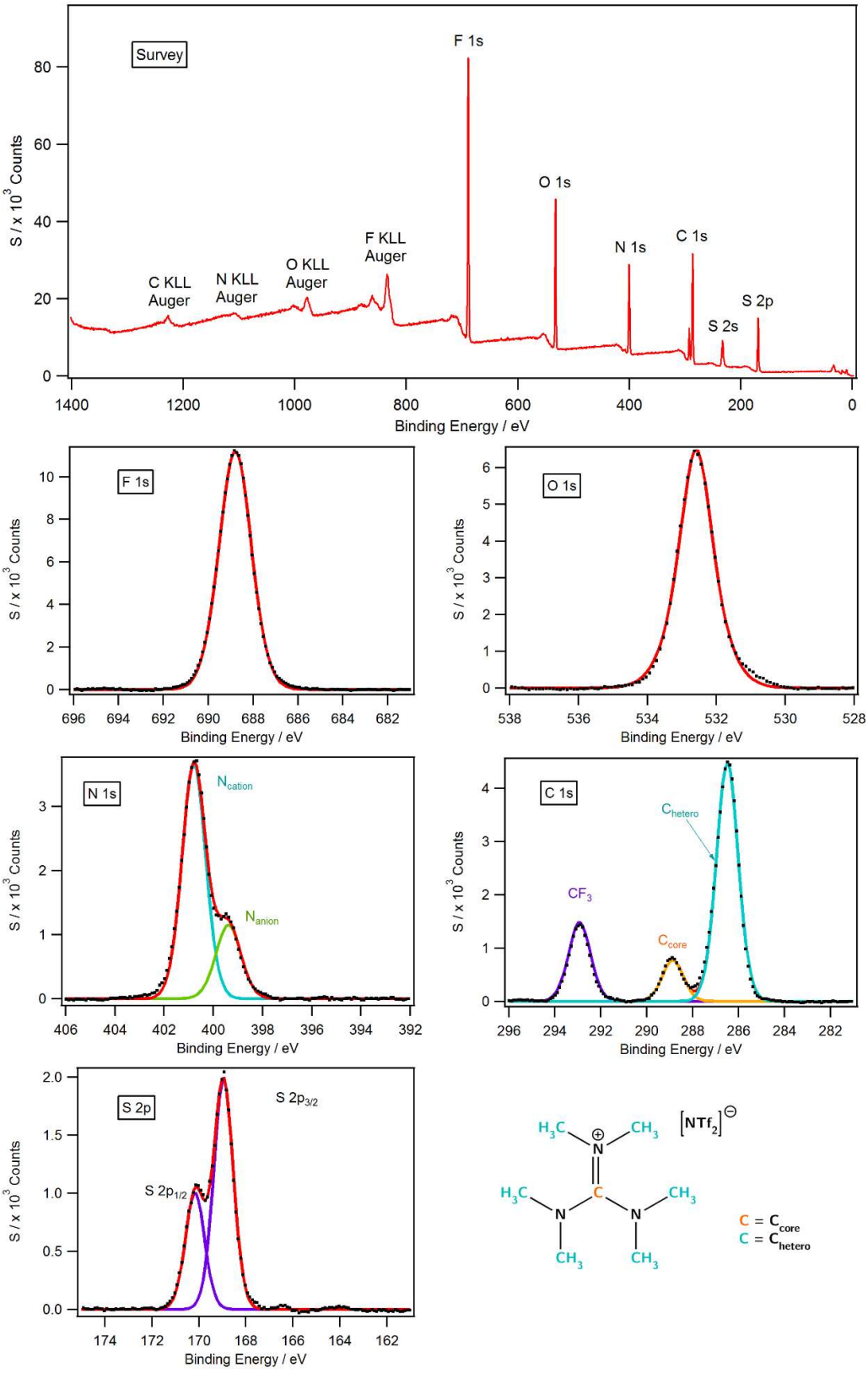
Appendix B: XP Spectra for Chapter 4

Spectra are charge corrected by indirect charge referencing as all the ionic liquids in *Chapter 4* have short alkyl chains ($n < 8$). This was achieved by setting the F 1s component to 688.8 eV as all ionic liquids studied share the $[NTf_2]^-$ anion. This agrees with the F 1s literature binding energy attributed to the $[NTf_2]^-$ anion for various ionic liquid families.[108, 125, 127]

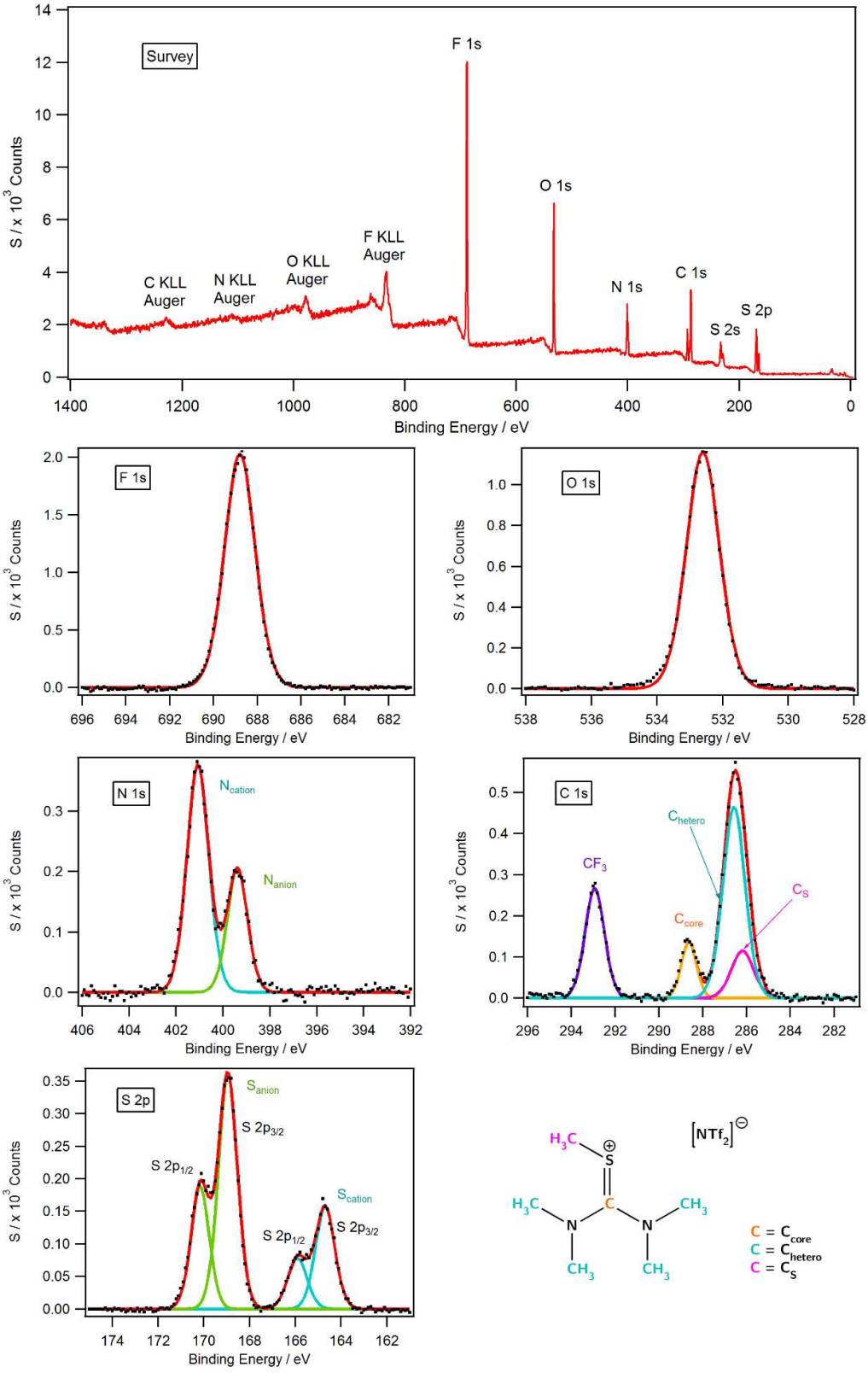
C 1s high-resolution spectra were fitted according to the models described within *Chapter 4, Section 4.2.2*. S 2p high-resolution spectra was fitted taking into account spin-orbit coupling, whereby the area ratio of $2p_{1/2}$: $2p_{3/2}$ components is set to 1 : 2. The O 1s and S 2p high-resolution spectra for ionic liquids containing the $[NTf_2]^-$ anion are affected by shake up/off phenomena and a 4% intensity loss (per oxygen/sulfur atom involved in double bonding) was taken into account when calculating atomic percentages for these elements. This was also applied to the sulfur in the cation when involved in double bonding. Likewise, the $C_{2/core}$ 1s and N_{cation} 1s high-resolution spectra of all cations are affected by shake up/off phenomena and a 20% and 12%, respectively, intensity loss (per carbon/nitrogen atom involved in double bonding) was taken into account when calculating atomic percentages for these elements.[74]

Binding energies, full width at half maximum and composition tables for all guanidinium-, imidazolium- and sulfur-based ionic liquids investigated in *Chapter 4* can be found at the end of *Appendix B*.

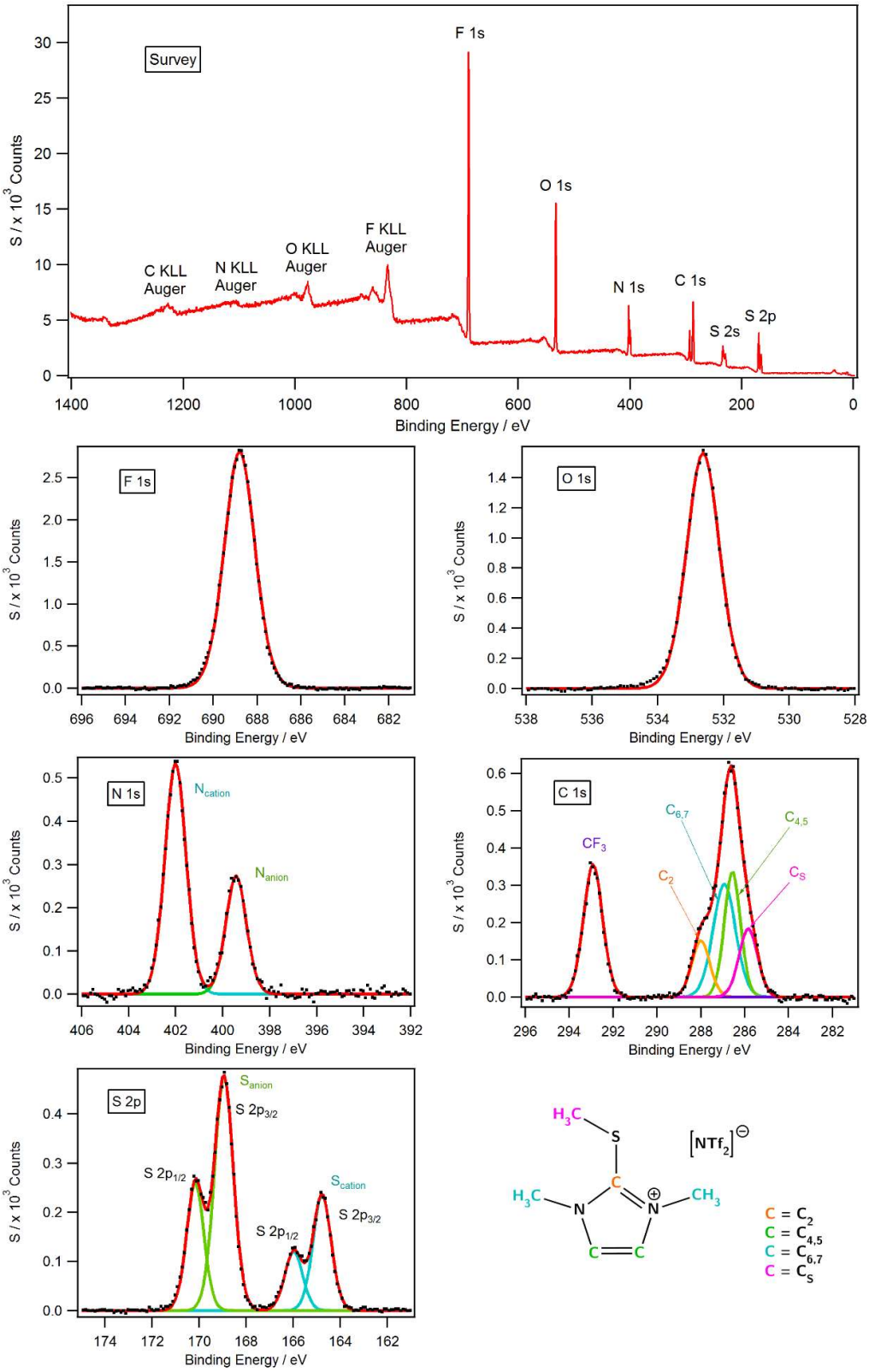
7.3.1. $[(C_1C_1)_2dmg][NTf_2]$ survey and high-resolution scans



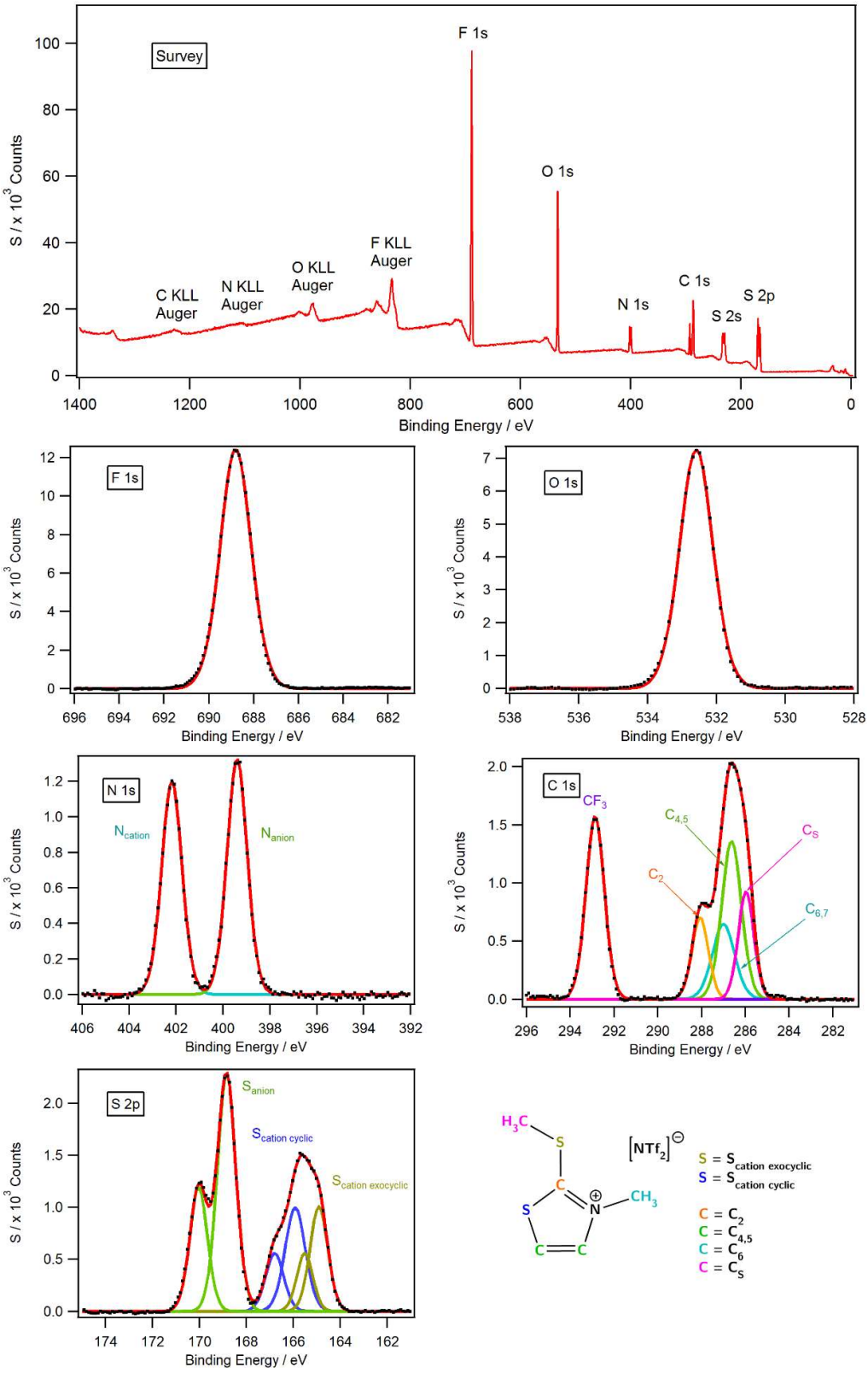
7.5.19. $[(C_1)_5TU][NTf_2]$ survey and high-resolution scans



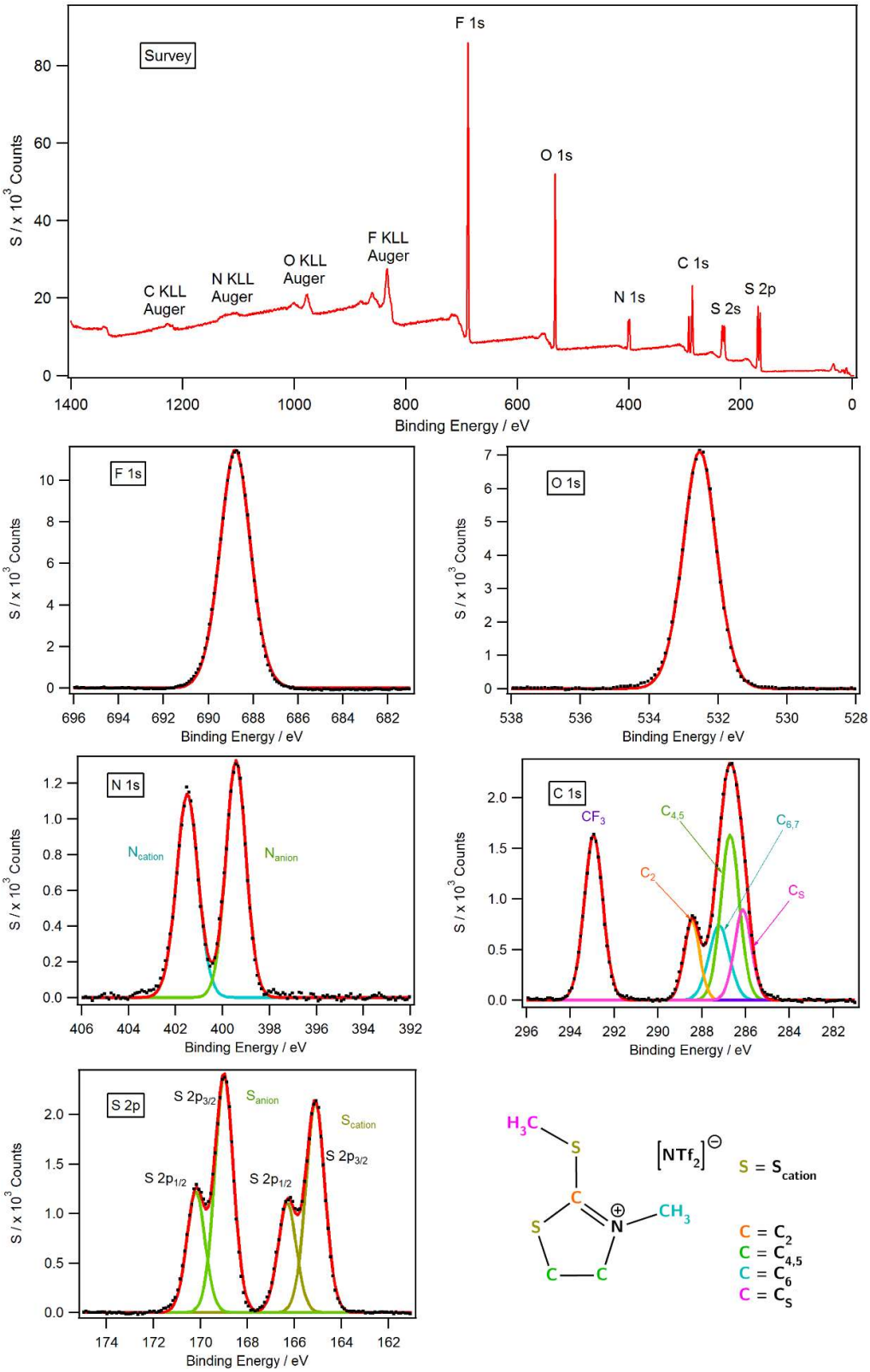
7.5.22. $[C_1(C_1)_2ThioIm][NTf_2]$ survey and high-resolution scans



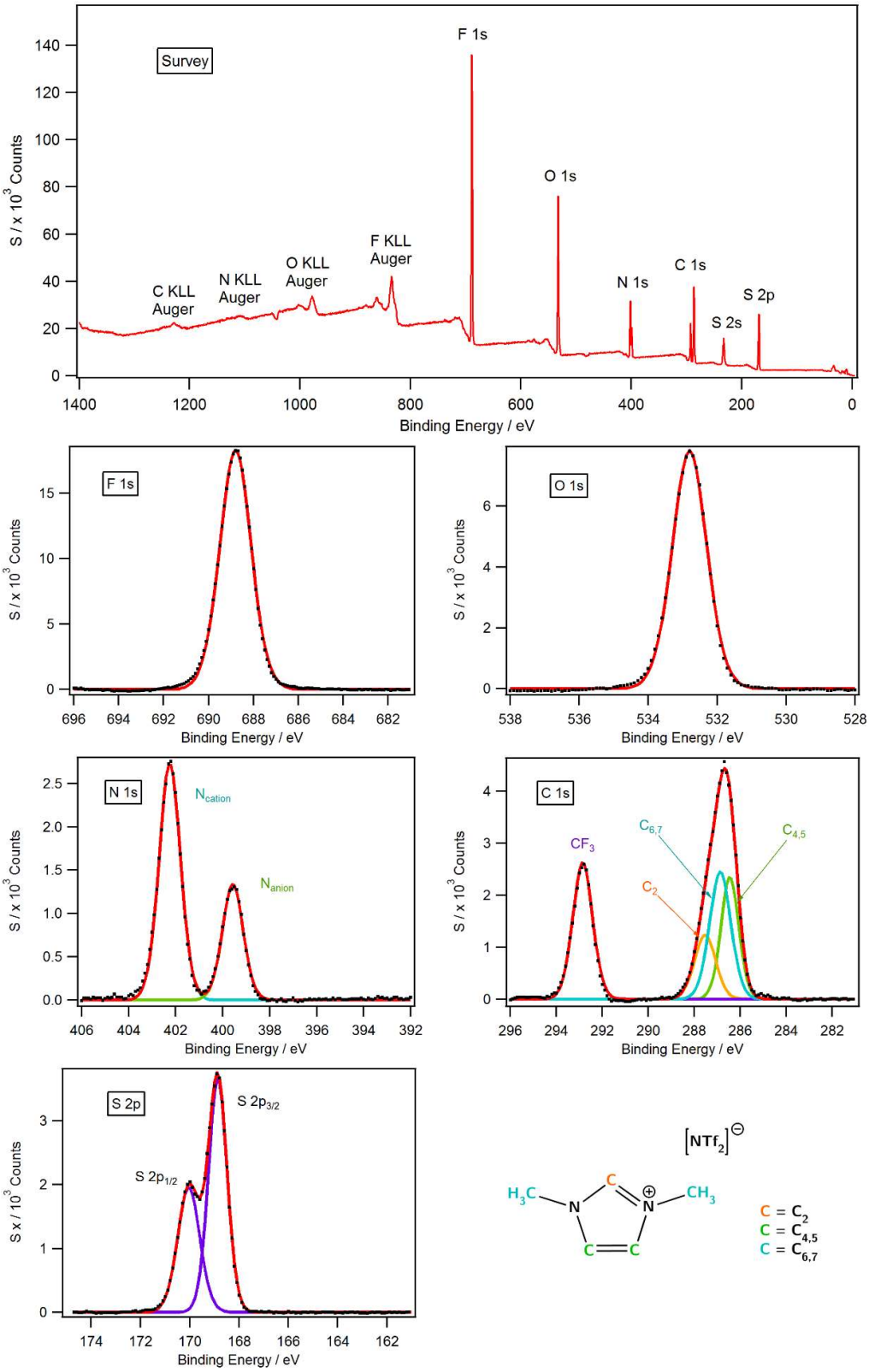
7.5.36. $[(C_1)_2Thio][NTf_2]$ survey and high-resolution scans



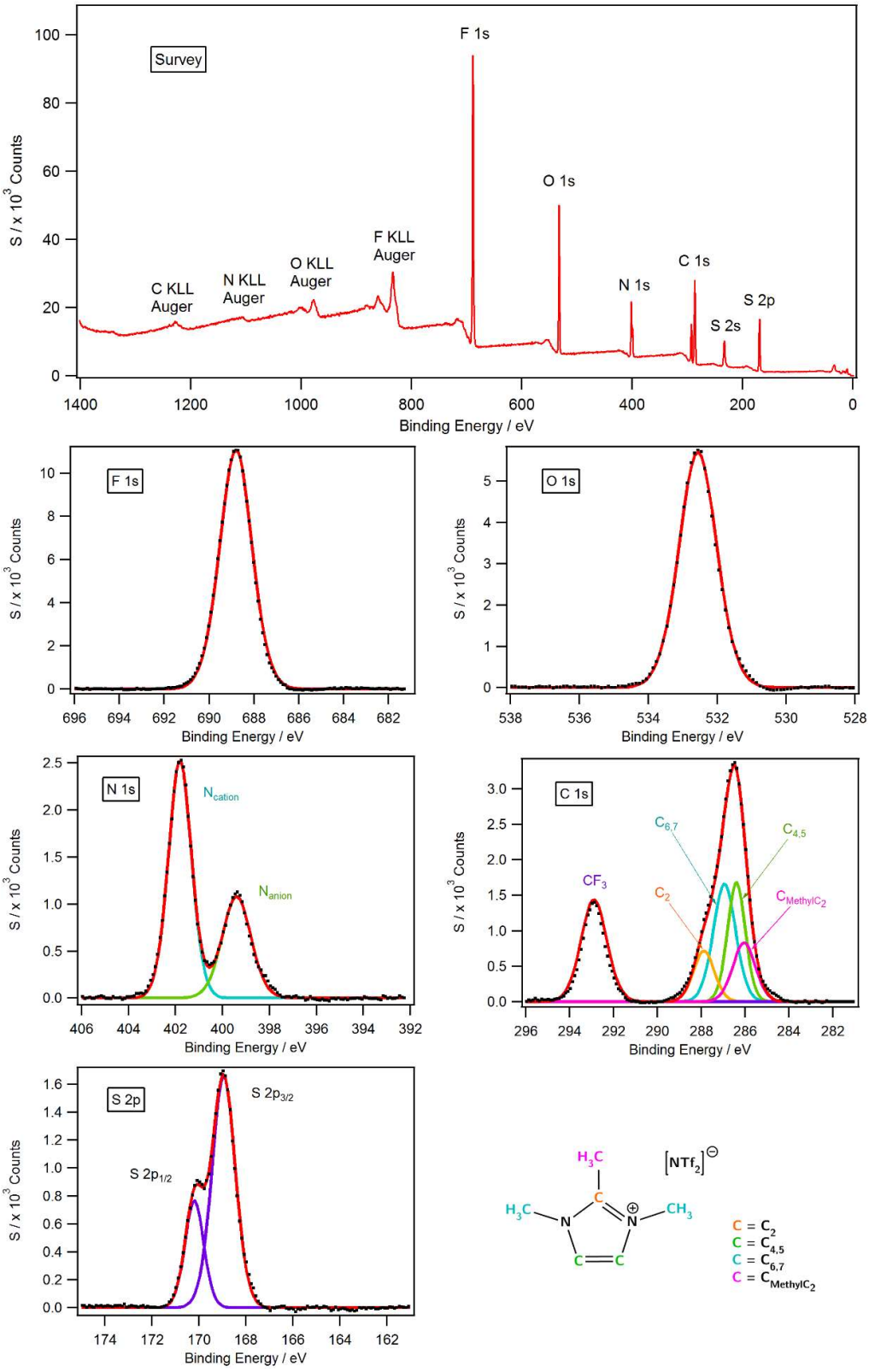
7.5.38. $[(C_1)_2Thiz][NTf_2]$ survey and high-resolution scans



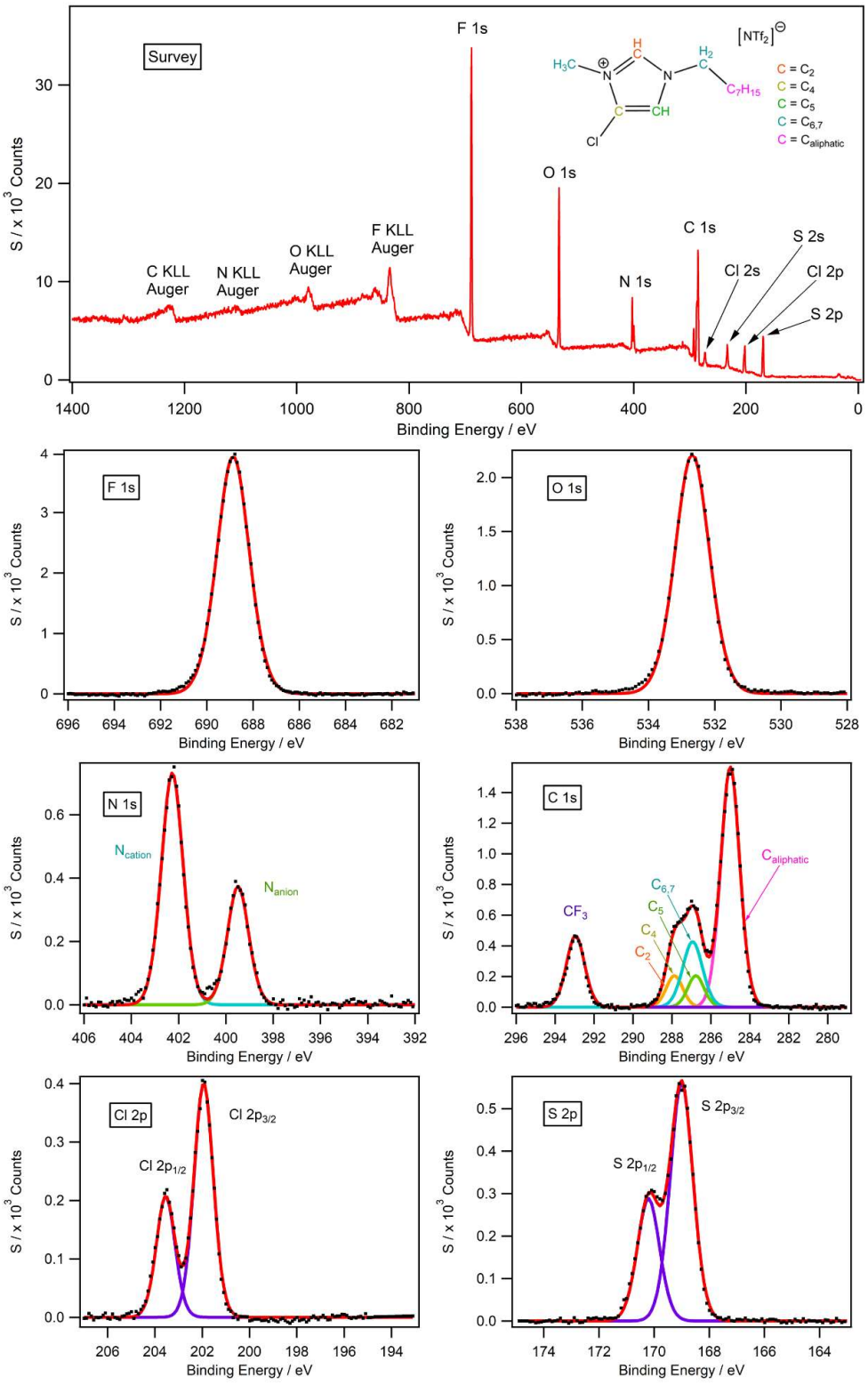
7.5.4. $[C_1C_1Im][NTf_2]$ survey and high-resolution scans



7.5.2. $[C_1C_1C_1Im][NTf_2]$ survey and high-resolution scans

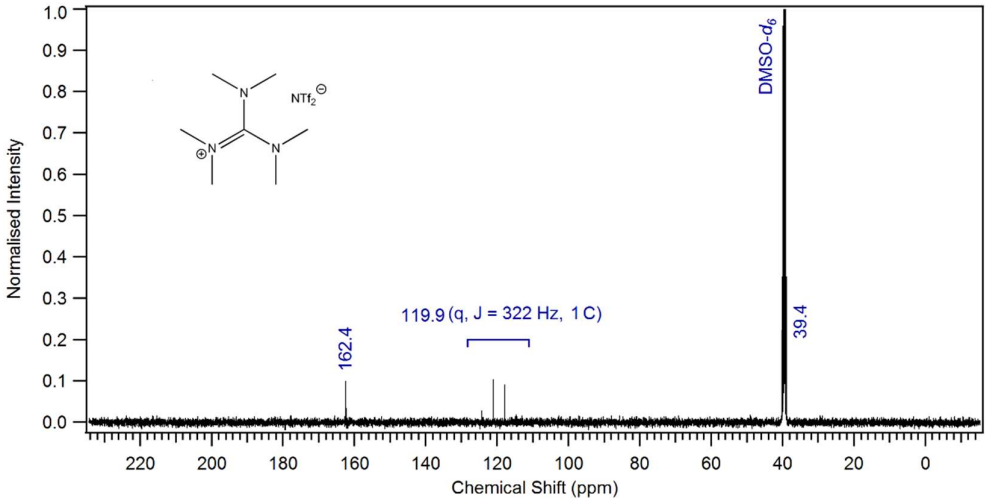


$[C_1C_8\text{-4-ClIm}][NTf_2]$ survey and high-resolution scans***

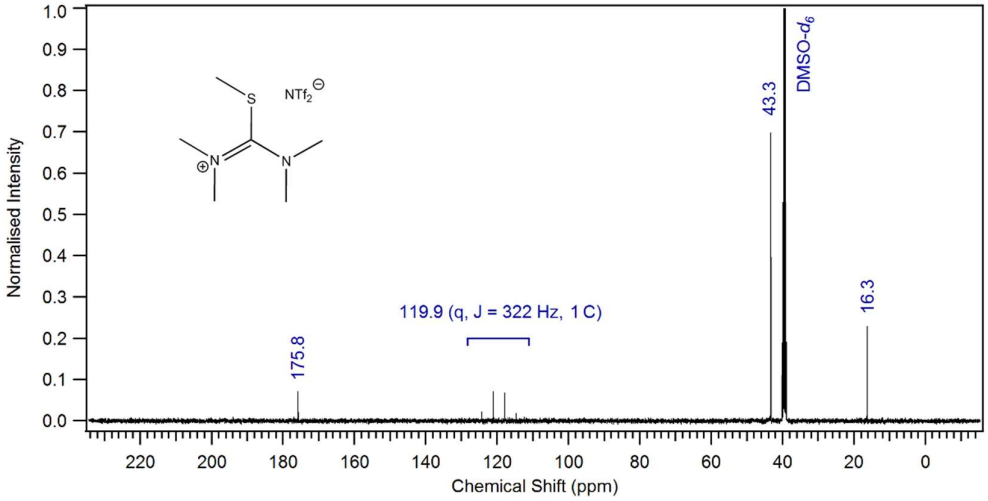


*** Experimental data in agreement with reference 191.

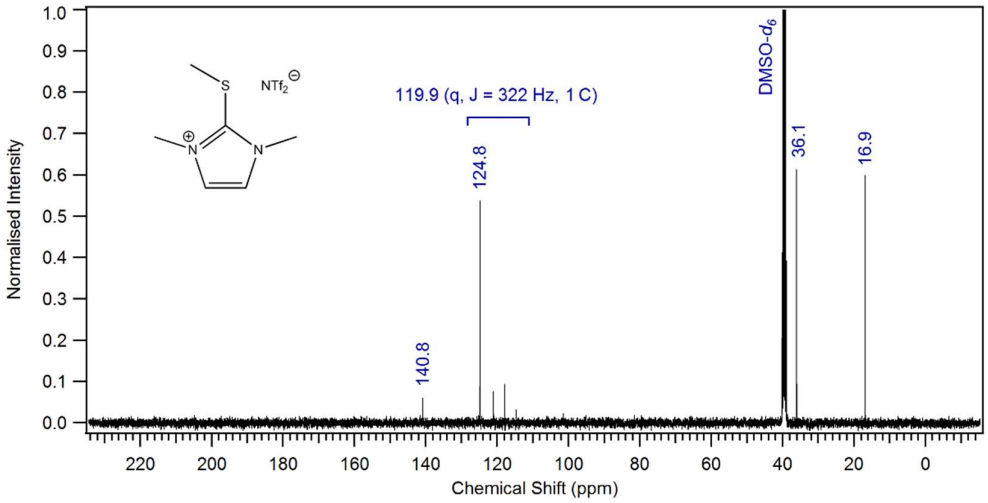
7.3.1. $[(C_1C_1)_2dmg][NTf_2]$ ^{13}C NMR spectrum



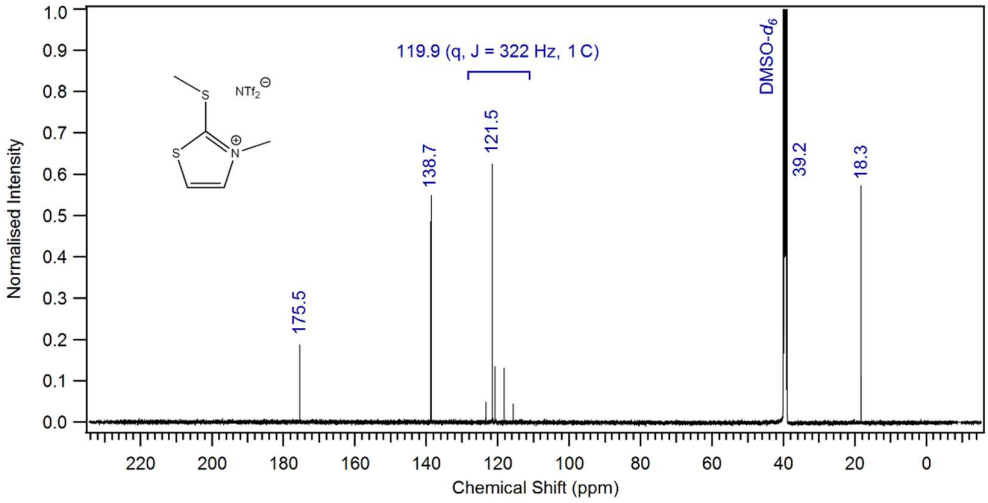
7.5.19. $[(C_1)_5TU][NTf_2]$ ^{13}C NMR spectrum



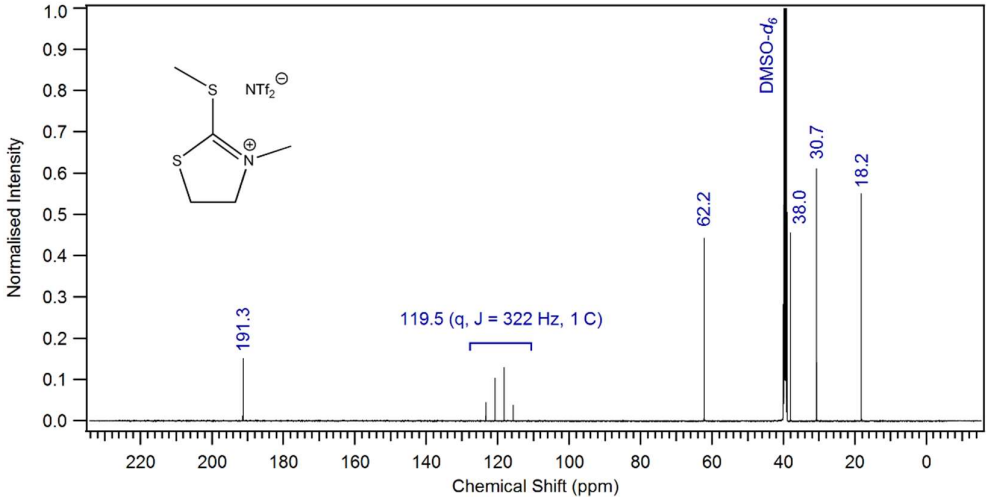
7.5.22. $[C_1(C_1)_2ThioIm][NTf_2]$ ^{13}C NMR spectrum



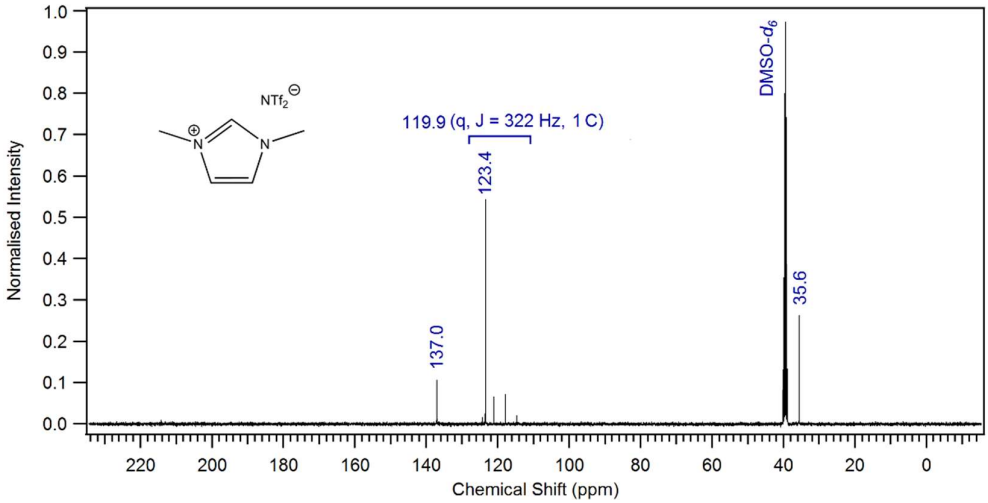
7.5.36. $[(C_1)_2Thio][NTf_2]$ ^{13}C NMR spectrum



7.5.38. $[(C_1)_2Thiz][NTf_2]$ ^{13}C NMR spectrum



7.5.4. $[C_1C_1Im][NTf_2]$ ^{13}C NMR spectrum



7.5.2. $[C_1C_1C_1Im][NTf_2]$ ^{13}C NMR spectrum

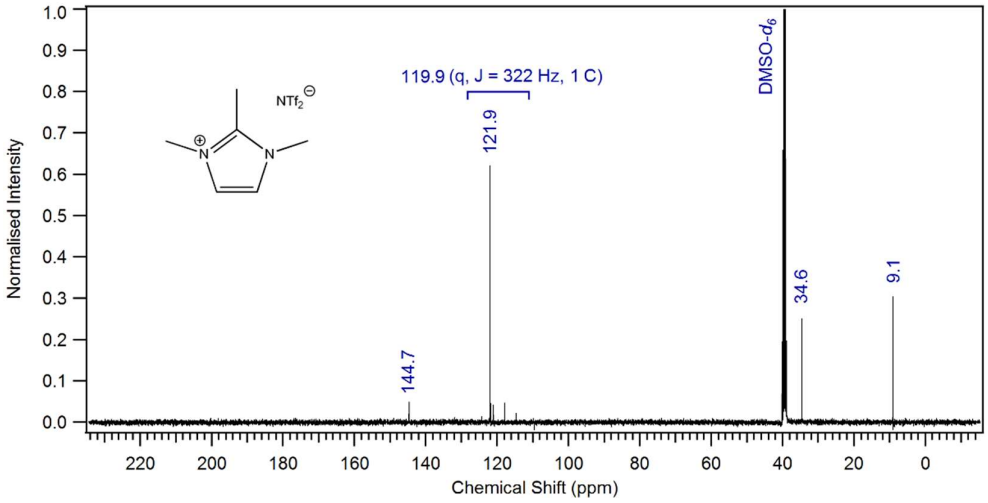


Table 4.1. Measured experimental and nominal (in brackets) stoichiometries for guanidinium, sulfur and imidazolium based ionic liquids studied in this work. Associated experimental error is ± 10 - 20%.

	Composition (%)				
Compound	C 1s	N 1s	O 1s	F 1s	S 2p
[a]RSF[74,134]	0.278	0.477	0.780	1.000	0.668
$[(C_1C_1)_2dmg][NTf_2]$	39.9 (36.0)	16.7 (16.0)	14.4 (16.0)	22.6 (24.0)	6.4 (8.0)
$[(C_1)_5TU][NTf_2]$	37.8 (33.3)	11.5 (12.5)	14.2 (16.7)	23.3 (25.0)	13.3 (12.5)
$[C_1(C_1)_2ThioIm][NTf_2]$	36.6 (33.3)	11.7 (12.5)	14.2 (16.7)	24.4 (25.0)	13.1 (12.5)
$[(C_1)_2Thio][NTf_2]$	32.3 (30.4)	9.1 (8.7)	16.4 (17.4)	27.2 (26.1)	15.0 (17.4)
$[(C_1)_2Thiz][NTf_2]$	33.8 (30.4)	9.1 (8.7)	16.2 (17.4)	25.0 (26.1)	15.8 (17.4)
$[C_1C_1Im][NTf_2]$	35.3 (31.8)	14.3 (13.6)	16.0 (18.2)	25.9 (27.3)	8.5 (9.1)
$[C_1C_1C_1Im][NTf_2]$	38.2 (34.8)	14.6 (13.0)	15.8 (17.4)	23.4 (26.1)	8.1 (8.7)

[a] Relative sensitivity factors (RSF) taken from the Kratos Library. *N.B.* Hydrogen is undetectable by XPS due its low photoionisation cross-section; consequently, reported stoichiometries are determined without consideration of hydrogen content.[132]

Table 4.2. Experimental binding energies in eV for guanidinium, sulfur-based and imidazolium ionic liquids studied in this work. The associated experimental error is 0.1 eV. All compounds charge corrected by setting F 1s to 688.8 eV of the corresponding $[NTf_2]^-$ anion.

Compound		Binding Energy / eV												
		Cation							Anion					
Cation	Anion	$C_{2/core}$ 1s	$C_{6,7/hetero}$ 1s	$C_{4,5/inter}$ 1s	$C_{S/MethylC2}$ 1s	N_{cation} 1s	$S_{exocyclic}$ $2p_{3/2}$	S_{cyclic} $2p_{3/2}$	C_{CF_3} 1s	N_{anion} 1s	O 1s	F 1s	S_{anion} $2p_{3/2}$
$[(C_1C_1)_2dmg]^+$	$[NTf_2]^-$	288.9	286.5	-	-	400.8	-	-	292.9	399.4	532.6	688.8	169.0
$[(C_1)_5TU]^+$	$[NTf_2]^-$	288.6	286.6	-	286.2	401.1	164.7	-	292.9	399.4	532.6	688.8	169.0
$[C_1(C_1)_2ThioIm]^+$	$[NTf_2]^-$	288.0	286.9	286.6	285.8	402.0	164.8	-	292.9	399.4	532.6	688.8	168.9
$[(C_1)_2Thio]^+$	$[NTf_2]^-$	288.1	286.9	286.6	285.9	402.2	164.9	165.9	292.9	399.4	532.6	688.8	168.9
$[(C_1)_2Thiz]^+$	$[NTf_2]^-$	288.4	286.9	286.7	286.1	401.5	165.1	-	292.9	399.4	532.6	688.8	169.0
$[C_1C_1Im]^+$	$[NTf_2]^-$	287.6	286.9	286.5	-	402.1	-	-	292.9	399.4	532.6	688.8	168.9
$[C_1C_1C_1Im]^+$	$[NTf_2]^-$	287.9	286.9	286.4	286.1	401.8	-	-	292.9	399.4	532.6	688.8	168.9

Table 4.3. FWHM in eV for guanidinium, sulfur-based and imidazolium ionic liquids studied in this work.

Compound		FWHM / eV											
		Cation							Anion				
Cation	Anion	$C_{2/core}$ 1s	$C_{6,7/hetero}$ 1s	$C_{4,5/inter}$ 1s	$C_{S/MethylC2}$ 1s	N_{cation} 1s	$S_{exocyclic}$ $2p_{3/2}$	S_{cyclic} $2p_{3/2}$	C_{CF_3} 1s	N_{anion} 1s	O 1s	F 1s	S_{anion} $2p_{3/2}$
$[(C_1C_1)_2dmg]^+$	$[NTf_2]^-$	1.0	1.1	-	-	1.1	-	-	1.1	1.2	1.2	1.7	1.0
$[(C_1)_5TU]^+$	$[NTf_2]^-$	0.8	1.2	-	1.2	1.1	1.0	-	1.0	1.0	1.2	1.6	1.0
$[C_1(C_1)_2ThioIm]^+$	$[NTf_2]^-$	0.9	1.2	0.9	1.0	1.0	0.9	-	1.0	1.0	1.2	1.6	0.9
$[(C_1)_2Thio]^+$	$[NTf_2]^-$	0.8	1.2	0.9	0.9	1.0	1.1	1.0	0.9	1.0	1.1	1.6	0.9
$[(C_1)_2Thiz]^+$	$[NTf_2]^-$	0.8	1.1	1.1	1.0	1.1	0.9	-	1.0	1.0	1.1	1.6	0.9
$[C_1C_1Im]^+$	$[NTf_2]^-$	1.0	1.1	0.9	-	1.0	-	-	1.0	1.0	1.2	1.6	0.9
$[C_1C_1C_1Im]^+$	$[NTf_2]^-$	1.0	1.2	1.0	1.2	1.1	-	-	1.1	1.2	1.2	1.7	1.0

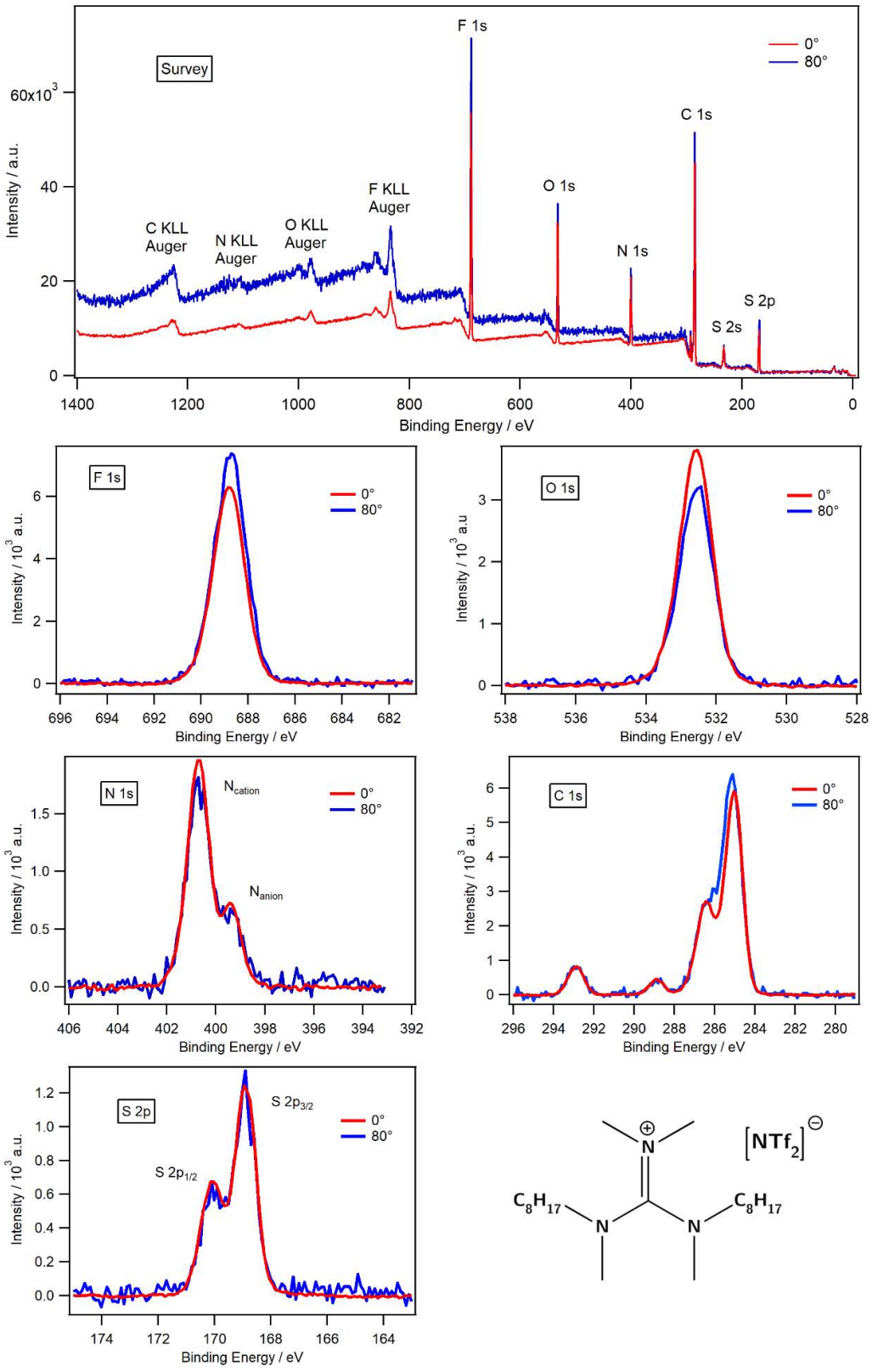
Appendix C: XP Spectra for Chapter 5

Spectra are charge corrected using an established internal reference method of setting the $C_{aliphatic}$ 1s component to 285.0 eV for ionic liquids with longer alkyl chains ($n \geq 8$). For ionic liquids with shorter alkyl chains ($n < 8$), indirect charge referencing is achieved by setting the measured binding energy of N_{cation} 1s equal to that of their long-chain equivalent A full description of this procedure is described within *Chapter 3, Section 3.2.3*.

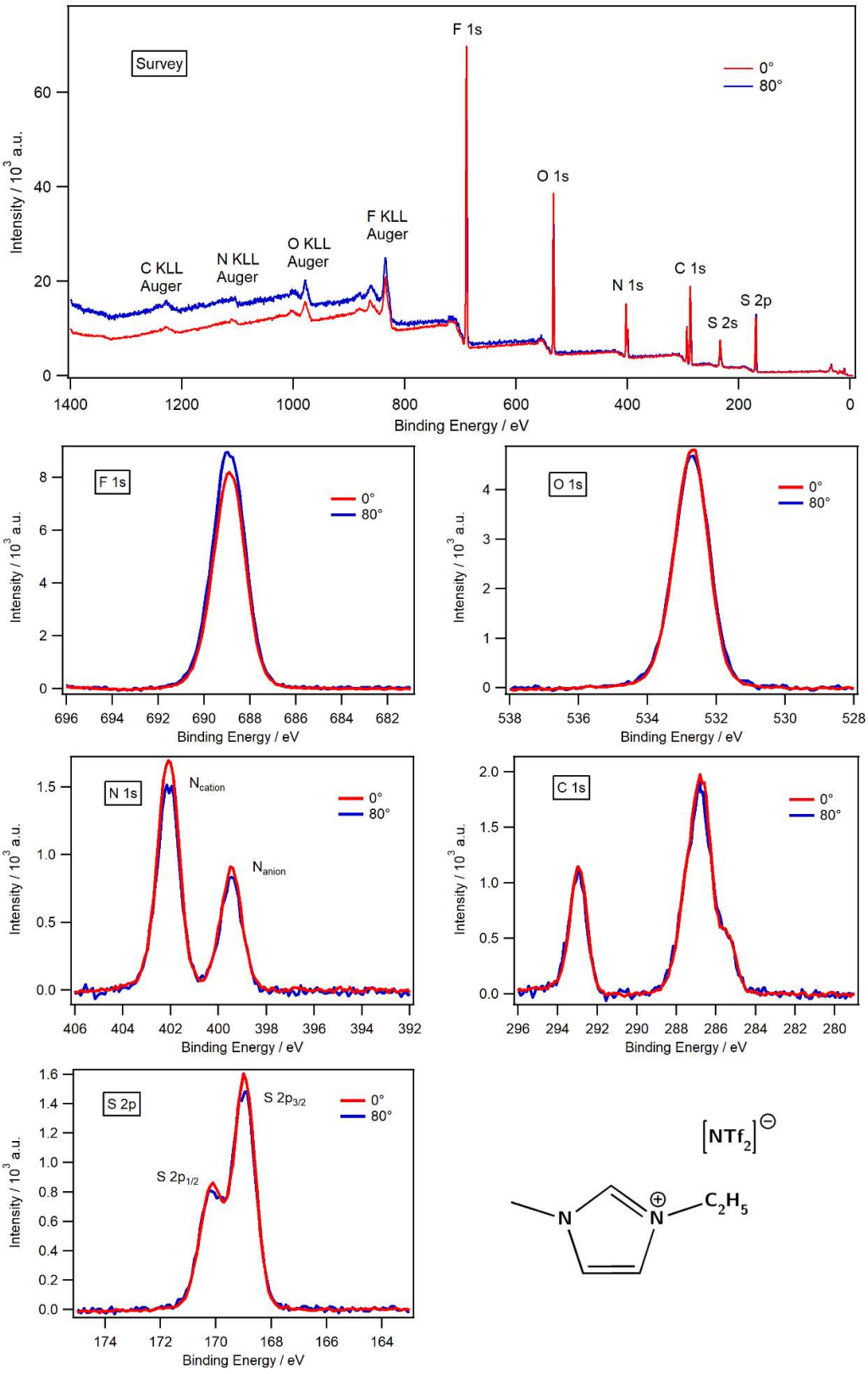
C 1s high-resolution spectra were fitted according to the models described within *Chapter 3, Section 3.2.2 and Chapter 4, Section 4.2.2*. S 2p and Cl 2p high-resolution spectra were fitted taking into account spin-orbit coupling; whereby the area ratio of $2p_{1/2} : 2p_{3/2}$ components are set to 1 : 2. The O 1s and S 2p high-resolution spectra for ionic liquid containing the $[NTf_2]^-$ anion are affected by shake up/off phenomena and a 4% intensity loss (per oxygen/sulfur atom involved in double bonding) was taken into account when calculating atomic percentages for these elements. Any carbon or nitrogen atoms involved in conjugated bonding are affected by shake up/off phenomena and a respective 20% and 12% intensity loss is taken into account.[74]

Binding energies, full width at half maximum and composition tables for all imidazolium-, thioimidazolium- and guanidinium-based ionic liquids investigated in *Chapter 5* can be found at the end of *Appendix C*.

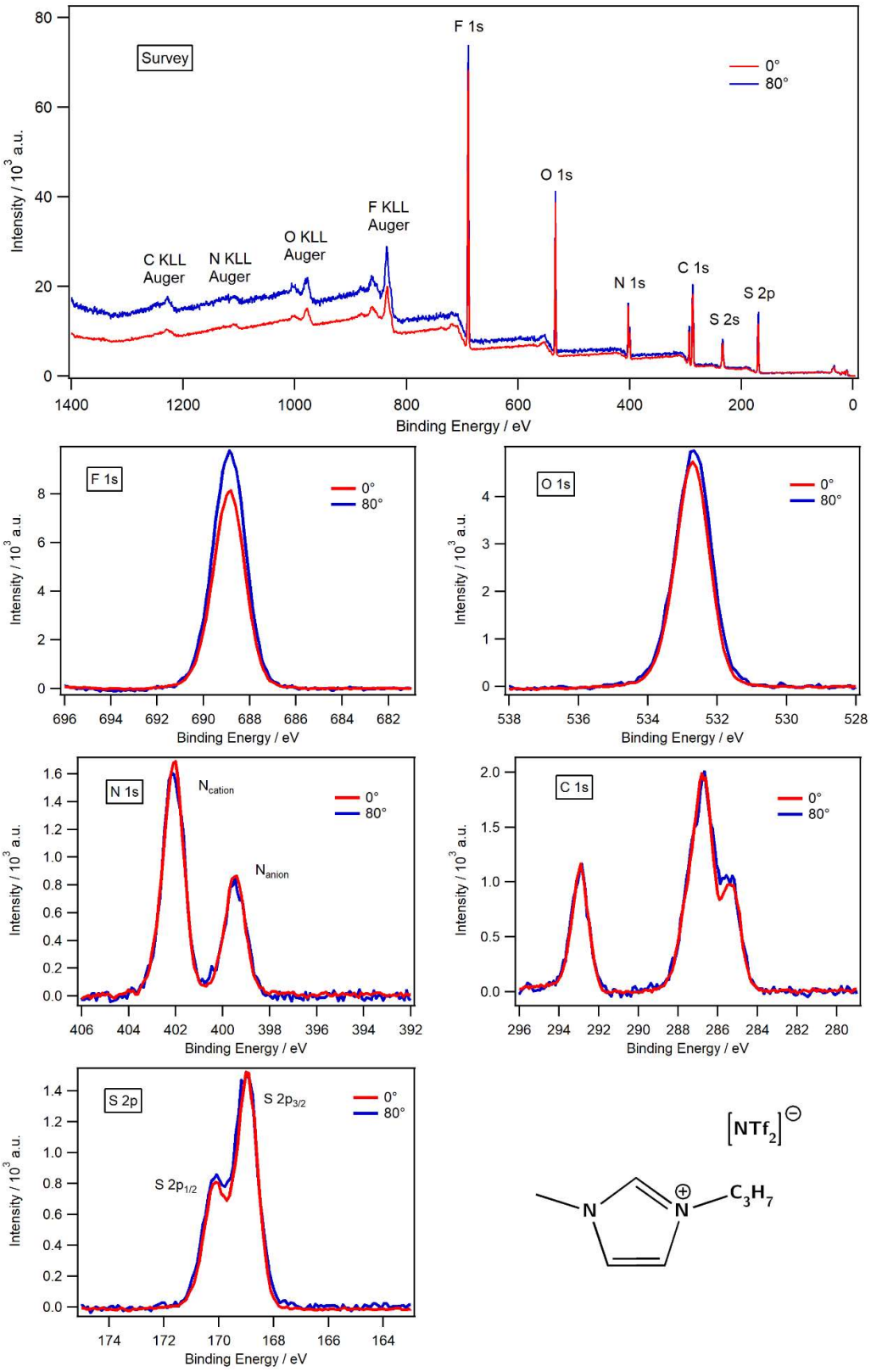
7.3.13. $[(C_8C_1)_2dmg][NTf_2]$ XP spectra recorded at θ = 0 and 80°



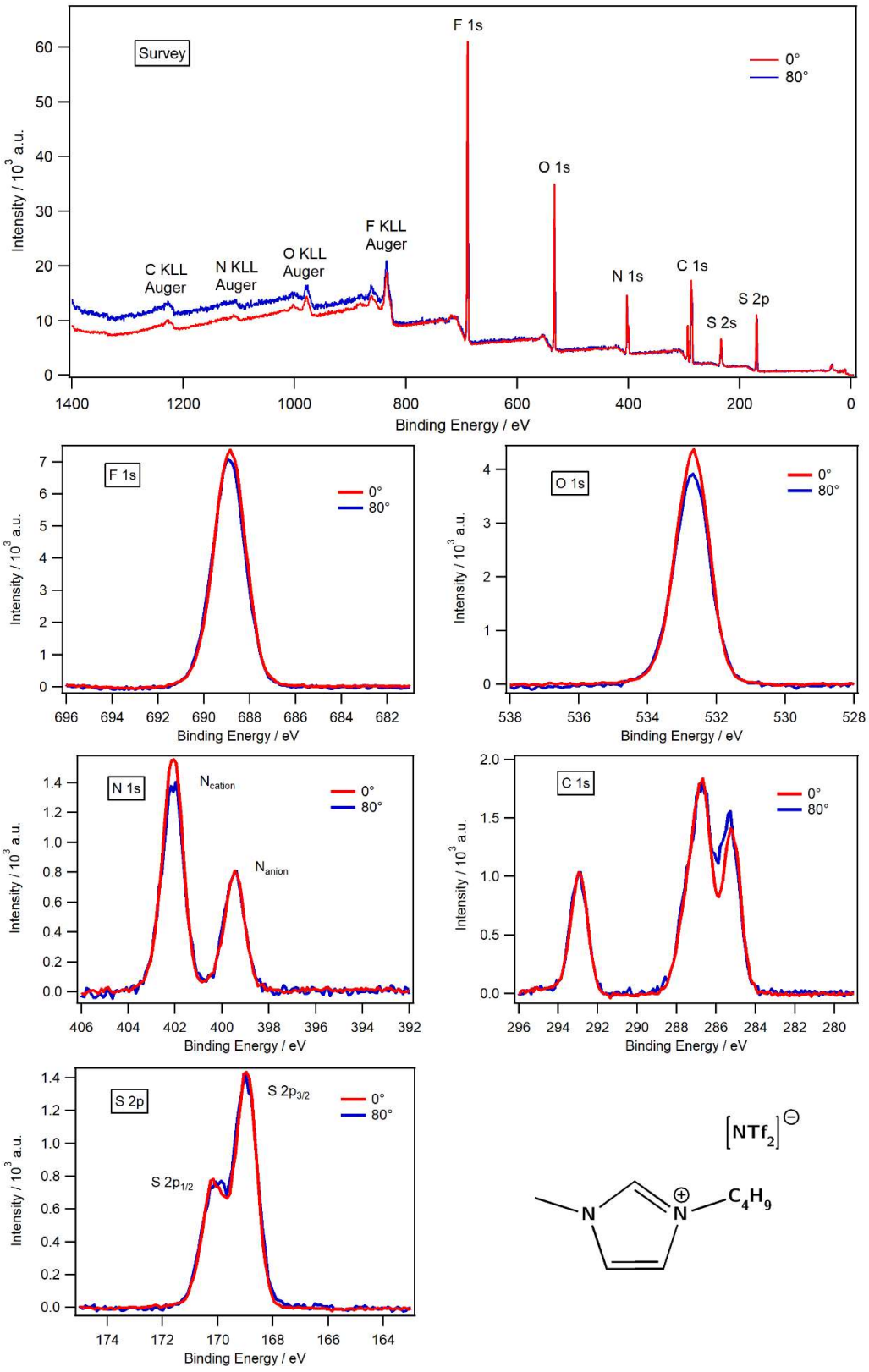
7.5.5. $[C_2C_1Im][NTf_2]$ XP spectra recorded at θ = 0 and 80°



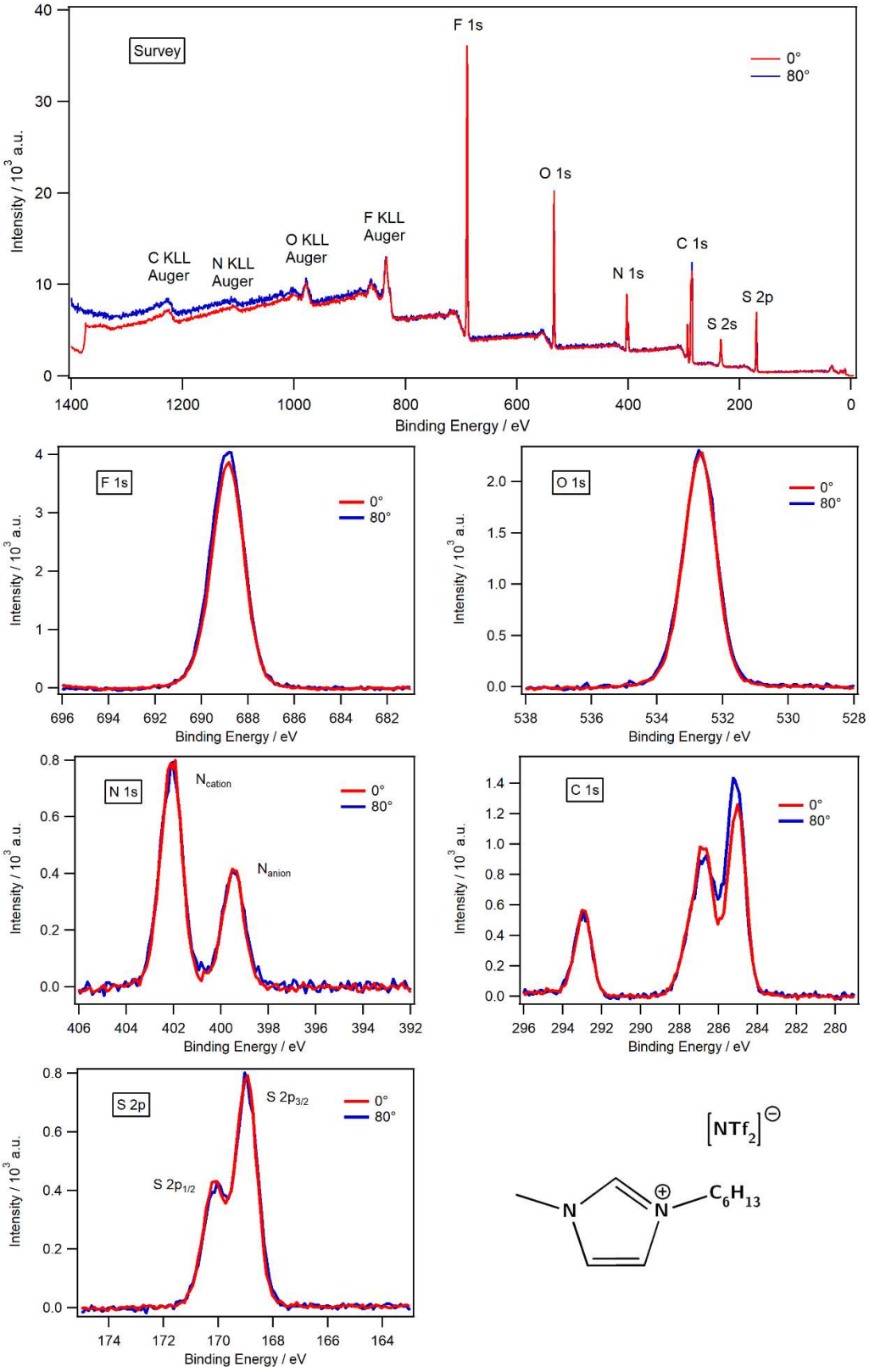
7.5.7. $[C_3C_1Im][NTf_2]$ XP spectra recorded at θ = 0 and 80°



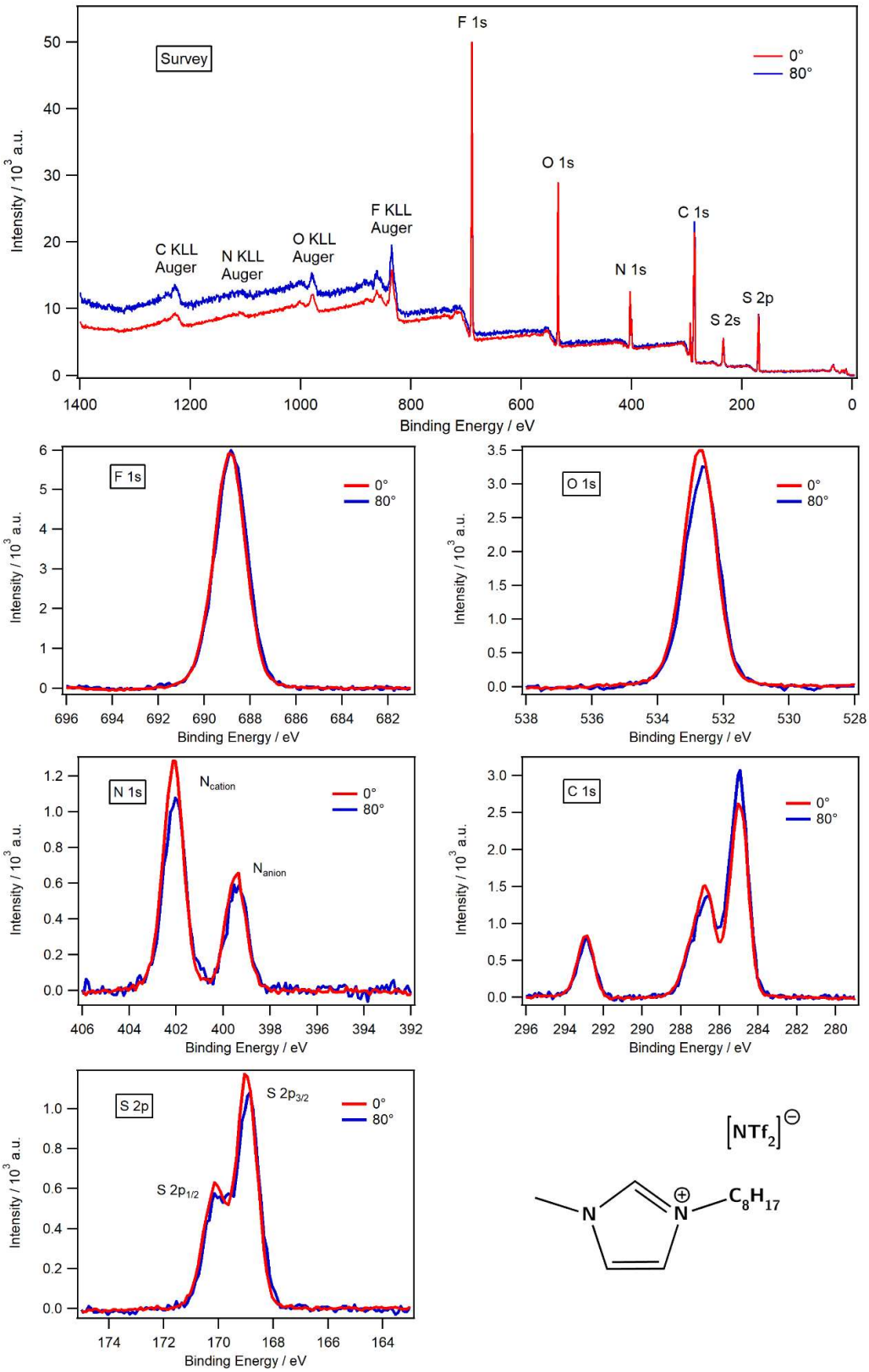
7.5.9. $[C_4C_1Im][NTf_2]$ XP spectra recorded at θ = 0 and 80°



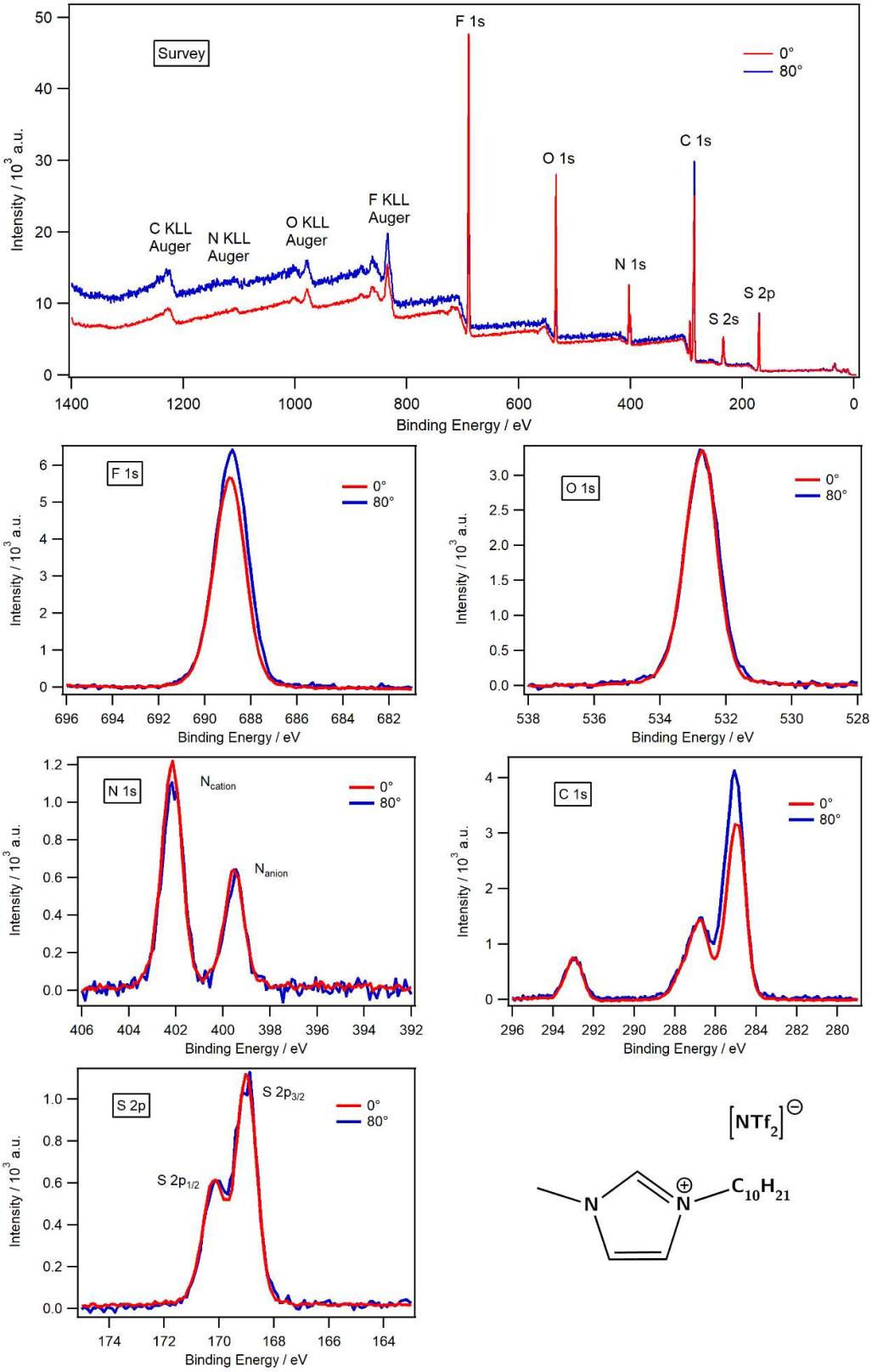
7.5.11. $[C_6C_1Im][NTf_2]$ XP spectra recorded at θ = 0 and 80°



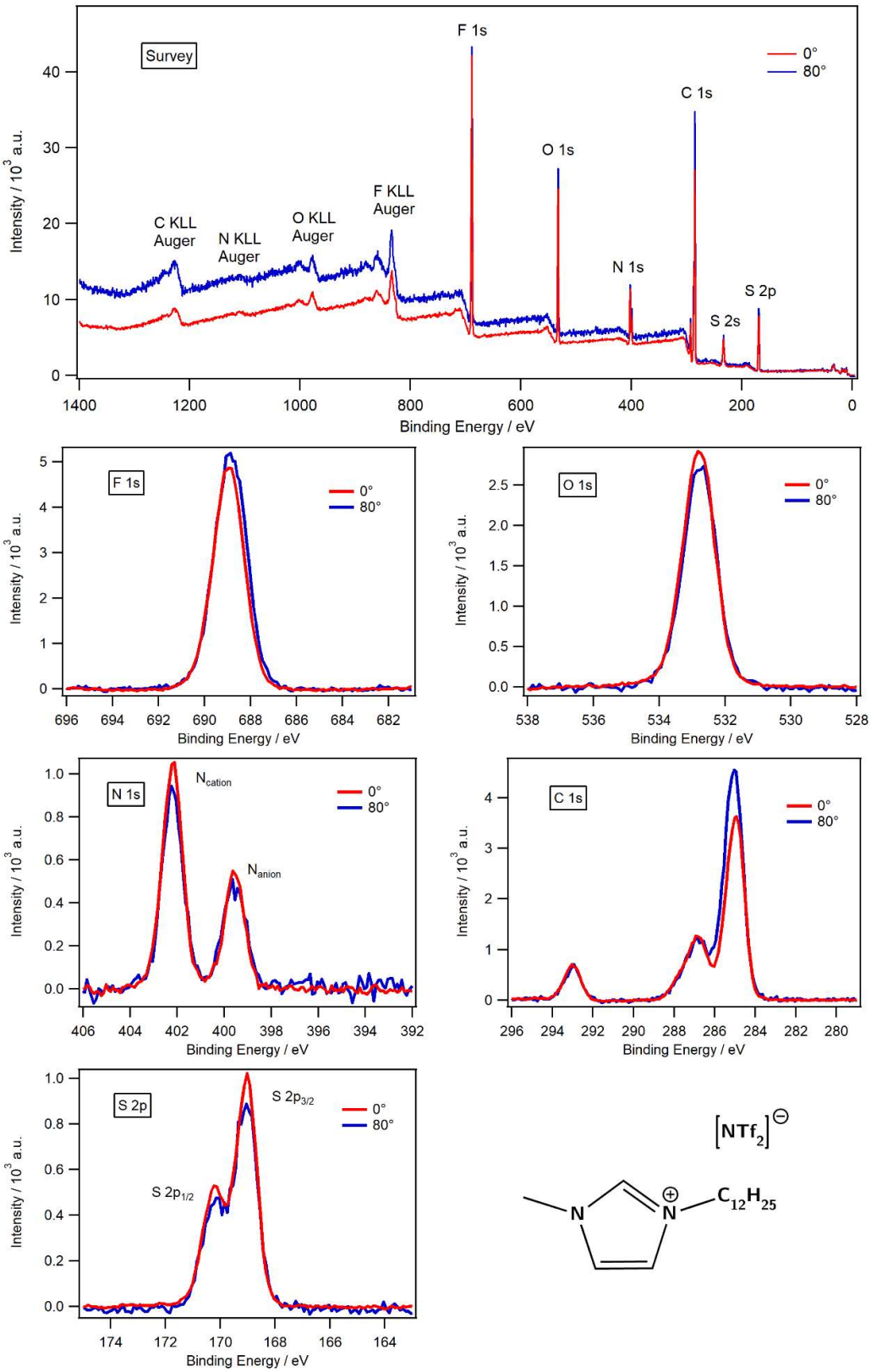
7.5.13. $[C_8C_1Im][NTf_2]$ XP spectra recorded at θ = 0 and 80°



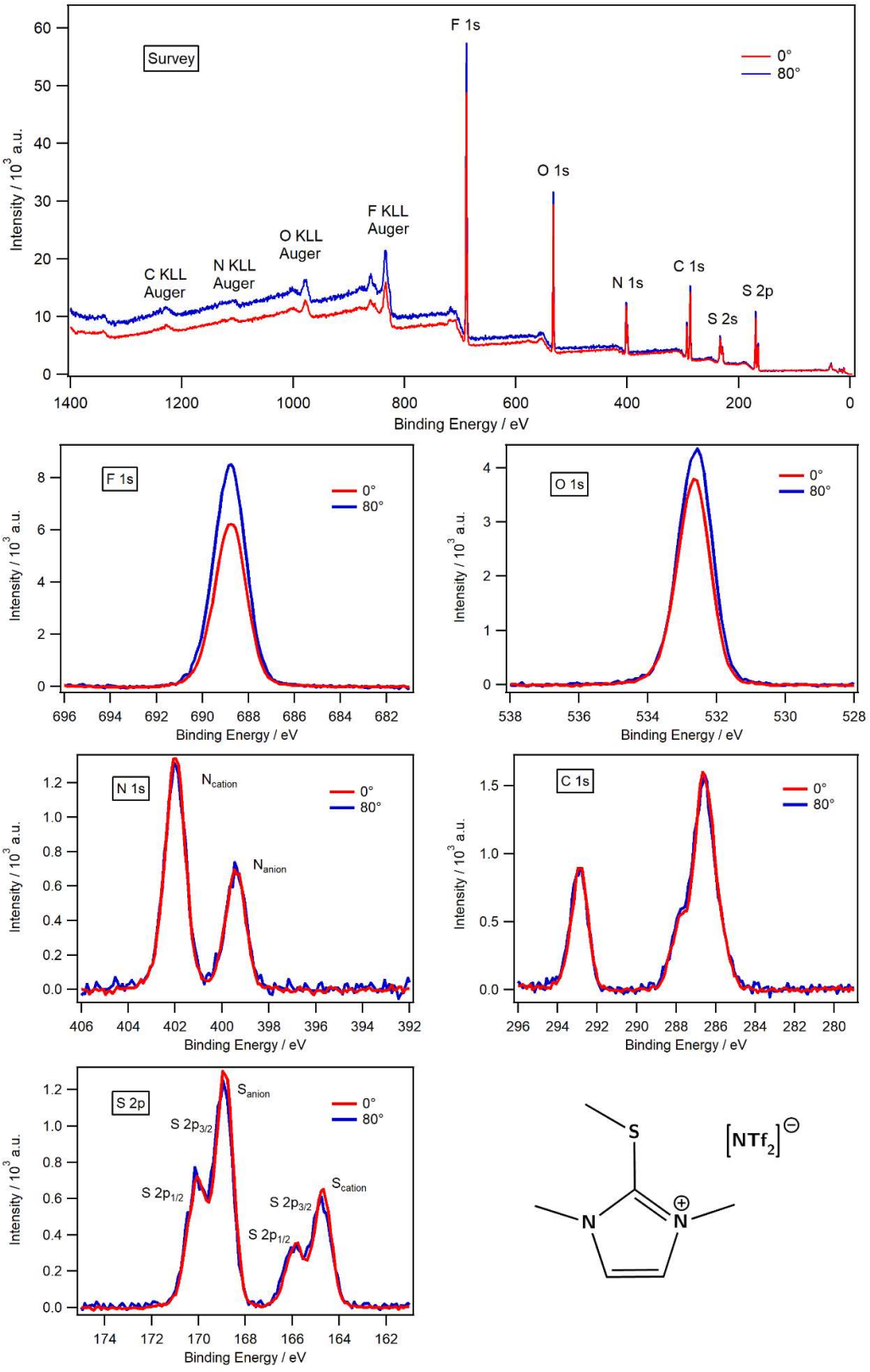
7.5.15. $[C_{10}C_1Im][NTf_2]$ XP spectra recorded at θ = 0 and 80°



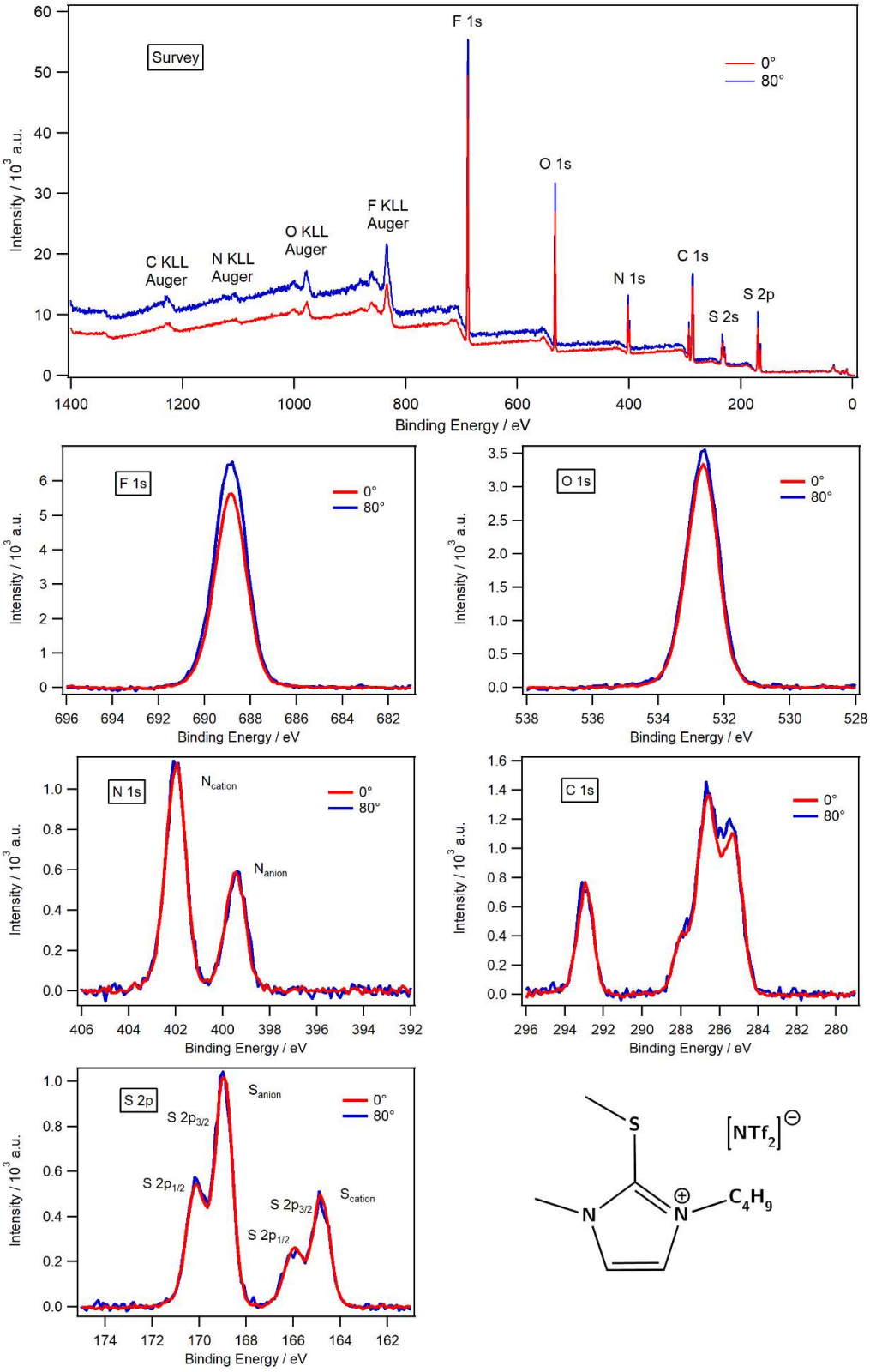
7.5.17. $[C_{12}C_1Im][NTf_2]$ XP spectra recorded at θ = 0 and 80°



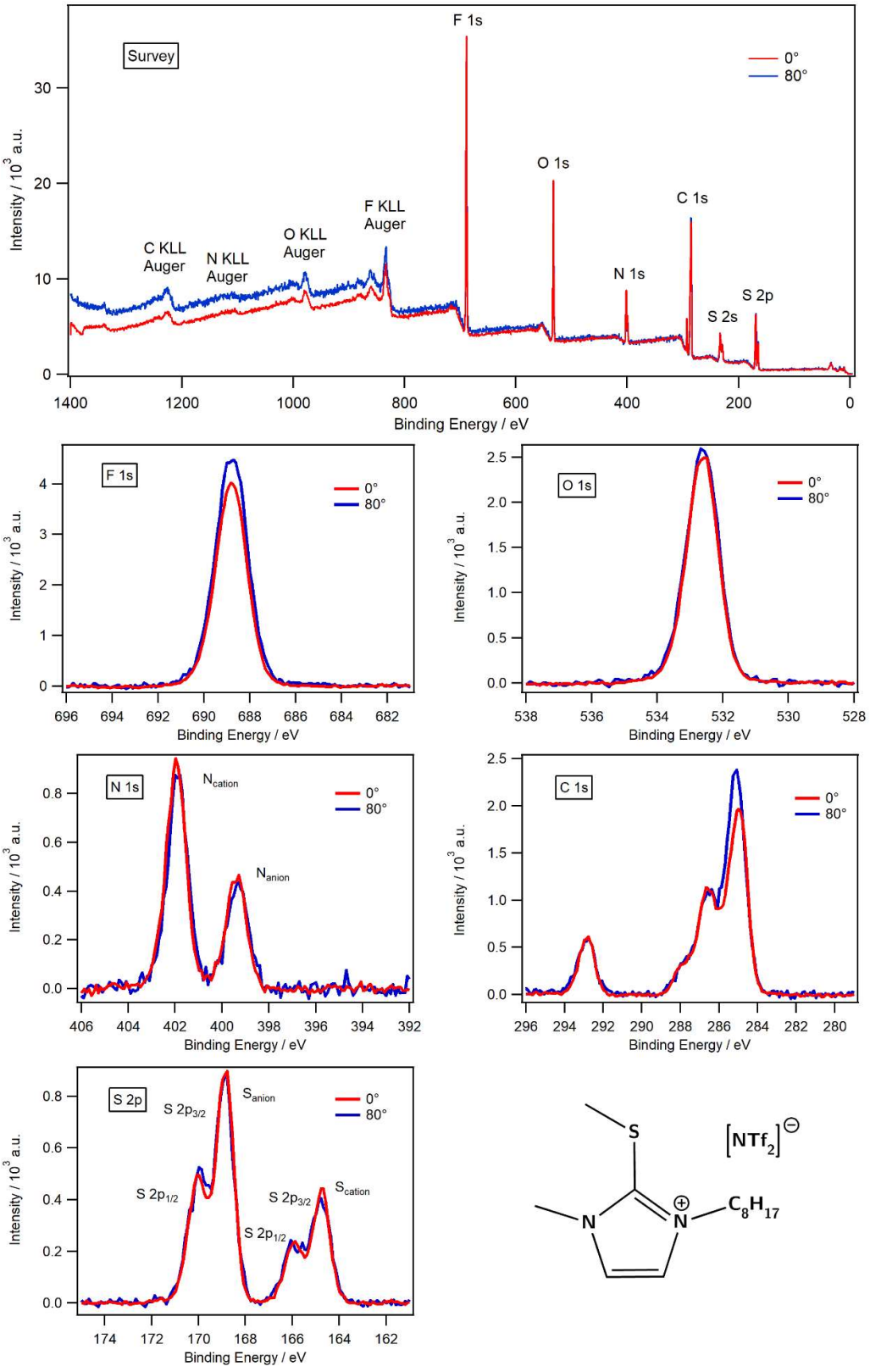
7.5.22. $[C_1(C_1)_2ThioIm][NTf_2]$ XP spectra recorded at θ = 0 and 80°



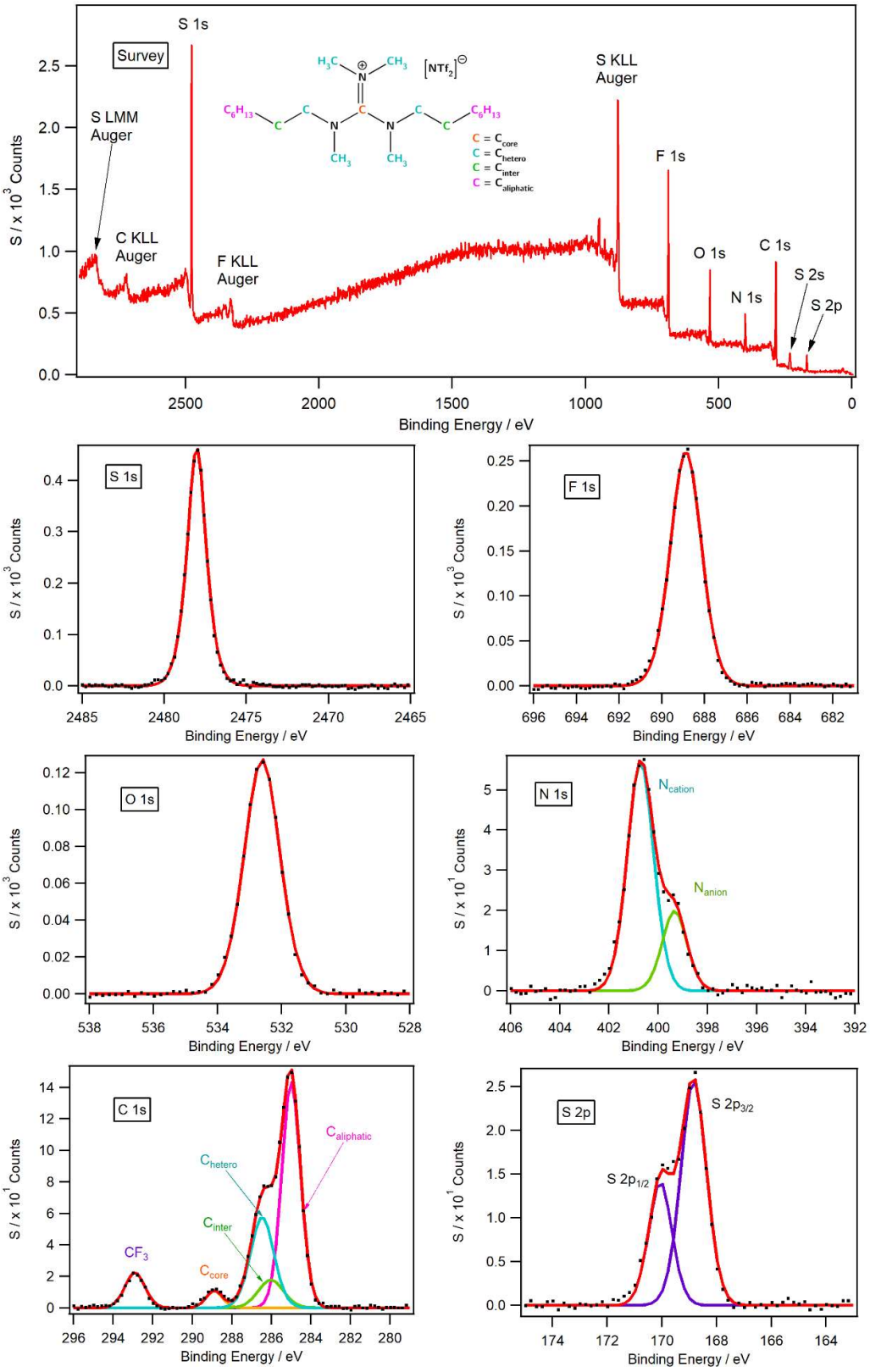
7.5.28. $[C_4(C_1)_2ThioIm][NTf_2]$ XP spectra recorded at θ = 0 and 80°



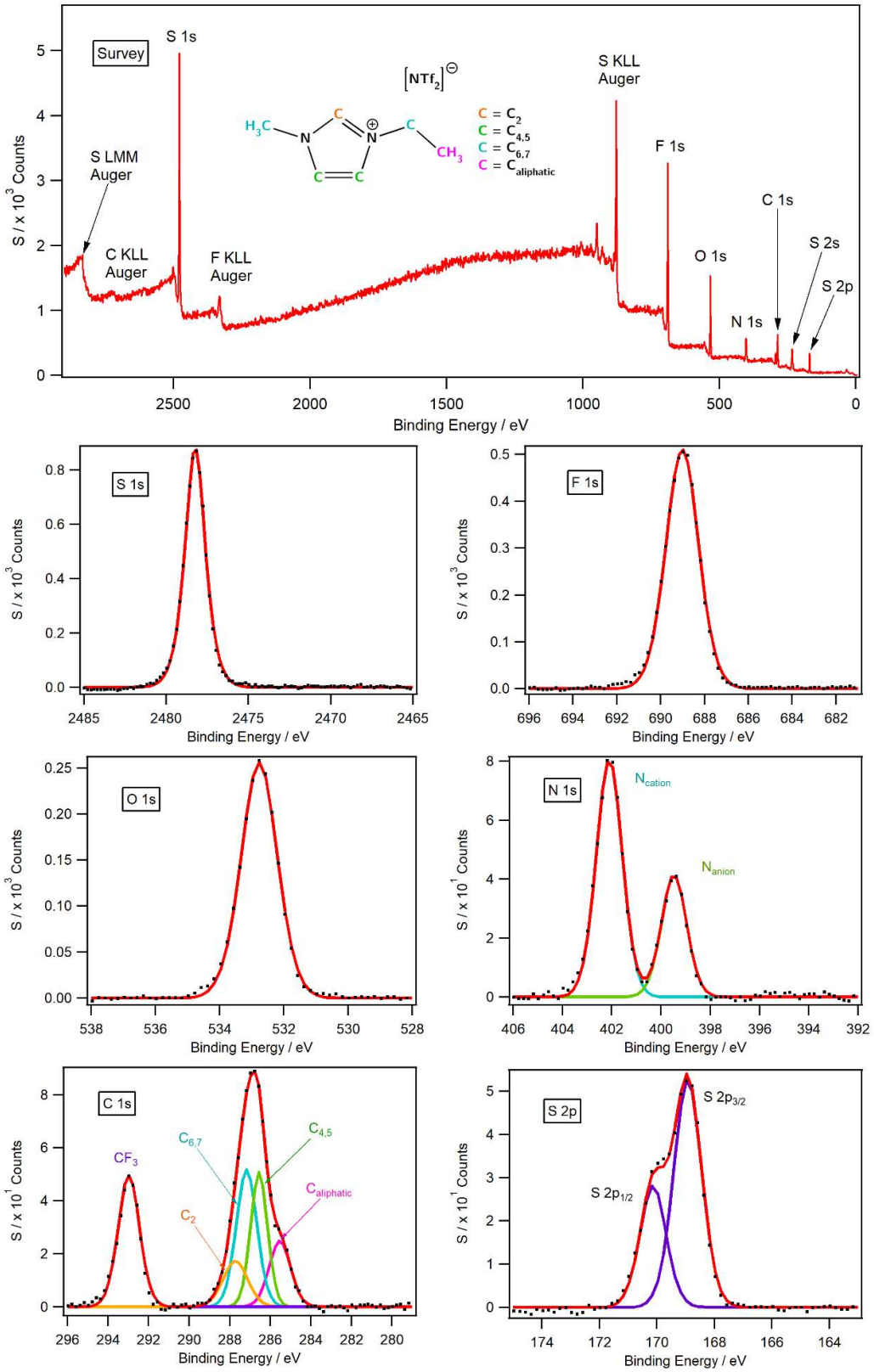
7.5.34. $[C_8(C_1)_2ThioIm][NTf_2]$ XP spectra recorded at θ = 0 and 80°



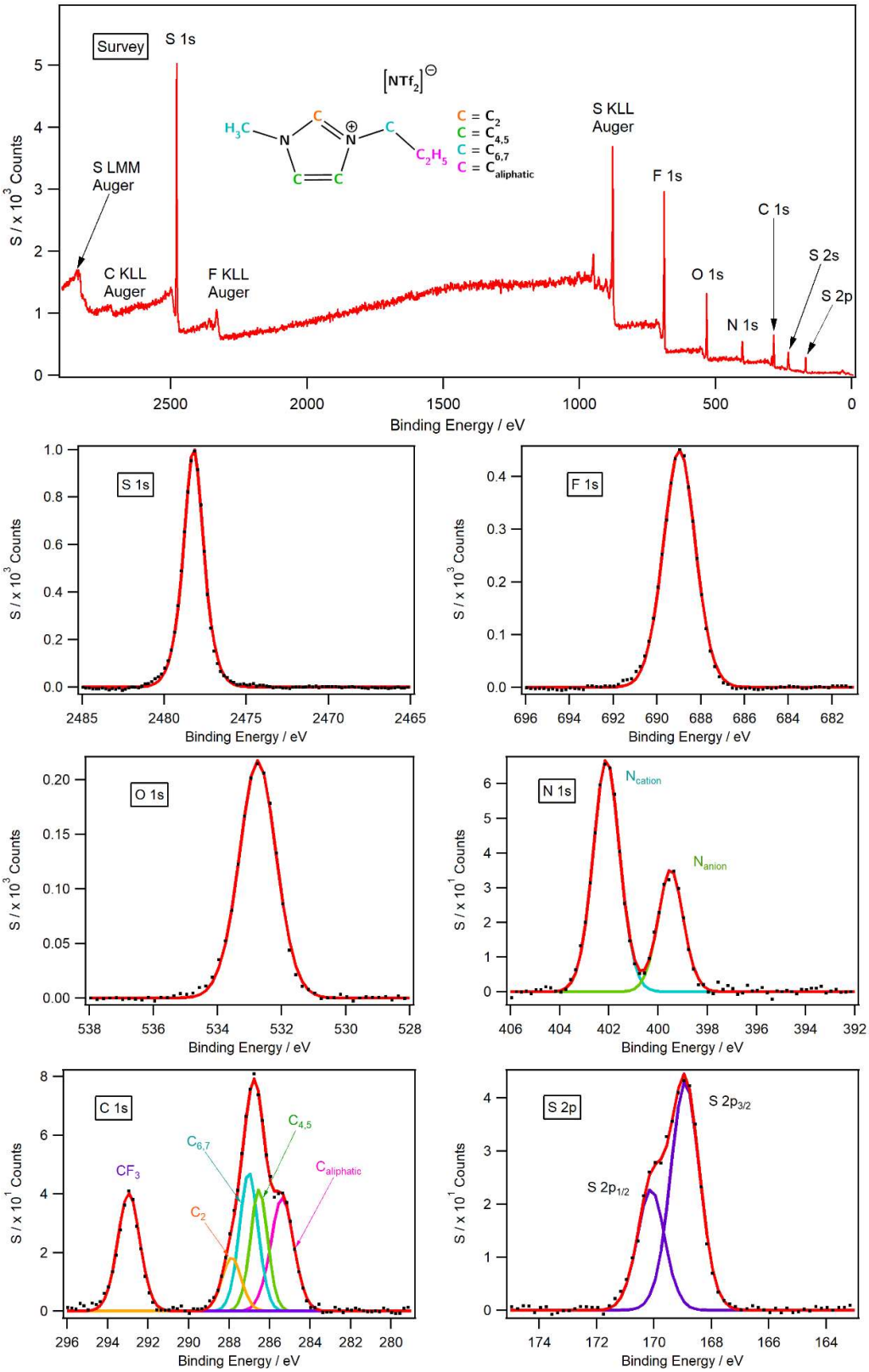
7.3.13. $[(C_8C_1)_2dmg][NTf_2]$ Ag L_α' X-ray source XP Spectra



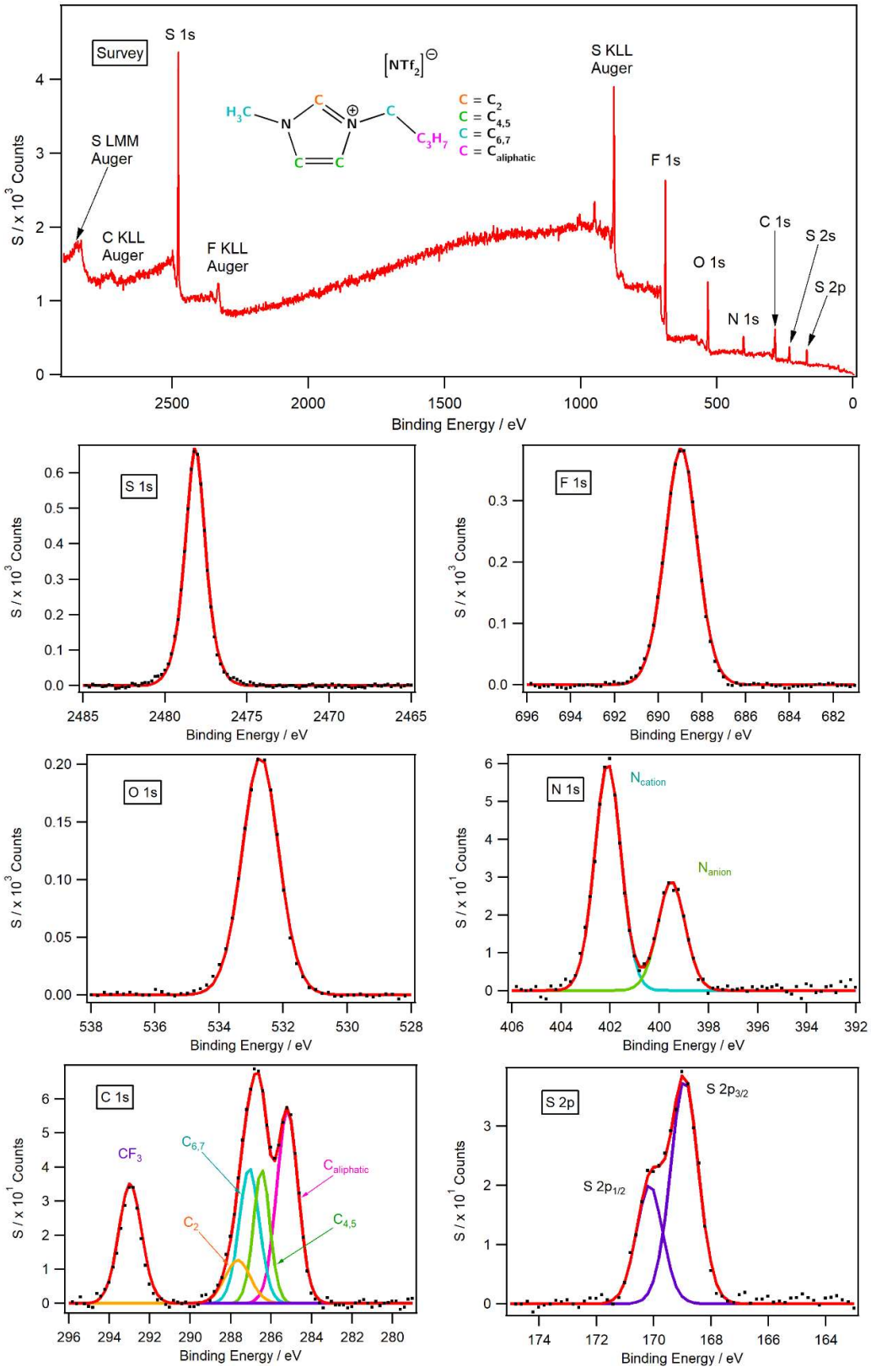
7.5.5. $[C_2C_1Im][NTf_2]$ Ag L_α' X-ray source XP Spectra



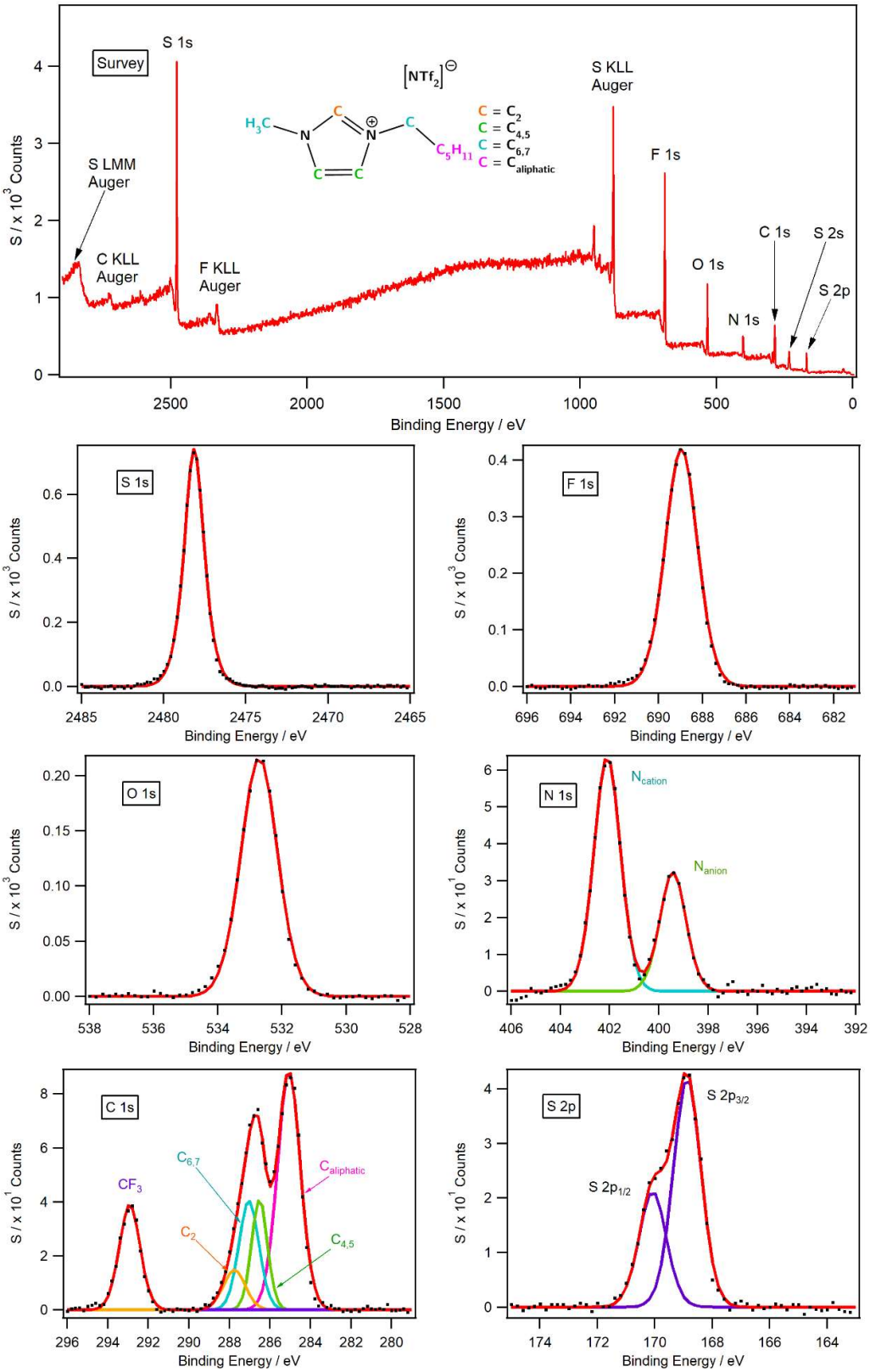
7.5.7. $[C_3C_1Im][NTf_2]$ Ag L_α' X-ray source XP Spectra



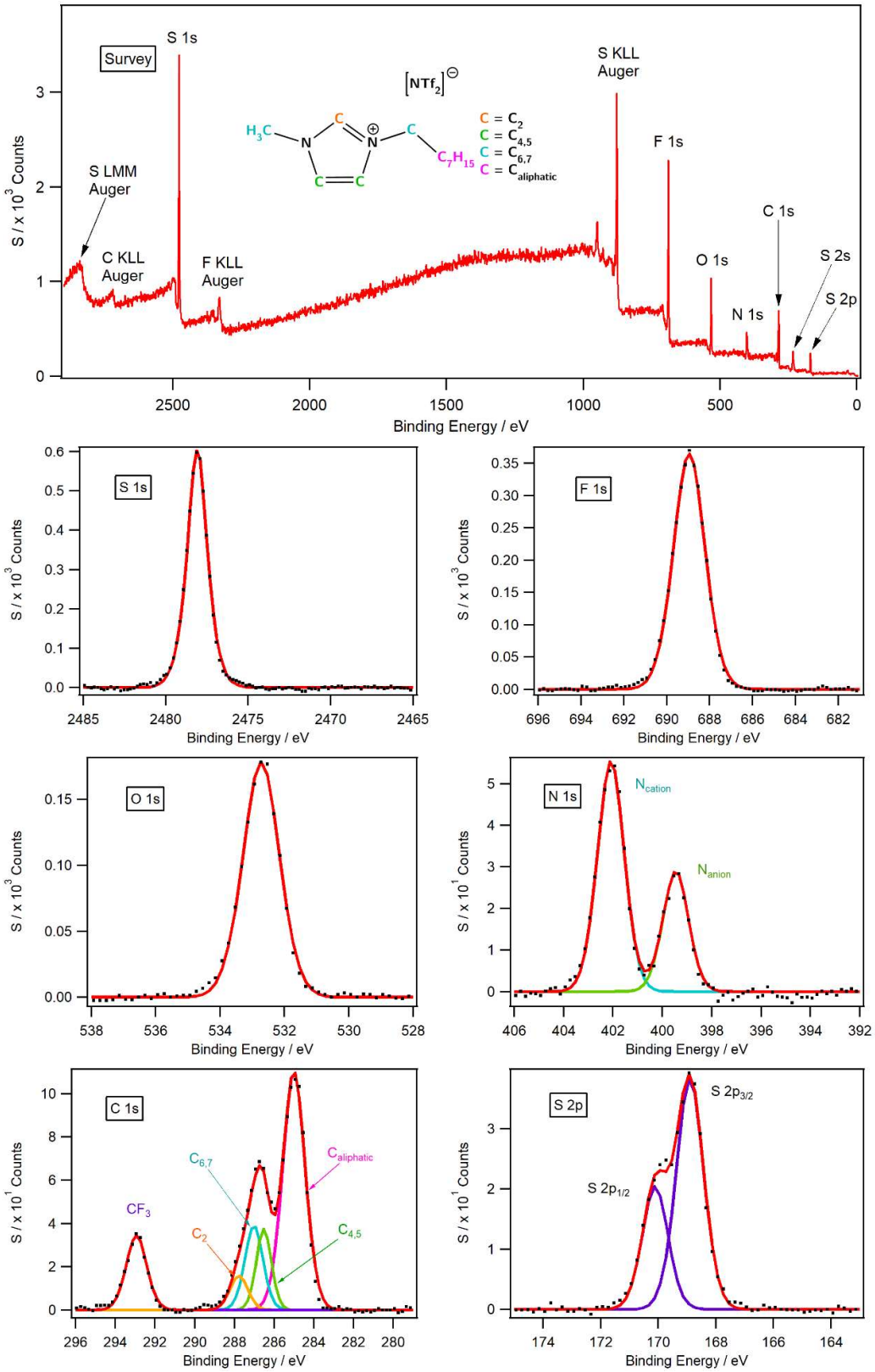
7.5.9. $[C_4C_1Im][NTf_2]$ Ag L_α' X-ray source XP Spectra



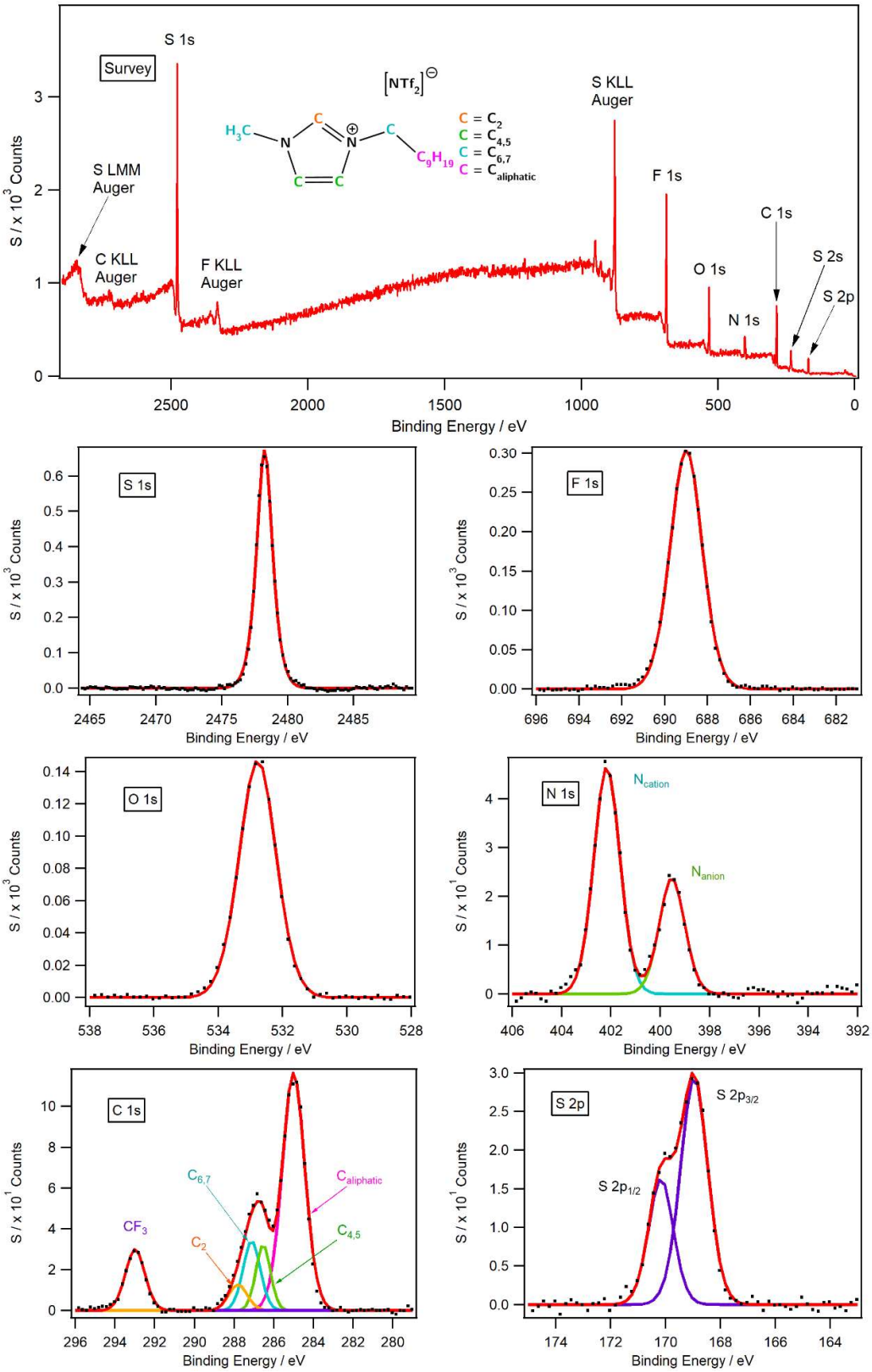
7.5.11. $[C_6C_1Im][NTf_2]$ Ag L_α' X-ray source XP Spectra



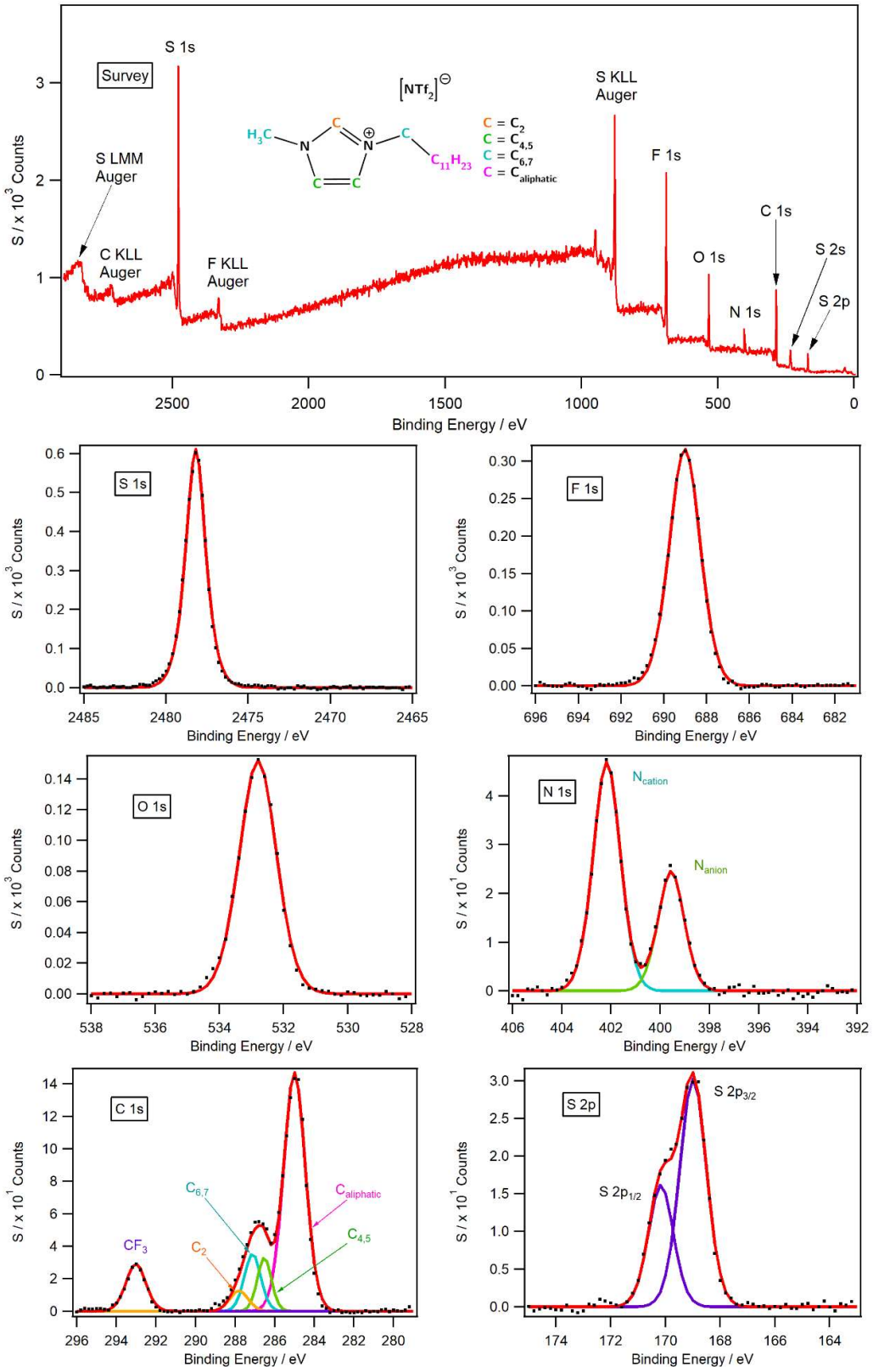
7.5.13. $[C_8C_1Im][NTf_2]$ Ag L_α' X-ray source XP Spectra



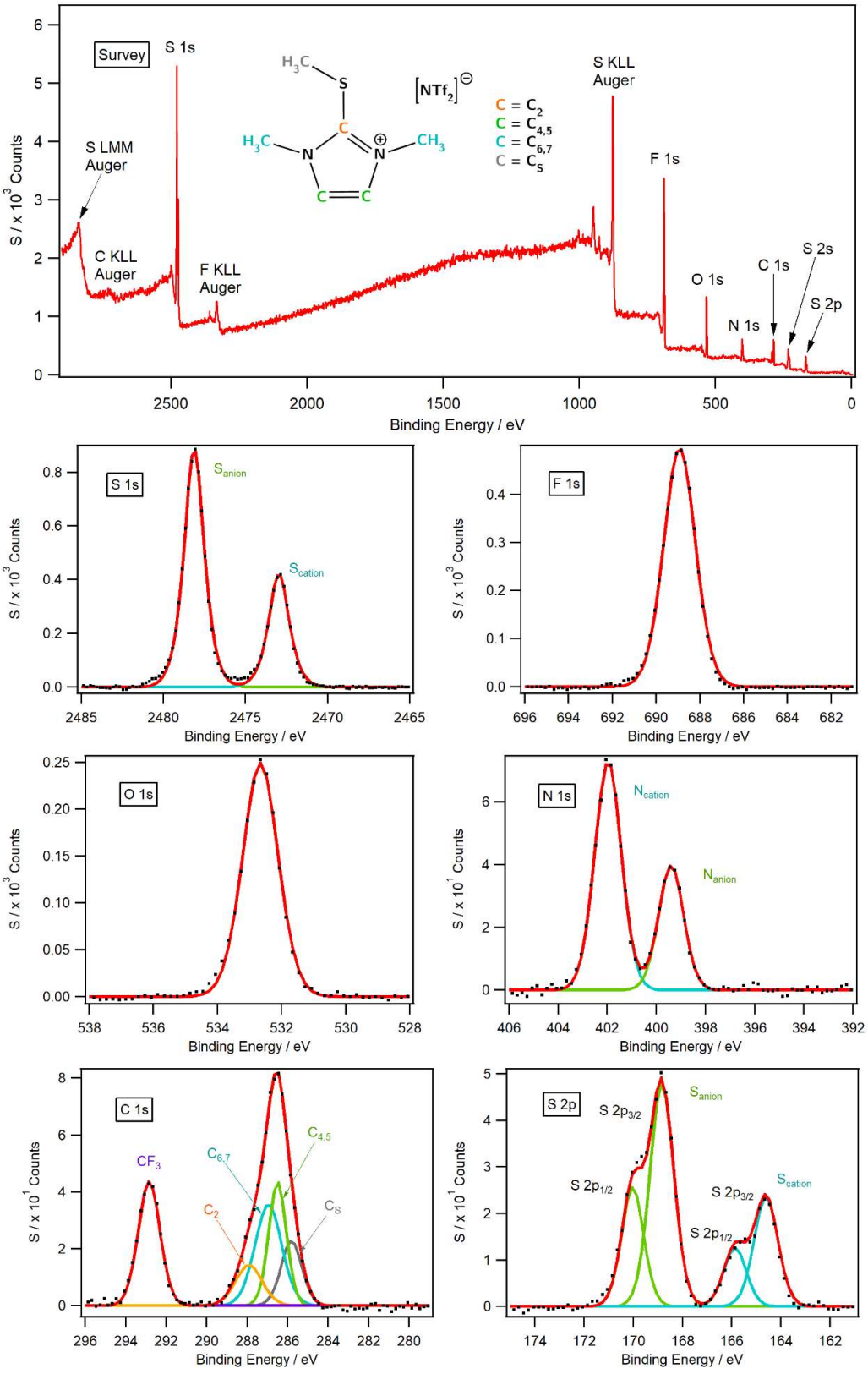
7.5.15. $[C_{10}C_1Im][NTf_2]$ Ag L_α' X-ray source XP Spectra



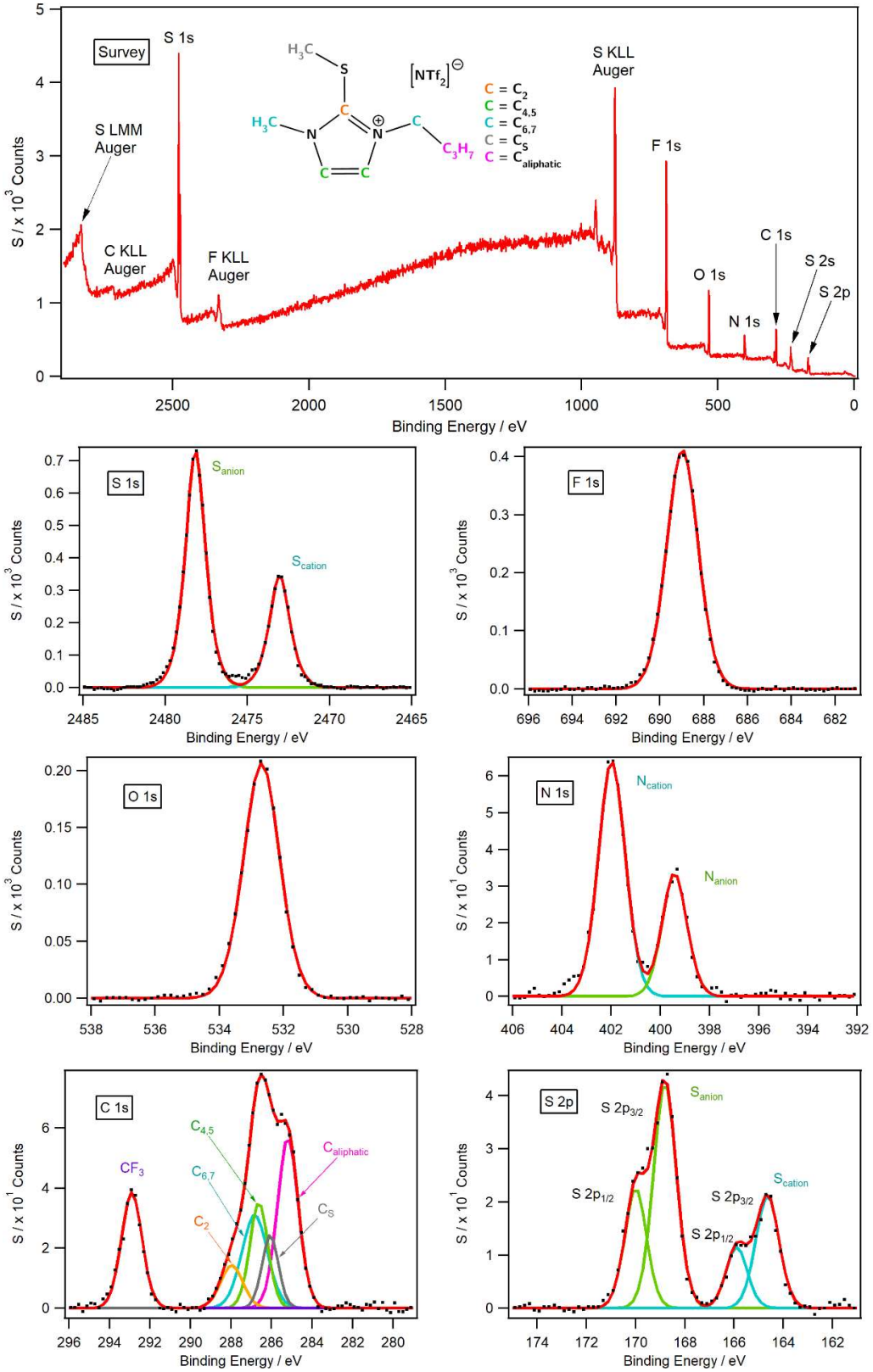
7.5.17. $[C_{12}C_1Im][NTf_2]$ Ag L_α' X-ray source XP Spectra



7.5.22. $[C_1(C_1)_2ThioIm][NTf_2]$ Ag L_α' X-ray source XP Spectra



7.5.28. $[C_4(C_1)_2ThioIm][NTf_2]$ Ag L_α' X-ray source XP Spectra



7.5.34. $[C_8(C_1)_2ThioIm][NTf_2]$ Ag L_α' X-ray source XP Spectra

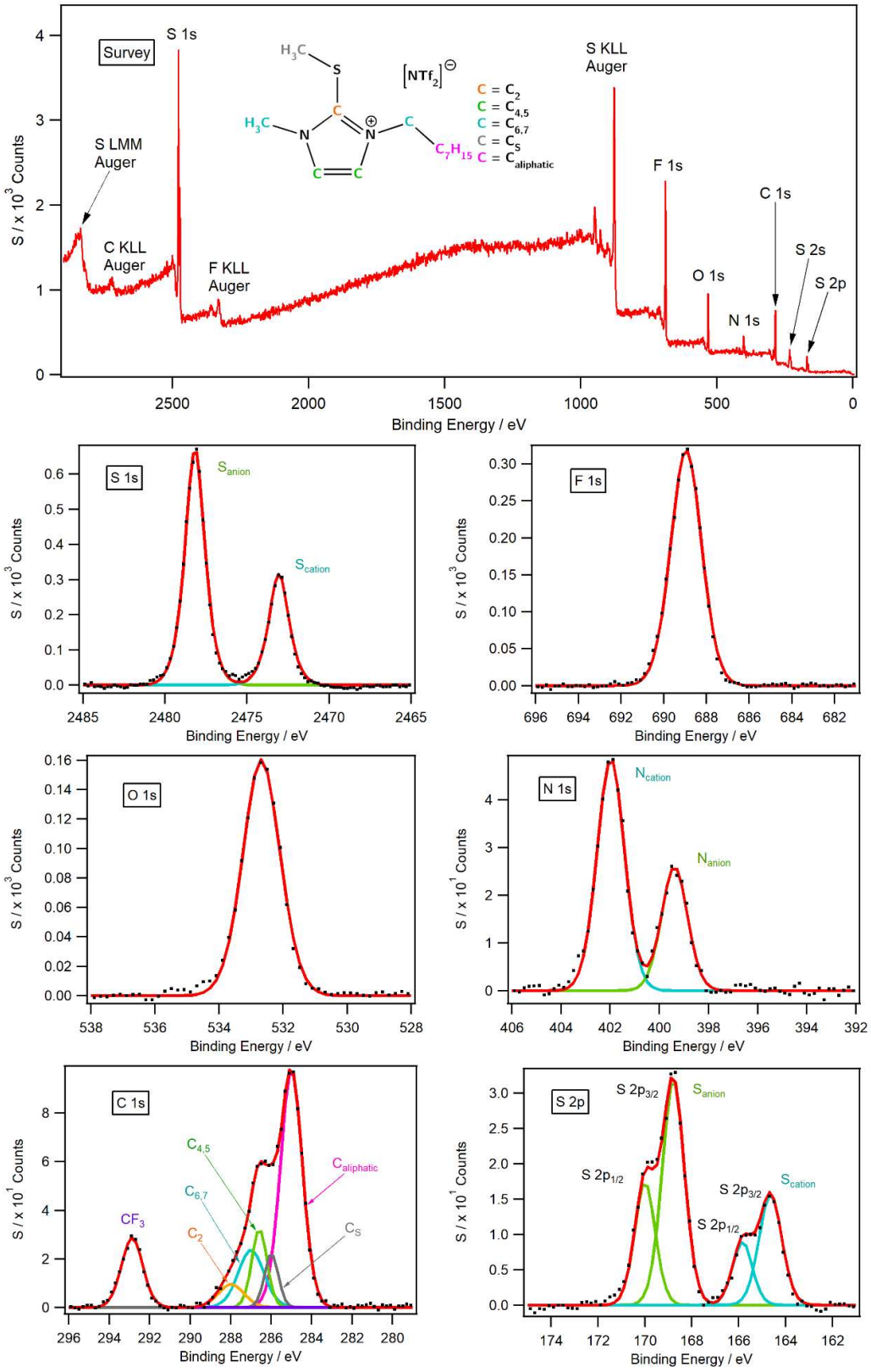


Table 5.1. Measured experimental and nominal stoichiometries (in number of atoms) for the imidazolium-based ionic liquids studied with ARXPS in this work. The experimental values are obtained from XP spectra at θ = 0° and 80°. Associated experimental error is ± 10 - 20%.

		Composition (number of atoms)									
		Cation				Anion					
Compound		$C_{aliphatic}$ 1s	$C_{4,5}$ 1s	$C_{6,7}$ 1s	C_2 1s	N_{cation} 1s	C_{CF_3} 1s	N_{anion} 1s	O 1s	F 1s	S 2p
	[a]RSF[74,134]	0.278	0.278	0.278	0.278	0.477	0.278	0.477	0.780	1.000	0.668
$[C_2C_1Im][NTf_2]$	**Nominal**	**1**	**2**	**2**	**1**	**2**	**2**	**1**	**4**	**6**	**2**
	0°	1.2	1.9	2.3	0.9	2.0	2.3	1.0	3.5	6.0	1.8
	80°	1.2	1.8	2.2	0.9	1.8	2.2	1.0	3.5	6.5	1.8
$[C_3C_1Im][NTf_2]$	**Nominal**	**2**	**2**	**2**	**1**	**2**	**2**	**1**	**4**	**6**	**2**
	0°	2.3	1.9	2.3	0.9	2.0	2.3	1.0	3.5	6.0	1.8
	80°	2.3	1.8	2.1	0.9	1.8	2.2	0.9	3.5	6.7	1.7
$[C_4C_1Im][NTf_2]$	**Nominal**	**4**	**2**	**2**	**1**	**2**	**2**	**1**	**4**	**6**	**2**
	0°	3.5	1.9	2.3	0.9	2.0	2.3	1.0	3.5	5.9	1.8
	80°	3.8	1.9	2.3	0.9	1.9	2.3	1.0	3.3	5.7	1.9
$[C_6C_1Im][NTf_2]$	**Nominal**	**6**	**2**	**2**	**1**	**2**	**2**	**1**	**4**	**6**	**2**
	0°	5.7	1.8	2.3	0.9	1.9	2.3	1.0	3.4	5.7	1.9
	80°	5.8	1.9	2.3	1.1	1.9	2.2	1.0	3.3	5.8	1.8
$[C_8C_1Im][NTf_2]$	**Nominal**	**8**	**2**	**2**	**1**	**2**	**2**	**1**	**4**	**6**	**2**
	0°	7.9	1.8	2.3	0.9	1.9	2.3	1.0	3.4	5.7	1.8
	80°	8.4	1.8	2.3	0.9	1.7	2.3	0.9	3.2	5.8	1.7
$[C_{10}C_1Im][NTf_2]$	**Nominal**	**10**	**2**	**2**	**1**	**2**	**2**	**1**	**4**	**6**	**2**
	0°	10.0	1.8	2.2	0.9	1.9	2.2	1.0	3.5	5.8	1.8
	80°	10.7	1.8	2.2	0.9	1.6	2.2	0.9	3.2	5.9	1.6
$[C_{12}C_1Im][NTf_2]$	**Nominal**	**12**	**2**	**2**	**1**	**2**	**2**	**1**	**4**	**6**	**2**
	0°	12.2	1.8	2.2	0.9	1.9	2.2	1.0	3.4	5.6	1.8
	80°	13.7	1.7	2.1	0.9	1.6	2.2	0.9	3.0	5.5	1.6

[a] Relative sensitivity factors (RSF) taken from the Kratos Library. Stoichiometries determined without consideration of H content.

Table 5.2. Experimental binding energies in eV for the imidazolium bis(trifluoromethanesulfonyl)imide-based ionic liquids studied. The associated experimental error is ± 0.1 eV. $[C_nC_1Im][NTf_2]$ with $n \geq 8$ charge corrected by referencing $C_{aliphatic}$ 1s to 285.0 eV. $[C_nC_1Im][NTf_2]$ with $n < 8$ charge corrected by referencing N_{cation} 1s to the value obtained for $[C_8C_1Im][NTf_2]$ using the same X-ray source.

		Binding Energy / eV										
		Cation					Anion					
Ionic Liquid		$C_{aliphatic}$ 1s	$C_{4,5}$ 1s	$C_{6,7}$ 1s	C_2 1s	N_{cation} 1s	C_{CF_3} 1s	N_{anion} 1s	O 1s	F 1s	S_{anion} $2p_{3/2}$	S_{anion} 1s
Al K_α Source												
$[C_2C_1Im]$	$[NTf_2]$	285.5	286.6	287.0	287.7	402.1	293.0	399.5	532.7	688.9	169.0	-
$[C_3C_1Im]$	$[NTf_2]$	285.4	286.5	287.0	287.7	402.1	292.9	399.5	532.7	688.9	168.9	-
$[C_4C_1Im]$	$[NTf_2]$	285.2	286.6	287.0	287.7	402.1	292.9	399.5	532.7	688.9	169.0	-
$[C_6C_1Im]$	$[NTf_2]$	285.1	286.5	287.0	287.7	402.1	292.9	399.5	532.7	688.9	169.0	-
$[C_8C_1Im]$	$[NTf_2]$	285.0	286.5	287.0	287.7	402.1	292.9	399.5	532.7	688.9	169.0	-
$[C_{10}C_1Im]$	$[NTf_2]$	285.0	286.6	287.0	287.7	402.1	293.0	399.5	532.7	688.9	169.0	-
$[C_{12}C_1Im]$	$[NTf_2]$	285.0	286.6	287.0	287.7	402.1	293.0	399.5	532.7	688.9	169.0	-
Ag L_α' Source												
$[C_2C_1Im]$	$[NTf_2]$	285.5	286.6	287.2	287.7	402.1	293.0	399.5	532.7	689.0	168.9	2478.2
$[C_3C_1Im]$	$[NTf_2]$	285.4	286.5	287.0	287.8	402.1	293.0	399.5	532.7	689.0	168.9	2478.2
$[C_4C_1Im]$	$[NTf_2]$	285.2	286.5	287.1	287.7	402.1	293.0	399.5	532.7	689.0	168.9	2478.2
$[C_6C_1Im]$	$[NTf_2]$	285.1	286.5	287.0	287.8	402.1	293.0	399.5	532.7	689.0	168.9	2478.2
$[C_8C_1Im]$	$[NTf_2]$	285.0	286.5	287.0	287.8	402.1	293.0	399.5	532.7	688.9	168.9	2478.2
$[C_{10}C_1Im]$	$[NTf_2]$	285.0	286.5	287.1	287.7	402.1	293.0	399.5	532.7	689.0	169.0	2478.2
$[C_{12}C_1Im]$	$[NTf_2]$	285.0	286.5	287.1	287.8	402.1	293.0	399.5	532.7	689.0	169.0	2478.2

Table 5.3. Experimental binding energies in eV for the Thioimidazolium bis(trifluoromethanesulfonyl)imide-based ionic liquids studied. The associated experimental error is ± 0.1 eV. $[C_8(C_1)_2ThioIm][NTf_2]$ charge corrected by referencing $C_{aliphatic}$ 1s to 285.0 eV. $[C_1(C_1)_2ThioIm][NTf_2]$ and $[C_4(C_1)_2ThioIm][NTf_2]$ charge corrected by referencing N_{cation} 1s to the value obtained for $[C_8(C_1)_2ThioIm][NTf_2]$ using the same X-ray source.

Compound		Binding Energy / eV													
		Cation								Anion					
Cation	Anion	C_2 1s	$C_{6,7}$ 1s	$C_{4,5}$ 1s	C_S 1s	$C_{aliphatic}$ 1s	N_{cation} 1s	$S_{exocyclic}$ $2p_{3/2}$	$S_{exocyclic}$ 1s	C_{CF_3} 1s	N_{anion} 1s	O 1s	F 1s	S_{anion} $2p_{3/2}$	S_{anion} 1s
Al K_α Source															
$[C_1(C_1)_2ThioIm]$	$[NTf_2]$	288.0	286.9	286.6	285.8	-	402.0	164.8	-	292.9	399.4	532.6	688.8	168.9	-
$[C_4(C_1)_2ThioIm]$	$[NTf_2]$	288.0	286.9	286.5	285.9	285.2	402.0	164.8	-	292.9	399.4	532.6	688.8	168.9	-
$[C_8(C_1)_2ThioIm]$	$[NTf_2]$	287.9	286.9	286.5	285.9	285.0	402.0	164.8	-	292.9	399.4	532.6	688.9	168.9	-
Ag L_α' Source															
$[C_1(C_1)_2ThioIm]$	$[NTf_2]$	287.9	286.9	286.5	285.8	-	402.0	164.7	2473.0	292.9	399.4	532.7	688.9	168.8	2478.2
$[C_4(C_1)_2ThioIm]$	$[NTf_2]$	288.0	286.8	286.6	286.0	285.2	402.0	164.7	2473.0	292.9	399.4	532.7	688.9	168.8	2478.2
$[C_8(C_1)_2ThioIm]$	$[NTf_2]$	288.0	286.9	286.6	286.0	285.0	402.0	164.7	2473.0	292.9	399.4	532.7	689.0	168.8	2478.2

Table 5.8. Experimental binding energies in eV for the guanidinium bis(trifluoromethanesulfonyl)imide-based ionic liquid studied in this *Chapter*. The associated experimental error is ± 0.1 eV. $[(C_8C_1)_2dmg][NTf_2]$ charge corrected by referencing $C_{aliphatic}$ 1s to 285.0 eV.

Compound		Binding Energy / eV											
		Cation					Anion						
Cation	Anion	C_{core} 1s	C_{hetero} 1s	C_{inter} 1s	$C_{aliphatic}$ 1s	N_{cation} 1s	C_{CF_3} 1s	N_{anion} 1s	O 1s	F 1s	S_{anion} $2p_{3/2}$	S_{anion} 1s
Al K_α Source												
$[(C_8C_1)_2dmg]^+$	$[NTf_2]$	288.9	286.5	285.5	285.0	400.7	292.9	399.3	532.6	688.8	168.9	-
Ag L_α' Source												
$[(C_8C_1)_2dmg]^+$	$[NTf_2]$	288.9	286.5	285.6	285.0	400.7	292.9	399.4	532.6	688.8	168.8	2478.1

Table 5.9. Measured experimental and nominal stoichiometries (in number of atoms) for $[(C_8C_1)_2dmg][NTf_2]$ ionic liquid studied with ARXPS in this work. The experimental values are obtained from XP spectra at θ = 0° and 80°. Associated experimental error is ± 10 - 20%.

		Composition (number of atoms)									
		Cation				Anion					
Compound		$C_{aliphatic}$ 1s	C_{inter} 1s	C_{hetero} 1s	C_{core} 1s	N_{cation} 1s	C_{CF_3} 1s	N_{anion} 1s	O 1s	F 1s	S 2p
	[a]RSF[74,134]	0.278	0.278	0.278	0.278	0.477	0.278	0.477	0.780	1.000	0.668
$[(C_8C_1)_2dmg][NTf_2]$	**Nominal**	**12**	**2**	**6**	**1**	**3**	**2**	**1**	**4**	**6**	**2**
	0°	12.3	1.9	6.2	1.0	3.0	2.3	1.0	3.5	5.8	1.9
	80°	12.8	2.1	6.2	1.0	2.7	2.3	0.9	3.3	6.0	1.9

[a] Relative sensitivity factors (RSF) taken from the Kratos Library. Stoichiometries determined without consideration of H content.

Table 5.10. Measured experimental and nominal stoichiometries (in number of atoms) for $[(C_n(C_1)_2ThioIm][NTf_2]$ ionic liquids studied with ARXPS in this work. The experimental values are obtained from XP spectra at θ = 0° and 80°. Associated experimental error is ± 10 - 20%.

		Composition (number of atoms)											
		Cation							Anion				
Compound		C_2 1s	$C_{6,7}$ 1s	$C_{4,5}$ 1s	C_S 1s	$C_{aliphatic}$ 1s	N_{cation} 1s	$S_{exocyclic}$ 2p	C_{CF_3} 1s	N_{anion} 1s	O 1s	F 1s	S_{anion} 2p
	[a]RSF[74,134]	0.278	0.278	0.278	0.278	0.278	0.477	0.668	0.278	0.477	0.780	1.000	0.668
$[C_1(C_1)_2ThioIm][NTf_2]$	**Nominal**	**1**	**2**	**2**	**1**	-	**2**	**1**	**2**	**1**	**4**	**6**	**2**
	0°	1.1	2.3	2.0	1.1	-	2.0	0.9	2.3	1.0	3.6	5.8	1.9
	80°	1.0	2.1	1.8	1.0	-	1.9	0.8	2.1	0.9	3.7	7.0	1.7
$[C_4(C_1)_2ThioIm][NTf_2]$	**Nominal**	**1**	**2**	**2**	**1**	**3**	**2**	**1**	**2**	**1**	**4**	**6**	**2**
	0°	1.1	2.2	1.9	1.1	3.2	2.0	0.8	2.2	1.0	3.7	6.1	1.7
	80°	1.3	1.9	1.7	0.8	3.5	1.9	0.8	2.0	0.9	3.7	6.7	1.7
$[C_8(C_1)_2ThioIm][NTf_2]$	**Nominal**	**1**	**2**	**2**	**1**	**7**	**2**	**1**	**2**	**1**	**4**	**6**	**2**
	0°	1.1	2.2	2.0	1.1	7.8	2.0	0.9	2.2	1.0	3.5	5.4	1.9
	80°	1.1	2.1	1.6	1.1	8.6	1.8	0.8	2.1	0.9	3.4	5.8	1.8

[a] Relative sensitivity factors (RSF) taken from the Kratos Library. Stoichiometries determined without consideration of H content.

Table 5.11. Measured experimental full width at half maximum for the imidazolium ionic liquids studied in this work. The associated experimental error is ± 0.1 eV.

Compound		FWHM / eV										
		Cation					Anion					
Cation	Anion	$C_{aliphatic}$ 1s	$C_{4,5}$ 1s	$C_{6,7}$ 1s	C_{c_2} 1s	N_{cation} 1s	C_{CF_3} 1s	N_{anion} 1s	O 1s	F 1s	S_{anion} $2p_{3/2}$	S_{anion} 1s
Al K_α Source												
$[C_2C_1Im]^+$	$[NTf_2]^-$	1.1	0.9	1.1	1.1	1.1	1.0	1.1	1.2	1.6	0.9	-
$[C_3C_1Im]^+$	$[NTf_2]^-$	1.1	0.9	1.1	1.1	1.1	1.0	1.0	1.2	1.6	0.9	-
$[C_4C_1Im]^+$	$[NTf_2]^-$	1.1	0.9	1.0	1.0	1.0	1.0	1.0	1.2	1.6	0.9	-
$[C_6C_1Im]^+$	$[NTf_2]^-$	1.1	0.9	1.0	0.9	1.1	1.0	1.0	1.2	1.6	0.9	-
$[C_8C_1Im]^+$	$[NTf_2]^-$	1.1	0.9	0.9	0.9	1.0	1.0	1.0	1.2	1.6	0.9	-
$[C_{10}C_1Im]^+$	$[NTf_2]^-$	1.1	0.9	1.0	0.9	1.0	1.0	1.0	1.2	1.6	0.9	-
$[C_{12}C_1Im]^+$	$[NTf_2]^-$	1.1	1.0	1.1	0.9	1.0	1.0	1.0	1.2	1.6	0.9	-
Ag L_α' Source												
$[C_2C_1Im]^+$	$[NTf_2]^-$	1.2	1.0	1.2	1.3	1.2	1.2	1.2	1.3	1.7	1.1	1.4
$[C_3C_1Im]^+$	$[NTf_2]^-$	1.3	1.0	1.1	1.1	1.2	1.2	1.2	1.3	1.7	1.1	1.4
$[C_4C_1Im]^+$	$[NTf_2]^-$	1.2	1.0	1.1	1.1	1.2	1.2	1.2	1.3	1.7	1.1	1.4
$[C_6C_1Im]^+$	$[NTf_2]^-$	1.3	0.9	1.1	1.2	1.2	1.2	1.2	1.3	1.7	1.1	1.4
$[C_8C_1Im]^+$	$[NTf_2]^-$	1.3	0.9	1.1	1.0	1.2	1.2	1.2	1.3	1.7	1.1	1.4
$[C_{10}C_1Im]^+$	$[NTf_2]^-$	1.3	0.9	1.0	1.1	1.2	1.2	1.2	1.3	1.7	1.1	1.4
$[C_{12}C_1Im]^+$	$[NTf_2]^-$	1.3	0.9	1.0	1.1	1.2	1.2	1.2	1.3	1.7	1.1	1.4

Table 5.12. Measured experimental full width at half maximum for the guanidinium ionic liquid studied in this work. The associated experimental error is ± 0.1 eV.

Compound		FWHM / eV										
		Cation					Anion					
Cation	Anion	C_{core} 1s	C_{hetero} 1s	C_{inter} 1s	$C_{aliphatic}$ 1s	N_{cation} 1s	C_{CF_3} 1s	N_{anion} 1s	O 1s	F 1s	S_{anion} $2p_{3/2}$	S_{anion} 1s
Al K_α Source												
$[(C_8C_1)_2dmg]^+$	$[NTf_2]$	0.9	1.1	1.1	1.0	1.1	1.0	1.0	1.2	1.6	0.9	-
Ag L_α' Source												
$[(C_8C_1)_2dmg]^+$	$[NTf_2]$	1.0	1.2	1.3	1.1	1.2	1.2	1.2	1.3	1.7	1.1	1.4

Table 5.13. Measured experimental full width at half maximum for the thioimidazolium ionic liquids studied in this work. The associated experimental error is ± 0.1 eV.

Compound		FWHM / eV													
		Cation								Anion					
Cation	Anion	C_2 1s	$C_{6,7}$ 1s	$C_{4,5}$ 1s	C_S 1s	$C_{aliphatic}$ 1s	N_{cation} 1s	$S_{exocyclic}$ $2p_{3/2}$	$S_{exocyclic}$ 1s	C_{CF_3} 1s	N_{anion} 1s	O 1s	F 1s	S_{anion} $2p_{3/2}$	S_{anion} 1s
Al K_α Source															
$[C_1(C_1)_2ThioIm]^+$	$[NTf_2]^-$	0.9	1.2	0.9	1.0	-	1.0	0.9	-	1.0	1.0	1.2	1.6	0.9	-
$[C_4(C_1)_2ThioIm]^+$	$[NTf_2]^-$	0.9	1.1	0.9	0.9	1.1	1.0	0.9	-	1.0	1.0	1.2	1.6	0.9	-
$[C_8(C_1)_2ThioIm]^+$	$[NTf_2]^-$	0.9	1.1	0.9	0.9	1.1	1.0	0.9	-	1.0	1.0	1.2	1.6	0.9	-
Ag L_α' Source															
$[C_1(C_1)_2ThioIm]^+$	$[NTf_2]^-$	1.1	1.3	1.0	1.2	-	1.2	1.1	1.5	1.2	1.2	1.3	1.7	1.1	1.4
$[C_4(C_1)_2ThioIm]^+$	$[NTf_2]^-$	1.1	1.3	1.0	1.0	1.2	1.2	1.1	1.5	1.2	1.2	1.3	1.7	1.1	1.4
$[C_8(C_1)_2ThioIm]^+$	$[NTf_2]^-$	1.2	1.3	0.9	0.9	1.3	1.2	1.1	1.4	1.2	1.2	1.3	1.7	1.1	1.4